ZIRCON TYPOLOGY AND CHEMISTRY OF THE GRANITOIDS FROM CENTRAL ANATOLIA, TURKEY

A THESIS SUBMITTED TO
THE GRADUATE SCHOOL OF NATURAL AND APPLIED SCIENCES
OF
MIDDLE EAST TECHNICAL UNIVERSITY

BY

SERHAT KÖKSAL

IN PARTIAL FULFILLMENT OF THE REQUIREMENTS
FOR
THE DEGREE OF DOCTOR OF PHILOSOPHY
IN
GEOLOGICAL ENGINEERING

JANUARY 2005

Approval of the Graduate School of Natural and Applied Sciences

Prof. Dr. Canan ÖZGEN
Director

I certify that this thesis satisfies all the requirements as a thesis for the degree of Doctor of Philosophy.

Prof. Dr. Asuman G. TÜRKMENOĞLU
Head of Department

This is to certify that we have read this thesis and that in our opinion it is fully adequate, in scope and quality, as a thesis for the degree of Doctor of Philosophy.

Prof. Dr. M. Cemal GÖNCÜOĞLU
Supervisor

Examining Committee Members

Prof. Dr. Asuman G. TÜRKMENOĞLU (METU, GEOE) ____________________

Prof. Dr. M. Cemal GÖNCÜOĞLU (METU, GEOE) ____________________

Prof. Dr. Durmuş BOZTUĞ (Cumhuriyet Univ., GEOE) ____________________

Assoc. Prof. Dr. Taylan LÜNEL (METU, GEOE) ____________________

Assoc. Prof. Dr. Sönmez SAYILI (Ankara Univ., GEOE) ____________________

I hereby declare that all information in this document has been obtained and presented in accordance with academic rules and ethical conduct. I also declare that, as required by these rules and conduct, I have fully cited and referenced all material and results that are not original to this work.

Name, Last name	: Serhat KÖKSAL
Signature	:

ABSTRACT

ZIRCON TYPOLOGY AND CHEMISTRY OF THE GRANITOIDS FROM CENTRAL ANATOLIA, TURKEY

KÖKSAL, Serhat
Ph.D., Department of Geological Engineering
Supervisor: Prof. Dr. M. Cemal Göncüoğlu

January 2005, 314 pages

This thesis investigates the morphological, chemical and growth characteristics of zircon mineral in relation with the granitoid petrology. Physical and chemical variations recorded within zircon crystals during evolution of the Central Anatolian Granitoids are discussed.

The thesis focuses on twelve granitoid samples from the Ekecikdağ, Ağaçören and Terlemez regions from western part of central Anatolia. These granitoids are differentiated into S- and H-type granitoids on the basis of field, petrographical and whole-rock geochemical aspects.

In granitoids concerned, zircon is associated with biotite, allanite and plagioclase, and zircon populations mainly comprise P- and S-type zircon crystals, with rare G-, L- and J-types.

Typology method combined with cathodoluminescence imaging revealed that S- and H-type granitoids show intrusive aluminous autochthonous and hybrid character, respectively. Zircons generally have euhedral to subhedral cores exhibiting zoning, although sometimes faint, but inherent and embayed cores also exist. Large scale, first order, and/or small-scale second order oscillatory zoning and effects of late stage recrystallization are observed within zircon crystals.

Multi-corrosion zones within zircons are characterized by sharp changes in crystal forms with decreased Zr and Si, and increased U, Th and REE+Y contents, beside infrequent increase in Hf, Sc, Ta, Ti, Ca, Al and Fe elements. These zones are interpreted to be formed by transient heating of the resident felsic magma due to mafic melt contribution, at the time of mixing/mingling processes of the H-type granitoids, and then zircons re-grow in magma source reflecting a mafic character.

Corrosion stages within zircons of S-type granitoids, on the other hand, were probably formed by mantle-derived melts producing heat for resorption of zircons without direct contribution.

Keywords: Zircon, Granitoid, Typology, Chemistry, Central Anatolia

ÖZ

ORTA ANADOLU’DAKİ (TÜRKİYE) GRANİTOYİDLERİN ZİRKON TİPOLOJİSİ VE KİMYASI

KÖKSAL, Serhat
Doktora, Jeoloji Mühendisliği Bölümü
Tez Yöneticisi: Prof. Dr. M. Cemal Göncüoğlu

Ocak 2005, 314 sayfa

Bu tez, zirkon mineralinin morfolojik, kimyasal ve oluşum özelliklerini granitoyid petrolojisiyle ilişkilendirilerek araştırmaktadır. Orta Anadolu Granitoyidlerinin oluşumu sırasında, zirkon kristallerinde kaydedilen fiziksel ve kimyasal değişimler tartışılmaktadır.

Bu tez Orta Anadolu’nun batı kesiminde yeralan Ekecikdağ, Ağaçören ve Terlemez bölgelerinden seçilen oniki granitoyid örneği üzerinde odaklanmıştır. Bu granitoyidler, arazi, petrografik ve tüm-kayaç jeokimyasal özelliklerine dayanarak S- ve H-tipi granitoyidler olarak ayırtlanmıştır.

Sözkonusu granitoyidlerde, zirkon, biyotit, allanit ve plajiyoklas ile birlikte bulunurken, zirkon populasyonları temel olarak P- ve S-tipi zirkon kristalleri ile nadiren G-, L- ve J-tiplerini kapsamaktadır.

Tipoloji metodu, katodoluminesans görüntülemesi ile birlikte değerlendirildiğinde, S-tipi granitoyidlerin otokton alüminus sokulum, H-tipi granitoyidlerin ise hibrid özellik gösterdiğini ortaya koymuştur.

Zirkonlar, genellikle özşekilliden yarı-özşekilliye değişen, bazen zayıf olmakla birlikte zonlanma gösteren çekirdekler içerir, fakat kalıt ve yenmiş çekirdekler de vardır. Zirkon kristallerinde, büyük çapta, birincil ve/veya küçük çapta ikincil salınan zonlanma ve son evre tekrar-kristallenme etkileri gözlenmektedir.

Zirkon kristallerindeki çoklu-korozyon zonları, kristal formlarındaki keskin değişimlerle, azalan Zr, Si ve yükselen U, Th, NTE+Y içerikleri ve nadiren Hf, Sc, Ta, Ti, Ca, Al ile Fe elementlerindeki yükselimle nitelendirilmektedir. Bu zonların; H-tipi granitoyidlerin karışım süreçleri sırasında, yerleşik felsik magmanın mafik ergiyik katılımı sonucu geçici ısıtılmasıyla oluştuğu yorumu getirilmiştir. Zirkonlar, mafik özellik gösteren bu magma kaynağında oluşumlarına devam etmiştir.

Diğer taraftan; S-tipi granitoyid zirkonlarındaki korozyon aşamaları ise, olasılıkla zirkonların emilmelerine yolaçan ısıyı üreten mantodan-türemiş ergiyiklerle, direkt katılım olmaksızın oluşmuştur.

Anahtar Kelimeler: Zirkon, Granitoyid, Tipoloji, Kimya, Orta Anadolu

To My Wife Fatma

ACKNOWLEDGMENTS

I would like to thank to my supervisor Prof. Dr. M. Cemal Göncüoğlu for providing the incentive to choose this interesting subject. I am also greatly indebted to him for his supervision and encouragement throughout the research and for valuable criticisms and warm guidance.

I would like to express my sincere gratitude to Dr. Andreas Möller from the Geology Department of Potsdam University, Germany for valuable discussions about zircon sample preparation, evaluation and interpretation of petrographic thin sections, SEM and CL images.

I am grateful to the Geological Research Center (Geoforschungs-zentrum Potsdam-GFZ) for the free of charge laboratory facilities comprising of scanning electron microscope (SEM), cathodoluminescence (CL) and electron microprobe (EMP) analyses during my ten months stay in Potsdam, Germany.

I would like to thank to Dr. Helga Kemnitz for providing SEM and CL analyses and to Dr. Dieter Rhede for EMP analyses at GFZ.

I am grateful to Prof. Dr. Roland Oberhänsli from Potsdam University due to his friendly logistic support for laboratory work including mineral enrichment and office facilities at the Geology Department of Potsdam University. I would like to thank to Prof. Dr. Rolf L. Romer from GFZ for his valuable comments and criticisms. I also thank to Assist. Prof. Gültekin Topuz from İstanbul Technical University for his valuable comments.

I acknowledge the Scientific and Technical Research Council of Turkey (TÜBİTAK; project code YDABÇAG-101Y051) for supporting the geochemical analyses. The financial support for laboratory materials for sample enrichment was provided by Middle East Technical University (METU) Research Fund Project (AFP) code: AFP-99.03.09.01. I also thank to Mining Engineering Department of

Middle East Technical University for providing part of the mineral enrichment process.

I wish to express my thanks to technical staff from the Geology Department of Potsdam University and the Geological Research Center (Geoforschungszentrum-GFZ) in Potsdam/Germany, especially Mrs. Oona Appelt for conducting EMP analyses, Mrs. Chstian Fischer for preparing polished and petrographic thin sections, Mrs. Arnold for preparing CL slides and Mrs. Ursula Glenz for spectacular work on SEM and CL.

I am grateful to Prof. Dr. Çiğdem Erçelebi from Central Laboratory, METU for her understanding and encouragements during my study period.

I appreciatively thank to Mr. Özgür Demirci from General Directorate of Mineral Research and Exploration for supporting fieldwork with his car and help in sample collection. Mr. Orhan Karaman at the Department of Geological Engineering, METU is acknowledged for his support in preparation of polished and petrographic thin sections.

I extend my gratitude to my parents for their patience and encouragement throughout my study.

My wife, Dr. Fatma Toksoy-Köksal from the Geological Engineering Department, METU, helped to improve the focus of the thesis by her valuable comments. Additionally, she helped the fieldwork, mineral enrichment and petrographical studies. Moreover, she drew and revised most of the figures in this thesis, including sketch SEM and CL figures and thin-section photographs. She also prepared some supplementary sections such as Table of Contents and List of Figures. My sincere thanks are to her not only for these valuable contributions to preparation of this thesis, but also for her endless patience and encouragement throughout my study.

TABLE OF CONTENTS

CHAPTER

APPENDICES

LIST OF TABLES

TABLE

LIST OF FIGURES

FIGURE

CHAPTER 1

INTRODUCTION

1.1. Purpose and Scope

Evaluating the petrology of granitic rocks crucially bases on understanding the mineral growth histories and mechanisms besides geological and whole-rock geochemical characteristics. This is a driven factor for geologists intending to resolve physical and chemical aspects of minerals by in-depth investigations.

Progress in the analytical methods, e.g. scanning electron microscopy, electron microprobe and ion-probe techniques made in-situ analysis of the minerals possible. In this manner, studies on individual minerals in terms of crystallography and chemistry provide important clues about the evolution of the granitoids.

Among the minerals, zircon is remarkable, because of its ubiquity in the earth's crust. Its low solubility in almost all melts and fluid compositions and chemical and physical durability during transport enables zircon to survive almost any crustal processes (Hanchar and Miller, 1993). Zircon, being a subject of numerous studies, is a key mineral recording footprints of magmatic evolution. Moreover, it is particularly an important mineral because of its tendency to incorporate trace elements (including radionuclides) and considerable resistance to high-temperature diffusive re-equilibration (Cherniak et al., 1997; Belousova et al., 2002).

Although zircon abundance is commonly low as a trace amount, it may strongly affect the behavior of many trace elements during the crystallization of magma, and understanding its compositional variation is hence important for petrological modeling (Watson, 1979; Schaltegger et al., 1999; Hoskin et al., 2000; Möller et al., 2001; Belousova et al., 2002). In addition, Wark and Miller (1993) showed that the chemistry of accessory minerals, especially zircon not only controls much of the trace element chemistry of the granitoids, but in general way also records compositional changes in melt during differentiation. All these interpretations put forward that detailed studies on a zircon mineral can provide reliable information for petrogenetic inferences.

Present research aims to provide contribution to the studies on zircons and their link with the granitoid petrology, and the Central Anatolian Granitoids (CAG) were chosen as a case study in this manner.

A variety of approaches (geological, geochemical, isotopical and geochronometric) have been used to interpret the source, petrogenesis and evolution histories of granitoids of central Anatolia (e.g. Erler et al., 1991; Akıman et al., 1993; Göncüoğlu and Türeli, 1993, 1994; Erler and Bayhan, 1995; Erler and Göncüoğlu, 1996; Göncüoğlu et al., 1997; Güleç and Kadıoğlu, 1998; Aydın et al., 1998; Boztuğ, 1998, 2000; Düzgören-Aydın et al., 2001; Kadıoğlu et al., 2003; İlbeyli et al., 2004; Köksal et al., 2004a). In spite of numerous studies, gaps remain in our understanding of the petrological characteristics of the CAG. Studies concerning geology and whole-rock and isotope geochemistry supplied detailed data; however, it is needed to provide new approaches to the petrology of them to overcome current shortcomings. In this way, this is the first effort discussing zircon mineral for petrological implications of the granitoids in central Anatolia.

Zircon typology introduced by Pupin (1980) is one of the methods taken into consideration in this research. Moreover, internal structures of zircon minerals were investigated by cathodoluminescence imaging, considering that not only the crystal outlines but also the inner structures would provide more detailed and exact data. Furthermore, zircon crystals were analyzed by electron microprobe to investigate their chemical characteristics to enlighten the evolution histories. Supplementary information was provided by additional geological, petrographical and whole-rock geochemical studies on the concerned granitoids.

It is expected that these different approaches would contribute to the existing knowledge on the zircons, considering their external and internal structures and growth histories, and provide new insights into the petrology of the granitoids in central Anatolia. Additionally, present study intends to form basis for future dating studies on zircons from granitoids in central Anatolia, which would be essential in geodynamic modeling.

1.2. Methods of the Study

The morphological and intracrystalline characteristics of zircons from the granitoids of central Anatolia were planned to investigate, considering zircon as an important key mineral to evaluate the petrology of the granitoids.

The first part of the study covered the sampling of the granitoids from the selected localities of the central Anatolia. Granitoid outcrops were sampled from each of the selected 13 different locations in a range of 4-20 kg. Totally 141.193 kg rock samples were collected for petrographical and typological studies. The sample localities are shown in Figure 1.1.

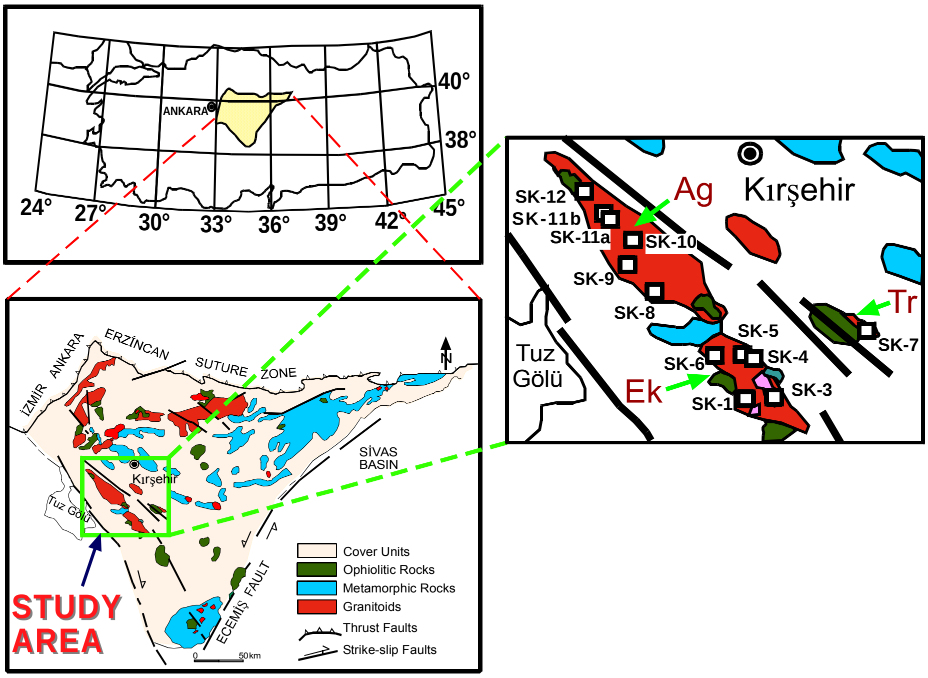

Figure 1.1. Location map of the study area and sample locations (Ek: Ekecikdağ pluton, Ag: Ağaçören pluton; Tr: Terlemez granitoid; SK-1: sample location)

The present study focused on the granitoids located in the western part of central Anatolia. Granitoids, which are concerned in this research, are from Ekecikdağ, Ağaçören and Terlemez plutons.

The sampled granitoids were chosen from the type localities that were reported in the previous studies. Granitoid samples are collected from Borucu, Kalebalta, Hisarkaya, Sinandı (Ekecikdağ area), Çatalçeşme, Yenişabanlı, Torunobası, Camili, Çimkalesi (Ağaçören area) and Terlemez around Aksaray. These are all well-defined granitoid bodies that are either major or minor phases in the CAG as proposed by previous authors (Göncüoğlu et al., 1991; Türeli, 1991; Kadıoğlu, 1996; Göncüoğlu and Türeli, 1993, 1994; Yalınız, 1996; Yalınız et al., 1999; Düzgören-Aydın et al., 2001).

Ekecikdağ pluton exposed in the southern end of the NW-SE trending granitoid belt is located in the western part of central Anatolia. The subunits of the Ekecikdağ pluton differentiated by Türeli (1991), namely Borucu Granodiorite-Monzogranite (SK-1), Kalebalta Leucogranite (SK-3), Hisarkaya Porphyritic Granite (SK-4 and 5) and Sinandı Microgranite (SK-6) are sampled from the Ekecikdağ area.

Ağaçören suite is situated on the NW of the Ekecikdağ suite and was studied by Kadıoğlu (1996) around Ağaçören area. In the scope of this research, granitoid samples were collected from Namlıkışla biotite-granite (SK-8), Yenişabanlı biotite-amphibole granite (SK-9), Sipahiler amphibole-biotite granite (SK-10), Torunobası granite porphyry (SK-11a), Camili alkali feldspar granite (SK-11b) and Çimkalesi monzonite (SK-12) which were defined in detail by Kadıoğlu (1996) in the Ağaçören area.

Terlemez quartz monzonite (SK-7) is exposed to the east of the Ekecikdağ suite. Yalınız (1996) and Yalınız et al. (1999) presented the geological and geochemical characteristics of the Terlemez pluton.

The petrographical study was performed to detect the main petrographical characteristics of the samples and contents and the mean diameters of zircon minerals to form the basis of the enrichment procedures.

Afterwards, rock samples were enriched for heavy minerals through routine enrichment procedures. Then, zircon fractions were purified and examined under binocular microscope to determine their typological features. Scanning Electron Microscope (SEM) studies were carried out on the selected crystals for detailed morphological descriptions. After SEM studies, same samples were re-prepared and cathodoluminescence (CL) studies were achieved. Furthermore chemical investigation was performed on the selected zircon grains.

Details of sample preparation and analytical techniques, beside discussion on previous studies related to these applications are presented in the following chapters.

CHAPTER 2

REGIONAL GEOLOGICAL SETTING, AGE AND PETROLOGICAL BACKGROUND OF THE CENTRAL ANATOLIAN GRANITOIDS

Anatolia is a geologically remarkable region where it is possible to discuss the history of the configuration of continents throughout the opening and closure episodes of Tethys Ocean. The present geology of Anatolia was mainly drawn by the Alpine Orogeny represented by the closure of various branches of Neotethys Ocean, i.e. Mesozoic ocean, in this realm.

The oldest lithologies of the Central Anatolian Crystalline Complex (CACC) are Precambrian-Palaeozoic-Mesozoic metamorphic rocks, consisting of gneisses, schists, calc-schists, phyllites, and marbles (Figure 2.1). These HT/LP metamorphic rocks, forming similar successions with the Tauride Platform, were intruded by S-type granitoids (Göncüoğlu et al., 1991). Both the metamorphic and S-type granitic rocks were thrusted by supra-subduction-zone type ophiolitic rocks (Figure 2.2). H-type granitoids intruded the ophiolitic rocks and the S-type granitoids besides the metamorphic basement (Göncüoğlu et al., 1993). The syenitoids intruding not only the older units but also the granitoids and their extrusive equivalents, which are found as blocks and boulders within the non-metamorphic Upper Maastrichtian-Lower Palaeocene cover units, marked the subsequent extensional magmatic episode in the complex. Palaeocene-Eocene volcanic, volcanoclastic, and carbonate rocks, Oligocene-Miocene evaporites and continental clastic rocks, and Upper Miocene-Pliocene continental clastic, volcanoclastic, and volcanic rocks represent the cover units within CACC (Göncüoğlu et al., 1991).

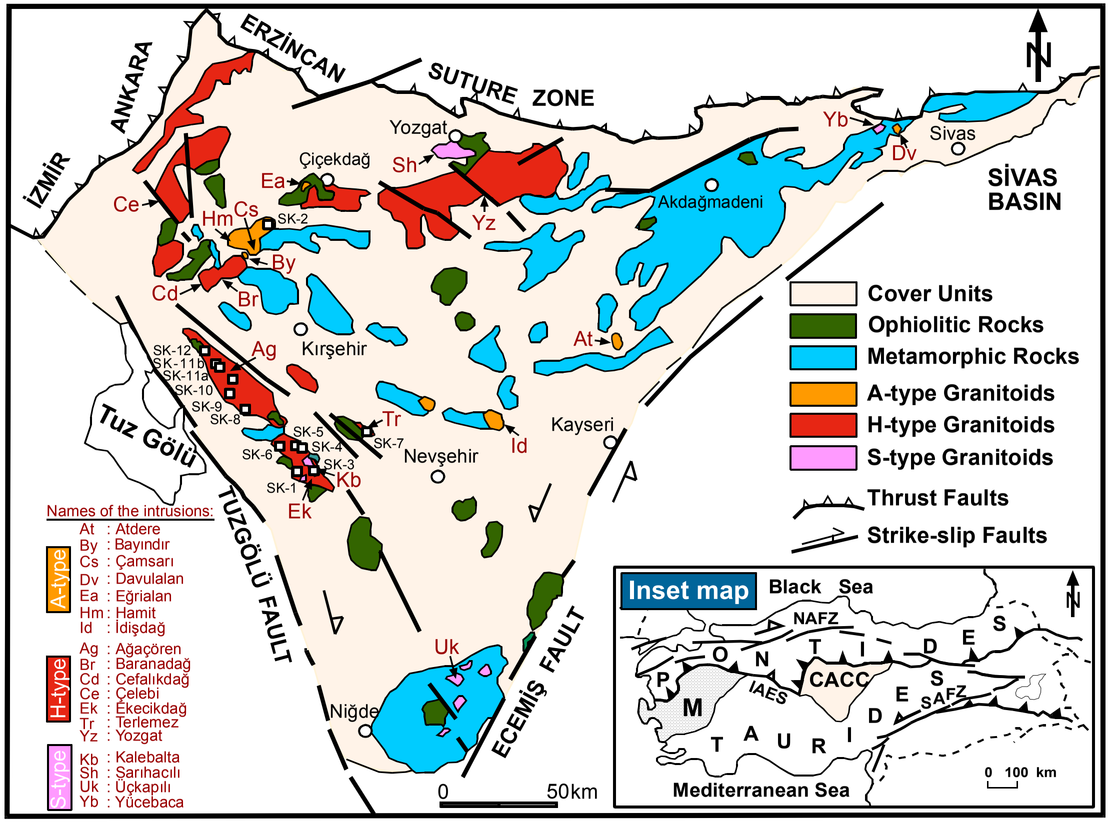

Figure 2.1. Simplified geological map of the CACC (Modified after Göncüoğlu et al., 1991; Toksoy-Köksal et al., 2001; Düzgören-Aydın et al., 2001; Boztuğ, 2000) including the sample locations. Inset map shows the locations of main tectonic units in Turkey (modified after Toksoy-Köksal et al., 2001). M: Menderes Massif, IAES: İzmir-Ankara-Erzincan Suture Zone, NAFZ: North Anatolian Fault Zone, SAFZ: South Anatolian Fault Zone.

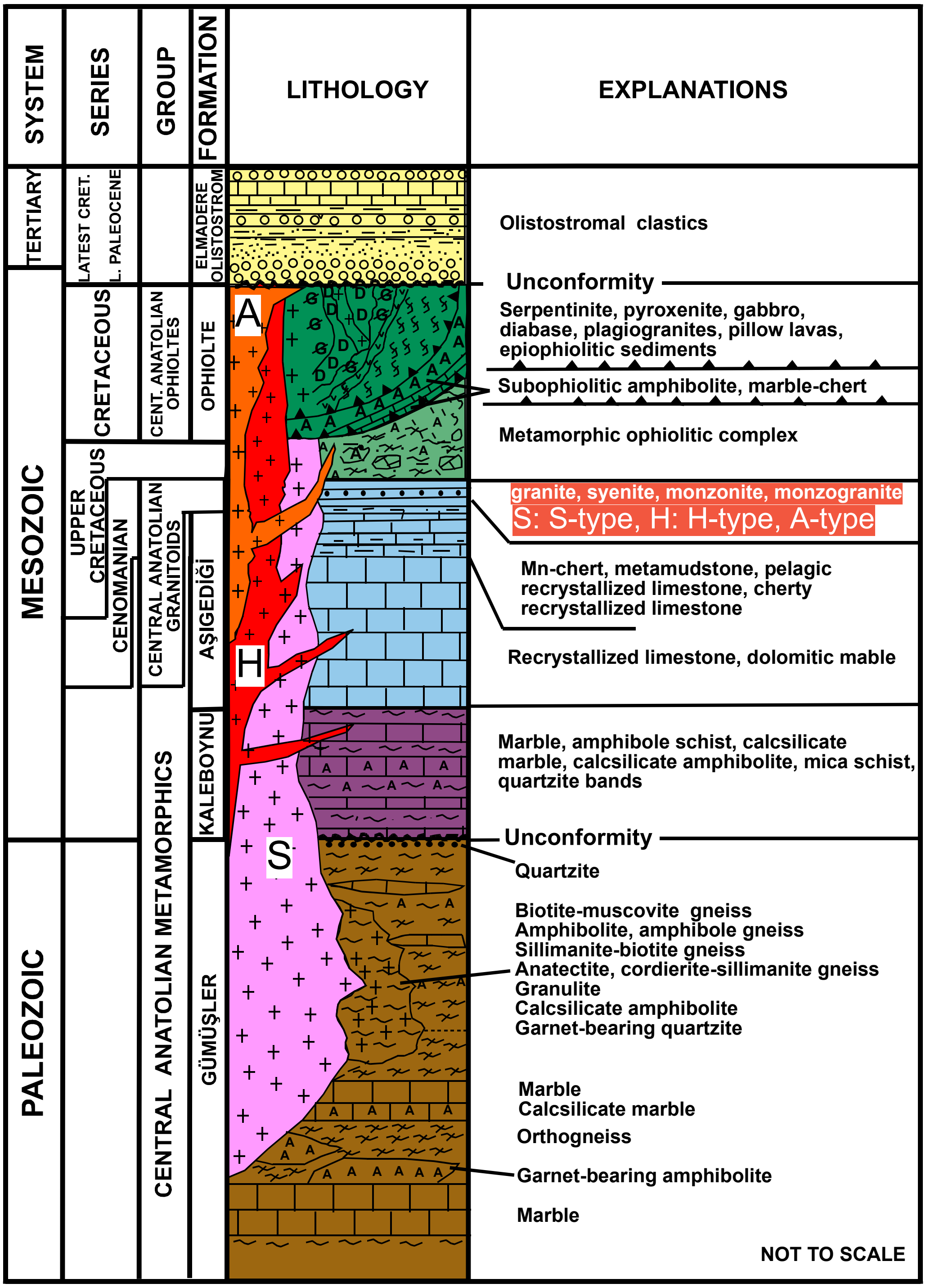

Figure 2.2. Generalized columnar section of the CACC (Modified after Göncüoğlu et al., 1991; Toksoy-Köksal et al., 2001; Düzgören-Aydın et al., 2001; Boztuğ, 2000).

The CAG comprise the S-, H- and A-type granitoids in this area. The formation of the CAG is attributed by Görür et al. (1984) to the closure of the “Inner Tauride Ocean” separating the Tauride block from Anatolides, along which the Menderes-Taurus block collided with the Sakarya Continent and the Kırşehir block (i.e. the CACC) during Late Paleocene-Early Eocene. The subduction of the oceanic lithosphere of the “Inner Tauride Ocean” beneath the Kırşehir Block is considered by these authors as the main mechanism for the formation of granitoids in central Anatolia.

However, Göncüoğlu et al. (1993) opposed this opinion and indicated that the CACC represented (together with the Menderes Massif in the west) the metamorphosed and telescoped northern passive margin of the Tauride-Anatolide Platform facing the İzmir-Ankara-Erzincan (IAE) branch of the northern Neotethys Ocean. The closure of IAE branch led to the evolution of voluminous granitoids within the CACC during the collision, post-collision and subsequent extension periods.

These contrasting models eventually suggest that the fingerprints of distinct events are inherent in the geological and petrological nature of these granitoids. That is why the petrology of the CAG is accepted as one of the major concepts for understanding the Alpine geological history of Anatolia.

2.1. General Petrological Characteristics of the Central Anatolian Granitoids

In central Anatolia, Alpine collision-related magmatism started with the formation of S-type granitoids, generally represented by garnet-bearing leucogranites (e.g. Üçkapılı granitoid: Göncüoğlu, 1986; Yozgat granitoid: Erler and Göncüoğlu, 1996; Sarıhacılı granitoid: Ekici and Boztuğ, 1997). Calc-alkaline H-type to A-type granitoids were generated during the post-collisional stage (Göncüoğlu et al., 1991, 1992, 1993, 1997; Göncüoğlu and Türeli, 1993, 1994; Erler and Göncüoğlu, 1996; İlbeyli and Pearce, 1997; Boztuğ, 1998, 2000; Aydın et al., 1998; Köksal et al., 2001; Düzgören-Aydın et al., 2001).

Geological and petrographical studies on the S-, H- and A-type CAG reveal different types of granitoids can be recognized by their distinct features.

S-type granitoids are typically white leucogranites with a fine to medium grained texture or alternatively medium grained granodiorites. S-type granitoids containing K-feldspar, quartz, plagioclase, two-mica (biotite+muscovite) with accessory amounts of garnet, zircon, apatite and opaque minerals, do not include any mafic enclaves (e.g. Göncüoğlu, 1986; Göncüoğlu and Türeli, 1994).

H-type granitoids can be characterized by their medium to coarse-grained porphyritic texture with pinkish K-feldspar megacrysts and mafic microgranular enclaves. They are in granitic, monzogranitic, quartz-monzonitic, and/or granodioritic compositions with K-feldspar, plagioclase (oligoclase), quartz ± hornblende ± biotite ± clinopyroxene ± chlorite, and with accessory minerals such as zircon, titanite, allanite, and opaque minerals (e.g. Aydın et al., 1998; Düzgören-Aydın et al., 2001; Yalınız et al., 1999).

A-type granitoids are typically pink medium-fine grained syenitoids. They can be discriminated in two groups as (i) silica saturated group including quartz-syenites (containing K-feldspar, quartz, plagioclase (low-An) ± hornblende ± biotite ± clinopyroxene with accessory amounts of fluorite, titanite, zircon, apatite, and opaque minerals) and (ii) silica undersaturated group including feldspathoid-bearing syenites (containing K-feldspar, nepheline, sodalite, cancrinite, melanite, with accessory amount of biotite, aegerine-augite, fluorite, zircon, titanite) (e.g. Otlu and Boztuğ, 1998; Boztuğ, 1998, 2000).

Geochemical studies also make it possible to discriminate and define different types of the granitoids in the Central Anatolia. In a plot of Na_2O+K_2O vs. SiO_2 (Figure 2.3), the data from the H- and S-type granitoids are plotted in the sub-alkaline field, while those of A-type ones are plotted in the alkaline field.

Data of H-type granitoids plotted on AFM ternary diagram (Figure 2.4) indicate that the hybrid granitoids have calc-alkaline features.

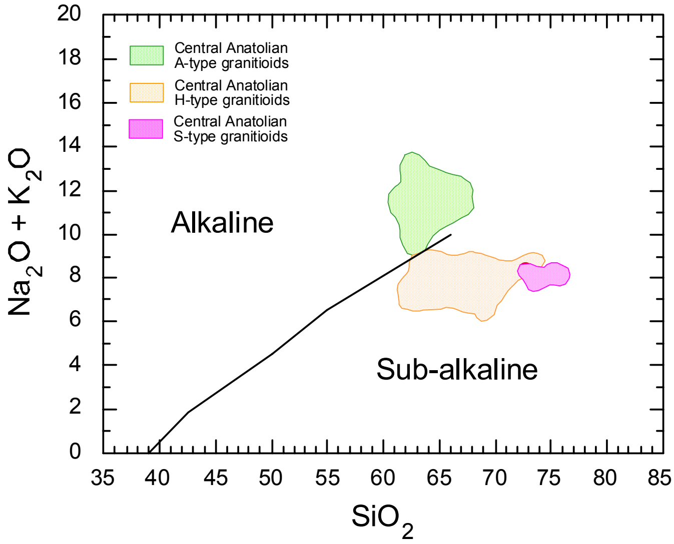

Figure 2.3. Total alkali vs. silica diagram (after Irvine and Baragar, 1971) of central Anatolian S-, H- and A-type granitoids (see Appendix A for data source).

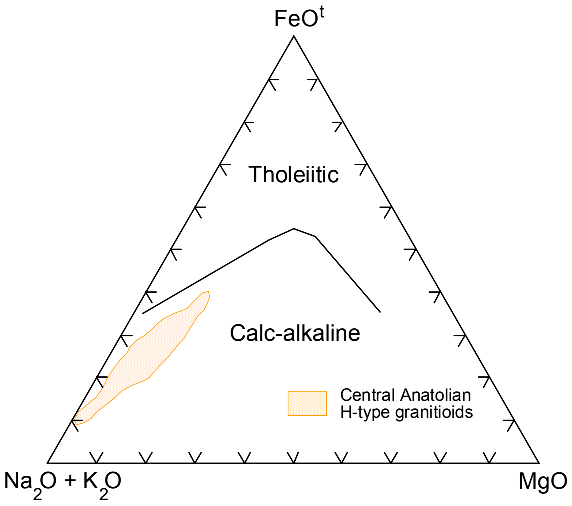

Figure 2.4. AFM ternary diagram (after Irvine and Baragar, 1971) of central Anatolian H-type granitoids (see Appendix A for data source).

Different behavior of the data from the different types of granitoids can also be recognized by immobile element diagrams such as Zr vs. TiO_2 (Figure 2.5). A-type granitoid commonly have higher Zr content than those of typical H- and S-type granitoids, which is also the case for the CAG. Some of the other diagrams including immobile trace elements also reflect distinct trends and distribution patterns (not shown).

In the trace element discrimination diagram (Figure 2.6) of Pearce et al. (1984), while the samples from the A-type CAG plot clearly on the WPG field, the H-type CAG plot close to the triple junction of within-plate-granite (WPG), syn-collision granite (Syn-COLG), and volcanic arc granite (VAG) fields that is typical for post-collision granites (Pearce et al., 1984; Pearce, 1996). On the other hand, S-type granitoids are mainly localized within the syn-COLG field. Distribution of the samples in the Rb vs. Y+Nb diagram, and the correlation with the typical examples from the similar tectonic settings suggest that the H-type CAG have post-collisional, S-type ones have syn-collisional, and A-type ones have within-plate natures.

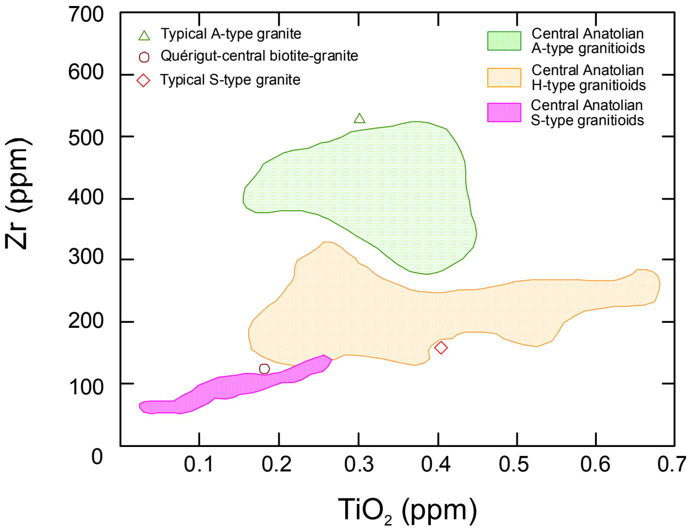

Figure 2.5. The distribution of the central Anatolian S-, H- and A-type granitoids on the Zr vs. TiO_2 diagram in comparison with the typical S-, post-collision- and A-type granitoids (see Appendix A for data source).

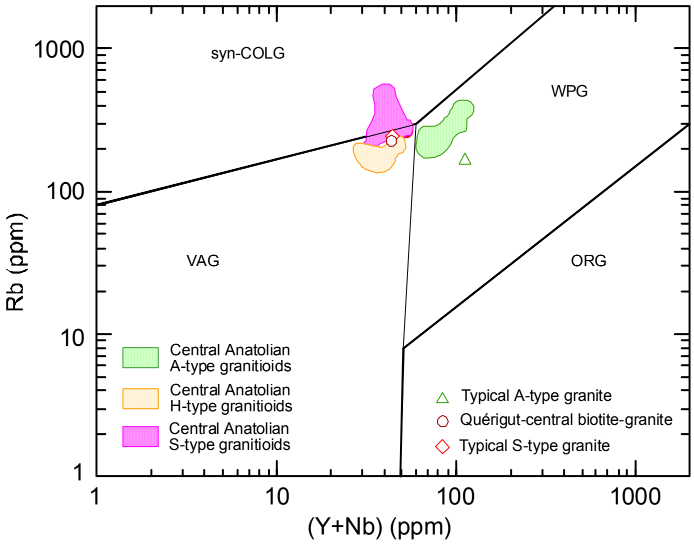

Figure 2.6. The distribution of the central Anatolian S-, H- and A-type granitoids on the Rb vs. (Y+Nb) tectono-magmatic discrimination diagram of Pearce et al. (1984) in comparison with the typical S-, post-collision- and A-type granitoids (see Appendix A for data source).

The multi-element variation patterns (Figure 2.7) normalized to the continental-crust of Taylor and McLennan (1985) reveal that the central Anatolian S-type granitoid group, display gull-wing-shaped patterns for Ba, Nb, Sr and Ti, and positive Th, La and Yb anomalies with enrichment in LILE (especially in Rb) with respect to HFSE suggesting a depleted and crustal source with inherent subduction-component. Central Anatolian H-type granitoid group, has similar trend with the S-type granitoids with a more pronounced subduction-component as recognized in Nb-depletion. Additionally, samples from the A-type CAG display similar patterns for Ba, Nb, Sr and Ti, but higher concentrations of Th, Nb, Zr and Y than the samples from H- and S-type granitoids. The patterns suggest enriched mantle source with variable, but significant crustal contamination for the A-type CAG. Also shown, for comparison, are data on the typical S-, post-collision and A-type granitoids from different orogens in Figure 2.7. Although there are some variances due to the enrichment levels it can be concluded that the typical S-, H- and A-type granitoids roughly show similar trends with S-, post-collision and the A-type CAG, respectively.

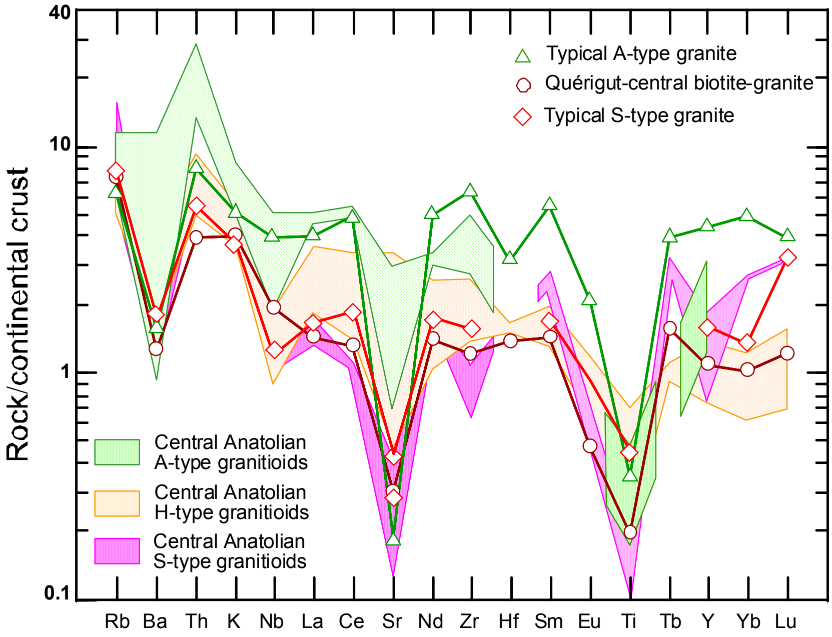

Figure 2.7. Continental-crust-normalized (after Taylor and McLennan, 1985) multi-element variation diagrams of the central Anatolian S-, H- and A-type granitoids in comparison with the typical S-, post-collision- and A-type granitoids (see Appendix A for data source).

Besides geochemical database there are also some available isotope data from the CAG (Table 2.1). These data indicate that the S-type Hisarkaya granitoid is likely to have more crust dominant source characteristics, while A-type Hamit granitoid (and also Baranadağ granitoid that characterizes mature stage of H-type plutonism, e.g. Düzgören-Aydın et al., 2001; İlbeyli et al., 2004) has mantle dominant source characteristics. The H-type CAG, on the other hand, can be characterized by subduction modified hybrid magma sources with large continental crustal components (e.g. Göncüoğlu and Türeli, 1994; İlbeyli et al., 2004).

Table 2.1. Available isotope data from the CAG.

Name of Intrusion	εNd	$^{87}Sr/^{86}Sr$	Granitoid Type	Authors
Ekecikdağ pluton (Hisarkaya)	-6.1	0.722029±37(2σ)	S-type	Türeli (1991)
Ekecikdağ pluton (Borucu)	(-6.1)- (-7.1)	0.715459-0.715723 (2σ)	H-type	Türeli (1991)
Ağaçören pluton (Yenişabanlı)		0.711245-0.712702 (2σ)	H-type	Güleç (1994)
Behrekdağ pluton	-6.3	0.71004± 11 (1σ)	H-type	İlbeyli et al. (2004)
Cefalıkdağ pluton	(-5.7)- (-6.7)	0.70972-0.71087 (1σ)	H-type	İlbeyli et al. (2004)
Çelebi pluton	-5.5	0.71028± 35 (1σ)	H-type	İlbeyli et al. (2004)
Baranadağ pluton	-5.2	0.70873± 11 (1σ)	H-type	İlbeyli et al. (2004)
Hamit pluton	(-4.8)- (-5.5)	0.70875-0.71275 (1σ)	A-type	İlbeyli et al. (2004)

2.2. Existing Age Constraints on the Central Anatolian Granitoids

Table 2.2 shows a summary of efforts to constrain the timing of magmatism in central Anatolia. The geochronological studies on the CAG and the geological data show that some uncertainties inherent in interpretation of the timing of magmatism.

The geochronological data on the syn-collision granitoids are available for the Üçkapılı and Behrekdağ plutons. Göncüoğlu (1986), using both Rb/Sr and K/Ar methods determined the crystallization age of the Üçkapılı granodiorite to be 95±11 Ma, with a cooling age of 77.8±1.2 Ma. On the other hand, Whitney and Dilek (1997) reported a 20-13.7 Ma U-Pb monazite age for the Üçkapılı granodiorite, considering the evolution of the pluton during the exhumation of the Niğde Massif in Late Oligocene-Early Miocene. However, Gautier et al. (2001) stated that the exhumation of the Niğde metamorphics was older than the Eocene. Furthermore, Fayon et al. (2001) indicated that the data of Göncüoğlu (1986) was consistent with regional geologic constraints for the timing of closure of the southern Neotethyan seaway, while younger age interpretation (Whitney and Dilek, 1997) might be related with the emplacement of a later phase. However, it is indicated by Göncüoğlu (1986) that the Upper Maastrichtian basal conglomerates, bearing pebbles of the

Üçkapılı granodiorite, disconformably covers this pluton and the metamorphic rocks. U/Pb SHRIMP studies have shown that zircon cores in Üçkapılı Granitoid record Proterozoic through Mesozoic ages, whereas rims consistently yield Late Cretaceous (92-85 Ma) ages that is in accordance with Ar/Ar mineral age data yielding 79.5±1.2 Ma (Whitney et al., 2003). Age data from the northwest of the CACC are only available for Behrekdağ composite pluton which yield K/Ar mineral ages of 69.1±1.4 to 71.5±1.5 Ma for S-type granitoids (Tatar et al., 2003).

First geochronological study on the H-type CAG resulted in an age of ca. 54 Ma by the total Pb method on a single zircon grain for the Baranadağ quartz monzonite (Ayan, 1963). İlbeyli et al. (2004) determined the age of the Baranadağ quartz-monzonite as 76.4±1.3 by K/Ar mineral (hornblende) method.

Ataman (1972) calculated a 71±1 Ma (73.5±1 Ma if recalculated by the decay constant recommended by Steiger and Jäger, 1977) isochron age for the Cefalıkdağ granitoid (Rb/Sr method). Erkan and Ataman (1981), obtained similar ages (69.0±1.7 to 74.2±2.7 Ma) using K/Ar mineral dating method to be an intrusion/cooling age for these intrusive rocks. On the other hand, İlbeyli et al. (2004) determined the age of the Cefalıkdağ granitoid as 66.6±1.1 Ma by K/Ar mineral method. K/Ar mineral ages of the H-type granitoids from the Behrekdağ area determined as 68.8±1.4 to 81.2±3.4 Ma by Tatar et al. (2003), and as 79.5±1.7 Ma by İlbeyli et al. (2004).

Güleç (1994) obtained an intrusion age of the Ağaçören granitoid (Yenişabanlı biotite-amphibole granite) as 110±14 Ma by Rb/Sr whole-rock method, whereas Ar/Ar muscovite data yield an age of 77.6±0.3 Ma (Kadıoğlu et al., 2003) for this granitoid. The K-Ar isotopic determinations for the Terlemez quartz-monzonite yielded ages range from 81.5±1.9 (interpreted as intrusion age) to 67.1±1.3 Ma (interpreted as cooling age) (Yalınız et al., 1999).

Available age data from the H-type CAG yield a broad age range of some 20 to 30 Ma. Similar wide age span is also present for the A-type CAG.

Alkaline intrusions from the Kaman region gave Rb/Sr WR ages of 70.7±1.1 Ma (Bayındır feldspathoidal syenites; Gündoğdu et al., 1988), 70.5±3.4 Ma (foyaites and volcanic rocks; Kuruç, 1990), 71.8±0.1 Ma (miaskites; Kuruç, 1990), 84.4±0.9 Ma (sodalite syenites; Kuruç, 1990), and 85.1±3.6 Ma (quartz syenites; Kuruç, 1990).

Depending on the U-Pb method, Köksal et al. (2004a) indicated that both the post-collisional H-type and A-type CAG were evolved in the Campanian. U-Pb titanite age of the Baranadağ quartz-monzonite representing the mature stage of H-type magmatism is 74.0±2.8 Ma, while that of the Çamsarı quartz-syenite representing A-type magmatism is 74.1±0.7 Ma (Köksal et al., 2004a). These ages documented a coeval H-type and A-type magmatism, in a post-collision setting postdating the Alpine thickening within the passive margin of the Tauride-Anatolide Platform in the central Anatolia (Köksal et al., 2004a).

Some paleontological and stratigraphical studies also accommodate for constraining the age of granitoids in central Anatolia. For instance, Terlemez quartz-monzonite is determined to have a clear intrusive contact with the Middle Turonian-Lower Santonian pelagic rocks that is associated with the pillow basalts of the allochthonous Sarıkaraman Ophiolite (Yalınız et al., 1999). Additionally, the basal conglomerates of the latest Maastrichtian sediments, disconformably covering the CACC, are dominated by well-rounded pebbles of granites, syenites and monzonites of the underlying CAG. In this way, the intrusion age of the H- and A-type granitoids is also geologically bracketed between Early Santonian and Latest Maastrichtian (e.g. Köksal et al., 2001).

2.3. Evolutionary Models for the Central Anatolian Granitoids

There are some different petrogenetic and geodynamic interpretations about the evolution of the CAG. Şengör and Yılmaz (1981) considered these granitoids as the consequence of the calc-alkaline magmatism related to the northward-subduction of the inner Tauride Ocean beneath the CACC during Lower Paleocene-Eocene. Görür et al. (1984, 1998) on the other hand, relate the granitoids with the Andean-type arc magmatism generated via the eastward subduction of the Inner Tauride Ocean during Paleocene-Early Eocene.

Table 2.2. Available geochronological data from the CAG.

Name of Intrusion	**Method**	**Age (Ma)**	**Granitoid Type**	**Authors**
Üçkapılı granitoid	Rb-Sr (whole rock)	95±11	S-type	Göncüoğlu (1986)
Üçkapılı granitoid	Rb-Sr (mineral)	77.8±1.2	S-type	Göncüoğlu (1986)
Üçkapılı granitoid	K-Ar (mineral)	78-75	S-type	Göncüoğlu (1986)
Üçkapılı granitoid	U-Pb (monazite)	20-13.7	S-type	Whitney and Dilek (1997)
Üçkapılı granitoid	U-Pb SHRIMP (zircon)	92-85	S-type	Whitney et al. (2003)
Üçkapılı granitoid	^{40}Ar-^{39}Ar plateau age (mineral)	79.5±1.2	S-type	Whitney et al. (2003)
Behrekdağ composite pluton	K-Ar (mineral)	71.5-69.1	S-type	Tatar et al. (2003)
Baranadağ quartz-monzonite	Total Pb method (zircon)	54	H-type	Ayan (1963)
Baranadağ monzonite	K-Ar (mineral)	76.4±1.3	H-type	İlbeyli et al. (2004)
Baranadağ quartz-monzonite	U-Pb (mineral)	74.0±2.8	H-type	Köksal et al. (2004a)
Cefalıkdağ granitoid	Rb-Sr (whole rock)	73.5±1.0[a]	H-type	Ataman (1972)
Cefalıkdağ quartz-monzonite	K-Ar (mineral)	66.6±1.1	H-type	İlbeyli et al. (2004)
Ağaçören granitoid	Rb-Sr (whole rock)	110±14	H-type	Güleç (1994)
Ağaçören granitoid	Ar-Ar (mineral)	77.6±0.3	H-type	Kadıoğlu et al. (2003)
Terlemez quartz-monzonite	K-Ar (mineral)	81-67	H-type	Yalınız et al. (1997)
Behrekdağ composite pluton	K-Ar (mineral)	81.2-68.8	H-type	Tatar et al. (2003)
Behrekdağ granite	K-Ar (mineral)	79.5±1.7	H-type	İlbeyli et al. (2004)
Çamsarı quartz syenite	U-Pb (mineral)	74.1±0.7	A-type	Köksal et al. (2004a)
Bayındır feldspathoidal syenite	Rb-Sr (whole rock)	70.7±1.1	A-type	Gündoğdu et al. (1988)
Bayındır quartz syenite	Rb-Sr (whole rock)	85.1±3.6	A-type	Kuruç (1990)
Bayındır sodalite syenite	Rb-Sr (whole rock)	84.4±0.9	A-type	Kuruç (1990)
Bayındır miaskite	Rb-Sr (whole rock)	71.8±0.1	A-type	Kuruç (1990)
Bayındır foyaites and volcanic rocks	Rb-Sr (whole rock)	70.5±3.4	A-type	Kuruç (1990)

[a] recalculated using the decay constant recommended by Steiger and Jäger (1977)

Alternatively, Boztuğ (2000) stated that the crustal metasediments of the CACC could have been affected by inverted metamorphism resulting from the Anatolide-Pontide collision at the northern margin of the Anatolide-Tauride segment. According to Boztuğ (2000), S-type or C_{ST}-type (crustal-shearing, thrusting-type; cf. Barbarin, 1990) granitoids formed from minimum melt composition anatectic melts derived from supracrustal material during collision of the Anatolides and Pontides. Boztuğ (2000) further suggested that the following crustal thickening during Late Cretaceous-Early Tertiary yielded post-collision H_{LO}-type (hybrid-late orogenic type; cf. Barbarin, 1990) granitoids, and the subsequent lithospheric attenuation during the core complex development (Whitney and Dilek, 1997) resulted in the A-type, within-plate alkaline silica-oversaturated and silica-undersaturated syenitic magmatism.

İlbeyli et al. (2004) subdivided the intrusive rocks of the CACC into three main groups on the basis of their major trace element and isotopic characteristics, as (i) calc-alkaline (Behrekdağ, Cefalıkdağ, and Çelebi); (ii) subalkaline-transitional (Baranadağ); and (iii) alkaline (Hamit). These plutonic rocks show isotopic and trace element data reflecting a crustal component which is thought to originate from source enrichment associated with a subduction zone, and/or from crustal contamination that takes place via assimilation and fractional crystallization during magmatic ascent through the thickened central Anatolian crust (İlbeyli et al., 2004). The coexistence of calc-alkaline and alkaline magmatism in the CACC may be attributed to mantle source heterogeneity before collision according to İlbeyli et al. (2004). The authors stating that there is no evidence for localized extension in the CACC described the mechanism for the initiation of the post-collisional central Anatolian magmatism as either thermal perturbation of the metasomatized lithosphere by delamination of the thermal boundary layer, or removal of a subducted plate (slab breakoff).

On the contrary, Göncüoğlu and his collaborates (e.g. Göncüoğlu et al., 1991, 1992, 1993, 1997; Göncüoğlu and Türeli, 1993, 1994; Yalınız et al., 1999; Aydın et al., 1998; Düzgören-Aydın et al., 2001) described the granitoids as evolved through the collision of CACC with the Sakarya Continent during Early Upper Cretaceous following the closure of northern branch of Neotethys. They classify the granitoids as S-type syn-collision granitoids formed just after the climax of a collision of CACC with the Sakarya microcontinent, H-type post-collision granitoids evolved from the underplating mantle-derived mafic magma formed due to the crustal thickening followed by lithospheric delamination, and A-type granitoids representing the advanced and final and extensional stages of post-collisional period.

Floyd et al. (2000) indicated that the southward stacking of the Sakarya subduction zone material along the CACC margin was prior to the metamorphism and coeval collisional magmatism in Mid-Cretaceous times. According to them, further compression produced slicing and imbrications of the supra-subduction-zone ophiolitic rocks, which evolved within the oceanic segment left after the initial collision of CACC with the Sakarya continent. The eventual obduction of the supra-subduction-zone-type fragments over the CACC metamorphic basement followed by intrusion of post-collison granitoids in Campanian (Yalınız et al., 1999; Floyd et al., 2000).

Thermal relaxation during the Late Maastrichtian to Paleocene resulted in the formation of extensional basins such as Kızılırmak, Ulukışla and Sivas in the central Anatolia (Göncüoğlu et al., 1993; Dirik et al., 1999; Alpaslan et al., 2004). The basin margin sediments during Maastrichtian are characterized by mass-flows and the thickness of the basin-fill reaches up to 5000 m. Olistoliths of volcanic rocks in these basins are chemically related to shallow intrusions that represent equivalents of the deeper level A-type granitoids (Göncüoğlu et al., 1997; Köksal et al., 2001). Geochemical and isotope data from Early Tertiary volcanic rocks formed in these basins also supports the geological data on the extensional regime (Gökten and Floyd, 1987; Çevikbaş and Öztunalı, 1992; Köksal et al., 2001; Alpaslan et al., 2004).

CHAPTER 3

DETAILED GEOLOGY, PETROGRAPHY AND WHOLE-ROCK GEOCHEMISTRY OF THE STUDIED PLUTONS

Previous work on the plutons selected for zircon studies covers the detailed and precise geological mapping, geochemistry, including major, trace and rare-earth elements, isotope geochemistry and geochronology. The following summary is given to understand the general geological and petrological features of these granitoids and provide basis for the correlation of the findings from the zircon typology and further studies with that of previous work.

The granitoids concerned were interpreted to have some differences with each other in geological, petrographical and geochemical aspects, but similarities to other granitoids in the CACC. Borucu Granodiorite-Monzogranite (SK-1), Sinandı Microgranite (SK-6) from the Ekecikdağ area, Namlıkışla biotite-granite (SK-8), Yenişabanlı biotite-amphibole granite (SK-9), Sipahiler amphibole-biotite granite (SK-10), Torunobası granite porphyry (SK-11a), Camili alkali feldspar granite (SK-11b) and Çimkalesi monzonite (SK-12) from the Ağaçören suite, and Terlemez quartz monzonite (SK-7) characterized by high-K calc-alkaline nature with mafic microgranular enclaves is similar to the other central Anatolian H-type granitoids (e.g. Türeli, 1991; Kadıoğlu, 1996; Göncüoglu and Türeli, 1993, 1994; Yalınız, 1996; Yalınız et al., 1999; Aydın et al., 1998; Düzgören-Aydın et al., 2001). On the other hand, Kalebalta Leucogranite (SK-3) and Hisarkaya Porphyritic Granite (SK-4 and 5) from the Ekecikdağ suite with high Rb and low Ba abundances, and free of mafic microgranular enclaves are similar to other S-type granitoids in central Anatolia regarding the mineralogy and geochemistry (e.g. Düzgören-Aydın et al., 2001).

To simplify the evaluation of geology, petrography and geochemistry of the granitoids from three different regions, samples are grouped based on the classification suggested in the previous studies given above, as H-type granitoids and S-type granitoids. In spite of the present discussion on the origin and tectonic setting of these granitoids, it is reasonable basically to describe H-type granitoids (SK-1 and SK-6 from Ekecikdağ; SK-7 from Terlemez; SK-8, 9, 10, 11a, 11b, 12 from Ağaçören areas) as having calc-alkaline H-type characteristics and S-type granitoids (SK-3, 4 and 5 from Ekecikdağ area) as exhibiting some distinct features with respect to the H-type ones. This roughly grouping provides advantages in presenting general features of the studied granitoids. On the other hand, care also taken to interpret different characteristics observed within each group.

The geological and petrological features of the Ekecikdağ, Ağaçören and Terlemez plutons were given in detail in the previous studies (e.g. Türeli, 1991; Kadıoğlu, 1996; Yalınız, 1996). Brief explanation of the geological, petrographical and geochemical characteristics of the granitoids in concern is presented in this section.

3.1. Geology

The study area is located within the western part of the CACC. Previous field studies on the selected granitic bodies presenting their main geological characteristics are summarized below.

3.1.1. Ekecikdağ Suite

Ekecikdağ pluton comprises one of the most important segments of the CAG in the western part of the CACC. Field relations and petrological features of the pluton have been described by Türeli (1991), Göncüoğlu and Türeli (1993, 1994). Ekecikdağ pluton intruded both metamorphic rocks and ophiolitic rocks that were overthrusted the metamorphic rocks (Türeli, 1991).

Türeli (1991) differentiated Ekecikdağ pluton into subunits as Borucu granodiorite-monzogranite, Kalebalta leucogranite, Hisarkaya porphyritic granite and Sinandı microgranite. All of these four granitoids were sampled (Borucu: SK-1; Kalebalta: SK-3; Hisarkaya: SK-4 and 5; Sinandı: SK-6) in the scope of present research. Borucu granodiorite-monzogranite exposing in the form of large, oval shaped bodies, is characterized by grayish color with high biotite content and coarsely crystalline, phaneritic texture with K-feldspar phenocrysts. Irregular angular or subrounded microgranular mafic enclaves are common throughout the granitoid. Kalebalta leucogranite is a pinkish white, medium equigranular granitoid with very low mafic mineral content without mafic enclaves, exhibiting sharp contacts with Borucu granitoid and gabbroic rocks in the area. Hisarkaya porphyritic granite intrudes to Borucu granitoid and is characterized by light grayish color with feldspar phenocrysts. Sinandı microgranite displaying microgranular texture with dark grayish color, occur as series of small intrusions that cut Borucu granitoid (Türeli, 1991).

Türeli (1991) suggested that, the Borucu granodiorite-monzogranite is the main granitic phase in the area, while other granitic subunits were evolved through the process of magmatic differentiation. According to Türeli (1991), the Ekecikdağ pluton is a post-collision granitoid formed due to the ophiolite emplacement, which caused crustal thickening and increase in the geothermal gradient, and gave rise to the partial melting of the pre-existing continental rocks. Furthermore, Düzgören-Aydın et al. (2001) stated that the Kalebalta leucogranite is the crustal-type granitoid representing the early stages of post-collision magmatism, while the Borucu granodiorite-monzogranite is the H-type granitoid representing the mature stages of post-collision magmatism.

3.1.2. Ağaçören Suite

Geological and petrological characteristics of the granitoids around Ağaçören area were described by Kadıoğlu (1996), Güleç (1994), Güleç and Kadıoğlu (1998), Kadıoğlu and Güleç (1999), Kadıoğlu et al. (2003). Kadıoğlu (1996) differentiated the Ağaçören pluton into following subtypes: Namlıkışla biotite-granite, Yenişabanlı biotite-amphibole granite, Sipahiler amphibole-biotite granite, Torunobası granite porphyry, Çimkalesi monzonite, Camili alkali-feldspar granite, Cebirli quartz-monzonite, Boğazköy microcline granite and Yurtlak quartz-monzonite porphyry, from which Namlıkışla (SK-8), Yenişabanlı (SK-9), Sipahiler (SK-10), Torunobası (SK-11a), Camili (SK-11b) and Çimkalesi (SK-12) granitoids were selected in the scope of the present research.

Kadıoğlu (1996) indicated that almost all the subunits of the Ağaçören granitoid include mafic microgranular enclaves related with the magma mixing/mingling events. He further suggested that first less felsic subunits (e.g. Çimkalesi and Namlıkışla granitoids) were formed by mixing, and then more felsic units (e.g. Sipahiler, Yenişabanlı granitoids) were formed by mingling due to the fractional crystallization of hybrid magma source. In the latter subunits, mafic microgranular enclaves are larger and more abundant (Kadıoğlu, 1996). Ağaçören granitoids have sinusoidal and irregular contacts with the gabbros, and there is compositional changing within the gabbros along these contacts suggesting synchronous forming of granitoids with gabbros in the Ağaçören suite according to Kadıoğlu (1996). Some other studies, e.g. Kadıoğlu (1996), Kadıoğlu and Güleç (1999), Güleç and Kadıoğlu (1998), Kadıoğlu et al. (2003), also suggested that the granitoid to gabbroid plutons were coeval in the Ağaçören area.

Kadıoğlu (1996) described the Namlıkışla biotite granite as phaneritic, light gray to pinkish granitoid with feldspar megacrysts, abundant amphibole minerals and mafic enclaves. The Çimkalesi monzonite, on the other hand, is characterized by its dark gray color, porphyro-phaneritic texture with plagioclase megacrysts and oval shaped mafic enclaves (Kadıoğlu, 1996). The Yenişabanlı biotite-amphibole granite exhibiting phaneritic and porphyritic texture characterized by megacrysts of plagioclase and orthoclase has contact relationships with the Namllıkışla and Sipahiler granitoids (Kadıoğlu, 1996). Higher abundance of the mafic enclaves is characteristic feature for the Yenişabanlı granitoid (e.g. Kadıoğlu, 1996). The Sipahiler amphibole-biotite granite displaying transitional contacts with the Namlıkışla and Yenişabanlı granitoids is light gray, with fine crystalline and phaneritic texture and abundant amphibole minerals and without microcline or feldspar megacrysts (Kadıoğlu, 1996). The Torunobası granite porphyry is light gray to light brownish gray, porphyritic granite that cut the Namlıkışla granitoid (Kadıoğlu, 1996). The Camili alkali feldspar granite exposing as small dykes cutting the Yenişabanlı granitoid and other subunits, is pinkish, fine-grained granitoid free of mafic enclaves (Kadıoğlu, 1996).

3.1.3. Terlemez Suite

The Terlemez quartz monzonite exposed to the east of the NW-SE trending granitoid belt including the Ekecikdağ and Ağaçören plutons. Yalınız (1996) described the Terlemez quartz monzonite as medium- to coarse-grained compact and massive granitoid with granoblastic texture. Terlemez granitoid is indicated to have chilled margins close to the contact with the ophiolitic basic rocks (Yalınız, 1996). It is essentially composed of quartz, plagioclase, hornblende and K-feldspar and variable contents of biotite, and characteristically includes K-feldspar megacrysts, besides irregular angular or sub-rounded micro-mafic granular enclaves (Yalınız, 1996). In addition to xenoliths within the Terlemez granitoid, large ‘roof-pendants’ of gabbroic composition likely to be derived from the ophiolitic rocks are also found on top of the granitoid in some locations in the area (Yalınız, 1996).

Yalınız et al. (1999) suggested that the Terlemez quartz monzonite was a H-type (hybrid type) post-collisional granitoid that requires significant input from a mantle-derived mafic magma. The Terlemez quartz monzonite has a clear intrusive contact with the Middle Turonian-Lower Santonian Sarıkaraman ophiolitic rocks suggesting that the post-collisional magmatism post-dates the emplacement of ophiolitic rocks in the Terlemez area (Yalınız et al., 1999).

3.2. Petrography

A petrographic study was carried out on the selected 12 granitoid samples not only to interpret the general petrographical features of the rocks but also to investigate the sizes and textural relationships of the zircon crystals with their surroundings.

In general, both H- and S-type granitoids are composed mainly of quartz, orthoclase, plagioclase, biotite in varying amounts, and invariably altered to chlorite, kaoline and sericite. The rocks with varying amounts of major minerals are mainly grayish (e.g. Borucu, Hisarkaya and Yenişabanlı granitoids) to dark gray (e.g. Namlıkışla and Çimkalesi granitoids), while white (e.g. Kalebalta Leucogranite) and yellowish (e.g. Camili granitoid) varieties are also present.

The H-type granitoids from the Ekecikdağ area consist essentially of quartz, orthoclase, microcline, plagioclase, biotite, and minor amounts of hornblende (Figure 3.1). Chlorite is the most common alteration mineral of these rocks. In addition, they have opaques, zircon, titanite, allanite and apatite as accessory phases (Table 3.1).

The Ağaçören H-type granitoids exhibit similar major minerals to those from the Ekecikdağ area. The granitoids from both areas differ only in mineral contents with the presence of an epidote as an alteration product of plagioclase in the Ağaçören granitoids. Çimkalesi and Namlıkışla granitoids represent the most mafic members of the Ağaçören suite while the Camili granitoid may be defined as the most felsic member. The Camili alkali feldspar granite (SK-11b) locally contains muscovite instead of biotite.

The Terlemez quartz-monzonite, similar to other H-type granitoids, consists of quartz, orthoclase, plagioclase and biotite as major phases, and opaque minerals and zircon as accessory phases (Table 3.1).

In general, the H-type granitoids, which are composed of subhedral and anhedral crystals, are characterized by phaneritic and granitic textures. They also display graphic and myrmekitic textures. Orthoclase crystals display commonly perthitic form together with Carlsbad twins. Phenocrysts of orthoclase and plagioclase are abundant in most of the granitoids except equigranular or microgranular ones. Undolatory extinction is a common feature of quartz crystals. Microgranular enclaves encompassing hornblende and minor plagioclase are common within the H-type CAG (Figure 3.2).

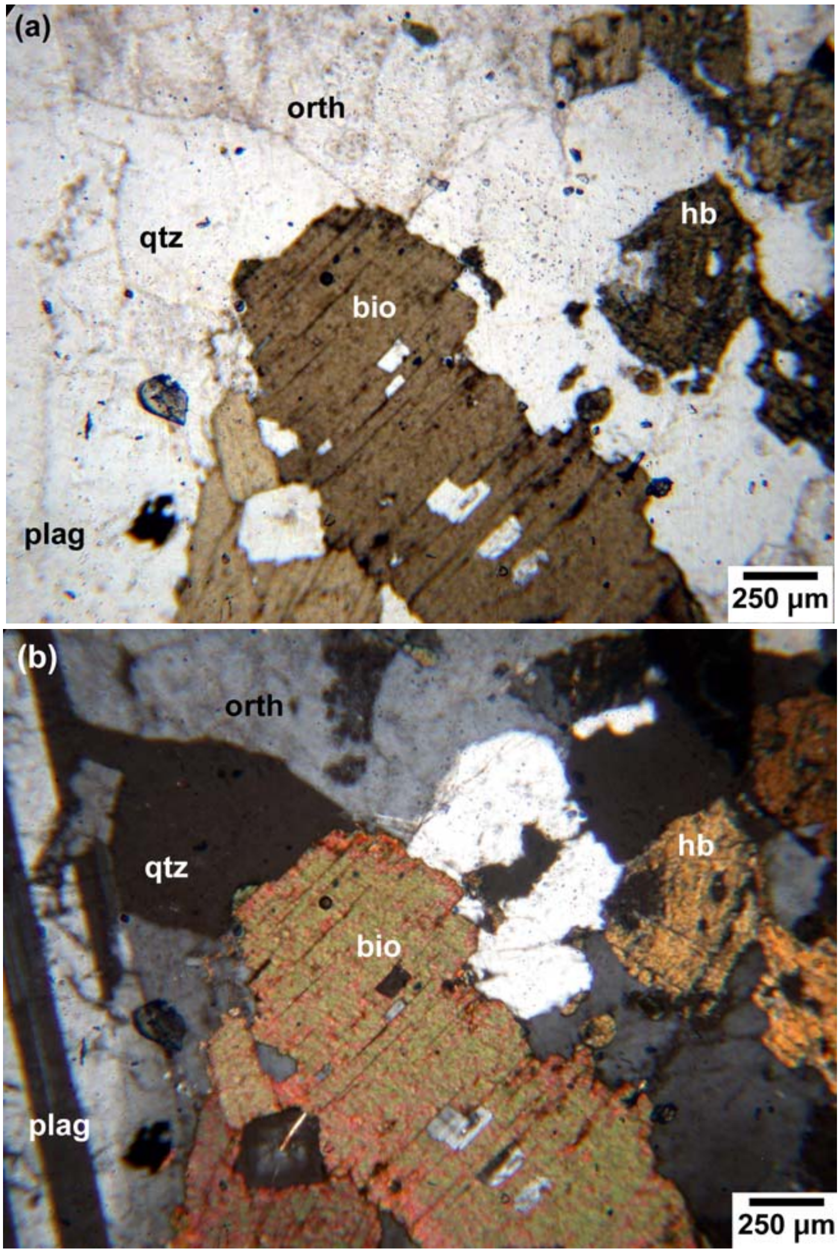

Figure 3.1. Photomicrograph showing the mineral assemblages of the H-type granitoid from central Anatolia (Çimkalesi-sample SK-12): (a) analyzer out and (b) analyzer in position (qtz: quartz, orth: orthoclase, plag: plagioclase, bio: biotite, hb: hornblende).

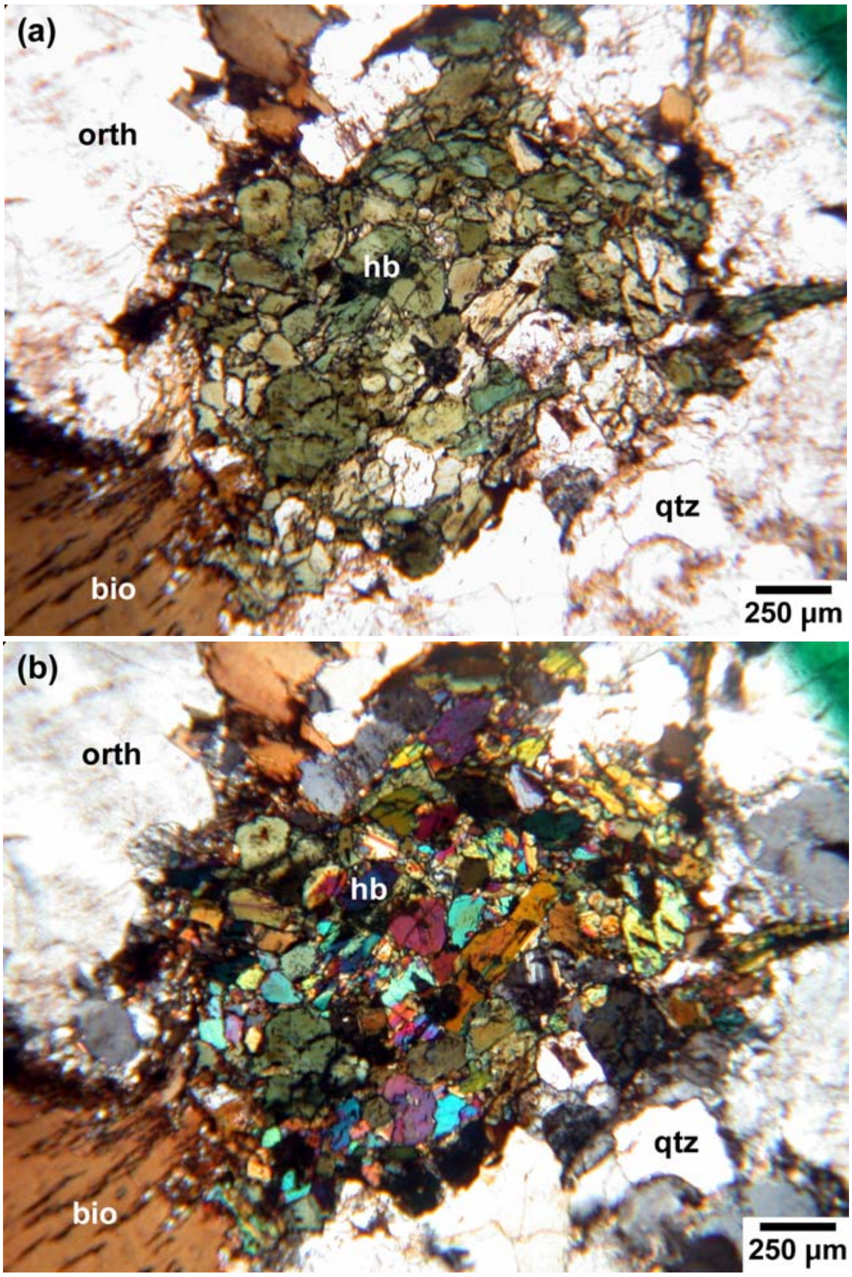

Figure 3.2. Photomicrograph showing microgranitoid enclave within H-type Borucu granitoid (Sample SK-1): (a) analyzer out and (b) analyzer in position (qtz: quartz, orth: orthoclase, bio: biotite, hb: hornblende).

The Ekecikdağ H-type granitoids have either porphyritic texture (Borucu granitoid) or microgranular texture (Sinandı granitoid). Ağaçören H-type granitoids display heterogeneous textures ranging from porphyritic varieties (Çimkalesi and Yenişabanlı granitoids) to more equigranular types (Namlıkışla and Sipahiler granitoids). On the other hand, Terlemez granitoid has porphyritic texture that is characterized by feldspar megacrysts.

S-type granitoids from the Ekecikdağ area are composed of quartz, orthoclase, plagioclase and biotite as major phases, whereas muscovite, titanite, apatite, allanite, zircon, and opaque minerals are also present in accessory amounts. The S-type CAG in this area display granitic texture and coexistence of muscovite and biotite (Table 3.1, Figure 3.3).

Moreover, they exhibit either porphyritic texture with larger orthoclase crystals in a medium-grained matrix consisting of quartz, plagioclase, orthoclase, biotite (e.g. Hisarkaya granitoid) or equigranular leucocratic texture with quartz, orthoclase, and minor amounts of biotite with accessory amounts of muscovite (e.g. Kalebalta granitoid). Porphyritic Hisarkaya granitoid differs from equigranular Kalebalta granitoid by presence of allanite (Figure 3.4a) and higher amount of biotite.

Table 3.1. Modal mineralogical compositions of the granitoids concerned.

sample Mineral	●(1) SK-1	▲ SK-3	▲ SK-4	▲ SK-5	● SK-6	♦ SK-7	▼ SK-8	▼ SK-9	▼ SK-10	▼ SK-11a	▼ SK-11b	▼ SK-12
Quartz	26	33	29	38	32	22	16	24	17	36	39	11
Orthoclase	14	34	40	34	20	21	31	21	30	29	45	13
Plagioclase	24	21	16	17	27	31	13	30	29	20	5	30
Microcline	7				2							
Biotite	14	6	12	7	13	9	28	15	10	11	1	6
Muscovite		2						2			9	
Hornblende	12		2	2	3	16	8	3	8	3		23
Pyroxene							1					11
Chlorite	2	3			2		1	3	2			2
Epidote				1			1		1			1
Opaque	1	1	1	1	1	1	1	2	3	1	1	3
Zircon	+	+	+	+	+	+	+	+	+	+	+	+
Titanite	+					+	+	+	+			+
Apatite	+	+	+	+	+	+	+	+	+	+	+	+
Allanite			+	+		+						

(1) **Symbols:** ●: Ekecikdağ H-type granitoids (SK-1, 6); ▼: Ağaçören H-type granitoids (SK-8, 9, 10, 11a, 11b, 12); ♦: Terlemez quartz-monzonite (SK-7); ▲: Ekecikdağ S-type granitoids (SK-3, 4, 5).

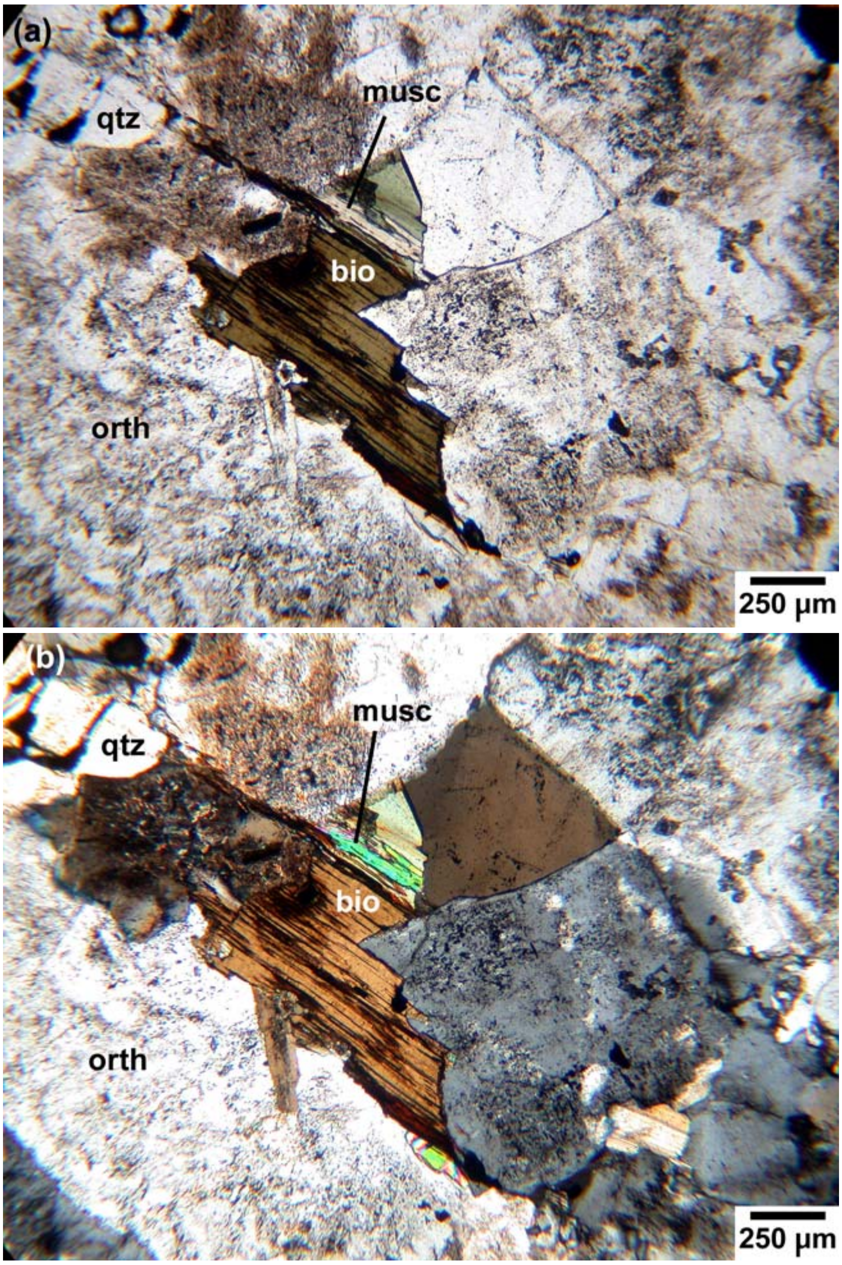

Figure 3.3. Photomicrograph showing S-type granitoid from central Anatolia (Kalebalta-sample SK-3): (a) analyzer out and (b) analyzer in position. (qtz: quartz, orth: orthoclase, bio: biotite, musc: muscovite)

Zircon, one of the most common accessory minerals present in both H- and S-type granitoids, is found in contact with major phases (biotite, quartz, orthoclase, and plagioclase) and as inclusions in these minerals. Furthermore, contemporaneous growth of zircon with allanite is characteristic (Figure 3.4b).

Commonly, zircons show zoning visible under microscope and their contacts with host biotite minerals often form pleochroic haloes due to metamictization (Figure 3.5). Petrographic study showed that diameters of zircon crystals range from 10 µ to 400 µ, and mean diameter is ca. 100-150 µ.

3.3. Geochemistry

The categorization of the granitoids into H- and S-type varieties is also used for interpretation of general geochemical characteristics of the studied granitoids. It is important to note that the grouping of these granitoids into H- and S-types is primarily based on the previous studies. This classification was accepted only to be the starting point for the petrological evaluations, e.g. geochemistry, zircon typology, in the scope of this research.

New whole-rock geochemical data including rare earth elements (REE) were obtained from 12 samples in the present study (Table 3.2) to better constrain the geochemical features and relationship of these granitoids.

Both of H- and S-type granitoids are subalkaline based on the Irvine and Baragar (1971)'s classification (Figure 3.6), similar to the other H- and S-type CAG.

H-type granitoids from both Ekecikdağ and Ağaçören areas exhibit metaluminous to peraluminous features, based on Shand index, while Terlemez granitoid shows metaluminous character (Figure 3.7a). However, the H-type granitoid samples with agpaitic index (AI)<0.87 have calc-alkaline metaluminous feature (Figure 3.7b).

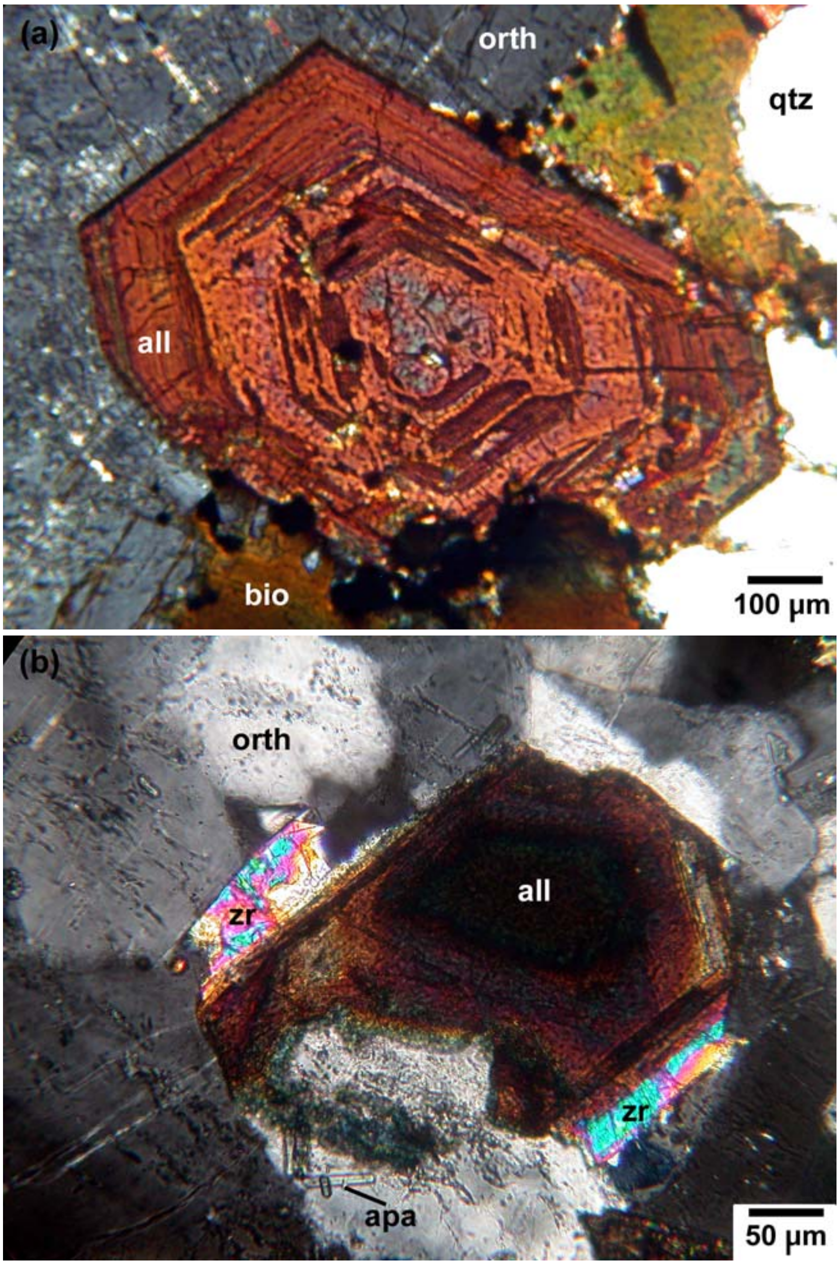

Figure 3.4. Photomicrograph showing allanite occurrences in the CAG: (a) zoned and large allanite mineral from the Hisarkaya granitoid (SK-4), (b) coexistence of allanite and zircon (from Terlemez granitoid, SK-7) (zr: zircon, all: allanite, apa: apatite, qtz: quartz, orth: orthoclase, bio: biotite).

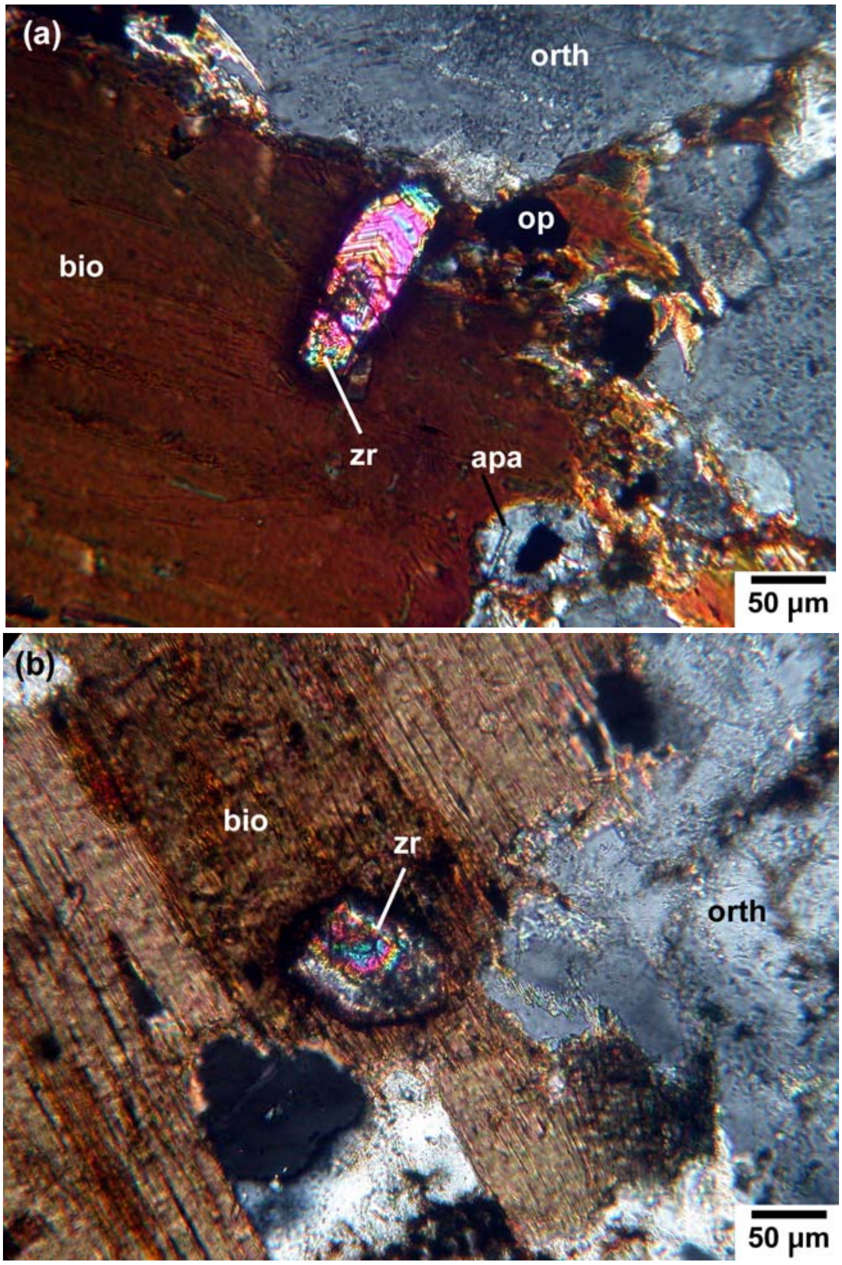

Figure 3.5. Photomicrograph showing zoned zircons within biotites from the Hisarkaya granitoid (a) sample SK-4, (b) sample SK-5 (zr: zircon, apa: apatite, op: opaque, orth: orthoclase, bio: biotite).

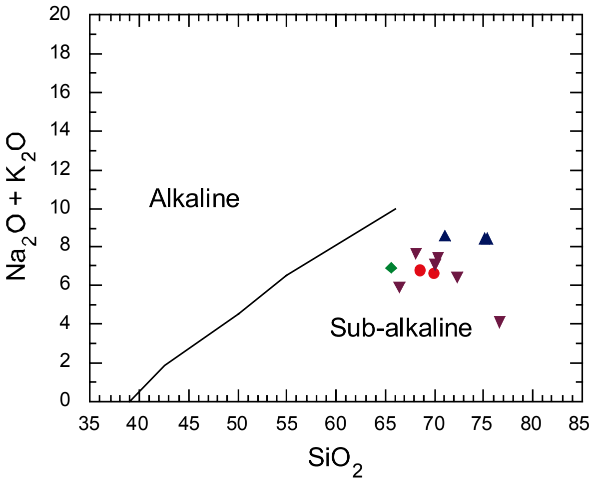

Figure 3.6. Distribution of the samples in the $Na_2O+K_2O-SiO_2$ diagram (Irvine and Baragar, 1971). Symbols as in Table 3.1.

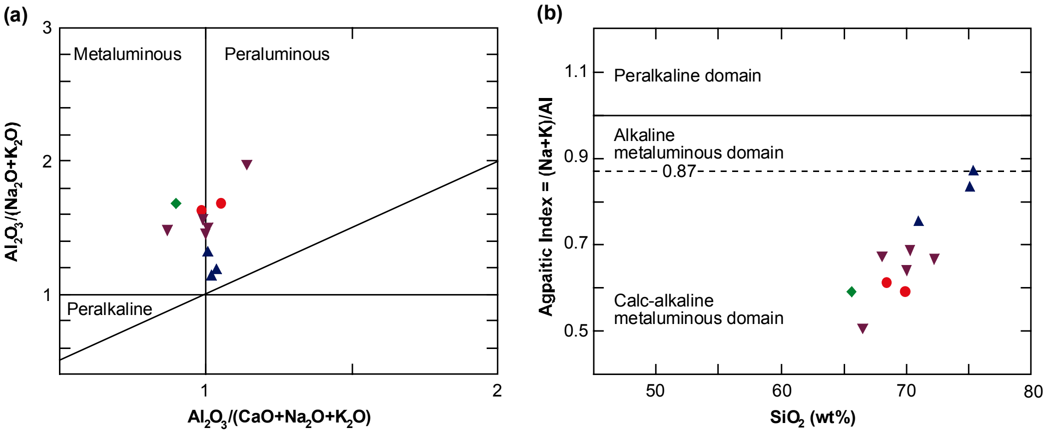

Figure 3.7. (a) Plot of Shand index for the Ekecikdağ, Ağaçören and Terlemez granitoids, discrimination fields are from Maniar and Piccoli (1989); (b) Agpaitic index (AI) vs. SiO_2 diagram. The dashed line [AI=0.87 (Liégeois and Black 1987)] separates alkaline and calc-alkaline granite series. Symbols as in Table 3.1.

Table 3.2. Geochemical analyses⁽¹⁾ from the granitoids concerned.

Sample► **Element▼**	● (2) **SK-1**	▲ **SK-3**	▲ **SK-4**	▲ **SK-5**	● **SK-6**	◆ **SK-7**	▼ **SK-8**	▼ **SK-9**	▼ **SK-10**	▼ **SK-11a**	▼ **SK-11b**	▼ **SK-12**
SiO_2	68.5	75.4	71.0	75.1	69.9	65.6	66.5	70.0	72.3	70.4	76.7	68.1
Al_2O_3	14.7	12.7	15.0	13.0	14.8	15.4	15.2	14.9	13.0	14.5	13.3	14.5
$Fe_2O_3^{tot}$	3.58	1.13	2.06	1.41	3.04	4.33	5.14	3.19	2.65	3.02	2.04	3.62
MgO	1.26	0.17	0.51	0.23	0.79	1.2	2.29	0.76	0.57	0.86	0.11	1.3
CaO	3.26	0.77	1.95	0.92	2.91	4.42	3.11	3.02	2.34	2.52	0.09	3.83
Na_2O	2.83	3.41	3.55	3.1	2.76	2.84	2.17	3.28	2.99	3.31	0.04	2.64
K_2O	4.02	5.06	5.09	5.37	3.89	4.12	3.81	3.83	3.46	4.13	4.1	5.01
TiO_2	0.34	0.07	0.17	0.10	0.40	0.60	0.63	0.24	0.18	0.24	0.13	0.36
P_2O_5	0.05	< .01	0.02	< .01	0.13	0.14	0.12	0.07	0.07	0.05	0.01	0.09
MnO	0.06	0.08	0.08	0.07	0.06	0.08	0.09	0.07	0.08	0.06	< .01	0.08
Cr_2O_3	0.059	0.039	0.06	0.044	0.033	0.063	0.056	0.064	0.062	0.04	0.025	0.051
LOI	1.1	0.7	0.6	0.6	1.4	1.1	1.2	0.7	2.5	1.2	3.8	0.4
TOTAL	**99.8**	**99.6**	**100.2**	**100.0**	**100.2**	**100.0**	**100.4**	**100.2**	**100.3**	**100.3**	**100.4**	**100.0**
Ba	369	130	435	290	755	904	648	713	451	678	511	478
Sc	7	4	3	2	7	5	14	4	4	4	2	6
Co	8	2	3	2	4	6	13	5	3	6	2	7
Cs	10.4	9.4	6.8	34.3	4.2	7.3	6	4.1	3.2	5.6	5.1	11.1
Ga	17	15	17	15	19	25	22	17	14	14	17	17
Hf	4.7	3.5	3	3.4	4.7	6.8	5.6	4.1	4	3.7	4.2	5.1
Nb	10	26	14	19	12	19	12	8	10	10	12	15
Rb	171	418	266	382	128	175	145	138	132	156	154	189
Sn	6	3	3	3	2	3	3	2	2	2	4	4
Sr	137	28	119	47	226	634	183	170	186	189	48	467
Ta	1.0	4.0	1.8	3.3	1.0	1.3	0.8	0.7	0.9	1.1	1.3	1.2
Th	25	33	32	35	13	22	16	14	16	18	37	43
U	6.3	11.0	8.9	10.2	2.6	3.6	2.0	3.0	5.3	5.3	6.5	5.4
V	47	8	24	14	21	53	95	31	22	40	32	51
Zr	133	75	87	73	160	223	182	144	122	125	129	171
Y	20	55	23	30	25	21	23	18	18	18	22	23
Cu	22	8	15	9	7	15	34	14	14	18	6	14
Pb	8.3	8.5	6	6.9	3.5	9.4	6.1	4.1	3.9	10.9	19.4	25.2
Zn	32	15	33	21	62	49	83	44	41	27	19	34
Ni	24	13	24	13	11	25	45	25	20	28	14	19
La	30	21	23	25	38	52	42	33	33	32	62	49
Ce	62	47	42	43	72	99	82	55	55	54	99	87
Pr	6.1	4.7	3.9	4.0	7.2	9.4	8.2	5.1	5.2	4.8	9.1	8.2
Nd	22.9	18.8	14.5	15.3	30.1	37.3	35.3	19.9	20.0	18.0	33.5	30.1
Sm	4.0	4.2	3.1	2.9	6.2	6.8	6.6	3.4	3.2	3.0	5.3	5.8
Eu	0.8	0.2	0.5	0.3	1.2	1.3	1.2	0.7	0.6	0.6	0.6	1.0
Gd	3.24	5.25	2.54	2.96	5.36	5.21	5.78	3.55	3.17	2.48	4.71	4.56
Tb	0.56	1.07	0.53	0.59	0.77	0.71	0.79	0.48	0.46	0.42	0.64	0.68
Dy	3.1	7.4	3.4	4.0	4.4	3.5	4.0	2.9	2.7	2.5	3.5	3.5
Ho	0.67	1.75	0.63	0.81	0.79	0.68	0.75	0.49	0.48	0.48	0.61	0.64
Er	2.1	5.7	2.3	3.1	2.1	2.0	2.1	1.5	1.6	1.7	2.0	2.1
Tm	0.28	0.77	0.34	0.62	0.28	0.28	0.3	0.23	0.24	0.24	0.3	0.29
Yb	2.2	6.3	2.6	4.1	2.2	2.2	2.4	1.8	1.9	2.1	2.3	2.4
Lu	0.30	0.84	0.45	0.68	0.35	0.31	0.37	0.32	0.29	0.31	0.35	0.38
Ba/Nb	36.9	5.0	31.1	15.3	62.9	47.6	54.0	89.1	45.1	67.8	42.6	31.9
Ba/La	12.3	6.2	18.9	11.6	19.9	17.4	15.4	21.6	13.7	21.2	8.2	9.8
Ce/Pb	7.5	5.5	7.0	6.2	20.6	10.5	13.4	13.4	14.1	5.0	5.1	3.5
Ba/Zr	2.8	1.7	5.0	4.0	4.7	4.1	3.6	5.0	3.7	5.4	4.0	2.8
La/Nb	3.0	0.8	1.6	1.3	3.2	2.7	3.5	4.1	3.3	3.2	5.2	3.3

(1) Geochemical analyses were performed in ACME Analytical Laboratories Ltd. (Canada). Major elements, Ba, and Sc were measured by ICP-AES. Trace elements excluding Ba and Sc were measured by ICP-MS, and LOI is Loss of Ignition; tot: total Fe as Fe_2O_3 ; major elements in wt%; trace elements in ppm

(2) For symbols see Table 3.1.

S-type granitoids also plot into calc-alkaline metaluminous domain based on agpaitic index (AI<0.87), while they are peraluminous (A/NK>1, A/CNK>1) depending on Shand index (Figure 3.7). Collectively, the H-type granitoids can be described to have calc-alkaline metaluminous to peraluminous characters, S-type samples, on the other hand, can be classified as calc-alkaline peraluminous granitoids.

H- and S-type granitoids exhibit distinct geochemical trends on the Harker diagrams (Figure 3.8). In general, the H-type granitoids display higher concentrations of TiO_2, $Fe_2O_3^{(tot)}$, MgO, CaO, P_2O_5, Ba, Sr, Zr, V and lower abundances of SiO_2, K_2O and Rb than those of S-type granitoids.

Ekecikdağ H- and S-type granitoids have distinct trends in SiO_2 vs. TiO_2, Al_2O_3, K_2O, P_2O_5, Rb, Sr, Ba, Th, Zr diagrams. They also display parallel or different sloped trends in SiO_2 vs. MgO, CaO, $Fe_2O_3^{(tot)}$, Nb, V diagrams. It can be deduced that H- and S-type granitoids from the Ekecikdağ area are not likely to be evolved by fractional crystallization, i.e. they have different source characteristics. Due to the limited number of samples it is not possible to make an interpretation about the chemical variation of either H- or S-type Ekecikdağ granitoids within themselves.

For the Ağaçören H-type granitoids, the chemical variations characterized by negative trends, especially on SiO_2 vs. TiO_2, $Fe_2O_3^{(tot)}$, MgO, CaO, P_2O_5 diagrams, can be described as representative of fractional crystallization patterns. Ağaçören H-type granitoids are scattered in the K_2O, Na_2O, and trace element plots. It is also remarkable that the single Terlemez granitoid sample has major and trace element compositions very different than the other rock samples, while the Ekecikdağ and Ağaçören H-type granitoids have similar major and trace elements contents (Figure 3.8).

Continental crust-normalized multi-element plots for H-type granitoids, in general, display enrichment in LILE (Rb, Ba, Th, K) and LREE (La, Ce) relative to HSFE (Nb, Zr, Hf, Sm, Y) and HREE (Figure 3.9). H-type granitoids are characterized by negative anomalies of Ba, Nb, and Ti. Particularly, the Terlemez granitoid has higher concentrations of Ba, Nb, Sr, Zr, Hf and Ti than those of the other H-type granitoids.

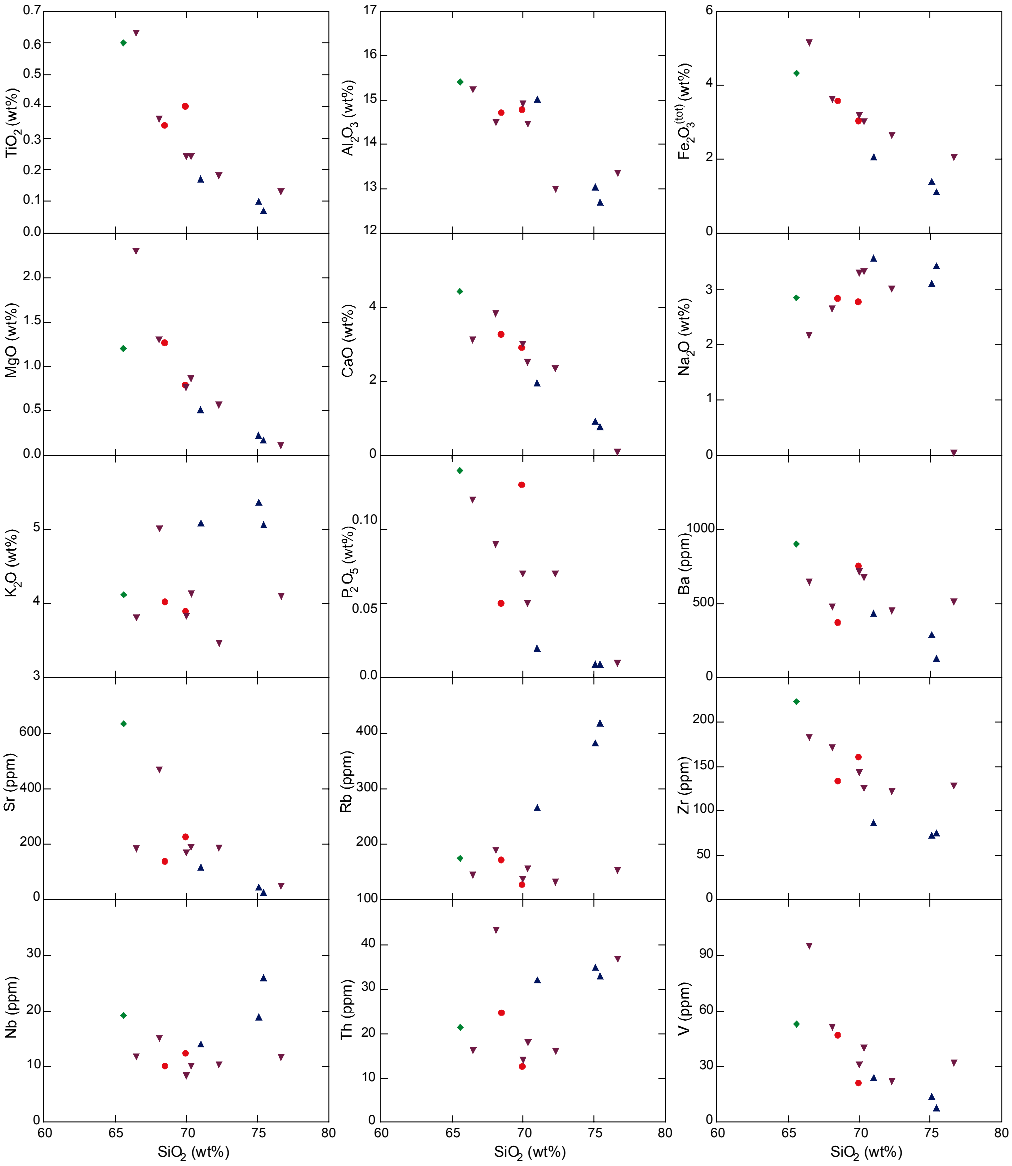

Figure 3.8. Harker variation plots for selected major and trace elements of the Ekecikdağ, Ağaçören and Terlemez granitoid samples. Symbols as in Table 3.1.

S-type granitoids differ from H-type ones by their strong depletions in Ba, Sr and Ti, and enrichment in HREE than those of H-type granitoids. S-type granitoids are strongly enriched in Rb and Th, and depleted in LREE, Zr, Nd, Sm and Eu with respect to H-type granitoids. Nb depletion is less pronounced in the S-type granitoids (Figure 3.9). The observed features and differences, revealed from spider diagrams, are very common for other H- and S-type granitoids within the CACC (for comparison see Figure 2.7).

On the ocean-ridge granite normalized multi-element variation diagram (Figure 3.10), patterns of S-type granitoids show similarities to those of syn-collision granitoids, i.e. LILE enrichment and HFSE, HREE depletion (cf. Pearce et al., 1984). On the other hand, patterns of H-type granitoids exhibit similar characteristics to the post-collisional granitoids, again LILE enrichment and HFSE, HREE depletion, with lower abundances of Rb and Th than those of S-type ones (cf. Pearce et al., 1984).

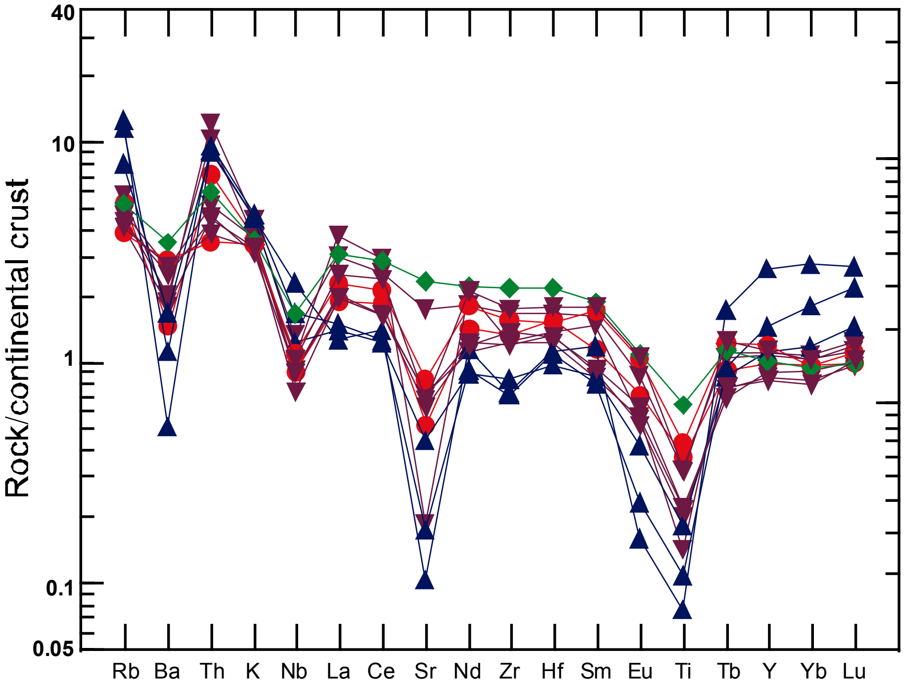

Figure 3.9. Continental-crust-normalized (after Taylor and McLennan, 1985) multi-element variation plots of the Ekecikdağ, Ağaçören and Terlemez granitoids. Symbols as in Table 3.1.

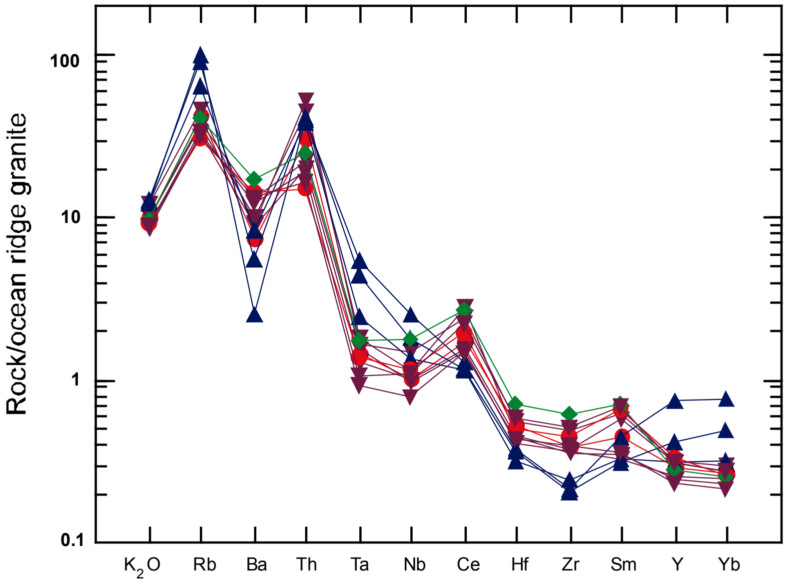

Figure 3.10. Ocean-ridge granite-normalized (after Pearce et al., 1984) multi-element variation plots of the Ekecikdağ, Ağaçören and Terlemez granitoids. Symbols as in Table 3.1.

Chondrite-normalized REE patterns of the H- and S-type granitoids have steep LREE-enriched and almost flat HREE patterns (Figure 3.11). The H-type granitoids, in general, differ from S-type ones by higher LREE enrichment levels and lower MREE and HREE contents with concave-upward patterns. Both granitoid types have negative Eu-anomalies [$(Eu/Eu^*)_N$] but these anomalies are less pronounced in the H-type granitoids than those in the S-type granitoids (0.39-0.69 for H-type granitoids; 0.12-0.52 for S-type granitoids). H-type granitoids have high $(La/Yb)_N$ ratios (10.05-19.30), whereas S-type granitoids exhibit lower $(La/Yb)_N$ ratios (2.40-6.28).

In general, both of the H- and S-type granitoids seem to display arc affinity based on their Nb and Ti negative anomalies and Th enrichment levels relative to La. H-type granitoids having Ba concentrations higher than average continental crust (ACC; Taylor and McLennan, 1985) are characterized by high Ba/Nb (32-89), Ba/La (8.2-22), Ba/Zr (2.8-5.4), La/Nb (2.7-5.2) and low Ce/Pb (3.5-14) incompatible element ratios.

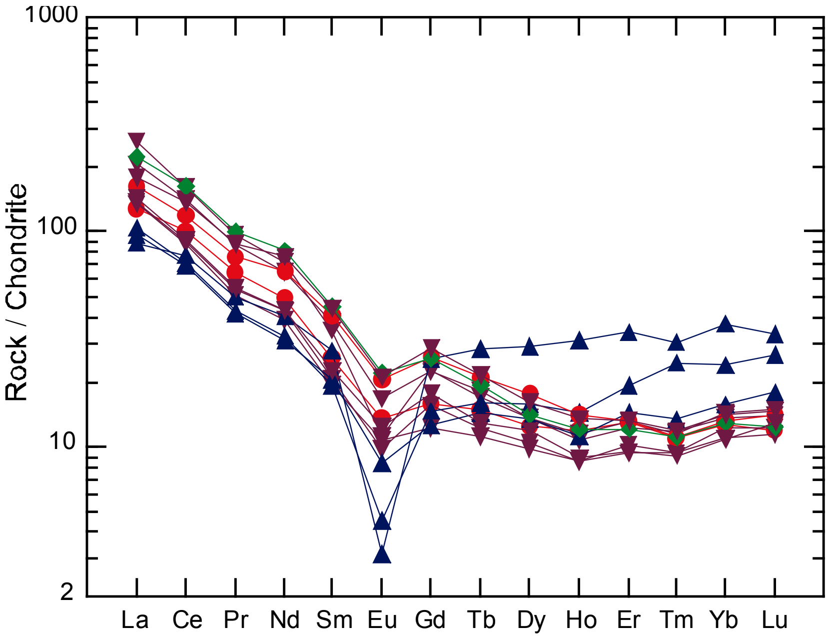

Figure 3.11. Chondrite-normalized (after Sun and McDonough, 1989) rare earth element patterns for the Ekecikdağ, Ağaçören and Terlemez granitoids. Symbols as in Table 3.1.

However, S-type granitoids have lower Ba/Nb (5.0-31) and La/Nb (0.8-1.6) ratios with respect to those of H-type ones, but similar Ba/Zr (1.7-5.0), Ba/La (6.2-18) and Ce/Pb (5.5-7.0) ratios. Subduction related magmas have Ba/Nb ratios (>30; Gill, 1981), high La/Nb ratios (Hawkesworth et al., 1995), high Ba/La, Ba/Zr and low Ce/Pb ratios (Ajaji et al. 1998), and average Nb of 11(±4) (Whalen et al., 1987). Especially the H-type granitoids show similar characteristics to the subduction-related magmas. However, these geochemical features are reported not only from arc environment but also from enriched sources related to post-collisional environment (Whalen et al., 1996; Wenzel et al., 1997; Ajaji et al., 1998). Ajaji et al. (1998) described such enrichment in post-collisional setting as likely to be related with an earlier subduction event that created a subduction-modified sub-continental lithospheric mantle (SCLM) source.

Moreover, available isotope data suggests for granitoids from the Ağaçören pluton that the relative proportion of mantle and crustal components exceeds the limits for complete hybridization, but falls into the range for commingling (incomplete mixing) of mafic and felsic magmas (Güleç and Kadıoğlu, 1998).

In the Rb-(Nb+Y) diagram (Figure 3.12a) of Pearce et al. (1984), S-type granitoids plot on the syn-collision (syn-COLG) field. H-type granitoids, on the other hand, are clustered in the volcanic arc granite (VAG) field near to the triple junction of the VAG, within-plate granite (WPG) and syn-COLG fields in the Rb-(Nb+Y) diagram as recognized for most post-collision granitoids (Pearce et al., 1984). Pearce (1996) stated that some of the post-collision granitoids might show subduction-like mantle sources and have many of the characteristics of volcanic-arc granites on this diagram. Moreover, extensive interaction between the mantle-derived sources and crust results in movement of all compositions into the VAG field, and consequence is a restricted range of compositions for post-collision granitoids that overlap the fields of other magma types (Pearce, 1996).

It should also be noted that in the Rb vs. (Nb+Y) diagram there exist some ambiguities especially in the case of complex or polyphase orogenies due to the mixing of source rocks of different provenances (Förster et al., 1997; Romer et al., 2001). This is reported as a common situation for collisional settings, which is also closely associated in space and time with extensional regime like the case of central Anatolia (e.g. Förster et al., 1997). Moreover, the compositional trends that are produced by differentiation may cross the field boundaries, which can cause misclassification (Förster et al, 1997).

In the tectonic discrimination diagram of Harris et al. (1986) (Figure 3.12b), S-type granitoids fall into the Group II field that comprises syn-collision peraluminous intrusions. H-type granitoids plot onto the pre-collision or volcanic-arc type calc-alkaline intrusions (Group I) field (except two samples SK-11a and SK-11b).

Despite of limitations mentioned above, these tectonomagmatic discrimination diagrams (Figure 3.12) suggest syn-collision character for the S-type, and post-collisional character for the H-type granitoids.

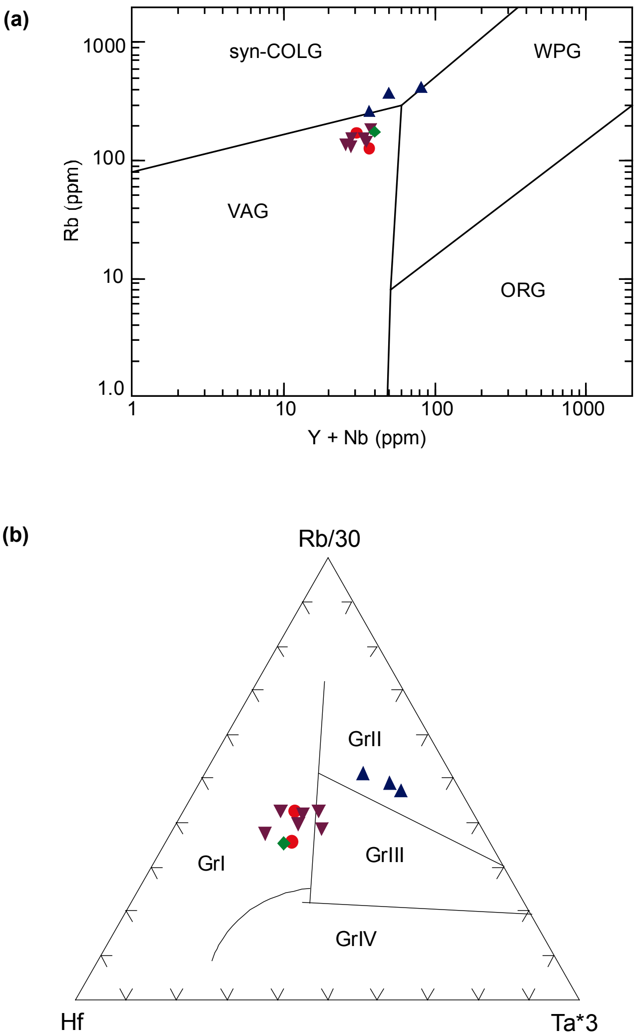

Figure 3.12. Distribution of the Ekecikdağ, Ağaçören and Terlemez granitoids on the tectonomagmatic discrimination diagrams: (a) Rb vs. Y+Nb diagram (after Pearce et al., 1984), syn-COLG: syn-collision, WPG: within-plate, VAG: volcanic arc, and ORG: ocean ridge granitoids; (b) Hf-Rb/30-Ta*3 diagram (after Harris et al., 1986). Gr I: pre-collision calc-alkaline (volcanic arc), Gr II: syn-collision peraluminous, Gr III: late or post-collision calc-alkaline, and Gr IV: post-collision alkaline intrusions. Symbols as in Table 3.1.

$(La/Lu)_N$ ratios of H-type granitoids decrease with increasing $(Eu/Eu^*)_N$, while those of S-type granitoids increase (Figure 3.13a). Furthermore $(La/Yb)_N$ ratios of H-type granitoids increase with increasing $(Ce)_N$, whereas those of S-type granitoids decrease (Figure 3.13b).

$(Eu/Eu^*)_N$ values are variable and smaller in the S-type granitoids than the H-type ones. Additionally H-type granitoids have higher LREE/HREE ratios than the S-type ones. Both of the diagrams reflecting REE fractionation of the granitoids (cf. Rollinson, 1993) indicate different source characteristics for the H- and S-type CAG.

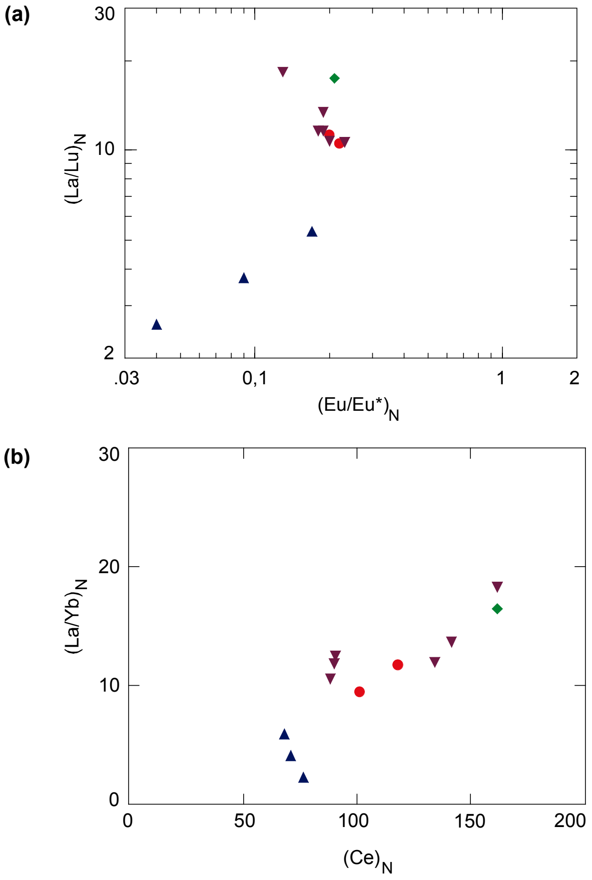

Figure 3.13. Distribution of the Ekecikdağ, Ağaçören and Terlemez granitoids on the REE ratio diagrams: (a) $(La/Lu)_N$–$(Eu/Eu^*)_N$ diagram; (b) $(La/Yb)_N$–$(Ce)_N$ diagram. Symbols as in Table 3.1.

Consequently, both of the granitoid types seem to be generated in a collisional setting, in which S-type represents collision, and H-type represents post-collision stage. Available geochemical data infer that H-type granitoids have enriched mantle sources modified by subduction-related component.

Moreover, H-type granitoids exhibit hybridized source with evidences of magma mingling/mixing processes, and S-type reflects common features of collisional granitoids.

The present research did not principally direct towards a detailed geochemical study, thus systematic sampling was not performed for geochemical analysis. Therefore, it is important to note that, geochemical interpretations above are based on limited data, and only provide basis for detailed investigations on zircon minerals.

CHAPTER 4

ZIRCON TYPOLOGY

4.1. Background

4.1.1. Zircon: The Key Mineral

Zircon ($ZrSiO_4$ - zirconium orthosilicate) belonging to tetragonal group is polymorphous and naturally occurring dimorph mineral (Speer, 1982). The principal structural unit in zircon is a chain of alternating, edge sharing [SiO_4] tetrahedra and [ZrO_8] triangular dodecahedra extending parallel to c along which the four-fold screw axes formally insist on an axial development and the chains are joined laterally by edge-sharing dodecahedra (Speer, 1982). The interatomic distances Zr-Si are 2.991 Ǻ, Zr-Zr' 3.626 Ǻ and Zr'-Si 3.629 Ǻ, and the c/a ratio is 0.909, underlining a typical pseudoisometric atomic arrangement (Kostov and Kostov, 1999).

Zircon displays crystal habits varying from bipyramidal to pseudoisometric and prismatic, scarcely acicular or spherulitic (Kostov and Kostov, 1999).

Zircon is chemically inert and a refractory mineral which can survive both weathering and transport processes as well as high temperature metamorphism and anatexis (Hinton and Upton, 1991). New growth can occur during metamorphism or onto older relict cores during igneous processes, therefore each individual crystal, or parts of that crystal, may have a different origin (Hinton and Upton, 1991).

Considering the wide spectrum of the geological and petrological studies on this mineral, it is plausible to describe zircon as a key mineral. Not only its crystallography but also chemistry is a subject of numerous studies.

4.1.2. Main Aspects of the Zircon Typology Method

The application of primary zircon morphology as an indicator of the origin of granites was developed by Poldervaart (1956) and co-workers, leading to the studies of Pupin and Turco (1972) and Pupin (1980) who proposed a scheme relating the external zircon morphology to a genetic classification of the granite host and temperature of crystallization of the granite magma.

Pupin and Turco (1972) introduced a zircon typology method that is basically a method for petrogenetic classification of granitic rocks by depending on the population study concerning the morphologies of zircons. Pupin (1980) gave the basics of the zircon typology method in which an arrangement of given prismatic and pyramidal crystal faces constitute population types. Further studies considering the typological features of zircon is being applied to different granitoid bodies (Broska and Uher, 1991; Vavra, 1990, 1993, 1994; Vavra et al., 1996, 1999; Pupin and Persoz, 1999; Klötzli et al., 2001).

The crystal forms encountered on natural zircon are the prisms {100} and {110}, the pyramids {011} and {211}, and much less commonly, the steep pyramid {031} and the flat pyramid {112} (Vavra, 1993).

According to Pupin (1980), the main zircon types show 0, 1 or 2 prisms, i.e. {100}, {110} in combination with either one of the three pyramids {101}, {211} or {301}, or the arrangement {101} + {211}. Pupin (1980) suggested that the main types and subtypes of zircon minerals can be arranged to place on a square board, i.e. zircon typologic diagram, depending upon the relative development of the prisms and pyramids, and disregarding the crystal elongation (Figure 4.1). S-type, which is the most abundant habitus that can be found in endogenous and exogenous rocks, forms, then, the diagram’s main point, the other main types logically arranged around. Pupin (1980) also stated that among the thirty natural types eight types are only frequent (D, G, J, L, N, P, S, U) where some main types staying purely theoretical (i.e.: C, I, R, F) are emplaced at the right part of the diagram (Figure 4.1).

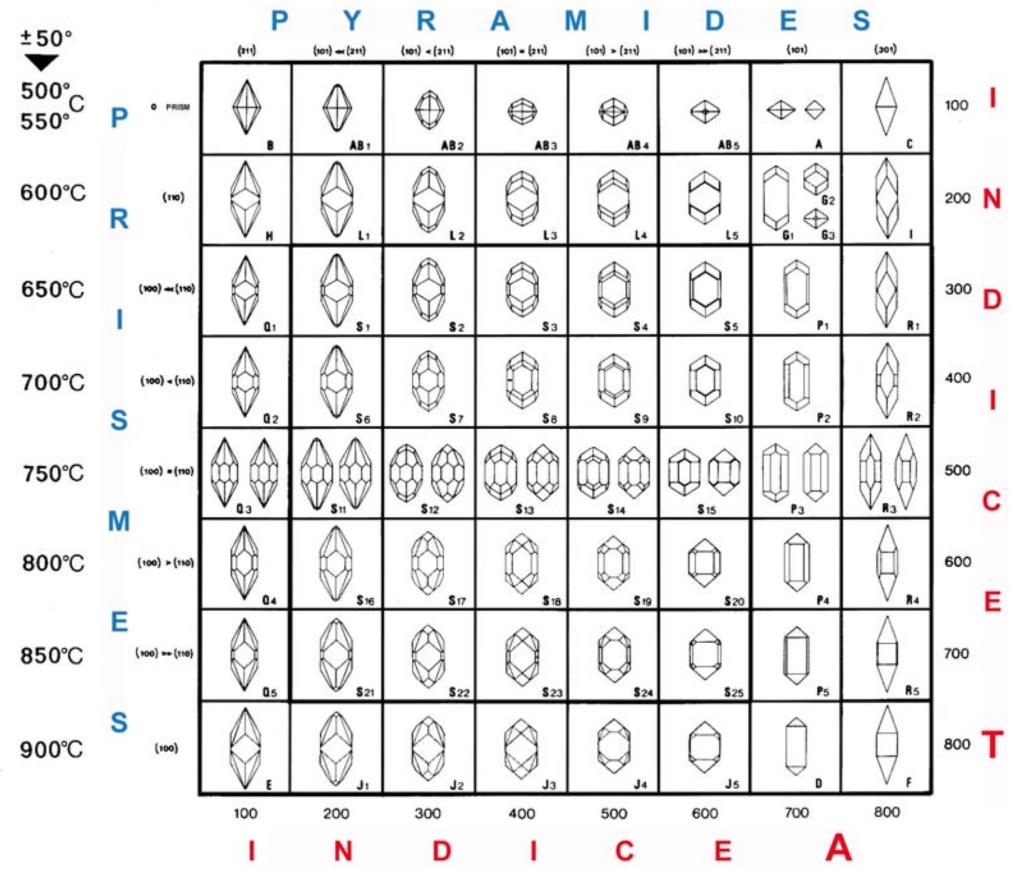

Figure 4.1. Zircon typology diagram (Pupin, 1980).

The secondary types have been derived from the above main types from which they can be deduced by adding one or more extra pyramids, with usually a minor development (Pupin, 1980). For instance S-type crystal (S_1 to S_{25}) with additional {301} pyramid is named as V-type (V_1 to V_{25}). Moreover in alkaline rocks by addition of {301} pyramid to P (P_1 to P_5) and D types, T (T_1 to T_5) and K types are formed (cf. Pupin, 1980).

The typologic distribution has been determined on the basis of the examination of 100 to 150 unbroken zircon crystal whenever possible, and the coordinates (I.Ā. and I.Ť.) are computed (Pupin, 1980) (Figure 4.2).

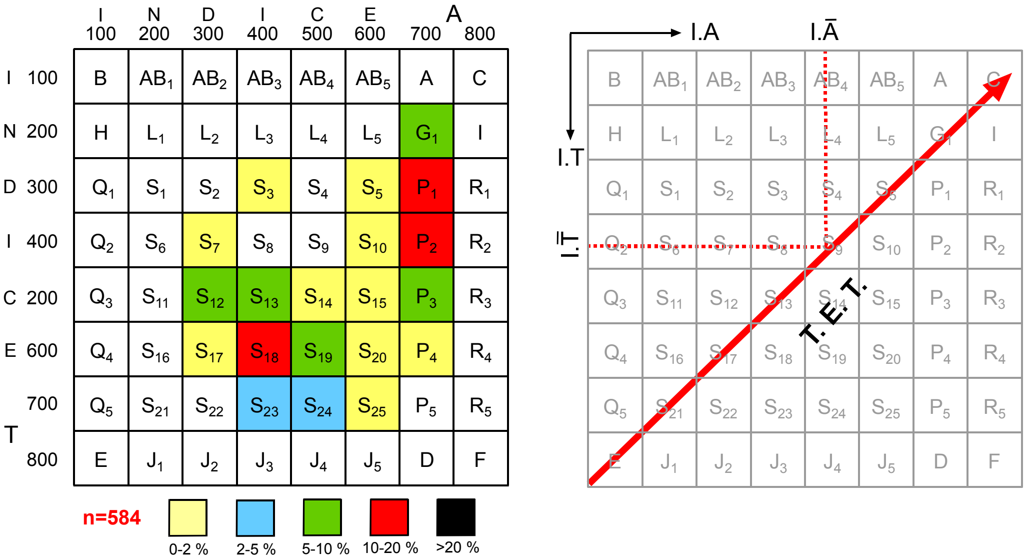

	I 100	N 200	D 300	I 400	C 500	E 600	A 700	800
I 100	B	AB_1	AB_2	AB_3	AB_4	AB_5	A	C
N 200	H	L_1	L_2	L_3	L_4	L_5	G_1 🟩	I
D 300	Q_1	S_1	S_2	S_3 🟨	S_4	S_5 🟨	P_1 🟥	R_1
I 400	Q_2	S_6	S_7 🟨	S_8	S_9	S_{10} 🟨	P_2 🟥	R_2
C 200	Q_3	S_{11}	S_{12} 🟩	S_{13} 🟩	S_{14} 🟨	S_{15} 🟨	P_3 🟩	R_3
E 600	Q_4	S_{16}	S_{17} 🟨	S_{18} 🟥	S_{19} 🟩	S_{20} 🟨	P_4 🟨	R_4
T 700	Q_5	S_{21}	S_{22}	S_{23} 🟦	S_{24} 🟦	S_{25} 🟨	P_5	R_5
800	E	J_1	J_2	J_3	J_4	J_5	D	F

n=584 🟨 0-2 % 🟦 2-5 % 🟩 5-10 % 🟥 10-20 % ⬛ >20 %

Figure 4.2. Zircon population representation: Typologic frequency distribution of the population (left side), and mean point (I. Ā. and I. Ť.) in the (I.A., I.T.) diagram with calculated "Typological Evolutionary Trend" (T.E.T.) of the population (cf. Pupin, 1980) (right side).

I.Ā. and I.Ť. indices are calculated by the following formulas:

$$\text{I. }\bar{\text{A}}\text{.} = \sum_{\text{I.A.} = 100}^{800} \text{I.A. x } n_{\text{I.A.}} \qquad \text{I. }\check{\text{T}}\text{.} = \sum_{\text{I.T.} = 100}^{800} \text{I.T. x } n_{\text{I.T.}}$$

where $n_{\text{I.A.}}$ and $n_{\text{I.T.}}$ are the respective frequencies for each value of I.A. or I.T. ($\Sigma n_{\text{I.A.}} = \Sigma n_{\text{I.T.}} = 1$). The T.E.T. is drawn through the mean point (I. Ā. and I. Ť.) with a slope $a = S_T / S_A$ which is the tangent of the angle between the T.E.T. axis and the I.A. axis.

Standard deviation of A index = $S_A = \sqrt{(A - A)^2 / N}$

Standard deviation of T index = $S_T = \sqrt{(T - T)^2 / N}$
N = number of determined crystals

Pupin (1980) stated that the chemical characteristics of the crystallization medium play a leading role in the origin and relative growth of zircon pyramids. He indicated that zircon originating in a hyperaluminous or hyperalkaline medium show well developed {211} pyramid whereas those grown in an hyperalkaline or hyperaluminous medium have well developed {101} pyramid. The {301} pyramid is remarkable with its development in T-and K-type zircon crystals formed in an potassium-rich alkaline medium, on the other hand, the {112} pyramid mainly occurs in hyperaluminous media (e.g. Pupin, 1980). Thus Pupin (1980) suggested that the Al/alkaline ratio controls the zircon population index Ā. Pupin (1980) also suggested that the relative development of the zircon prisms was depended on the temperature of the crystallization medium, and temperature controlled the index Ť, therefore zircon could be proposed as a geothermometer (Figure 4.1).

The role of water in development of crystal faces in zircon is another subject that should be taken into consideration (e.g. Pupin, 1980). Pupin (1980) stated that in water-poor magmas zircon crystallizes during an early magmatic period whereas in magmas rich in water zircon crystallization begins early in the magmatic period and continues up to the end with the development of trace elements, e.g. U, Th, Y, rich-hydrozircon. In the granitoids formed from water-rich magmas simultaneous crystallization of late zircon with interstitial quartz results in the lowering of the zircon population's index Ť (Pupin, 1980).

Pupin (1980) also stated that metamictization of this hydrozircon commences with time and results in overgrowths with a distinctive zoned structure. Accordingly, Williams (1992) indicated that the decay of radioactive elements (e.g. U and Th showing variation in small-scale zones) not only generates a correlated zonation in the concentration of radiogenic Pb but also, if the temperature remains below that at which zircon anneals, creates a zonation in the extent to which the crystal structure becomes damaged by radiation. He further interpreted that the effect of that damage is to cause a differential expansion of the crystal lattice (Holland and Gottfried, 1955 in Williams, 1992), resulting in the fracturing of the lower Th-U, less damaged zones and a physical weakening of the whole crystal. Metamictization is the end state in conditions of severe radiation damage resulting in the destruction of all trace of the zircon crystal lattice (Williams, 1992). Therefore strong volume expansion of zircon occurs during metamictization (Murakami et al., 1991). Additionally heterogeneous distribution of U and Th in zircon may cause heterogeneous metamictization (Nasdala et al., 1998) leading to local stress and formation of micro-fissures and cracks due to heterogeneous expansion (Nasdala et al., 2001).

It should be noted that the zircon typology studies have to be accompanied by petrographical and mineralogical studies concerning the associations of other main and accessory minerals, and on the field by investigating the presence or absence of basic microgranular xenoliths, associated microgranites, rhyolites or basic rocks (Pupin, 1980).

Pupin (1980) stated that the typologic study of zircon populations from granitic rocks lead to the proposition of a genetic classification with three main divisions as (a) granitoids of crustal (or mainly crustal) origin, (b) hybrid (crustal+mantle origin) granitoids and (c) granitoids of mantle (or mainly mantle) origin. Brief descriptions of these groups are presented below.

(a) Granites of crustal or mainly crustal origin

These granites can be assumed to be identical to S-type or syn-collisional granitoids characterized by crustal or mainly crustal origin.

1. _Autochthonous and intrusive aluminous leucogranites_: The zircon populations of this group are characterized by very low Ā and Ť indices (260-390) (Figure 4.3) with subtypes $L_{1-2,}$ and $S_{1-2-3-6-7}$. They are generally holo-leucocratic granites rich in quartz, two feldspars, biotite and some primary muscovite ± aluminous silicates (andalusite, sillimanite) ± cordierite ± zircon ± apatite ± monazite ± anatase ± garnet ± tourmaline. They thought to be formed by the anatexis of hydrous crystalline schists under low P-T conditions (e.g. Pupin, 1980).

2. _(Sub)autochthonous monzogranites and granodiorites_: The zircon populations of this group are characterized by low Ā (~300) and Ť (~350) indices (Figure 4.3) with subtypes $S_{1-2-3-6-7}$. These granitoids have anatectic origin since they can be traced to the migmatites without any break on the field. They are generally biotite granites including cordierite nodules with accessory mineral suite similar to that of aluminous leucogranites (zircon, apatite, anatase-brookite, monazite ± garnet ± tourmaline) (Pupin, 1980).

3. _Intrusive aluminous monzogranites and granodiorites_: The zircon populations of this group have low Ā and Ť indices (250-440) (Figure 4.3) with subtypes $S_{1-2-3-7-8-12}$. These granitoids are typically porphyroid granites and/or cognate granodiorites with quartz, K-feldspar, oligoclase-andesine, biotite, secondary muscovite + (idiomorphic) cordierite + monazite + zircon + apatite +

anatase (very rarely titanite) ± garnet ± tourmaline. Granitoids of this group include basic microgranular xenoliths indicating little mantle contribution, i.e. hybridization (Pupin, 1980).

(b) Granites of crustal+mantle origin, hybrid granites

These granites can be assumed to be identical to H-type or I-type granitoids having sources hybridized by crustal and mantle sources.

4. *Calc-alkaline series granites*: They typically include basic microgranular xenoliths in varying quantities and sometimes associated with basic rocks (gabbro, quartz gabbro, diorite, quartz diorite). This group is characterized by zircon populations having large ranges of Ā (higher than those of first 3 group) and Ť (from very high to low) indices, and has been divided into three main stocks (4 a-c) depending on their mineral contents and T.E.T.'s (Pupin, 1980).

Stock 4a: biotite granodiorite - biotite ± secondary muscovite monzogranite – biotite ± secondary muscovite alkaline granite. Subtypes G, P_1, and $S_{4\text{-}5\text{-}10}$ are common in this stock (Pupin, 1980).

Stock 4b: biotite ± amphibole granodiorite – biotite ± amphibole monzogranite – biotite ± secondary muscovite monzogranite - biotite ± secondary muscovite alkaline granite. Subtypes G, P_1, L_5 and $S_{5\text{-}10\text{-}13\text{-}14\text{-}18\text{-}19}$ are common in this stock (Pupin, 1980).

Stock 4c: biotite ± amphibole ± pyroxene granodiorite - biotite ± amphibole ± pyroxene monzogranite - biotite ± secondary muscovite alkaline granite. Subtypes $S_{5\text{-}10\text{-}15\text{-}18\text{-}19\text{-}20\text{-}23\text{-}24\text{-}25}$, and $P_{2\text{-}3\text{-}4}$ are common in this stock (Pupin, 1980).

Granitoids of stock 4c include greater amounts of microgranular basic xenoliths. At the end of differentiation (or at the end of crystallization of the more differentiated rocks), all these stocks converge on the G-type (Pupin, 1980) (Figure 4.3).

5. *Sub-alkaline series granites*: The zircon population of this group display distribution between calc-alkaline and alkaline series (but also overlap the calc-alkaline series) with higher Ā and variable Ť indices (Figure 4.3). At the end of differentiation (or at the end of crystallization of the more differentiated rocks), the stock converges on the G-type as in the calc-alkaline series. The rocks of this group exhibiting primarily mantle origin are generally monzogranite, syenogranite with quartz microcline – oligoclase – biotite – hornblende, biotite monzogranite, or biotite + secondary muscovite leucomonzogranite (Pupin, 1980).

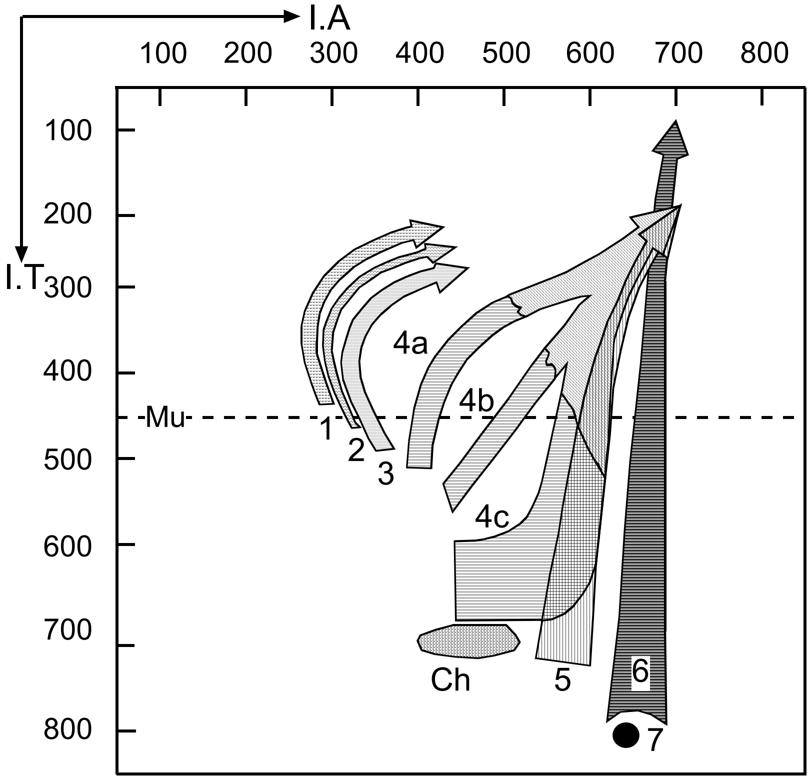

Figure 4.3. Distribution of mean points and mean T.E.T. of zircon populations from: *Granites of crustal or mainly crustal origin* [(1) aluminous leucogranites; (2) (sub) autochthonous monzogranites and granodiorites; (3) intrusive aluminous monzogranites and granodiorites], *granites of crustal+mantle origin or hybrid granites* [(4a, b, c) calc-alkaline series granites (horizontal stripped area = granodiorites + monzogranites, oblique stripped area = monzogranites + alkaline granites); (5) sub-alkaline series granites], *granites of mantle or mainly mantle origin* [(6) alkaline series granites; (7) tholeiitic series granites. Mu: limit of muscovite granites, Ch: magmatic charnockites area.

(c) Granites of mantle or mainly mantle origin

6. *Alkaline series granites*: Alkaline and hyperalkaline granitoids that are found in subvolcanic, anorogenic complexes are interpreted to be involved in this group (Pupin, 1980). Post-orogenic A-type granitoids also belong to this group (Bonin et al., 1998). These granitoids showing string perthites constitute iron-rich minerals such as fayalite, ferro-augite, hedenbergite, aegerine, hastingsite, riebeckite, arfvedsonite and biotite (near the annite composition). Zircon types locate along the right hand-side part of the typology diagram with very high Ā and Ť indices. Zircon crystals typically demonstrate preferential development of {101} pyramid and remarkable occurrence of {301} pyramid (e.g. in K and T types). This stock trends towards the G-type (then the A-type) with vertical T.E.T. (Figure 4.3) (Pupin, 1980).

7. *Tholeiitic series granites*: The zircon population of this group display very localized distribution as clustering right-bottom of the typology diagram with very high Ā and Ť indices (Figure 4.3), and common distinct subtypes as N_5 and K_1. Plagiogranites with trondhjemitic composition are assumed to characterize the rocks of this group (Pupin, 1980).

Pupin's method was received many critiques since it introduced a spectacular theory in to a granitoid petrogenesis. Benisek and Finger (1993) indicated that morphology of granite zircons is not a reliable geothermometer as suggested by Pupin (1980), since the size relations of two zircon prisms are strongly dependent on the chemistry of the growth medium.

Experimental works carried out by Watson (1979) showed that the zircon saturation level in felsic liquids depends strongly on the molar $(Na_2O+K_2O)/Al_2O_3$ ratio of the melts, but less sensitive to temperature. Accordingly, Benisek and Finger (1993) stated that development of a {110} dominated prism form is favored by a high abundance of U cations in the granite melt, which produces a growth blocking effect on {110} crystal surfaces of zircons. They further stated that the presence of a $Y(REE)PO_4$ solid solution component in the zircon lattice may also produce crystals with {110} forms. Therefore as a cooling granite melt will very often become enriched in U, Th, Y(REE) by fractional crystallization, there should be a general tendency for zircons to crystallize with {110} forms in cooler magmas yielding plausible results of Pupin’s zircon thermometer (Benisek and Finger, 1993). Additionally a renewed magma or fluid input into the system, or fractionation of minerals, which save the capacity to capture, U and Y may be responsible, given that zircons with a 100}-dominated outer form may well develop also during cooling of granite (Benisek and Finger, 1993). That’s why in this study zircon is not used for geothermometric descriptions.

In spite of ongoing discussion, the method is applicable to various granitoids from several settings and environments, and consistent results were demonstrated by many studies (e.g. Pupin and Persoz, 1999; Sheepers et al., 1999; Fekkak et al., 2000; Klötzli et al., 2001; Tikhomirova, 2002; Willner et al., 2003; Köksal et al., 2004b).

4.2. Methods of Typology Study

4.2.1. Enrichment

Zircon crystals were enriched through standard enrichment techniques. Thirteen granitoid samples (i.e. SK-1, 2, 3, 4, 5, 6, 7, 8, 9, 10, 11a, 11b, 12) collected from the field were finely crushed in three steps. At the first step samples were crushed into the pieces of 100-150 g in weight. At the second step they were further crushed into 1-2 cm in diameter. At the final step the pieces that were obtained at the second step were finely crushed into max 0.5 cm in diameter using Spex 4200 model jaw crusher and prepared for powdering. The samples were finely crushed and ground by the roller crusher in the Mining Engineering Department of M.E.T.U. Samples are then sieved, and <500 μm fractions were obtained. Samples range in <500 μm were enriched in heavy minerals by using the Sturtevant 1964 model shaking table in the Mining Engineering Department of M.E.T.U. The total weight of samples at the beginning of the separation, and weight of samples after shaking table step are presented in Table 4.1. During shaking table step the heavy fraction was selected as large as possible to prevent sample loss.

Table 4.1. Distribution of samples into heavy fractions after shaking table step.

Sample No	Total Weight (g)	Weight After Shaking Table Step (g)
SK-1	8012	477.93
SK-2	5864	374.05
SK-3	19538	490.52
SK-4	13308	298.34
SK-5	6177	256.51
SK-6	6187	294.66
SK-7	12262	377.40
SK-8	20771	477.68
SK-9	7724	180.07
Sk-10	11041	685.44
SK-11a	8035	113.14
SK-11b	6162	86.92
SK-12	16112	394.90
TOTAL	**141193**	**4507.56**

The separation of the heavy minerals by heavy liquid was performed on the samples obtained after shaking table step. Bromoform with density of 2.82 g/cm^3 was used for this process. The heavy liquid separation and separation of magnetic minerals by using the Frantz isodynamic magnetic separator were conducted in the Mineral Separation Laboratories of Geological Engineering Department of M.E.T.U.

The obtained portions were purified under microscope by separation of zircon crystals from other heavy minerals by handpicking under binocular stereomicroscope. Zircon picking step was partly made in the Mineral Separation Laboratories of Geological Engineering Department of M.E.T.U. and continued in the Optic Mineralogy Laboratory of Geology Department of Potsdam University (Potsdam/Germany). During this step, zircon crystals were picked without considering whether they were unbroken, euhedral or not.

By this way, it was aimed to collect all zircon crystals within the samples. Among the collected samples, from SK-2, which was taken from the silica-undersaturated alkaline granitoid around the Çanhoca Hill in the Akpınar area, it was not possible to obtain zircon crystals adequate for the typology study. This occasion was assumed to be related to the mineralogical characteristics and scarce zircon content of this sample. Hence studies were carried out on the other twelve granitoid samples.

4.2.2. Sample Preparation for Scanning Electron Microscope (SEM) Study

After getting all the available zircon crystals from the samples, unbroken and euhedral zircon crystals which represent the zircon populations of the granitoids separated for SEM and cathodoluminescence (CL) investigations. For most of the samples two or more steps of the separation procedure were needed for providing the most representative fraction. From each sample at least 12 crystals were selected for SEM and CL studies. Zircon samples for SEM investigations were prepared in the Optic Mineralogy Laboratory of the Geology Department of Potsdam University (Germany).

Under the binocular microscope, zircon crystals were mounted row by row onto the double-sided sticky tape, which is placed on top of the sample disc. Crystals from different granitoid samples were mounted onto the different discs. Each crystal was coded depending on the sample name and crystal order [e.g., second crystal of granitoid sample SK-8 was coded as Z8(2)] to avoid of mixing of SEM images. Same crystal codes were used throughout the whole study. Crystals in each row were selected to be the similar in thickness to prevent sample loose during etching for CL study. Then samples were coated for the morphological imaging by sputter coating device SCD 050 (BALTEC), using carbon alloy.

4.2.3. Analytical Methods

SEM study was carried out in the SEM Laboratory of GFZ by the scanning electron microscope DSM 962/Zeiss equipped with Zeiss cathodoluminescence detector using a 15 kV accelerating potential. Overviews and the morphological images of single zircons were done using the BSE (Back Scattered Electrons) detector which receive its signals from the sample straight vertically beneath it.

SEM imaging was performed in two steps: first totally 295 crystals were imaged three by three (or four by four) by 100x - 150x magnification. These overview images were studied in detail on the computer screen to choose the most typical, representative and informative euhedral and unbroken, and in some cases the crystals with interesting features. Totally 54 crystals (out of 295) were chosen for high-resolution SEM imaging. In the second step high-resolution SEM imaging was performed on these crystals by 250x - 500x magnification.

By using the information from SEM study, zircon crystals were counted under the binocular microscope to determine the amounts/percentages of the different typologies within the population.

4.2.4. Typology Study

Typologic investigation was performed on the separated zircon crystals under binocular microscope along with the images obtained by SEM study. Zircon crystals were examined depending on the method explained by Pupin (1980). Each crystal was described considering its relative development of the crystal surfaces. About 100 or more grains were selected from each sample and classified into the zircon types (cf. Pupin, 1980).

Typology method to define the zircon populations was applied to the granitoid samples after counting and classifying all obtained zircon crystals based on the methodology explained briefly in Section 4.1.

4.3. Application of Zircon Typology Method to the Central Anatolian Granitoids

Granitoid samples from central Anatolia were investigated by using the zircon typology method, which is described in detail by Pupin (1980), and explained briefly in Section 4.1. The calculated mean points (i.e. I.Ā and I.Ť indices), standard deviations (i.e. S_A and S_T), slopes (a) and angle (α) of the "Typological Evolutionary Trend" are shown in Table 4.2. Totally 3001 crystals were examined under binocular microscope to infer comprehensive implications.

Zircon crystals enriched from the granitoids of the Ekecikdağ, Ağaçören and Terlemez plutons are generally colorless, transparent, white, yellow, pale yellow, brownish yellow with some brown to dark brown varieties. Most of the crystals are euhedral with well defined crystal surfaces but corroded and metamictized grains are also present. Zircon crystals consist titanite and apatite inclusions, but clear and inclusion free crystals rarely exist.

Zircon crystals of the studied granitoids range from <60 μm to ~500 μm, with abundance within the range of 75 to150 μm.

Table 4.2. Statistical zircon typology elements (cf. Pupin, 1980) of the Ekecikdağ, Ağaçören and Terlemez plutons.

SAMPLE	I.Ā	I.Ť	S_A	S_T	A	α(°)	n
SK-1	555	474	147.88	148.00	1.00	45	584
SK-3	682	314	64.18	104.92	1.64	59	230
SK-4	679	376	67.26	115.53	1.72	60	387
SK-5	700	333	6.70	89.82	13.41	86	223
SK-6	374	526	74.47	83.51	1.12	48	57
SK-7	501	526	66.78	83.51	1.25	51	223
SK-8	290	397	68.78	96.00	1.40	54	312
SK-9	579	538	110.69	63.76	0.58	30	214
SK-10	673	346	75.31	86.18	1.14	49	212
SK-11a	421	485	89.96	103.13	1.15	49	104
SK-11b	423	620	62.94	70.52	1.12	48	103
SK-12	471	692	79.76	43.01	0.54	28	352

4.3.1. Ekecikdağ Pluton

4.3.1.1. Borucu Granodiorite-Monzogranite

Zircons of the Borucu Granodiorite-monzogranite are commonly white, yellow, pale yellow, brownish yellow and rarely dark brown. Zircon types are $S_{18-19-23-24-12-13-5-10}$, P_{1-2-3} and G_1 among which S_{18}, P_1 and P_2 are the dominant ones (Figure 4.4).

In Figure 4.5 zircon crystal [Z1(2)] showing larger {100} prism than asymmetric {110} prism and including {101} pyramid but not {211} pyramid is of P_4 type. On the other hand, [Z1(5)] (Figure 4.6) with {100}>{110} and {101}={211} typological characteristics is a S_{18} type crystal. Figure 4.7 illustrates S_{12} type crystal [Z1(21)] with {100}={110} and {101}<{211} typological characteristics. P_2 which is one of the most common crystal type in the Borucu granitoid is represented by [Z1(30)] illustrated in Figure 4.8. The zircon types of Borucu granitoid show a distribution from middle to upper right part of the typology diagram reaching to the type G_1 (e.g. [Z1(44)] in Figure 4.9). They are generally short prismatic but long crystals (e.g. [Z1(4)] and [Z1(51)] in Figure 4.4; [Z1(45)] in Figure 4.10) are also present.

T.E.T. of the Borucu granitoid is comparable with that of 4b-type, which is defined as calc-alkaline hybrid type by Pupin (1980) (Figure 4.11).

4.3.1.2. Kalebalta Leucogranite

The Kalebalta leucogranite is one of the most distinct types among the studied granitoid samples. Zircon crystals exhibit preferential presence of G_1, P_1 and P_2 types (Figures 4.12, 4.13) with rare P_{3-4}, $S_{5-10-13-14-20}$ (Figures 4.12, 4.14, 4.15), S_{15} (with {001} pinacoid surface) and G_3 types.

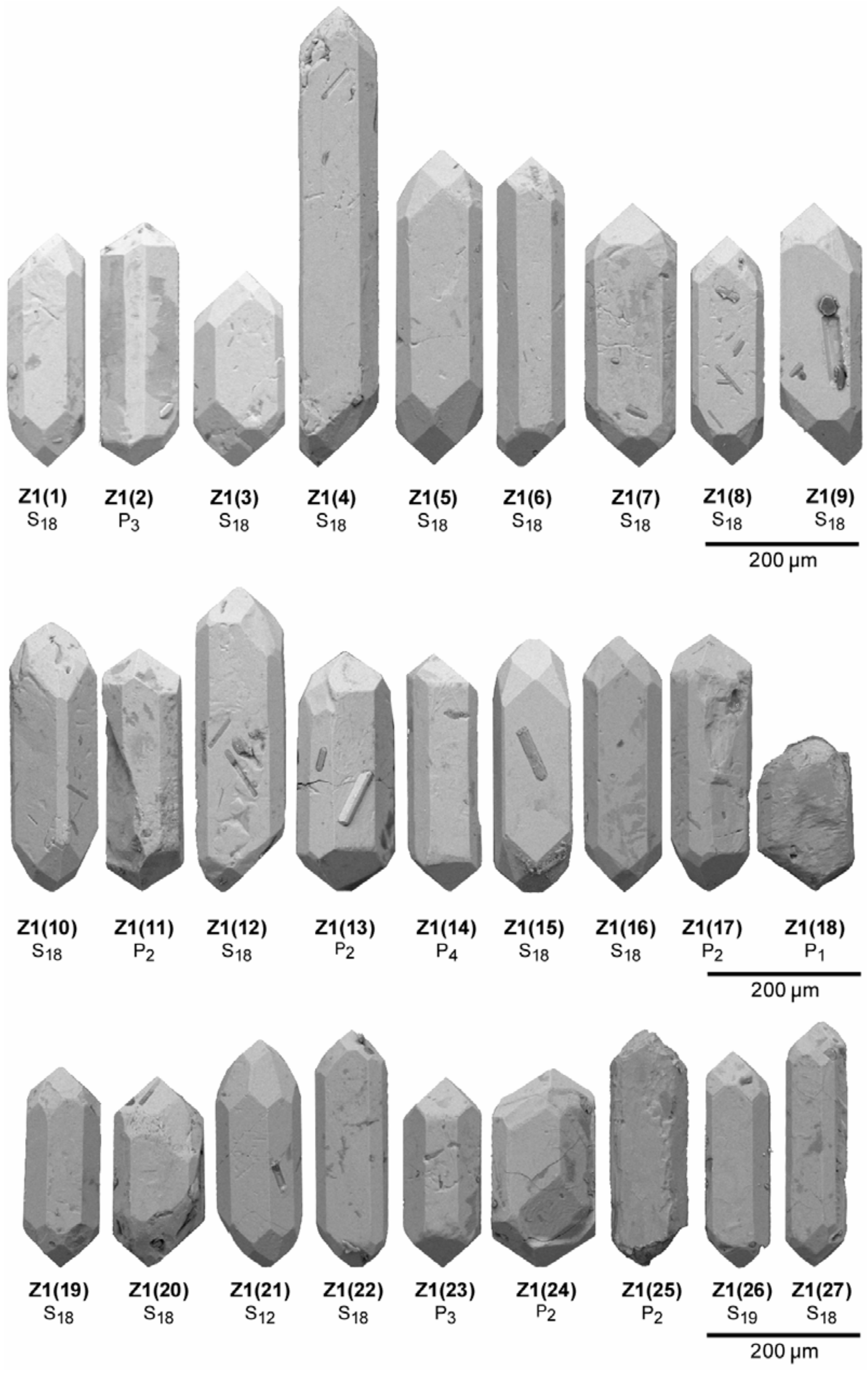

Figure 4.4. SEM images of the selected zircon crystals from the Borucu granodiorite-monzogranite (SK-1).

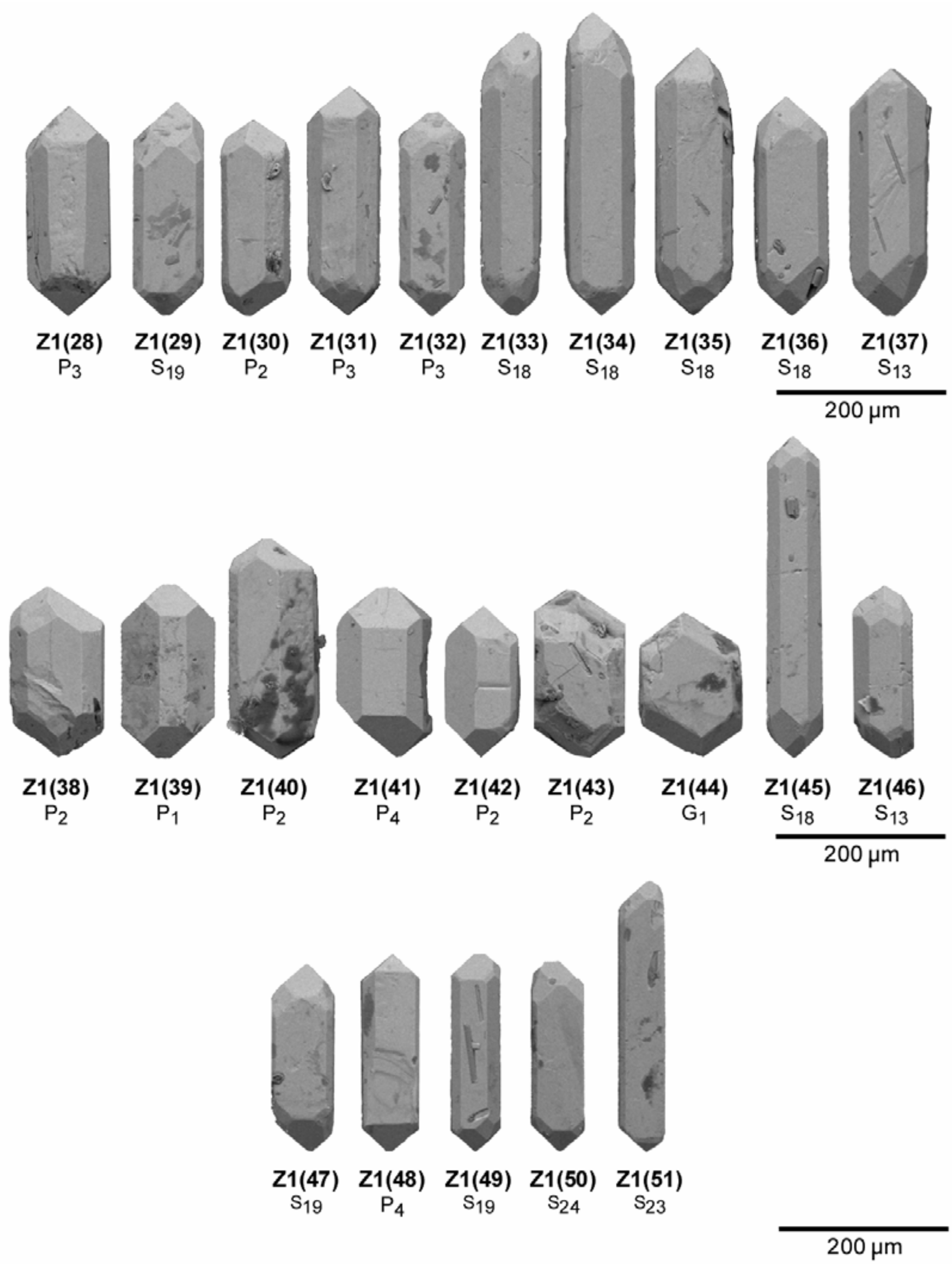

Figure 4.4 (cont'd).

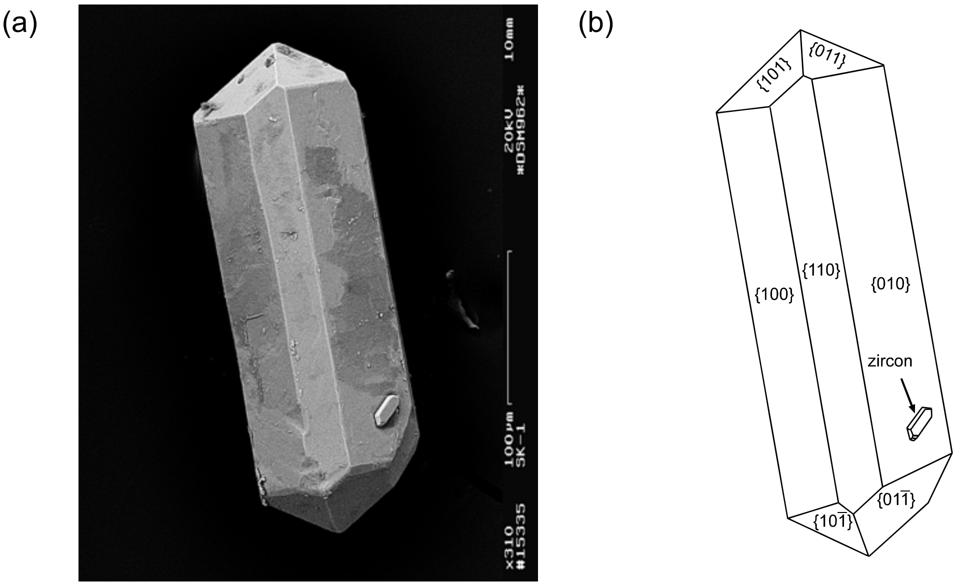

Figure 4.5. Zircon crystal [Z1(2)] from the Borucu granodiorite-monzogranite (sample SK-1): (a) High-resolution SEM photograph, (b) Sketch model showing the crystal surfaces.

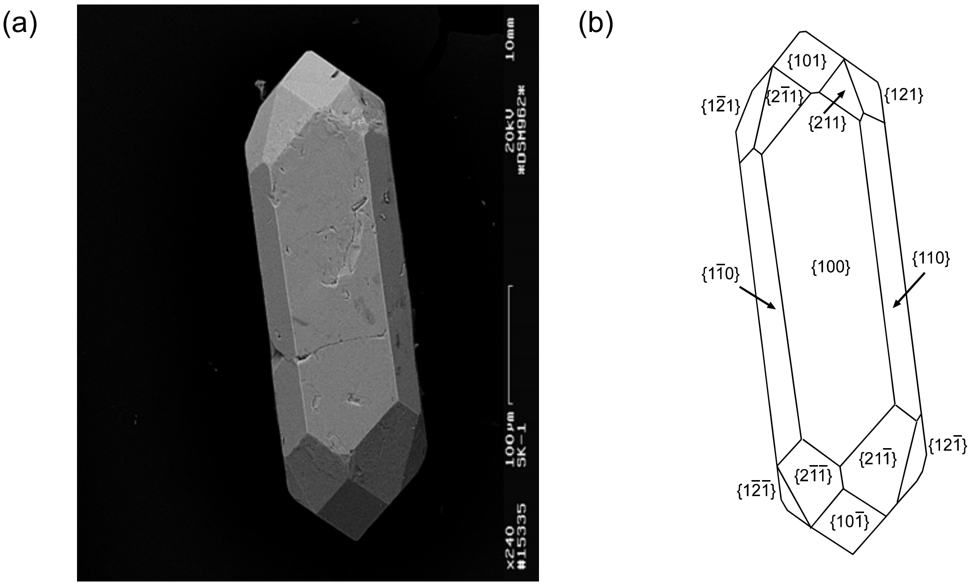

Figure 4.6. Zircon crystal [Z1(5)] from the Borucu granodiorite-monzogranite (sample SK-1): (a) High-resolution SEM photograph, (b) Sketch model showing the crystal surfaces.

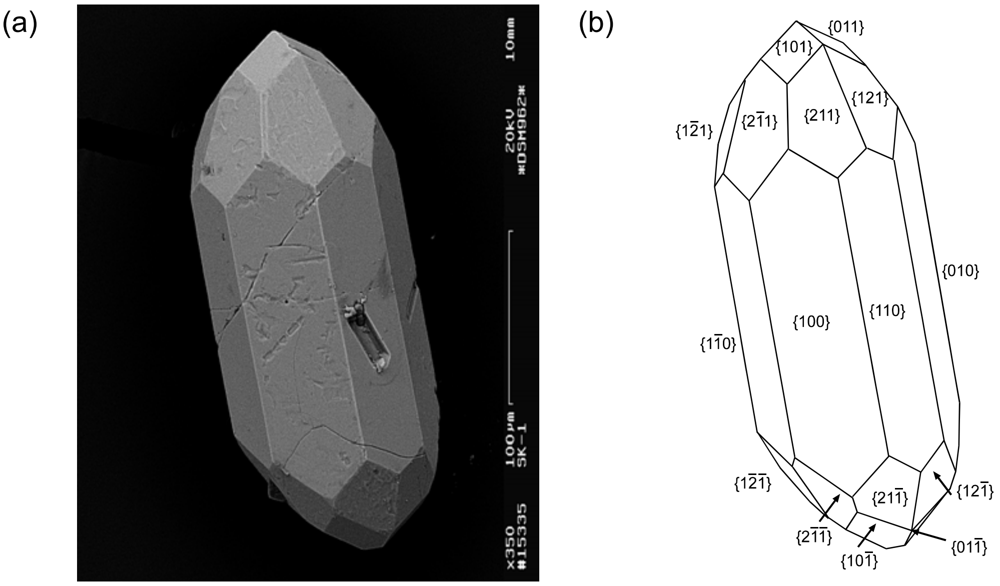

Figure 4.7. Zircon crystal [Z1(21)] from the Borucu granodiorite-monzogranite (sample SK-1): (a) High-resolution SEM photograph, (b) Sketch model showing the crystal surfaces.

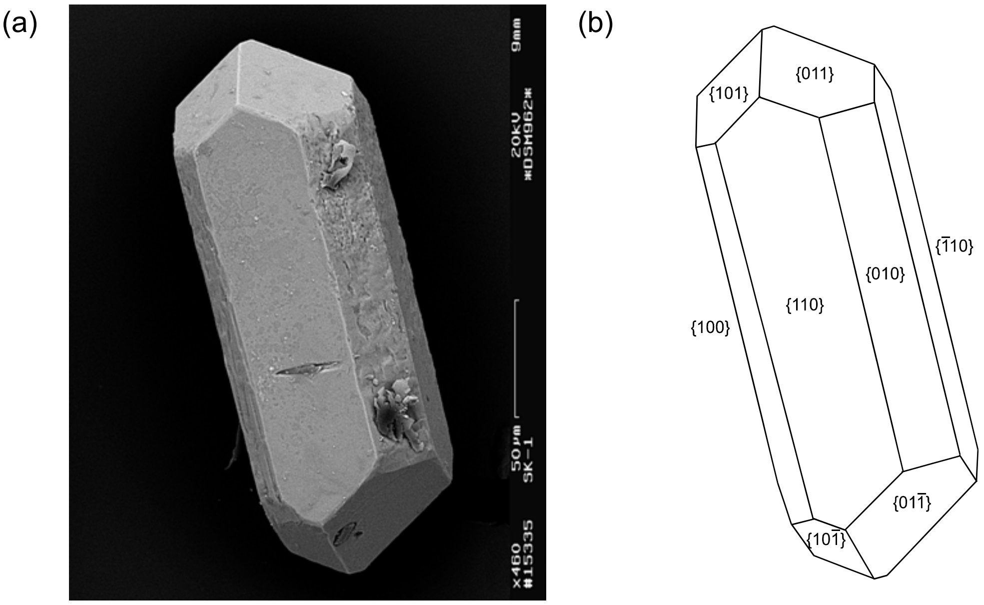

Figure 4.8. Zircon crystal [Z1(30)] from the Borucu granodiorite-monzogranite (sample SK-1): (a) High-resolution SEM photograph, (b) Sketch model showing the crystal surfaces.

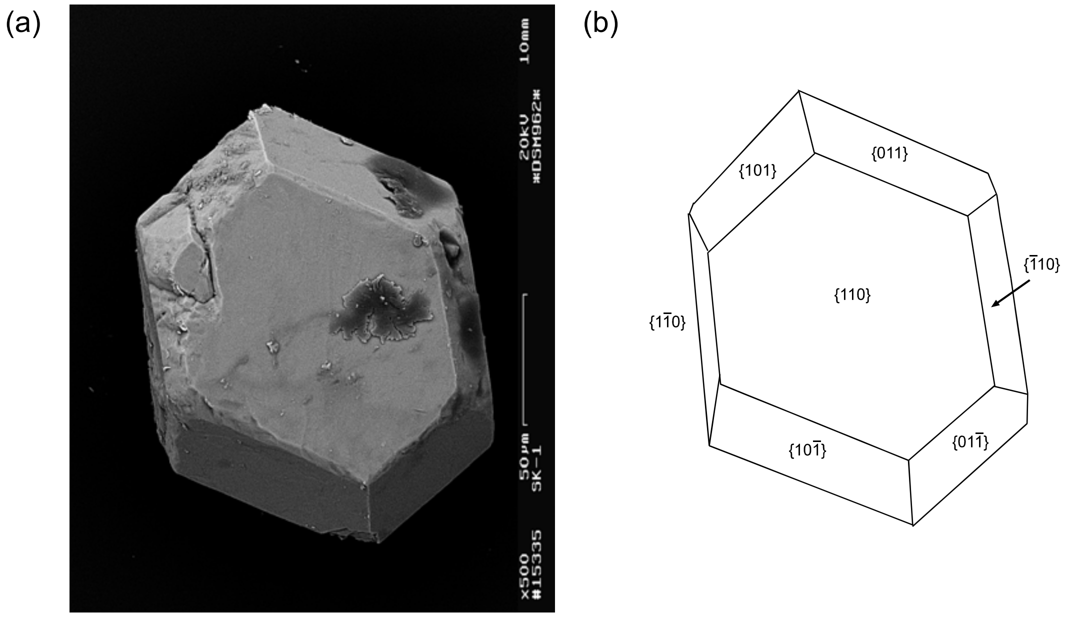

Figure 4.9. Zircon crystal [Z1(44)] from the Borucu granodiorite-monzogranite (sample SK-1): (a) High-resolution SEM photograph, (b) Sketch model showing the crystal surfaces.

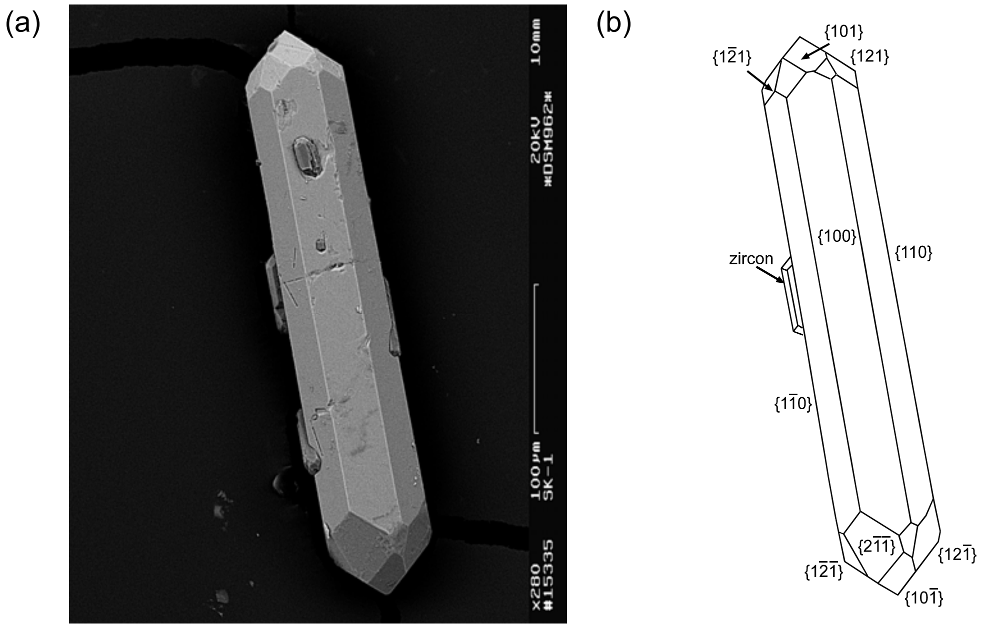

Figure 4.10. Zircon crystal [Z1(45)] from the Borucu granodiorite-monzogranite (sample SK-1): a) High-resolution SEM photograph, (b) Sketch model showing the crystal surfaces.

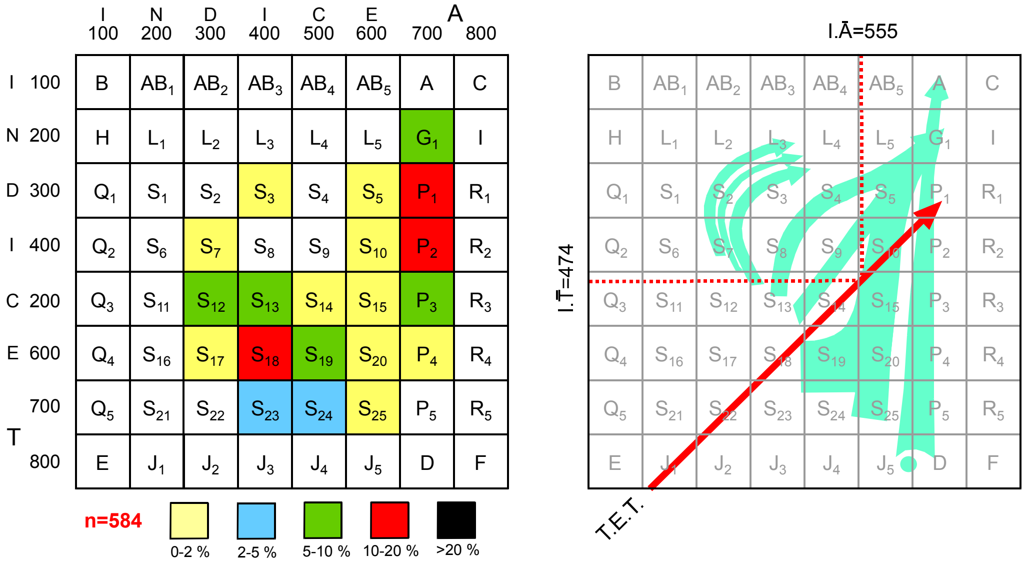

Figure 4.11. Distribution of the zircon crystals from the SK-1 (Borucu granodiorite-monzogranite) sample on the Pupin (1980)'s typologic diagram (left side), and Typologic Evolution Trend with the mean points (I. Ā. and I. Ť.) (right side).

Zircon crystals of the Kalebalta granitoids are highly corroded, white, colorless, pink, pale yellow, reddish and brownish crystals with radial cracks pointing metamictization (Figures 4.16 and 4.17).

T.E.T. of the Kalebalta leucogranite fit with that of the Stock 4b (cf. Pupin, 1980), which represents the hybrid granitoids (Figures 4.18), although the field and geochemical features discussed in the Chapter 3 suggest mainly crustal origin (e.g. Group 1, 2 or 3). However epitaxial overgrowth of the crystals (e.g. [Z3(13)] in Figure 4.19) and complex features with numerous inclusions and parallel (should be revealed by CL) overgrowths (e.g. [Z3(26)] in Figure 4.20 and [Z3(40)] in Figure 4.21), indicating discontinuous growth history of the mineral, suggest that the final zircon population does not likely represent the main characteristics of the granitoid.

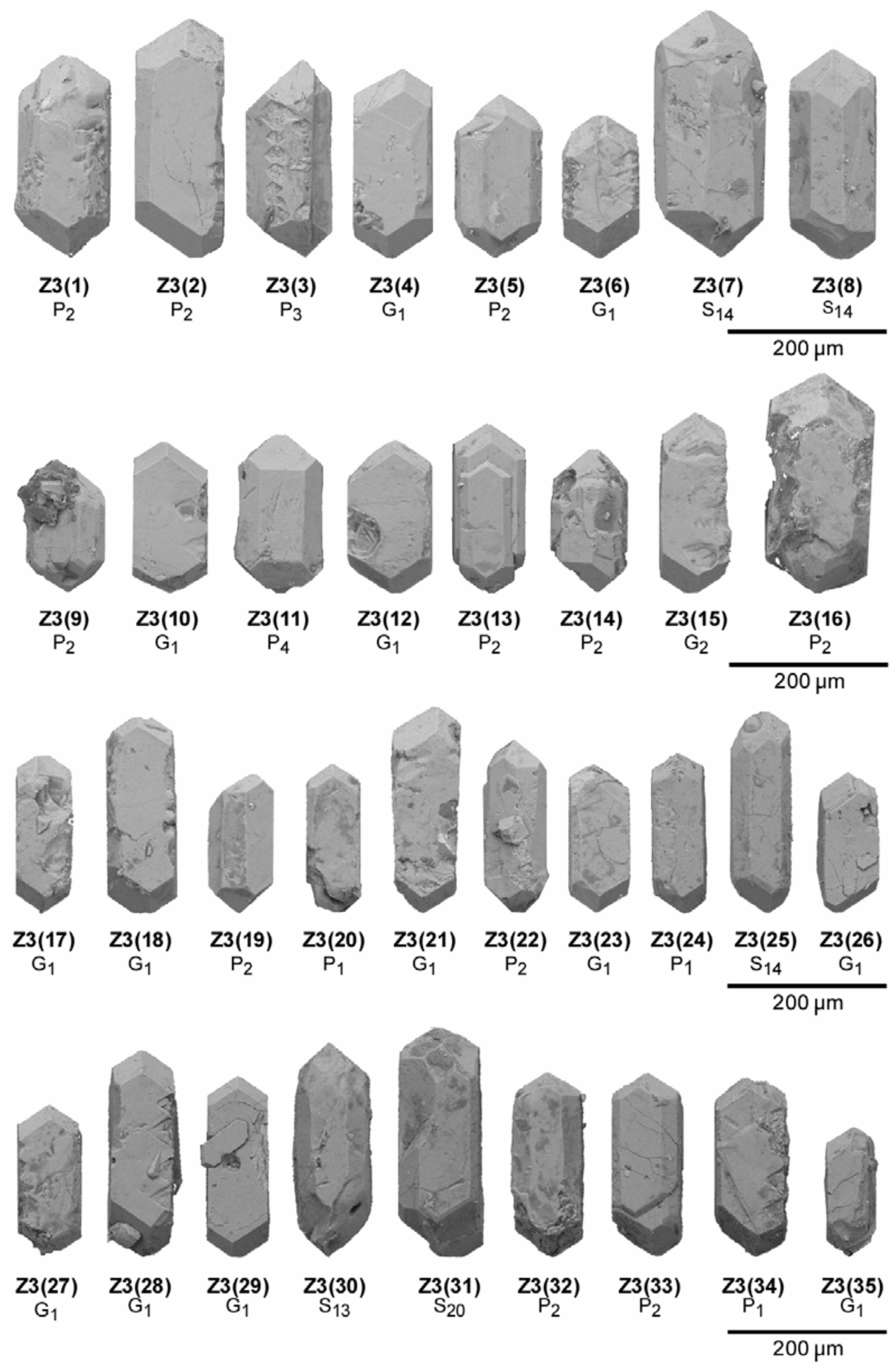

Figure 4.12. SEM images of the selected zircon crystals from the Kalebalta leucogranite (SK-3).

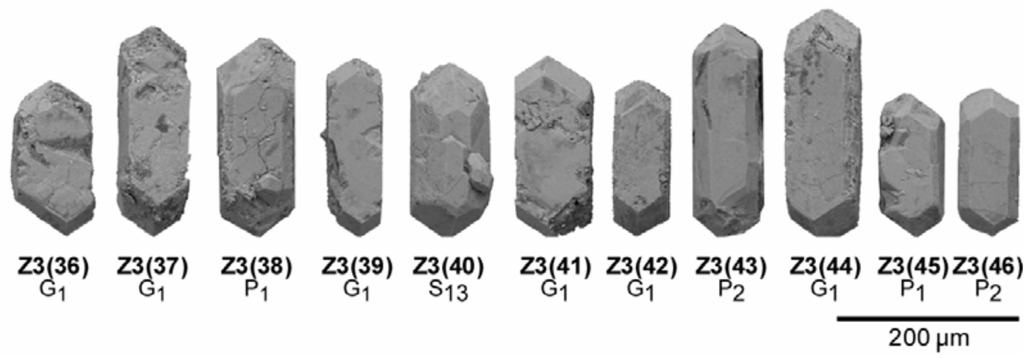

Figure 4.12 (cont'd).

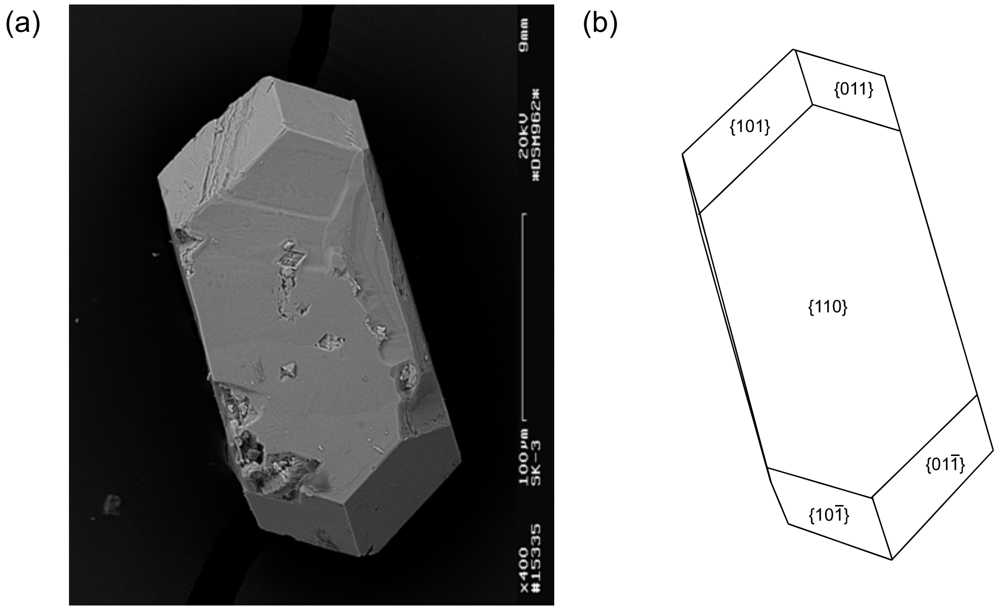

Figure 4.13. Zircon crystal [Z3(4)] from the Kalebalta leucogranite (sample SK-3): (a) High-resolution SEM photograph, (b) Sketch model showing the crystal surfaces.

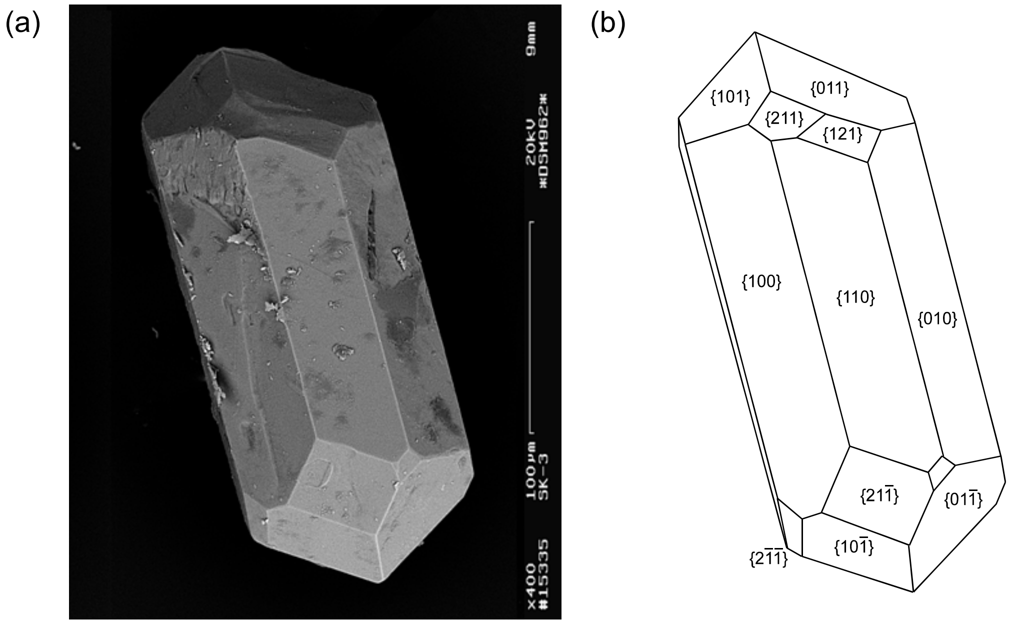

Figure 4.14. Zircon crystal [Z3(8)] from the Kalebalta leucogranite (sample SK-3): (a) High-resolution SEM photograph, (b) Sketch model showing the crystal surfaces.

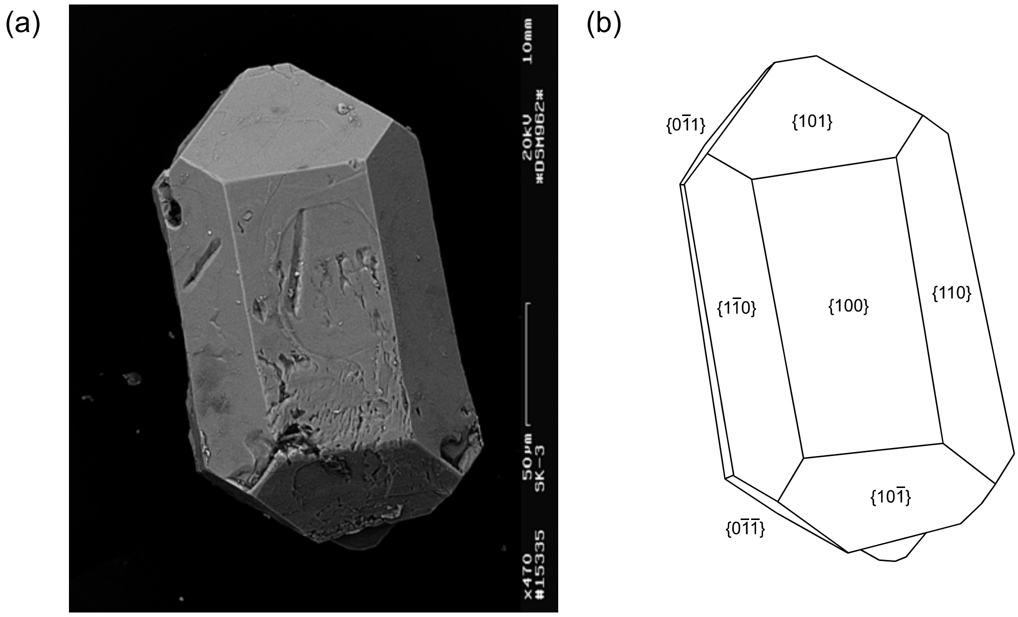

Figure 4.15. Zircon crystal [Z3(11)] from the Kalebalta leucogranite (sample SK-3): (a) High-resolution SEM photograph, (b) Sketch model showing the crystal surfaces.

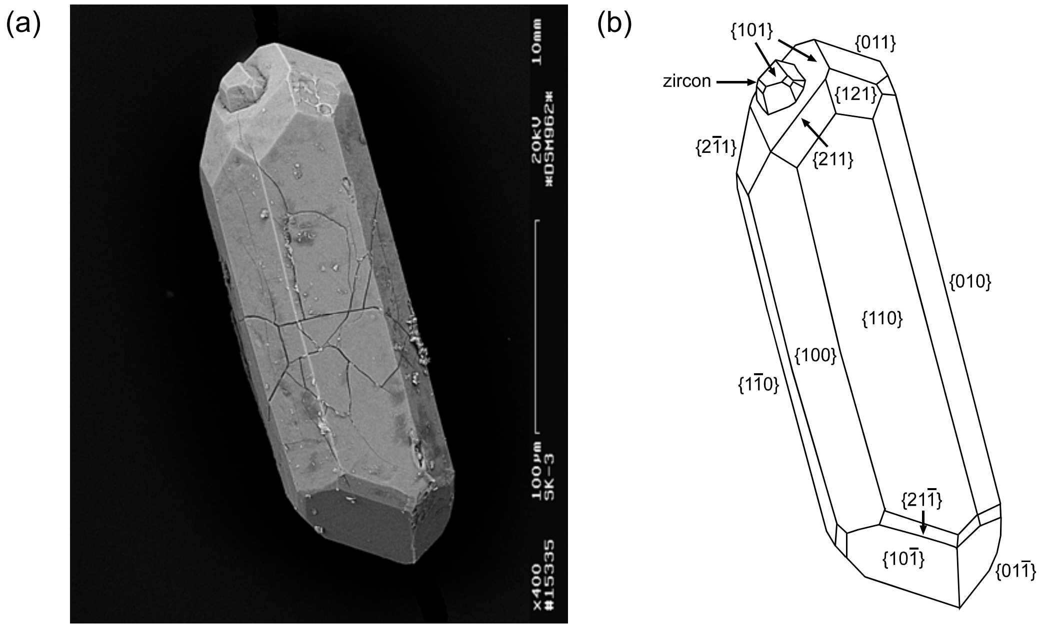

Figure 4.16. Zircon crystal [Z3(25)] from the Kalebalta leucogranite (sample SK-3): (a) High-resolution SEM photograph, (b) Sketch model showing the crystal surfaces.

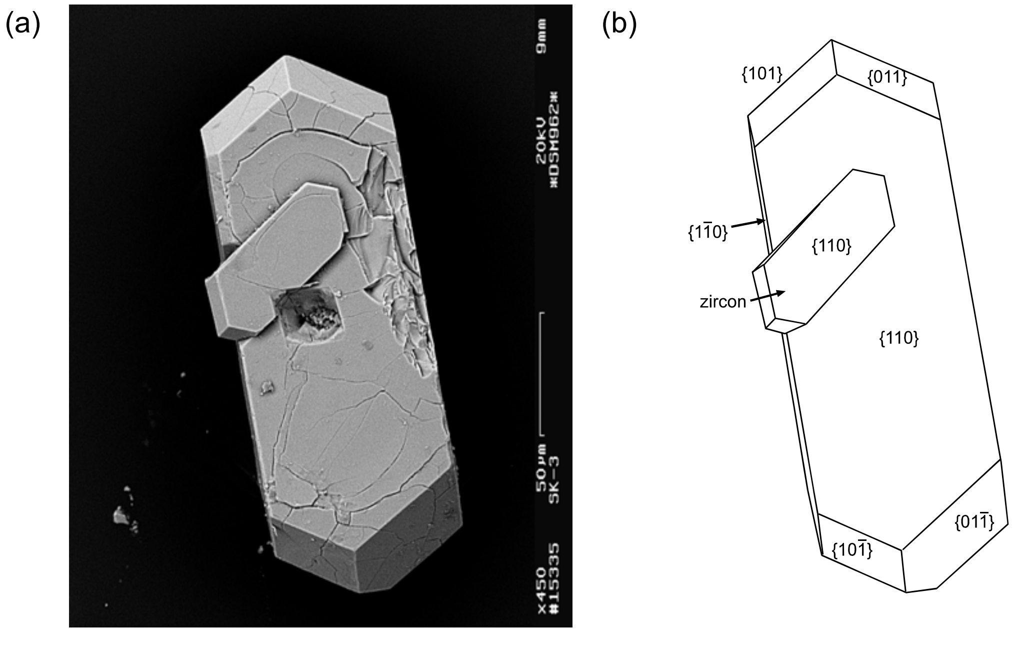

Figure 4.17. Zircon crystal [Z3(29)] from the Kalebalta leucogranite (sample SK-3): (a) High-resolution SEM photograph, (b) Sketch model showing the crystal surfaces.

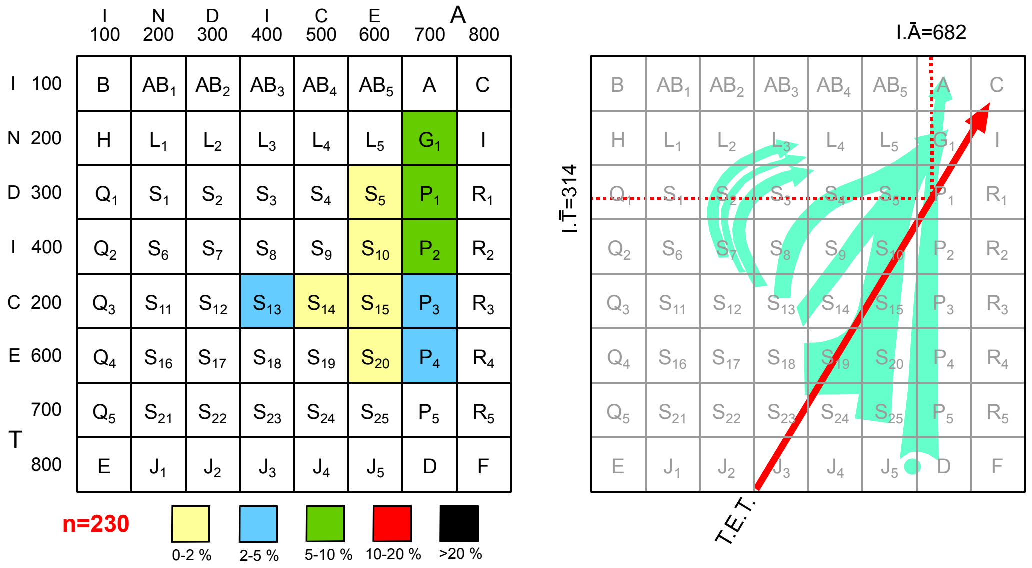

	I 100	N 200	D 300	I 400	C 500	E 600	700	A 800
I 100	B	AB_1	AB_2	AB_3	AB_4	AB_5	A	C
N 200	H	L_1	L_2	L_3	L_4	L_5	🟩 G_1	I
D 300	Q_1	S_1	S_2	S_3	S_4	🟨 S_5	🟩 P_1	R_1
I 400	Q_2	S_6	S_7	S_8	S_9	🟨 S_{10}	🟩 P_2	R_2
C 200	Q_3	S_{11}	S_{12}	🟦 S_{13}	🟨 S_{14}	🟨 S_{15}	🟦 P_3	R_3
E 600	Q_4	S_{16}	S_{17}	S_{18}	S_{19}	🟨 S_{20}	🟦 P_4	R_4
700	Q_5	S_{21}	S_{22}	S_{23}	S_{24}	S_{25}	P_5	R_5
T 800	E	J_1	J_2	J_3	J_4	J_5	D	F

n=230

🟨 0-2 % 🟦 2-5 % 🟩 5-10 % 🟥 10-20 % ⬛ >20 %

Figure 4.18. Distribution of the zircon crystals from the SK-3 (Kalebalta leucogranite) sample on the Pupin (1980)'s typologic diagram (left side), and Typologic Evolution Trend with the mean points (I. Ā. and I. Ť.) (right side).

Mutual orientation of two different crystals on top of each other, both having fitting rows of atomic arrays, is defined as epitaxy, and if both of the crystals belong to same substance, e.g. zircon, autoepitaxy would be a more convenient term (e.g. Kostov and Kostov, 1999). (Auto)epitaxial overgrowth of the later generation zircon (e.g. [Z3(13)]) being one of the common features for the authochtonous granitoids (e.g. Speer, 1982) may infer that the Kalebalta leucogranite is of S-type. Additionally, absence of microgranular mafic enclaves along with other petrographic and geochemical features suggests that the Kalebalta leucogranite belongs to Group 1 (autochthonous and intrusive aluminous leucogranites) of Pupin (1980).

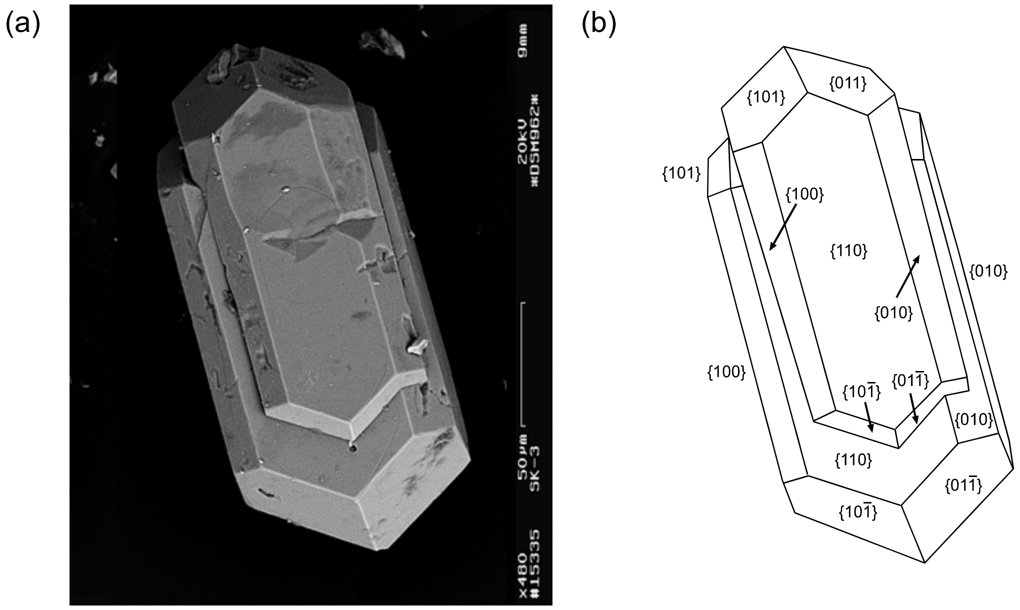

Figure 4.19. Zircon crystal [Z3(13)] from the Kalebalta leucogranite (sample SK-3):a) High-resolution SEM photograph, (b) Sketch model showing the crystal surfaces.

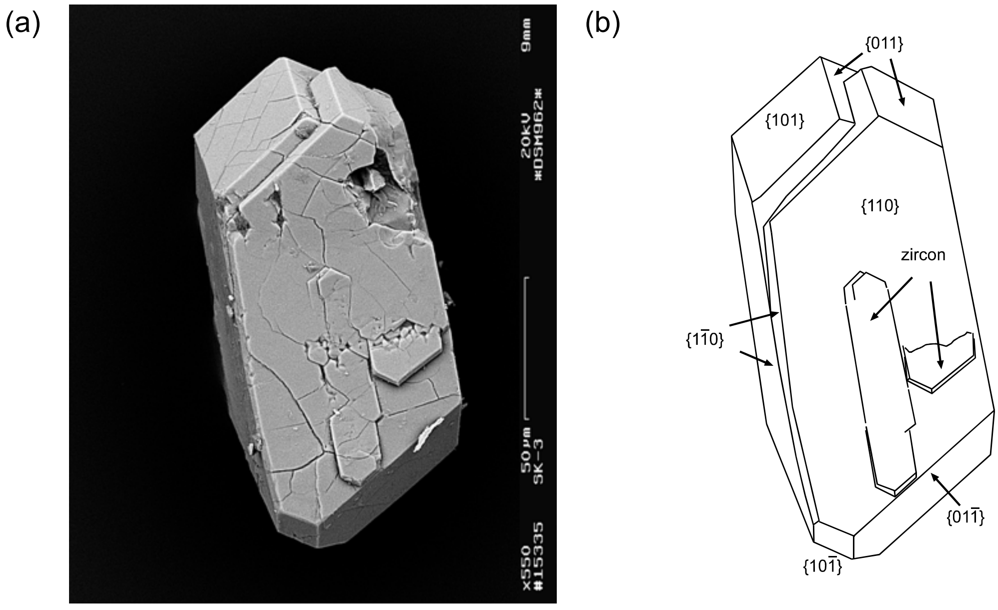

Figure 4.20. Zircon crystal [Z3(26)] from the Kalebalta leucogranite (sample SK-3): (a) High-resolution SEM photograph, (b) Sketch model showing the crystal surfaces.

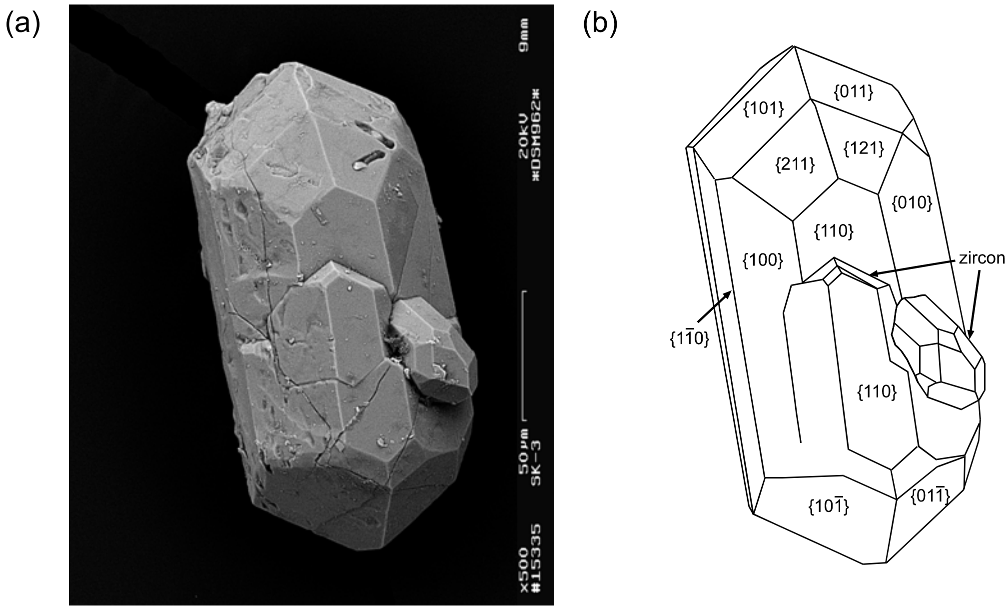

Figure 4.21. Zircon crystal [Z3(40)] from the Kalebalta leucogranite (sample SK-3): (a) High-resolution SEM photograph, (b) Sketch model showing the crystal surfaces.

4.3.1.3. Hisarkaya Porphyritic Granite

Hisarkaya porphyritic granite is sampled from two different stocks (i.e.. samples SK-4 and SK-5) to investigate whether typological differences are possible within the same granitoid type.

The zircon population of the Hisarkaya granitoid is mainly characterized by dark brownish, pale yellow with some colorless or white varieties. In general, zircon types in samples SK-4 and SK-5 are similar, but SK-5 contains smaller number of types. Major zircon types are $P_{1\text{-}2\text{-}3}$ and G_1, while P_4 and $S_{4\text{-}5\text{-}7\text{-}9\text{-}10\text{-}11\text{-}12\text{-}13\text{-}14\text{-}15\text{-}19\text{-}20}$ are rarely present (Figures 4.22, 4.23). G_2 and G_3 types are rare in SK-4, but abundant in SK-5.

Zircon crystals in Figures 4.24, 4.25, 4.26 and 4.27 are examples of P_2, P_4, S_4 and P_2 type crystals in the sample SK-4, respectively.

Pyramidal surfaces of the crystals do not show symmetrical evolution always. It is also possible to observe asymmetrical or unsymmetrical evolution of the pyramid surfaces in the zircon crystals (Figures 4.28, 4.29).

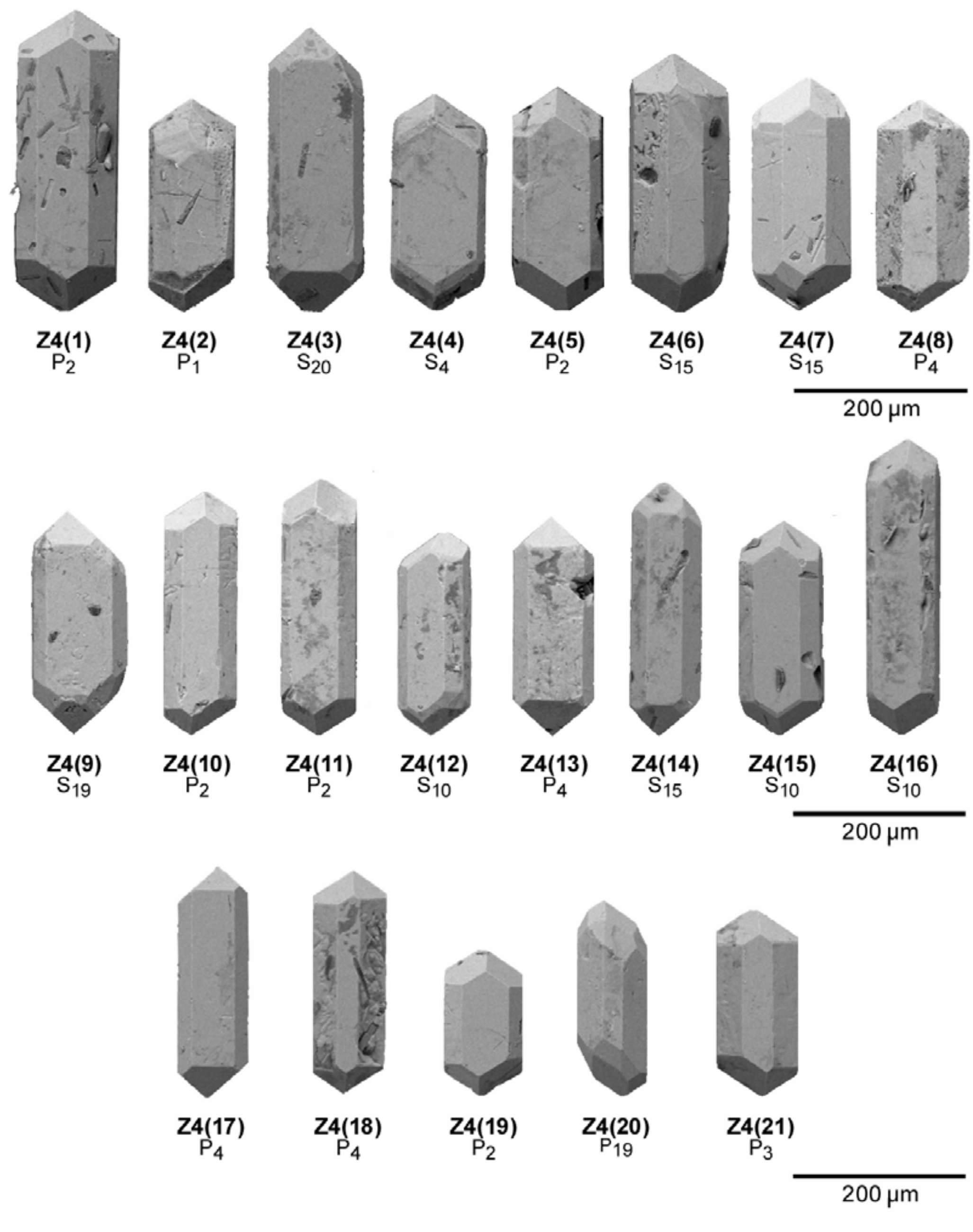

Figure 4.22. SEM images of the selected zircon crystals from the Hisarkaya porphyritic granite (SK-4).

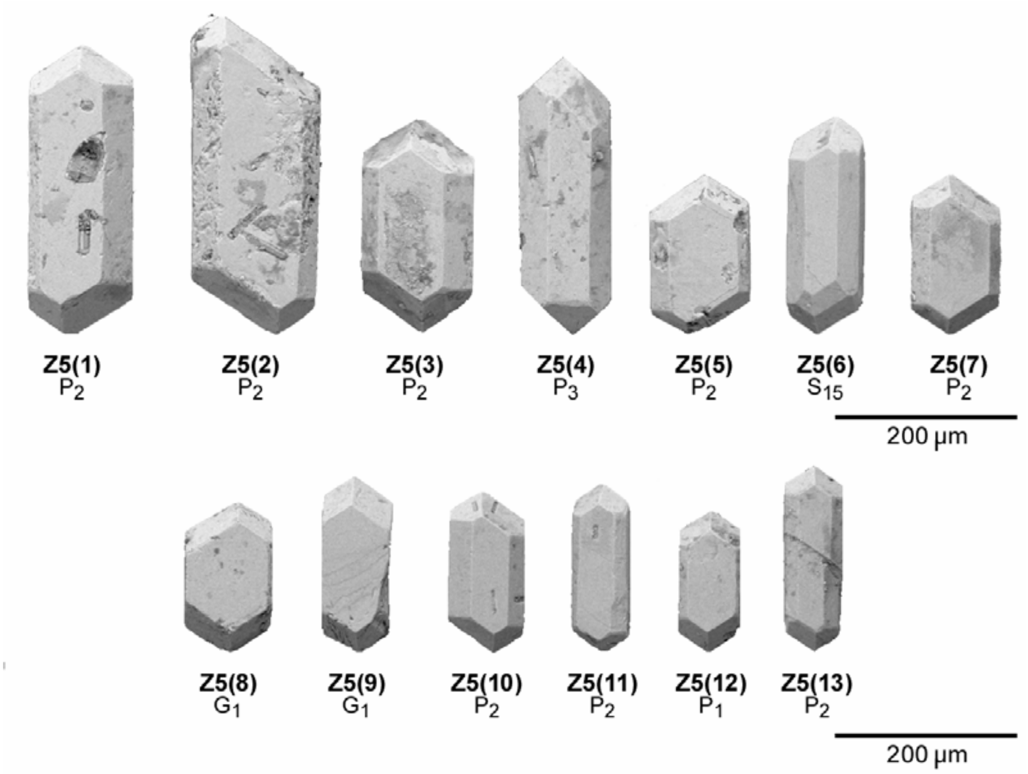

Figure 4.23. SEM images of the selected zircon crystals from the Hisarkaya porphyritic granite (SK-5).

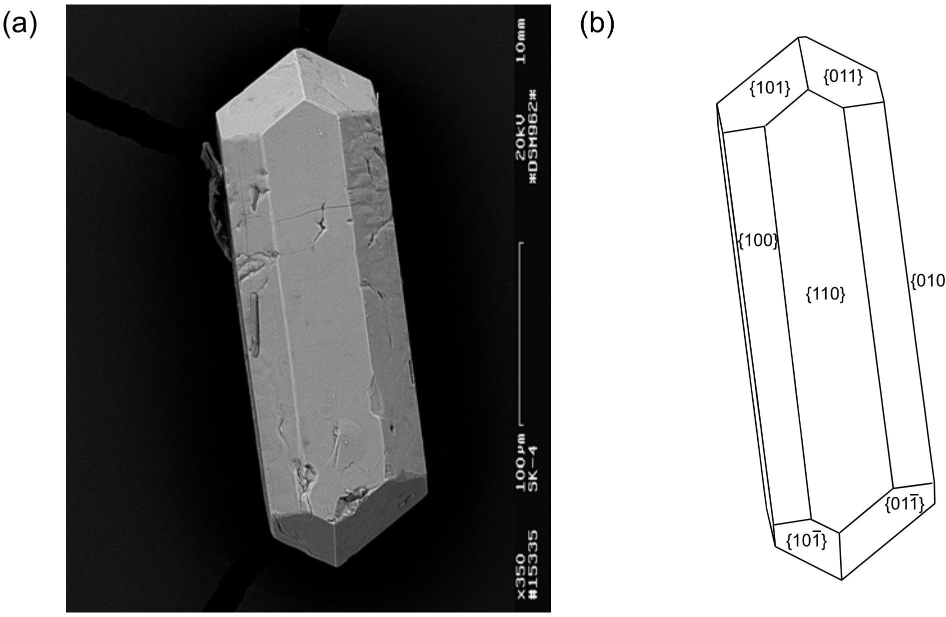

Figure 4.24. Zircon crystal [Z4(10)] from the Hisarkaya porphyritic granite (sample SK-4): (a) High-resolution SEM photograph, (b) Sketch model showing the crystal surfaces.

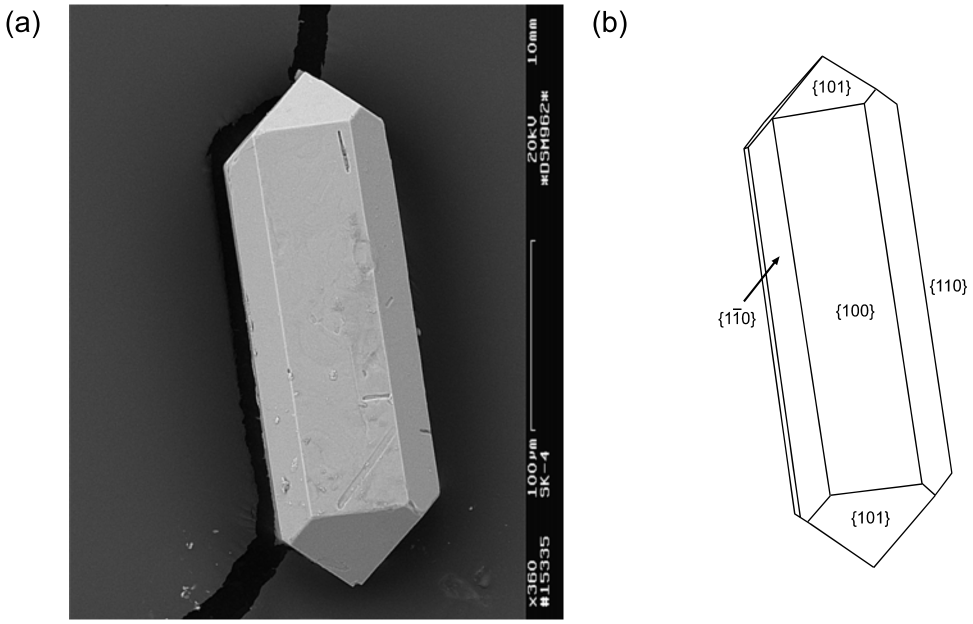

Figure 4.25. Zircon crystal [Z4(17)] from the Hisarkaya porphyritic granite (sample SK-4): (a) High-resolution SEM photograph, (b) Sketch model showing the crystal surfaces.

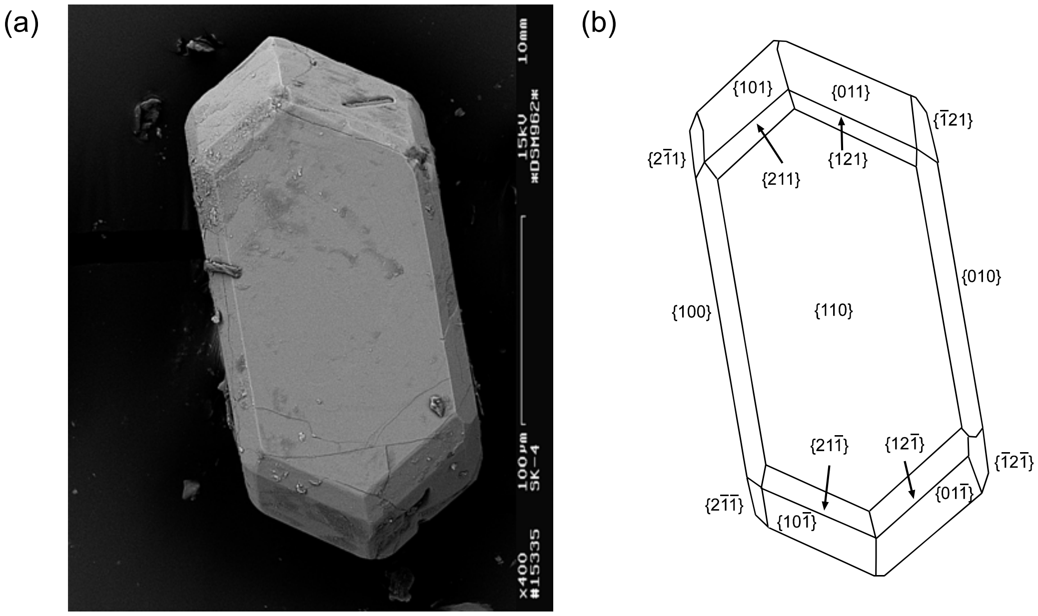

Figure 4.26. Zircon crystal [Z4(4)] from the Hisarkaya porphyritic granite (sample SK-4): (a) High-resolution SEM photograph, (b) Sketch model showing the crystal surfaces.

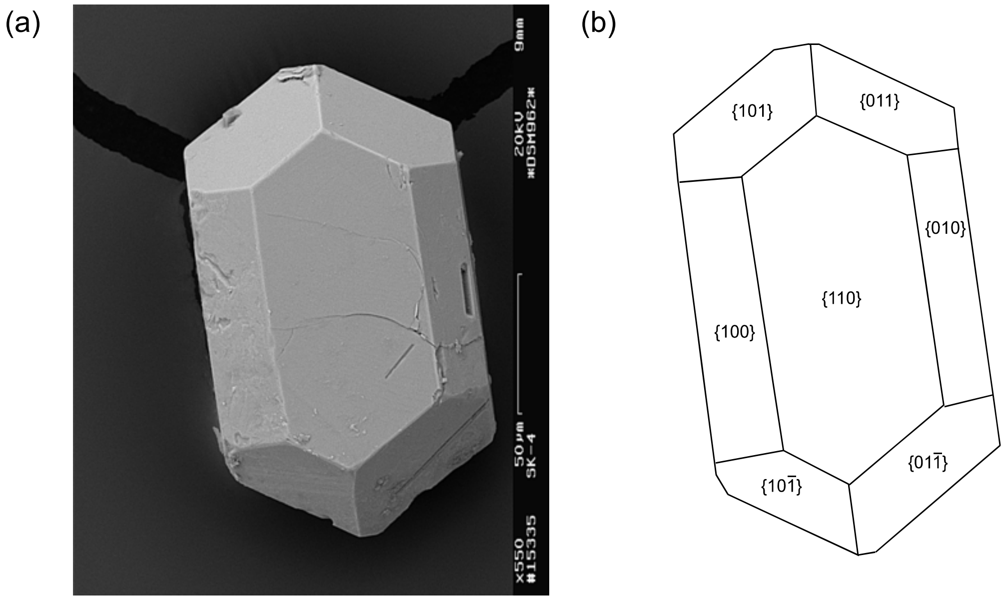

Figure 4.27. Zircon crystal [Z4(19)] from the Hisarkaya porphyritic granite (sample SK-4): (a) High-resolution SEM photograph, (b) Sketch model showing the crystal surfaces.

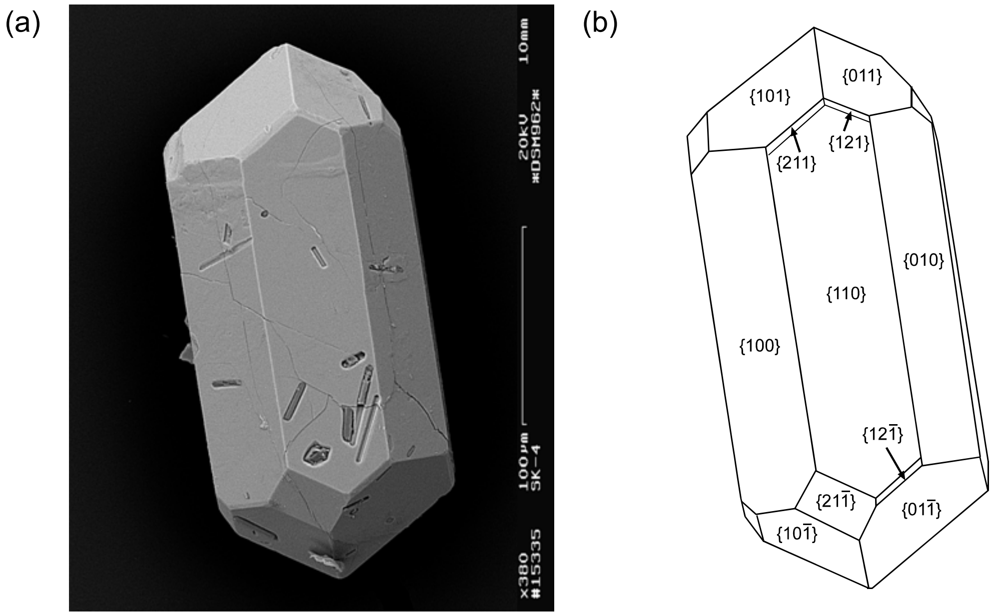

Figure 4.28. Zircon crystal [Z4(7)] from the Hisarkaya porphyritic granite (sample SK-4): (a) High-resolution SEM photograph, (b) Sketch model showing the crystal surfaces.

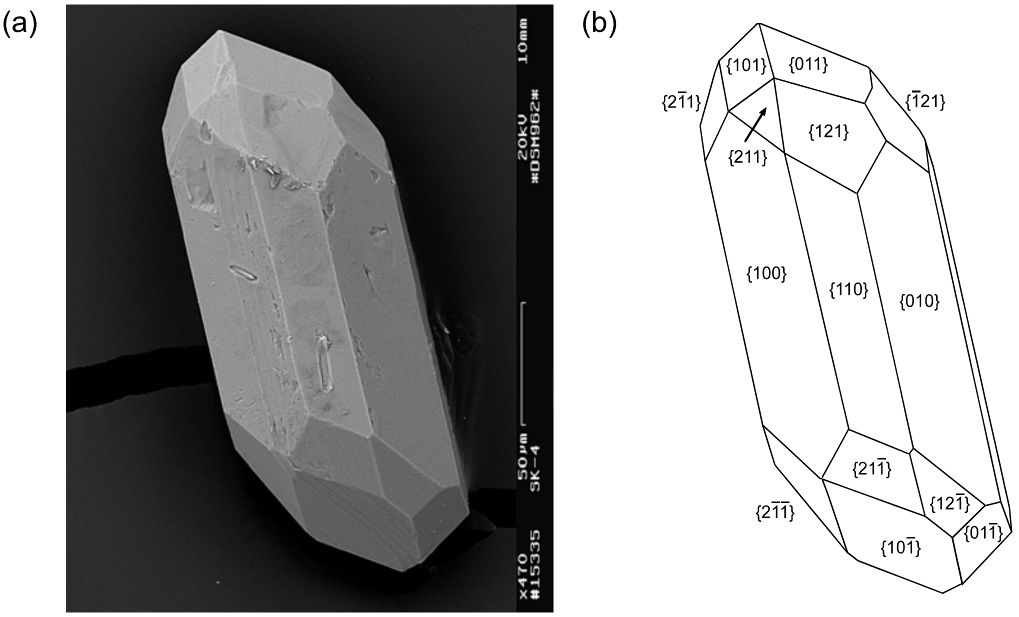

Figure 4.29. Zircon crystal [Z4(20)] from the Hisarkaya porphyritic granite (sample SK-4): (a) High-resolution SEM photograph, (b) Sketch model showing the crystal surfaces.

Moreover, pyramid surface at one end of a mineral may fit to a certain zircon type while that at the other end may not, e.g. [Z5(4)] (Figure 4.23) and [Z5(6)] in the (Figure 4.30).

In the sample SK-5, P_2 type characterized by {100}<{110} and {101} as only pyramid surface is the most abundant crystal type (e.g. [Z5(7)] in Figure 4.31 and [Z5(10)] in Figure 4.32). Some asymmetric P_2 type varieties, e.g. [Z5(2)] (Figure 4.23) are also present in this sample. G_1 type is also common in the sample SK-5 and illustrated by [Z5(8)] crystal in Figure 4.33.

Zircon population in the sample SK-5 clustering in the right part of the typology diagram shows rather limited distribution on the typologic diagram with respect to that of the sample SK-4 (Figure 4.34 and 4.35). Moreover T.E.T. of SK-5 is steeper than the SK-4. These differences may be due to the presence of limited number of types in SK-5. However, in general terms granitoid samples SK-4 and SK-5 have very similar typological characteristics. Therefore, zircon typology method can be useful in comparing outcrops of the same unit.

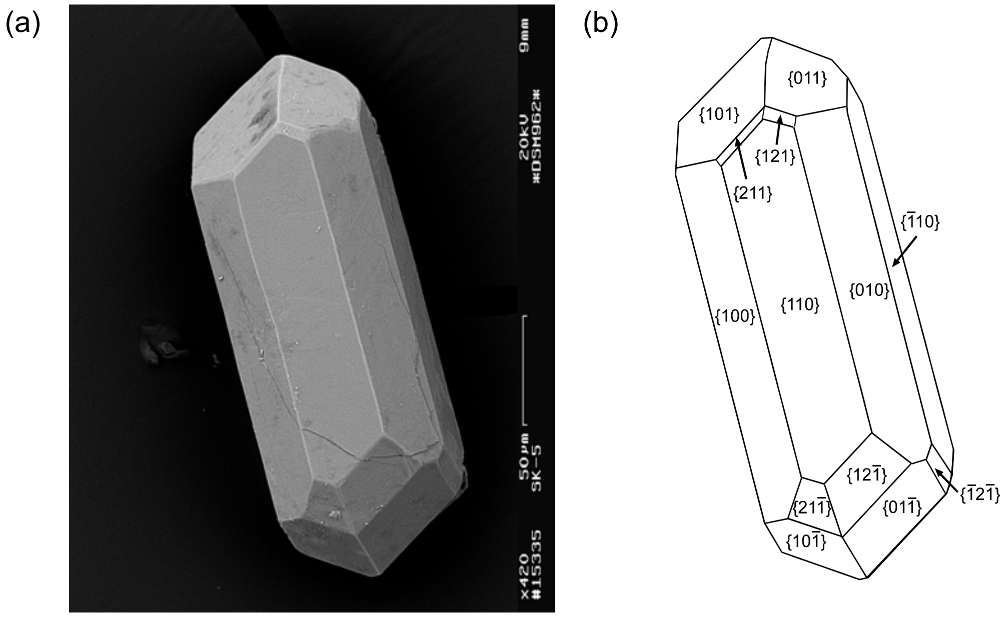

Figure 4.30. Zircon crystal [Z5(6)] from the Hisarkaya porphyritic granite (sample SK-5): (a) High-resolution SEM photograph, (b) Sketch model showing the crystal surfaces.

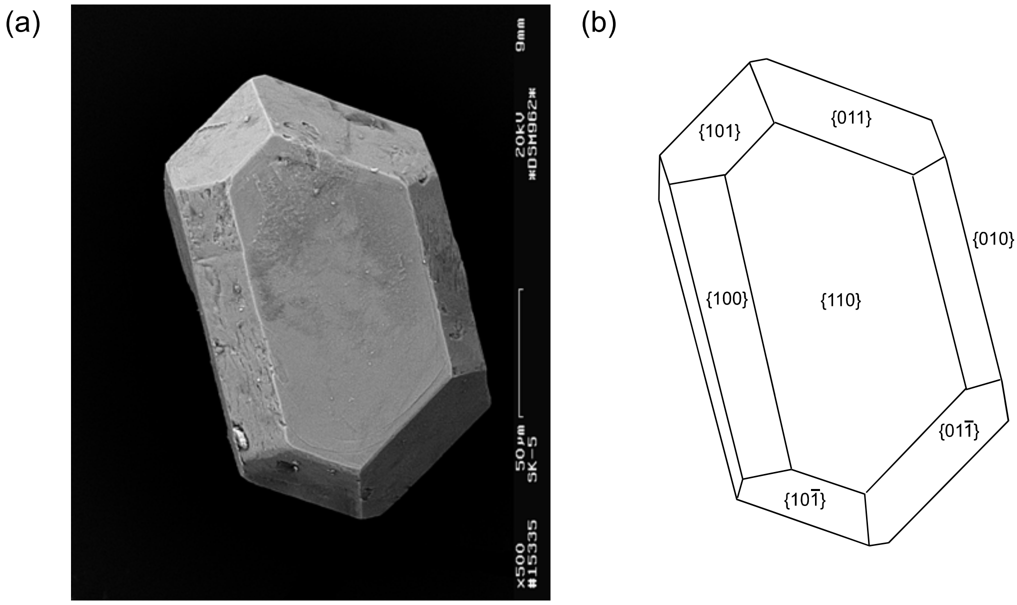

Figure 4.31. Zircon crystal [Z5(7)] from the Hisarkaya porphyritic granite (sample SK-5): (a) High-resolution SEM photograph, (b) Sketch model showing the crystal surfaces.

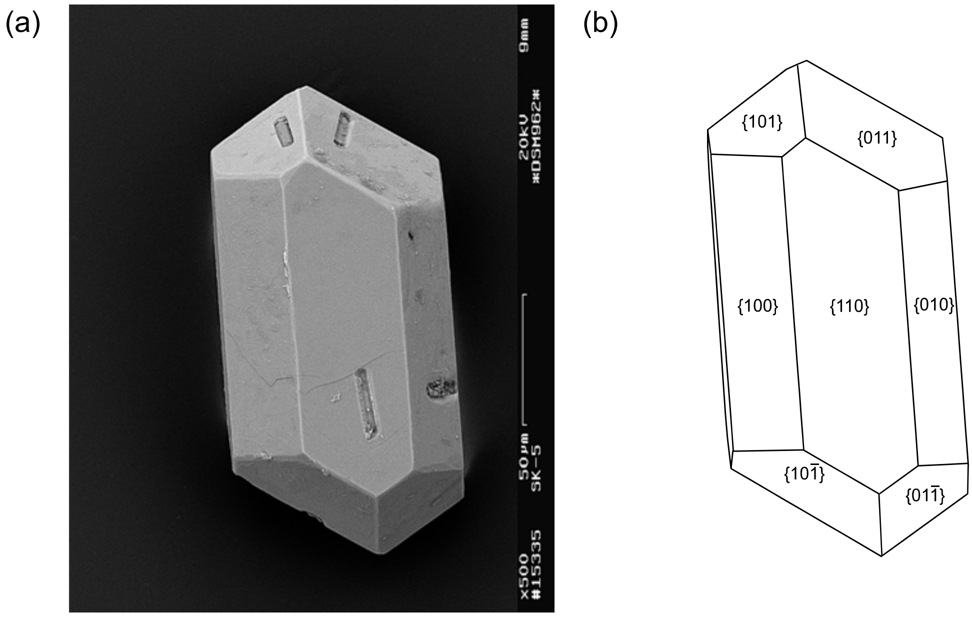

Figure 4.32. Zircon crystal [Z5(10)] from the Hisarkaya porphyritic granite (sample SK-5): (a) High-resolution SEM photograph, (b) Sketch model showing the crystal surfaces.

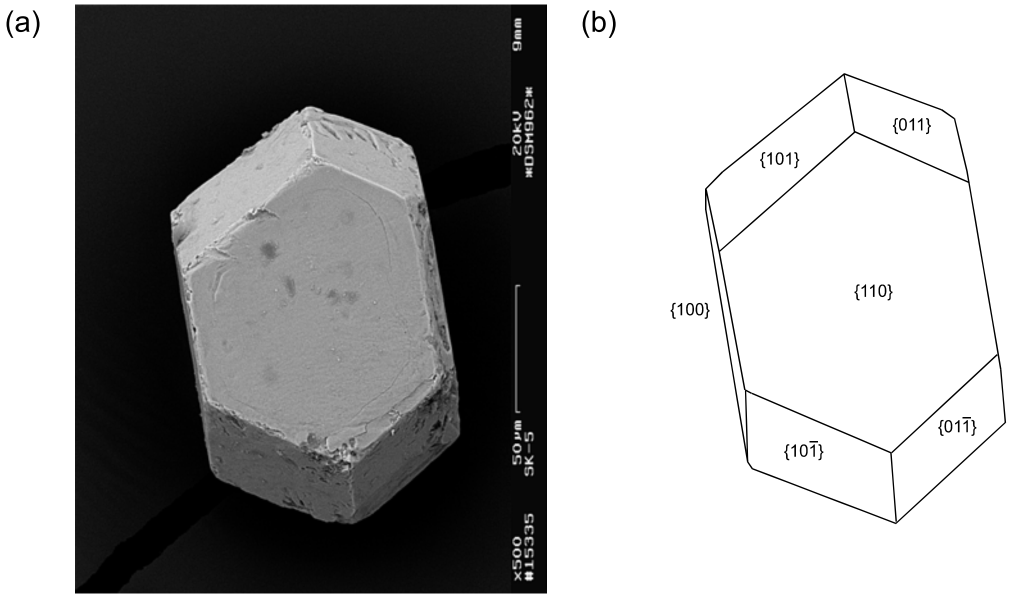

Figure 4.33. Zircon crystal [Z5(8)] from the Hisarkaya porphyritic granite (sample SK-5): (a) High-resolution SEM photograph, (b) Sketch model showing the crystal surfaces.

The zircon population of the Hisarkaya granitoid tends to G-type on its end of evolution trend, and resembles Stock 4b for SK-4 and Group 5 for SK-5 samples. Depending on the T.E.T.s' of samples SK-4 and SK-5, Hisarkaya granitoid maybe described as hybrid granitoid. However the data on the observed types and T.E.T.s' are not concrete enough to define this granitoid as hybrid, since partial overgrowths (observed under binocular microscope) are common in the Hisarkaya granitoid as in the case of the Kalebalta leucogranite. Therefore the zircon minerals of the Hisarkaya porphyritic granite are described to have discontinuities in their growth, referring the possibility of crust dominated source region and/or collision orogen, suggesting that this granitoid should be of Group 1 of Pupin (1980)'s classification.

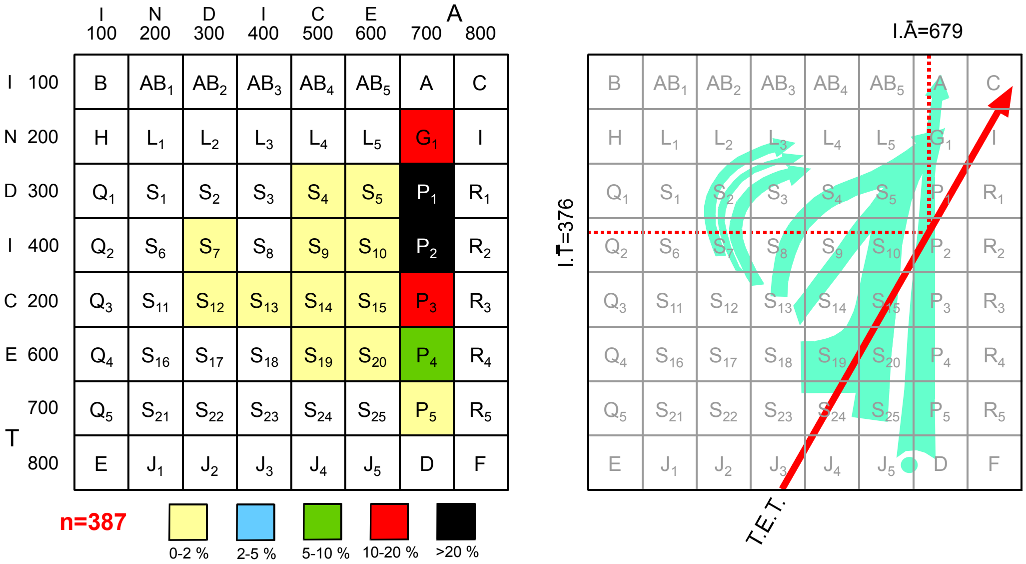

Figure 4.34. Distribution of the zircon crystals from the SK-4 (Hisarkaya porphyritic granite) sample on the Pupin (1980)'s typologic diagram (left side), and Typologic Evolution Trend with the mean points (I. Ā. and I. Ť.) (right side).

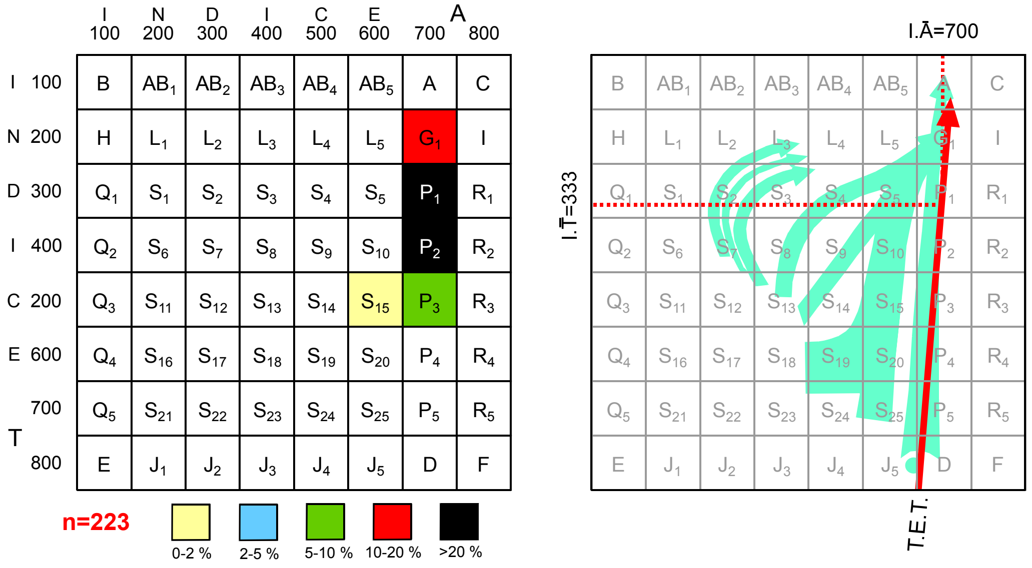

Figure 4.35. Distribution of the zircon crystals from the SK-5 (Hisarkaya porphyritic granite) sample on the Pupin (1980)'s typologic diagram (left side), and Typologic Evolution Trend with the mean points (I. Ā. and I. Ť.) (right side).

4.3.1.4. Sinandı Microgranite

Sinandı microgranite is characterized by zircon types of $S_{7-12-13-18}$ abundantly and of $S_{2-9-10-17-19-23-24}$ scarcely (Figure 4.36). Zircons are generally colorless, yellow and pale-yellow.

Crystal [Z6(7)] (Figure 4.37) exhibiting {100}<<{110} and {101}<{211} surfaces is a good example for the S_2 type crystals in the Sinandı microgranite. Figure 4.38 shows an unsymmetrical evolution of pyramidal surfaces in S_{18} type crystal in the Sinandı microgranite. S_{12} type is one of the most abundant crystal types in the Sinandı microgranite present either in short ([Z6(13)] in Figure 4.39) or long ([Z6(14)] in Figure 4.39) prismatic forms.

Zircon crystal types of this granitoid mainly confined to the middle part of the typology diagram. T.E.T. of the Sinandı microgranite is similar to that of Stock 4b (calc-alkaline hybrid granitoid) of Pupin (1980)'s classification (Figure 4.41).

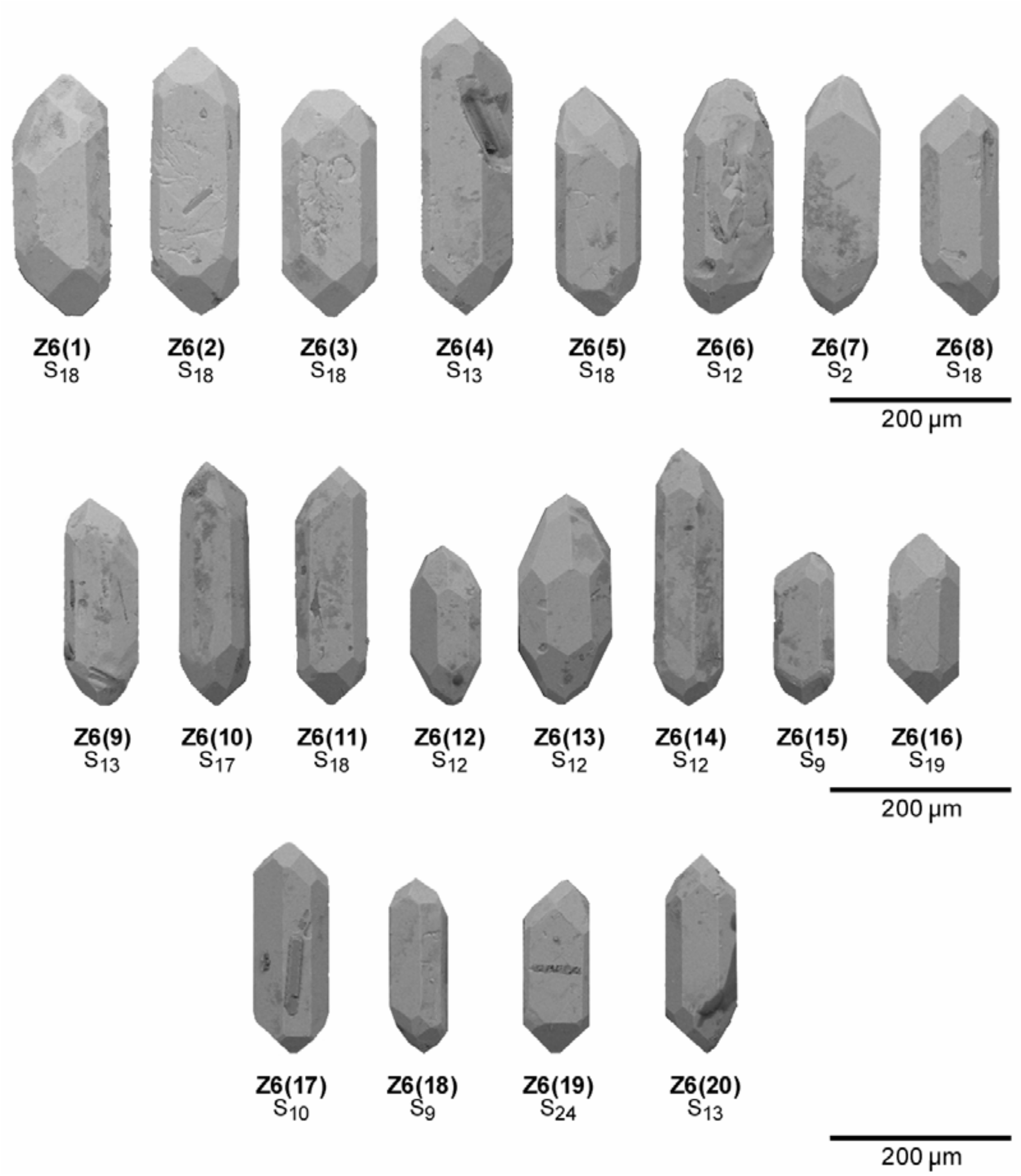

Figure 4.36. SEM images of the selected zircon crystals from the Sinandı microgranite (SK-6).

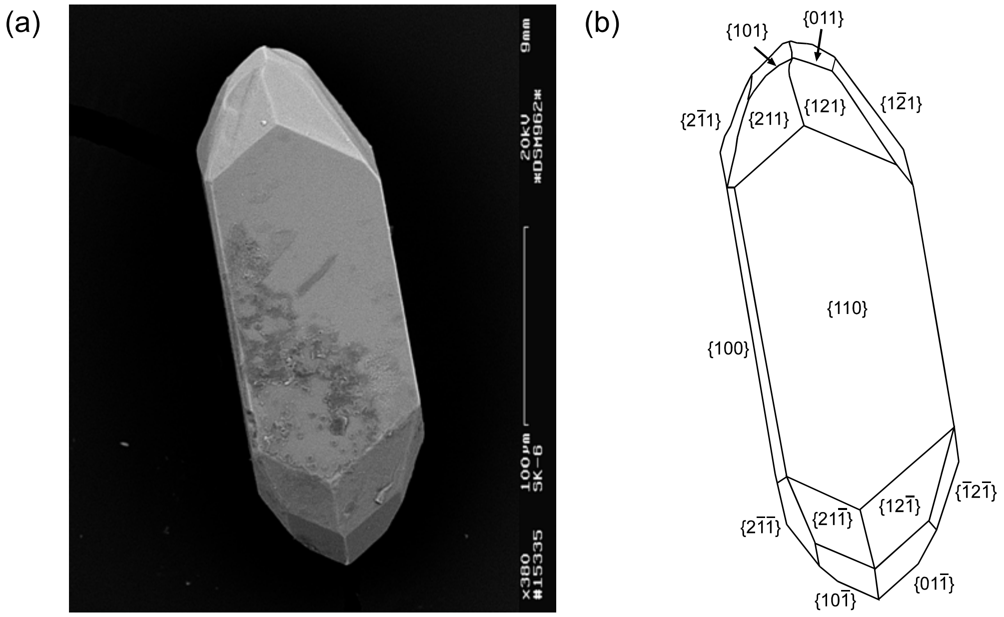

Figure 4.37. Zircon crystal [Z6(7)] from the Sinandı microgranite (sample SK-6): (a) High-resolution SEM photograph, (b) Sketch model showing the crystal surfaces.

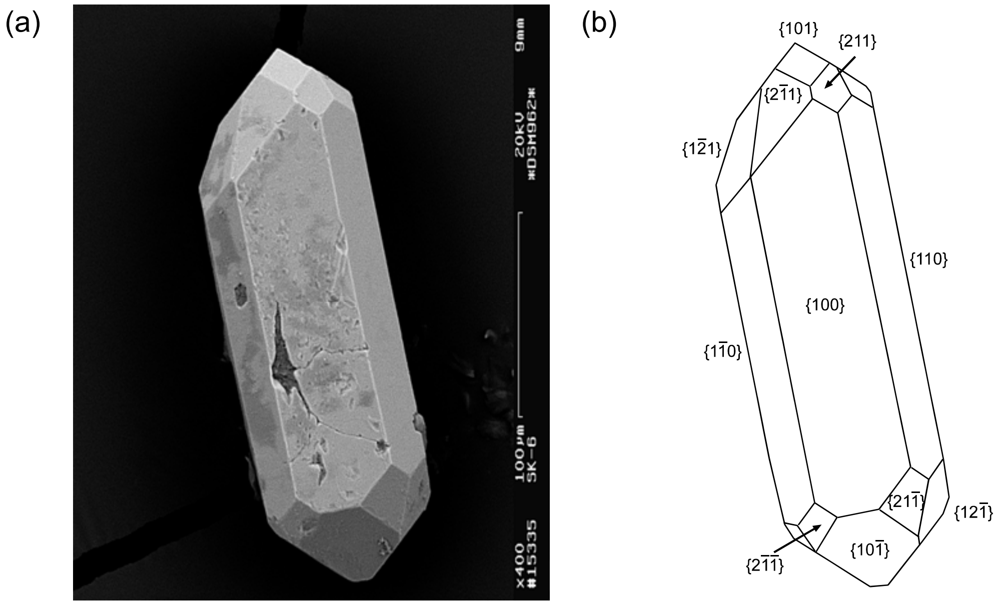

Figure 4.38. Zircon crystal [Z6(11)] from the Sinandı microgranite (sample SK-6): (a) High-resolution SEM photograph, (b) Sketch model showing the crystal surfaces.

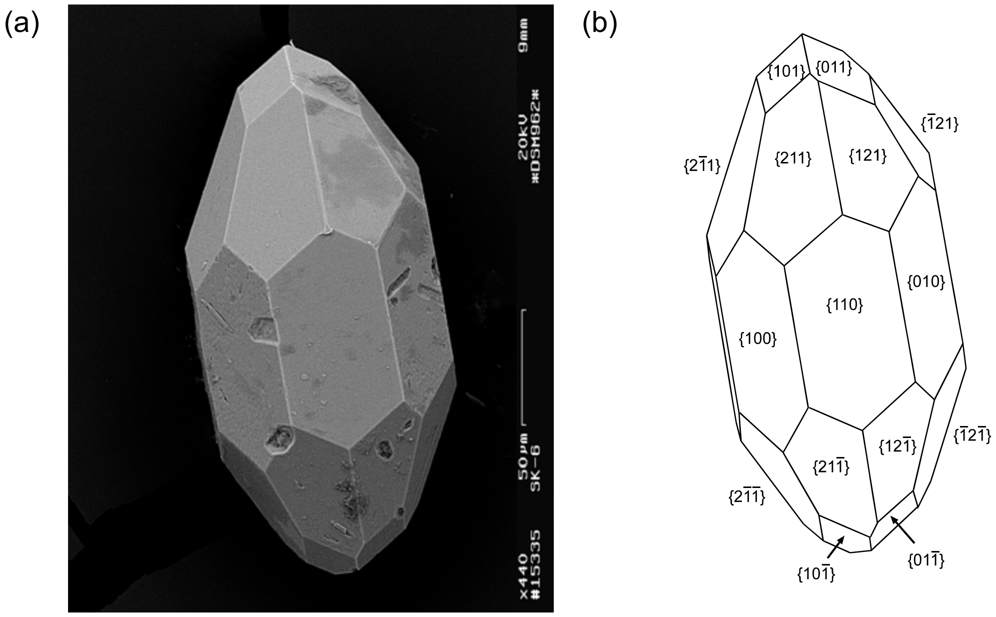

Figure 4.39. Zircon crystal [Z6(13)] from the Sinandı microgranite (sample SK-6): (a) High-resolution SEM photograph, (b) Sketch model showing the crystal surfaces.

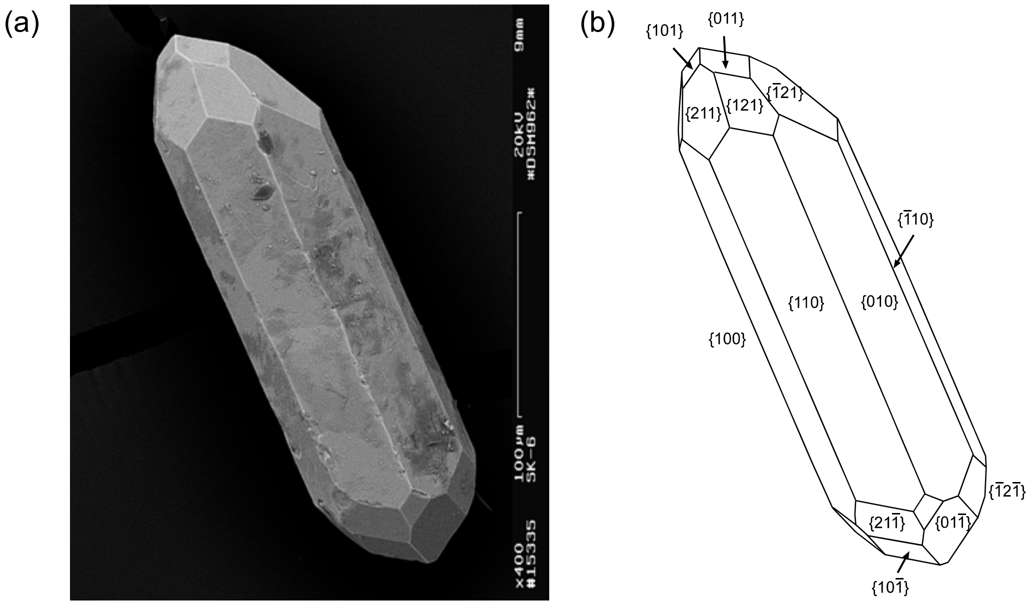

Figure 4.40. Zircon crystal [Z6(14)] from the Sinandı microgranite (sample SK-6): (a) High-resolution SEM photograph, (b) Sketch model showing the crystal surfaces.

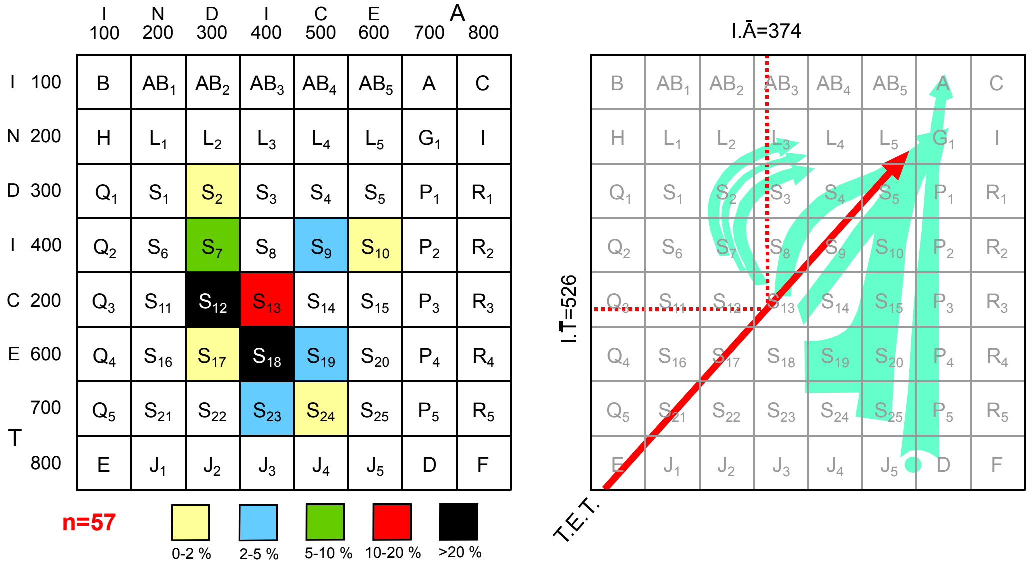

Figure 4.41. Distribution of the zircon crystals from the SK-6 (Sinandı microgranite) sample on the Pupin (1980)'s typologic diagram (left side), and Typologic Evolution Trend with the mean points (I. Ā. and I. Ť.) (right side).

4.3.2. Ağaçören Pluton

4.3.2.1. Namlıkışla Biotite-Granite

Zircon crystals of Namlıkışla biotite-granite are limpid, yellow to pale yellow with well-defined crystal surfaces and minor inclusions. Zircon population of the Namlıkışla biotite-granite is represented by low Ā and Ť indices with preferential development of S_{2-7-12} types besides $S_{1-3-4-5-6-8-11-13-16}$ and $L_{1-2-3-4-5}$ types in lesser percentage (Figure 4.42). Long prismatic crystals such as [Z8(16)] (in Figure 4.42) and [Z8(18)] (Figure 4.43) are present in the Namlıkışla granitoid.

S_{12} and S_7 are the most abundant types in the Namlıkışla granitoid. [Z8(1)] (Figure 4.44) and [Z8(3)] (Figure 4.45) showing {100}={110} and {101}<{211} characteristics are good examples for the S_{12} type crystals in the Namlıkışla granitoid. Additionally, [Z8(12)] (Figure 4.46) and [Z8(20)] (Figure 4.47) exhibiting typology with surfaces {100}<{110} and {101}<{211} are the representatives of the S_7 type crystals in this granitoid.

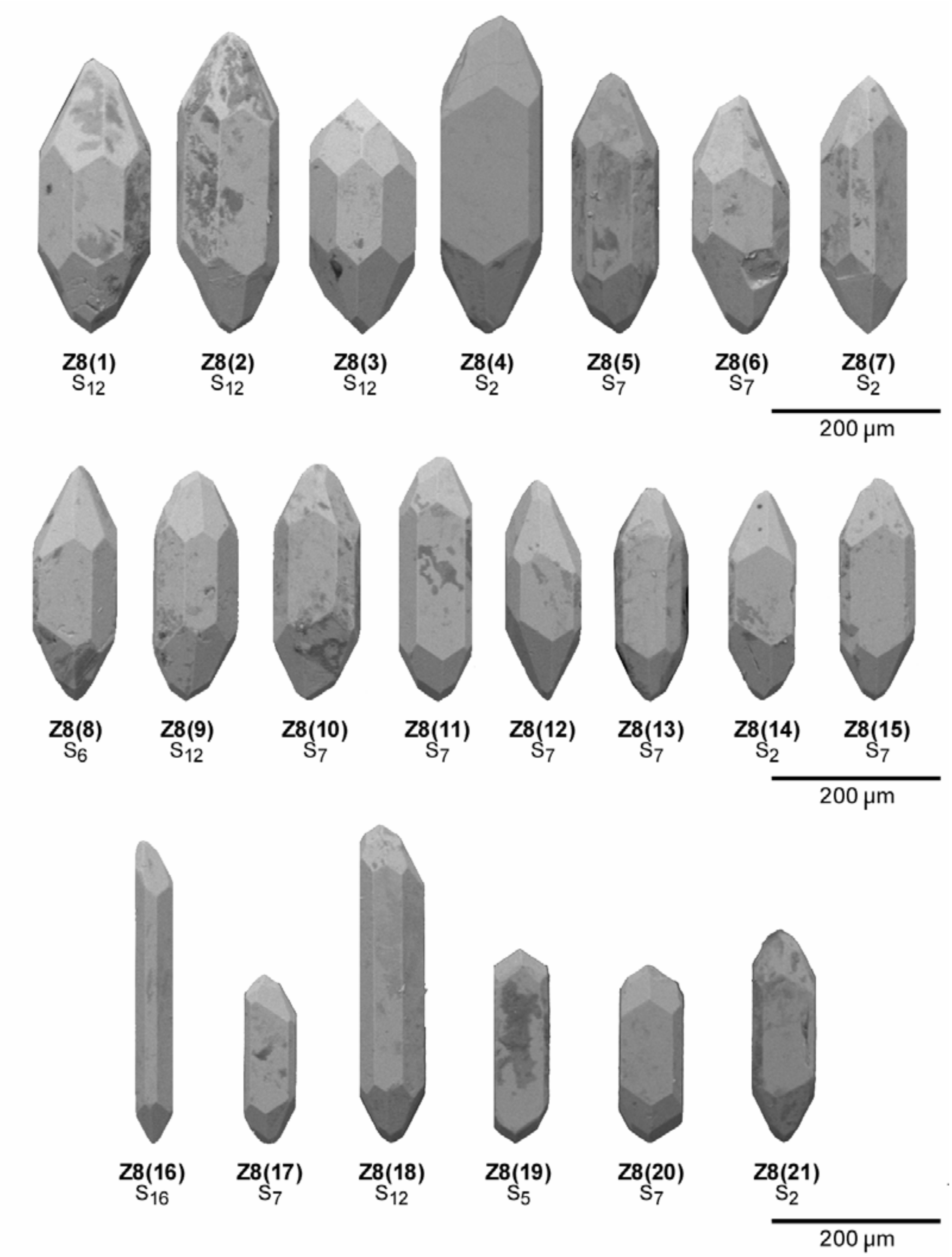

Figure 4.42. SEM images of the selected zircon crystals from the Namlıkışla biotite-granite (SK-8).

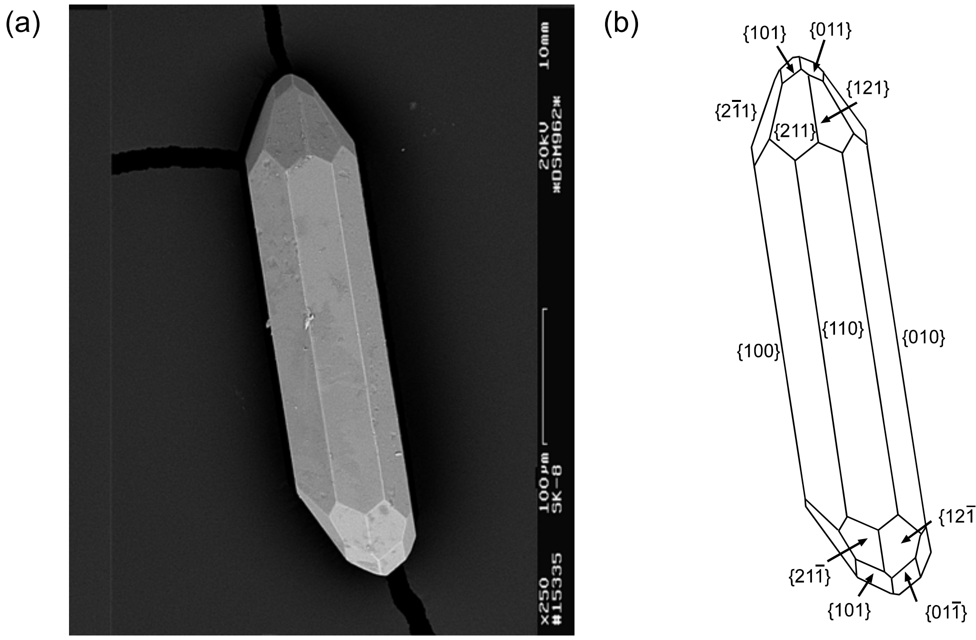

Figure 4.43. Zircon crystal [Z8(18)] from the Namlıkışla biotite-granite (sample SK-8): (a) High-resolution SEM photograph, (b) Sketch model showing the crystal surfaces.

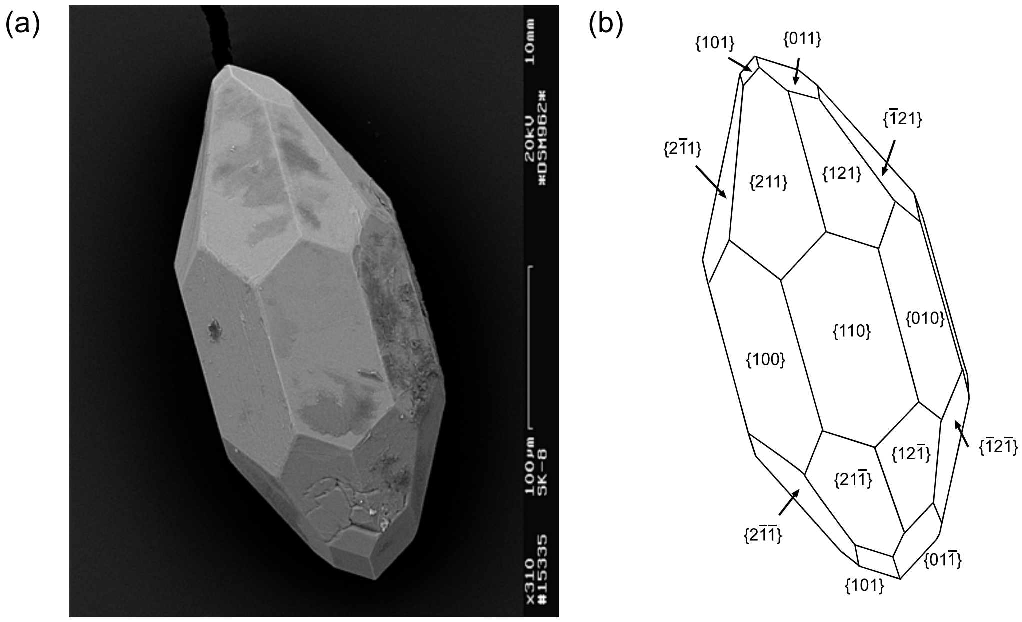

Figure 4.44. Zircon crystal [Z8(1)] from the Namlıkışla biotite-granite (sample SK-8): (a) High-resolution SEM photograph, (b) Sketch model showing the crystal surfaces.

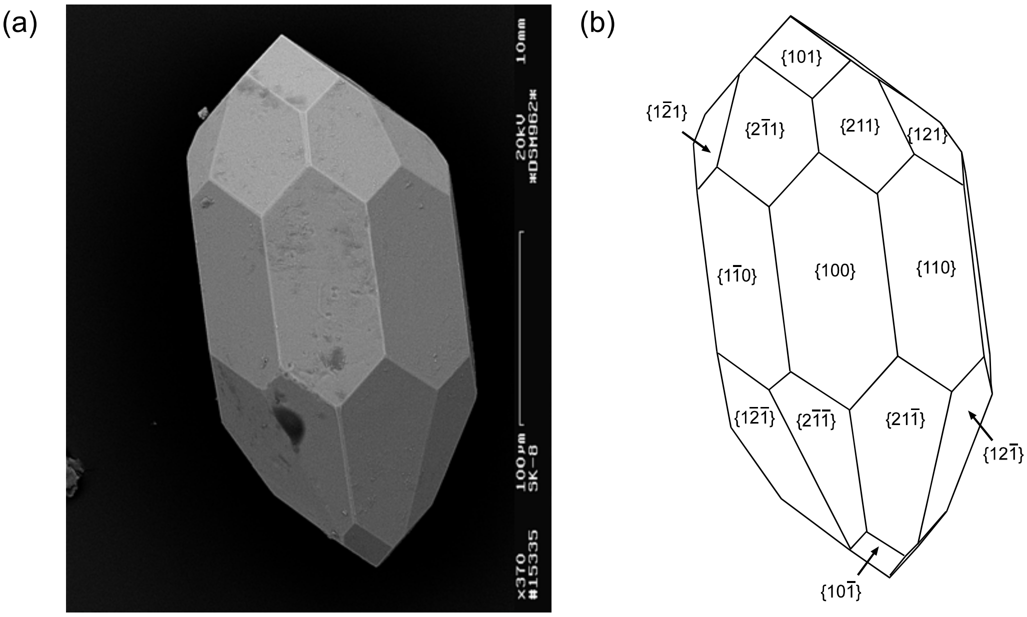

Figure 4.45. Zircon crystal [Z8(3)] from the Namlıkışla biotite-granite (sample SK-8): (a) High-resolution SEM photograph, (b) Sketch model showing the crystal surfaces.

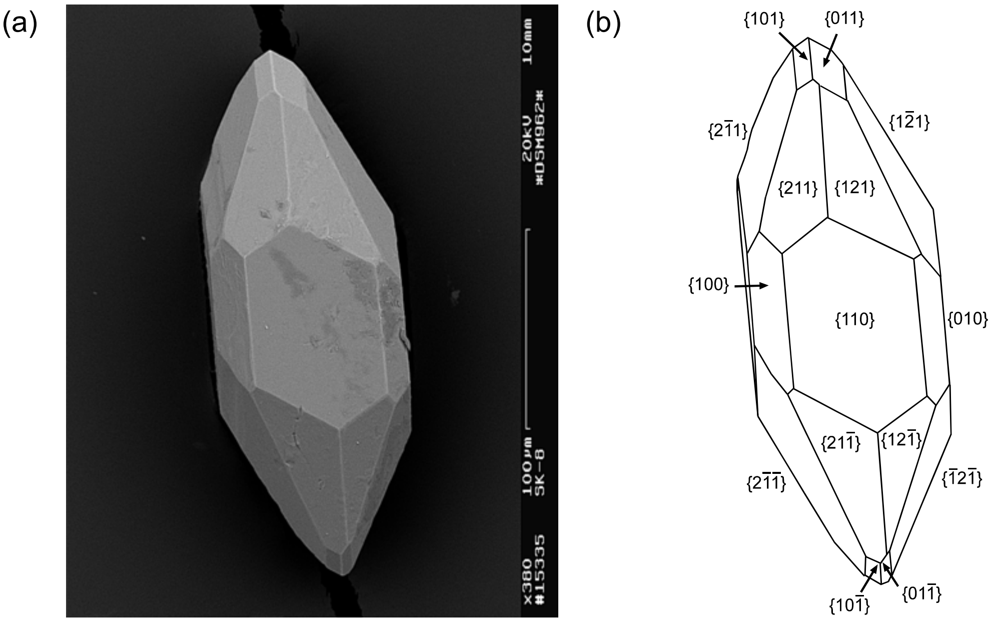

Figure 4.46. Zircon crystal [Z8(12)] from the Namlıkışla biotite-granite (sample SK-8): (a) High-resolution SEM photograph, (b) Sketch model showing the crystal surfaces.

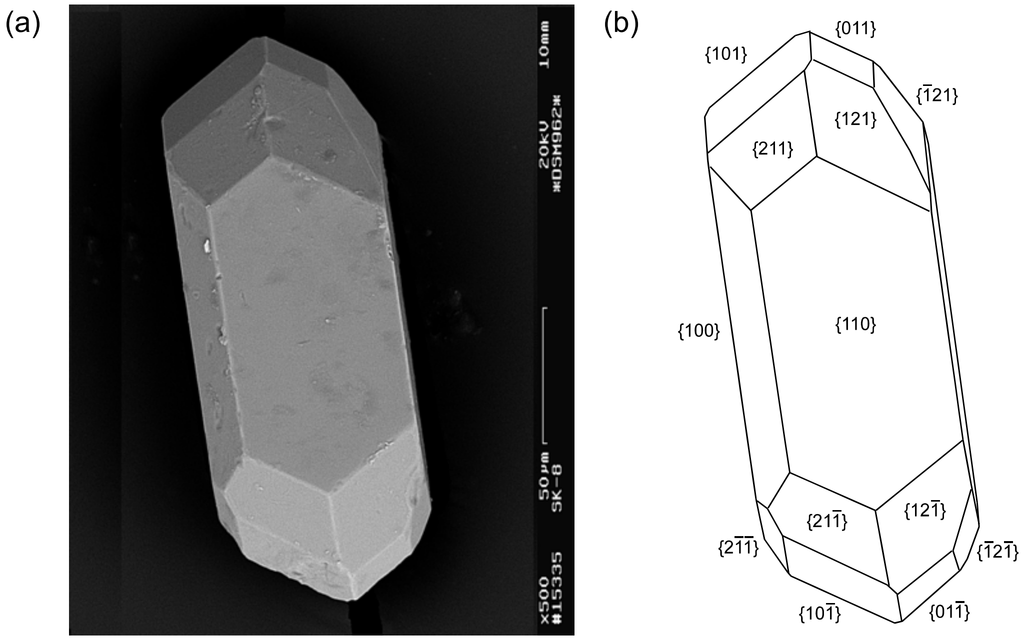

Figure 4.47. Zircon crystal [Z8(20)] from the Namlıkışla biotite-granite (sample SK-8): (a) High-resolution SEM photograph, (b) Sketch model showing the crystal surfaces.

Moreover, crystal [Z8(4)] (Figure 4.48) is an example of S_2 type zircons in the Namlıkışla granitoid with its {100}<<{110} and {101}<{211} typologic characteristics.

Considering the trend of T.E.T. the Namlıkışla granitoid can be characterized as intrusive aluminous autochthonous granitoid (Group-3 of Pupin, 1980), which demonstrates crustal source with minor mantle contribution (Figure 4.49).

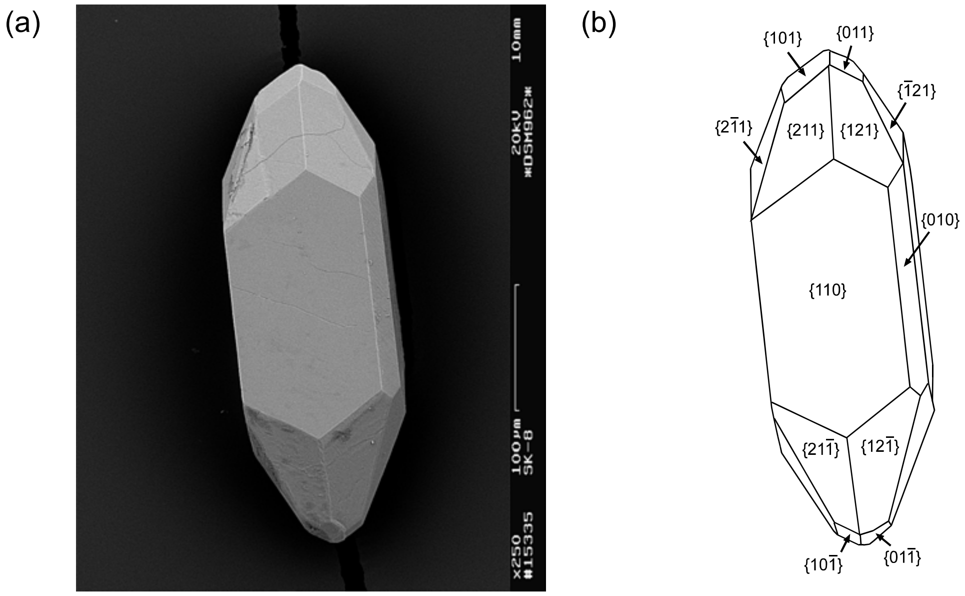

Figure 4.48. Zircon crystal [Z8(4)] from the Namlıkışla biotite-granite (sample SK-8): (a) High-resolution SEM photograph, (b) Sketch model showing the crystal surfaces.

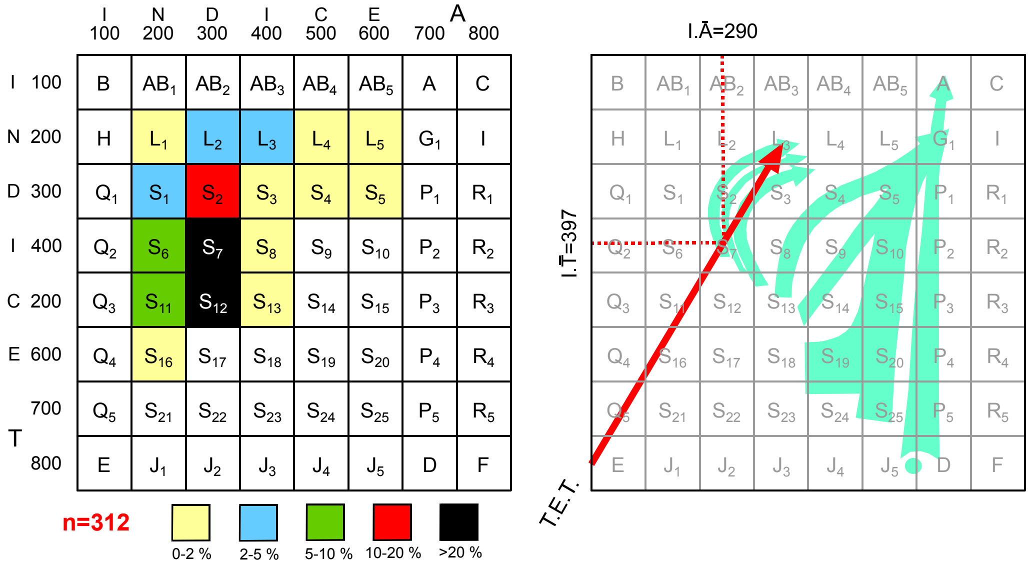

	I 100	N 200	D 300	I 400	C 500	E 600	700	A 800
I 100	B	AB_1	AB_2	AB_3	AB_4	AB_5	A	C
N 200	H	🟨 L_1	🟦 L_2	🟦 L_3	🟨 L_4	🟨 L_5	G_1	I
D 300	Q_1	🟦 S_1	🟥 S_2	🟨 S_3	🟨 S_4	🟨 S_5	P_1	R_1
I 400	Q_2	🟩 S_6	⬛ S_7	🟨 S_8	S_9	S_{10}	P_2	R_2
C 200	Q_3	🟩 S_{11}	⬛ S_{12}	🟨 S_{13}	S_{14}	S_{15}	P_3	R_3
E 600	Q_4	🟨 S_{16}	S_{17}	S_{18}	S_{19}	S_{20}	P_4	R_4
700	Q_5	S_{21}	S_{22}	S_{23}	S_{24}	S_{25}	P_5	R_5
T 800	E	J_1	J_2	J_3	J_4	J_5	D	F

n=312

🟨 0-2 %
🟦 2-5 %
🟩 5-10 %
🟥 10-20 %
⬛ >20 %

Figure 4.49. Distribution of the zircon crystals from the SK-8 (Namlıkışla biotite granite) sample on the Pupin (1980)'s typologic diagram (left side), and Typologic Evolution Trend with the mean points (I. Ā. and I. Ť.) (right side).

4.3.2.2. Yenişabanlı Biotite-Amphibole Granite

Yenişabanlı biotite-amphibole granite has zircon crystal types $S_{14-19-20}$ and P_{3-4} types dominantly and $S_{9-10-13-15-18}$ and P_2 types scarcely (Figure 4.50). Zircons of Yenişabanlı granitoid are generally large yellow, pale yellow, brownish yellow and white crystals with some inclusions and long prismatic varieties, e.g. [Z9(14)] (Figure 4.51).

Crystals [Z9(11)] (Figure 4.52) and [Z9(12)] (Figure 4.53) can be described as S_{12} and S_{13} types, respectively depending on their relative development of pyramid developments while {100} and {110} prisms are almost equal.

Yenişabanlı granitoid with T.E.T. trend adjusting to Stock 4c of Pupin (1980) can be described as hybrid granitoid (Figure 4.54).

4.3.2.3. Sipahiler Amphibole-Biotite Granite

Zircon crystals are generally colorless, yellow, and pale yellow, while brownish and white varieties are also present in the Sipahiler amphibole-biotite granite. They typically bear inclusions. Sipahiler granitoid is characterized by predominant long prismatic G_1, P_1 and P_2 types, with fewer P_3, $S_{5-8-9-10-13-14}$ types (Figure 4.55).

Figure 4.56 illustrates a P_2 type (crystal [Z10(10)]) which is very common in the Sipahiler granitoid. The cracks resulting from heterogeneous metamictization are visible on the crystal. Moreover [Z10(18)] is a typical example of S_5 type with its minor {211} pyramid development and larger {110} prism than {100} prism (Figure 4.57). On the other hand to describe crystal [Z10(13)] as transitional from S_8 to S_9 is plausible since {211} pyramid is considerably smaller at one corner of the crystal (Figure 4.58).

T.E.T. of the Sipahiler granitoid adapts to that of Stock 4b of Pupin (1980) (Figure 4.59).

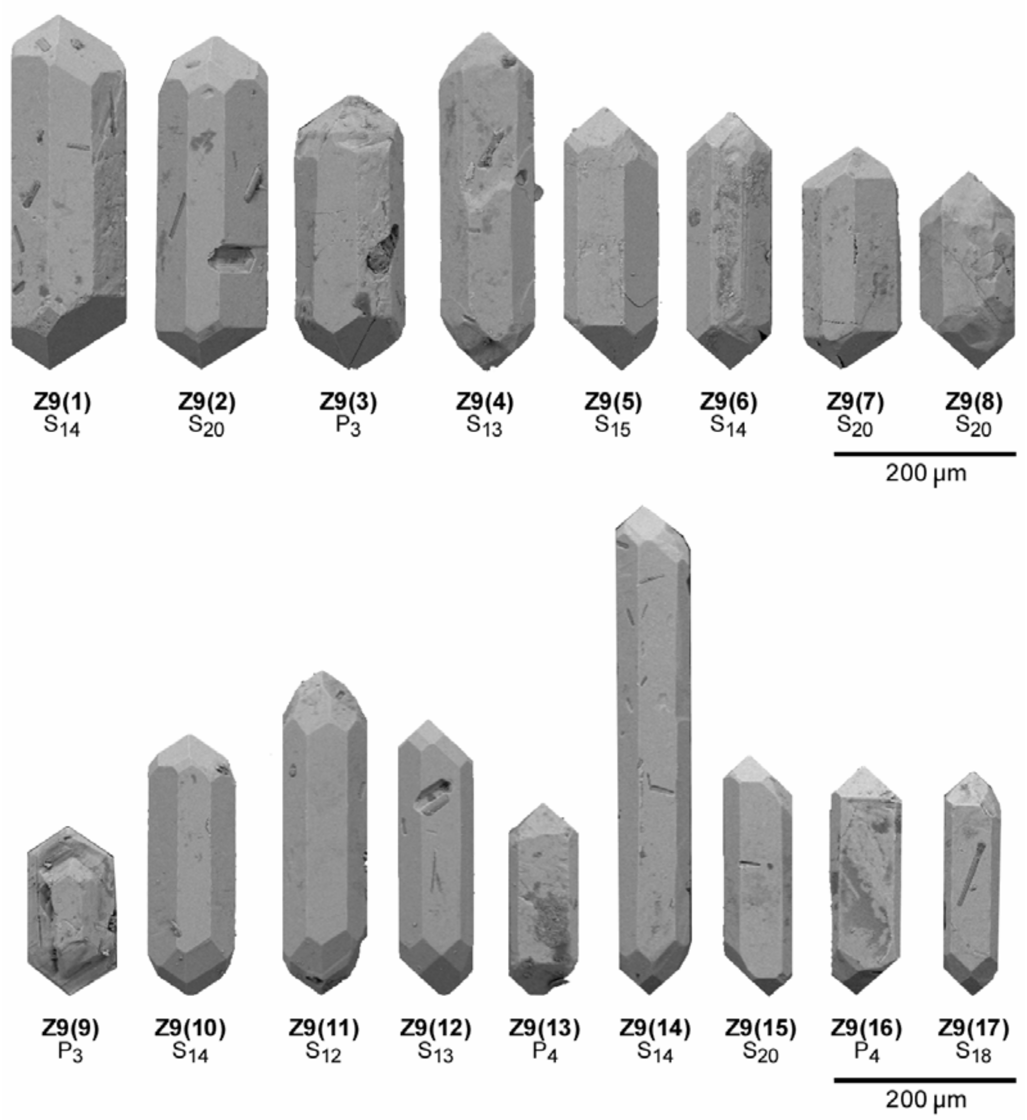

Figure 4.50. SEM images of the selected zircon crystals from the Yenişabanlı biotite-amphibole granite (SK-9).

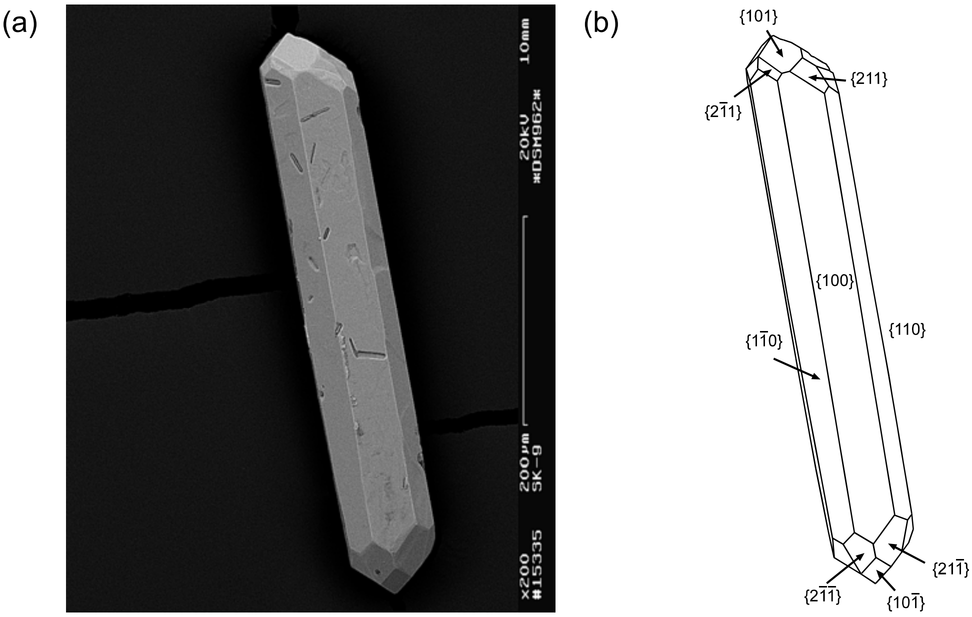

Figure 4.51. Zircon crystal [Z9(14)] from the Yenişabanlı biotite-amphibole granite (sample SK-9): (a) High-resolution SEM photograph, (b) Sketch model showing the crystal surfaces.

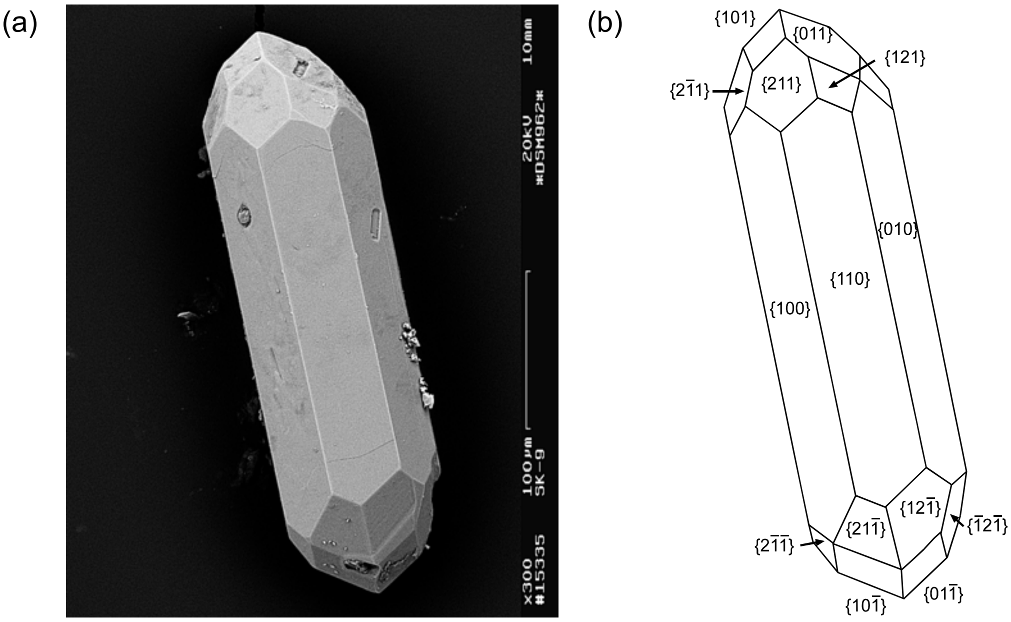

Figure 4.52. Zircon crystal [Z9(11)] from the Yenişabanlı biotite-amphibole granite (sample SK-9): (a) High-resolution SEM photograph, (b) Sketch model showing the crystal surfaces.

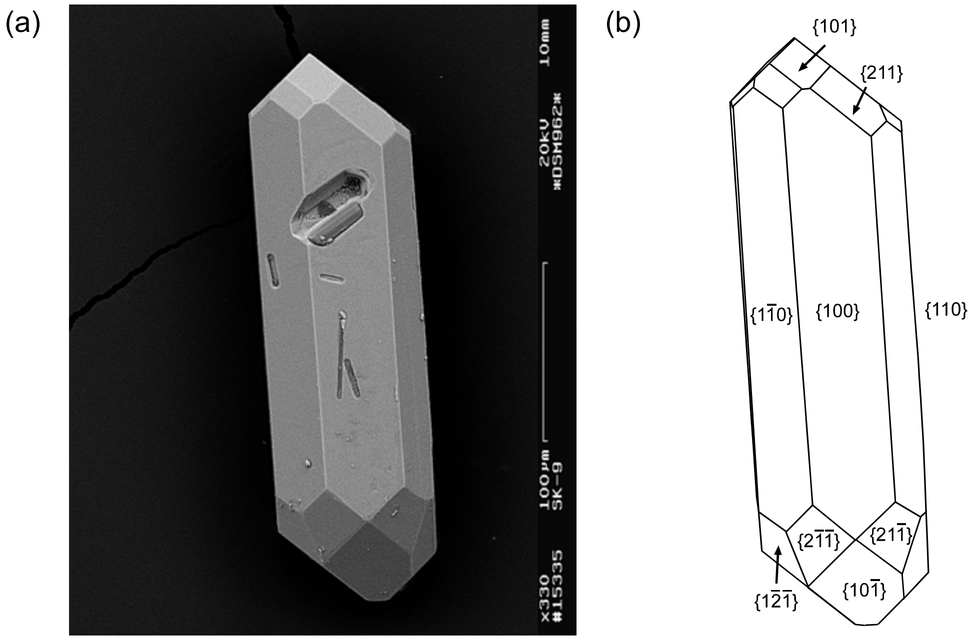

Figure 4.53. Zircon crystal [Z9(12)] from the Yenişabanlı biotite-amphibole granite (sample SK-9): (a) High-resolution SEM photograph, (b) Sketch model showing the crystal surfaces.

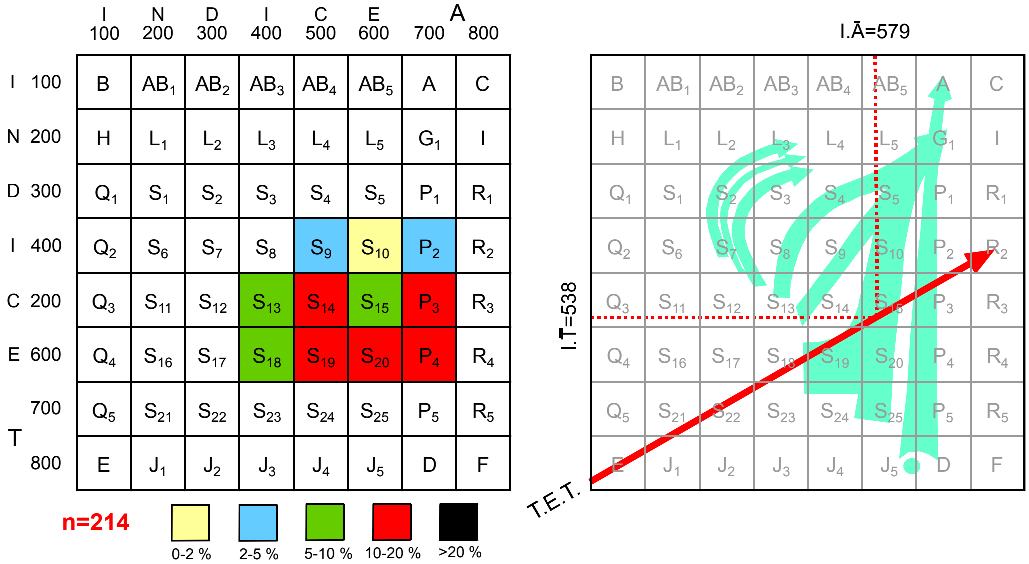

	I 100	N 200	D 300	I 400	C 500	E 600	A 700	800
I 100	B	AB$_1$	AB$_2$	AB$_3$	AB$_4$	AB$_5$	A	C
N 200	H	L$_1$	L$_2$	L$_3$	L$_4$	L$_5$	G$_1$	I
D 300	Q$_1$	S$_1$	S$_2$	S$_3$	S$_4$	S$_5$	P$_1$	R$_1$
I 400	Q$_2$	S$_6$	S$_7$	S$_8$	🟦 S$_9$	🟨 S$_{10}$	🟦 P$_2$	R$_2$
C 200	Q$_3$	S$_{11}$	S$_{12}$	🟩 S$_{13}$	🟥 S$_{14}$	🟩 S$_{15}$	🟥 P$_3$	R$_3$
E 600	Q$_4$	S$_{16}$	S$_{17}$	🟩 S$_{18}$	🟥 S$_{19}$	🟥 S$_{20}$	🟥 P$_4$	R$_4$
T 700	Q$_5$	S$_{21}$	S$_{22}$	S$_{23}$	S$_{24}$	S$_{25}$	P$_5$	R$_5$
800	E	J$_1$	J$_2$	J$_3$	J$_4$	J$_5$	D	F

n=214 🟨 0-2 % 🟦 2-5 % 🟩 5-10 % 🟥 10-20 % ⬛ >20 %

Figure 4.54. Distribution of the zircon crystals from the SK-9 (Yenişabanlı biotite-amphibole granite) sample on the Pupin (1980)'s typologic diagram (left side), and Typologic Evolution Trend with the mean points (I. Ā. and I. Ť.) (right side).

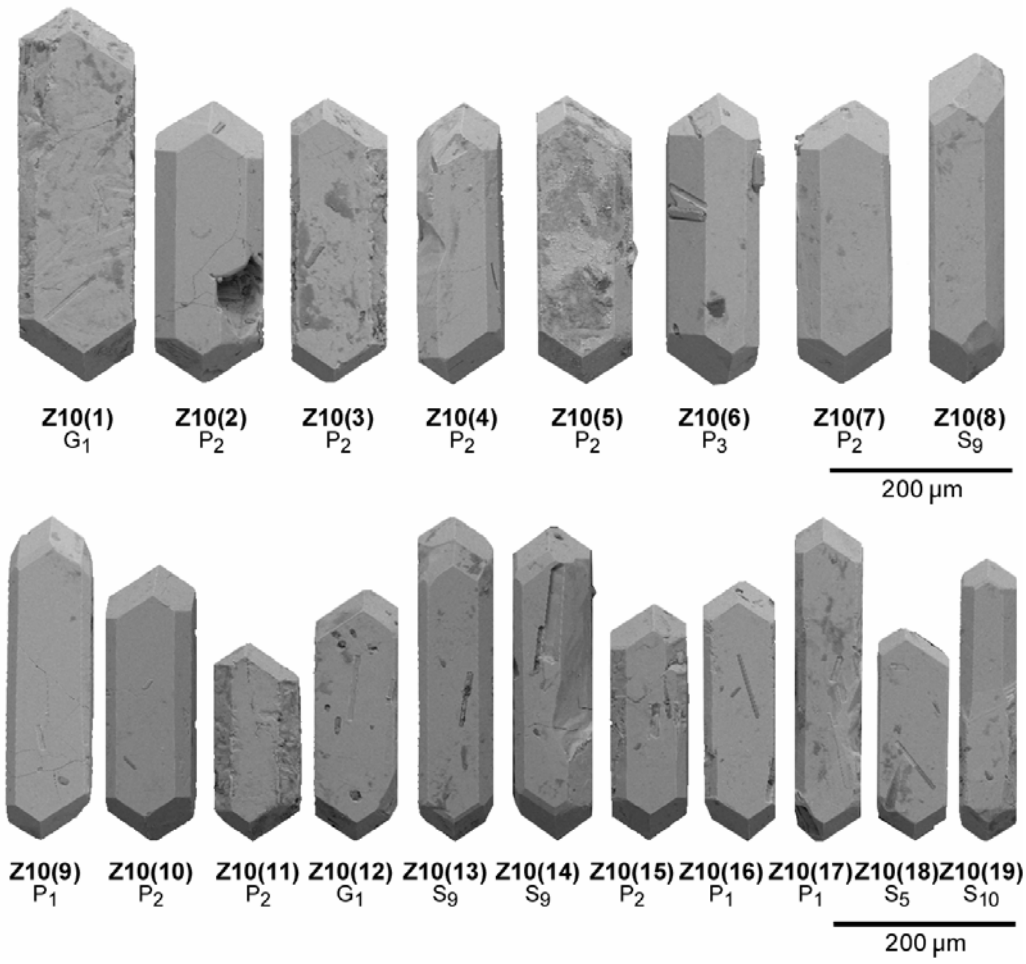

Figure 4.55. SEM images of the selected zircon crystals from the Sipahiler amphibole-biotite granite (SK-10).

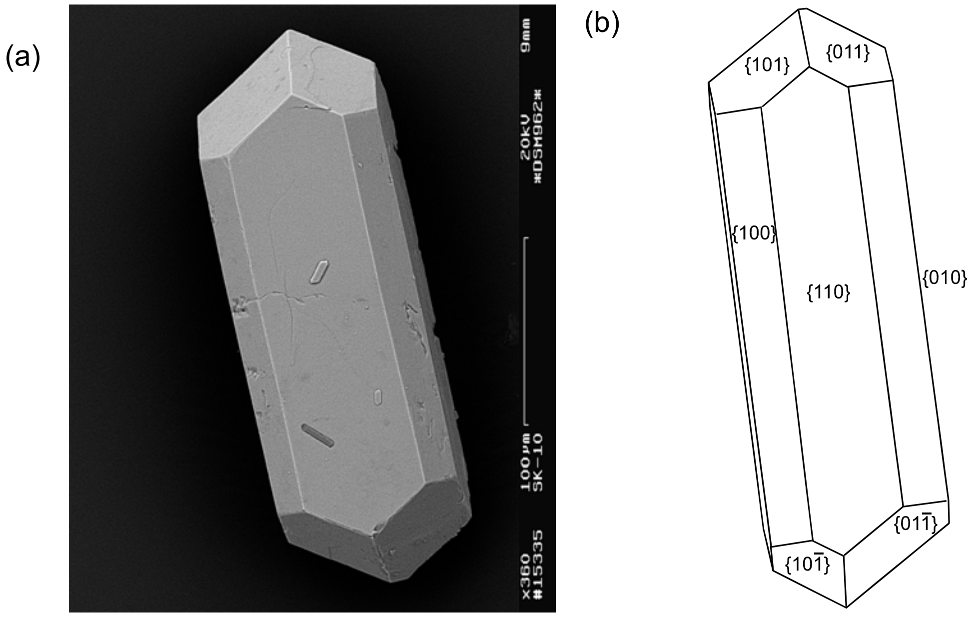

Figure 4.56. Zircon crystal [Z10(10)] from the Sipahiler amphibole-biotite granite (sample SK-10): (a) High-resolution SEM photograph, (b) Sketch model showing the crystal surfaces.

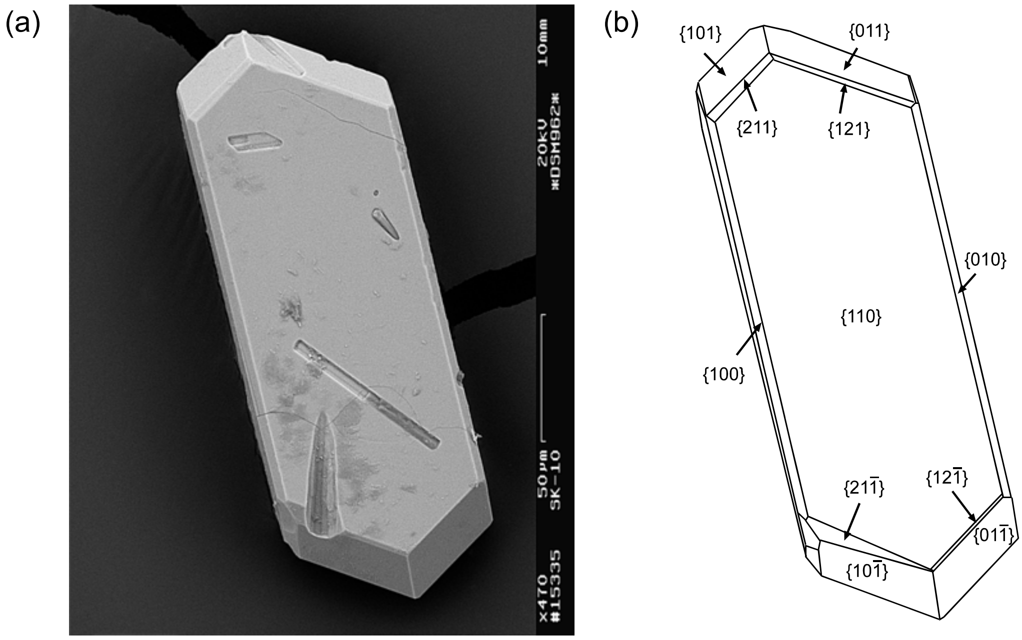

Figure 4.57. Zircon crystal [Z10(18)] from the Sipahiler amphibole-biotite granite (sample SK-10): (a) High-resolution SEM photograph, (b) Sketch model showing the crystal surfaces.

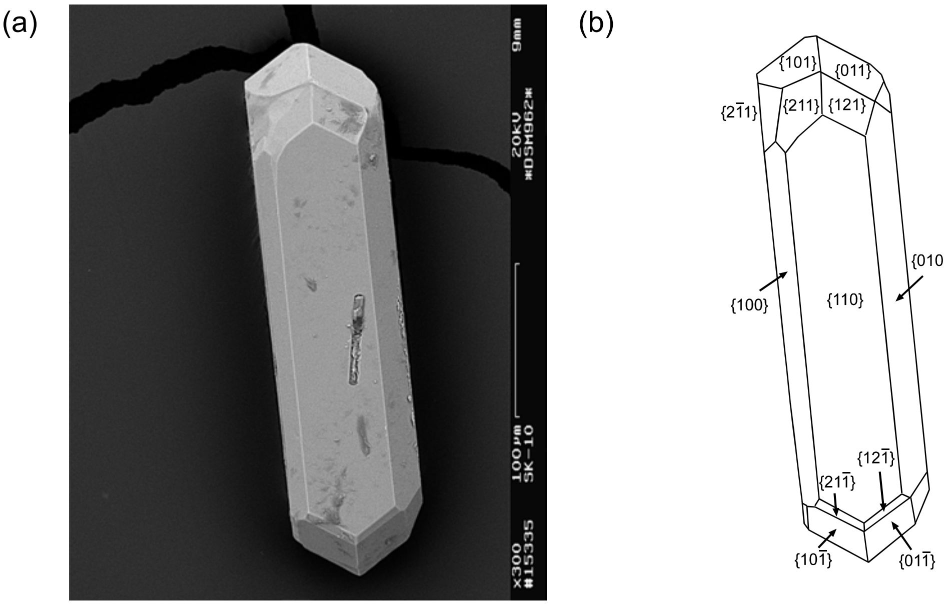

Figure 4.58. Zircon crystal [Z10(13)] from the Sipahiler amphibole-biotite granite (sample SK-10): (a) High-resolution SEM photograph, (b) Sketch model showing the crystal surfaces.

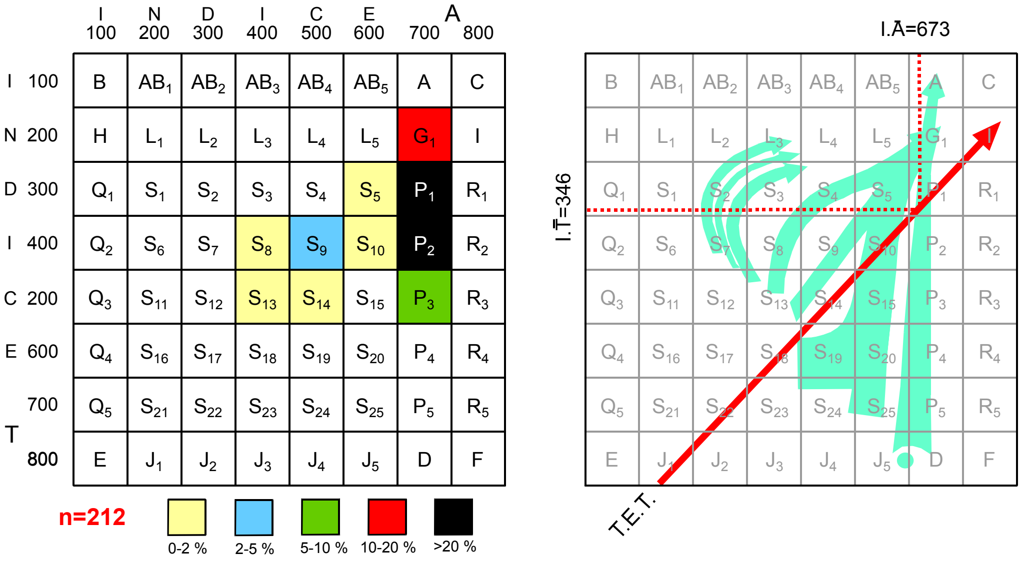

	I 100	N 200	D 300	I 400	C 500	E 600	A 700	800
I 100	B	AB_1	AB_2	AB_3	AB_4	AB_5	A	C
N 200	H	L_1	L_2	L_3	L_4	L_5	G_1	I
D 300	Q_1	S_1	S_2	S_3	S_4	S_5	P_1	R_1
I 400	Q_2	S_6	S_7	S_8	S_9	S_{10}	P_2	R_2
C 200	Q_3	S_{11}	S_{12}	S_{13}	S_{14}	S_{15}	P_3	R_3
E 600	Q_4	S_{16}	S_{17}	S_{18}	S_{19}	S_{20}	P_4	R_4
700	Q_5	S_{21}	S_{22}	S_{23}	S_{24}	S_{25}	P_5	R_5
T 800	E	J_1	J_2	J_3	J_4	J_5	D	F

n=212

🟨 0-2 %
🟦 2-5 %
🟩 5-10 %
🟥 10-20 %
⬛ >20 %

Figure 4.59. Distribution of the zircon crystals from the SK-10 (Sipahiler amphibole-biotite granite) sample on the Pupin (1980)'s typologic diagram (left side), and Typologic Evolution Trend with the mean points (I. Ā. and I. Ť.) (right side).

4.3.2.4. Torunobası Granite Porphyry

Common crystal types exist in the Torunobası granite porphyry are $S_{8-9-12-13-18}$ (Figure 4.60).

Additionally $S_{4-5-7-10-14-15-17-19-23-24}$ and G_1 types also exist in lesser percentage of abundance (Figure 4.60). Dark brownish yellow zircon crystals, bearing inclusions, as well as clear white, yellow, pale yellow or limpid varieties are observed. Moreover crystals demonstrating partial overgrowth are rarely present in the Torunobası granitoid.

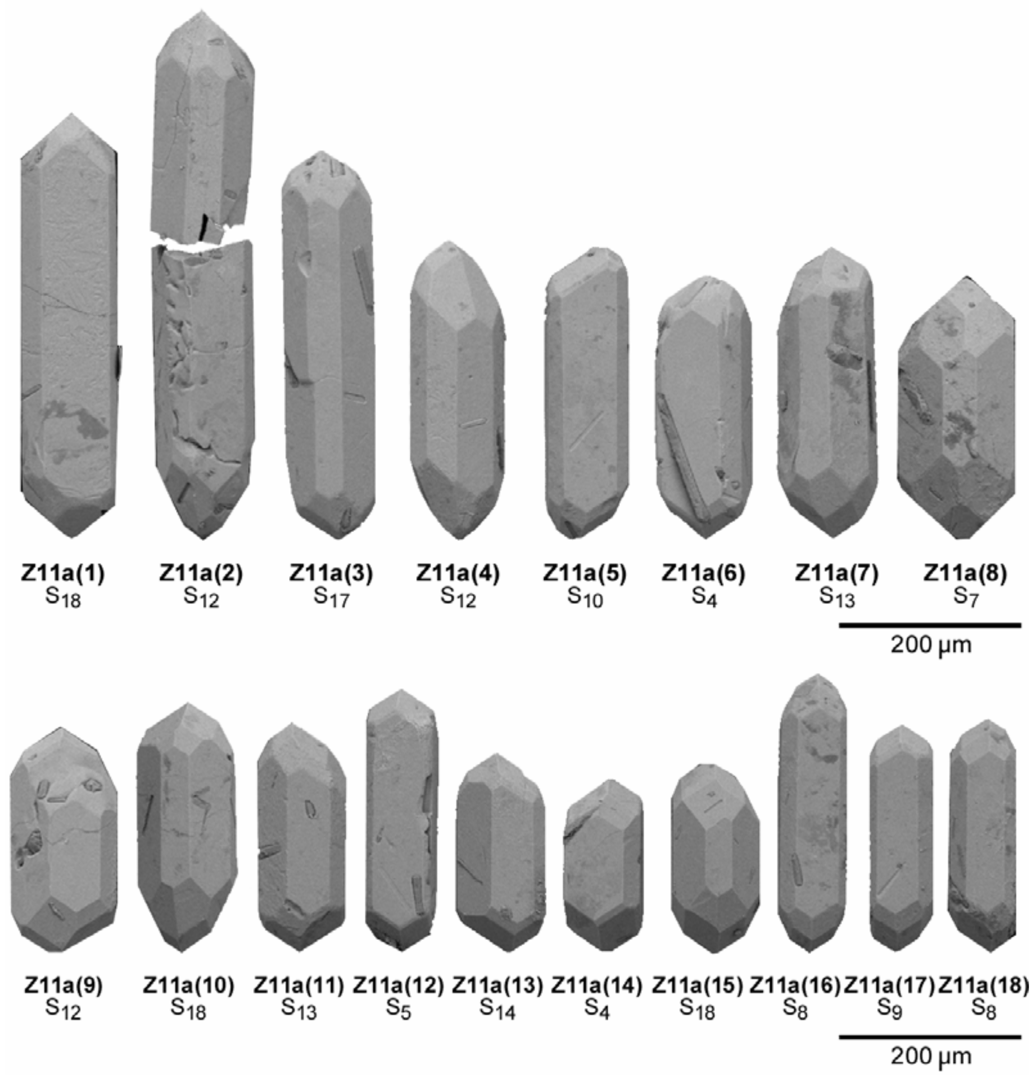

Figure 4.60. SEM images of the selected zircon crystals from the Torunobası granite porphyry (SK-11a).

[Z11a(1)] in Figure 4.61 illustrates S_{18} type which is the most common one in this granitoid. In addition, crystal [Z11a(3)] is the example of S_{17} type (Figure 4.62).

In the Figure 4.63 differential development of pyramids in a S_{17} to S_{18} type crystal can be recognized. It is also the case in Figure 4.64 in which crystal is transitional from S_8 to S_9 type.

Torunobası granite porphyry regarding the crystal types presented in Figure 4.60 and T.E.T. given in Figure 4.65 can be described as calc-alkaline hybrid granitoid (e.g. Stock 4b of Pupin, 1980).

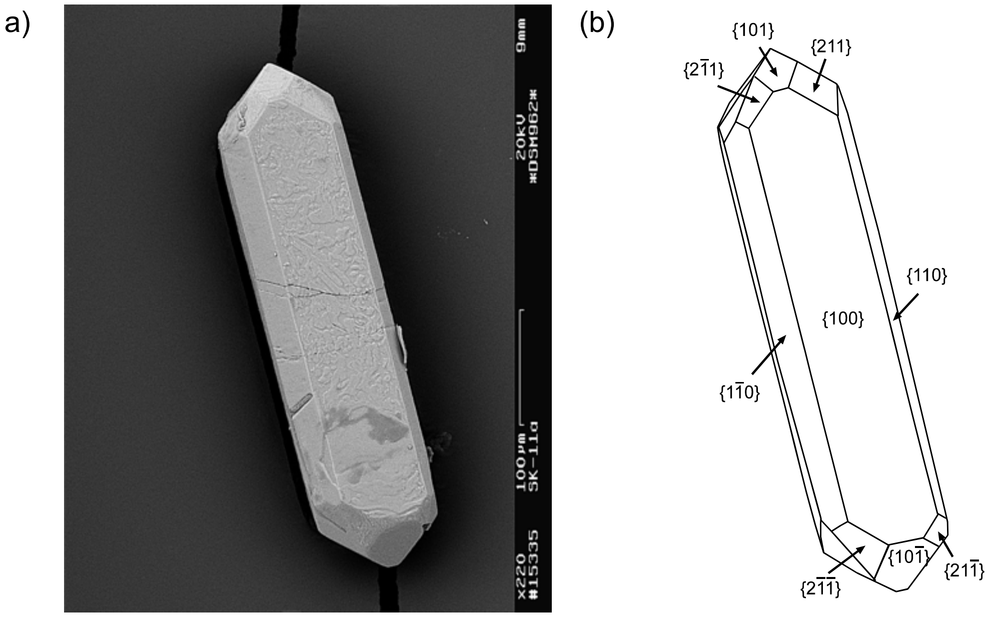

Figure 4.61. Zircon crystal [Z11a(1)] from the Torunobası granite porphyry (sample SK-11a): (a) High-resolution SEM photograph, (b) Sketch model showing the crystal surfaces.

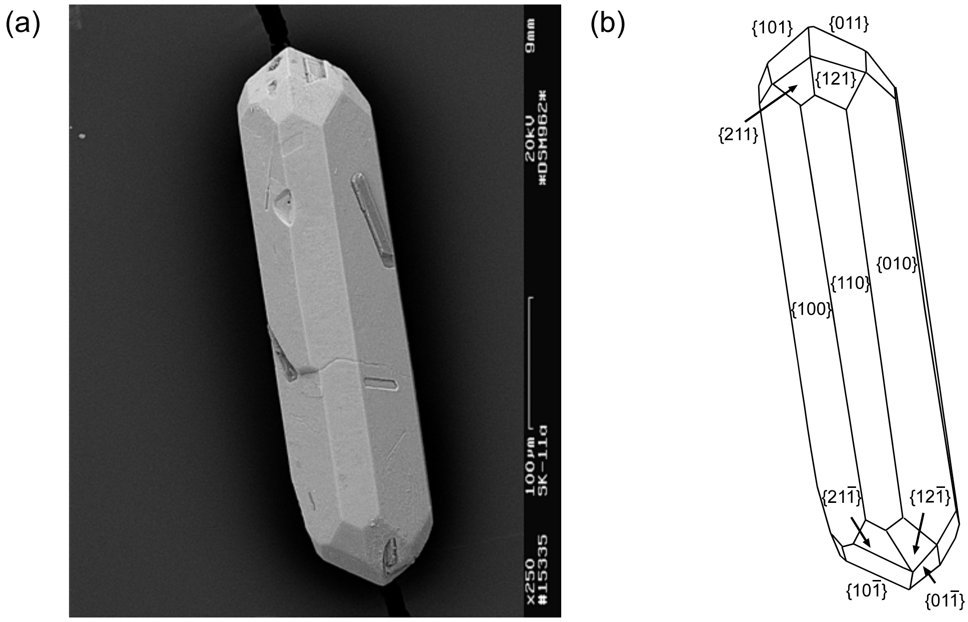

Figure 4.62. Zircon crystal [Z11a(3)] from the Torunobası granite porphyry (sample SK-11a): (a) High-resolution SEM photograph, (b) Sketch model showing the crystal surfaces.

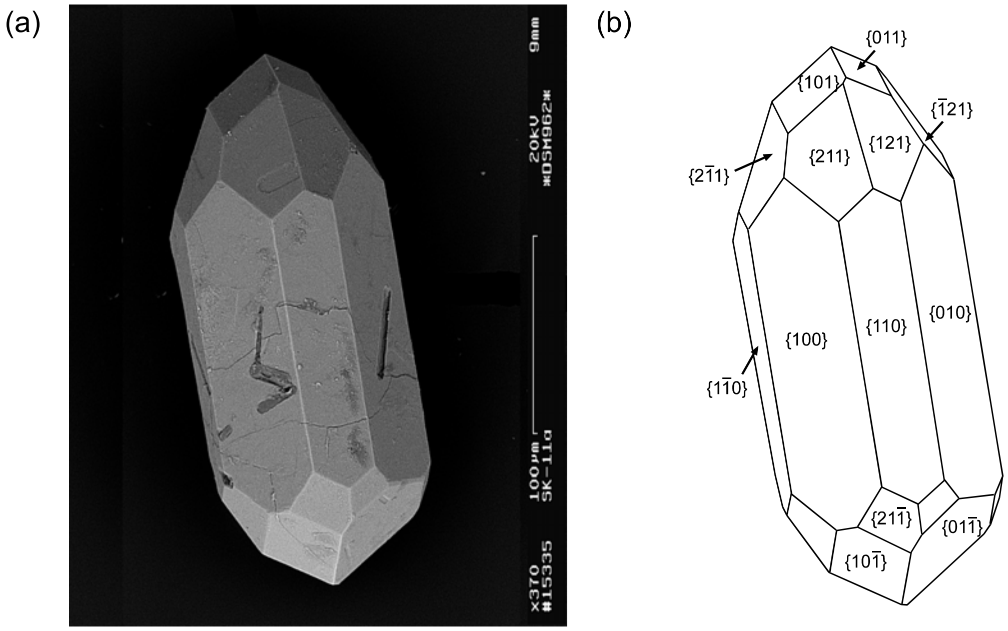

Figure 4.63. Zircon crystal [Z11a(10)] from the Torunobası granite porphyry (sample SK-11a): (a) High-resolution SEM photograph, (b) Sketch model showing the crystal surfaces.

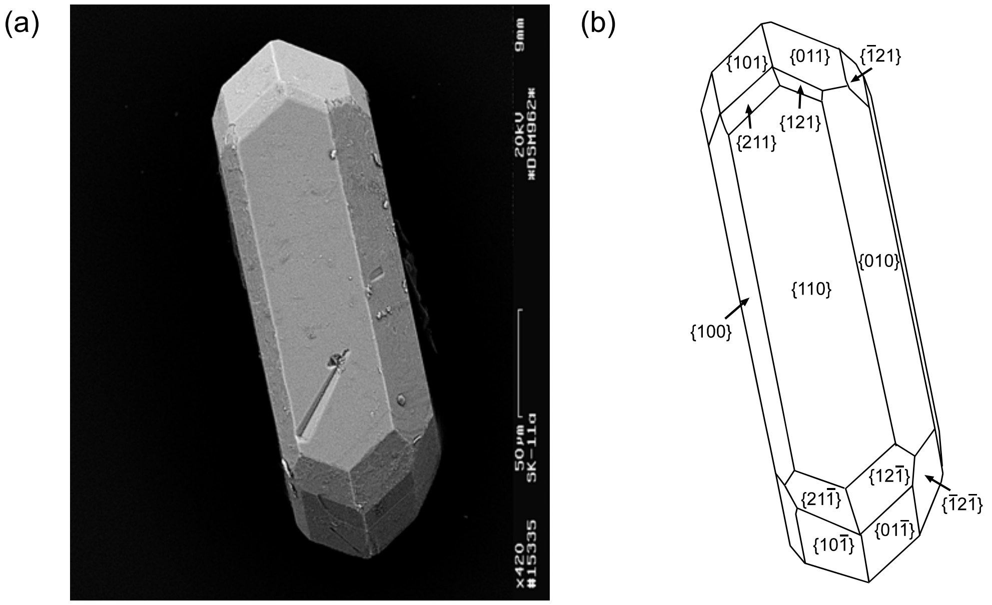

Figure 4.64. Zircon crystal [Z11a(17)] from the Torunobası granite porphyry (sample SK-11a): (a) High-resolution SEM photograph, (b) Sketch model showing the crystal surfaces.

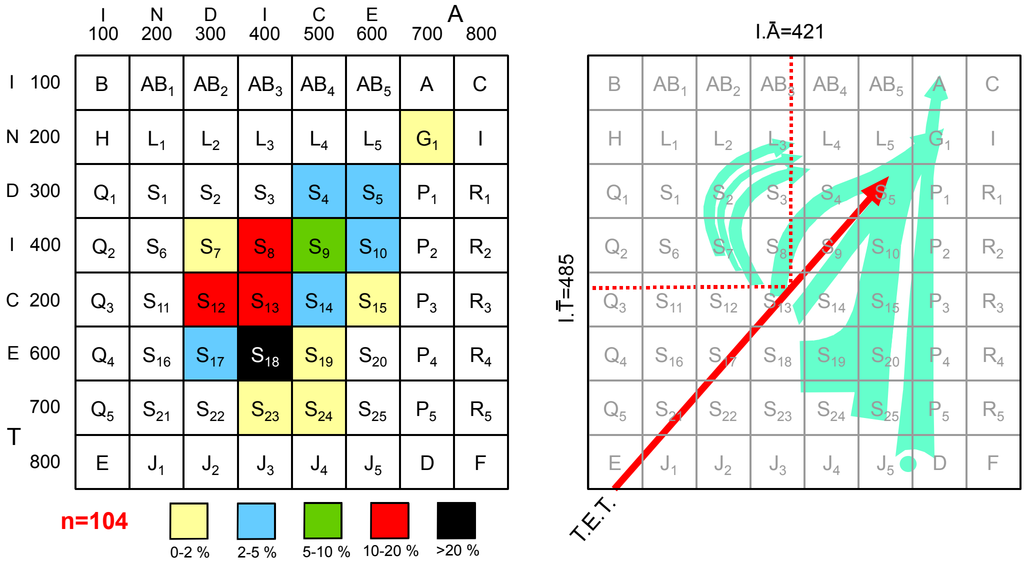

	I 100	N 200	D 300	I 400	C 500	E 600	A 700	800
I 100	B	AB_1	AB_2	AB_3	AB_4	AB_5	A	C
N 200	H	L_1	L_2	L_3	L_4	L_5	G_1 🟨	I
D 300	Q_1	S_1	S_2	S_3	S_4 🟦	S_5 🟦	P_1	R_1
I 400	Q_2	S_6	S_7 🟨	S_8 🟥	S_9 🟩	S_{10} 🟦	P_2	R_2
C 200	Q_3	S_{11}	S_{12} 🟥	S_{13} 🟥	S_{14} 🟦	S_{15} 🟨	P_3	R_3
E 600	Q_4	S_{16}	S_{17} 🟦	S_{18} ⬛	S_{19} 🟨	S_{20}	P_4	R_4
T 700	Q_5	S_{21}	S_{22}	S_{23} 🟨	S_{24} 🟨	S_{25}	P_5	R_5
800	E	J_1	J_2	J_3	J_4	J_5	D	F

n=104

🟨 0-2 %
🟦 2-5 %
🟩 5-10 %
🟥 10-20 %
⬛ >20 %

Figure 4.65. Distribution of the zircon crystals from the SK-11a (Torunobası granite porphyry) sample on the Pupin (1980)'s typologic diagram (left side), and Typologic Evolution Trend with the mean points (I. Ā. and I. Ť.) (right side).

4.3.2.5. Camili Alkali Feldspar Granite

Extensively corroded, euhedral to subhedral long prismatic colorless, pale yellow to brownish yellow zircon crystals with many inclusions are characteristic for the Camili alkali feldspar granite (Figure 4.66; 4.67). S_{18} is the most abundant type (e.g. [Z11b(5)] in Figure 4.68), while S_{13} (e.g. [Z11b(16)] in Figure 4.69) and S_{23} are other predominant crystal types. $S_{12-17-19-22-24}$ and J_{3-4} types are also present in minor amount.

T.E.T. of the Camili granitoid along with its high index Ť is conformable with the features of stock 4b, i.e. calc-alkaline hybrid type (Figure 4.70).

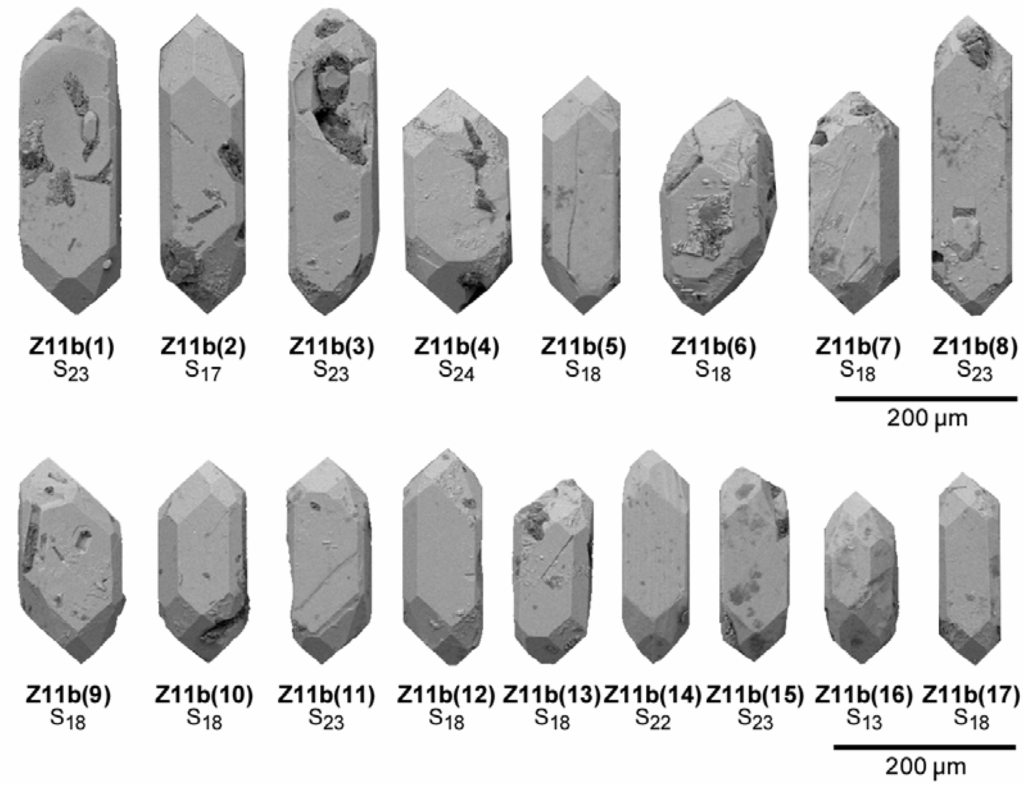

Figure 4.66. SEM images of the selected zircon crystals from the Camili alkali feldspar granite (SK-11b).

4.3.2.6. Çimkalesi Monzogranite

Çimkalesi monzogranite is characterized by idimorphic long prismatic $S_{23\text{-}24\text{-}25}$ type zircon crystals mainly and $S_{13\text{-}17\text{-}18\text{-}19\text{-}20\text{-}22}$ and $J_{3\text{-}4\text{-}5}$ types in lesser amounts (Figure 4.71). Zircons are yellow to pale yellow with various inclusions (e.g. Figure 4.72; 4.73), while limpid varieties also exist.

In the Çimkalesi granitoid S_{24} is the abundant type and represented by [Z12(11)] (Figure 4.72), [Z12(20)] (Figure 4.73) and [Z12(27)] (Figure 4.74) crystals all of which characterized by {100}>{110} and {101}={211}. [Z12(32)] (Figure 4.75) on the other hand is an example of S_{13} type in this granitoid.

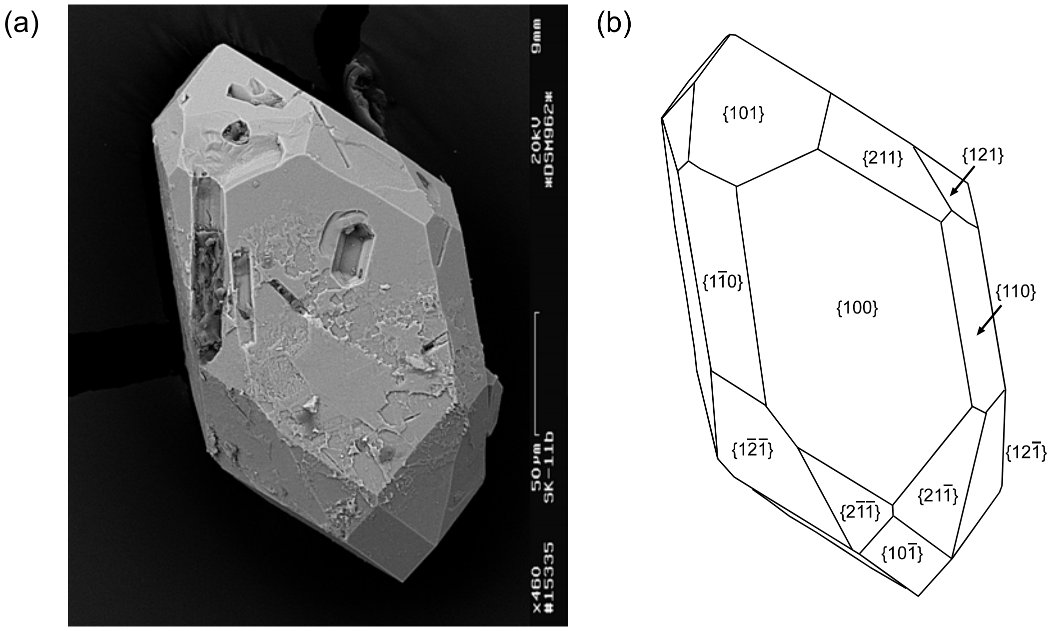

Figure 4.67. Zircon crystal [Z11b(9)] from the Camili alkali-feldspar granite (sample SK-11b): (a) High-resolution SEM photograph, (b) Sketch model showing the crystal surfaces.

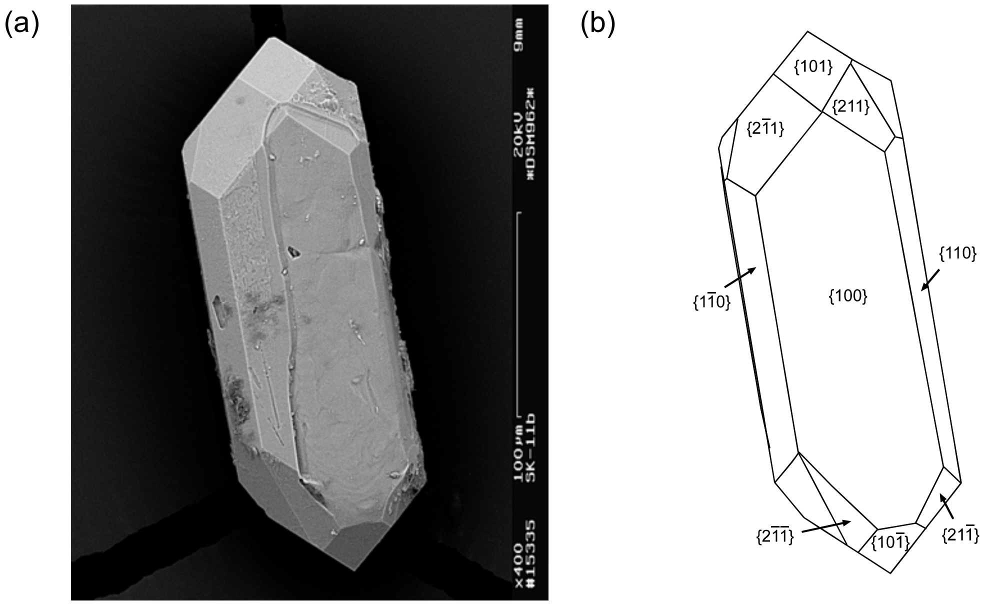

Figure 4.68. Zircon crystal [Z11b(5)] from the Camili alkali-feldspar granite (sample SK-11b): (a) High-resolution SEM photograph, (b) Sketch model showing the crystal surfaces.

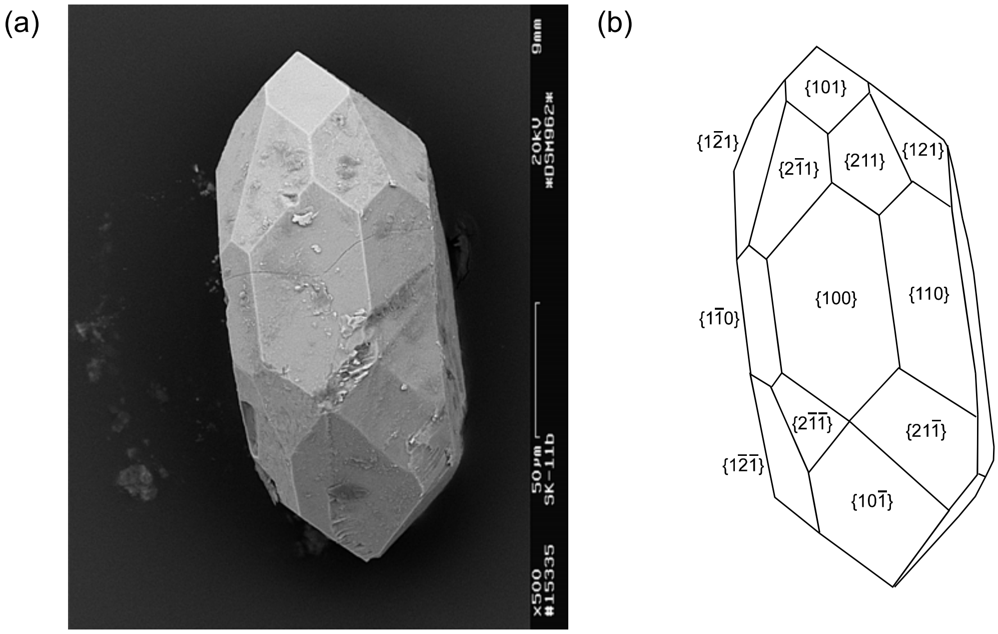

Figure 4.69. Zircon crystal [Z11b(16)] from the Camili alkali-feldspar granite (sample SK-11b): (a) High-resolution SEM photograph, (b) Sketch model showing the crystal surfaces.

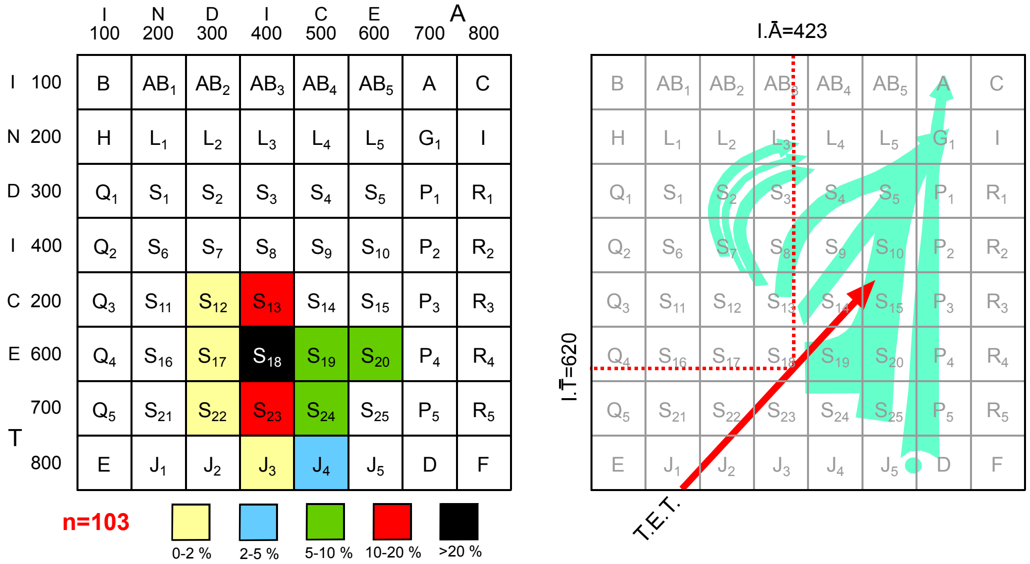

Figure 4.70. Distribution of the zircon crystals from the SK-11b (Camili alkali feldspar granite) sample on the Pupin (1980)'s typologic diagram (left side), and Typologic Evolution Trend with the mean points (I. Ā. and I. Ť.) (right side).

Zircon populations showing restricted distribution on the typology diagram are characterized by their high index Ť and T.E.T. which is similar to the stock 4c of Pupin (1980) (Figure 4.76).

4.3.3. Terlemez Quartz-Monzonite

Zircon crystals of the Terlemez quartz-monzonite are colorless, yellow to pale yellow. Long prismatic crystals with extensive presence of inclusions are characteristic feature for the zircon population of the Terlemez granitoid (Figure 4.77).

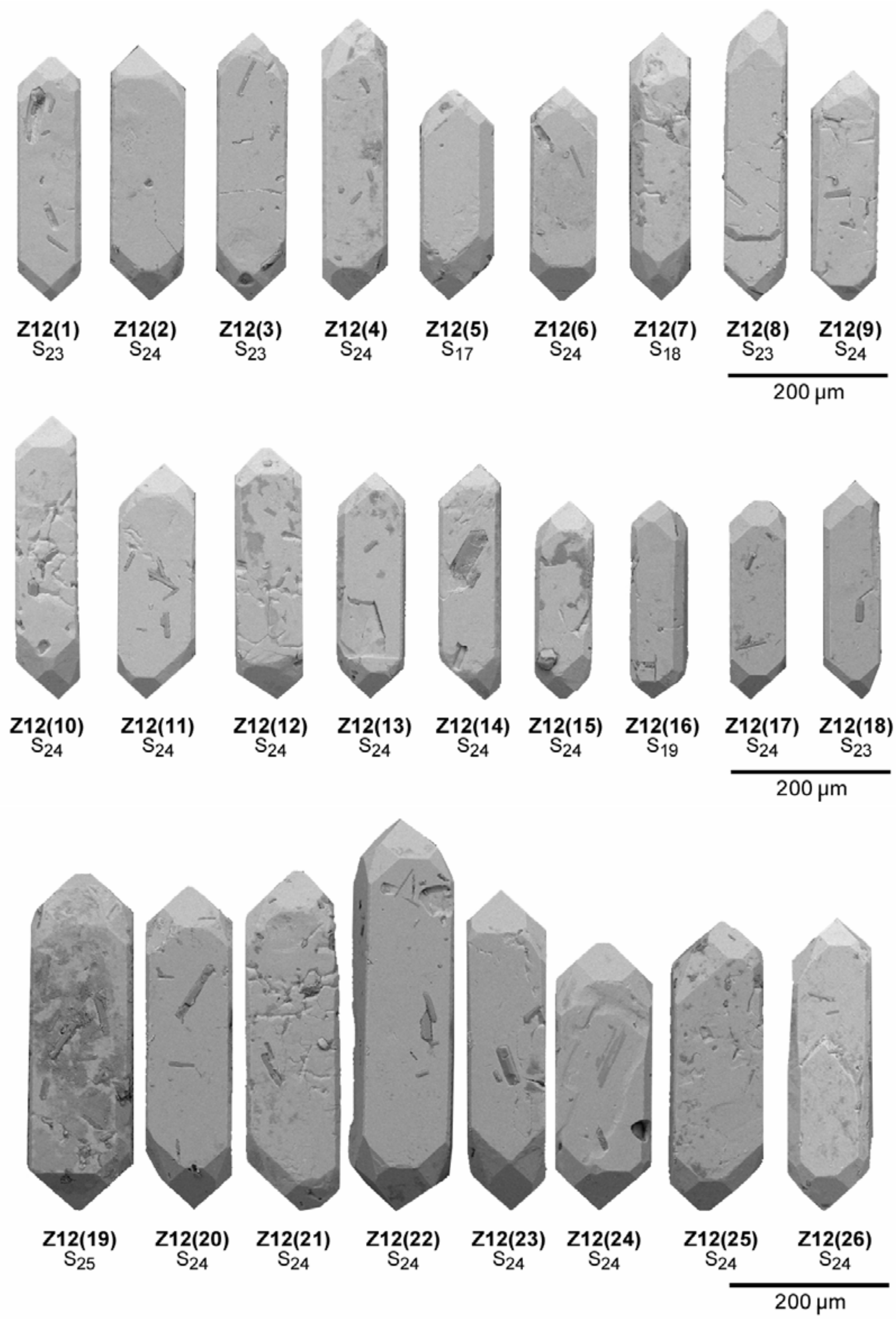

Figure 4.71. SEM images of the selected zircon crystals from the Çimkalesi monzogranite (SK-12).

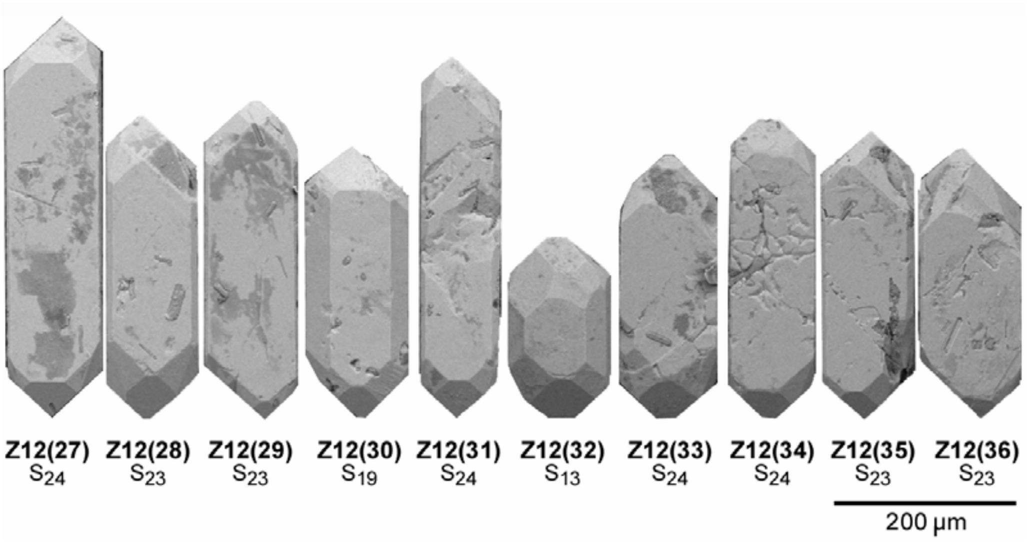

Figure 4.71 (cont'd).

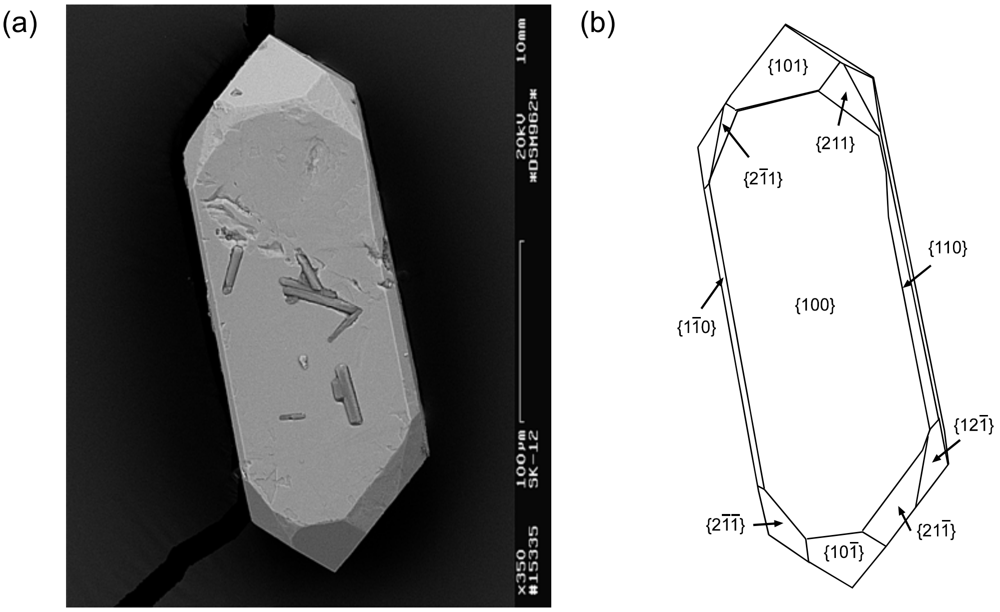

Figure 4.72. Zircon crystal [Z12(11)] from the Çimkalesi monzogranite (sample SK-12): (a) High-resolution SEM photograph, (b) Sketch model showing the crystal surfaces.

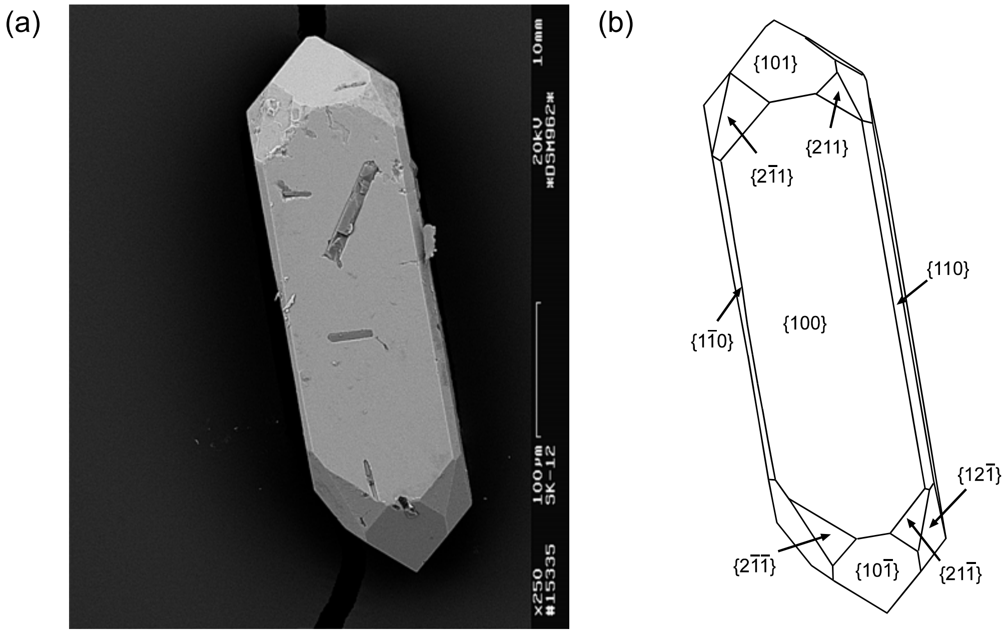

Figure 4.73. Zircon crystal [Z12(20)] from the Çimkalesi monzogranite (sample SK-12): (a) High-resolution SEM photograph, (b) Sketch model showing the crystal surfaces.

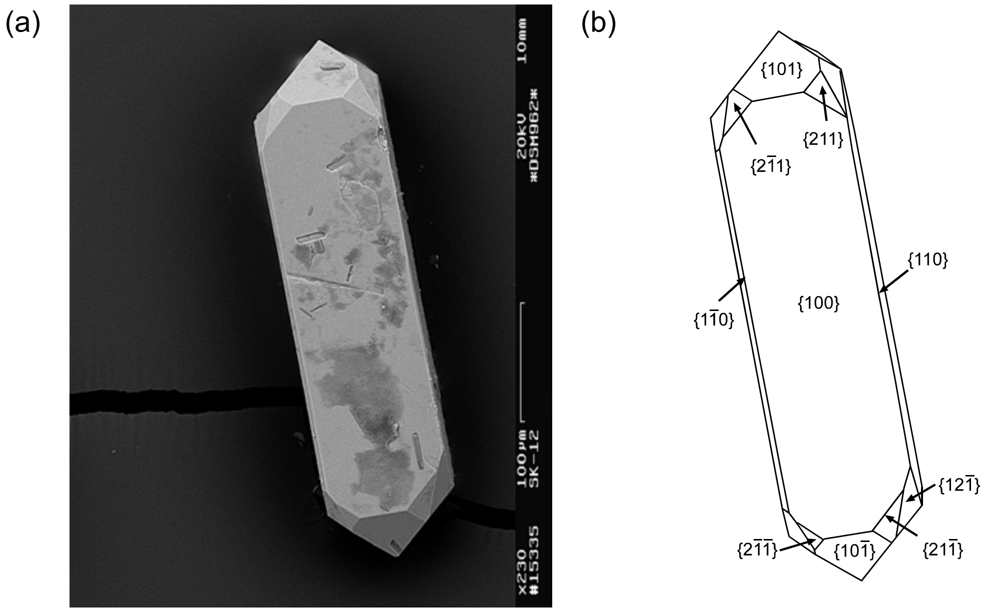

Figure 4.74. Zircon crystal [Z12(27)] from the Çimkalesi monzogranite (sample SK-12): (a) High-resolution SEM photograph, (b) Sketch model showing the crystal surfaces.

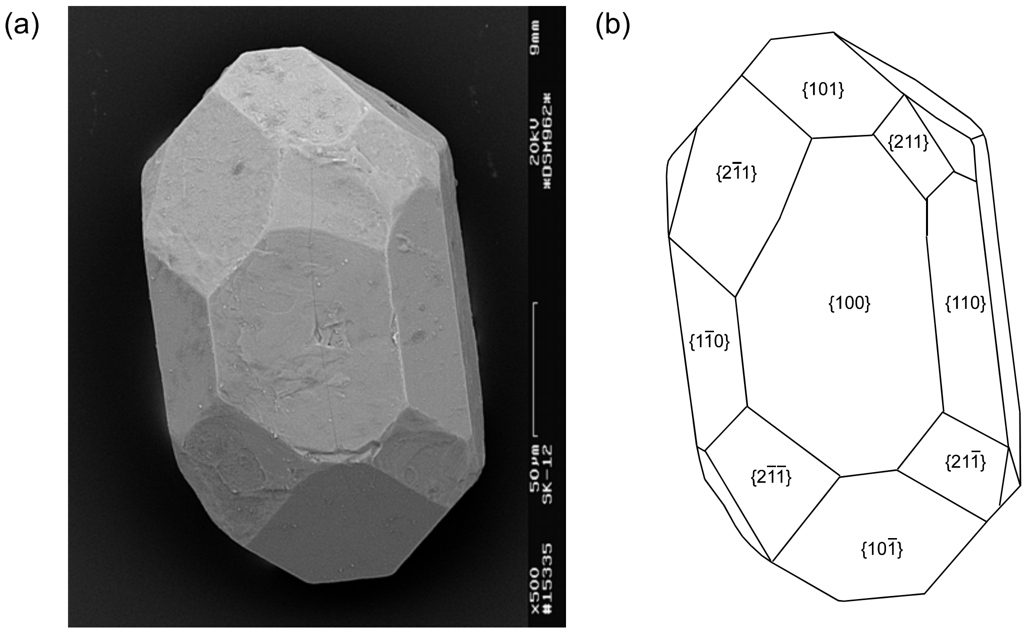

Figure 4.75. Zircon crystal [Z12(32)] from the Çimkalesi monzogranite (sample SK-12): (a) High-resolution SEM photograph, (b) Sketch model showing the crystal surfaces.

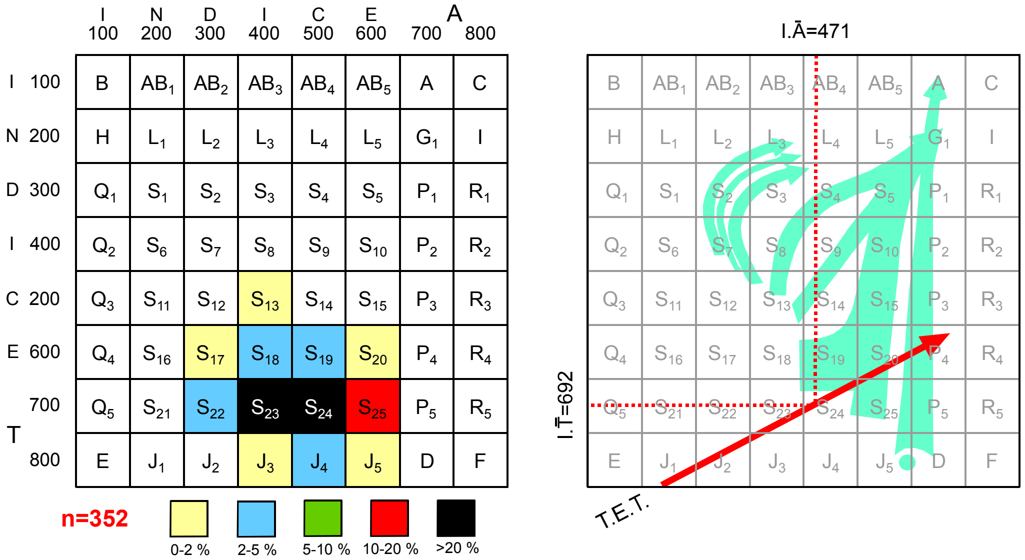

	I 100	N 200	D 300	I 400	C 500	E 600	700	A 800
I 100	B	AB_1	AB_2	AB_3	AB_4	AB_5	A	C
N 200	H	L_1	L_2	L_3	L_4	L_5	G_1	I
D 300	Q_1	S_1	S_2	S_3	S_4	S_5	P_1	R_1
I 400	Q_2	S_6	S_7	S_8	S_9	S_{10}	P_2	R_2
C 200	Q_3	S_{11}	S_{12}	🟨 S_{13}	S_{14}	S_{15}	P_3	R_3
E 600	Q_4	S_{16}	🟨 S_{17}	🟦 S_{18}	🟦 S_{19}	🟨 S_{20}	P_4	R_4
700	Q_5	S_{21}	🟦 S_{22}	⬛ S_{23}	⬛ S_{24}	🟥 S_{25}	P_5	R_5
T 800	E	J_1	J_2	🟨 J_3	🟦 J_4	🟨 J_5	D	F

n=352

🟨 0-2 %
🟦 2-5 %
🟩 5-10 %
🟥 10-20 %
⬛ >20 %

Figure 4.76. Distribution of the zircon crystals from the SK-12 (Çimkalesi monzogranite) sample on the Pupin (1980)'s typologic diagram (left side), and Typologic Evolution Trend with the mean points (I. Ā. and I. Ť.) (right side).

The Terlemez granitoid shows main types of S_{24} (e.g. Figures 4.78 and 4.79) and S_{25} (e.g. Figure 4.80) and lesser types of $S_{13\text{-}18\text{-}19\text{-}20\text{-}23}$.

Although the zircon types are limited as in the case of stock 4c with one of the most restricted distribution on the typology diagram among the studied samples, T.E.T. of the Terlemez granitoid is similar to stock 4b (Figure 4.81).

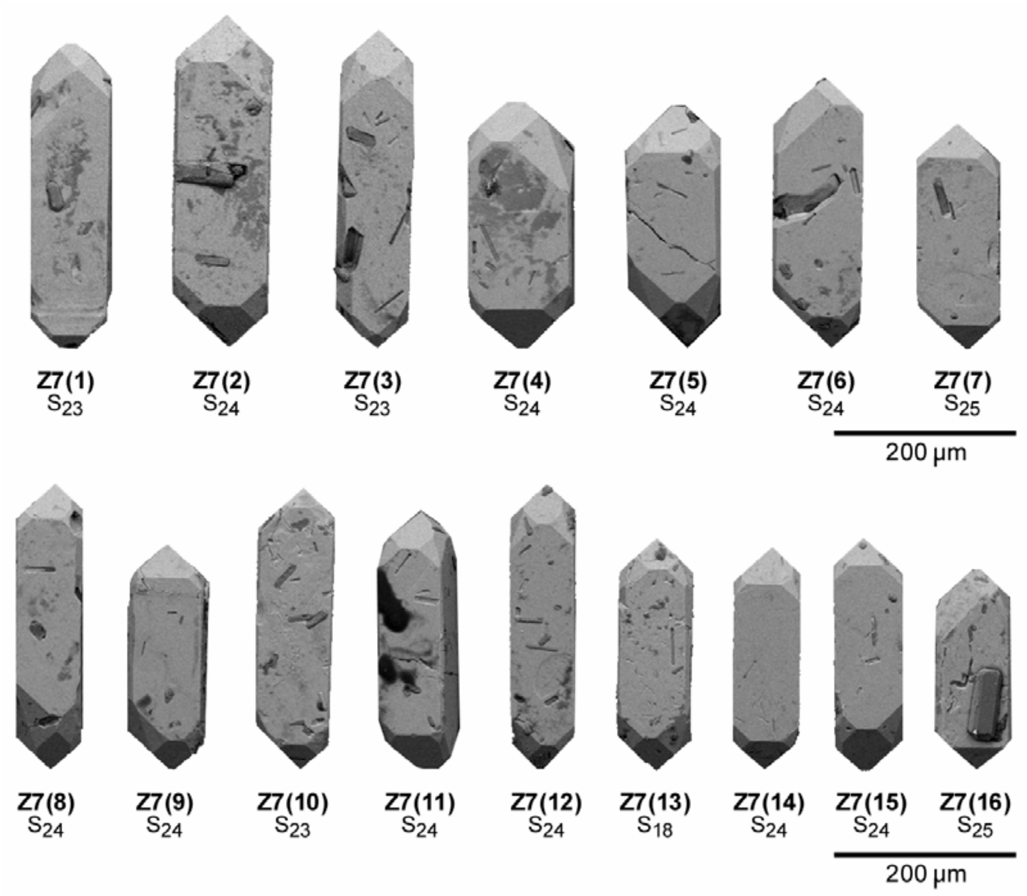

Figure 4.77. SEM images of the selected zircon crystals from the Terlemez quartz-monzonite (SK-7).

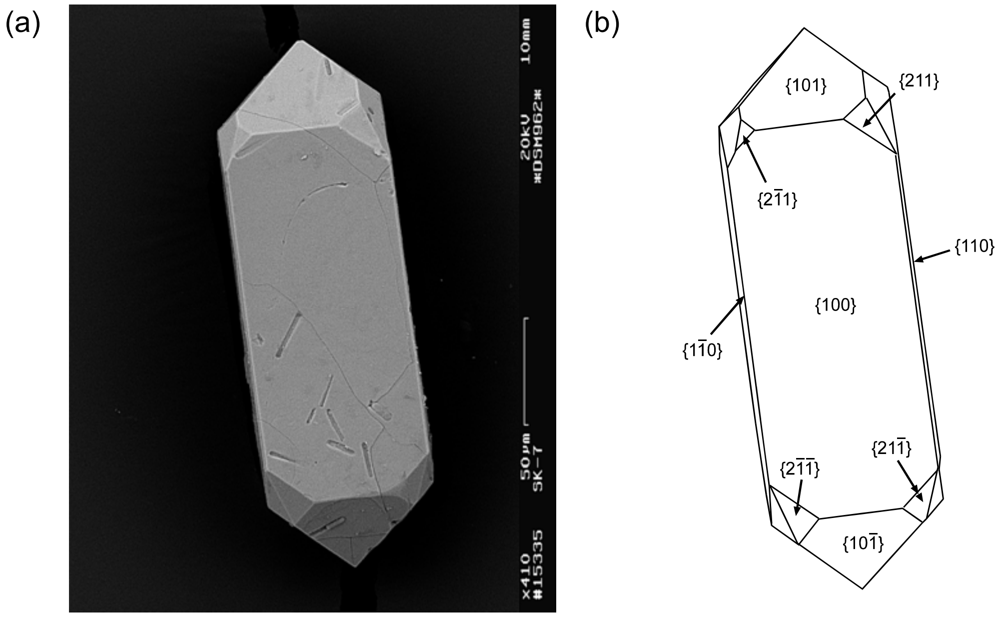

Figure 4.78. Zircon crystal [Z7(14)] from the Terlemez quartz-monzonite (sample SK-7): (a) High-resolution SEM photograph, (b) Sketch model showing the crystal surfaces.

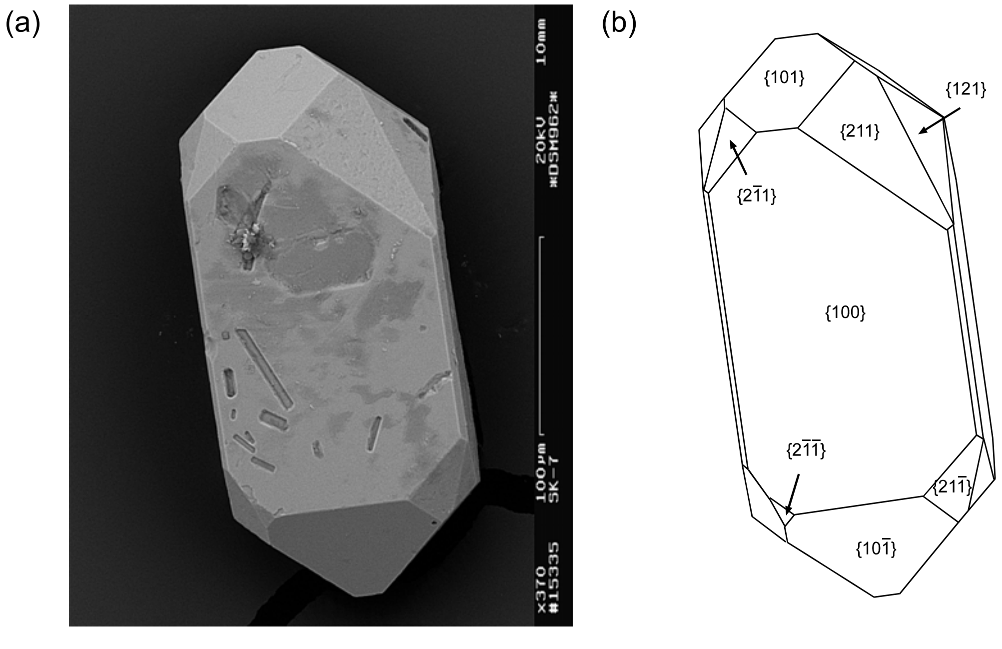

Figure 4.79. Zircon crystal [Z7(4)] from the Terlemez quartz-monzonite (sample SK-7): (a) High-resolution SEM photograph, (b) Sketch model showing the crystal surfaces.

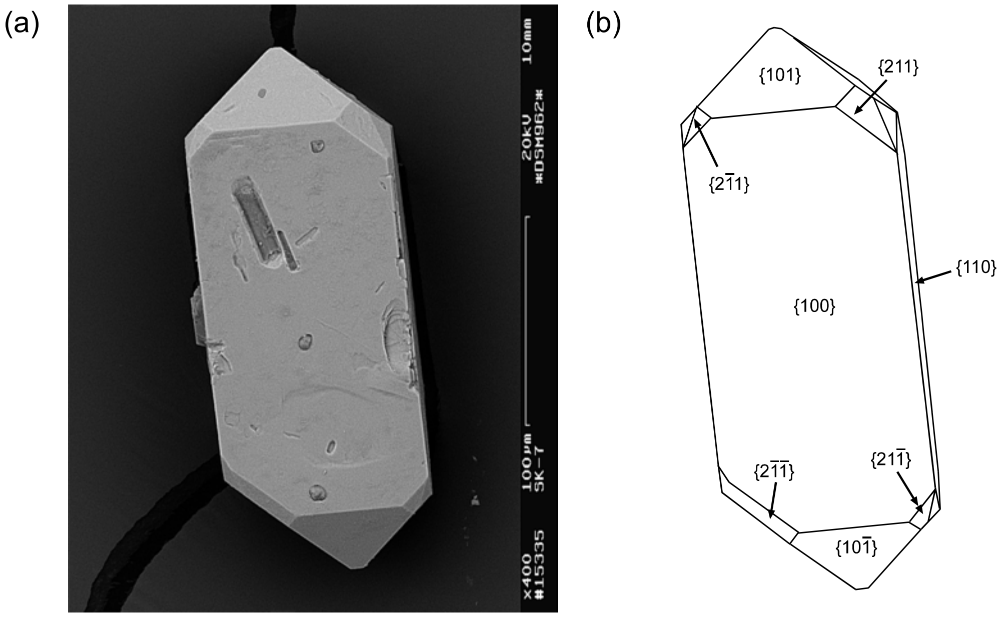

Figure 4.80. Zircon crystal [Z7(7)] from the Terlemez quartz-monzonite (sample SK-7): (a) High-resolution SEM photograph, (b) Sketch model showing the crystal surfaces.

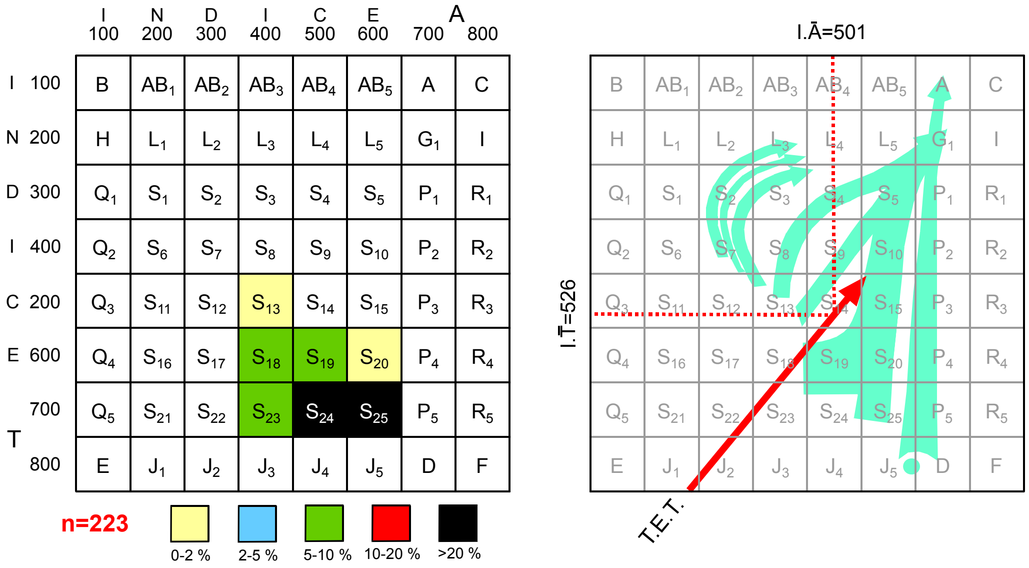

	I 100	N 200	D 300	I 400	C 500	E 600	700	A 800
I 100	B	AB_1	AB_2	AB_3	AB_4	AB_5	A	C
N 200	H	L_1	L_2	L_3	L_4	L_5	G_1	I
D 300	Q_1	S_1	S_2	S_3	S_4	S_5	P_1	R_1
I 400	Q_2	S_6	S_7	S_8	S_9	S_{10}	P_2	R_2
C 200	Q_3	S_{11}	S_{12}	🟨 S_{13}	S_{14}	S_{15}	P_3	R_3
E 600	Q_4	S_{16}	S_{17}	🟩 S_{18}	🟩 S_{19}	🟨 S_{20}	P_4	R_4
700	Q_5	S_{21}	S_{22}	🟩 S_{23}	⬛ S_{24}	⬛ S_{25}	P_5	R_5
T 800	E	J_1	J_2	J_3	J_4	J_5	D	F

n=223

🟨 0-2 %
🟦 2-5 %
🟩 5-10 %
🟥 10-20 %
⬛ >20 %

Figure 4.81. Distribution of the zircon crystals from the SK-7 (Terlemez quartz monzonite) sample on the Pupin (1980)'s typologic diagram (left side), and Typologic Evolution Trend with the mean points (I. Ā. and I. Ť.) (right side).

CHAPTER 5

CATHODOLUMINESCENCE

5.1. Background

5.1.1. Cathodoluminescence, a Tool for Investigation of Inner Structures

When certain minerals are subjected to an electron bombardment they emit visible radiation or light (i.e. light falls within the uv-visible region of the spectrum) due to the excitation by high-energetic electrons, and this optical phenomenon is called as cathodoluminescence (CL) (Potts, 1987; Gucsik et al., 2002). In other words, CL is caused by an incident electron exciting a sample electron to a higher energy state (Marshall, 1988).

Electrons within the crystal lattice occupy two bands of energy, i.e. the ground state (or valence band) and a higher energy conduction band, which are separated by a forbidden energy region including intermediate “trapping” centers (Potts, 1987). During interactions between the primary electron beam and mineral, electrons are excited from valence to conduction bands, and after a short half-life in this excited state, the electron reverts to a lower level and emits the energy lost as a photon, and finally returned to the ground state directly or via intermediate energy levels (Marshall, 1988; Potts, 1987).

In some minerals, the energy difference between these bands is large enough to yield an electromagnetic radiation that can be determined by the CL detector (Potts, 1987). On the other hand, transitions of excited atoms to higher energy levels are not possible in conducting materials such as metals, so no CL is produced, while some minerals do not show any CL for some reasons, e.g. incorporated CL-quenching or suppressing elements, concentration quenching, or non-radiative energy transfer (Marshall, 1988).

Zircon is well suited for CL imaging, and studies of synthetic and natural crystals have shown a relationship between trace and rare earth element content and CL signal (Rémond et al., 1995; Poller et al., 2001). Moreover, CL is often accepted as a critical tool for both ion probe and isotope dilution single crystal analyses of zircons. Accordingly, the CL emission spectra may be used as a guide to identify different regions within a zircon crystal or homogeneity within a zircon population as a prior step of ion probe studies in geochronology (Hanchar and Rudnick, 1995).

Investigation of inner structures of zircon by CL is a matter of interest for igneous and metamorphic petrology since 1970s (Hanchar and Miller, 1993 and references therein) because internal structures (e.g. igneous growth zoning, metamorphic growth) and different color CL emissions of zircon crystals are records of different geologic events (Hanchar and Rudnick, 1995).

Hanchar and Miller (1993) indicated that CL reveals more information in depth on inner structures of zircon crystals compared to the other methods such as viewing of HF-etched zircon (mounted in epoxy and polished to its half thickness) by using reflected light microscopy (e.g. Black et al., 1984) or imaging by Backscattered Electron (BSE) microscopy (e.g. Paterson et al., 1992).

Zircon internal structures can be differentiated into primary and secondary structures of which the former is formed during crystallization of zircon while the latter is formed after crystallization of zircon (Pidgeon et al., 1998). CL is useful for detection of both primary and secondary features preserved in the crystal.

In most cases, the electron falls back to an intermediate “trapping” centers that are caused by imperfections in the structure of the crystal lattice or by the presence of impurity ions. If the impurity ions are excited then the emitted radiation characterizes these impurities in the mineral (Potts, 1987). By CL imaging, therefore, it is not only possible to investigate the face development of the crystal but also to delineate the impurities, i.e. concentration of foreign atoms, in the zircon structures.

5.1.2. Crystal Growth and Internal Structures of Zircon

It is widely known that the growth zones in zircons of igneous rocks result from physical and chemical variations in the melt or solutions from which the zircon crystallizes and lack of reequilibration (Speer, 1982), their origin in detail, however, has remained enigmatic. In the first half of the 19th century Niggli performed spectacular studies on the crystals forms and habits. He suggested that the principal zones of a crystal correspond to important lattice rows, the major growth forms, cleavage planes and plastic behavior also related to the important lattice nets containing important lattice rows (Niggli, 1926 in Kostov and Kostov, 1999). His studies lead to foregoing ideas trying to answer how a crystal grows. Kleber (1959 in Kostov and Kostov, 1999) suggested that the principal zones with shortest interatomic distances have strong bonds.

Hartman (1973) proposed the PBC (periodic-bond-chain) theory based on the significance of strong bonds in the structures of minerals. Hartman (1973) suggested that the PBCs corresponded to uninterrupted chains of strongly bound arrays of atoms in the structure, running parallel to edge of the crystal, hence differentiating three categories of faces, i.e. F (flat), S (stepped) and K (kinked) faces. He further offered that the F faces composed of slices d_{hkl} containing two or more PBCs, the S faces only one PBC and the K faces, no PBC at all. The slice thickness d_{hkl} represents the interplanar spacing of the (hkl) face (Hartman, 1973). Higher growth rates make zones become thicker, or vice versa. The attachment energy of a slice, defined as the energy per molecule released when a new slice is attached to the crystal face, is considered to be a measure for the growth rate of an F face, the latter being proportional to the growth rate (Hartman, 1973). The F faces grow slowly according to a layer-by-layer mechanism and are important, S faces and forms grow according to a one-dimensional nucleation, the K-faces and forms need no nucleation, grow very fast, and therefore are rarely found on a crystal (Kostov and Kostov, 1999). When other growth factors interfere, especially supersaturation and impurities, K and S faces may become more important in crystal evolution than F faces (Kostov and Kostov, 1999).

Vavra (1990) indicated that the F faces of zircon like {100} and {011} grow layer by layer by two-dimensional nucleation that is promoted by Zr-supersaturation of the melt. Adsorption of cations (Na, K, Al) on the charged {011} faces on the other hand, changes the relative surface energies of the possible structures and that this changes the growth mechanism and growth rate (Vavra, 1994). Additionally, growing of S faces of zircon such as {121} and {301} is related to the foreign atom adsorption that lowers the rate of growth (Vavra, 1990). Moreover, sizes of these pyramids maybe controlled by the growth rates of adjacent crystal forms like {011}, {010} or {110} (Vavra (1994). Vavra (1994) stated that the {110} prism being a S-form might show F-form characteristics by the adsorption of protons and become growth inhibited by the adsorption of H_2O or trace elements enriched in the residual liquid. However, small amount of corrosion at the crystal surface is sufficient to disrupt the adsorption layer (and H_2O effect) and allows crystal faces to return high growth rates until the adsorption layer is rebuilt (Vavra, 1994).

Trocellier and Delmas (2001) indicated that natural zircons intrinsically show heterogeneity, which has a chemical and radiation damage origin. The volumetric distribution of impurities in the crystal may be non-uniform due to the events occurred during zircon genesis and radiation damage by α rays and recoil nuclei follows the distribution of U and Th (Trocellier and Delmas, 2001). Accordingly, on the BSE images Paterson et al. (1992) demonstrated the cracks within the cores terminating the core/rim boundaries that are consequences of the differential expansion of the zircon structure due to slowly accumulated α-particle damage. Additionally, the α-recoil results in contrasting spatial distribution of parent and daughter and contrasting level of structural damage that may result in contrasting mobilization of U and Pb from zones of high and low recoil damage (Romer, 2003).

In magmatic stages, some processes cause changes in the atomic structure of zircon crystal. During these stages, due to the concentration of the trapped foreign atoms in the crystal lattice of zircons some heterogeneities and contaminations may result in (Sommerauer, 1974). The concentration of foreign atoms leads to formation of igneous zoning that can be easily recognized in CL images (Vavra, 1990). Igneous zoning is the theme of several studies (e.g. Sommerauer, 1974; Miller et al., 1992; Paterson et al., 1992; Hanchar and Miller, 1993; Hoskin, 2000; Fowler et al., 2002) since it carries considerable information regarding the history of zircon.

Oscillatory zoning being the most common type of igneous zoning is a series of parallel three-dimensional growth shells of differing width and trace element content that form an “onion ring” texture (Hoskin, 2000) which is formed during a single episode (Hanchar and Miller, 1993). Several models were developed to explain the oscillatory zoning, e.g. bulk-system-wide perturbations, dynamic feedback and compositional boundary layers, cyclic polymeric-monomeric oscillations, and isothermal undercooling (Hoskin, 2000 and references therein). These studies mainly focus on the nature of zoning to demonstrate if they are resulted from extrinsic processes, i.e. those related to bulk-system scale fluctuations, or intrinsic processes, i.e. those belong to basic nature of the crystal whose patterns are self-organized (Fowler et al., 2002).

Hoskin (2000) presented a complex model in which the oscillatory distribution of trace elements in zircon is suggested to be controlled by dynamics at the zircon/melt interface involving cation substitution, diffusion, and melt polymerization and structure generation.

Fowler et al. (2002) on the other hand, suggested that the small-scale oscillatory zoning is the consequence of a nonlinear feedback process where the melt layer close to the crystal became depleted in Zr and enriched in U, Th, and REEs relative to the bulk melt driving the crystal to a new composition and oscillatory growth zonation. Fowler et al. (2002) further postulated that the large-scale harmonic zones likely reflect changes in the bulk geochemistry of the system, e.g. periodic influxes of new material or other large-scale changes, from which the zircon grew, though they assumed that the oscillatory zoning was not the simple one-to-one reflection of changes within the bulk system. Moreover, Vavra (1990) stated that widely spaced zoning, interrupted by surfaces of dissolution, is related with low Zr-supersaturation, whilst narrowly spaced uninterrupted oscillatory zoning is a marker of high Zr-supersaturation of the melt.

Vavra (1993) manifested that to investigate morphological evolution of the crystal is more critical than to describe outer form solely. He established a method in which the morphological evolution of a crystal can be constrained by a set of normalized growth rate functions.

The first step of identifying the evolution stages of the zircon crystal is the indexing of growth bands (Vavra, 1993). Vavra (1993) proposed that if {100}- and {110}-parallel sections are prepared, the growth bands of each face can be identified by their characteristic orientation measured as the angle α between growth band and c-axis. The orientation of growth bands and their characteristic angles are shown in Table 5.1.

In order to identify an unknown growth banding that occurs in a cathodoluminescence image, the angle between the unknown band and the trace of any prism face is measured. The characteristic angle is independent from the central distance of the section plane.

Table 5.1. Characteristic angles of crystal face in zircon sections (after Vavra, 1993). CD: Distance of section from the crystal center.

	Face	**Angle of face at CD=0 (°)**	**Angle of face at CD=0.24 (°)**	**Angle of face at CD=0.44 (°)**
Growth banding in sections parallel to {100}	**{011}**	48.2	48.2	
	{112}	65.5	65.5	65.5
	{010}	0	0	
	{031}	20.2	20.2	
	{121}		29.3	29.3
	{101}		90	90
	{110}		0*	0
	{211}			48.2
	{301}			90*
Growth banding in sections parallel to {110}	**{011}**		57.4	57.4
	{112}	57.4	90	90
	{010}		0*	0
	{031}		27.4*	27.4
	{121}	27.4	27.4	57.4*
	{110}	0	0	

* Angle observed in inner zones of the crystal

However, some ambiguities may arise due to the non-central crystal sections cutting growth bands of additional faces. If the section is non-central, the distance from the center of the crystal (CD) should be taken under consideration while defining the growth bands (Vavra, 1993). Also there is no way to identify the flat pyramidal face {112} in {110}-parallel sections since the growth bands of {011} and {112} have exactly the same orientation ($\alpha = 57.4°$) (Vavra, 1993) (e.g. Table 5.1).

In the present study, prisms and pyramids of zircon crystals are indexed by using these characteristic angles. Accordingly, Vavra's approach is used to argue that growth rates and morphological development are essentially reflective of the physical and chemical factors encountered during evolution of the crystal and medium in which it grows.

5.2. Methods of Cathodoluminescence Study

5.2.1. Sample Preparation for Cathodoluminescence Study

CL sample preparation is directed to obtain CL images of the inner part of the crystals whose morphologies were imaged by SEM on the same orientation. To accomplish the scope of the research different sample preparation technique is developed in this study.

After completion of the SEM study, sticky tapes prepared for SEM study were released from the (SEM) measurement discs. The strips of the stick tapes with zircon crystals are attached onto the slides row by row considering the crystals with similar thickness to be mounted onto the same slides. For some samples it was necessary to separate the different rows of the same sample and stick to different slides, or combine the rows from different samples in the same slide regarding the thickness proximity. The slides were then covered by epoxide resin and waited for solidification. Afterwards, slides were etched up to their half-thickness, i.e. polished sufficiently to reveal cores, for better observation of the inner structures of the crystals and coated by carbon alloy. In spite of care taken during slide preparation some of the crystals were lost during etching and polishing processes. Slide preparation for CL was performed in the Slide Preparation Laboratory of the Geological Research Center (Geoforschungszentrum-GFZ) in Potsdam/Germany.

In the previous studies crystals selected for CL work are put into the epoxide resin, and they orient themselves along their dominant prism face (e.g. Vavra, 1990, 1993, 1994). But the crystals those placed in the epoxide resin would not give good and detailed SEM images as presented in this study. Additionally, by the sample preparation method introduced in this study it is also possible to obtain SEM or CL images from the crystal of which frontal face is not the dominant one (e.g. ([Z11a(10)]).

5.2.2. Analytical Methods

CL study was carried out in the SEM Laboratory of GFZ, as the SEM study, by the scanning electron microscope DSM 962/Zeiss equipped with Zeiss cathodoluminescence detector using a 15 kV accelerating potential. CL detector receives its signals from the sample straight vertically beneath as in the case of BSE.

Overview CL images were taken and crystals that were suitable for high-resolution CL images were chosen like in the SEM study. CL imaging was performed in two steps: first totally 138 crystals were imaged three by three (or four by four) by 150x magnification. These overview images were studied in detail on the computer screen to choose the most typical, representative and informative euhedral and unbroken, and in some cases the crystals with interesting features. Totally 43 crystals (out of 138) were selected for high-resolution SEM imaging. In the second step high-resolution SEM imaging was performed on these crystals by 250x - 600x magnification.

When possible, crystal surfaces are indexed based on to their characteristic angles (e.g. Figure 5.1), and denoted on the sketch views that are extracted directly from the CL images. Surfaces parallel to indexed ones were not labeled unless it was necessary. Cores, corrosion stages, and secondary features, such as recrystallization, trace element band thickening and flow structures, are shown on the CL images.

5.3. Investigation of the Inner Structures of the Zircon Crystals from the Central Anatolian Granitoids

Inner structures and evolution histories of the granitoid samples from Central Anatolia were investigated by using the CL imaging.

Zircon crystals enriched from the granitoids of the Ekecikdağ, Ağaçören and Terlemez plutons are generally of igneous origin, whereas some have inherent cores. Intra-crystalline structures of the zircon crystals were investigated by using CL for detection of the different episodes in the genesis of zircons and their host granitoids.

5.3.1. Ekecikdağ Pluton

5.3.1.1. Borucu Granodiorite-Monzogranite

Two zircon crystals ([Z1(23)] and [Z1(19)]) were imaged by CL from the Borucu granodiorite - monzogranite. Both of them show growth zoning (Figure 5.1 and 5.2). The growth-zones reflecting the trapping of foreign atoms in different concentrations outline the shape of the crystal at succeeding stages of growth (Vavra, 1990).

The zircon crystal [Z1(23)] is of P_3-type (Figure 4.4) and is sectioned parallel to the {100} prism face (Figure 5.1). Crystal faces are indexed as explained in section 5.1.2, and characteristic angles are denoted on the crystal faces to exemplify the measurement. Morphology of this crystal is characterized by combination of {100} and {110} prisms and {101} and {011} pyramids. However, examination of CL image (Figure 5.1) reveals that during its evolution this crystal had also {121} pyramidal face. In the final shape, the crystal [Z1(23)] does not have {121} pyramid, which exists in internal zones. In this manner, P-type description of this crystal (Chapter 4) interprets only the outer form, but not the crystal growth history. Accordingly, evolutionary stages of this crystal can be defined roughly as changing in the order of P-type – S-type – P-type based on the CL image (Figure 5.1).

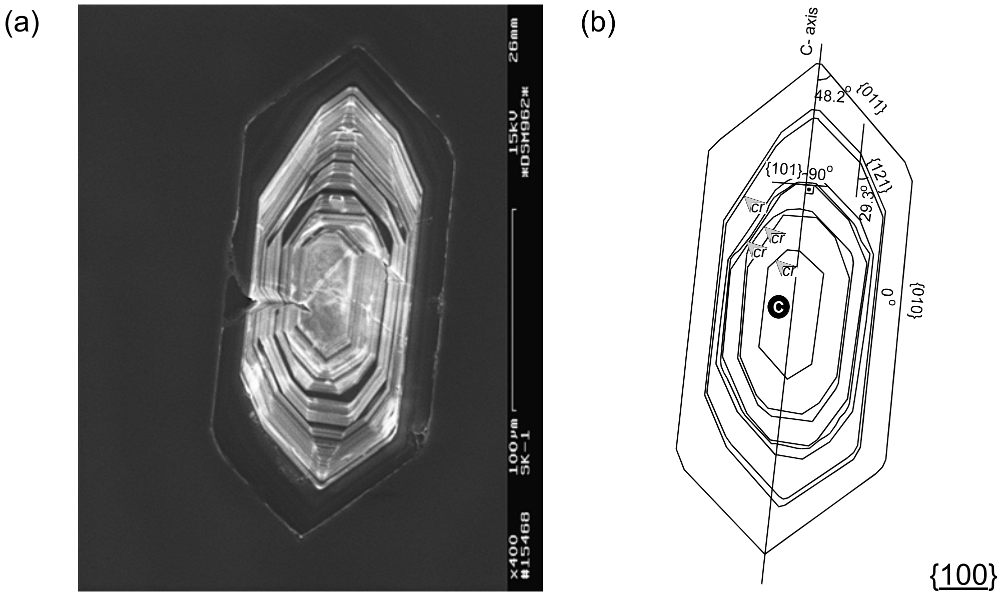

Figure 5.1. Zircon crystal [Z1(23)] from the Borucu granodiorite-monzogranite (sample SK-1): (a) High-resolution CL photograph, (b) Sketch model showing the inner structures.

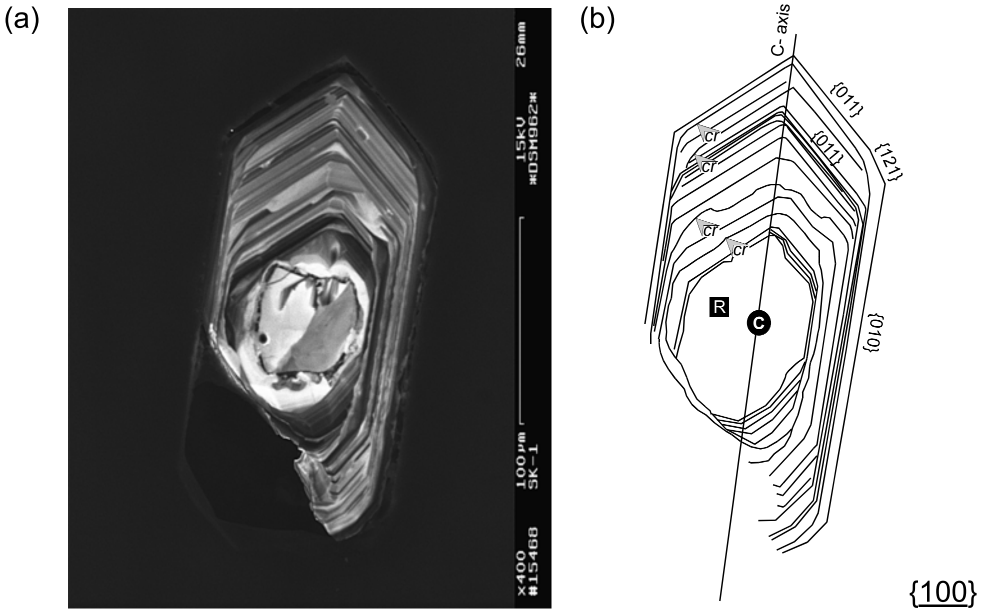

Figure 5.2. Zircon crystal [Z1(19)] from the Borucu granodiorite-monzogranite (sample SK-1): (a) High-resolution CL photograph, (b) Sketch model showing the inner structures.

Consequently, it is reasonable to indicate that the CL imaging reveals growth history of the zircon crystal that cannot be realized from its morphology.

In the innermost featureless part, which seems to be a core (marked as C; see Table 5.2), the crystal reflects {011} pyramid and {110} prism. In subsequent growth stages {101} and {121} pyramids appear in the section. Size of the {121} pyramidal face increases due to the rapid growth intervals of adjacent {011} faces (e.g. Vavra, 1994). Increasing growth rate of {011} faces suggests adsorption of cations like Na, K and Al (Vavra, 1994). The crystal is then surrounded by a smoothly rounded dissolution surface that is marked as "cr", which represents a corrosion event (e.g. Vavra, 1990, 1994). Corrosion of zircon occurred in the magma chamber, is possibly caused by renewed influx of fresh and hot magma (Vavra, 1994) therefore corrosion event is likely to be related to magma mixing in calcalkaline magmas (e.g. Vavra, 1994). Subsequent zonation overgrowing the corrosion surface is also interrupted by another corrosion stage. Subsequent faint oscillatory zonation continues near to rim where it is truncated by another corrosion stage.

The crystal reflects low intensity CL signals, i.e. darker areas, in its outer zones. This sharp morphological and chemical discontinuity (drop in cathodoluminescence) at the late stages of zircon crystallization is difficult to explain by changing cooling rate or Zr-supersaturation and chemical composition of the magma as indicated by Vavra (1994). Vavra (1994) suggested that the formation of large growth units (from smaller ionic entities) in the liquid, before they assembled on the crystal was likely to be the cause of this occasion. The formation of growth units starts when the magma attains sufficiently low temperatures and high concentration of elements essential for units (Vavra, 1994). Increased concentration of impurity elements like U, Th, Y, P and REEs results in the drop in CL intensity and growth units can dramatically change the morphological evolution of crystal (Vavra, 1994) as in the case of this crystal.

The S_{18}-type zircon crystal [Z1(19)] (Figure 4.4) is sectioned parallel to the {100} prism face (Figure 5.2). This crystal is characterized by recrystallized core surrounded by faint zoning and subsequent corrosion surface. It is reasonable to describe this corrosion to be related with the magma mixing as in the previous crystal. Faded zoning rounds this corrosion. Being a S_{18}-type crystal [Z1(19)] has {011} and {121} pyramidal faces on some parts of the CL section besides its outer form. {010} prism demonstrates very low growth rate. Vavra (1994) interpreted that the cooling rate of the crystallizing magma is the fundamental factor controlling the Zr-supersaturation and accordingly the relative growth rate of {010} prism. Additionally, growth intervals, which are repeatedly interrupted by crystal corrosion, would yield low Zr-supersaturation and low growth rate of {010} prism (Vavra, 1994). Intermittent periods of corrosion possibly cause low growth rate of {010} prism in this crystal. Outer zones of the crystal are characterized by low CL-intensity.

Considering the structures described in these two CL images it can be suggested that zircons of the Borucu granitoid show growth history with morphologically distinctive periods combined with stages of dissolution that might be related with magma mixing events. Incorporation of cations such as Na, K and Al, and impurity elements like U, Th, Y, P and REE lead to the differential growth rates of the crystal faces.

Table 5.2. Explanations of the symbols and abbreviations used in Figures 5.1 to 5.52.

Symbol (or abbreviation)	**Explanation**
Ⓒ	Core
R	Recrystallized domains (or recrystallization patches)
cr	Corrosion
T	Thickened trace element band
F	Flow domain (or structure)
M	Metamictized domains
mi(?)	(Possible) melt inclusion

5.3.1.2. Kalebalta Leucogranite

Zircons of the Kalebalta leucogranite commonly reflect dark and featureless cores (e.g. [Z3(9)], [Z3(10)], [Z3(15)] and [Z3(17)] in Figure 5.3) which are generally interpreted as inherited (e.g. Paterson et al., 1992; Pidgeon and Compston, 1992; Vavra, 1994). These inherited cores commonly subjected to secondary events resulting in curved and irregularly thickened trace element banding (e.g. [Z3(1)] and [Z3(2)]) similar to those described by Pidgeon et al. (1998).

Fading and broadening of outer zones and thickening of inner zones due to secondary trace element concentration (Pidgeon et al., 1998) are also observable in the zircon crystals from the Kalebalta granitoid (e.g. [Z3(1)], [Z3(15)] and [Z3(19)]). Additionally, some crystals are highly metamictized ([Z3(6)] and [Z3(14)]).

The CL section of the zircon crystal [Z3(3)] which is P_3-type (Figure 4.12) is parallel to the {100} prism face (Figure 5.4). The section is non-central since frontal prism face {100} appears as an inherited core in the middle of the crystal. Note that the criterion for centrality of the section parallel to {100} is that the frontal prism face {100} does not appear by its rectangular outline (Vavra, 1993). The particles within the core were supposed to be caused by polishing, not to be related with the crystal properties. Surrounding part of the core is affected by recrystallization. {121}-pyramid is non-persistent, and disappeared in the outer form. Its size is increased by the rapid growth intervals of adjacent {011} faces. Subsequent zoning having interspersed corrosion stages ended at the edges of the crystal where low intensity band, which may represent the formation of large growth units from smaller ionic entities (e.g. Vavra, 1994), exists. Asymmetric growth of {011} pyramid at the mean time must be related with the different proportions of adsorbing cations due to differences in surface energies as Vavra (1994) indicated.

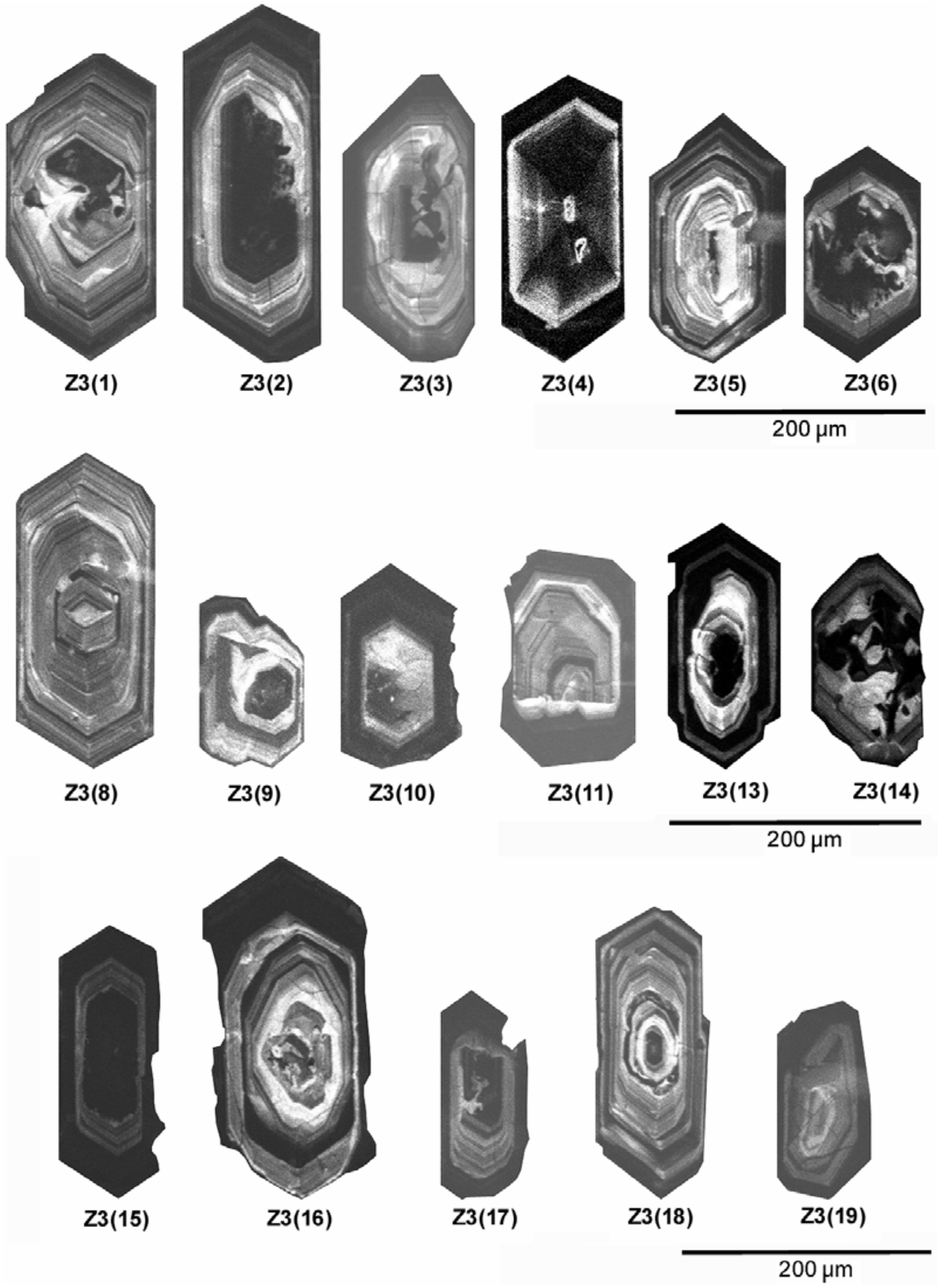

Figure 5.3. CL images of the selected zircon crystals from the Kalebalta leucogranite (SK-3).

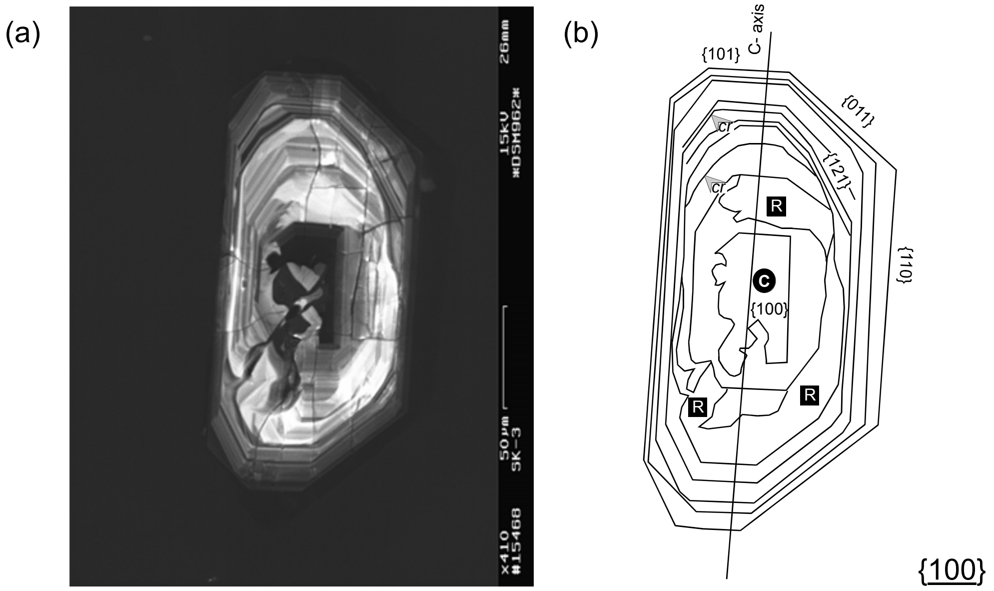

Figure 5.4. Zircon crystal [Z3(3)] from the Kalebalta leucogranite (sample SK-3): (a) High-resolution CL photograph, (b) Sketch model showing the inner structures.

The G_1-type zircon crystal [Z3(4)] (Figure 4.13) is sectioned parallel to the {110} prism face (Figure 5.5). The most striking feature of this crystal is the sector zoning (represented by dashed lines) which results from trapping of foreign atoms by individual crystal forms. Each sector is a pyramid, and its apex points of center of the crystal and its basal face corresponds to an advancing crystal face (Vavra, 1990). Sector zoning indicates the relatively rapid igneous (possibly fluid) growth (Hanchar and Miller, 1993). The outer low-CL rim may be related again with the growth units.

The zircon crystal [Z3(8)] which is an example of S_{14}-type (Figure 4.14) is sectioned parallel to the {110} prism face (Figure 5.6). Oscillatory zoning with intervening corroded and recrystallized parts overgrows the core and surrounding corrosion rim. Growth inhibition of {110} face reflects enrichment of water or trace elements in the growth medium (e.g. Vavra, 1994). Benisek and Finger (1993) explains growth inhibition of {110} face by the low concentration of U, Th, and Y (and possibly REE) elements. This interpretation is in accordance with the Vavra (1994)'s suggestions since enrichment of these elements in the residual liquid is related with the H_2O contribution.

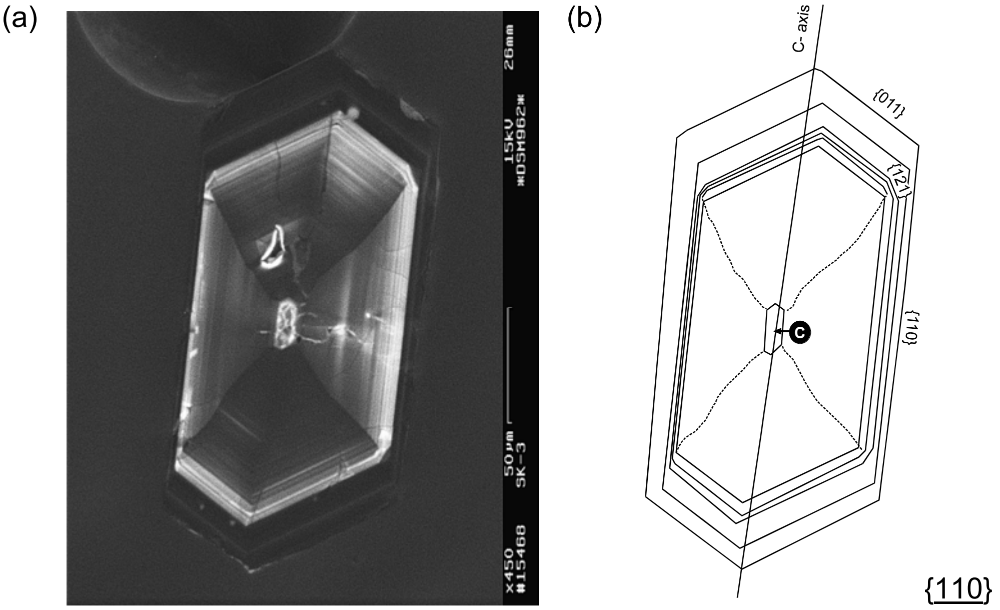

Figure 5.5. Zircon crystal [Z3(4)] from the Kalebalta leucogranite (sample SK-3): (a) High-resolution CL photograph, (b) Sketch model showing the inner structures.

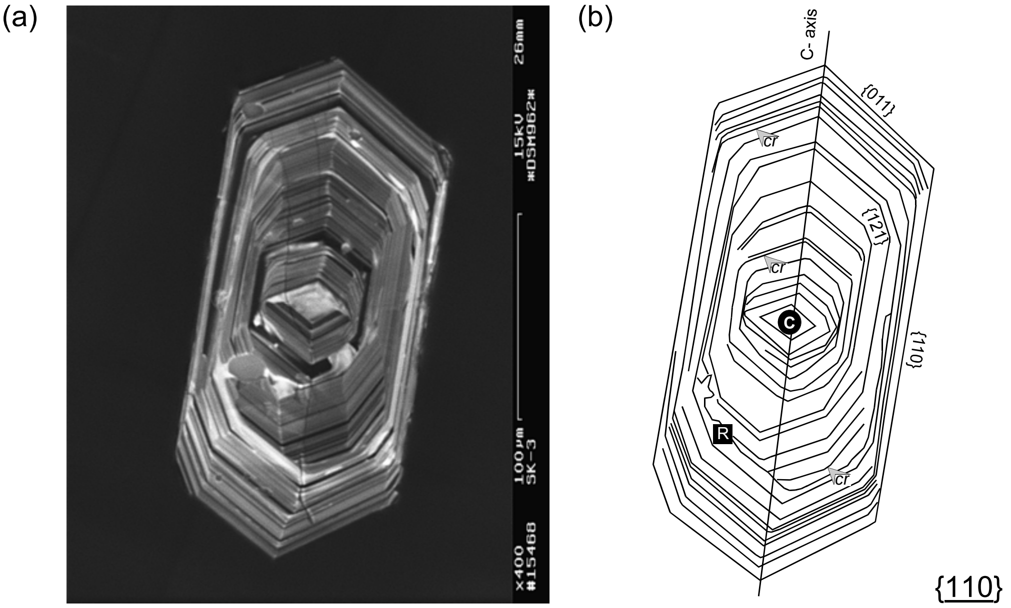

Figure 5.6. Zircon crystal [Z3(8)] from the Kalebalta leucogranite (sample SK-3): (a) High-resolution CL photograph, (b) Sketch model showing the inner structures.

Asymmetric growth of {011} pyramid can be explained by the different proportions of adsorbing cations due to different surface energies (e.g. Vavra, 1994).

Figure 5.7 (Zircon crystal [Z3(13)]) shows combination of two P_2-type crystals (Figure 4.19) both of which are sectioned parallel to the {110} prism faces. Dark inherent core with corrosion rim and covering faded and discontinuous zoning part of which is recrystallized are observable on CL photograph. The faded and broadened low luminescent zoning starts with a sharp transition. Robust explanation of this CL image is that the autoepitaxial overgrowth of zircon crystal on the other one resulting in the formation of a composite crystal (See Chapter 4). {121} face, which is predominant inside the crystal, does not exist in the outer form.

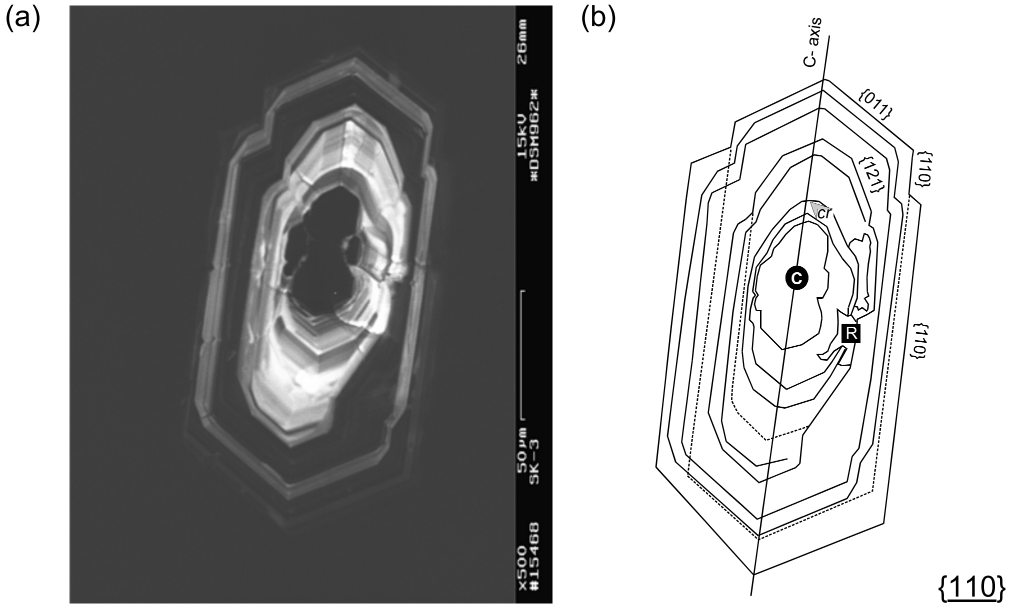

Figure 5.7. Zircon crystal [Z3(13)] from the Kalebalta leucogranite (sample SK-3): (a) High-resolution CL photograph, (b) Sketch model showing the inner structures.

The highly corroded zircon crystal [Z3(16)] is of P_2-type (Figure 4.12) and is sectioned parallel to the {110} prism face (Figure 5.8). In spite of the difficulty for representation due to recrystallization combined with flow structures, the central part can be suggested to be formed form multiple discrete cores (i.e. by igneous clustering). The relict crystal forms, i.e. cores with faint zoning although hardly recognizable (labeled by “lower case c”), in the central part may lead such a description. In the outer form {121} face does not exist (Figure 4.12), but it is almost continuously present inside the crystal (Figure 5.8). It shows increased sizes as a result of rapid growth intervals of adjacent {011} faces, which may accompany with the adsorption of cations (e.g. Vavra, 1994). A wide low-luminescent corrosion zone surrounds the crystal form showing dominant {121} face. Outer part of the crystal is characterized by faint and partly recrystallized fine oscillatory zoning. Outer rim seems to be lost during etching.

The CL section of the G_1-type zircon crystal [Z3(18)] (Figure 4.14) is parallel to the {110} prism face (Figure 5.9). Crystal is highly corroded and contains a relatively small core having {011} and {110} faces. Low-luminescent dark zone is truncated by oscillatory zone and formation of the {121} pyramidal face. New zonation started with asymmetric growth of {011} face at the rim of this zoning suggests that the crystal was broken and corroded.

Asymmetric zoning of {010} prism probably represents minor changes in the proportion of adsorbing cations (e.g. Vavra, 1994). The irregular low-luminescent corrosion zone is surrounded by oscillatory zone that is partly thickened and recrystallized.

As a summary, zircons from the Kalebalta granitoid show distinct features in the CL images, as recorded in SEM images. SEM images of the zircon crystals reveal complex features as partial and parallel growths, whilst CL images demonstrate additional structures involving inherent cores, recrystallization, and overgrowths.

Paterson et al. (1992) described the inherent zircon cores from Strontian and Kameruka (from the Bega Batholith-Australia) as representing refractory material that was incorporated into magma either during partial melting, or between that time and final crystallization, and were subsequently the sites of new, melt-precipitated zircon growth.

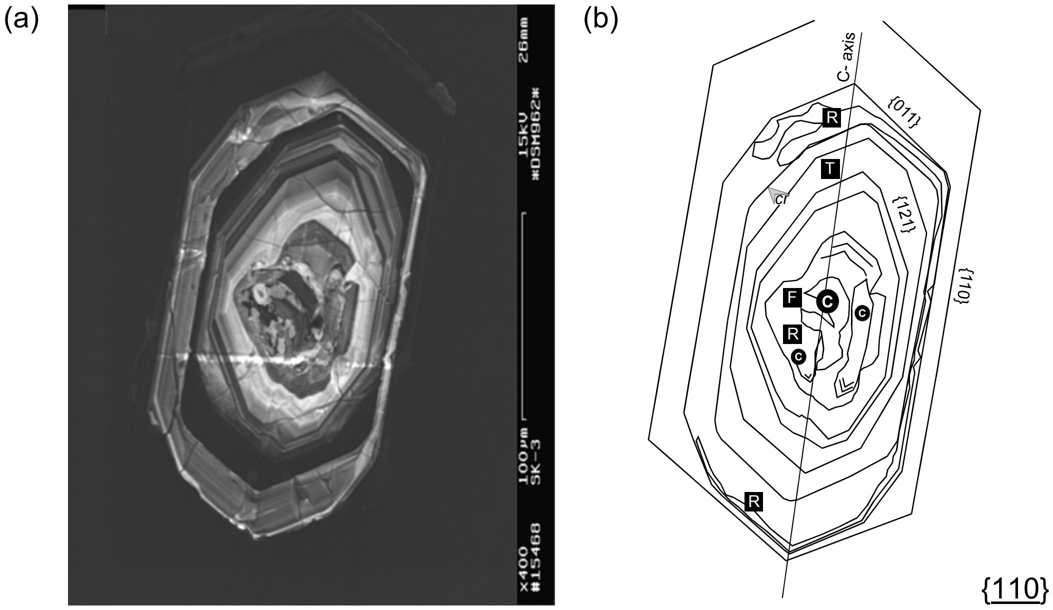

Figure 5.8. Zircon crystal [Z3(16)] from the Kalebalta leucogranite (sample SK-3): (a) High-resolution CL photograph, (b) Sketch model showing the inner structures.

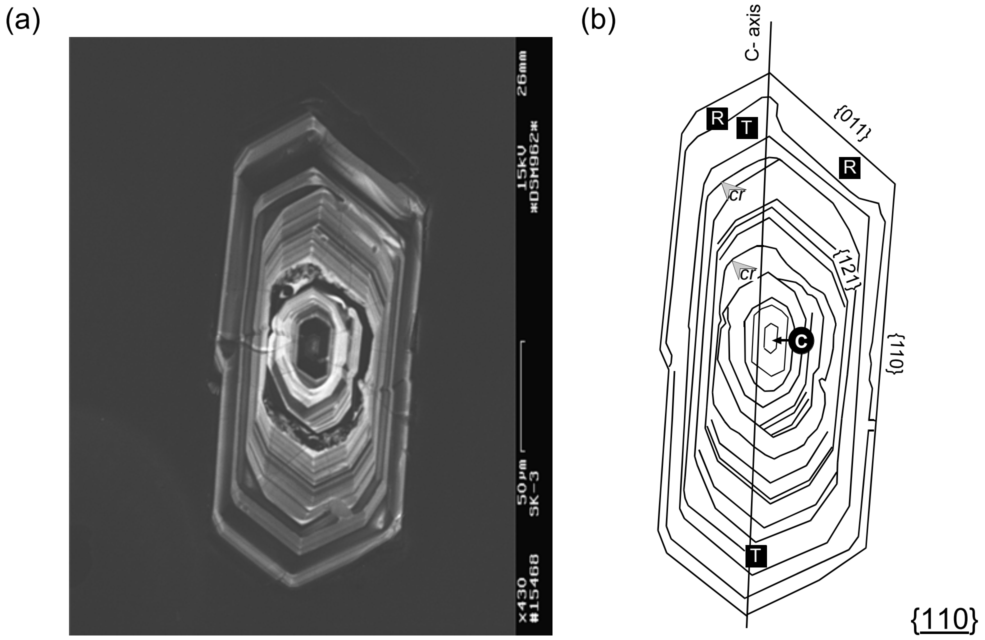

Figure 5.9. Zircon crystal [Z3(18)] from the Kalebalta leucogranite (sample SK-3): a) High-resolution CL photograph, (b) Sketch model showing the inner structures.

In the same manner, inherent cores and subsequent zoning detected in the Kalebalta zircon samples probably represent the different stages of growth history. Besides inherent cores, overgrowths observed within the crystals also support this interpretation. Along with the geochemical and morphological studies, CL imaging also provides an important contribution to the description of the Kalebalta leucogranite as S-type granitoid.

In the Kalebalta granitoid, cores of the zircon crystals generally overgrown by zoning, which is truncated by corrosion stages of low Zr-supersaturation. Beside the dissolution surfaces indicating corrosion, i.e. rounding of internal zones, sharp transitions to outer morphologically distinct and generally low luminescent growth zones are commonly present in the zircon crystals from the Kalebalta granitoid.

Outer rims are characterized by dominant {011} pyramid and {110} prism leading to formation of P or G type typology which results in inconsistency between the S-type definition of the Kalebalta granitoid and the results of the Pupin's zircon typology method. However careful investigation of CL images yields that, crystals show change in morphologies especially at the latest stages of growth. As indicated by Vavra (1994), increased concentration of impurity elements like U, Th, Y, P and REEs causes not only drop in CL intensity, but also change in the morphology of the crystal. Benisek and Finger (1993) demonstrated that the development of a {110} dominated prism form is favored by a high abundance of U cations in the granite melt and presence of a $Y(REE)PO_4$ solid solution component in the zircon lattice. They further postulated that a cooling granite become enriched in U, Th, Y(REE) by fractional crystallization. Moreover, during crystallization residual liquid was possibly enriched in water and possibly trace elements considering the growth the inhibition of {110} faces and metamictization observed in the zircon crystals. Therefore, it is assumed that the interplay of the chemical effects during the crystal growth is responsible for misinterpretation by the zircon typology method in the case of the Kalebalta granitoid.

5.3.1.3. Hisarkaya Porphyritic Granite

Hisarkaya porphyritic granite is characterized by CL structures commonly revealing inherent cores, sometimes metamictized, and surrounding relatively light luminescent zones which are then followed by low luminescent zones with {011} and {110} faces (Figure 5.10 and 5.11). Samples SK-4 and SK-5 show similar CL features, with slight differences, in accordance with their similarity in the morphological characteristics.

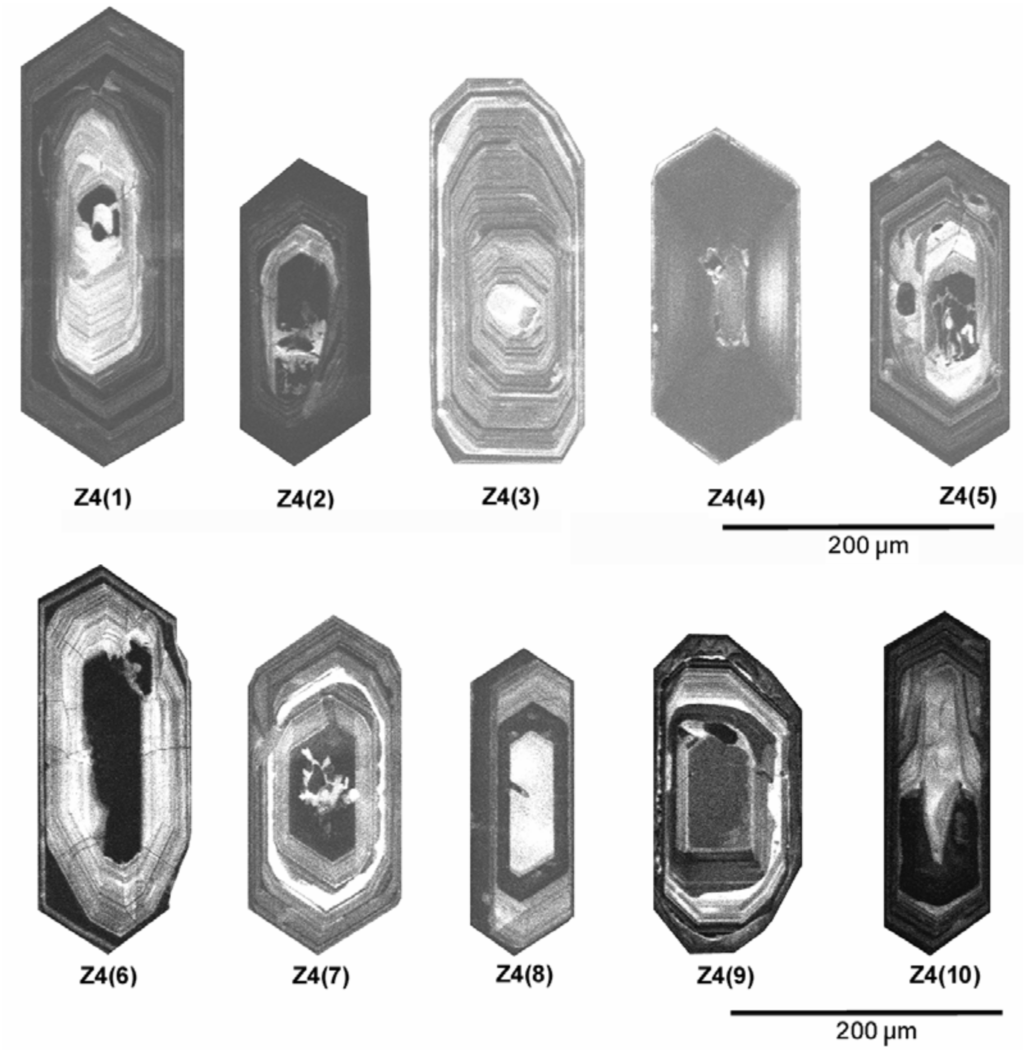

Figure 5.10. CL images of the selected zircon crystals from the Hisarkaya porphyritic granite (SK-4).

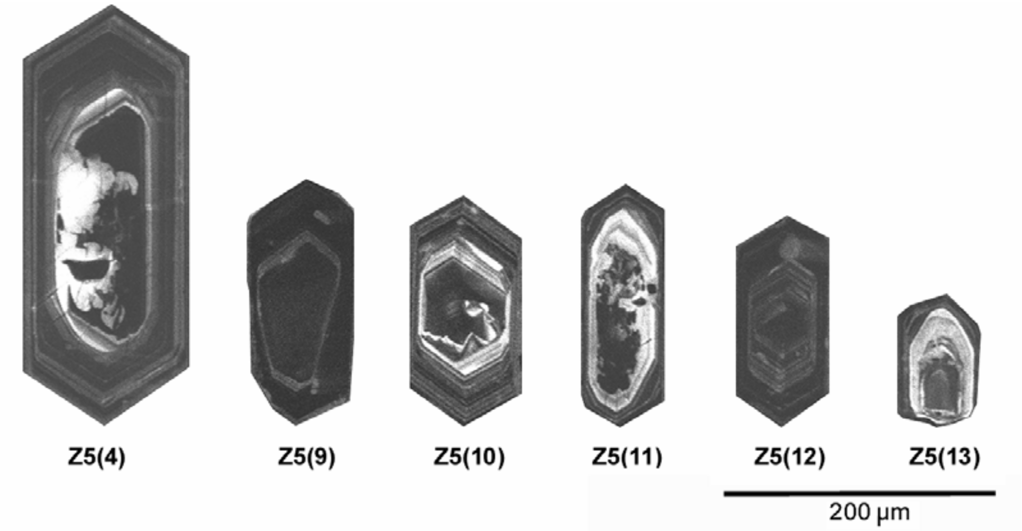

Figure 5.11. CL images of the selected zircon crystals from the Hisarkaya porphyritic granite (SK-5).

[Z4(1)] being a P_2-type zircon crystal (Figure 4.22) is sectioned parallel to the {110} prism face (Figure 5.12). It shows brightly luminescent oscillatory zoning surrounding an inherent core. At the inner zones rapid growth intervals of {011} faces increased the size of the adjacent {121} pyramids (e.g. Vavra, 1994). Adsorption of cations on the charged {011} faces changes the relative surface energies of the possible structures and growth rates of {011} faces (Vavra, 1994). Relatively low luminescent zoning, left part of which is broken or resorbed, overgrown by dark band that is not seems to be related with corrosion. This dark banding may be related with concentration of impurity elements (e.g. Vavra, 1994) or transportation and continuation of crystallization in a different part of magma chamber. Outer zoning with a corroded interlayer is characterized by reduced growth rate of {110} face.

The zircon crystal [Z4(6)] is of S_{15}-type (Figure 4.22) and is sectioned parallel to the {110} prism face (Figure 5.13). The large dark inherent core in this zircon shows is overgrown by brightly luminescent oscillatory zoning having sharp transition to the outer low-luminescent and morphologically distinct zone.

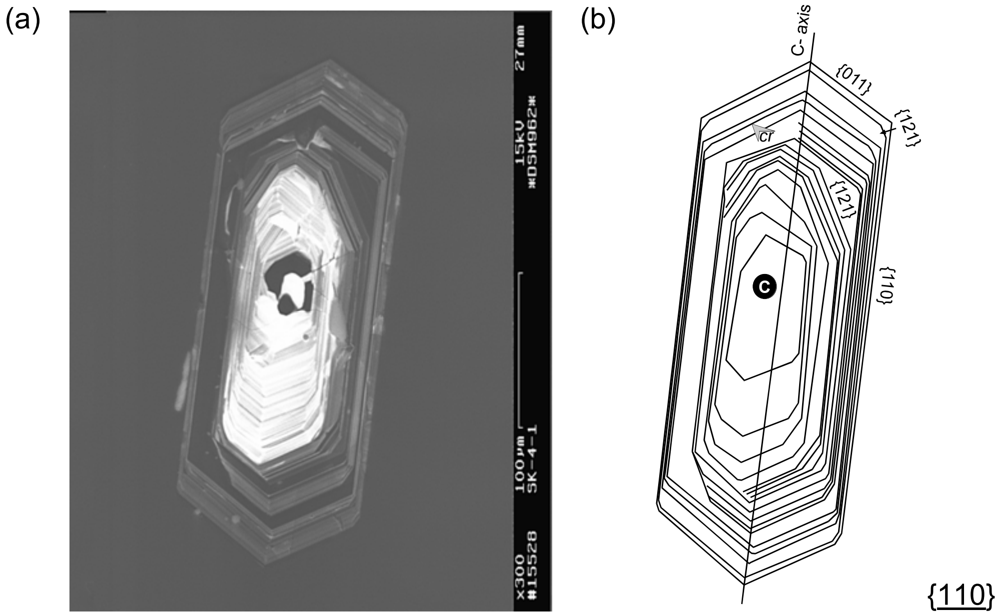

Figure 5.12. Zircon crystal [Z4(1)] from the Hisarkaya porphyritic granite (sample SK-4): (a) High-resolution CL photograph, (b) Sketch model showing the inner structures.

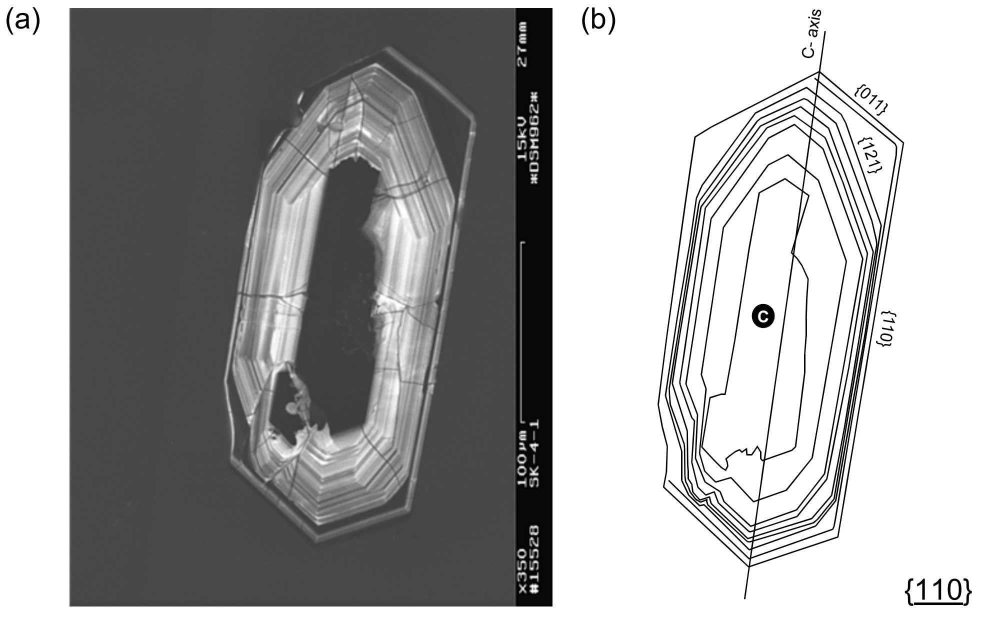

Figure 5.13. Zircon crystal [Z4(6)] from the Hisarkaya porphyritic granite (sample SK-4): (a) High-resolution CL photograph, (b) Sketch model showing the inner structures.

Upper part of this oscillatory zone is dominated by {121}-pyramid face whose size is increased because of the rapid growth intervals of adjacent {011} faces resulted by adsorbing cations (e.g. Vavra, 1994). Low left corner of this zoning is remarkably distorted probably due to a later event. Fluctuating growth rate of {110} prism is observable especially on the outer zones.

The zircon crystal [Z4(7)] as an example of S_{15}-type (Figure 4.28) is sectioned parallel to the {110} prism face (Figure 5.14). The large inherent and metamictized core with faint zoning can be described as frontal {110} face, which may indicate that the crystal section is not centered. Oscillatory zoning surrounding the core is truncated by bright and recrystallized zone, which may indicate a period of trace element loss within the crystallization history of the zircon (e.g. Pidgeon, 1992). Near to rim corrosion stage accompany by decreased growth rate of {010} prism.

The CL section of the S_{19}-type zircon crystal [Z4(9)] (Figure 4.22) is parallel to the {100} prism face (Figure 5.15). Being an inherent core rectangular shape of frontal {100} face suggests that the section is non-central. This core is overgrown by oscillatory zoning which is truncated by corrosion stages and bright recrystallized zone similar to that of the crystal [Z4(7)]. At the edge of this form there is a dark colored area resembling melt inclusion. However, this interpretation needs more detailed investigation. Outer zone also shows extensive distortion in relation with the secondary trace element migration.

The P_2-type zircon crystal [Z4(10)] (Figure 4.24) is sectioned parallel to the {110} prism face (Figure 5.16). The most striking feature of this crystal is the complex inner structure in contrast with its morphological simplicity. In its central part crystal shows fine convoluted banding, starting at resorbed crystal surface and invading towards the center, resembles flow structures that is reported by previous authors (e.g. Vavra et al., 1996; Pidgeon et al., 1998). This flow domain is likely formed during resorption at the surface of the crystal and triggered by the infiltration of some impurity components transgressing the resorbed faces (e.g. Vavra et al., 1996).

The CL section of the S_{13}- or P_3-type zircon crystal [Z5(4)] (Figure 4.23) is parallel to the {100} prism face (Figure 5.17).

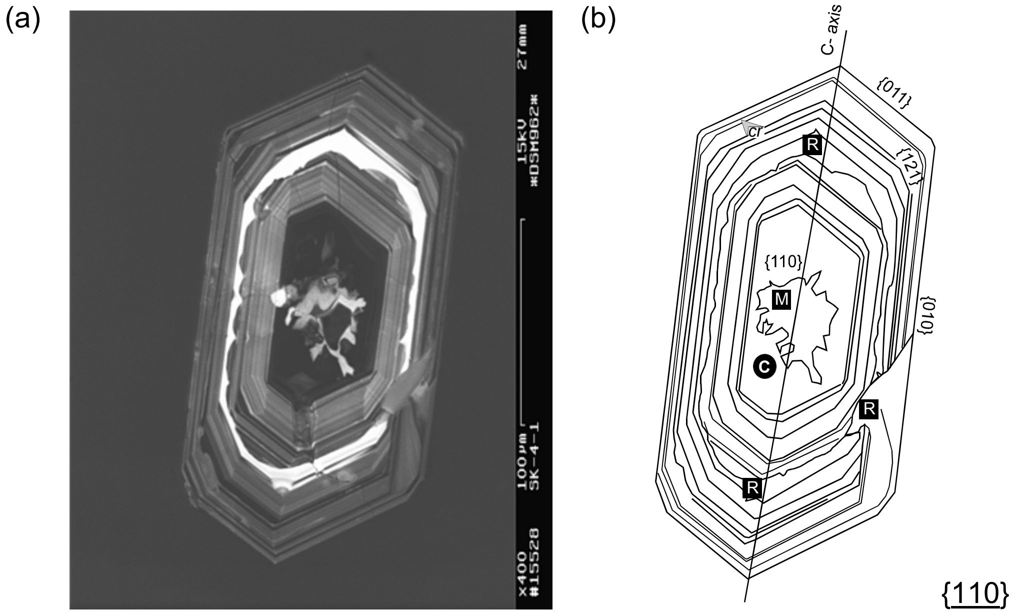

Figure 5.14. Zircon crystal [Z4(7)] from the Hisarkaya porphyritic granite (sample SK-4): (a) High-resolution CL photograph, (b) Sketch model showing the inner structures.

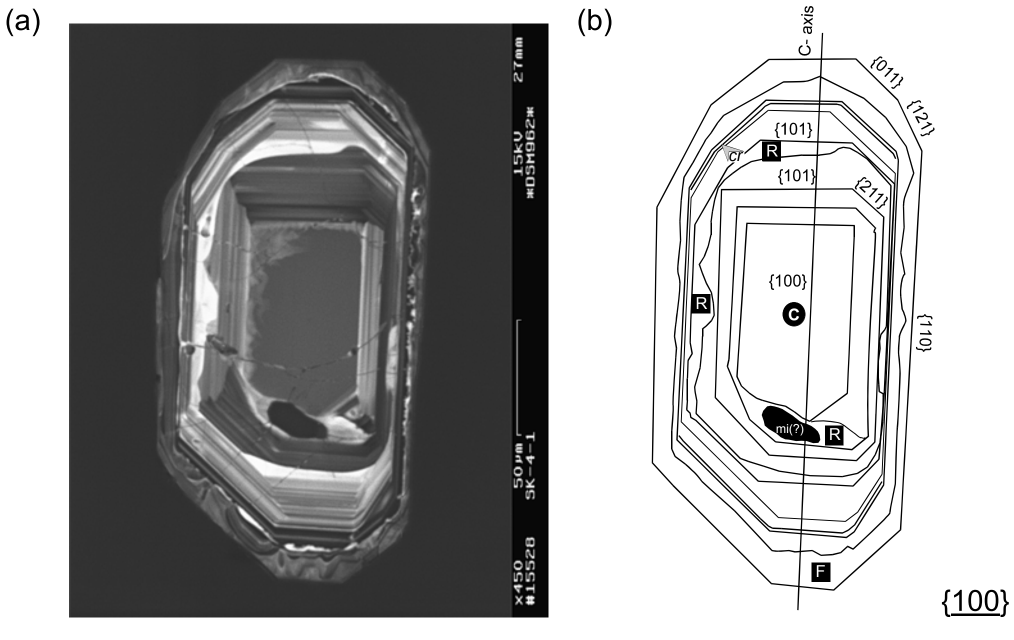

Figure 5.15. Zircon crystal [Z4(9)] from the Hisarkaya porphyritic granite (sample SK-4): (a) High-resolution CL photograph, (b) Sketch model showing the inner structures.

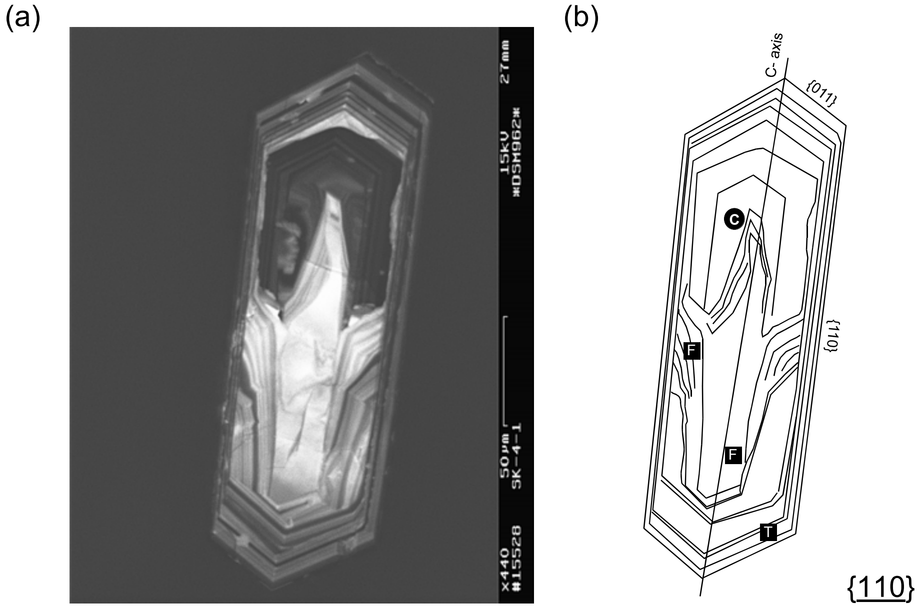

Figure 5.16. Zircon crystal [Z4(10)] from the Hisarkaya porphyritic granite (sample SK-4): (a) High-resolution CL photograph, (b) Sketch model showing the inner structures.

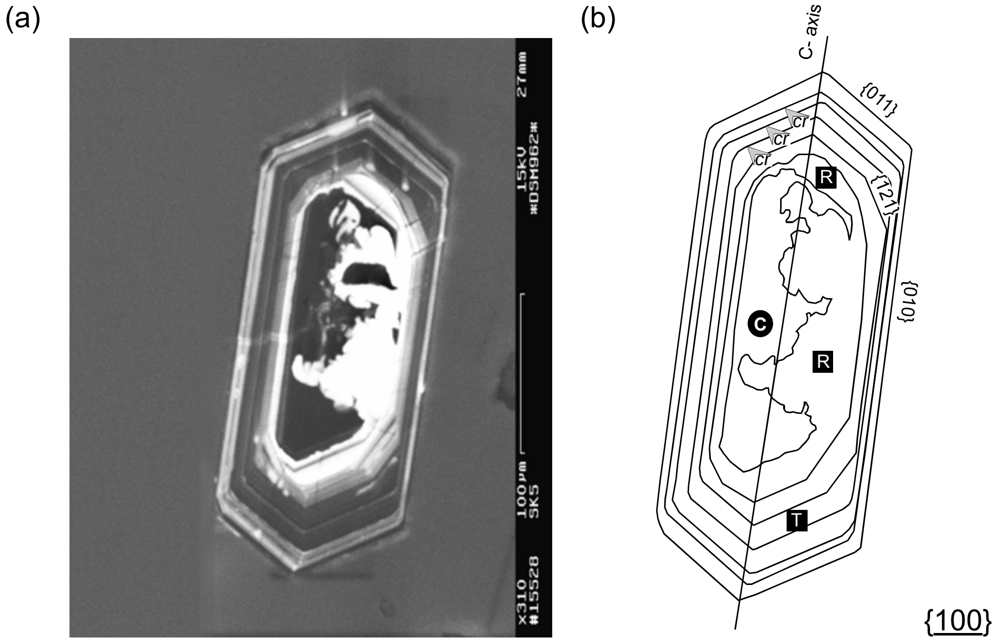

Figure 5.17. Zircon crystal [Z5(4)] from the Hisarkaya porphyritic granite (sample SK-5): (a) High-resolution CL photograph, (b) Sketch model showing the inner structures.

Partly recrystallized inherent core of the crystal [Z5(4)] is overgrown by zoning in varying luminescence of which diminishes at the outer rim. There are corrosion stages interrupting zoning and thickening of zones close to rim due to secondary trace element concentrations. Thickening of trace element bands or zones may point out a relatively slow cooling of the crystallizing granite (Pidgeon et al., 1998). Conditions of very low Zr-supersaturation can be assumed for low growth intervals of {010} prism, which are repeatedly interrupted by crystal corrosion towards rim (e.g. Vavra, 1994).

The zircon crystal [Z5(10)] is of P_2-type (Figure 4.32) and is sectioned parallel to the {110} prism face (Figure 5.18). Core showing faint zoning and metamictization is overgrown by zoning that reflects brighter CL-intensity on inner parts and interspersed corrosion stages in surrounding parts. {110} prism demonstrates growth inhibition on the outer zones.

Being a P_2-type, the zircon crystal [Z5(11)] (Figure 4.23) is sectioned parallel to the {110} prism face (Figure 5.19). This crystal has particularly different features with respect to the other Hisarkaya samples. The core is metamictized, and succeeding brightly luminescent zone is surrounded by thickened trace element band. Asymmetric evolution and size of {121} pyramid are probably controlled by growth rate of adjacent {011} faces. Outer rim of the crystal with P_2-type crystal morphology has low luminescence indicating formation of large growth units (from smaller ionic entities) in the liquid (Vavra, 1994).

In general zircon crystals from the Hisarkaya granitoid demonstrate considerable morphological changes in successive growth stages. Commonly they contain inherent cores overgrown by zoning up to the corrosion stages close to rim of crystals. Predominant {110} and {121} faces commonly characterize this zoning. Corrosion stages commonly interpret interface between high-CL-zone overgrowing inherent core and subsequent low-CL-zone outlining the shape of the crystal. In the late stages of evolution {010} prisms reflect low growth rate due to intercalated corrosion stages combined with low Zr-supersaturation, while {110} prisms had undergone growth inhibition possibly due to an enrichment of H_2O (or trace elements) in the growth medium. Moreover, {121} pyramids become smaller, or sometimes extinct through the outer zones.

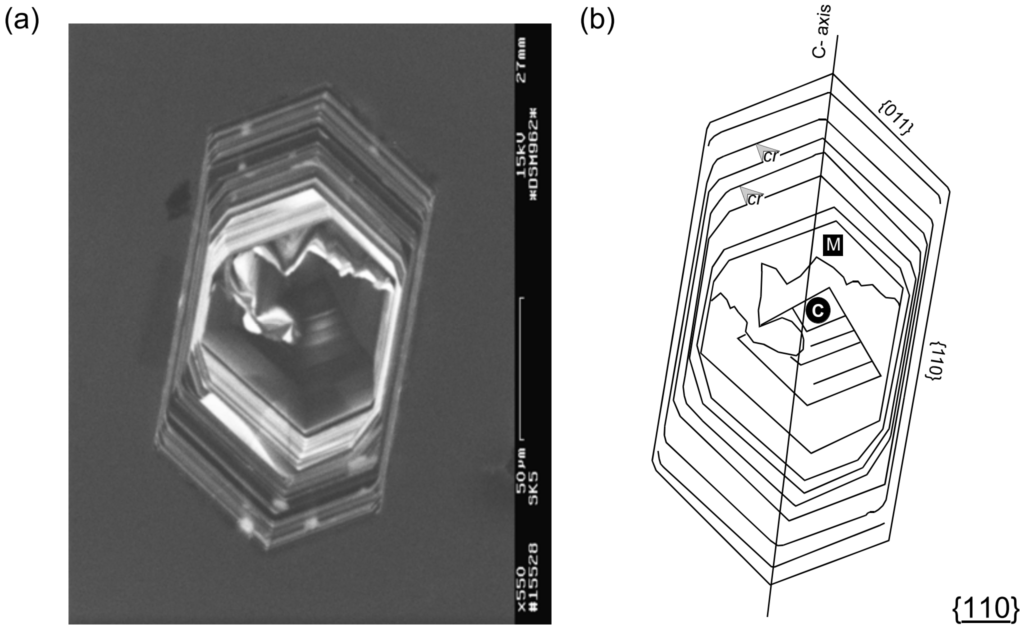

Figure 5.18. Zircon crystal [Z5(10)] from the Hisarkaya porphyritic granite (sample SK-5): (a) High-resolution CL photograph, (b) Sketch model showing the inner structures.

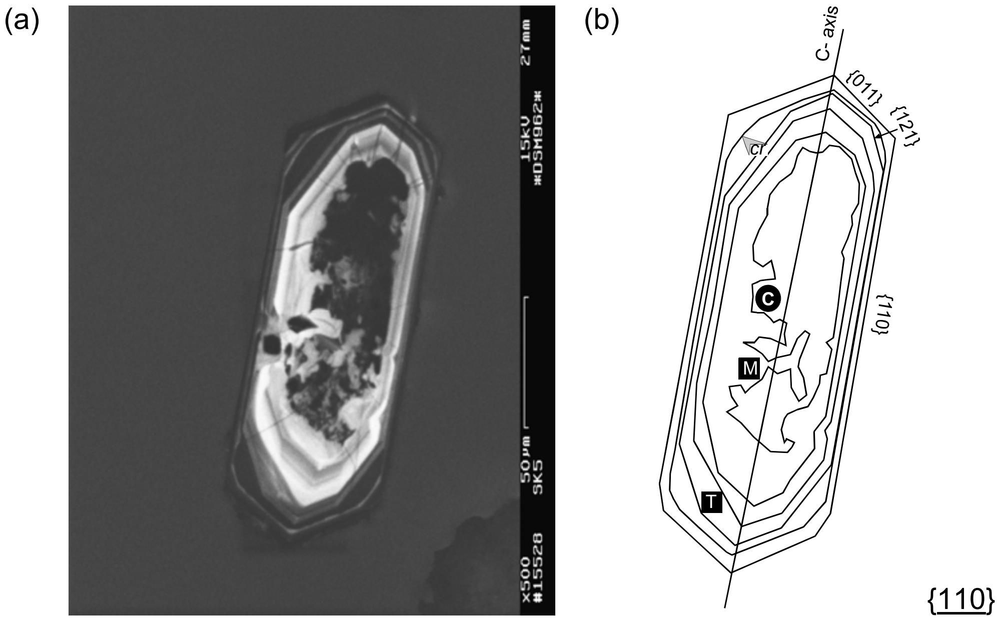

Figure 5.19. Zircon crystal [Z5(11)] from the Sinandı microgranite (sample SK-6): (a) High-resolution CL photograph, (b) Sketch model showing the inner structures.

As a consequence of these morphological changes, TET of the Hisarkaya granitoid does not coincide with that of S-type granitoid as in the case of the Kalebalta granitoid.

In addition, being separate outcrops of the Hisarkaya granitoid, SK-4 and SK-5 show similar features on the CL-images, but metamictization is more common in the latter.

5.3.1.4. Sinandı Microgranite

In the internal part of most zircon crystals from the Sinandı microgranite, brightly luminescent cores are overgrown by oscillatory zoning. In the outer zones CL intensity drops sharply. Recurrent stages of zircon corrosion, partly recrystallized in some crystals, are present (Figure 5.20).

Figure 5.20. CL images of the selected zircon crystals from the Sinandı microgranite (SK-6).

The S_{10}-type zircon crystal [Z6(17)] (Figure 4.36) is sectioned parallel to the {100} prism face (Figure 5.21). Bright and rounded core is overgrown by oscillatory zoning that is truncated by flow structures distorting the zonation. The crystal has consecutive oscillatory zoning stages interrupted by two intercalated corrosion surfaces accompanying with the low growth rate of {010} prism.

The zircon crystal [Z6(18)] is of S_9-type (Figure 4.36) and is sectioned almost parallel to the {100} prism face (Figure 5.22). Thin corrosion zone and following oscillatory zoning with decreasing CL intensity through outer zones surrounds featureless core. Two thickened bands in which the CL drops sharply are remarkable in the outer zones. Asymmetric growth of {011} maybe related with minor changes in proportions of adsorbing cations (e.g. Vavra, 1994).

The CL section of the S_{24}-type zircon crystal [Z6(19)] (Figure 4.36) is parallel to the {100} prism face (Figure 5.23). Zones of low CL intensity surround a very distinct core, showing bright CL with rounded and anhedral form. It is difficult to describe the core since it is featureless, probably due to the diffusion of trace elements to outer zones. Surrounding zones of very low CL show arrangement of face-parallel zoning within the zircon rims reflecting the shape of the core, and infer that the core/rim boundary represents a previous exterior surface of which the rim material was grown (e.g. Paterson et al., 1992). Subsequently, morphology is characterized by asymmetric growing of {121} pyramids controlled by asymmetric evolution and rapid growth intervals of {011} faces. Subsequent oscillatory zoning is truncated by thin corrosion surface and following zones with appearance of {101} pyramid resulting in external morphology. Dashed lines show irregular shaped sector boundaries.

Zircon crystals of the Sinandı granitoid generally contain rounded brightly luminescent cores probably indicating migration of trace elements to surrounding zones. Oscillatory zoning overgrowing cores continue to the dissolution surfaces, which represent corrosion event. Subsequent oscillatory zoning showing low-CL intensity combined with low growth rates of {010} prisms near to rims of the crystals represents periods of low Zr-supersaturation at the last stages of evolution.

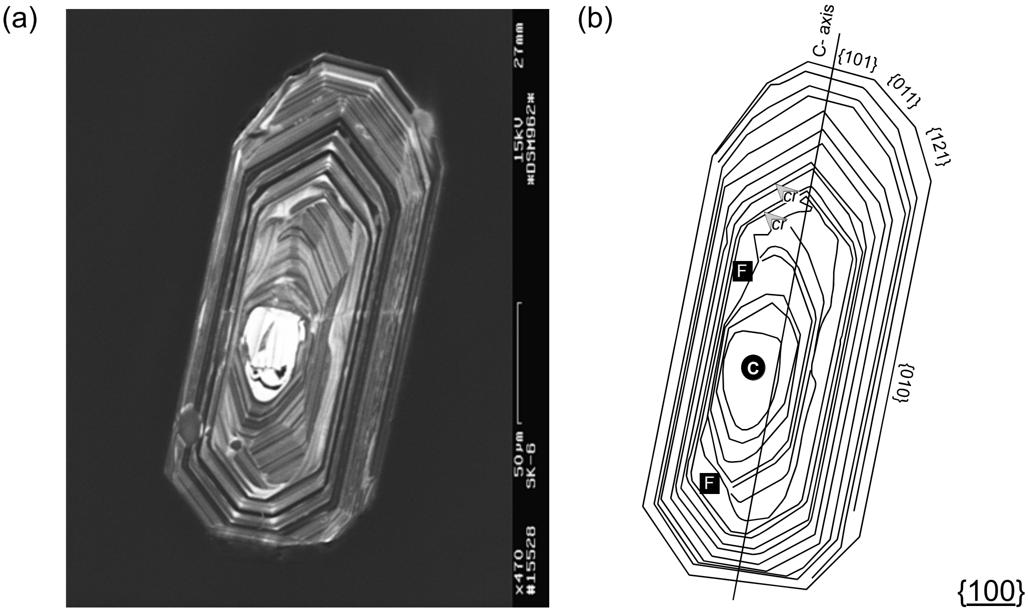

Figure 5.21. Zircon crystal [Z6(17)] from the Sinandı microgranite (sample SK-6): (a) High-resolution CL photograph, (b) Sketch model showing the inner structures.

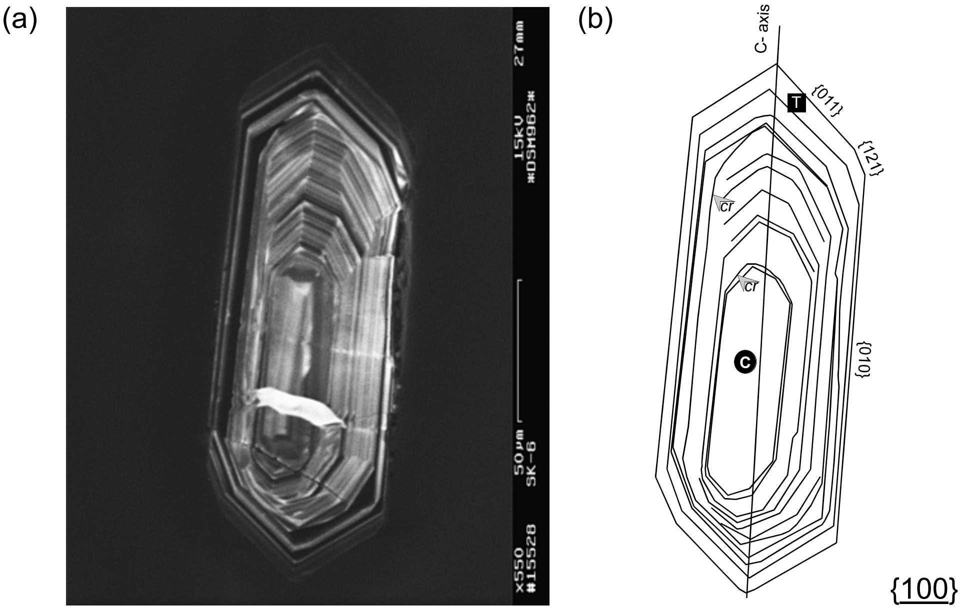

Figure 5.22. Zircon crystal [Z6(18)] from the Sinandı microgranite (sample SK-6): (a) High-resolution CL photograph, (b) Sketch model showing the inner structures.

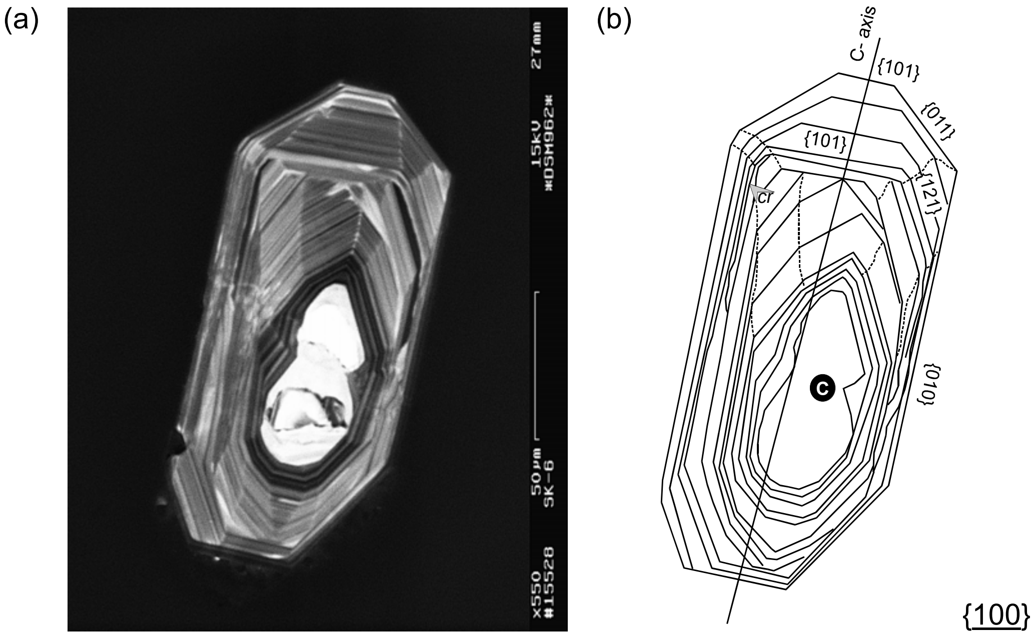

Figure 5.23. Zircon crystal [Z6(19)] from the Sinandı microgranite (sample SK-6): (a) High-resolution CL photograph, (b) Sketch model showing the inner structures.

5.3.2. Ağaçören Pluton

5.3.2.1. Namlıkışla Biotite-Granite

Namlıkışla biotite-granite reveals complex zircon intra-crystal structures. CL images of three zircon crystals reflect flow domains and periods of corrosion.

The zircon crystal [Z8(18)] is of S_{12}-type (Figure 4.43) and is sectioned parallel to the {110} prism face (Figure 5.24). The most distinguishing characteristic of this crystal is the convoluted zoning overprinting the oscillatory zoning in parts of a zoned zircon and extending to the inherent core. This is supposed to be the later event since it truncates the core and the outer zones. Other important features of the crystal are multi-stages of corrosion surrounding core and truncating the oscillatory zoning. Dark colored area may be a melt inclusion.

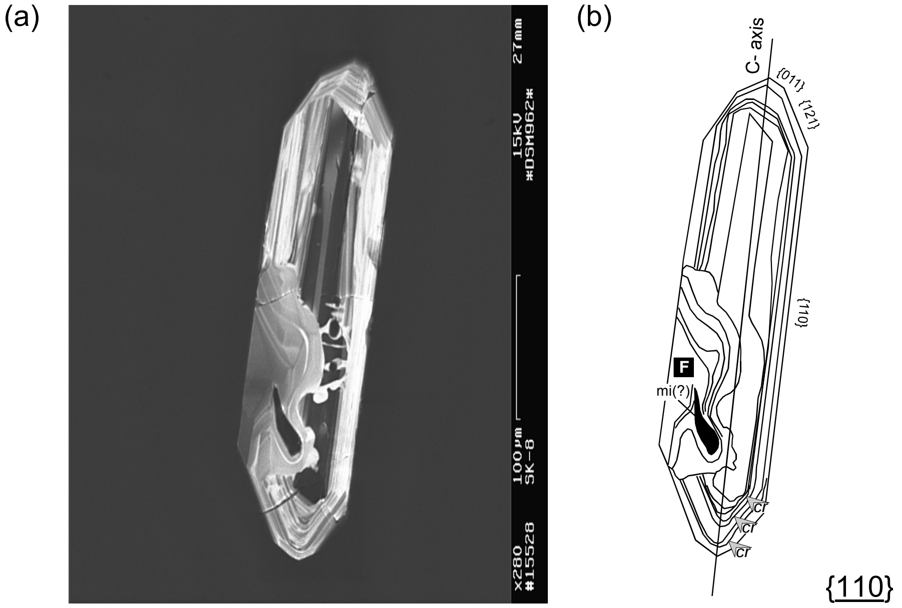

Figure 5.24. Zircon crystal [Z8(18)] from the Namlıkışla biotite-granite (sample SK-8): (a) High-resolution CL photograph, (b) Sketch model showing the inner structures.

The S_7-type zircon crystal [Z8(20)] (Figure 4.47) is sectioned parallel to the {110} prism face (Figure 5.25). It is not certain that the bright area in the center is related with zircon growth or sample preparation. The rounded interface between the almost continuous oscillatory zoning and the core formed from patches of low luminescence interprets the metamictization event. The rounded shape of the cores can either result from partial dissolution where transport in the melt is the rate-determining step, or from mechanical abrasion during sedimentary transport sometime before its incorporation in the melt as Paterson et al. (1992) suggested. Through to rim, zones are faded and thickened. {121} pyramid evolved asymmetrically due to rapid and changing growth rate of adjacent {011} faces which grown asymmetrically due to different proportions of adsorbing cations.

The zircon crystal [Z8(21)] which is S_2-type crystal (Figure 4.42) is sectioned parallel to the {110} prism face (Figure 5.26).

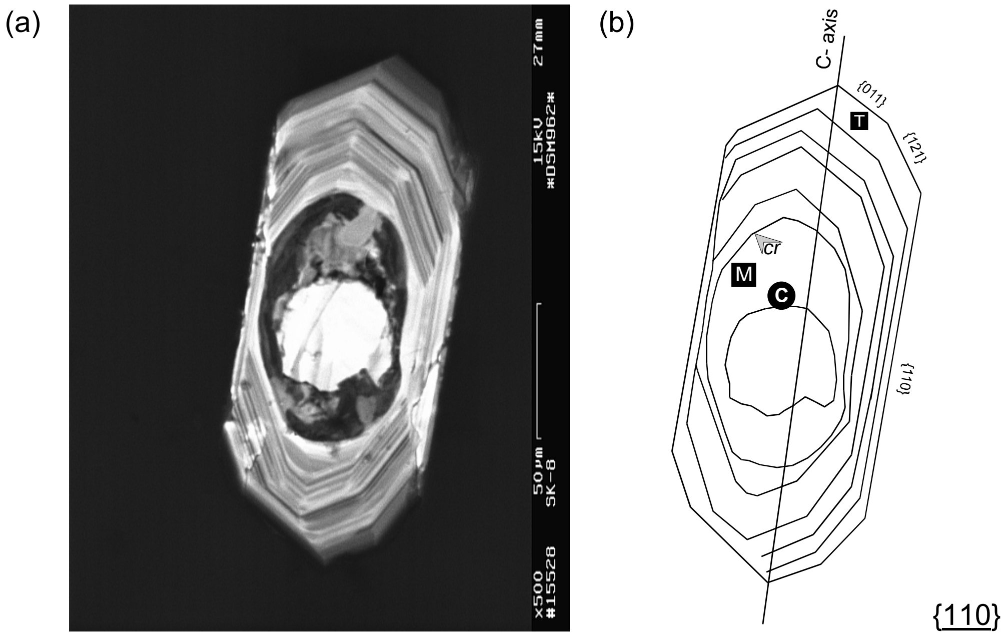

Figure 5.25. Zircon crystal [Z8(20)] from the Namlıkışla biotite-granite (sample SK-8): (a) High-resolution CL photograph, (b) Sketch model showing the inner structures.

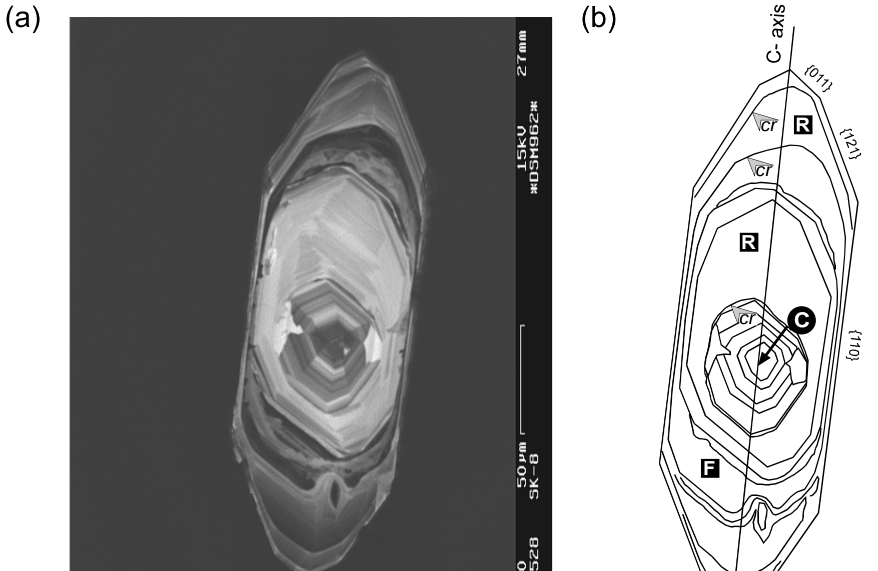

Figure 5.26. Zircon crystal [Z8(21)] from the Namlıkışla biotite-granite (sample SK-8): (a) High-resolution CL photograph, (b) Sketch model showing the inner structures.

The crystal [Z8(21)] is crystal is similar to [Z8(18)] in terms of convoluted zoning and series of corrosion stages. Curving of trace element band combined with formation of secondary zones and irregular thickening, and recrystallization due to trace element concentration suggests late stage interaction between zircon and fluids formed during cooling and crystallization of the granitoid (Pidgeon et al., 1998). Small patches of transgressive recrystallization in the central part are also indication of secondary trace element migration and loss (Pidgeon et al., 1998).

As a consequence, Namlıkışla granitoid generally displays complex zircon intracrystalline features. Secondary structures as flow domains and recrystallization are common in the zircon crystals. Besides large rounded corrosion interfaces between core structures and surrounding zoning, intermittent dissolution surfaces are also present in the succeeding stages. {110} and {121} faces are persistent throughout the growth history of the zircon crystals.

5.3.2.2. Yenişabanlı Biotite-Amphibole Granite

Zircon crystals from the Yenişabanlı granitoid generally show inherent cores and overgrown by oscillatory zoning with intermittent stages of corrosion (Figure 5.27).

In some crystal (e.g. [Z9(3)] and [Z9(7)] in Figure 5.27), trace element band develops curved, secondary zones are formed and irregular thickening occurs. Moreover, transgressive recrystallization patches are developed in some crystals (e.g. [Z9(6)], [Z9(7)] and [Z9(12)] in Figure 5.27). These described patterns closely resemble secondary structures those interpreted by Pidgeon et al. (1998).

Figure 5.27. CL images of the selected zircon crystals from the Yenişabanlı biotite-amphibole granite (SK-9).

The CL section of the S_{14}-type zircon crystal [Z9(1)] (Figure 4.50) is parallel to the {110} prism face (Figure 5.28). In terms of CL intensity crystal has three distinct zones. First of these zones is low-CL central part, which includes small core with faint zoning and surrounding oscillatory zoning with spasmodic corrosion surfaces. The core seems to be undergone series of corrosion and resorption, and consecutively truncated by another cycle of corrosion and resorption processes. The second zone having bright-CL overgrows the first zone along a corrosional interface. This zone has faded interspersed corrosion surfaces. Its rim also interprets a corrosion stage before growing of the outer zone. Third zone that has low-CL intensity shows almost continuous fine oscillatory zoning, which forms an asymmetrical outline. Asymmetric growth and increased sizes of {121} pyramids are probably governed by rapid growth intervals of the adjacent {011} pyramids by the adsorption of some cations.

The S_{20}-type zircon crystal [Z9(8)] (Figure 4.50) is sectioned parallel to the {100} prism face (Figure 5.29). This almost equant grain also reflects a complex history including series of corrosion. As previous crystal, this one also have low-CL part in the center and overgrowing relatively high-CL oscillatory zoning. The inherent core and corroded and recrystallized rim suggest that the chemistry of magma, in which zircon core grown, changed remarkably. Consecutive stages of dissolution indicated by rounded zones of corrosion (see Figure 5.29) also infer that repeatedly interruption of growth intervals of {010} prism is characterized by low Zr-supersaturation. Crystal also affected by secondary effects recorded by recrystallized zones and recrystallization patches. Traces of inclusions are also present throughout the crystal.

The zircon crystal [Z9(11)] is of S_{12}-type (Figure 4.52) and is sectioned parallel to the {110} prism face (Figure 5.30). It is not certain that the needle-shaped central zone of this crystal is a core. This central part closely resembles the zircons described by Vavra (1990) as initial skeletal crystal growth, which indicates a high Zr-supersaturation of the adjacent melt. Subsequent oscillatory zoning extending to the outer rim is interrupted by two stages of corrosion. Recrystallization patches and traces of inclusions are also noticeable in this crystal. Growth rate of {110} prism is reduced at the outer zones.

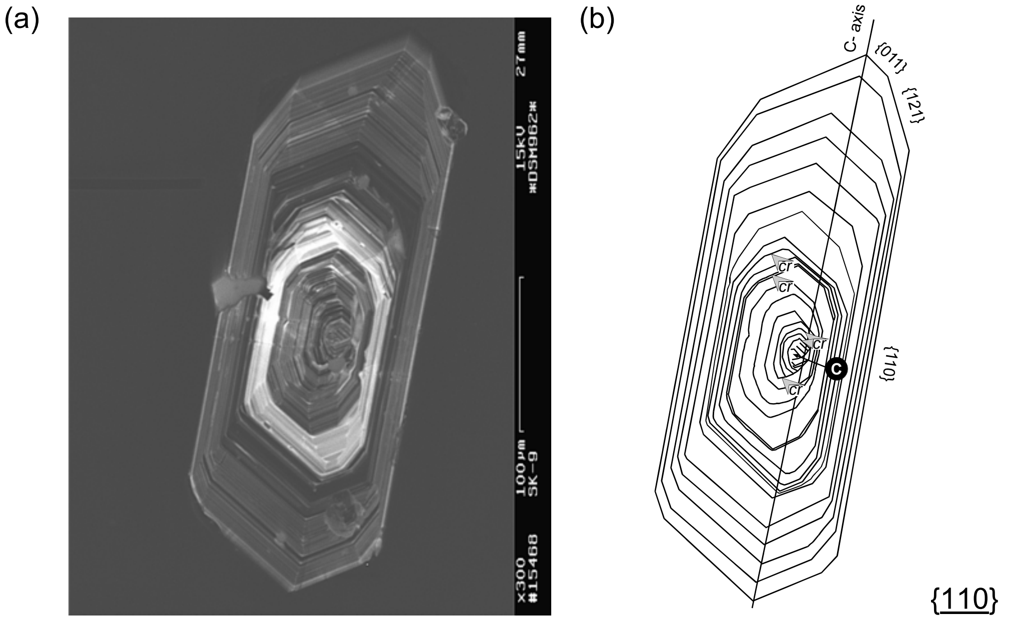

Figure 5.28. Zircon crystal [Z9(1)] from the Yenişabanlı biotite-amphibole granite (sample SK-9): (a) High-resolution CL photograph, (b) Sketch model showing the inner structures.

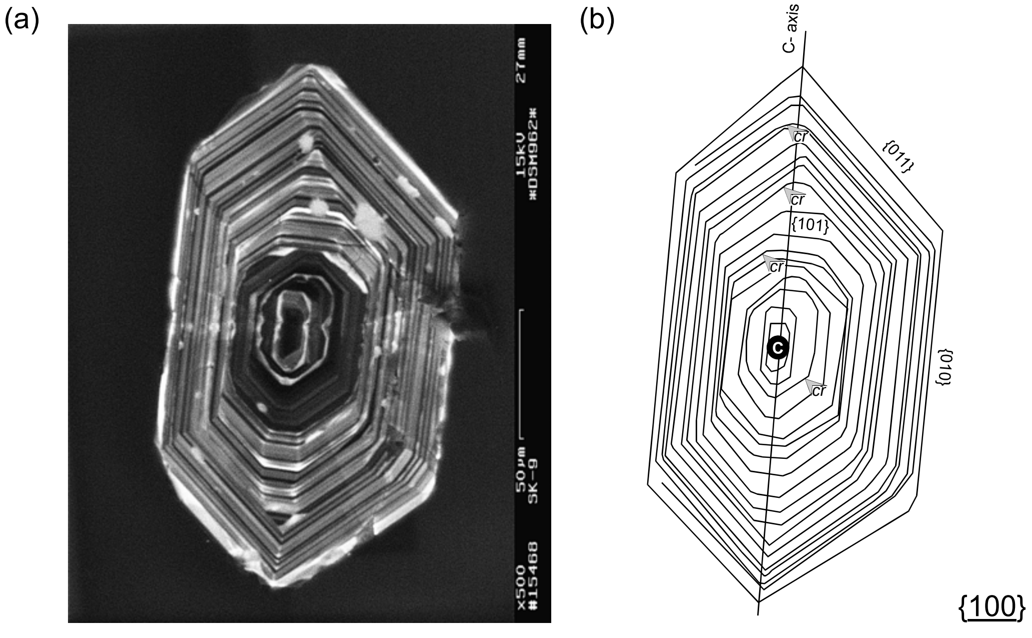

Figure 5.29. Zircon crystal [Z9(8)] from the Yenişabanlı biotite-amphibole granite (sample SK-9): (a) High-resolution CL photograph, (b) Sketch model showing the inner structures.

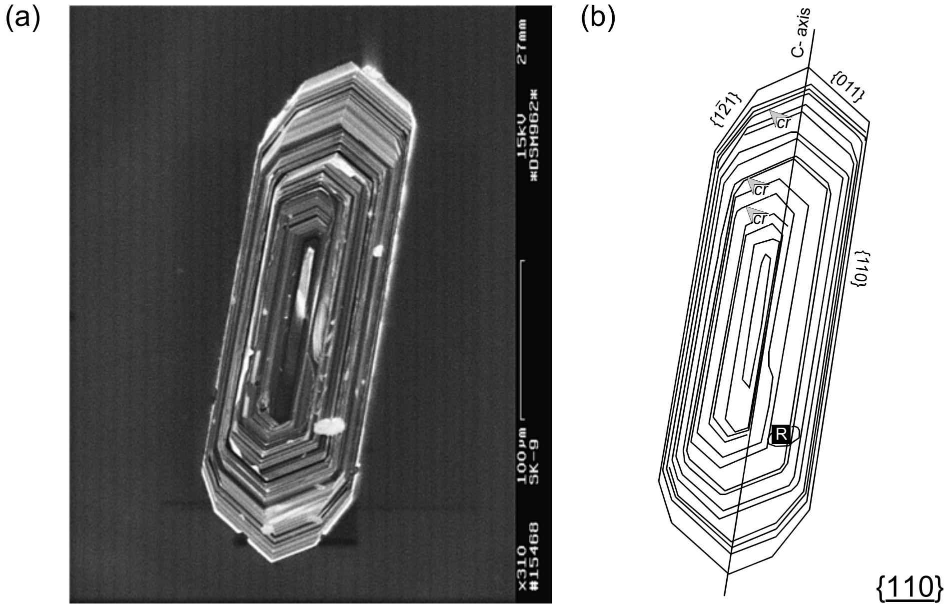

Figure 5.30. Zircon crystal [Z9(11)] from the Yenişabanlı biotite-amphibole granite (sample SK-9): (a) High-resolution CL photograph, (b) Sketch model showing the inner structures.

To sum up, zircons of the Yenişabanlı granitoid show oscillatory zoning from core to rim. Periods of corrosion interrupt the oscillatory zoning. However these corrosion zones are not so pronounced as in the case of the Kalebalta and Hisarkaya granitoids. Additionally, some crystals contain inherent cores.

5.3.2.3. Sipahiler Amphibole-Biotite Granite

Intra-crystal structures of the zircon crystals from the Sipahiler granitoid can be summarized as large inherent cores (e.g. [Z10(7)], [Z10(13)], [Z10(14)], [Z10(16)], [Z10(17)]), oscillatory zoning with intermittent corrosion stages (e.g. [Z10(1)], [Z10(6)], [Z10(13)]), metamictization (e.g. [Z10(9)]), flow domains (e.g. [Z10(4)]), low CL-intensity crystal rim (almost all crystals), recrystallized zones (e.g. [Z10(3)], [Z10(6)], [Z10(17)], and recrystallized patches (e.g. [Z10(12)] and [Z10(14)]) (Figure 5.31).

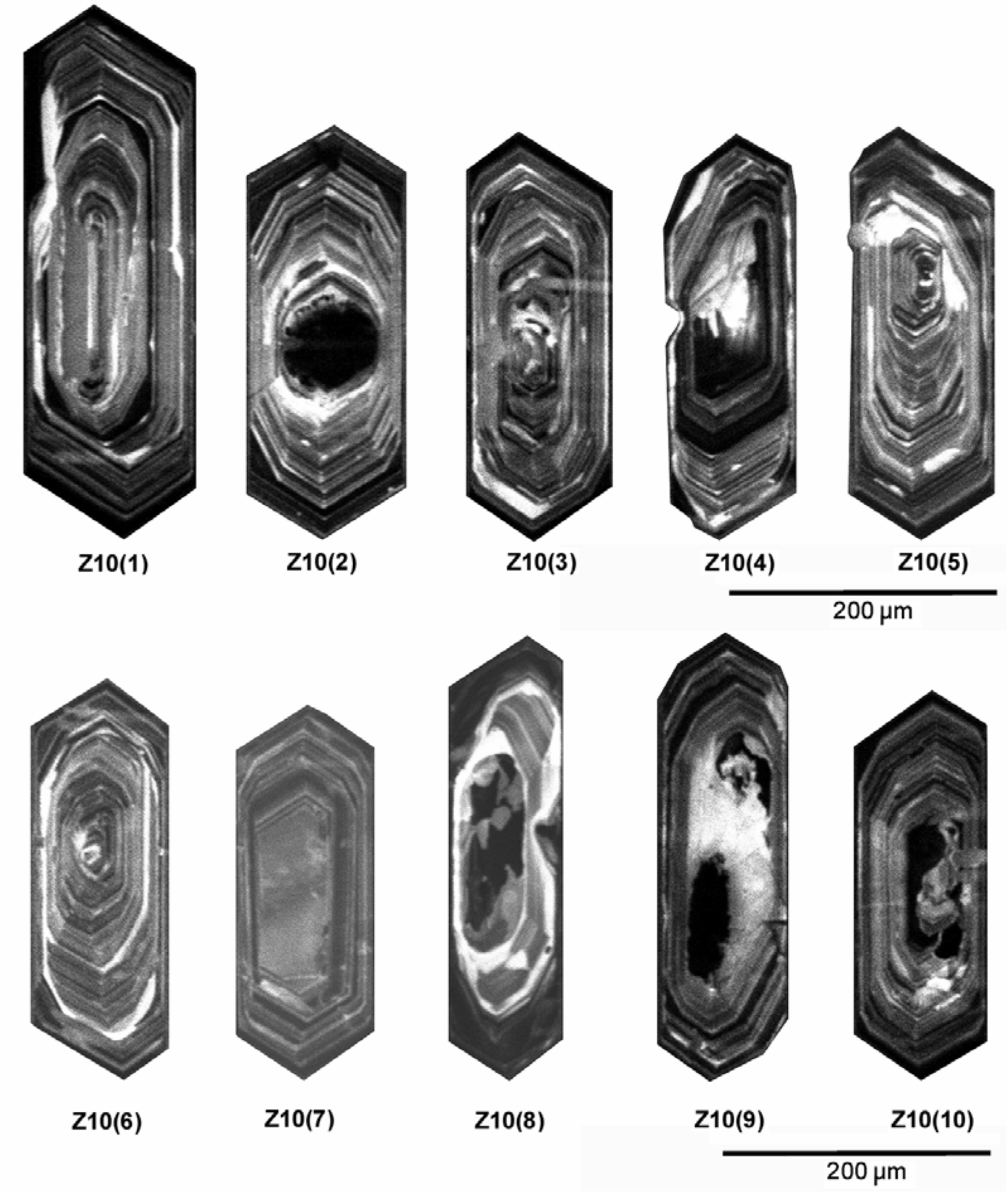

Figure 5.31. CL images of the selected zircon crystals from the Sipahiler amphibole-biotite granite (SK-10).

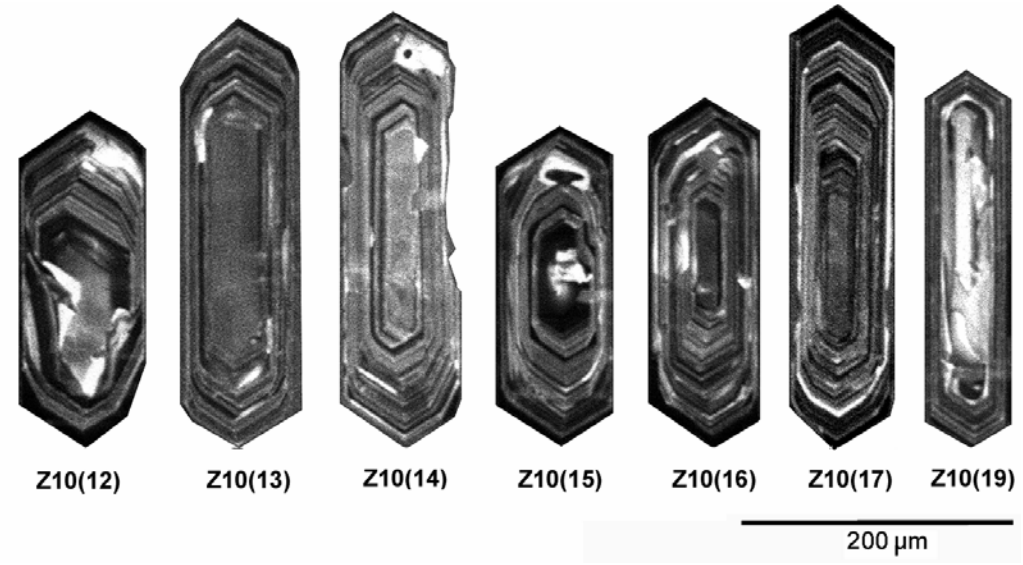

Figure 5.31 (cont'd).

The G_1-type zircon crystal [Z10(1)] (Figure 4.55) is sectioned parallel to the {110} prism face (Figure 5.32). The needle shape central part does not represent a core (similar to that observed in crystal [Z9(11)]). Subsequent oscillatory zoning, characterized by increased size of {121} pyramidal face, is truncated by corrosion stage after which fine oscillatory zoning represented by asymmetric growth of pyramid {011} overgrows. It is remarkable that the preceding and subsequent stages of corrosion are morphologically distinct. Outer rim of the crystal is characterized by low-CL intensity. Additionally, strongly reduced growth rate of {110} prism is remarkable at the outer zones combined with the effect of growth units (Vavra, 1994).

The zircon crystal [Z10(2)] is of P_2-type (Figure 4.55) and is sectioned parallel to the {110} prism face (Figure 5.33). The dark appearance in the central part of the crystal is probably related with etching processes during sample preparation (see Figure 4.55). Subsequently, oscillatory zoning is characterized by rapid disappearance of {121} surface at the outer zones following stage of low-CL. The rapid growth intervals of {011} pyramids are possibly responsible for increased sizes of adjacent {121} pyramidal faces as Vavra (1994) suggested. Growth rate of {010} face is governed by adsorption of cations (e.g. Na, K, Al). Moreover, growth rate of {010} face is decreased in the low Zr-supersaturation periods related with the crystal corrosion.

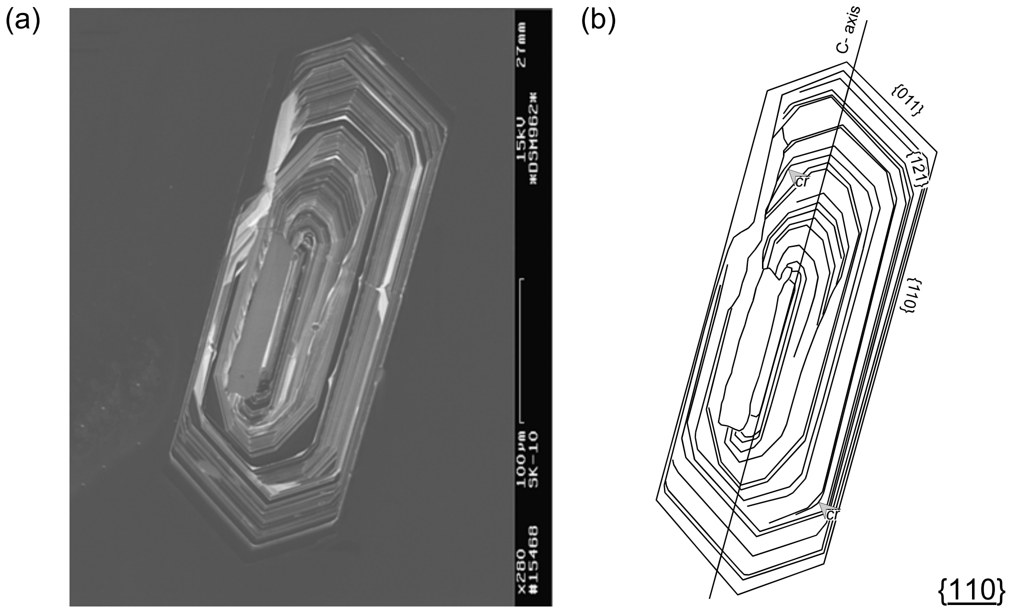

Figure 5.32. Zircon crystal [Z10(1)] from the Sipahiler amphibole-biotite granite (sample SK-10): (a) High-resolution CL photograph, (b) Sketch model showing the inner structures.

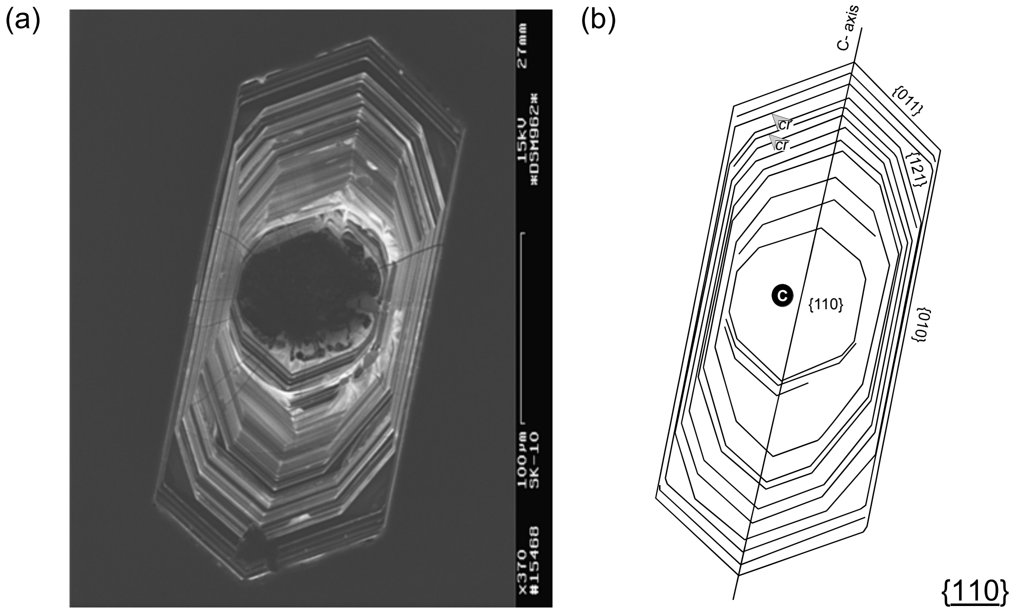

Figure 5.33. Zircon crystal [Z10(2)] from the Sipahiler amphibole-biotite granite (sample SK-10): (a) High-resolution CL photograph, (b) Sketch model showing the inner structures.

The CL section of the P_3-type zircon crystal [Z10(6)] (Figure 4.55) is parallel to the {110} prism face (Figure 5.34). In spite of its relatively simple morphology, this crystal seems to have a complex growth history. The small core has dissolution and recrystallization signatures. Fine oscillatory zoning comprising two intermittent corrosion stages surrounds the core and truncated by distinct pattern of zonation. Donaldson (1985) stated that non-planar boundaries can develop under conditions crystal growth, i.e. non-planar crystal interfaces should never be considered as a certain evidence of crystal dissolution. However, on the basis of this CL image, routine growth possibility can be confidently ruled out since truncation of oscillatory zoning is sudden and sharp, and combined with the dissolution surface of dropped CL. More plausible explanation would be that the crystal was broken and corroded (indicated by bold line), and overgrown by different stage of oscillatory zoning. Interruption and sudden disappearance of zones may be coeval with recrystallization (at the bottom part). Subsequent zones can be traced as surrounding the described inner part. {121} pyramidal faces in this period become larger due to the rapid growth intervals of adjacent {011} faces which maybe related with the adsorption of cations like Na, K and Al (e.g. Vavra, 1994). Afterwards, oscillatory zoning continues to the rim of the crystal, and can be characterized as asymmetric growth of pyramid {101} combined with disappearance of pyramid {112} at the outer zones, and low-CL zone at the outer rim. On the other hand, {110} face shows strongly reduced growth rate at the late stages of crystallization.

Sipahiler granitoid contains zircons with dominantly P- and G-type morphology. However investigation of intracrystalline structures infers that crystals undergone considerable morphological change during their growth. Crystals reflect oscillatory zoning up to the pronounced corrosional zone of low-CL intensity. Zoning, which outlines the crystal forms characterized by {110} and {010} faces surround these corrosional zones. Latest stages of growth are commonly represented by drop in CL-intensity probably related with the formation of growth units.

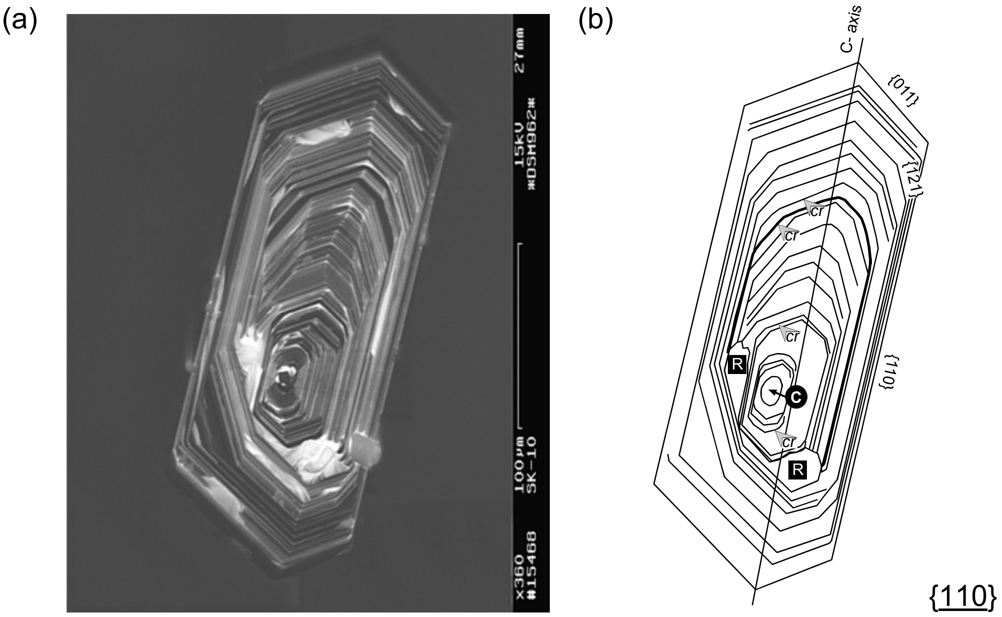

Figure 5.34. Zircon crystal [Z10(6)] from the Sipahiler amphibole-biotite granite (sample SK-10): (a) High-resolution CL photograph, (b) Sketch model showing the inner structures.

5.3.2.4. Torunobası Granite Porphyry

Torunobası granite porphyry is characterized by zircon population commonly (Figure 5.35) characterized by long tubular crystals exhibiting oscillatory zoning around an inherent core and with intermittent corrosion stages (e.g. [Z11a(1)], [Z11a(2)], [Z11a(3)] and [Z11a(12)]). Some of the crystals are metamictized (e.g. [Z11a(1)], [Z11a(9)], [Z11a(10)] and [Z11a(14)]), and some of have recrystallized intra-zones (e.g. [Z11a(6)] and [Z11a(7)]). In some crystals asymmetric growth is favored by the asymmetric form of the core (e.g. [Z11a(4)] and [Z11a(11)].

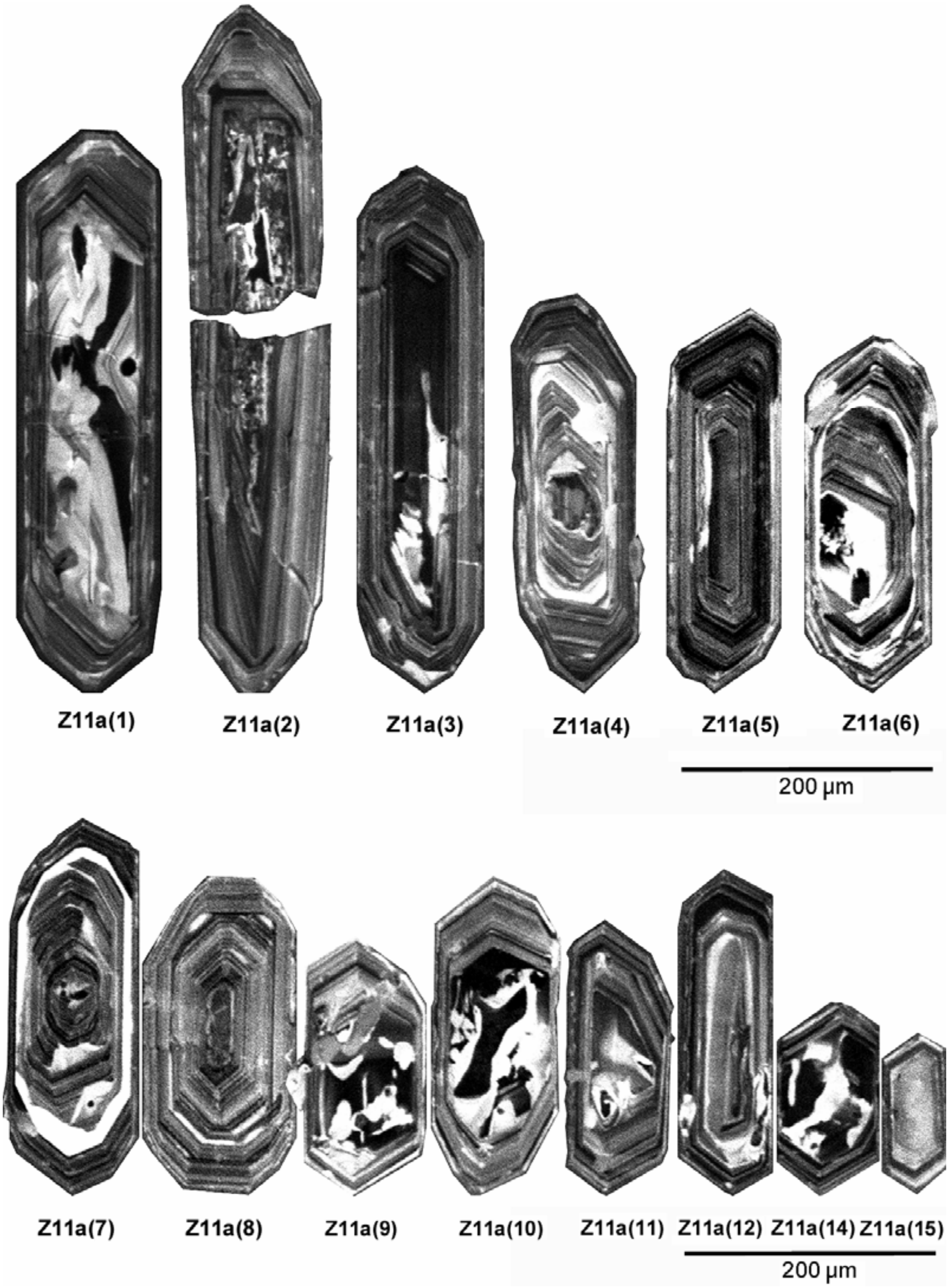

Figure 5.35. CL images of the selected zircon crystals from the Torunobası granite porphyry (SK-11a).

The zircon crystal [Z11a(3)] is of S_{17}-type (Figure 4.62) and is sectioned parallel to the {110} prism face (Figure 5.36). Long inherited core is overgrown by oscillatory zoning that is truncated by corrosion zone. Subsequent oscillatory zoning from corrosion zone to rim of the crystal is asymmetrically developed. Recrystallization patches are also visible in the crystal.

The zircon crystal [Z11a(10)] being an example of S_{18}-type (Figure 4.63) is sectioned parallel to the {110} prism face (Figure 5.37). This crystal is heterogeneously metamict, also detected by the radial cracks on the SEM image (Figure 4.63), suggesting U and Th in the zircon are heterogeneously distributed (e.g. Nasdala et al., 2001). This central part is covered by corrosion zone, which is then followed by zoning up to another corrosional zone close to exterior surface of crystal. Outer zones are characterized by increasing sizes of {121} pyramids probably due to the rapid growth rate of adjacent {011} faces according to Vavra (1994)'s suggestions. Adsorption of cations results in the increasing of the growth rate of {011} face (Vavra, 1994). Corrosion stage probably disrupts the adsorption layer (with H_2O component) and allows high growth rate of {110} prism as Vavra (1994) indicated.

As a summary, zircon crystals from the Torunobası granitoid display recrystallized and metamictized cores overgrown by oscillatory zoning with corrosion interface. This corrosion stage seems to represent the period between two growth stages. Subsequent oscillatory zoning continues to the outer zones with some intermittent corrosion stages one of which is near to rim.

5.3.2.5. Camili Alkali Feldspar Granite

CL-image of two crystals from the Camili granitoid is available. Both of them show oscillatory zoning with some corroded interlayers.

The zircon crystal [Z11b(15)] is of S_{23}-type (Figure 4.66) and is sectioned parallel to the {100} prism face (Figure 5.38).

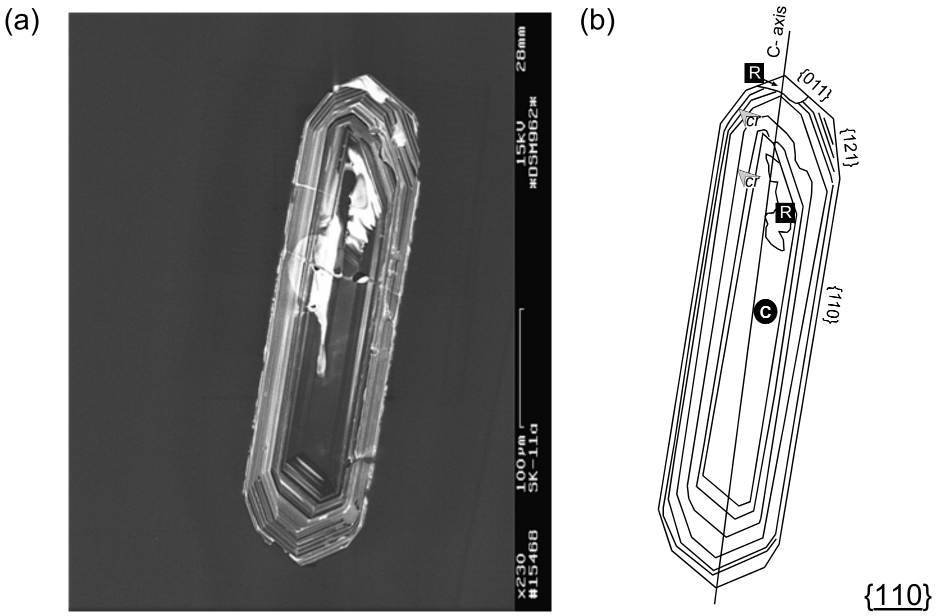

Figure 5.36. Zircon crystal [Z11a(3)] from the Torunobası granite porphyry (sample SK-11a): (a) High-resolution CL photograph, (b) Sketch model showing the inner structures.

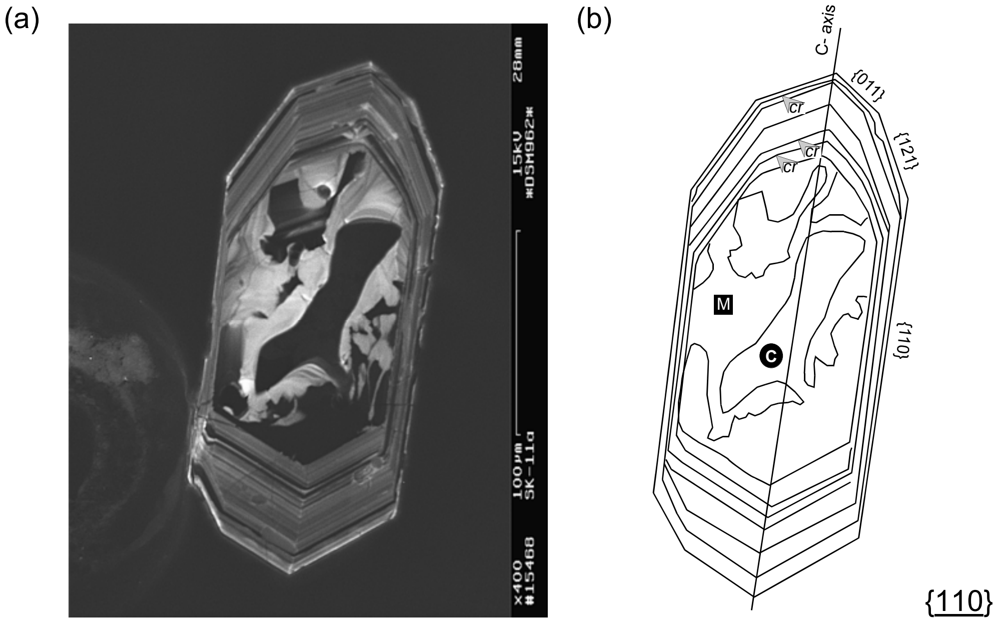

Figure 5.37. Zircon crystal [Z11a(10)] from the Torunobası granite porphyry (sample SK-11a): (a) High-resolution CL photograph, (b) Sketch model showing the inner structures.

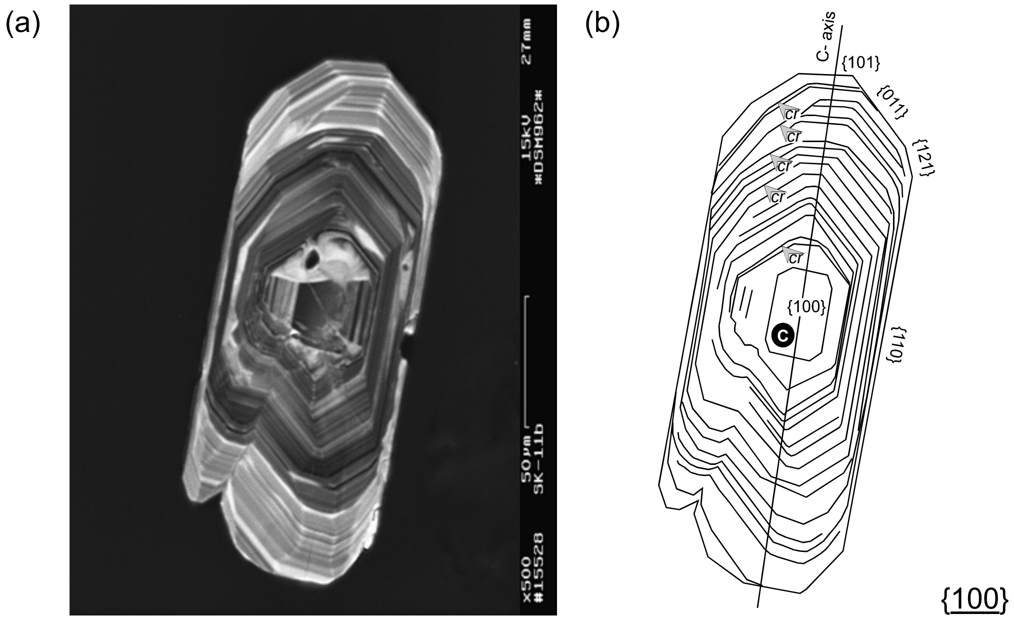

Figure 5.38. Zircon crystal [Z11b(15)] from the Camili alkali-feldspar granite (sample SK-11b): (a) High-resolution CL photograph, (b) Sketch model showing the inner structures.

The crystal [Z11b(15)] is distinct with different morphologies in its pyramid ends (Figure 4.66). This feature leads to a CL-image as if the crystal is twinned (Figure 5.38). However, the upper part of the crystal shows that zones are continuous, i.e. twinning is not the case. The zones are likely to be distorted. Apart from its distorted appearance, increase of CL-intensity in the outer zones is also remarkable. Corrosion stages are present not only in the inner lower-CL zones but also in the outer brighter zones. Additionally, {110} prism, at the late stages of evolution, shows growth inhibition suggesting H_2O or trace element enrichment in the residual liquid (Vavra, 1994).

The S_{13}-type zircon crystal [Z11b(16)] (Figure 4.69) is sectioned parallel to the {100} prism face (Figure 5.39). Intracrystalline structures are blurred probably due to the secondary events. The rectangular form of {100} prism visible in the center of the crystal as an inherent core indicates that the section is non-central (e.g. Vavra, 1993). Oscillatory zoning overgrowing the core is truncated by a corrosion zone, which is surrounded by another cycle of oscillatory zoning up to the crystal margin. Besides secondary flow structures and recrystallization patches, possible melt inclusion near to core is also observable in the crystal. {110} prism is growth inhibited as in the crystal [Z11b(15)].

Considering the intracrystalline features of the zircon crystals from the Camili granitoid, it can be concluded that the crystals have undergone successive corrosion events one of which is more notable than others. This corrosion interface probably separates first stage of growth, which includes inherent cores overgrown by zoning combined with recrystallization, from second stage of growth, which is characterized by higher luminescent oscillatory zoning with intermittent corrosion stages. On the other hand, at the late stages of crystallization, {110} prism faces become growth inhibited by the adsorption of H_2O or trace elements enriched in the residual liquid.

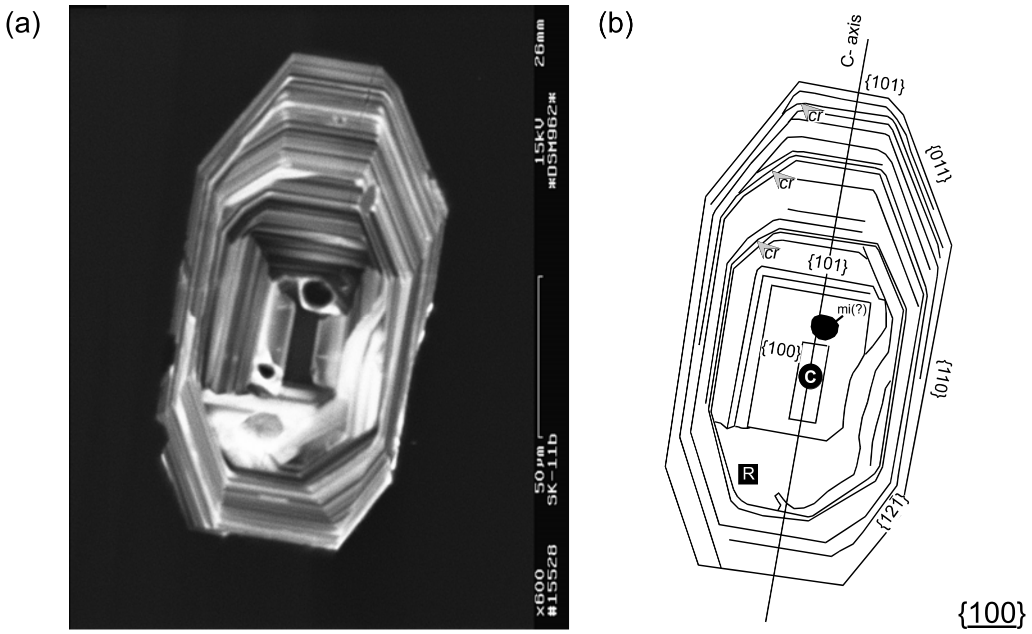

Figure 5.39. Zircon crystal [Z11b(16)] from the Camili alkali-feldspar granite (sample SK-11b): (a) High-resolution CL photograph, (b) Sketch model showing the inner structures.

5.3.2.6. Çimkalesi Monzogranite

The characteristics of the zircons from Çimkalesi monzogranite can be summed up in the following manner: (i) Corrosion zones generally surround cores, being sometimes inherent (e.g. [Z12(18)]). (ii) {011} pyramid overgrows these corrosion zones asymmetrically (e.g. [Z12(1)], and [Z12(11)]). (iii) Oscillatory zoning from core to rim is always present with intermittent corrosion stages. (iv) Sudden drop in the CL-intensity is common at the crystal margins. (v) In some crystals (e.g. [Z12(24)] and [Z12(35)]) core is a broken part of previously formed crystal. (vi) Some thick sections do not reveal well inner structures (e.g. [Z12(5)], [Z12(9)], [Z12(30)] and [Z12(33)]). (vii) Apatite and zircon inclusions are typical features (e.g. [Z12(2)] and [Z12(19)] (Figure 5.40).

The zircon crystal [Z12(1)] is of S_{23}-type (Figure 4.71) and is sectioned parallel to the {100} prism face (Figure 5.41). The rectangular shape of {100} prism that is an inherent core suggests that the section is not central. The truncation of linear compositional discontinuities within the core also defines the core/rim interface, which is convex outwards. This interface is characterized by asymmetrical growth behavior of {011} pyramid. Oscillatory zoning with intercalated corrosion stages continues to corrosion zone near to crystal rim. Following zones are distorted due to recrystallization, and outer rim is characterized by low-CL intensity. The rapid growth intervals of {011} faces, by adsorption of cations, increase the size of the adjacent {121} pyramids, while growth rate of {110} prism strongly decreases through the rim.

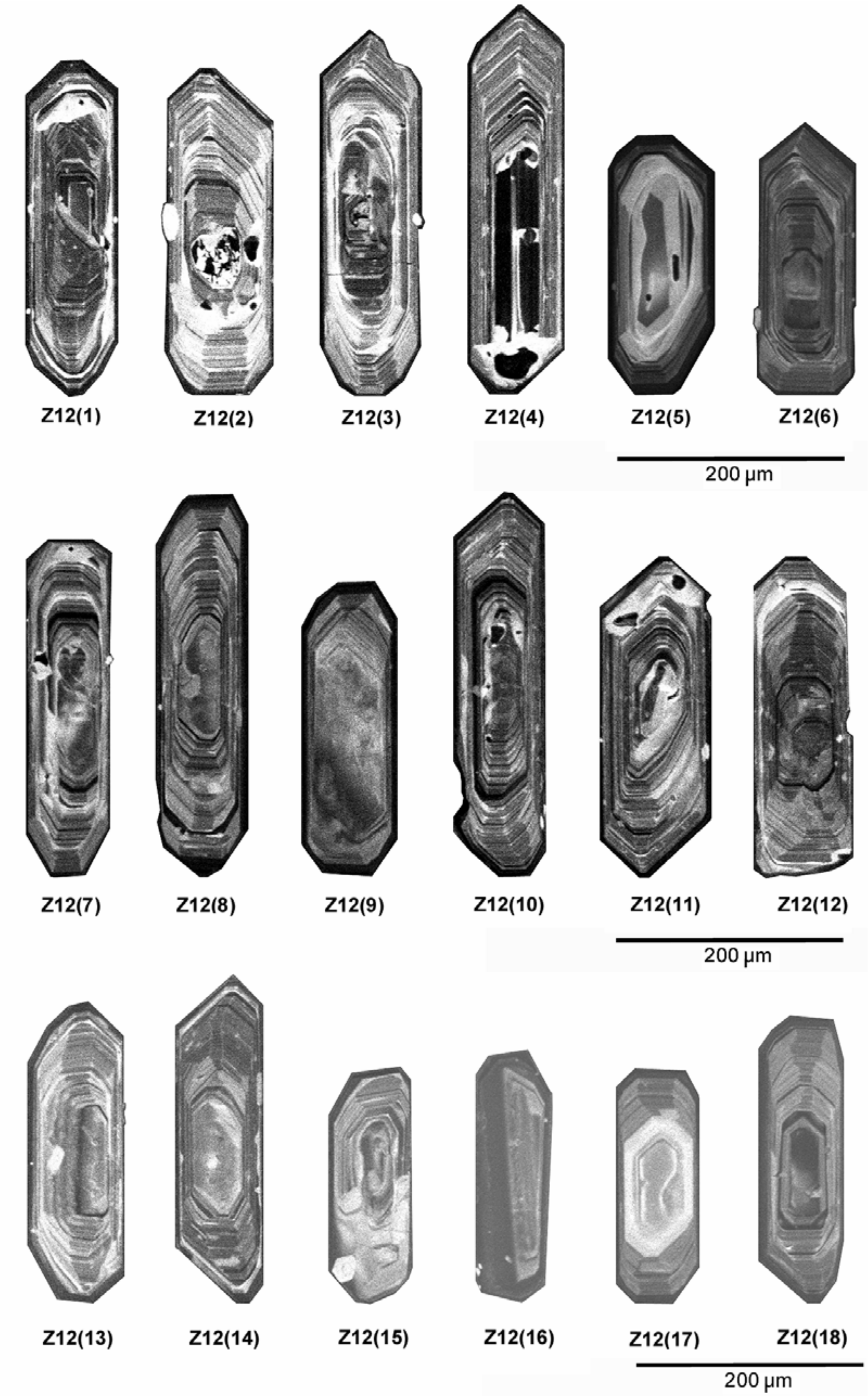

Figure 5.40. CL images of the selected zircon crystals from the Çimkalesi monzogranite (SK-12).

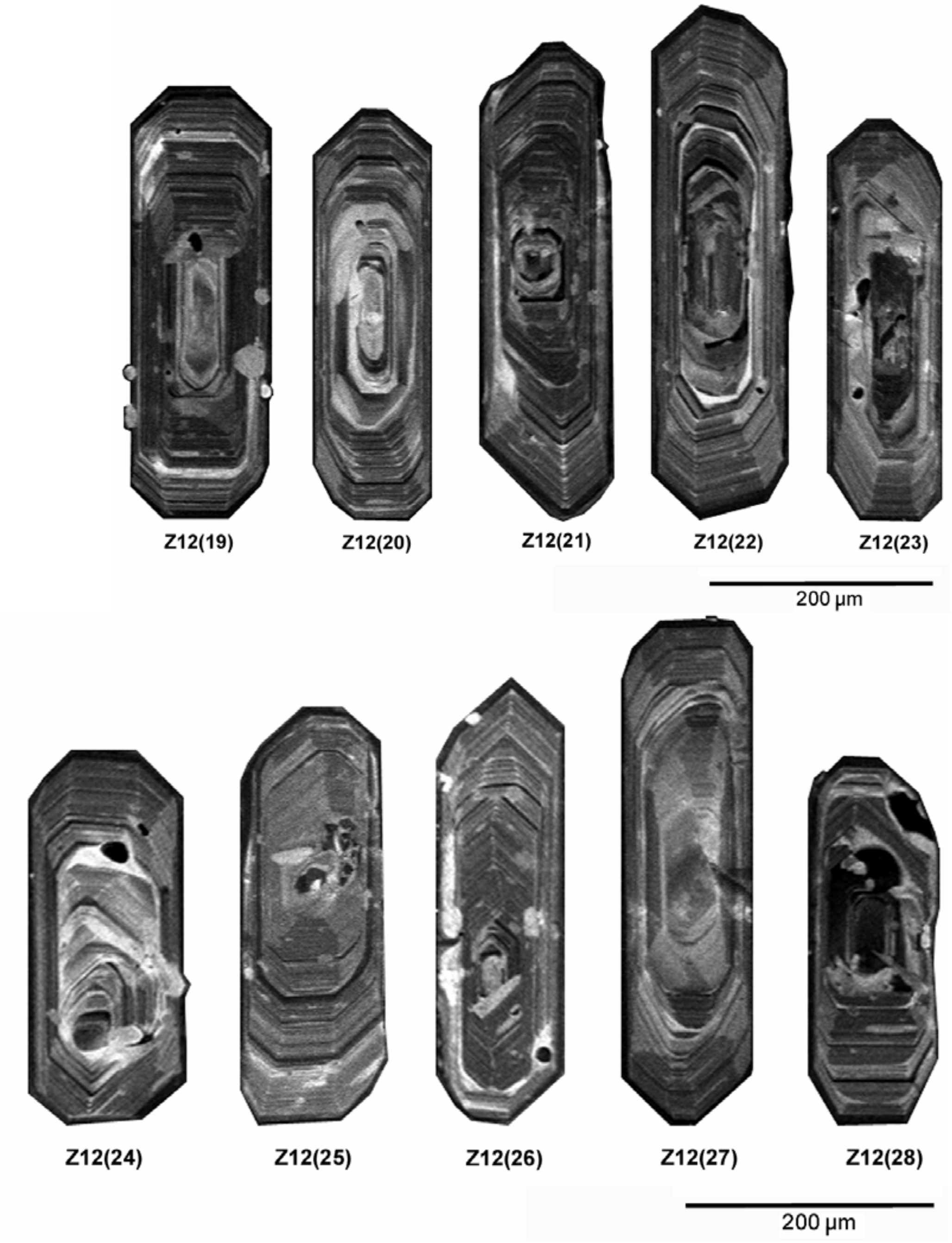

Figure 5.40 (cont’d).

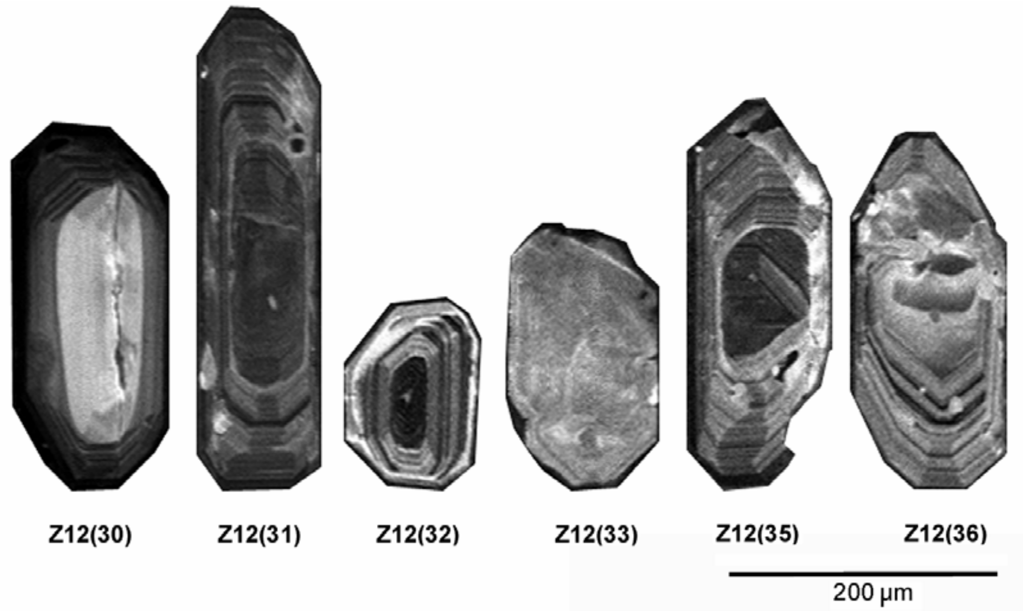

Figure 5.40 (cont'd).

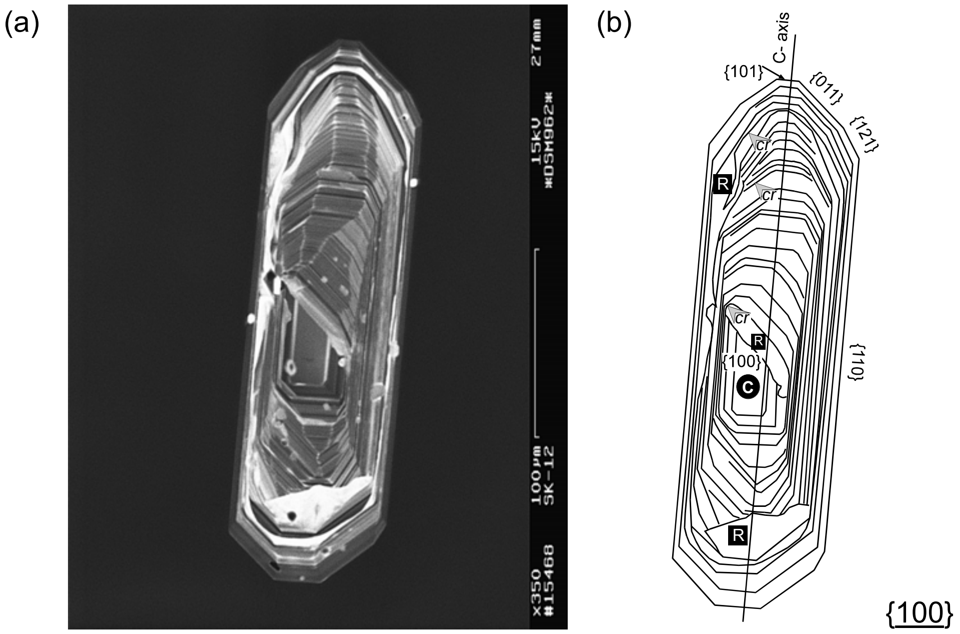

Figure 5.41. Zircon crystal [Z12(1)] from the Çimkalesi monzogranite (sample SK-12): (a) High-resolution CL photograph, (b) Sketch model showing the inner structures.

The S_{24}-type zircon crystal [Z12(11)] (Figure 4.72) is sectioned parallel to the {100} prism face (Figure 5.42). Asymmetric growth of {112} and {011} pyramids characterize crystal. Recrystallization concealed the core but subsequent corroded layers are visible. The outer corrosion zones are likely to be related with the episodic low Zr-supersaturation periods since they are narrowly spaced and frequent. Asymmetric evolution of the pyramid surfaces continues up to the rim. Reduced growth rate of {010} face indicates low Zr-supersaturation because of the intermittent corrosion stages (e.g. Vavra, 1994). Dashed lines interpret irregular sector boundaries. Near to rim of the crystal there exists a dark area, which resembles melt inclusion.

The zircon crystal [Z12(18)] is of S_{23}-type (Figure 4.71) and is sectioned parallel to the {100} prism face (Figure 5.43). A thick corrosion layer surrounds large inherent core. Subsequent zoning interrupted by two corrosion stages and low-CL zone takes place at the crystal margin. Dashed lines represent irregular shaped sector boundaries. During the corrosion stages growth rate of {110} faces increased in the inner zones whereas growth inhibition of {110} prism is observable on the outer zones.

The S_{24}-type zircon crystal [Z12(21)] (Figure 4.71) is sectioned parallel to the {100} prism face (Figure 5.44). Recrystallized and equant core and succeeding corrosion zone are surrounded by fine oscillatory zoning with recurrent corrosion stages. Recrystallized parts and inclusions are visible in the CL-image. Enrichment of trace elements or water in the magma may be concluded from the growth inhibition of the {110} face. Dashed lines show irregular shaped sector boundaries.

The zircon crystal [Z12(22)] being a S_{24}-type crystal (Figure 4.71) is sectioned parallel to the {100} prism face (Figure 5.45). The crystal growth is interrupted by several corrosion stages. The core has a faint zoning, which is partly recrystallized. Fine oscillatory zoning overgrows asymmetrically after a corrosion stage, and truncated by corroded layers. Outer rim has low-CL intensity. Moreover irregular shaped dashed lines designate sector boundaries. Additionally, {110} face become growth inhibited may be due to the adsorption of water or trace elements in the magma (e.g. Vavra, 1994).

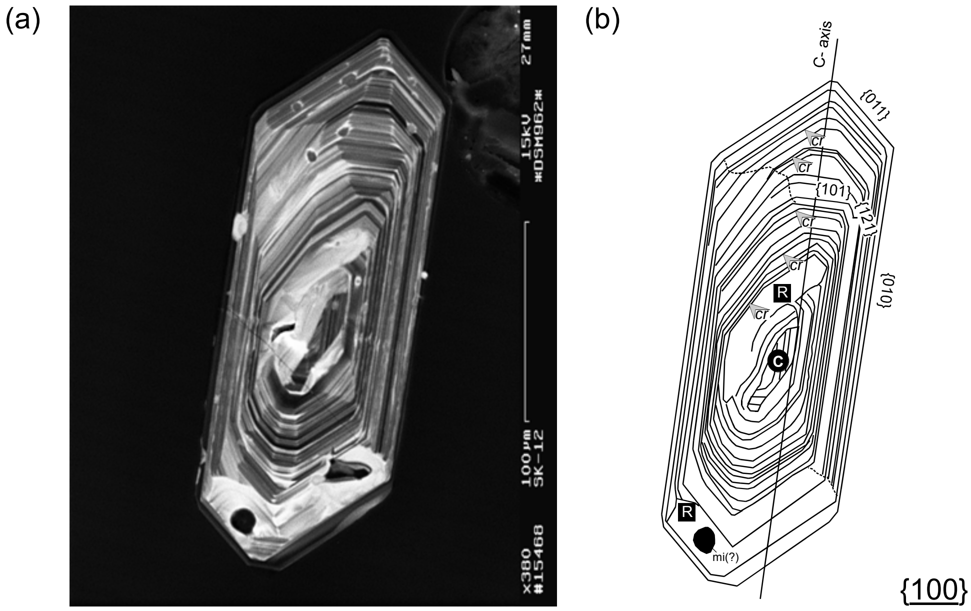

Figure 5.42. Zircon crystal [Z12(11)] from the Çimkalesi monzogranite (sample SK-12): (a) High-resolution CL photograph, (b) Sketch model showing the inner structures.

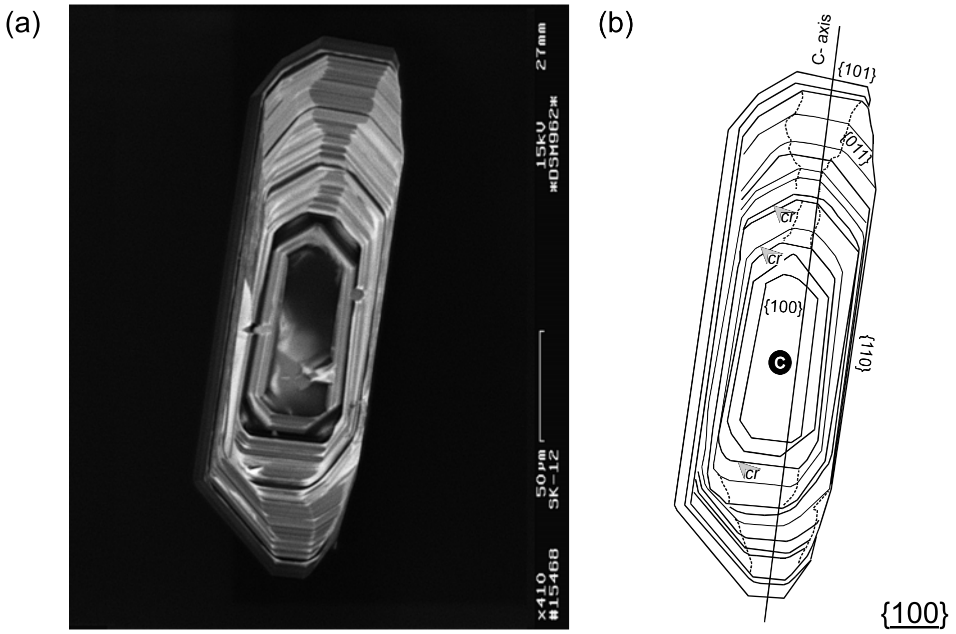

Figure 5.43. Zircon crystal [Z12(18)] from the Çimkalesi monzogranite (sample SK-12): (a) High-resolution CL photograph, (b) Sketch model showing the inner structures.

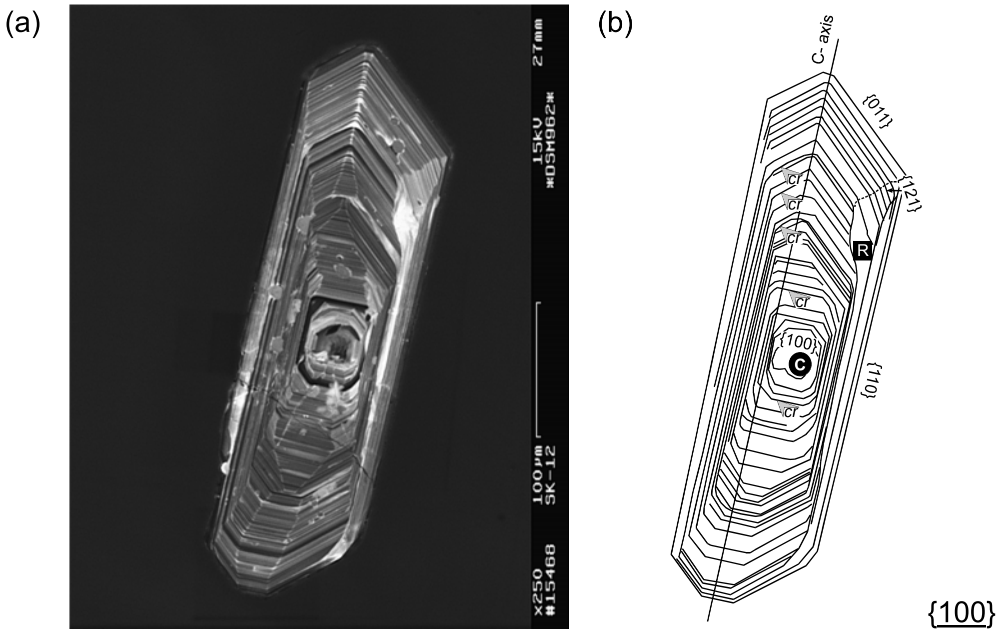

Figure 5.44. Zircon crystal [Z12(21)] from the Çimkalesi monzogranite (sample SK-12): (a) High-resolution CL photograph, (b) Sketch model showing the inner structures.

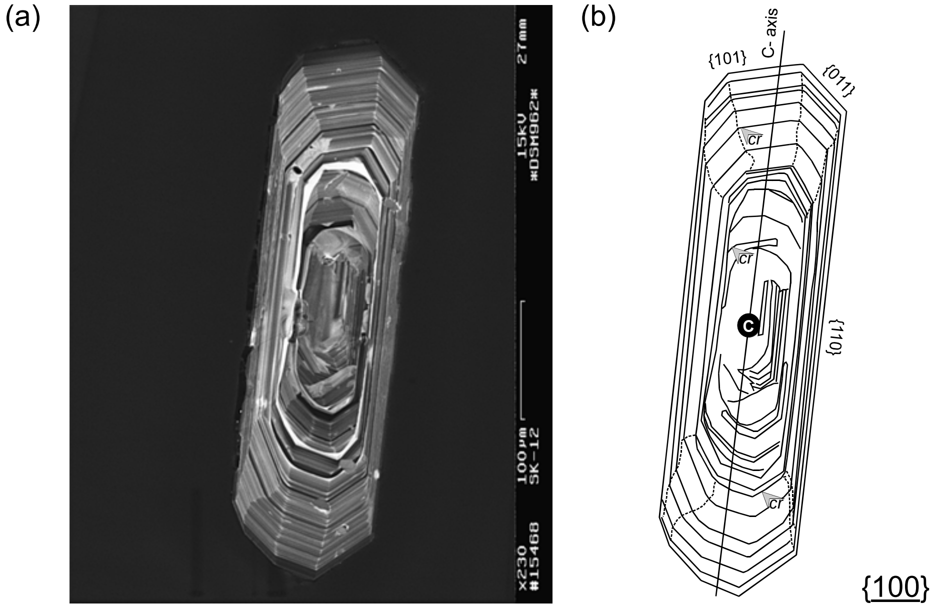

Figure 5.45. Zircon crystal [Z12(22)] from the Çimkalesi monzogranite (sample SK-12): (a) High-resolution CL photograph, (b) Sketch model showing the inner structures.

The CL section of the S_{24}-type zircon crystal [Z12(26)] (Figure 4.71) is parallel to the {100} prism face (Figure 5.46). The small inherent core is overgrown by subsequent stages of corrosion and oscillatory zoning in which the crystal is grown along C-axis. Outer zones are extensively recrystallized, and the crystal rim has low-CL intensity. Fluctuating growth rate of {010} prism points out varying Zr-supersaturation levels drastically lowered at the corrosion stages (e.g. Vavra, 1994). Additionally, inclusions are visible throughout the crystal. Dark colored point near to rim is possibly a melt inclusion, but it can be described only by a detailed investigation.

The zircon crystal [Z12(27)] which is of S_{24}-type (Figure 4.74) is sectioned parallel to the {100} prism face (Figure 5.47). Core is blurred and featureless, and overgrown by thickened trace element bands. Recrystallization of the outer zones hindered some details but the corrosion stages are visible within the oscillatory zoning. Dashed lines show irregular shaped sector boundaries. Crystal rim has very low-CL intensity. {010} face with reduced growth rate accompanied with intermittent corrosion stages infers that the Zr-supersaturation was low and cooling rate decreased in the last stages of crystal growth (e.g. Vavra, 1994).

Çimkalesi monzogranite is one of the samples in which the long zircon growth history can be traced. It seems that at the earliest stages of evolution, crystals were subjected to intense corrosion, which is distinguishable by remarkable dissolution surfaces around small cores. A noteworthy corrosion stage in the central part of the crystals truncates oscillatory zoning, which overgrows these dissolution surfaces. This corrosion combined with sharp transition in zoning probably characterizes an abrupt change in the growth history. Oscillatory zoning develops up to another pronounced corrosion event. Subsequently crystals exhibit new cycle of oscillatory zoning with minor interspersed corrosion events up to rims. Zircon rims generally showing low-CL are characterized by reduced growth rate of {010} prism and growth inhibition of {110} prism, which may indicate low Zr-supersaturation and enrichment of H_2O (and trace elements) in the growth medium at the latest stages of evolution. Recrystallization and inclusions are common in the zircon crystals from the Çimkalesi granitoid.

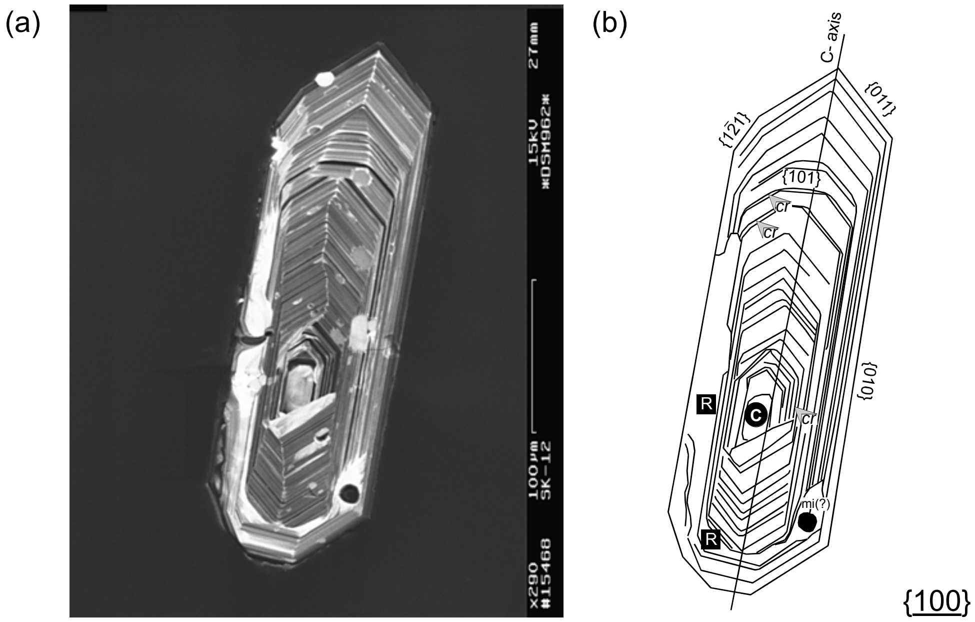

Figure 5.46. Zircon crystal [Z12(26)] from the Çimkalesi monzogranite (sample SK-12): (a) High-resolution CL photograph, (b) Sketch model showing the inner structures.

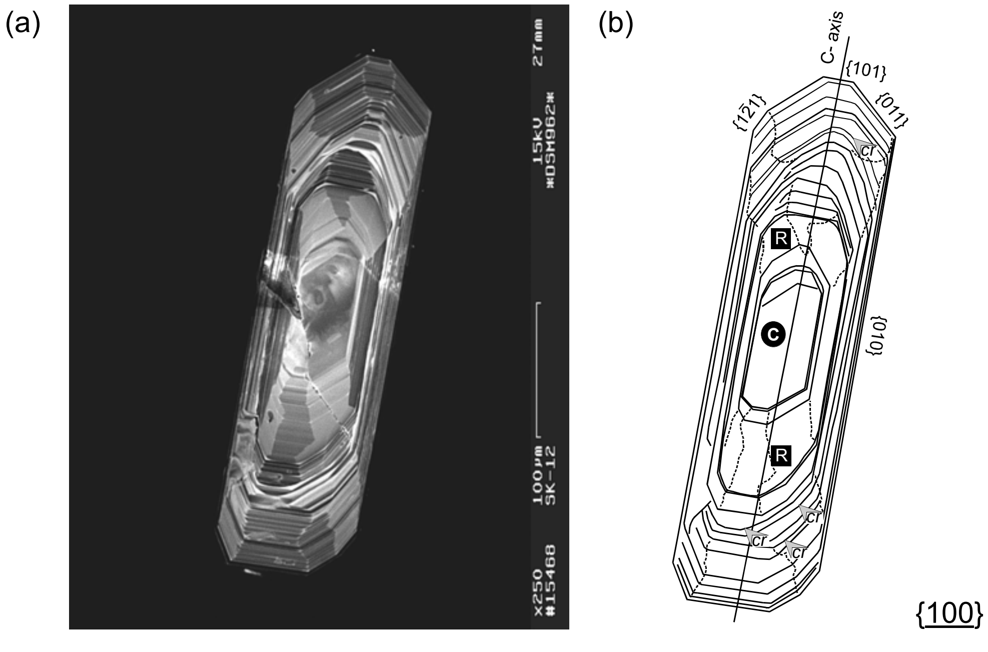

Figure 5.47. Zircon crystal [Z12(27)] from the Çimkalesi monzogranite (sample SK-12): (a) High-resolution CL photograph, (b) Sketch model showing the inner structures.

5.3.3. Terlemez Quartz-Monzonite

CL investigation of the zircons from the Terlemez quartz-monzonite is expected to form a basis of correlation with the other studied granitoids. Zircon cores are subjected to corrosion stages followed oscillatory zoning. Recrystallization patches and low-CL intensity outlines are typical features. Apatite and zircon inclusions are common in zircons of the Terlemez granitoid (Figure 5.48).

The S_{23}-type zircon crystal [Z7(3)] (Figure 4.77) is sectioned parallel to the {100} prism face (Figure 5.49). Oscillatory zoning showing spasmodic corrosion steps overgrows the core and surrounding corroded layer. During corrosion stages due to low Zr-supersaturation, {010} prisms form with low growth rate. Outer rim demonstrates flow structures and recrystallization. Irregular shaped dashed lines designate sector boundaries. Dark colored area resembles melt inclusion, but it should be determined by a detailed study. Surrounding this area there is a curving in the zones possibly related with the elevation in the temperature due to the inclusion.

Being a S_{25}-type, zircon crystal [Z7(7)] (Figure 4.80) is sectioned parallel to the {100} prism face (Figure 5.50). Oscillatory-zoned core is overgrown by corrosion zone. Truncation of zones suggests that crystal was broken, possibly transported, abraded and then corroded (supposed surface of the broken crystal is shown by bold line). Crystal's subsequent intra-structures can be divided into two zones as; (i) low-CL zone governed by corrosion stages, and (ii) oscillatory zoning with relatively higher CL intensity continues to the rim of crystal with corroded interlayers. Decreasing of growth rate of {010} prism is remarkable along the corroded layers. Dark point may represent melt inclusion but again needs more detailed study.

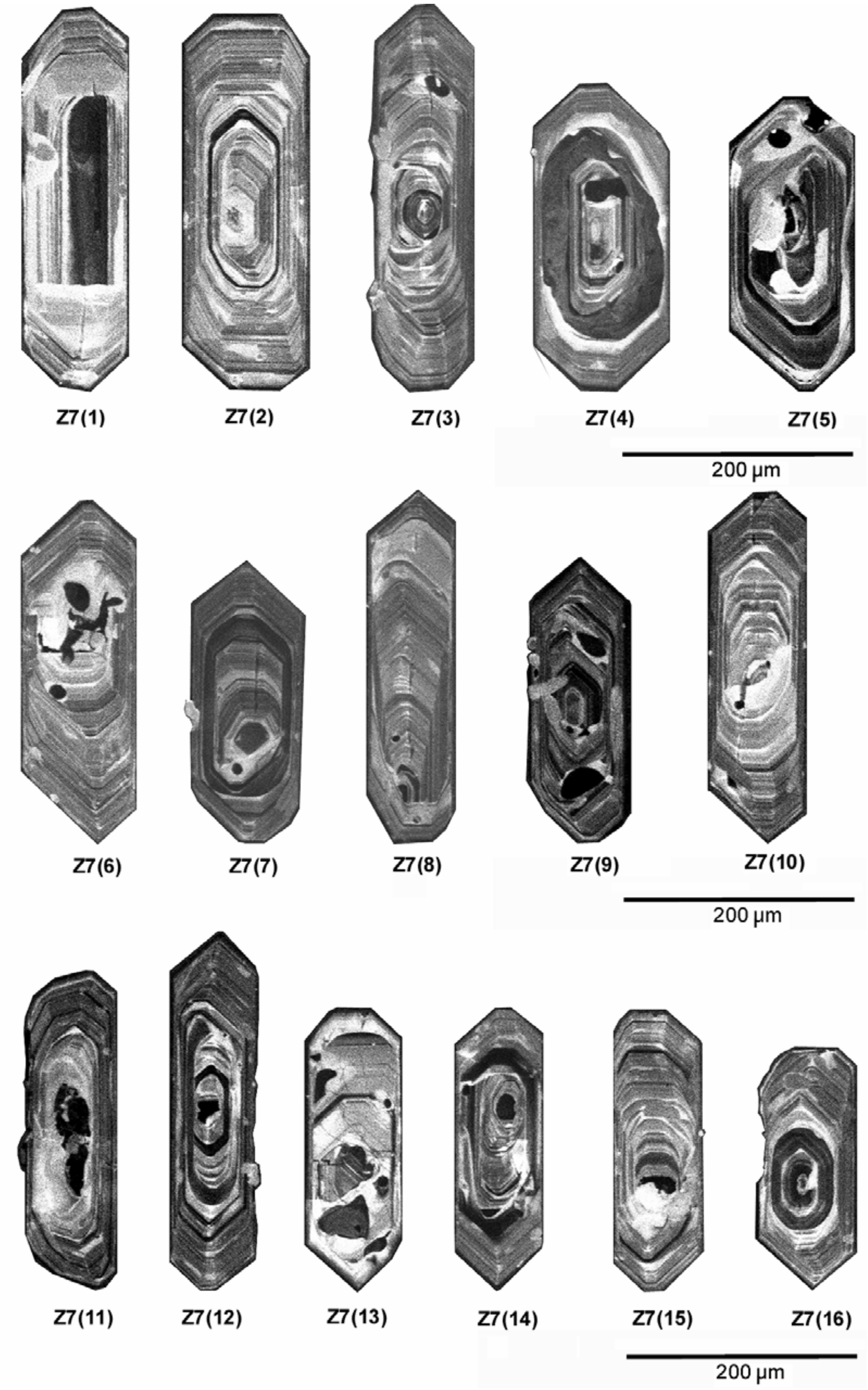

Figure 5.48. CL images of the selected zircon crystals from the Terlemez quartz-monzonite (SK-7).

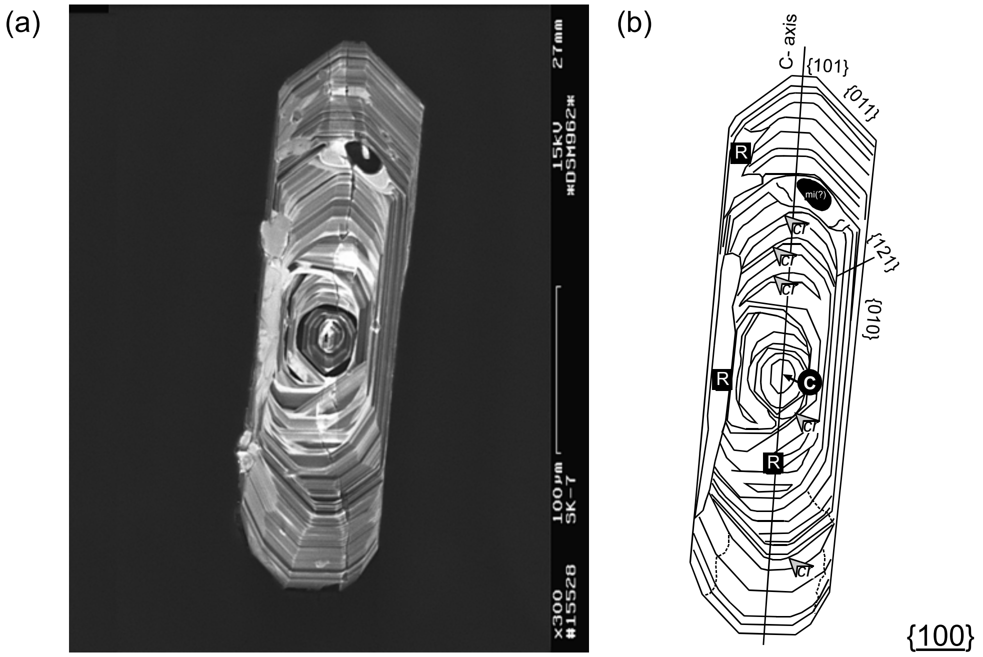

Figure 5.49. Zircon crystal [Z7(3)] from the Terlemez quartz-monzonite (sample SK-7): (a) High-resolution CL photograph, (b) Sketch model showing the inner structures.

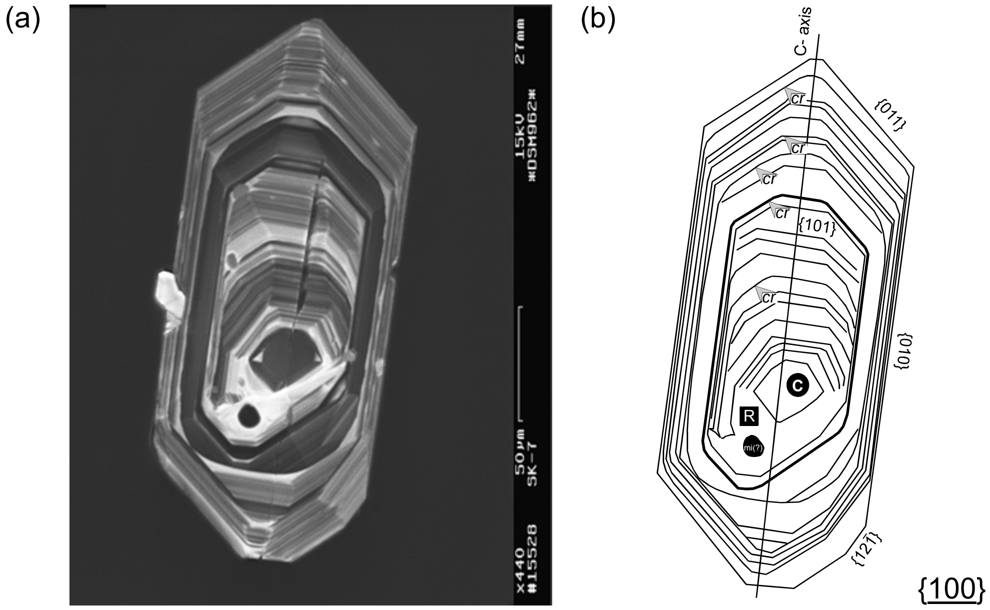

Figure 5.50. Zircon crystal [Z7(7)] from the Terlemez quartz-monzonite (sample SK-7): (a) High-resolution CL photograph, (b) Sketch model showing the inner structures.

The S_{24}-type zircon crystal [Z7(8)] (Figure 4.77) is sectioned parallel to the {100} prism face (Figure 5.51). The crystal reflects a history of development beginning with rapid growth of euhedral oscillatory zones, which rounds the small core and surrounding corrosion surface, in the direction of the c-axis. During this period of magmatic growth the elongate crystal was broken, but growth of zircon continued conformably onto the prism sides of the crystal while unconformably overlying the broken end (bold line represents the supposed frontier of the broken crystal). The evolution of crystal partly resembles that of the crystal [Z10(6)]. Subsequent to magmatic crystallization partial recrystallization causing blurring and rounding of the oscillatory zones has occurred but not inferred the later growth of new zircon (e.g. Pidgeon, 1992). Intermittent corrosion stages results in low growth rate of {010} face. Moreover dashed lines show irregular shaped sector boundaries. On the other hand dark points seem to be melt inclusions.

The zircon crystal [Z7(12)] is of S_{24}-type (Figure 4.77) and is sectioned parallel to the {100} prism face (Figure 5.52). Corrosion layer with faint zonation surrounds rounded core. Oscillatory zoning with multi corrosion stages accompany with low growth rate of {010} prism follows then up to the crystal rim. Inclusions are widespread in the crystal.

To sum up, zircons from the Terlemez granitoid can be characterized by successive stages of oscillatory zoning and corrosion. Small and sometimes inherited cores are overgrown by zoning, which is truncated by prominent corrosion stage. Subsequent oscillatory zoning starts then, and continues to the corrosion stage, perhaps the most pronounced one in the crystals. Ensuing oscillatory zoning develops through the outer parts with minor corrosion stages accompanying with reduced growth rate of {010} prism. Recrystallization and inclusions are widespread in the Terlemez zircons.

Despite of being afar and separate pluton, the Terlemez quartz-monzonite reveals very similar characteristics, in terms of zircon intracrystalline structures, with those of the Çimkalesi monzogranite.

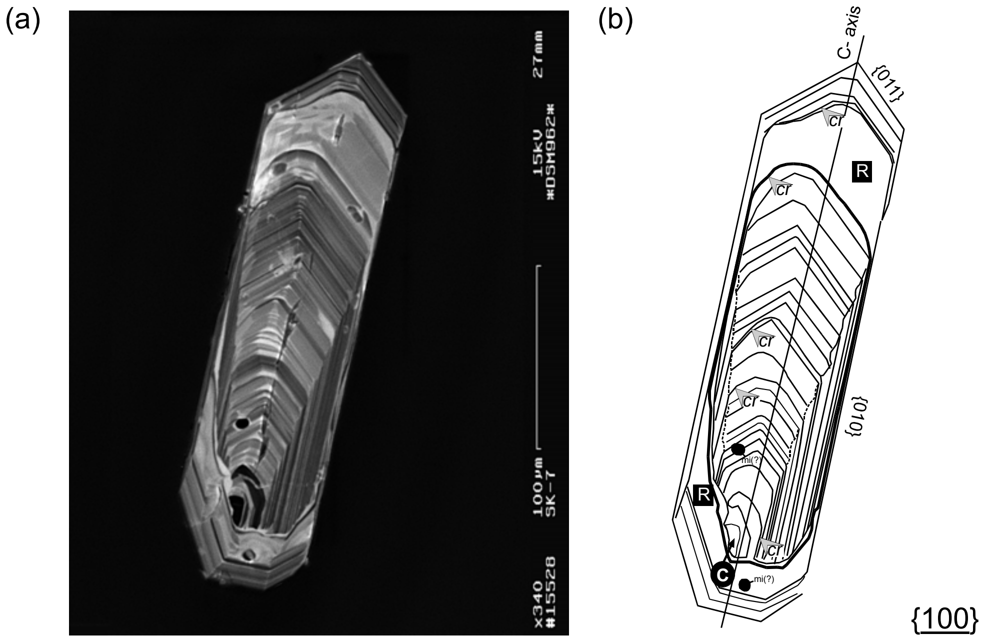

Figure 5.51. Zircon crystal [Z7(8)] from the Terlemez quartz-monzonite (sample SK-7): (a) High-resolution CL photograph, (b) Sketch model showing the inner structures.

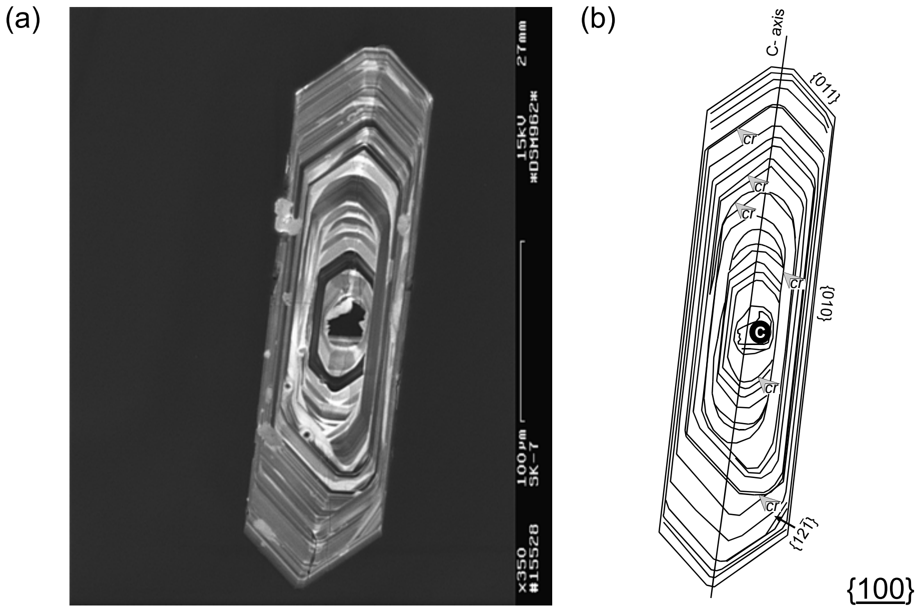

Figure 5.52. Zircon crystal [Z7(12)] from the Terlemez quartz-monzonite (sample SK-7): (a) High-resolution CL photograph, (b) Sketch model showing the inner structures.

As a consequence, CL imaging of the zircon crystals from the Central Anatolian Granitoids reveals hidden structures that cannot be recognized from their morphologies. Considering the kinematics of crystal growth, results obtained from the zircon typology method (Chapter 4) on the concerned granitoids are reviewed. In this manner, scope of typological study is extended from outer form to morphological evolution of the zircon crystals.

Investigated zircon crystals show fine or medium-scale oscillatory zoning, trace element bands or may instead be weakly zoned. Even though euhedral zircons are dominant within populations, some of them have anhedral, relict cores with euhedral overgrowths. In most cases multiple, internal surfaces of corrosion truncate crystal zoning.

Oscillatory zoning is distorted in some crystals at the pyramid end or interlayers of the zircon. Additionally, in some samples inclusions are widespread. Moreover, flow domains that may be originated from penetrative migration of impurity components in the crystal lattice (Vavra et al., 1996) are visible in the CL-images. Recrystallization and thickening of trace element bands are common in the crystals. These features demonstrate that the secondary events affecting the zircon crystal structures in the magma chamber are extensive (e.g. Pidgeon et al., 1998).

CHAPTER 6

ZIRCON CHEMISTRY

6.1. Background: Chemical Characteristics of Zircon

Chemically, zircon seems to be relatively simple; usually ZrO_2, HfO_2 and SiO_2 compose more than 99% of the total oxides (Hinton and Upton, 1991). ZrO_2 and SiO_2 contents are about 65% and 35%, respectively. Although there is a complete solid solution between zircon and hafnon ($HfSiO_4$), Hf content of most natural zircon crystals is only 1-3% HfO_2 (Speer, 1982). Complexity of the zircon chemistry comes from additional elements, which were reported to be present in minor amounts (Speer, 1982), among which the predominant ones are Y, REEs, Th, and U (Hinton and Upton, 1991; Benisek and Finger, 1993).

Trace elements, like Y, Th, U, Nb and Ta, and REEs being incompatible in many rock-forming silicate minerals because of their large ionic radii and high charge, generally become concentrated in the residual melts and are incorporated in the late-crystallizing zircon as the crystal structure of zircon accommodates widely varying proportions of these elements (Belousova et al., 2002). For instance, Miller and Wooden (2004) reported that within the sample population of zircons, the concentrations might vary over two orders of magnitude, and concentration ranges for U and Th observed within some zircons might vary by 10–20x.

The unique properties of zircon crystals coming from different sources attracted scientists to investigate the link between zircon chemistry and petrogenesis of host rocks.

Despite some chemical similarities between magmatic and metamorphic zircons, such as high Hf and Y contents (Rubatto, 2002), they demonstrate some particular features in terms of elemental contents and ratios. For instance, in metamorphic rocks or metamorphic rims that have overgrown magmatic or detrital cores, Th/U ratios characteristically show low ratios (<0.1) (Rubatto and Gebauer, 2000; Rubatto, 2002), while magmatic zircons generally show moderate to high Th/U ratios (>0.5) (Zeck and Williams, 2002). However, it is important to note that analyses of each sample may have a distinct range of Th/U regardless of magmatic or metamorphic growth (Möller et al., 2001).

Similarly, Zheng et al. (2004) interpreted that there are significant differences between the igneous and metamorphic zircon populations that they studied. Heaman et al. (1990) indicated that kimberlite zircons can be distinguished by extremely low abundances of U, Th, and the HREE and relatively unfractionated REE patterns; carbonatite and nepheline syenite zircons have anomalously low Hf contents (6000-8000 ppm) with correspondingly high Zr/Hf ratios (>60); zircon grains from mafic rocks have elevated levels of Sc (>80 ppm), highly fractionated chondrite normalized REE patterns, and high Th/U ratios (>1); and zircons from mafic volcanic rocks have some of the lowest known Hf contents (4100-5200 ppm).

Moreover, Moser and Heaman (1997) indicated that in the upper crust, grains are richer in radioactive Th and U (1000s of ppm), zircon from mantle depths on the other hand is characterized by low concentrations of U (several ppm to tens of ppm). Accordingly, Belousova et al. (2002) show that low contents of U, Th and Y are characteristic for mantle (or mainly mantle) derived rocks, while higher abundances of these elements are recorded when the crustal contribution increases. Some median trace element abundances of different rock types analyzed by Belousova et al. (2002) are presented in the Table 6.1. Considering the scope of present research chemical characteristics of zircons with magmatic nature are emphasized.

During magmatic crystallization, zircon grows with a changing quota of trace elements, mainly Hf, U, Y and P, successively accreting in concentric growth zones (Benisek and Finger, 1993).

Table 6.1. Some (median) trace element contents of zircons from a range of rock types (data from Belousova et al., 2002).

ELEMENT ROCK TYPE	U (ppm)	Th (ppm)	Hf (ppm)	Y (ppm)
Kimberlite	9.8	3.6	1.31	31
Carbonatite	0.29	212	1.04	379
Syenite	88	31	0.59	148
Basalt	106	64	0.61	417
Dolerite	274	331	0.95	2334
Granitoid	764	368	1.28	2515

The incorporation of foreign elements constitutes two possible sites (a tetragonal [Si] and a triangular dodecahedral site [Zr]) for cation substitution (Speer, 1982). Substitution of trace elements dominantly involves replacement of Zr in the larger triangular dodecahedral sites (Hinton and Upton, 1991), while coupled substitution of the REEs and PO_4 into zircon structure can results in substantial enrichment in REEs (Speer, 1982).

Y^{3+} and REEs readily incorporate into zircon due to their similarity in ionic radius. However, because of their ionic charges (i.e. 3+) they do not substitute as easily as U^{4+}, Th^{4+}, or Hf^{4+} in the Zr-site in the structure. The replacement of Zr^{4+} by the REE^{3+} requires compensation of the charge difference by, for example, P^{5+}, Nb^{5+}, or Ta^{5+} (Cesbron et al., 1995).

Although the REEs share similar characteristics, small differences in ionic radii and electronic configurations can lead to pronounced differences in geochemical behavior (Cherniak et al., 1997). Hinton and Upton (1991) indicated that the REE substitution into zircon is related to the size of the REE ion. They further stated that the Zr^{4+}, which normally occupies the triangular dodecahedral site, is smaller than the Lu^{3+} ion. The substitution into the zircon lattice becomes progressively easier for the higher atomic number REEs, because the ionic radii of the REEs decrease from La^{3+} to Lu^{3+} (Hinton and Upton, 1991). Zircon preferentially incorporates the smaller ionic radius HREE into its structure, sometimes; however, igneous zircon has LREE concentrations at higher than expected levels, a feature which may be accounted for several factors including disequilibrium crystallization and/or later disturbance (Whitehouse and Kamber, 2003).

Igneous zircons are generally typified by a steep positive slope from La-Lu in REE patterns, along with pronounced positive Ce and negative Eu anomalies (Murali et al., 1983; Barbey et al., 1995; Möller et al., 2001; Whitehouse and Kamber, 2002; Zheng et al., 2004). The positive Ce anomaly may be attributed to the presence in a melt of small amounts of Ce^{4+} a strongly compatible ion in zircon; the negative Eu anomaly probably records overall depletion of a melt in Eu by plagioclase fractionation (Whitehouse and Kamber, 2003). Whitehouse and Kamber (2003) stated that differences from the typical igneous zircon REE pattern are possible sometimes because of the compositional distinction of the partial melt from the melted-protolith, particularly for small-degree partial melts.

Hoskin et al. (2000) stated that abundances ranges of Th and U are much larger in mafic zones of granitoids relative to felsic zones. They further postulated that abundances ranges of Th and U are much smaller in felsic zones of an igneous body relative to mafic zones, with maximum abundances not exceeding 350 ppm and 470 ppm, respectively, whereas in mafic zones, zircon Th and U abundances may exceed 1000 ppm, possibly due to the co-crystallization of other Th- and U-bearing phases, allanite and monazite in particular.

Hoskin et al. (2000) also indicated that plots of Y and Yb reveal an increase in the lower limit of each abundance range for zircon populations from mafic whole-rock samples, and a decrease in felsic samples. What's more Sc content is reported as high in zircons from more mafic rocks (Heaman et al., 1990). Additionally, zircon HREE abundances increase in mafic zones and decrease in felsic zones, while Ce broadly increases in abundance from mafic to felsic (Hoskin et al., 2000).

Hoskin et al. (2000) interpreting that some trace elements (e.g. P, Ca, Sc, Nb, Hf, Ta) in zircon exhibit compositional variation with progressive differentiation of magma, stated that the normalized REE patterns and abundances (except Ce) do not vary because of limitations to both xenotime and complex xenotime-type coupled substitutions. Therefore, Hoskin et al.

(2000) indicated that zircon REE characteristics are not useful as those of other REE-rich accessory minerals as a petrogenetic indicator.

On the contrary, Barbey et al. (1995) demonstrated, depending on the REE patterns, that it is possible to test the genetic relationships between the granite and neighboring gneisses and leucosomes. In addition, Scherstérn et al. (2000) showed in their studies that REE-profiles show consistent differences between detrital, magmatic, and metamorphic zircon, typically differing in Lu/La_N, Ce/Ce*, and Eu/Eu*, and igneous zircon with marked positive Ce/Ce* and negative Eu/Eu*.

Moreover, according to Belousova et al. (2002) elemental abundances and the shape and slope of chondrite-normalized trace element patterns carry features characteristics for zircons of particular origin. They indicated that inherited cores in zircons of many felsic igneous rocks carry potential information on the original source rock. Poller et al. (2001) demonstrated that the chondrite-normalized REE patterns of cogenetic zircon rims are very similar, and inherited zircon cores from a single sample, but probably originating from different protoliths, can be distinguished by their REE patterns.

Consequently, in spite of existing controversy, unique chemical properties of zircon are drawing attention of scientists interested in igneous petrology. Therefore many studies are being directed towards the investigation of chemical characteristics of zircon to get some clues about the source and petrological features of the magma.

Relationships between zircon chemistry and CL intensity also form the subject of several studies. Sommerauer (1974) stated that the intensity of CL depends mainly on the concentration of foreign atoms in the zircon crystal lattice, either as growth or sector zoning. In the same manner, Hanchar and Rudnick (1995) indicated that concentrations of elements, such as Hf, Y, P, U and HREEs, in different growth zones are in relation with the data revealed with CL. Similar attempts were made to investigate if there is a correlation between chemistry and the CL-intensity.

Vavra (1990) interpreted that sectors belonging to the {110}-prism is distinguishable from other sectors by its high CL-intensity. Sommerauer (1974) suggested that this occasion could be related with the low total foreign-element concentration in the {110}-sectors. Additionally, Vavra (1994) suggested that drop in CL-intensity together with the sharp morphological change at the late stages of zircon crystallization is related with the increased concentrations of impurity elements like U, Th, Y, P, and REEs (see Chapter 5).

Hanchar and Miller (1993) indicated that the zonation in igneous zircons from granitoid rocks revealed with CL, as sharp-bounded zones of equal luminosity, where luminosity is primarily caused by Dy^{3+}, secondarily by Sm^{3+}, Eu^{3+}, Tb^{3+}, and Y^{3+}, and suppressed by U and Th. The contrast in CL emission between oscillatory zones reflects depletion or enrichment of trace elements (e.g. U and Y) at the crystal melt interface (Rubatto and Gebauer, 2000).

Rubatto and Gebauer (2000) determined that the brighter fluorescing domains are relatively poorer in U and Y than in the weaker fluorescing, i.e. dark, domains. In other words, CL emission in zircons is inversely correlated to their contents of U and Y (Rubatto and Gebauer, 2000). Miller and Wooden (2004) also explained the brightness contrasts in zircons as a function of U-content, i.e. high U-zones are corresponded to dark zones of crystals. Moreover, Hanchar and Miller (1993) and Williams et al. (1996) interpreted the dark luminescence area as having high U and Hf concentrations.

According to Poller et al. (2001) variations in CL-intensity show no direct correlation with the REEs, Y, or Th contents. Instead, they suggested that U (and possibly Hf) and related radiation may suppress the CL-intensity.

It should be kept in mind that the differences in interpretations might result from the physical and chemical characteristics of individual zircon samples. For instance, Koschek (1993) and Poller et al. (2001) suggested that discrepancies in CL spectra might originate from different intrinsic CL-centers, like lattice vacancies. Additionally, Poller et al. (2001) proposed that accumulated radiation damage from α-recoil, which disrupts the long-range crystallographic order, might contribute to a suppression of the CL signal.

However, based on above-mentioned electron and ion microprobe studies, it is plausible to conclude that the CL-intensity is negatively correlated with the concentrations of U and Hf (that acts similar to U). On the other hand, effect of other elements, such as Y, Th, and REEs remains controversial.

6.2. Methods of Zircon Chemistry Study

6.2.1. Sample Preparation for Zircon Chemistry

Thin-sections used in SEM and CL studies were used also for EMP analyses. Coating of well-polished sections with a 20 nm layer of carbon was performed in the Slide Preparation Laboratory of GFZ-Potsdam.

Fourteen zircon crystals were selected for EMP analyses from 7 granitoid samples in the scope of this study. Lines were drawn on the CL-photographs prior to analyses. Care was taken while drawing these lines to cut all the zones and important structures from center to rim. Point analyses were performed along these lines with equal distances (10 µ for crystals [Z4(7)], [Z8(20)], and [Z8(21)], 5 µ for others).

6.2.2. Analytical Methods

Major, minor and trace element compositions of the zircon crystals of the concerned granitoids were determined by using non-destructive in-situ microanalysis method, electron microprobe (EMP). The analyses on zircon crystals were performed for ca. 400 points using a fully automated CAMECA SX-50 electron microprobe, in the EMP Laboratory of GFZ-Potsdam.

The instrument operates in 4 wavelength-dispersion modes with 3 two-crystals spectrometers (LiF-PET, LiF-PET, TAP-PC3) and one 4-crystal spectrometer (PET-TAP-PC1-PC2). Instrument was accelerated to 20 kV electron-beam at 40 nA beam current with a spot (applied beam) size of 1 µm. PC1 Spectrometer was used for F, LiF was used for Hf, Fe, Ce, Nd, Sm, Gd, Dy, Yb and Ta, PET was used for Ti, Ca, P, Sc, Th, U, Pb, Nd, and TAP was used for Si, Zr, Al and Y analyses.

A variety of natural and synthetic standards were used for calibration. The following elements of silicates, oxides and sulphides have been analyzed using the standards: LiF for F; HfO_2 for Hf; Fe_2O_3 for Fe; $CePO_4$ for Ce and P; $NdPO_4$ for Nd; $SmPO_4$ for Sm; $GdPO_4$ for Gd; $DyPO_4$ for Dy; $YbPO_4$ for Yb; Ta for Ta; $MnTiO_3$ for Ti; wollaston for Ca; $ScPO_4$ for Sc; Th for Th; U for U; vanad for Pb; Nb for Nb; zircnau for Si and Zr; Al_2O_3 for Al and YPO_4 for Y. Matrix corrections were performed by the PAP/PhiRhoZ procedure in the CAMECA software.

In the scope of EMP analyses, SiO_2, ZrO_2, HfO_2, FeO, F, Al_2O_3, TiO_2, Y_2O_3, CaO, P_2O_5, Sc_2O_3, ThO_2, U_2O_3, PbO, Ce_2O_3, Nd_2O_3, Sm_2O_3, Gd_2O_3, Dy_2O_3, Yb_2O_3, Nb_2O_3, Ta_2O_5 were analyzed and results were obtained in terms of percentage. Results of analyses that are in oxide percentages were converted to elemental values in terms of ppm to provide better evaluation and comparison.

6.3. Investigation of Chemical Characteristics of the Zircon Crystals from the Central Anatolian Granitoids

General chemical properties and internal chemical variations of the zircon crystals from the CAG were investigated by using the EMP analyses. Four granitoid samples from the Ekecikdağ Pluton and three granitoid samples from Ağaçören Pluton were chosen for EMP study. Two zircon crystals were selected from each of seven granitoid samples for chemical analyses.

Results of EMP analysis and the elemental ratios of these zircon crystals are presented in Appendix B (Table B.1). In this table, elements with abundances below detection limits appear to have zero values, while ratios going infinity (since the divisor is zero) are left as blank. Moreover, it should be noted that it was relevant to overlook some of the corrosion zones since EMP analyses were performed point to point with some distances between them.

It is also important to note that inclusions or traces of inclusions within zircon are the sites of distinct chemical contents than the crystal. Depending on the type of the inclusion mineral different elements may show pronounced concentrations at the point of analysis. Likewise, other local or analytical effects may come across at the analyses. Therefore, chemical patterns are evaluated with the help of CL-images.

6.3.1. Ekecikdağ Pluton

6.3.1.1. Borucu Granodiorite-Monzogranite

Two zircon crystals ([Z1(19)] and [Z1(23)]) from the Borucu granitoid were analyzed chemically and results of chemical analyses are presented in Appendix B (Table B.1). As a summary of the Appendix B (Table B.1) some elemental median values and ranges are found in Table 6.2.

[Z1(19)] is characterized by median values of 64.62% (±15.09) ZrO_2, 32.29% (±7.27) SiO_2 and 1.47% (±0.39) HfO_2 (Table 6.2). Th and U values change between 0-606 ppm and 0-2980 ppm, respectively. Th/U ratio varies between 0-4.16. It should be noted that both U loss and Th enrichment would result in an increased Th/U ratio, while complete loss of Th would cause zero values.

Table 6.2. Median values and ranges for selected elements from zircon crystals of the CAG (B: Borucu; K: Kalebalta; H: Hisarkaya; S: Sinandı; N: Namlıkışla; Y: Yenişabanlı; Ç: Çimkalesi granitoids)

CRYSTAL		**ZrO_2 (%)**	**SiO_2 (%)**	**HfO_2 (%)**	**Th (ppm)**	**U (ppm)**	**Th/U**
[Z1(19)]	**B**	64.92±15.09	32.29±7.27	1.47±0.39	0-606	0-2980	0-4.16
[Z1(23)]	**B**	65.23±0.63	32.53±0.38	1.60±0.16	70-2197	999-8703	0.04-0.46
[Z3(16)]	**K**	65.84±8.30	32.51±2.49	1.56±0.25	0-6512	0-7758	0-11.53
[Z3(18)]	**K**	65.81±1.09	32.51±0.35	1.32±0.22	0-9298	191-9665	0-2.12
[Z4(1)]	**H**	65.86±0.99	31.88±0.65	1.42±0.19	0-2250	0-7858	0-9.51
[Z4(7)]	**H**	66.03±5.84	32.31±0.72	1.55±0.35	79-1397	518-10065	0.07-1.25
[Z6(17)]	**S**	63.83±6.99	30.66±2.30	1.51±0.20	0-1520	0-3988	0-0.95
[Z6(19]	**S**	65.08±0.50	31.52±0.17	1.59±0.15	0-1037	0-2925	0.06-4.51
[Z8(20)]	**N**	65.09±0.39	31.97±0.18	1.65±0.16	0-325	0-2262	0-3.29
[Z8(21)]	**N**	65.58±0.40	32.01±0.11	1.37±0.22	0-483	0-1790	0-15.96
[Z9(1)]	**Y**	65.92±0.69	32.50±0.57	1.53±0.27	0-2136	127-10174	0-1.45
[Z9(11)]	**Y**	65.52±0.35	32.33±0.12	1.51±0.26	0-1986	899-6958	0-0.62
[Z12(21)]	**Ç**	65.64±8.18	32.81±5.37	1.45±0.23	88-4262	454-5968	0.04-0.89
[Z21(22)]	**Ç**	65.70±0.27	32.26±0.23	1.41±0.12	0-2188	0-3225	0-1.21

Chondrite-normalized (values from Taylor and McLennan, 1985) trace element patterns of the zircon crystal [Z1(19)] are represented by enrichment in most of the elements, except for Fe, Ti and P (Figure 6.1). Belousova et al. (2002) conducted chemical analyses on 154 granitic zircons from the New England Batholith and the Lachlan Fold Belt, Australia, and from the Crimea Mountains, Ukraine. Considering the largeness of this database, averaged values of the data of Belousova et al. (2002) are used for comparison and also plotted on the same diagram (Figure 6.1).

[Z1(19)] shows depletion in Y, Fe and Ti, and enrichment in Ta, with respect to the data of Belousova et al. (2002). On the other hand, highest values of Th, U and Hf abundances of [Z1(19)] fit with the averaged granitoid values of Belousova et al. (2002). It should be considered that within the zircon crystal [Z1(19)] Nb values are zero or below detection limit. Contents below detection limit are the case for some other elements in the following chondrite-normalized spider-diagrams and chemical variation diagrams.

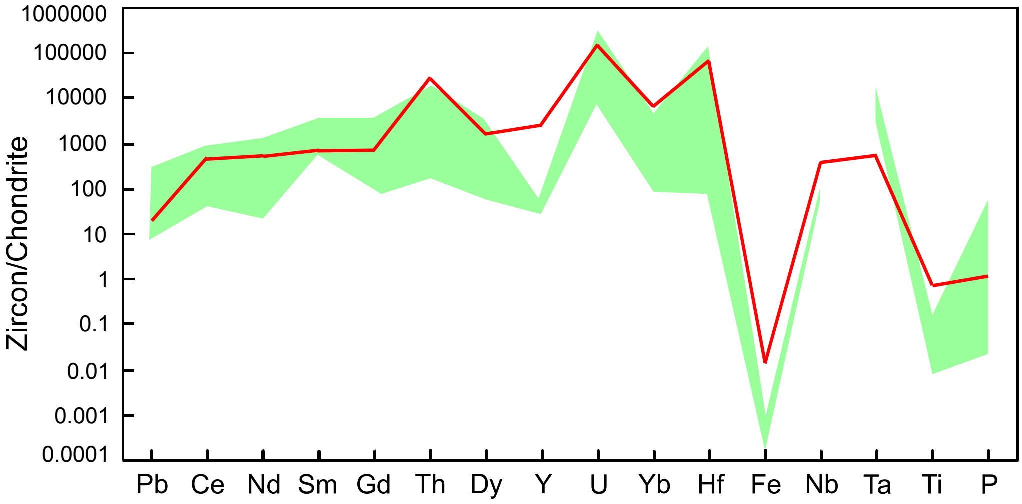

Figure 6.1. Chondrite-normalized trace element abundances of the zircon crystal [Z1(19)] from the Borucu granodiorite-monzogranite (sample SK-1) (shaded area) and the averaged values of zircons from granitoids (solid line) (average of 154 samples; data from Belousova et al., 2002). Chondrite values are from Taylor and McLennan (1985). Zero values are not plotted.

The elemental profiles drawn for the crystal [Z1(19)] are presented in the Figure 6.2. Chemical analyses of Zr, Si, U, Hf, Th, Y, Pb, Ta, Sc, Ti, Ce, Nd, Sm, Gd, Dy, Yb, Fe, Ca, Al elements are performed along the line A-B (Figure 6.2) with 5 µ intervals. Moreover, Th/U, U/Pb, Th/Yb, Ta/Yb ratios and available REE (Ce+Nd+Sm+Gd+Dy+Yb)+Y values along the same line are plotted in the Figure 6.2.

The zircon crystal [Z1(19)] can be characterized by its steady trend interrupted by two drastic decrease at the points 15 and 20 within the Zr and Si profiles. Both points correspond to low CL intensity, which is assumed to accompany with the Zr undersaturation (Chapter 5). Point 20 is at the rim of the crystal (Figure 6.2). The rim contains high abundances of Fe, Ca and Al elements, but very low contents of Hf, U, Th, Ta, Ti, Pb and REEs (some of which were completely lost) beside Zr and Si. The behavior of these elements at the rim can be explained by secondary events covering elemental escape as discussed in Chapter 5.

Point 15 is on the other hand at one of the corrosion zones, which was suggested based on CL image. At this point REE+Y content reaches its maximum value, while Hf decreases (Figure 6.2). Furthermore, this zone is astonishing with its very low Th/U ratio (0.015), under the lower limit for the igneous zircons (0.1), and plausibly represents the most important corrosion zone within the crystal.

The other remarkable analyses points are 5, 8 and 11 within the crystal. Point 5 placed within the core corresponds to slight decrease in Zr, Si, slight increase in REE+Y, but sharp increase in Sc and Ti. Point 8, on the other hand, is at the zone around core, and characterized by high Th/U ratio, whereas point 11 exhibits low Th/U ratio (0.016).

The compositions of the zircon crystal [Z1(23)] are: 65.23% (median value with standard deviation of ±0.63) ZrO_2, 32.53% (median value with standard deviation of ±0.38) SiO_2 and 1.60% (median value with standard deviation of ±0.16) HfO_2. Th/U ratio is between 0.04 and 0.46, while Th varies between 70-2197 ppm, and U varies between 999-8703 ppm (Table 6.2).

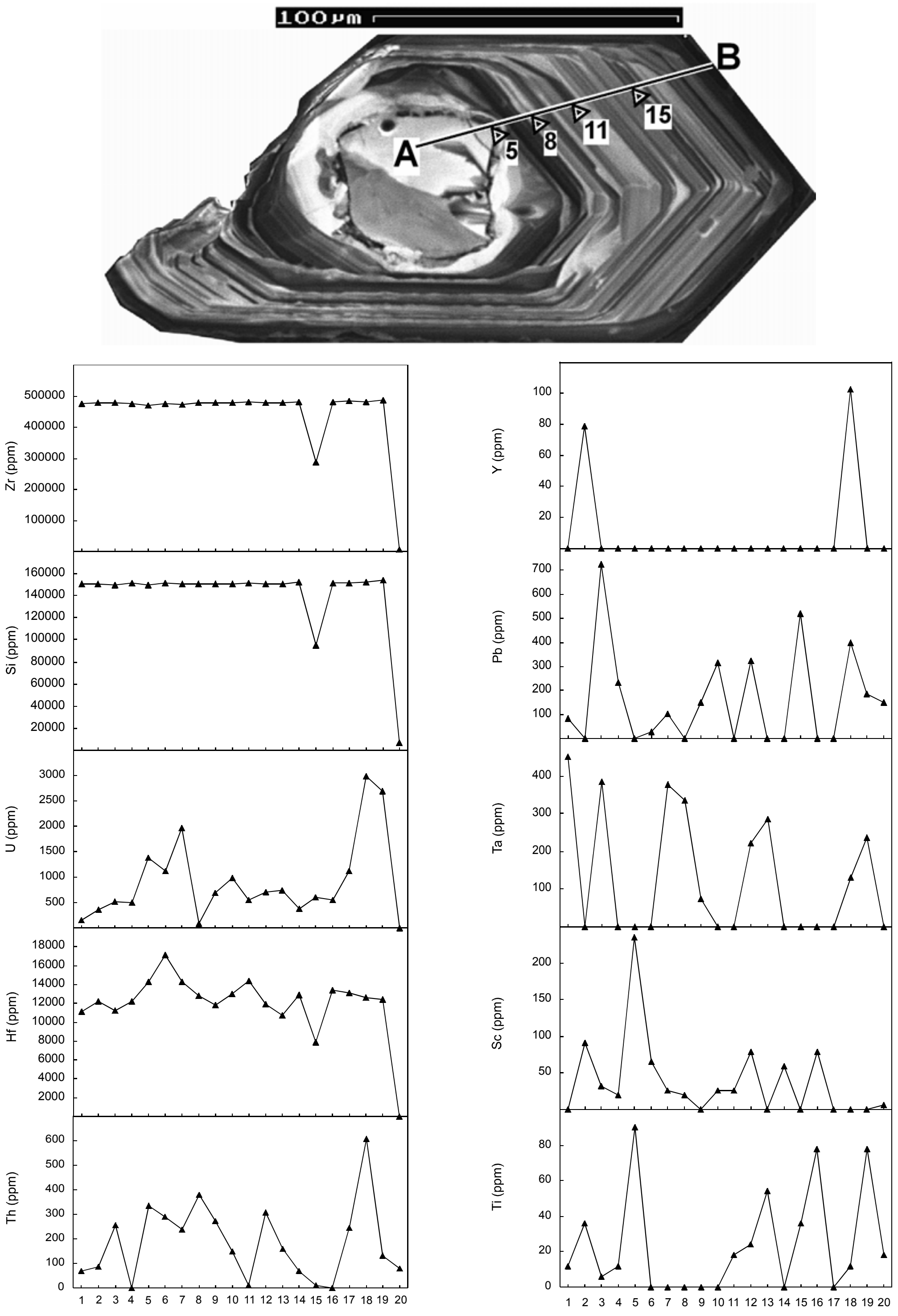

Figure 6.2. Chemical variations within the zircon crystal [Z1(19)] from the Borucu granodiorite-monzogranite (sample SK-1): Numbers on the x-axis of the diagrams denote analyzed points with equal distances along the line from A to B (in the photograph).

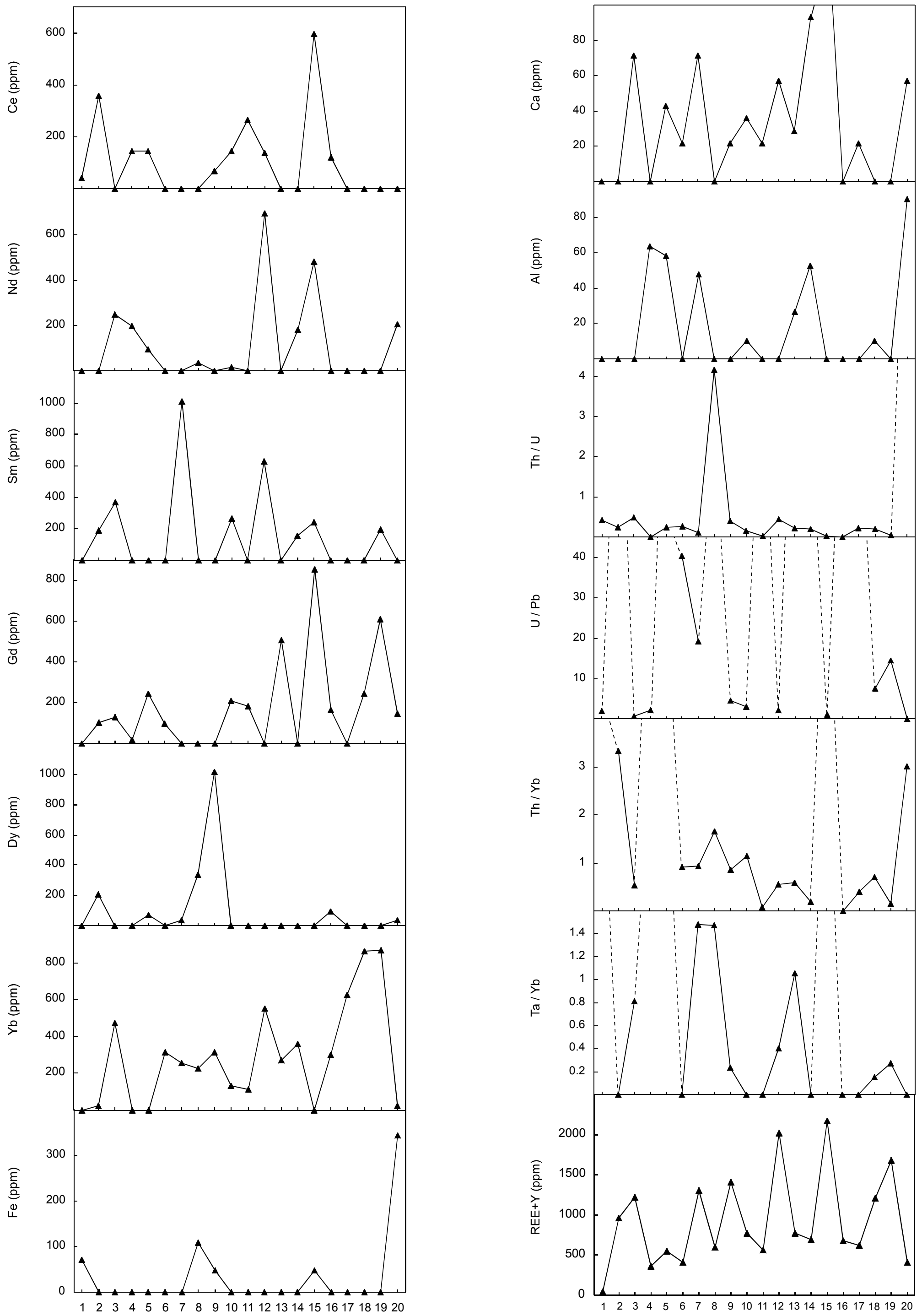

Figure 6.2 (cont’d).

Chondrite-normalized trace element patterns of the zircon crystal [Z1(23)] are characterized by depletion in Y, Fe and Ti, and enrichment Ta with respect to that of averaged granitic zircons of Belousova et al. (2002) (Figure 6.3). [Z1(23)] has similar patterns but respectively restricted ranges in comparison with those of the crystal [Z1(19)]. Th and U values are remarkably higher within [Z1(23)] than those of [Z1(19)].

Chemical variations within the crystal [Z1(23)] are shown in the Figure 6.4. The crystal is analyzed from core to rim along the line A-B. Within the core Zr abundance is around 483000 ppm, Si is around 152000 ppm, U is around 1100 ppm, Th is around 250 ppm, Hf is around 13750 ppm, and Th/U ratio is around 0.2. Tracing to the rim there are significant changes and variations not only in these elements, but also in other elements like REEs.

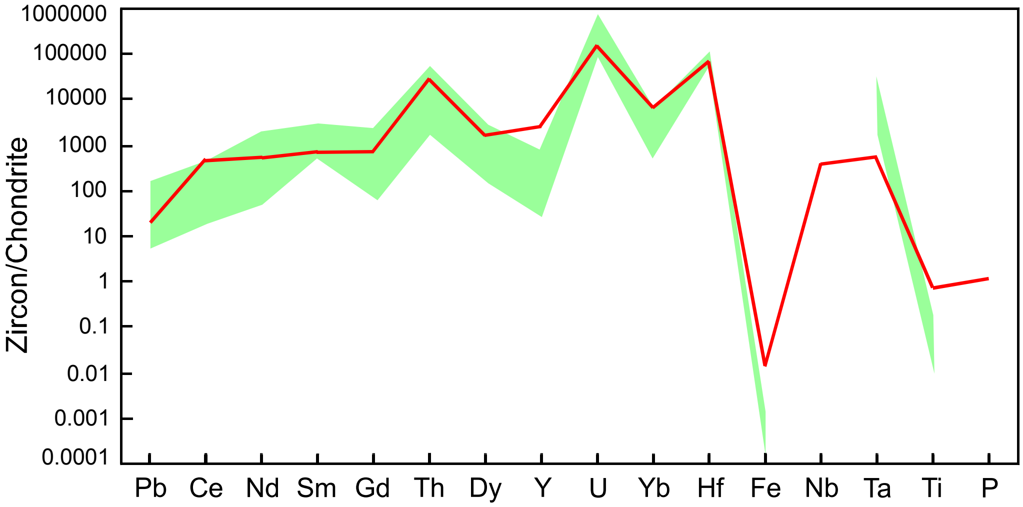

Figure 6.3. Chondrite-normalized trace element abundances of the zircon crystal [Z1(23)] from the Borucu granodiorite-monzogranite (sample SK-1) (shaded area) and the averaged values of zircons from granitoids (solid line) (average of 154 samples; data from Belousova et al., 2002). Chondrite values are from Taylor and McLennan (1985). Zero values are not plotted.

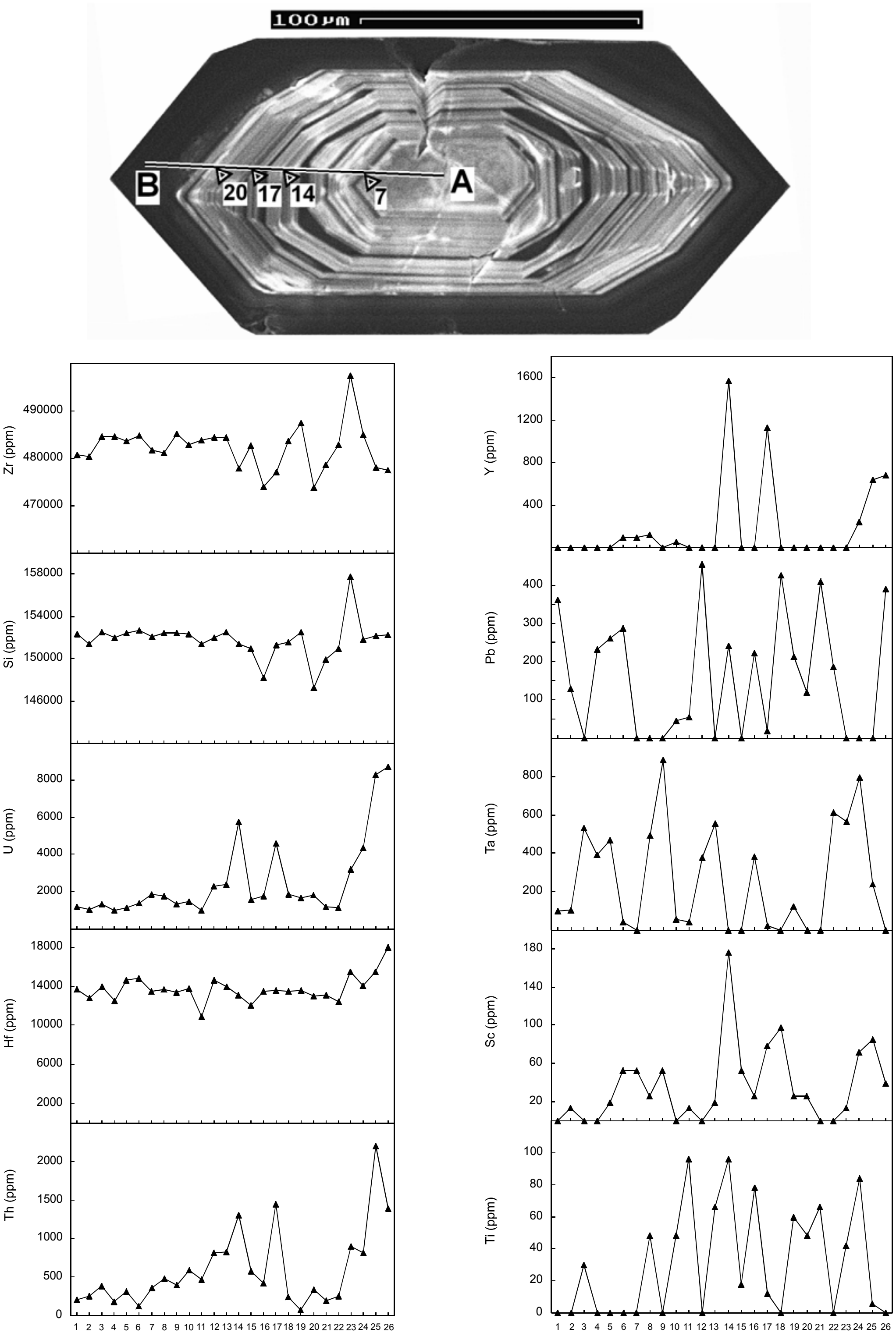

Figure 6.4. Chemical variations within the zircon crystal [Z1(23)] from the Borucu granodiorite-monzogranite (sample SK-1): Numbers on the x-axis of the diagrams denote analyzed points along the line from A to B (in the photograph) with an equal distance.

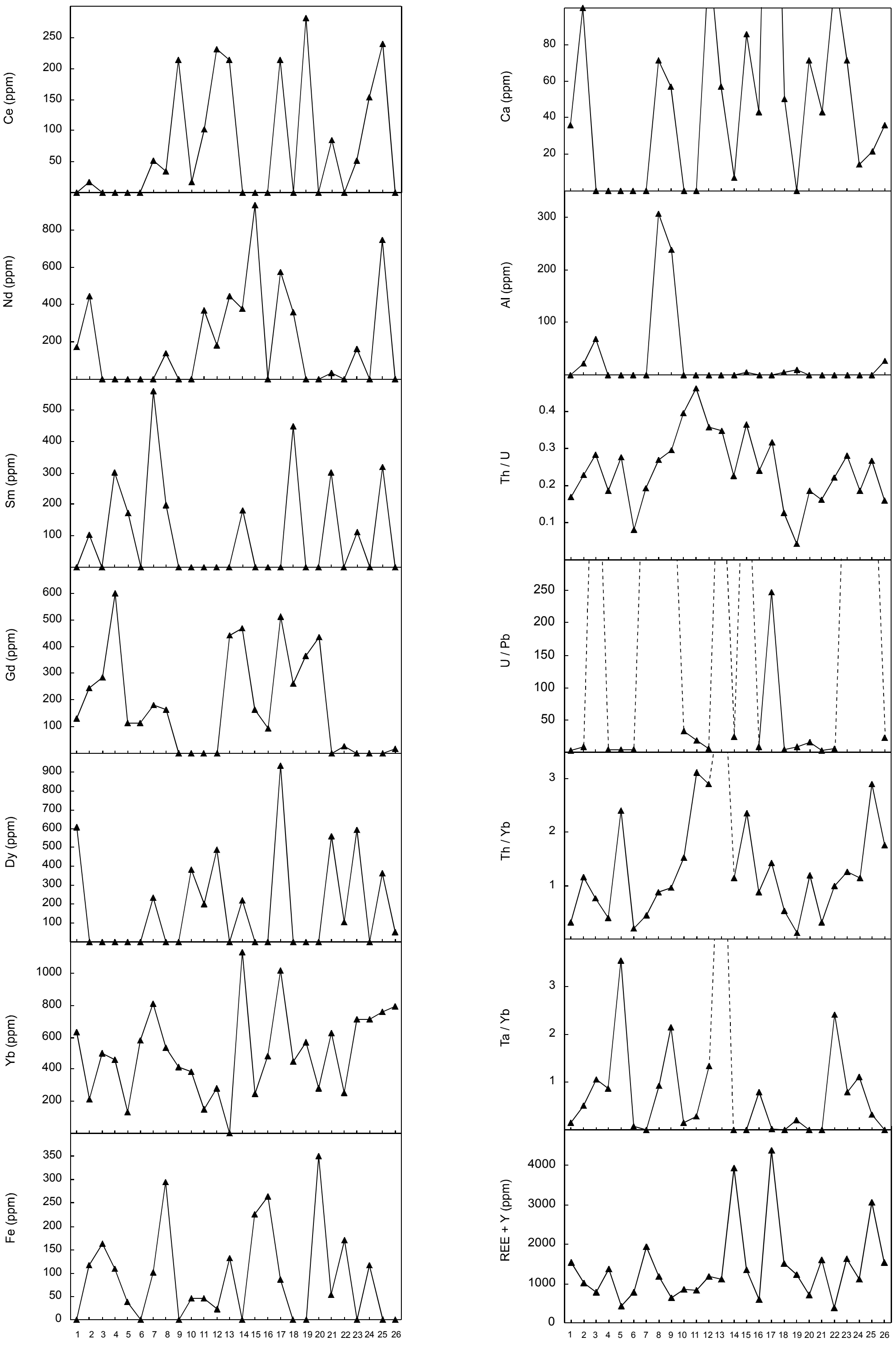

Figure 6.4 (cont'd).

The remarkable changes should be related to the chemical variations in the magma chamber. Accordingly, the sharp changes in elemental abundances correspond to compositional changes determined by CL imaging. In that manner point 7, which is at the dark zone overgrowing the core, exhibits decrease in Zr, Si, but increase in U, Th and REE+Y.

Point 14 is at a narrow corrosion zone revealed from CL image. Sharp increase in U, Th, Sc, Ti and REE+Y is accompanied by decrease in Zr, Si and Th/U. Point 17 is at a wider corrosion zone easily distinguishable in the CL image. Increased values of Th and Ca are observable at this point. Moreover, loss of Pb together with enrichment of U causes increase of U/Pb ratio. Additionally, REE+Y reaches its maximum value at this point. Y shows two notable peaks along the line A-B at points 14 and 17. At the outer zones U increases and suppresses the CL intensity. REE+Y value illustrates oscillation, and Th/U ratio shows slight variations around 0.2 at the outer zones, except for value of 0.042 at point 19, while Zr, Hf and Si demonstrate pronounced increase at point 20 (Figure 6.4).

6.3.1.2. Kalebalta Leucogranite

Complicated outer and internal features of the zircons from the Kalebalta leucogranite discussed in the previous chapters are investigated chemically. In this scope zircon crystals [Z3(16)] and [Z3(18)] were analyzed by EMP.

The chemical data for [Z3(16)] infers that the crystal has median values of 65.84% (±8.30) ZrO_2, 32.51% (±2.49) SiO_2 and 1.56% (±0.25) HfO_2 (Table 6.2). Th/U ratio is 0-11.53, while Th and U values varies between 0-6512 ppm and 0-7758 ppm, respectively.

Chondrite-normalized spider-diagram of the zircon crystal [Z3(16)] is given in the Figure 6.5. Trace elements of this crystal have abundances similar to that of averaged granitic zircons (Belousova et al., 2002), except for slight depletion in Ti.

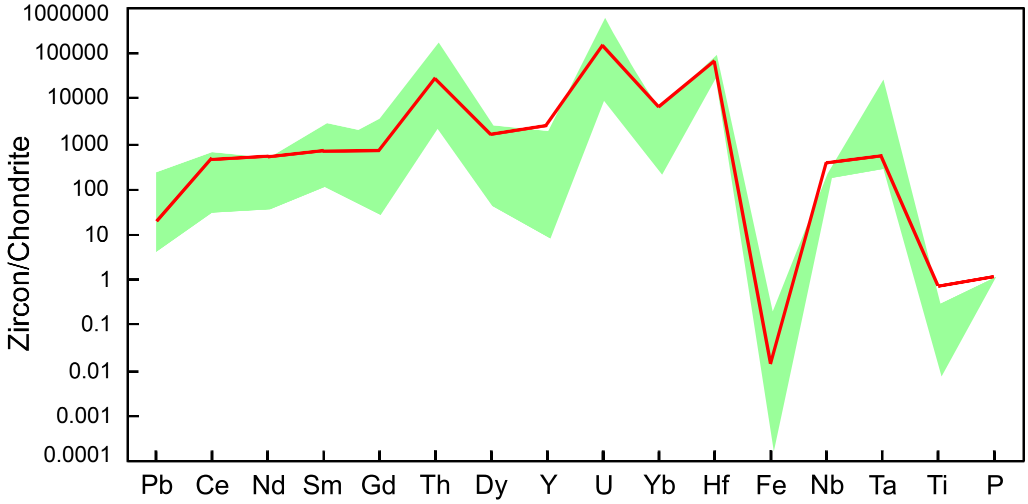

Figure 6.5. Chondrite-normalized trace element abundances of the zircon crystal [Z3(16)] from the Kalebalta leucogranite (sample SK-3) (shaded area) and the averaged values of zircons from granitoids (solid line) (average of 154 samples; data from Belousova et al., 2002). Chondrite values are from Taylor and McLennan (1985). Zero values are not plotted.

Figure 6.6 demonstrates the chemical variations within the zircon crystal [Z3(16)]. Point B represents the eleventh point on the profile along A-C. The crystal has complex inner structures as discussed in Chapter 5. In the Zr profile four sharp drops (points 3, 10, 14 and 22) interrupt the uniform trend. These drops are plausibly related with distinct chemical changes during the evolution history.

The core formed by igneous clustering (Chapter 5) has generally low CL intensity at the inner part. At point 3, Zr and Hf sharply decrease; Ti and Si remarkably increase while Ca and Al reach to anomalous levels. Brightly luminescent zone surrounds this inner part. Point 10 is located in this zone and characterized with decrease in Zr and Hf, and increase in Th, Fe and REEs, especially Dy and Sm. This bright zone is overgrown by relatively dark, i.e. grayish, CL-zone that includes point 14. At this point decrease in Zr and Hf is accompanied by increase in Th, Fe and REEs (Figure 6.6).

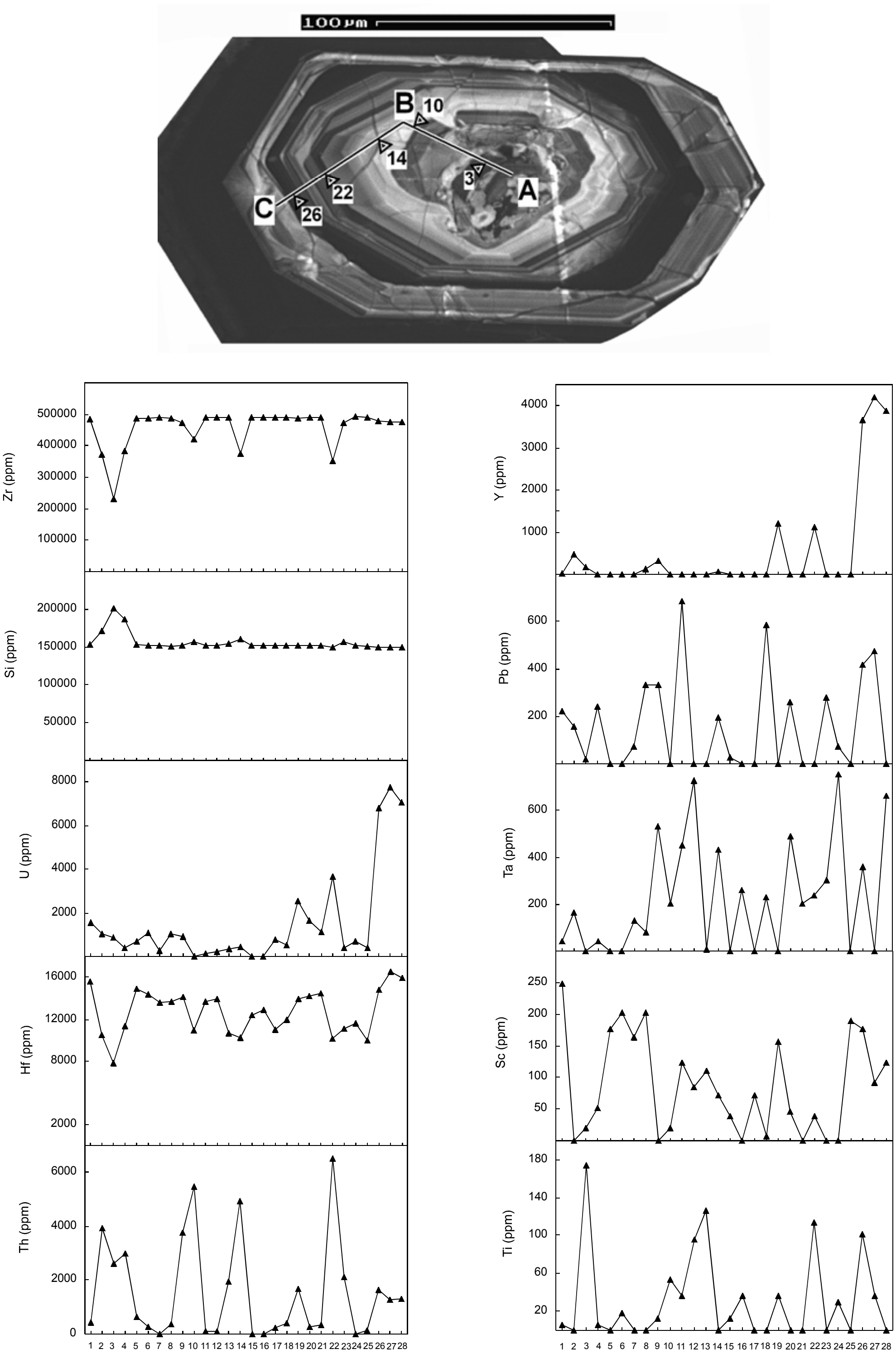

Figure 6.6. Chemical variations within the zircon crystal [Z3(16)] from the Kalebalta leucogranite (sample SK-3): Numbers on the x-axis of the diagrams denote analyzed points along the line from A to C (in the photograph) with an equal distance.

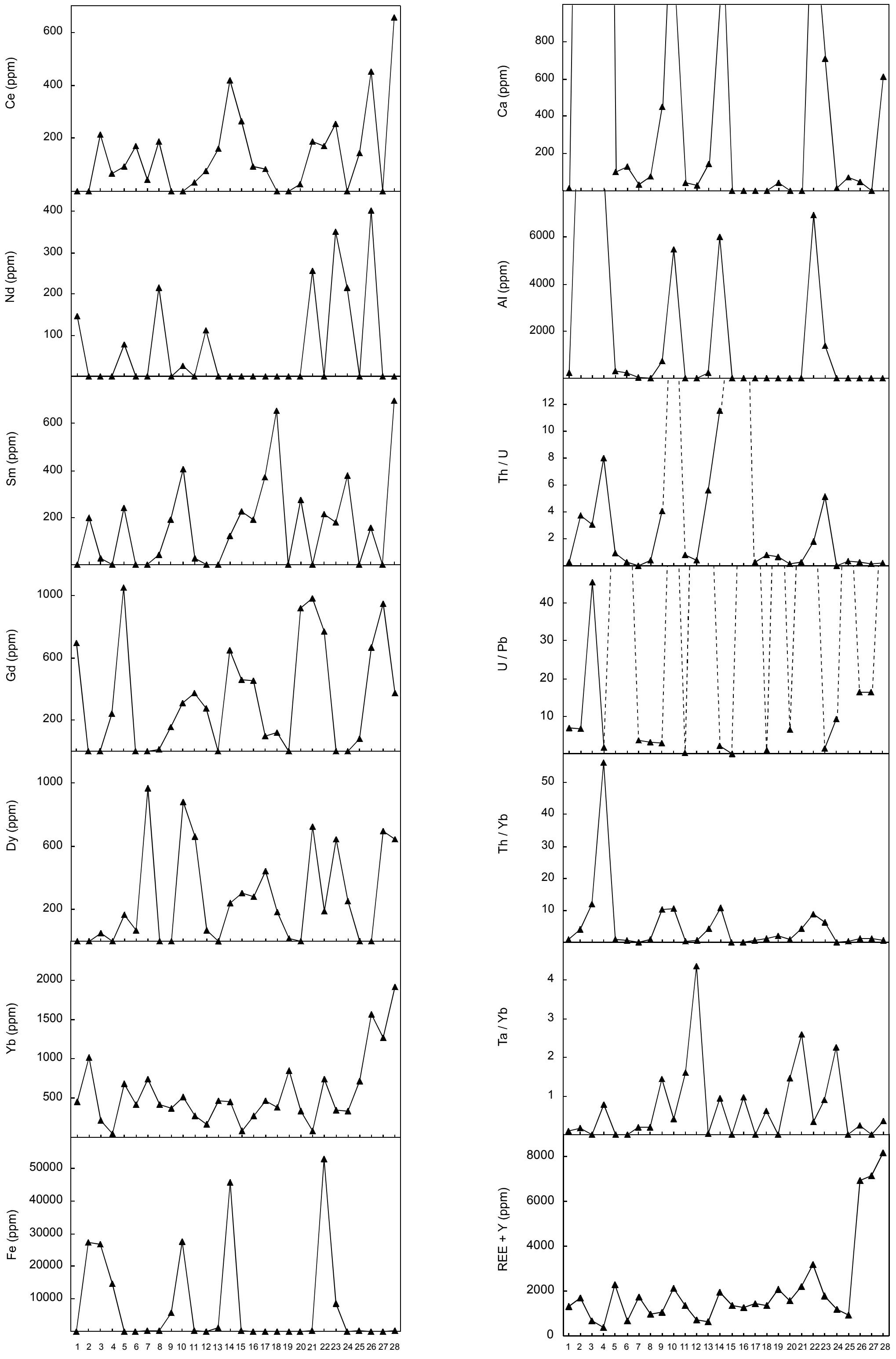

Figure 6.6 (cont'd).

Subsequently, there are two major drastic chemical changes corresponding to points 22 and 26, affect the crystal [Z3(16)]. Both of the points 22 and 26 fall upon the corrosion stages determined by the CL study in Chapter 5. Drop in Zr is notable especially at point 22. U, Y, Ti and REEs show considerable enrichments at points 22 and 26. At the outermost point of A-C profile Zr, Si and Hf elements show similar abundances as those in the core; on the other hand abundances of REE+Y and U are at the significantly higher levels.

The elemental compositions of the zircon crystal [Z3(18)] are: 65.81% (median value with standard deviation of ±1.09) ZrO_2, 32.51% (median value with standard deviation of ±0.35) SiO_2 and 1.32% (median value with standard deviation of ±0.22) HfO_2. [Z3(16)] is characterized by 0-2.12 Th/U ratio, and 0-9298 ppm Th and 191-9665 ppm U abundances (Table 6.2).

Chondrite-normalized trace element patterns of the zircon crystal [Z3(18)] are represented by lower Fe, and higher Nb and Ta abundances with respect to the crystal [Z3(16)] (Figure 6.7). [Z3(18)] shows depletion in Fe, and enrichment in Nb and Ta in comparison with the average chemical values of Belousova et al. (2002).

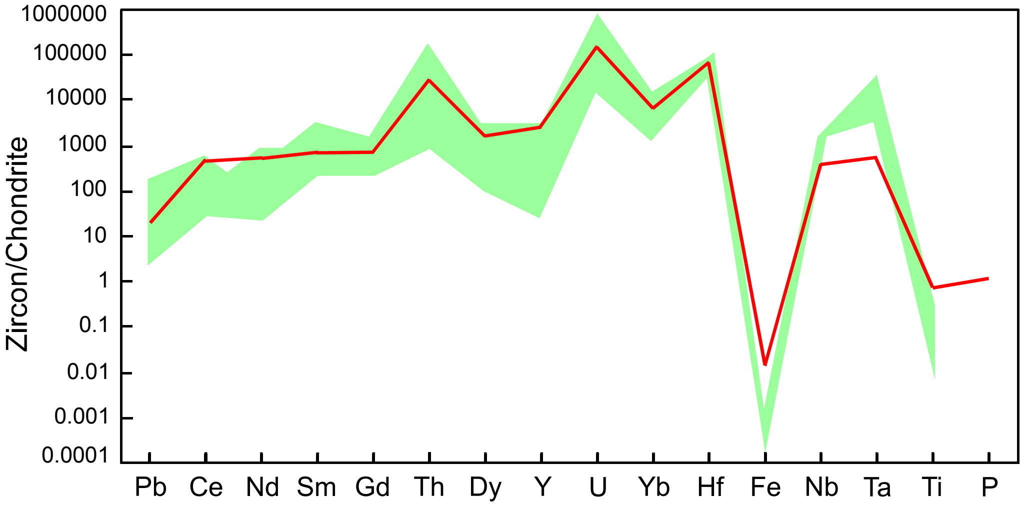

Figure 6.7. Chondrite-normalized trace element abundances of the zircon crystal [Z3(18)] from the Kalebalta leucogranite (sample SK-3) (shaded area) and the averaged values of zircons from granitoids (solid line) (average of 154 samples; data from Belousova et al., 2002). Chondrite values are from Taylor and McLennan (1985). Zero values are not plotted.

In general, trace element patterns of zircons of the Kalebalta granitoid exhibit similarities to those of Borucu granitoid, i.e. peaks at Th, U, Hf and Ta, and low values at Y, Yb, Fe and Ti, but show higher abundances of Th, Y, Nb and Fe, and lower abundances of Nd.

The elemental profiles drawn for the crystal [Z3(18)] are presented in the Figure 6.8. The small core has about 480000 ppm Zr, 150000 ppm Si, 11500 ppm Hf, and 3000 ppm U and Th. At point 4, Zr, Hf and Si decreased, whilst U, Th, Th/Yb increased. The core and surrounding near zones are seemed to have broken and corroded, and the main corrosion zone is noticeable by dark CL intensity on the CL image. Point 9 is at this corrosion zone, and reflects sharp drop in Zr and Si, but increase in U, Hf, Th, Y, Pb, Ta, Sc, Ti, Fe, Ca, Al and REEs. REE+Y abundance is of the highest value at this point. In the Zr diagram at point 14, within the oscillatory zonation overgrowing the corrosion zone, Zr and Si decreased, whereas Ca, Ce, Sm abundances and Th/U ratio show increased. Points 16 and 19 fall on the wide zones of low CL-intensity, and have low abundances of Zr, Si and Hf, and high abundances of Th and REE+Y. Point 16 characterizes subsequent corrosion stage, whereas Point 19 is at the thickened trace element band (Chapter 5).

6.3.1.3. Hisarkaya Porphyritic Granite

The chemical characteristics of the zircons from the Hisarkaya granitoid can be summed up in the following manner:

The zircon crystal [Z4(1)] is characterized by median values of 65.86% (±0.99) ZrO_2, 31.88% (±0.65) SiO_2 and 1.42% (±0.19) HfO_2 (Table 6.2). Within the crystal Th/U is 0-9.51, Th is 0-2250 ppm, and U is 0-7858 ppm.

Chondrite-normalized trace element patterns of the zircon crystal [Z4(1)] are marked by depletion in Y, Fe and Ti, and enrichment Ta with respect to that of averaged granitic zircons (Belousova et al., 2002) (Figure 6.9).

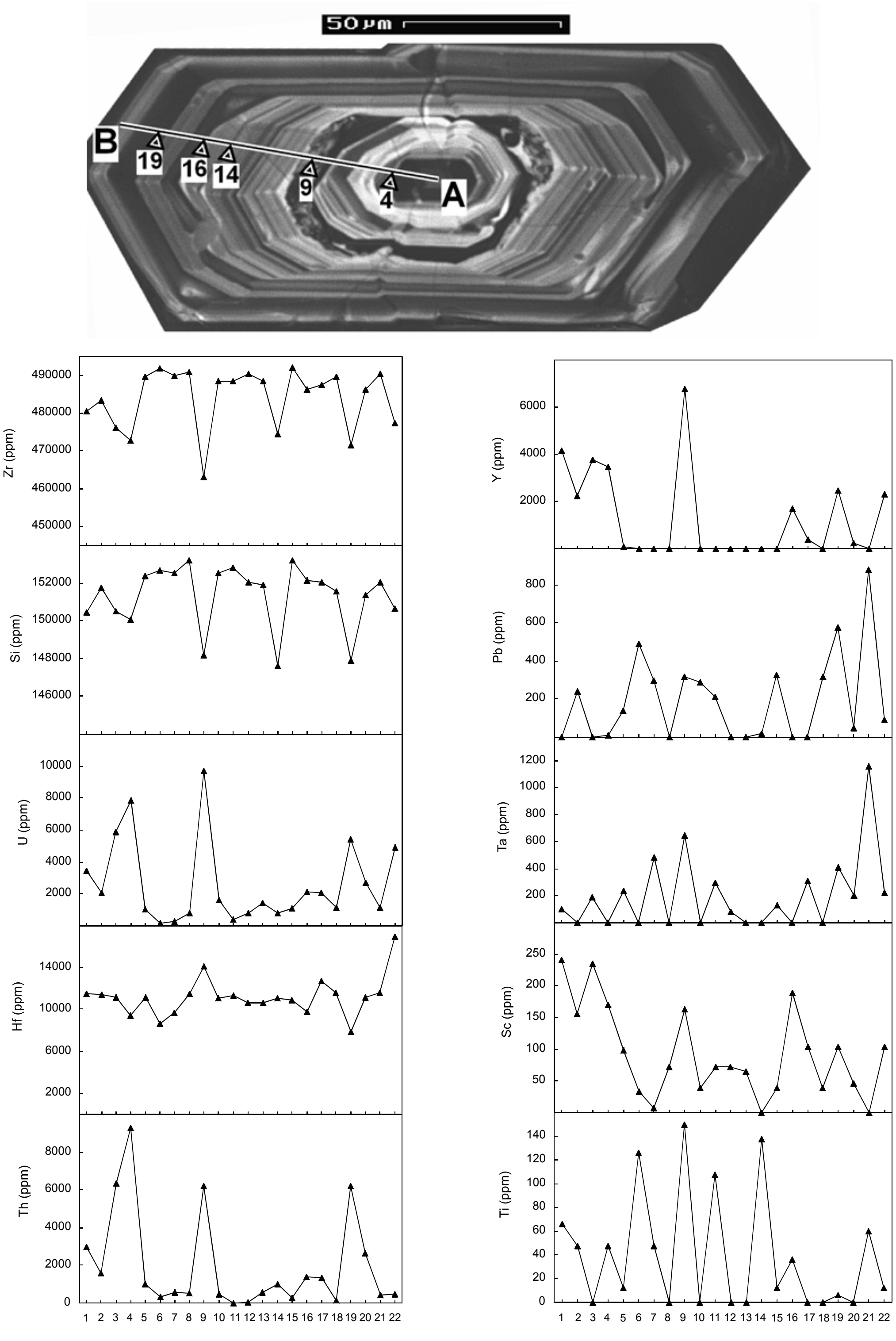

Figure 6.8. Chemical variations within the zircon crystal [Z3(18)] from the Kalebalta leucogranite (sample SK-3): Numbers on the x-axis of the diagrams denote analyzed points along the line from A to B (in the photograph) with an equal distance.

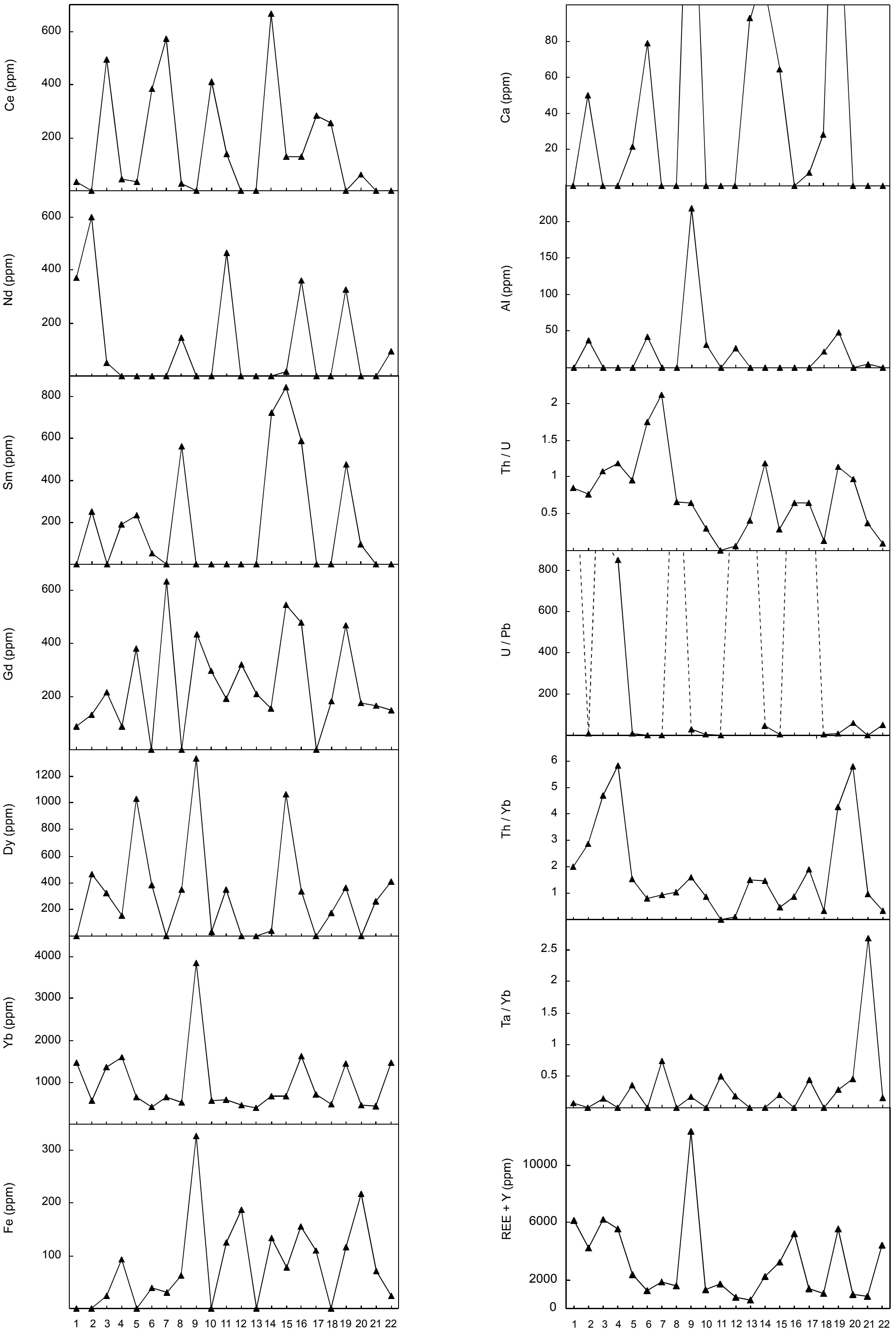

Figure 6.8. (cont’d)

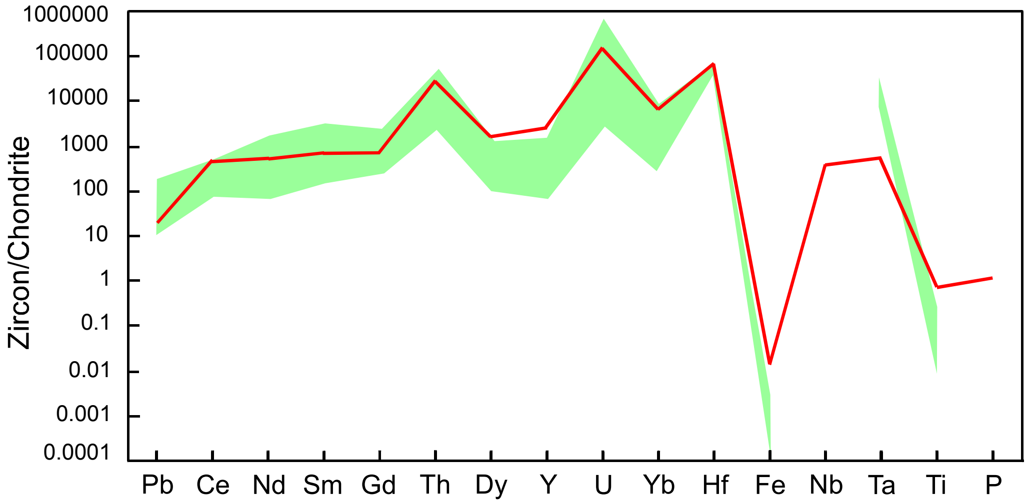

Figure 6.9. Chondrite-normalized trace element abundances of the zircon crystal [Z4(1)] from the Hisarkaya porphyritic granite (sample SK-4) (shaded area) and the averaged values of zircons from granitoids (solid line) (average of 154 samples; data from Belousova et al., 2002). Chondrite values are from Taylor and McLennan (1985). Zero values are not plotted.

Chemical variations within the crystal [Z4(1)] are shown in the Figures 6.10 and 6.11. A-B line cuts from core to surrounding brightly luminescent zones, while C-D line continues from the high CL-intensity zone to rim. The inherent core has low and high intensity areas, first of which is characterized by decreased Zr and Si, but increased REE+Y, U, Sc and Pb values relatively to the second one (Figure 6.10). Subsequent zones along A-B line show almost uniform appearance with some oscillations. Alternatively C-D line cuts the zone of corrosion stage at point 9 (Figure 6.11), defined based on the CL-image (Chapter 5), in which Zr and Si abundances are lowered and U, Sc and REE+Y values are elevated. Point D at the rim exhibits Zr undersaturation and REE enrichment at the latest stage of the crystallization (Figure 6.11).

The chemical data for [Z4(7)] demonstrates that the crystal has median values of 66.03% (±5.84) ZrO_2, 32.31% (±0.72) SiO_2 and 1.55% (±0.35) HfO_2 (Table 6.2). [Z4(7)] is represented by Th/U ratio between 0.07 and 1.25, Th values between 79 and 1397 ppm, and U values between 518 and 10065 ppm.

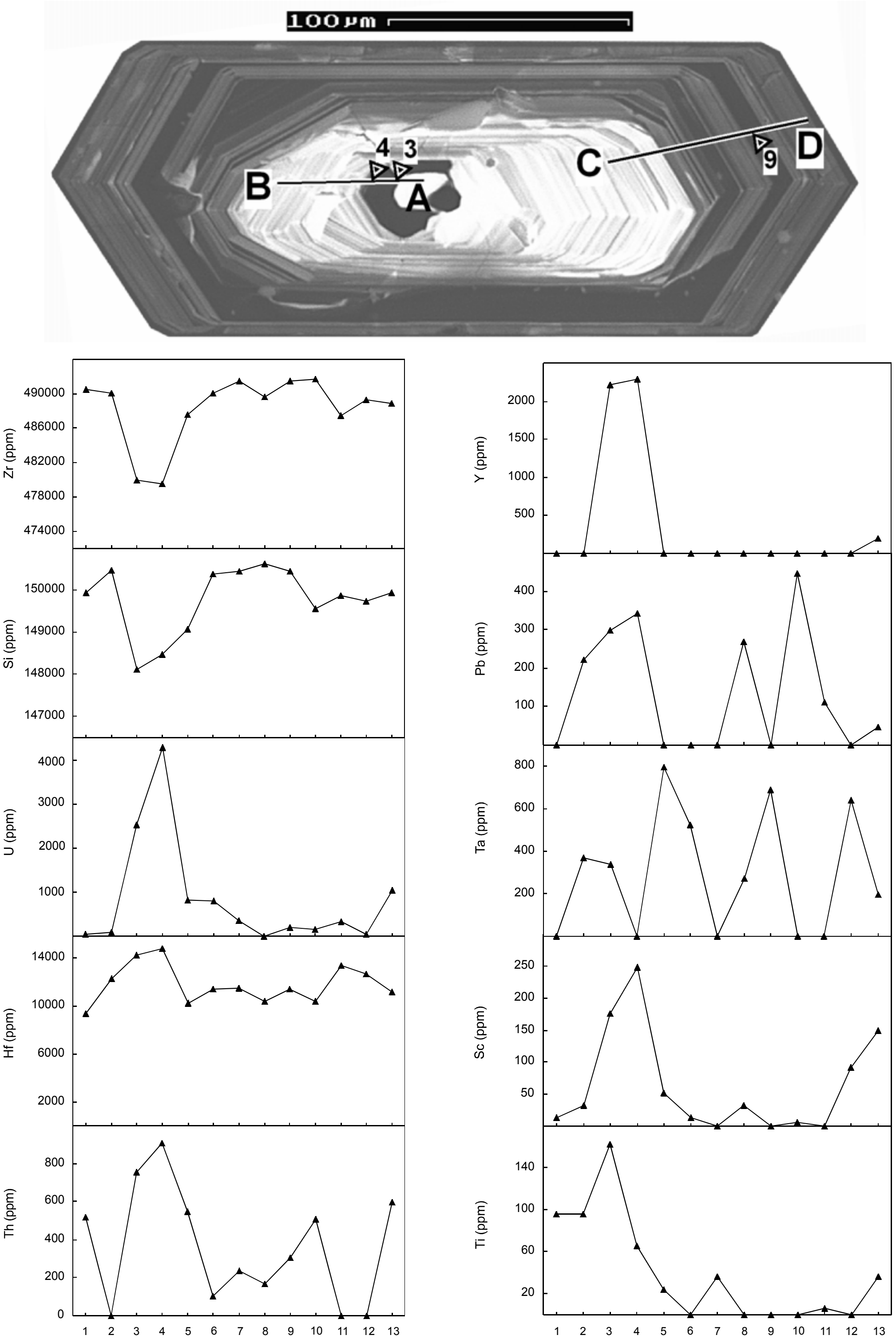

Figure 6.10. Chemical variations within the zircon crystal [Z4(1)] from the Hisarkaya porphyritic granite (sample SK-4): Numbers on the x-axis of the diagrams denote analyzed points along the line from A to B (in the photograph) with an equal distance.

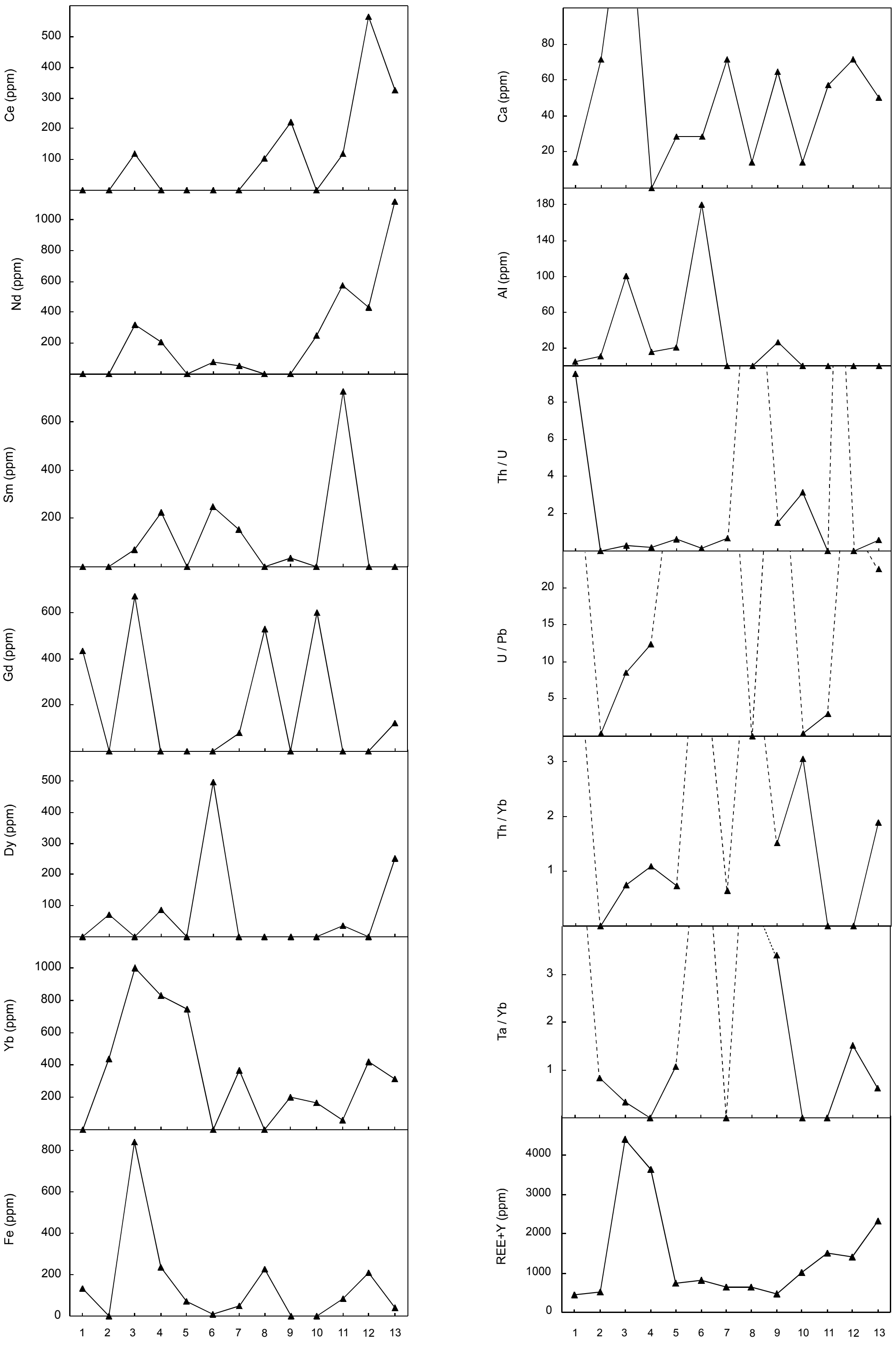

Figure 6.10 (cont'd).

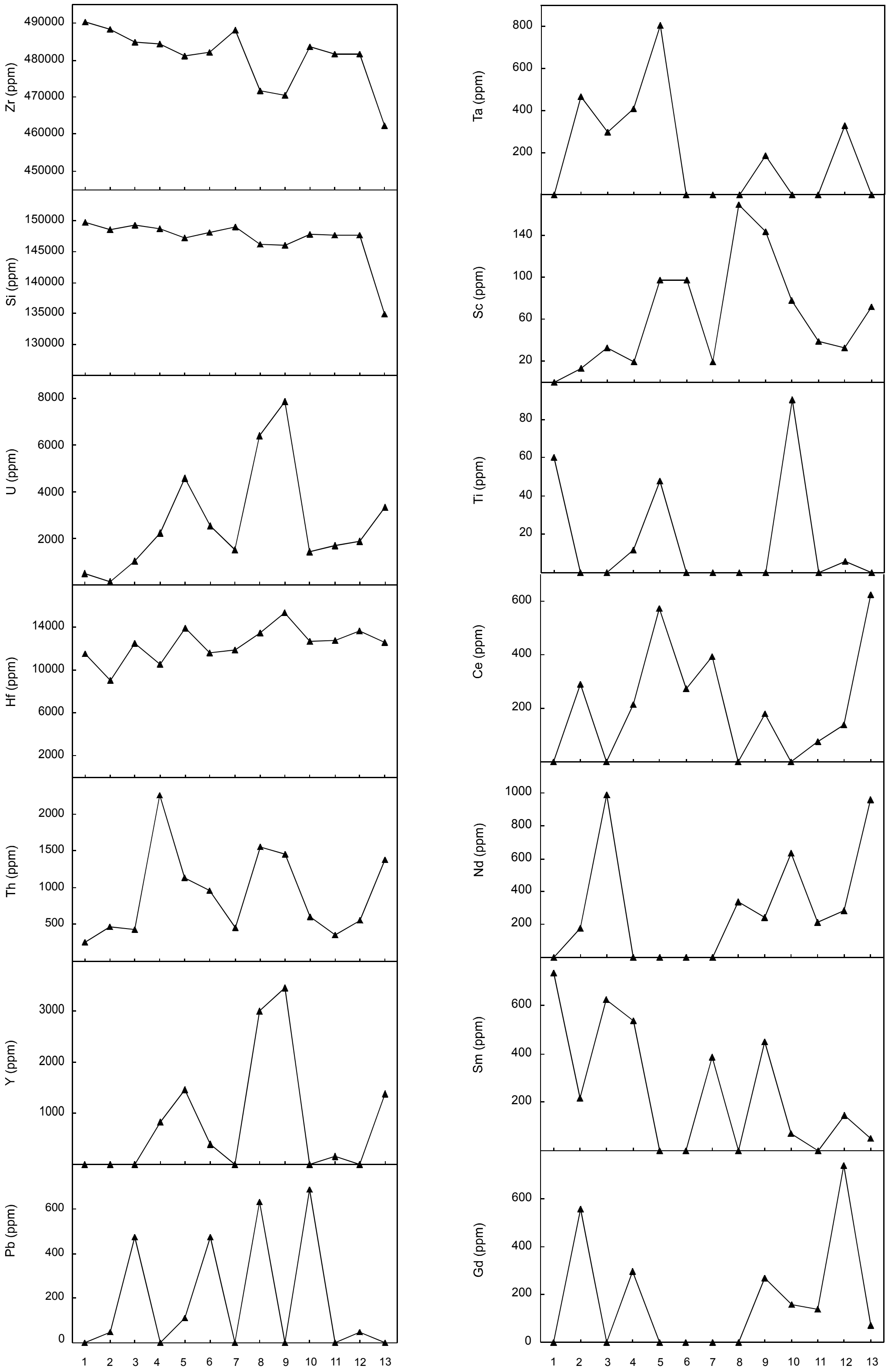

Figure 6.11. Chemical variations within the zircon crystal [Z4(1)] along the line from C to D (see CL-photograph in the Figure 6.10).

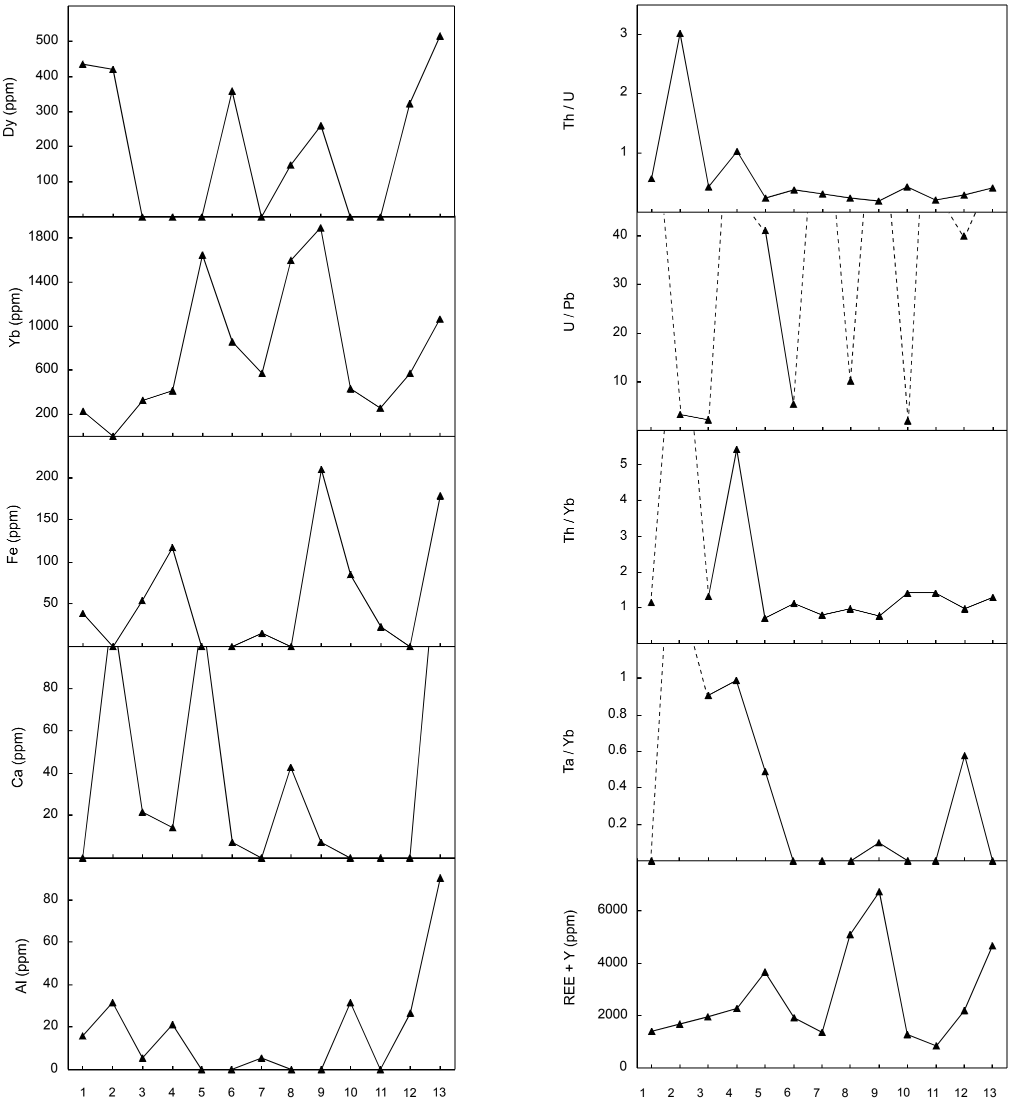

Figure 6.11 (cont'd).

Chondrite-normalized trace element patterns of the zircon crystal [Z4(7)] are similar to that of zircons analyzed by Belousova et al. (2002), but show wider ranges with respect to those of the crystal [Z4(1)] (Figure 6.12).

Chemical profiles of [Z4(7)] are shown in the Figure 6.13. Diagrams show almost steady profiles except for point 5 within the metamictized core. At this point Si, Ti, Fe, Ca and Al abundances are highly elevated, while Zr is decreased. Points 4, 5 and 6 within the metamictized core show low Th/U ratio as 0.074-0.087.

Near to rim at point 18, which is on the corrosion zone determined by CL study, there occurs slight decrease in Zr, but pronounced increase in U, Th and REE+Y. On the other hand, at B, the outmost point, there is no fundamental elemental change with respect to the core (Figure 6.13).

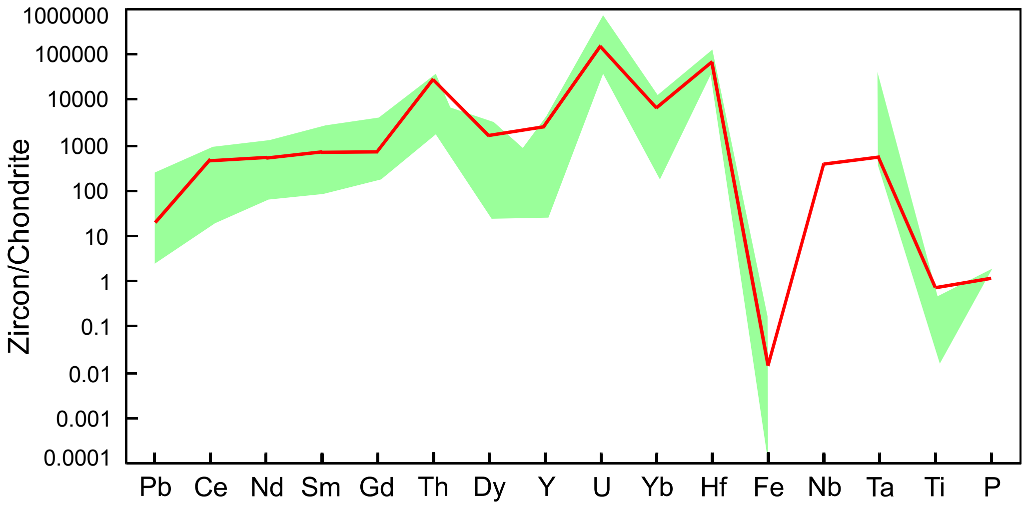

Figure 6.12. Chondrite-normalized trace element abundances of the zircon crystal [Z4(7)] from the Hisarkaya porphyritic granite (sample SK-4) (shaded area) and the averaged values of zircons from granitoids (solid line) (average of 154 samples; data from Belousova et al., 2002). Chondrite values are from Taylor and McLennan (1985). Zero values are not plotted.

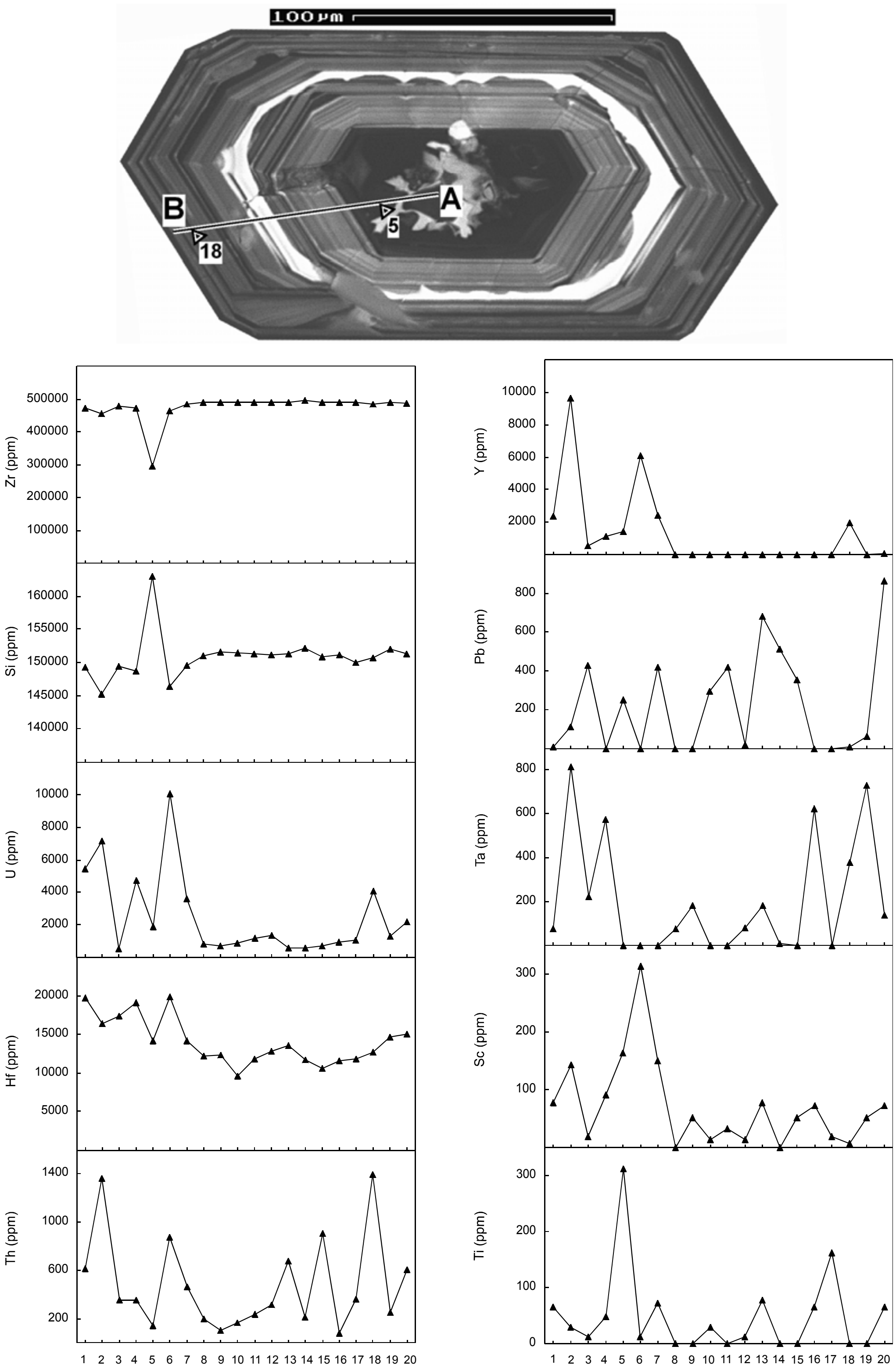

Figure 6.13. Chemical variations within the zircon crystal [Z4(7)] from the Hisarkaya porphyritic granite (sample SK-4): Numbers on the x-axis of the diagrams denote analyzed points along the line from A to B (in the photograph) with an equal distance.

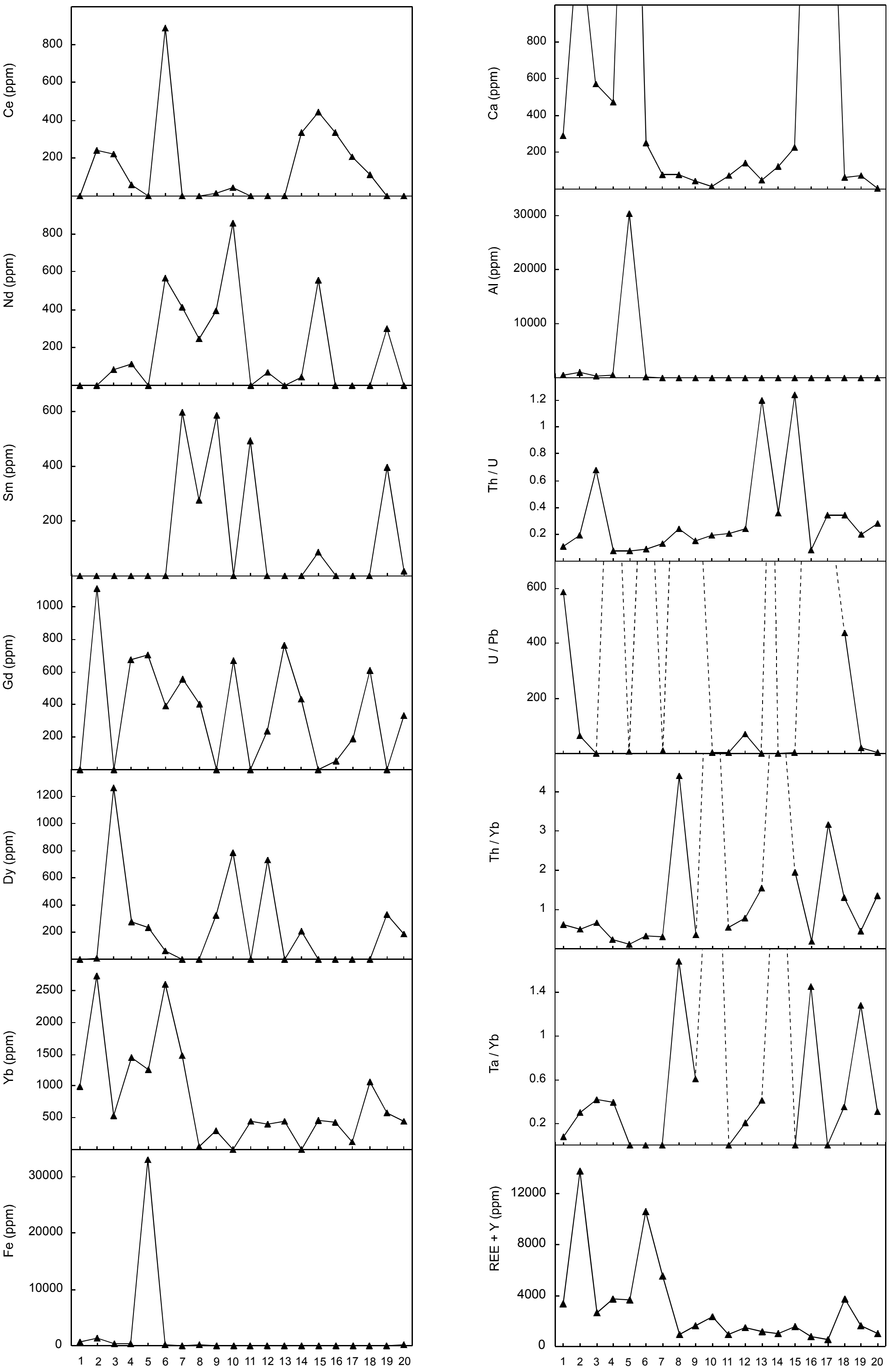

Figure 6.13 (cont'd).

6.3.1.4. Sinandı Microgranite

Two zircon crystals ([Z6(17)] and [Z6(19)]) from the Sinandı microgranite were analyzed chemically.

The compositions of the zircon crystal [Z6(17)] are: 63.83% (median value with standard deviation of ±6.99) ZrO_2, 30.66% (median value with standard deviation of ±2.30) SiO_2 and 1.51% (median value with standard deviation of ±0.20) HfO_2. It is further characterized by its Th/U ratio of 0-0.95, Th values of 0-1520 ppm, and U values of 0-3988 ppm (Table 6.2).

Chondrite-normalized trace element abundances of the zircon crystal [Z6(17)] are given in the Figure 6.14. Compared with the data of Belousova et al. (2002) depletions in Y, Fe and Ti, besides enrichments in Ta and P are recognizable.

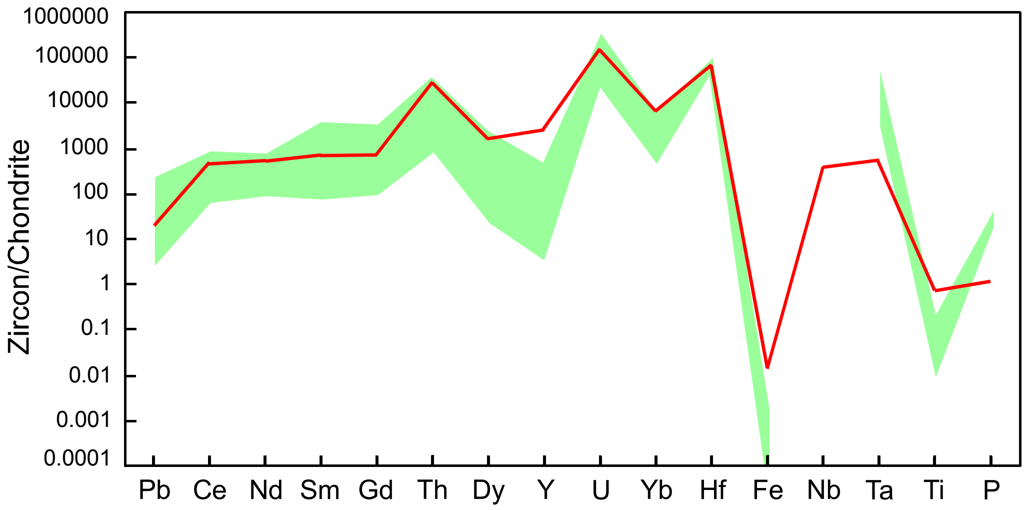

Figure 6.14. Chondrite-normalized trace element abundances of the zircon crystal [Z6(17)] from the Sinandı microgranite (sample SK-6) (shaded area) and the averaged values of zircons from granitoids (solid line) (average of 154 samples; data from Belousova et al., 2002). Chondrite values are from Taylor and McLennan (1985). Zero values are not plotted.

Elemental variations along the zones within the crystal [Z6(17)] are given in the Figures 6.15 and 6.16. The core is difficult to investigated because of its high CL-intensity. Sudden increases in U, Sc, Ta and REE+Y are noteworthy at point 3 that is at the narrow black stripe structure within the core. Through the oscillatory zones along the line A-B there are some oscillations (Figure 6.15).

Alternatively, the line C-D in the Figure 6.16 cuts some wide low-CL zones. At point 2, on a corrosion zone (Chapter 5), Zr and Si drop, whilst U, Th and REE+Y increase. Point 4 is on the thickened trace element band, where U, Th and REE+Y values are elevated, and Pb is lost. Point D has anomalously high Ca and Al content, with significantly decreased Zr and Si abundances (Figure 6.16).

The zircon crystal [Z6(19)] is characterized by median values of 65.08% (±0.50) ZrO_2, 31.52% (±0.17) SiO_2 and 1.59% (±0.15) HfO_2 (Table 6.2). Th/U ratio is between 0.06 and 4.51, while Th varies between 0-1037 ppm, and U varies between 0-2925 ppm.

Chondrite-normalized trace element patterns of the zircon crystal [Z6(19)] resemble those of [Z6(17)], disregarding slight enrichments in Y and Nd, depletion in Fe, and lack of P content (Figure 6.17).

Chemical variations within the crystal [Z6(19)] are shown in the Figures 6.18 and 6.19. The crystal has brightly luminescent core as [Z6(17)]. Point A which is at the dark strip structure (as the case in the crystal [Z6(17)]) has low Zr, but high Th/U and Th/Yb ratios besides U, Th, Pb, Ti, Fe, Al, Ca, REE+Y abundances (Figure 6.18). Overgrowing zones of high CL-intensity are characterized by Zr and Si decrease, and U, Th and REE+Y increase, especially at point 5 of A-B line (Figure 6.18). At points 4 and 7, Th/U ratio is about 0.060. Within the composite core at point 3 of C-D line (Figure 6.19) drop off Zr and Si, combined with rise in REE+Y is notable.

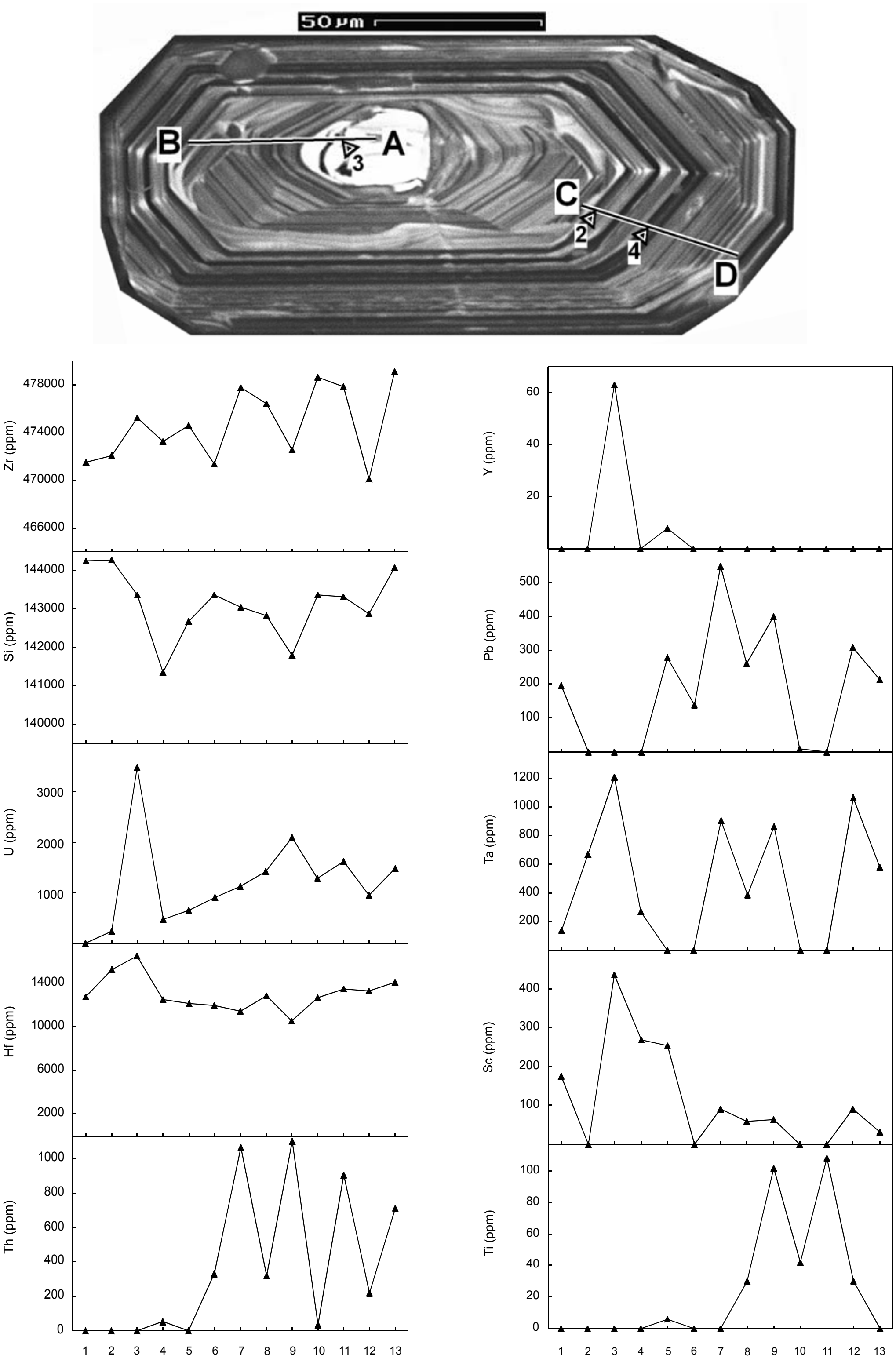

Figure 6.15. Chemical variations within the zircon crystal [Z6(17)] from the Sinandı microgranite (sample SK-6): Numbers on the x-axis of the diagrams denote analyzed points along the line from A to B (in the photograph) with an equal distance.

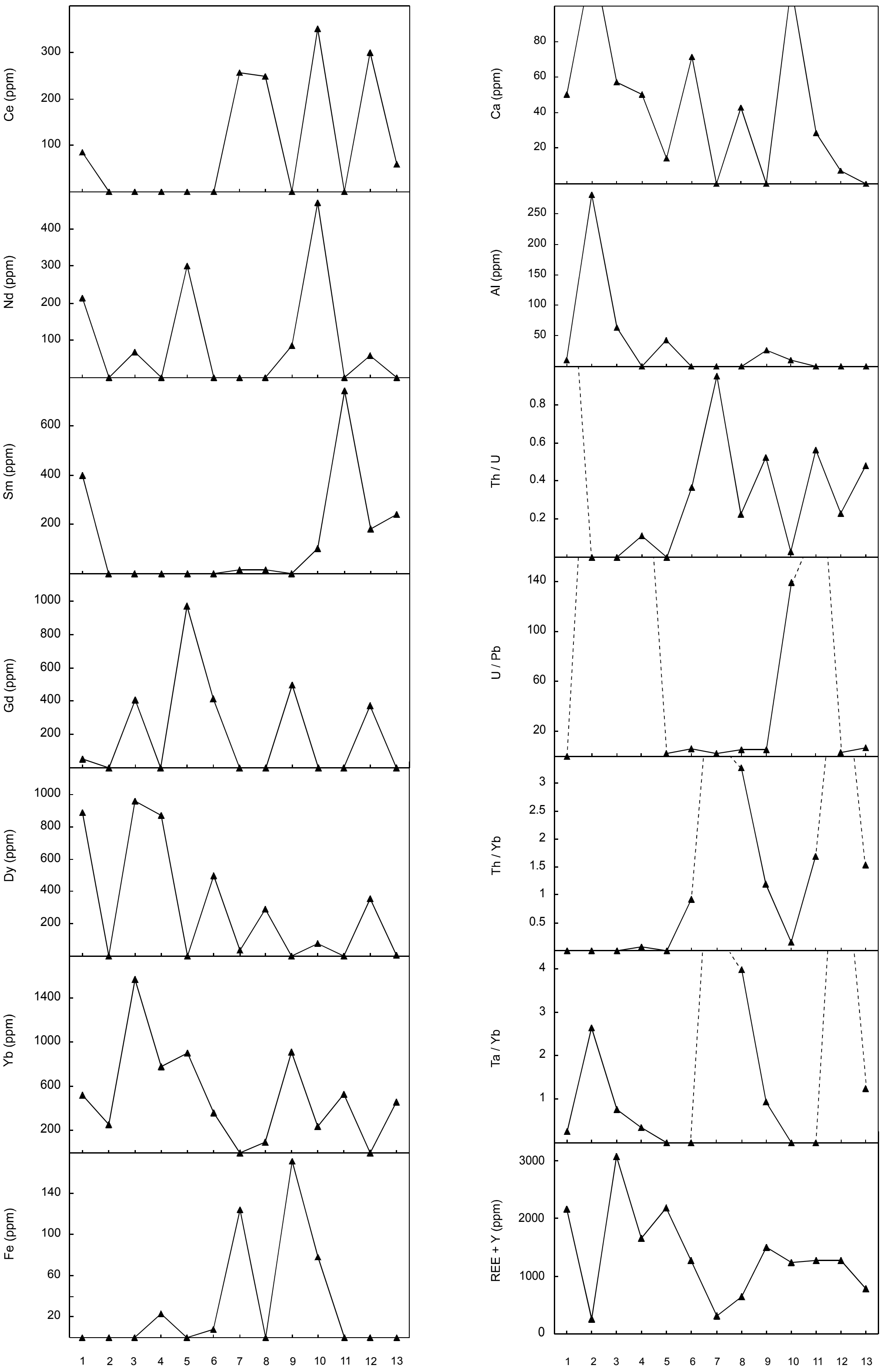

Figure 6.15. (cont'd).

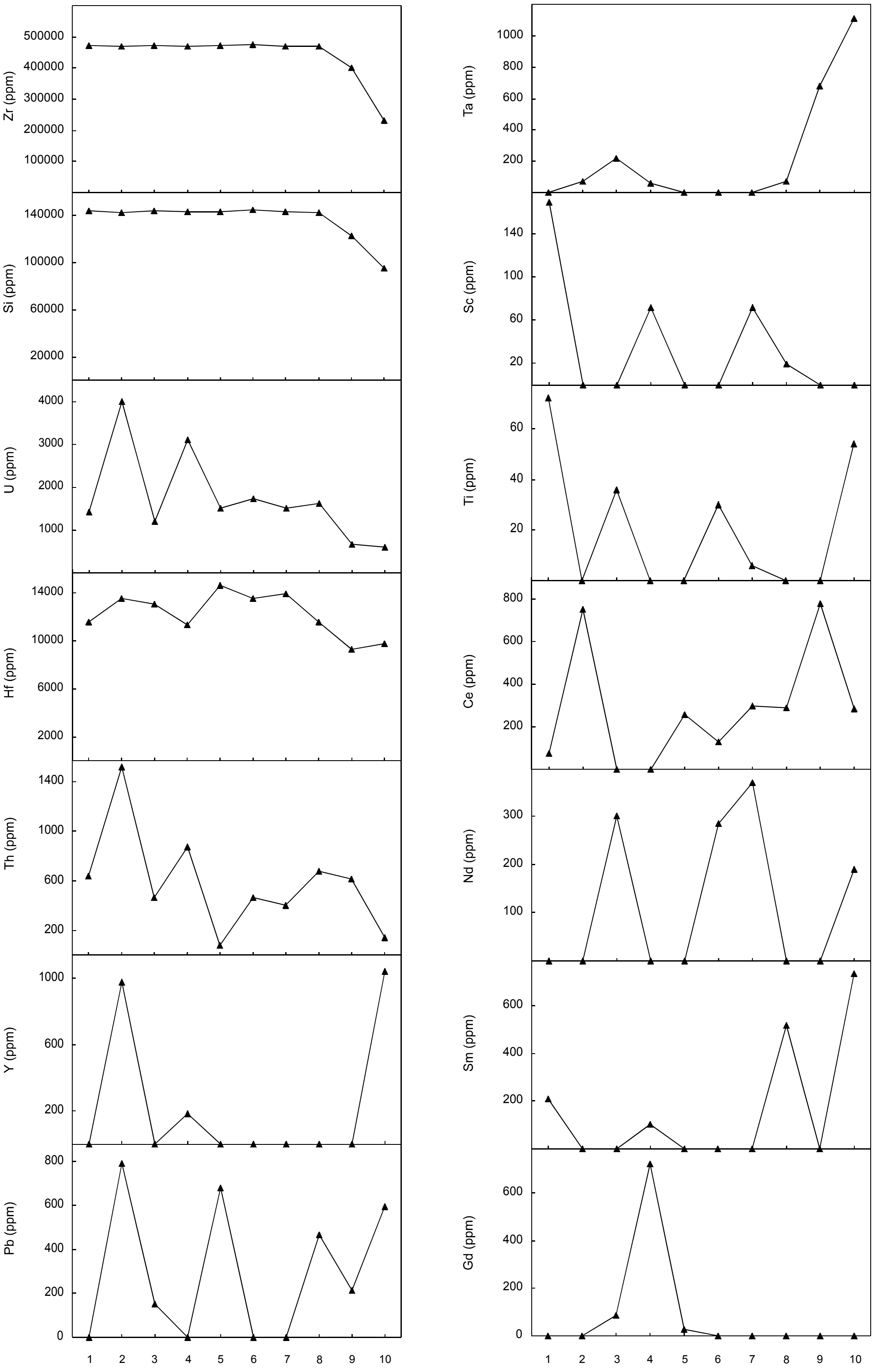

Figure 6.16. Chemical variations within the zircon crystal [Z6(17)] along the line from C to D (see CL-photograph in the Figure 6.15).

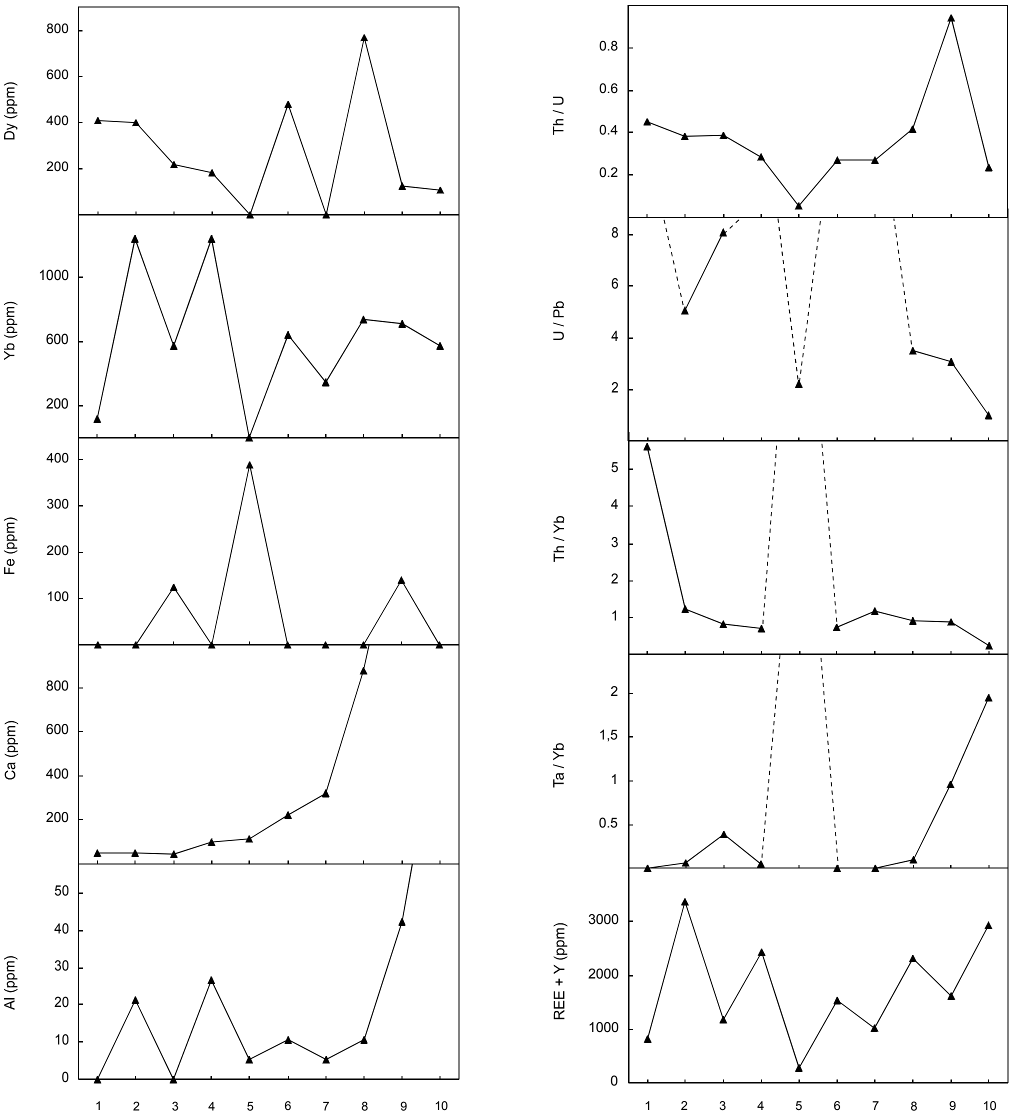

Figure 6.16 (cont'd).

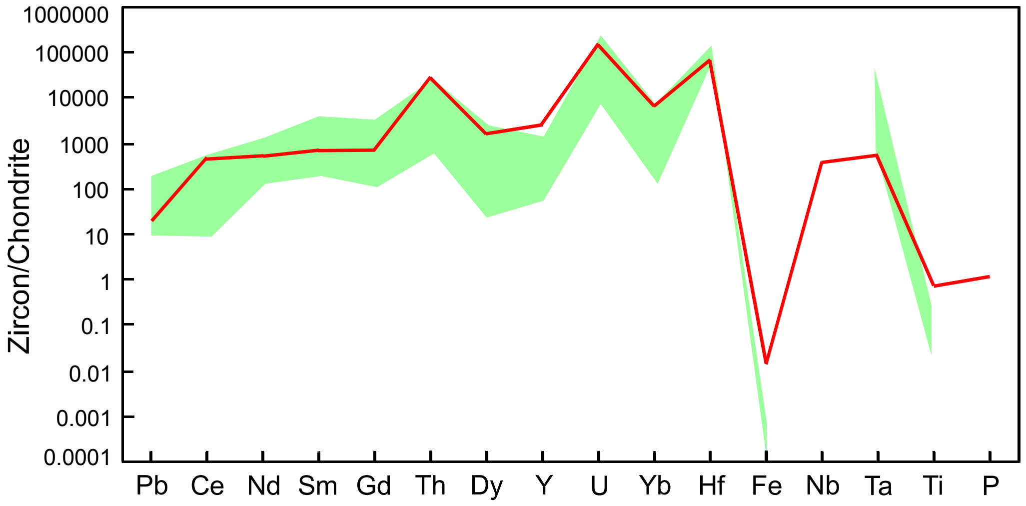

Figure 6.17. Chondrite-normalized trace element abundances of the zircon crystal [Z6(19)] from the Sinandı microgranite (sample SK-6) (shaded area) and the averaged values of zircons from granitoids (solid line) (average of 154 samples; data from Belousova et al., 2002). Chondrite values are from Taylor and McLennan (1985). Zero values are not plotted.

6.3.2. Ağaçören Pluton

6.3.2.1. Namlıkışla Biotite-Granite

[Z8(20)] and [Z8(21)] are the zircon crystals chosen for chemical analyses from the Namlıkışla granitoid.

The zircon crystal [Z8(20)] is characterized by median values of 65.09% (±0.39) ZrO_2, 31.97% (±0.18) SiO_2 and 1.65% (±0.16) HfO_2 (Table 6.2). Th/U ratio within the crystal is between 0 and 3.29. Moreover, Th values range from 0 to 325 ppm, and U values varies between 0 to 2262 ppm.

Chondrite-normalized trace element patterns of the zircon crystal [Z8(20)] are shown in the Figure 6.20. The most outstanding elemental characteristic of this crystal is low Th abundance in comparison with the averaged granitoid data of Belousova et al. (2002). Beside low Th, the crystal shows Y, Yb, Fe depletions, and Ta enrichment with respect to average granitoid zircons.

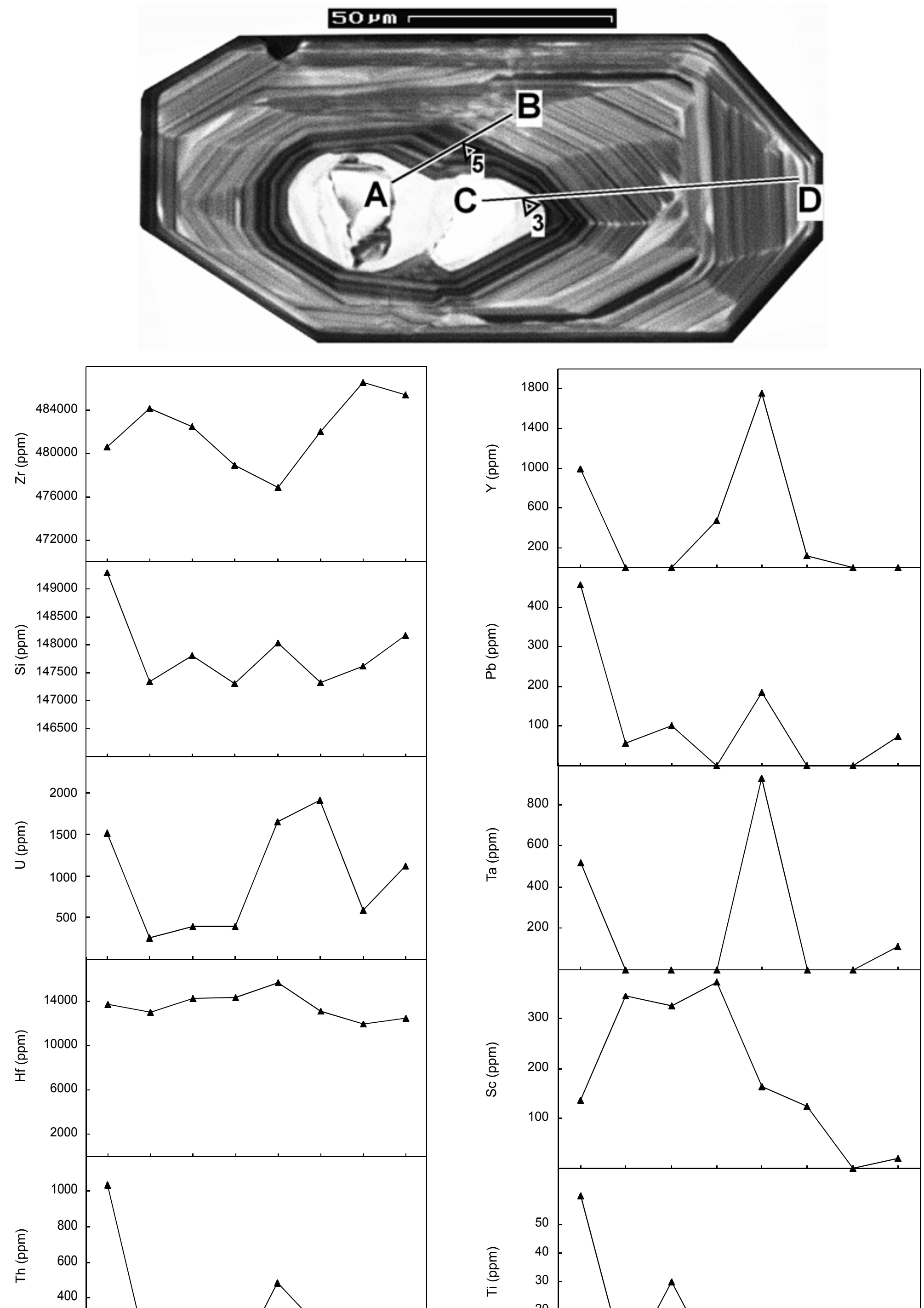

Figure 6.18. Chemical variations within the zircon crystal [Z6(19)] from the Sinandı microgranite (sample SK-6): Numbers on the x-axis of the diagrams denote analyzed points along the line from A to B (in the photograph) with an equal distance.

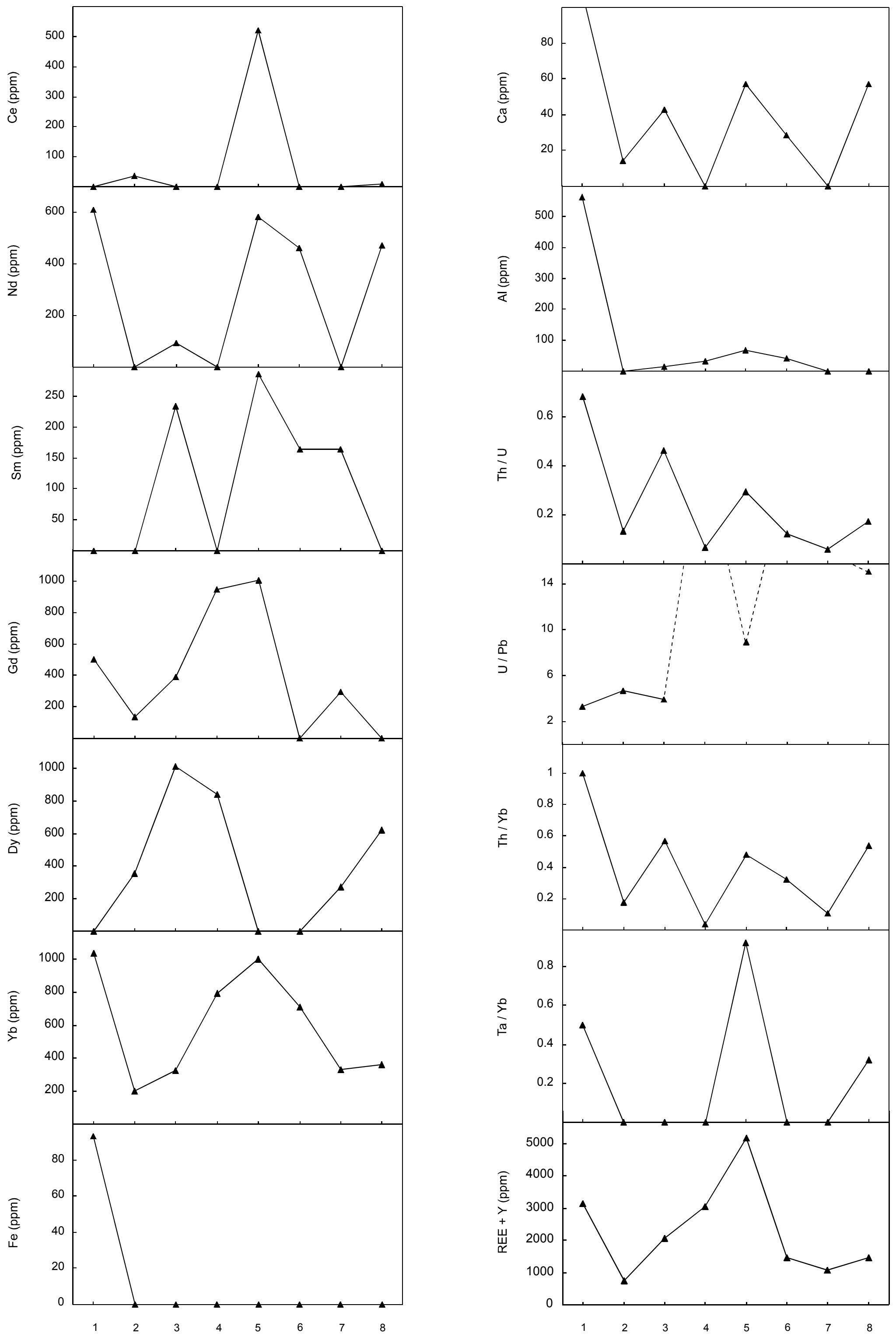

Figure 6.18 (cont'd).

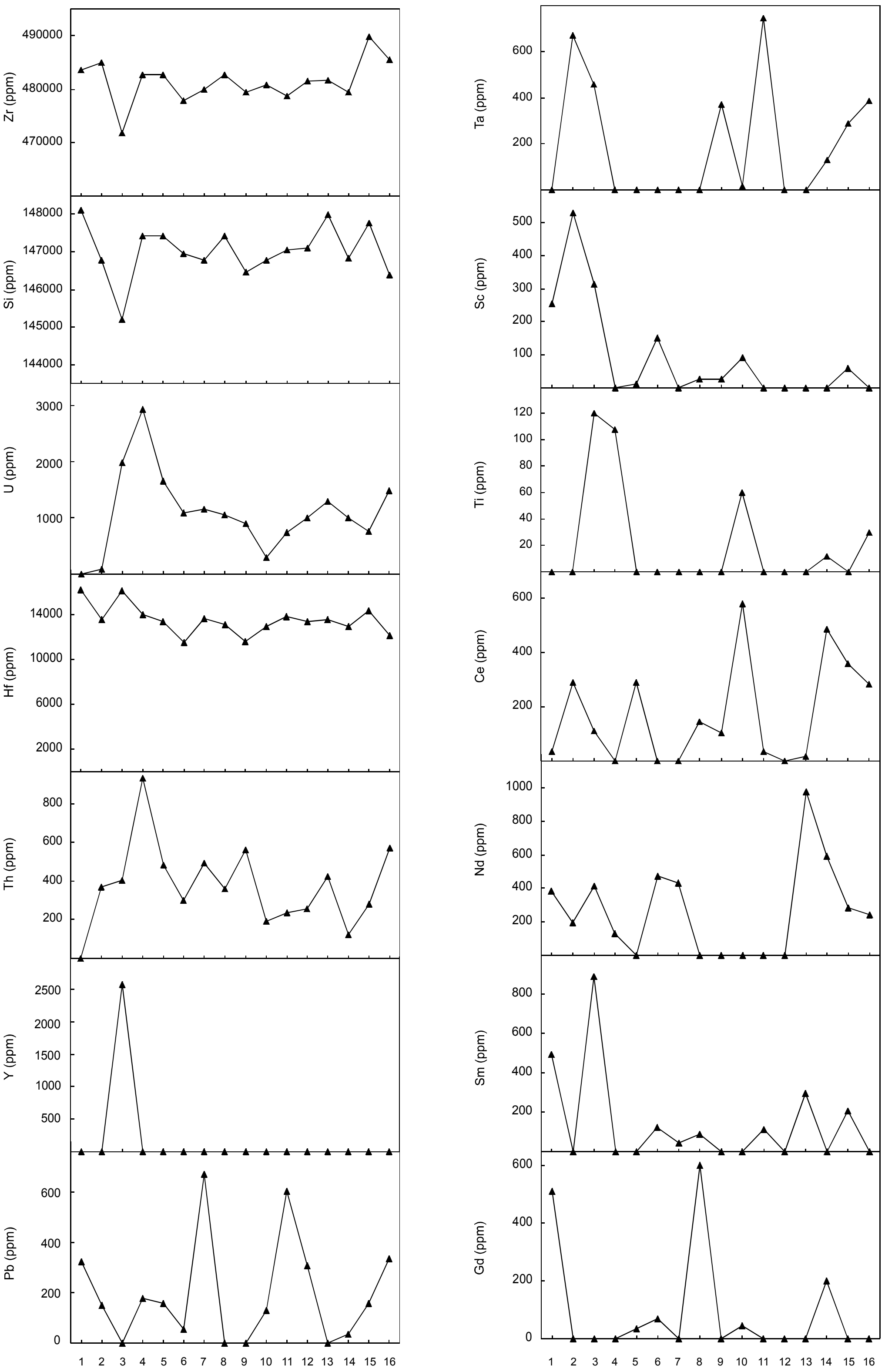

Figure 6.19. Chemical variations within the zircon crystal [Z6(19)] along the line from C to D (see CL-photograph in the Figure 6.18).

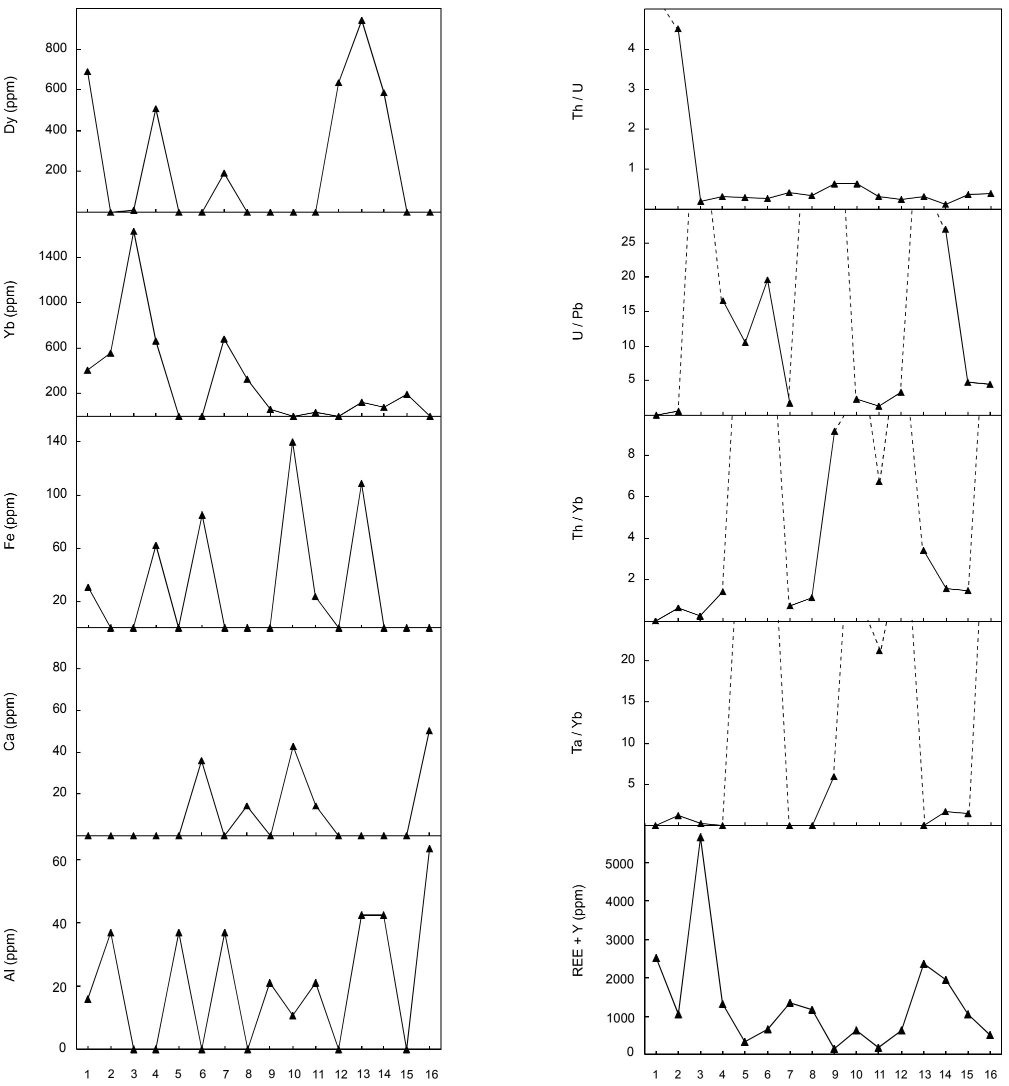

Figure 6.19 (cont’d).

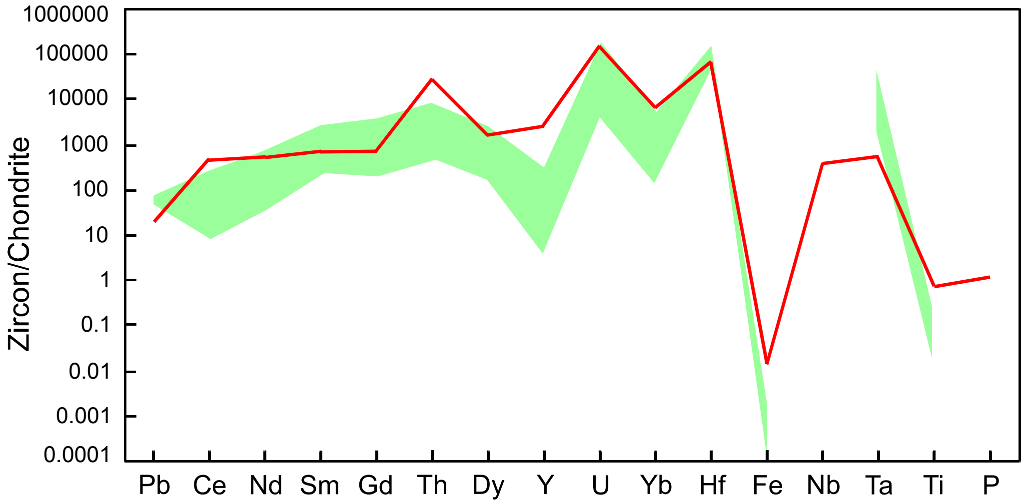

Figure 6.20. Chondrite-normalized trace element abundances of the zircon crystal [Z8(20)] from the Namlıkışla biotite-granite (sample SK-8) (shaded area) and the averaged values of zircons from granitoids (solid line) (average of 154 samples; data from Belousova et al., 2002). Chondrite values are from Taylor and McLennan (1985). Zero values are not plotted.

The elemental profiles drawn for the crystal [Z8(20)] are presented in the Figures 6.21 and 6.22. At the core elemental concentrations of U, Th, REE+Y etc. are very low (Figure 6.21) probably due to metamictization. Accordingly, Th/U ratio drops to 0.097 at point 6. Line C-D cuts rounded corrosion interface between core and overgrowing zones (Figure 6.22). Pb is lost through the outer zones, while REE+Y abundance is at higher levels with respect to core. Zr shows depletion at points 5 and 7, which correspond to thin low CL-bands. At point D, Th/U is 0.011, which is as low as that of metamorphic zircons. However, low Th/U values do not always exactly represent the metamorphic growth and maybe indicative of open system behavior in the rock (e.g. Möller et al., 2001).

The chemical data for [Z8(21)] shows that the crystal has median values of 65.58% (±0.40) ZrO_2, 32.01% (±0.11) SiO_2 and 1.37% (±0.22) HfO_2 (Table 6.2). Th/U ratio is varies from 0 to 15.96, on the other hand Th is of 0-483 ppm, and U is of 0-1790 ppm.

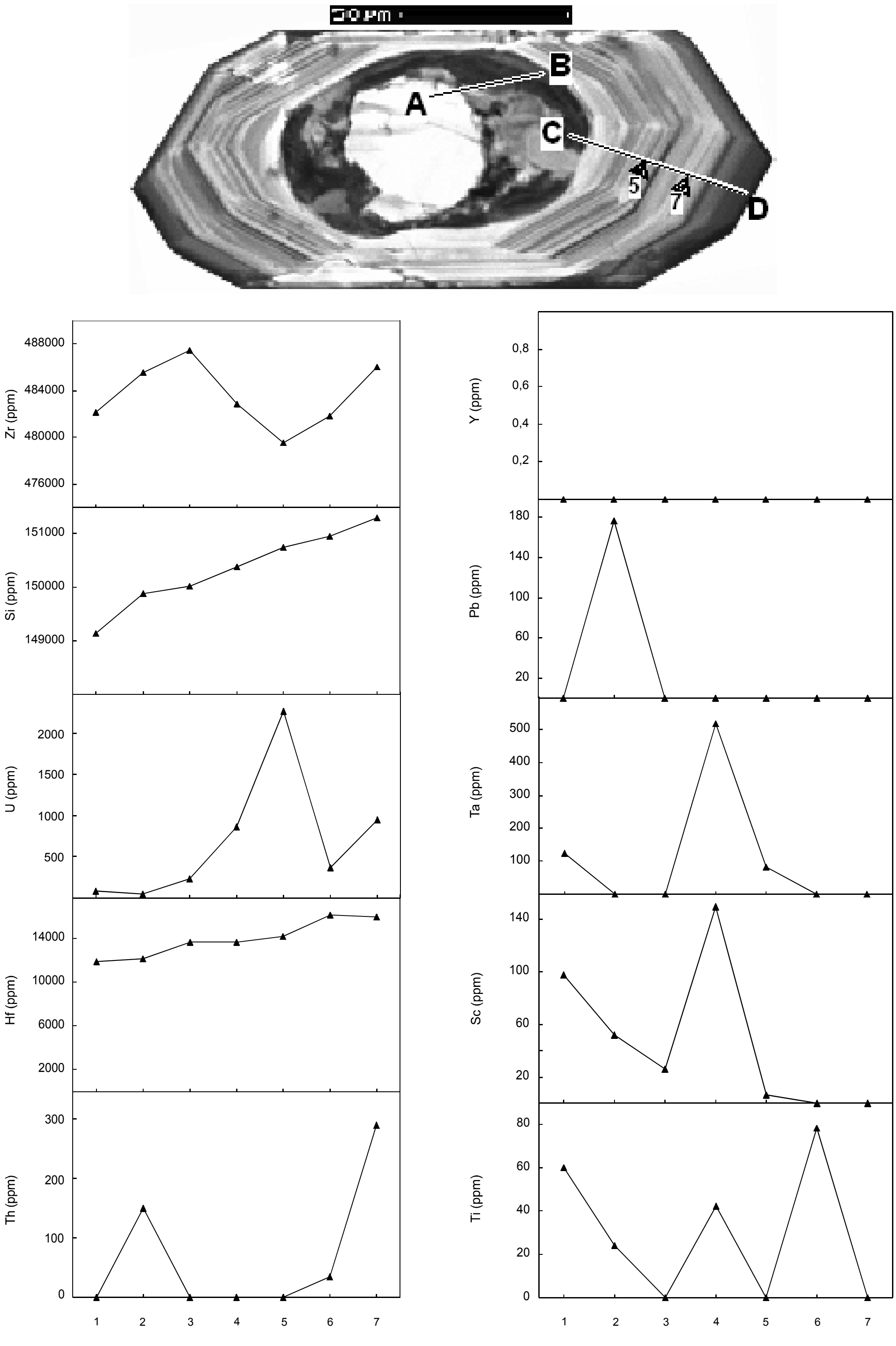

Figure 6.21. Chemical variations within the zircon crystal [Z8(20)] from the Namlıkışla biotite-granite (sample SK-8): Numbers on the x-axis of the diagrams denote analyzed points along the line from A to B (in the photograph) with an equal distance.

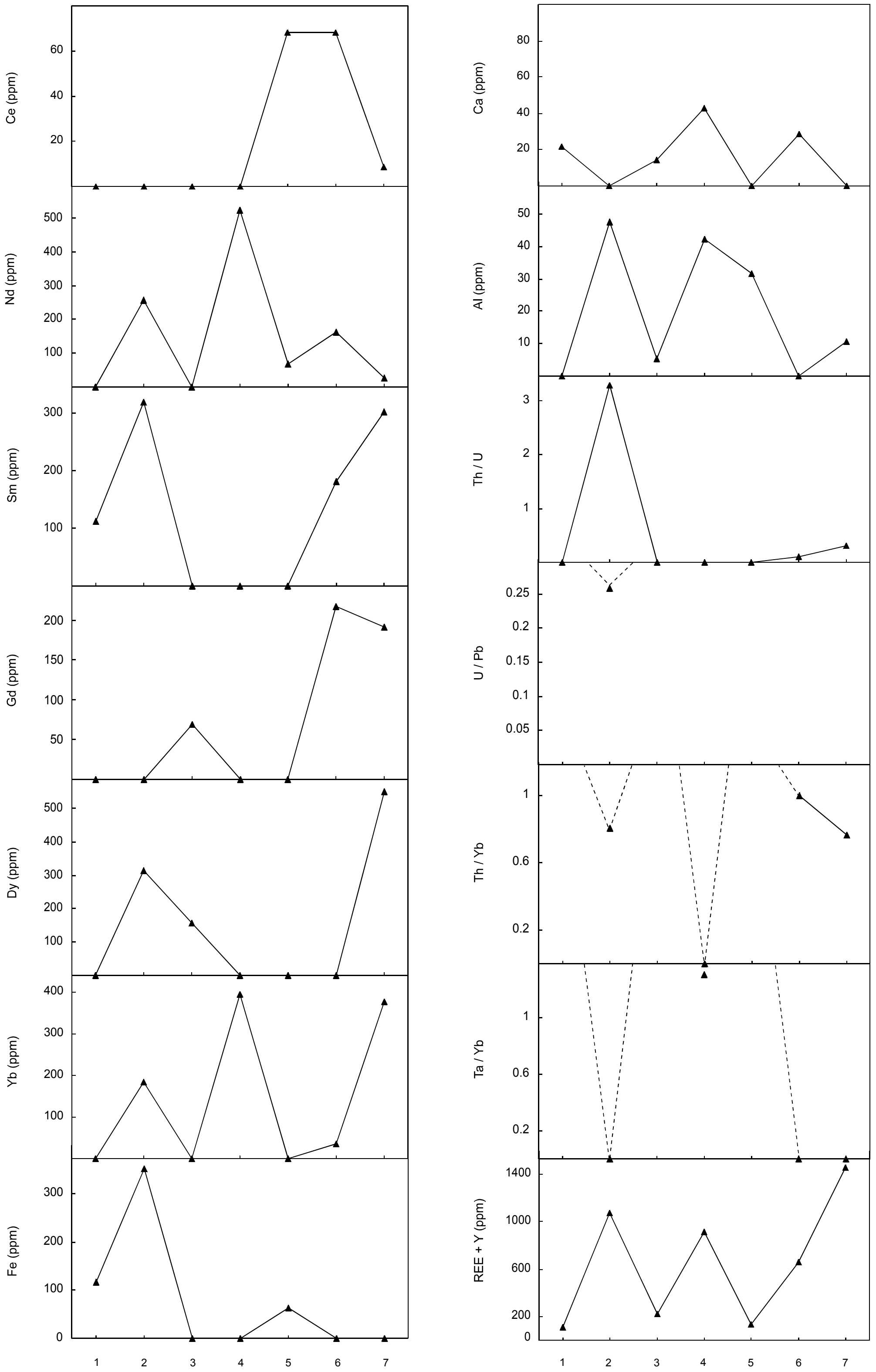

Figure 6.21 (cont'd).

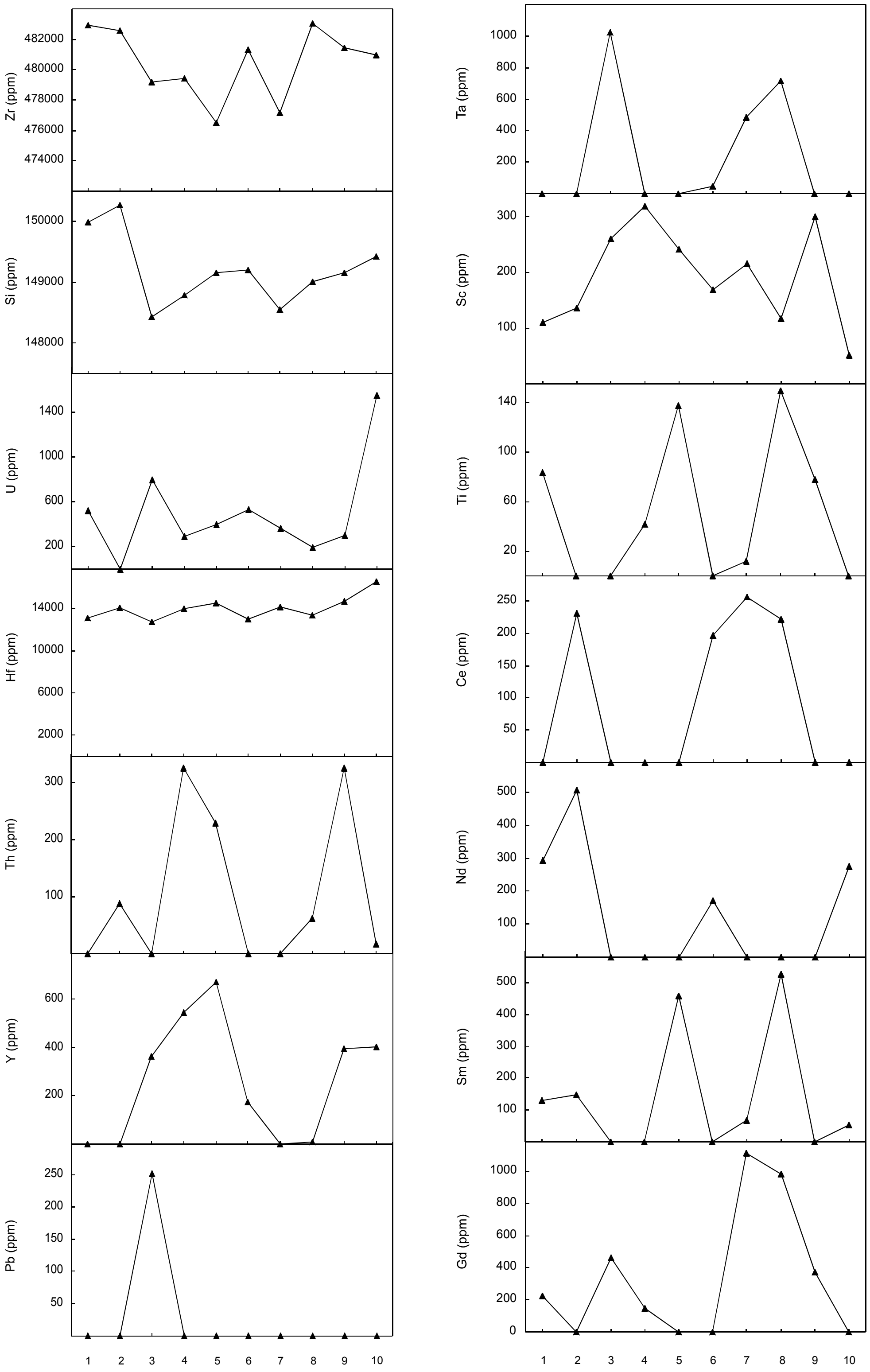

Figure 6.22. Chemical variations within the zircon crystal [Z8(20)] along the line from C to D (see CL-photograph in the Figure 6.21).

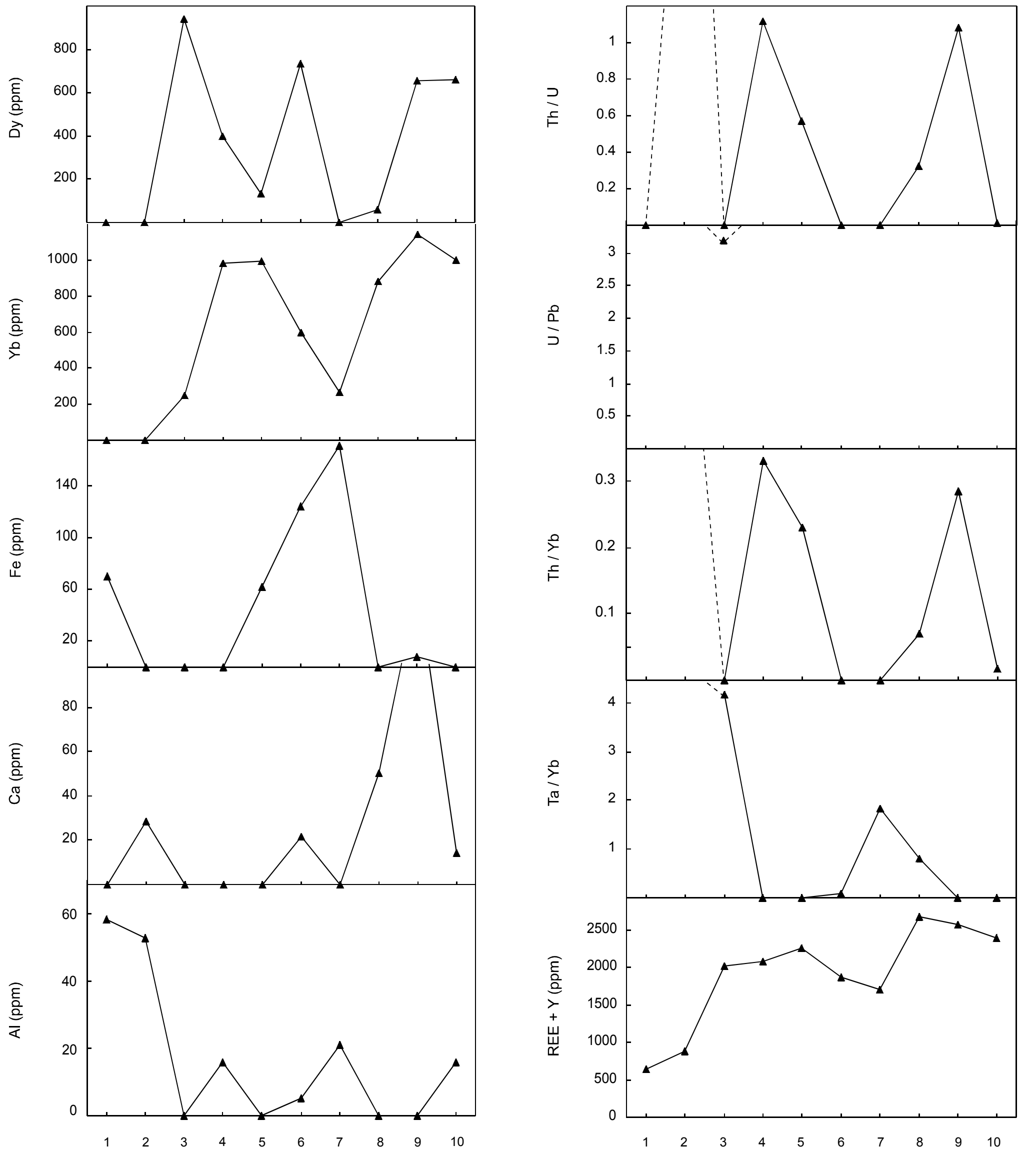

Figure 6.22 (cont'd).

Chondrite-normalized trace element patterns of the zircon crystal [Z8(21)] demonstrate low Th, Yb, Fe and Ti abundances as the case for [Z8(20)] (Figure 6.23).

Analyses along the lines from A to B and from C to D within the crystal [Z8(21)] are shown in the Figures 6.24 and 6.25. On the line A-B, at point 3 lying at the zone overgrowing the small core, there are depletions in Zr and U, but enrichments in Hf, Th, Ca, Al and REE+Y. Moreover, at point 7, which is on the thin zone with dark CL, Zr and Si drop, while U and REE+Y increase. In the succeeding stages there are oscillations in the elemental contents up to point B near to rounded interface between high intensity inner parts and zones of relatively lower CL-intensity (Figures 6.24). Line C-D on the other hand passes through this interface (Figures 6.25). Within the zone of corrosion at points from 3 to 7, Zr shows depletion, while REE+Y shows enrichment. Around this zone Th/U ratio is lowered less than 0.1. Additionally, inner parts of the crystal can be discriminated by their higher Zr, Si, Th contents and Th/U ratio, and low Hf, U, Sc and REE+Y contents than the outer parts. At point D, near to rim, Th/U ratio is 0.069 that is lower than that of igneous zircons, as in the case of [Z8(20)].

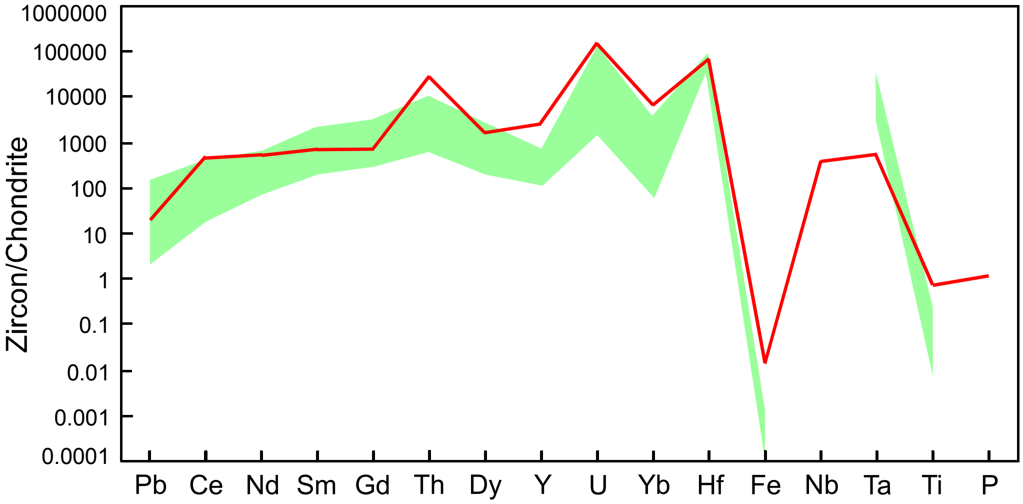

Figure 6.23. Chondrite-normalized trace element abundances of the zircon crystal [Z8(21)] from the Namlıkışla biotite-granite (sample SK-8) (shaded area) and the averaged values of zircons from granitoids (solid line) (average of 154 samples; data from Belousova et al., 2002). Chondrite values are from Taylor and McLennan (1985). Zero values are not plotted.

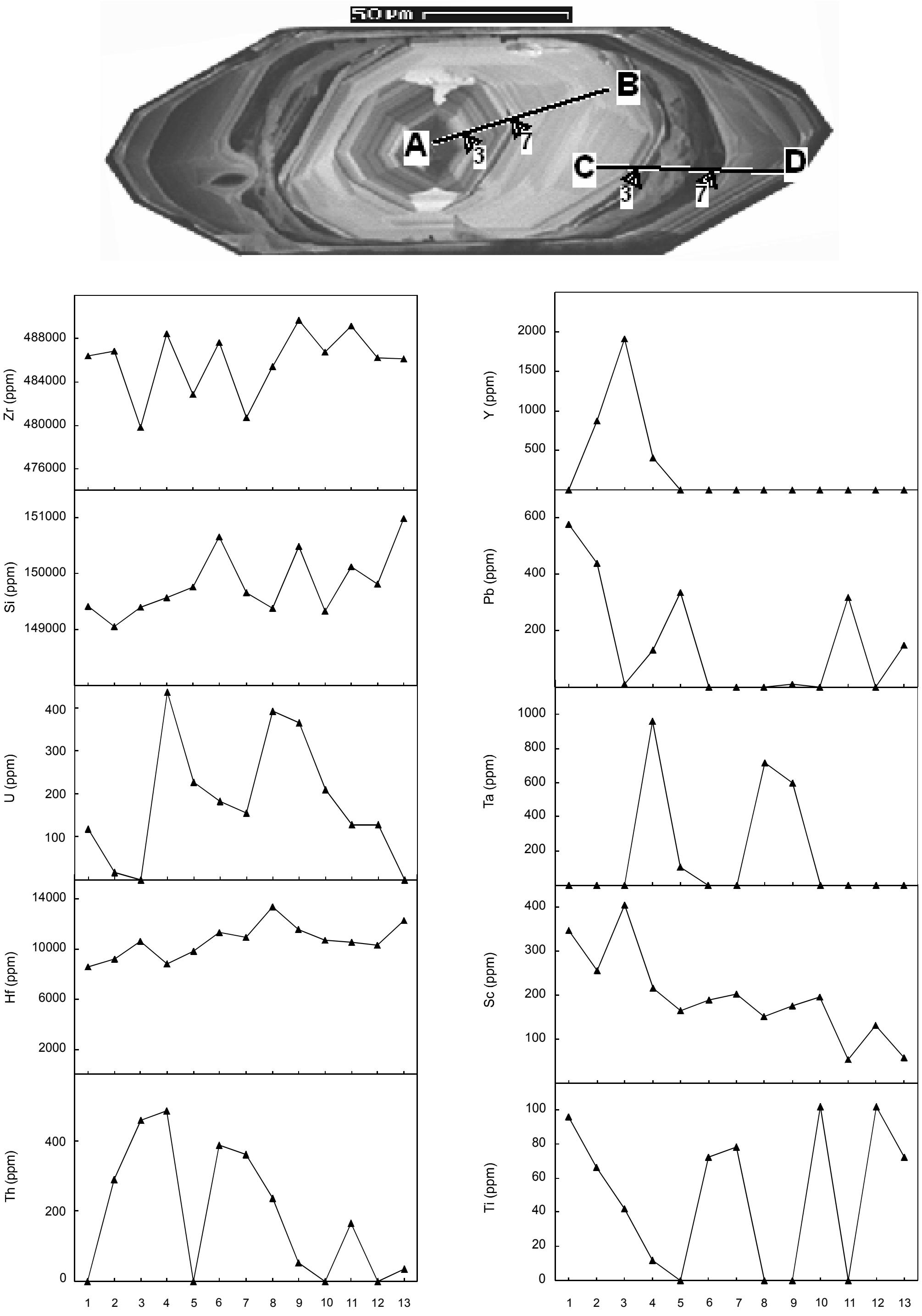

Figure 6.24. Chemical variations within the zircon crystal [Z8(21)] from the Namlıkışla biotite-granite (sample SK-8): Numbers on the x-axis of the diagrams denote analyzed points along the line from A to B (in the photograph) with an equal distance.

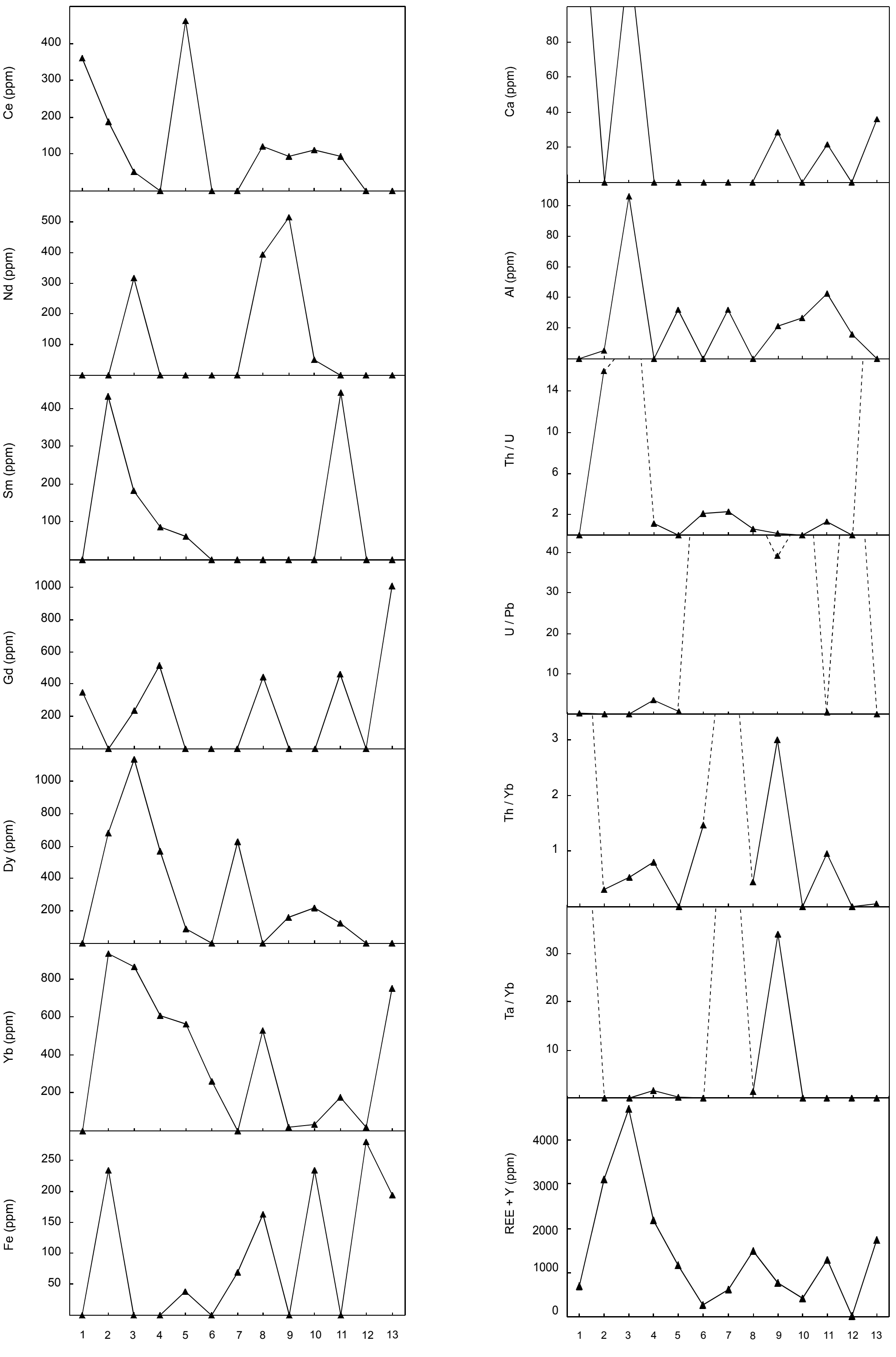

Figure 6.24 (cont'd).

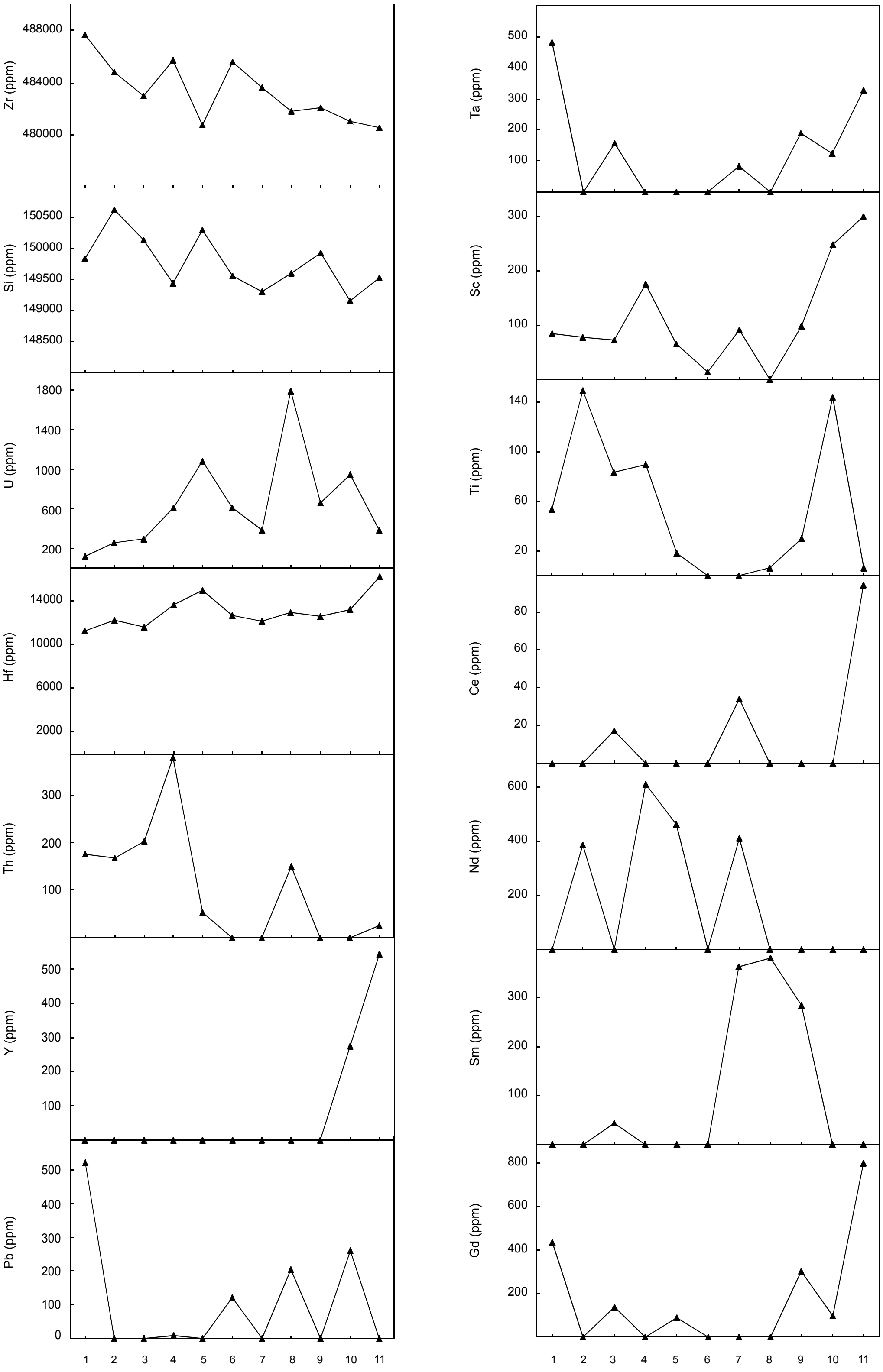

Figure 6.25. Chemical variations within the zircon crystal [Z8(21)] along the line from C to D (see CL-photograph in the Figure 6.24).

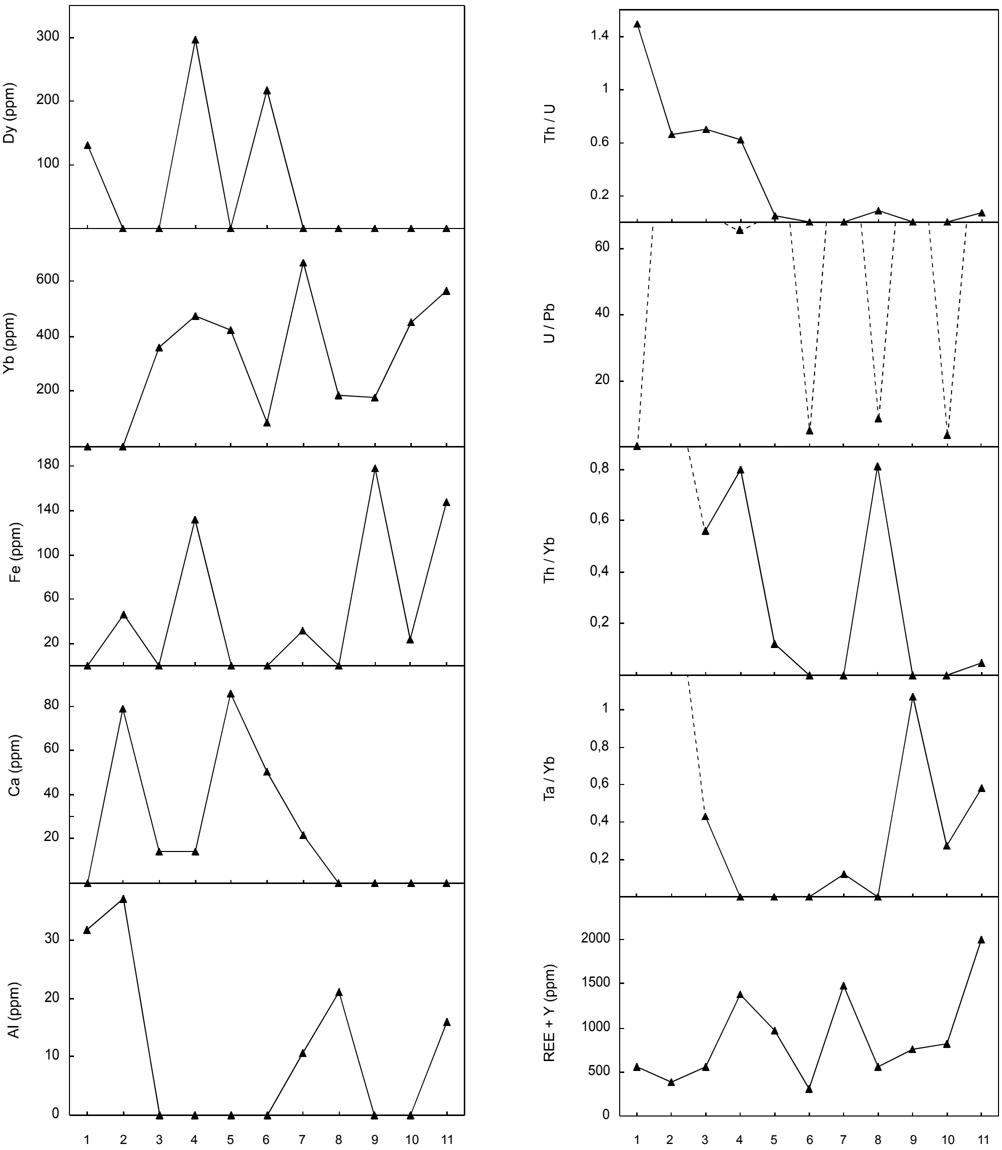

Figure 6.25 (cont'd).

6.3.2.2. Yenişabanlı Biotite-Amphibole Granite

From the Yenişabanlı granitoid two zircon crystals, namely [Z9(1)] and [Z9(11)], were chosen for chemical analyses.

The zircon crystal [Z9(1)] is represented by median values of 65.92% (±0.69) ZrO_2, 32.50% (±0.57) SiO_2 and 1.53% (±0.27) HfO_2 (Table 6.2). Th/U ratio within the crystal is of 0-1.45, Th is of 0-2136 ppm, and U is of 127-10174 ppm.

Chondrite-normalized trace elements of the zircon crystal [Z9(1)] are represented by their lower values of Y, Fe and Ti, and higher values Ta than that averaged granitic zircons of Belousova et al. (2002) (Figure 6.26).

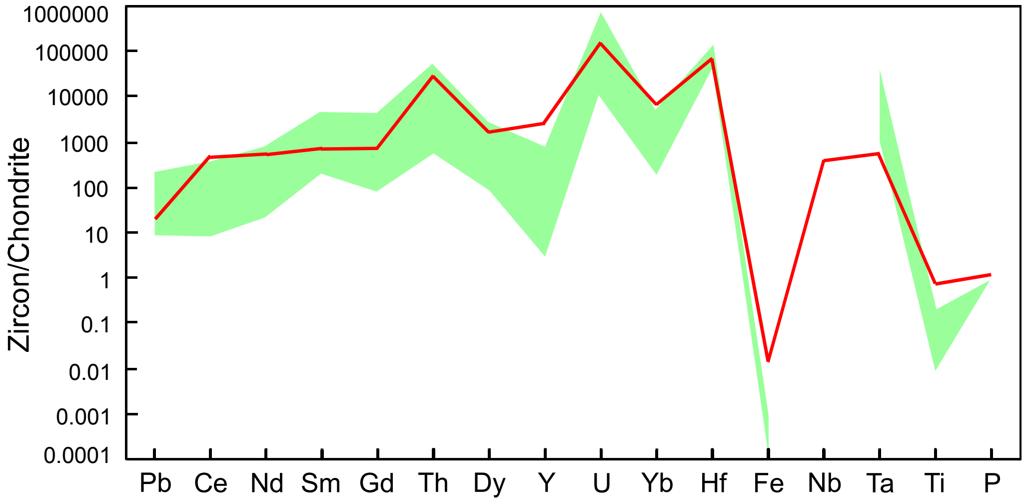

Figure 6.26. Chondrite-normalized trace element abundances of the zircon crystal [Z9(1)] from the Yenişabanlı granitoid (sample SK-9) (shaded area) and the averaged values of zircons from granitoids (solid line) (average of 154 samples; data from Belousova et al., 2002). Chondrite values are from Taylor and McLennan (1985). Zero values are not plotted.

Chemical variations within the zircon crystal [Z9(1)] are given in the Figure 6.27. The crystal has small core, which is overgrown by thin zones interrupted by multiple corrosion stages (Chapter 5). These interruptions are apparent in the chemical profiles with decreasing of Zr and Si, and increasing of U, Th and REE+Y. Chemical characteristics of the crystal at point 6 is remarkable in that manner. At point 22 where the trace elements form a relatively thick band, enrichment in U, Hf, Th, Ta, Al and REE+Y is visible. The last stages of crystallization are characterized by decreasing Zr and Si, but increasing U, Hf and REE+Y (at point B).

Th/U ratio varies along the line A-B within the crystal [Z9(1)], and decrease less than 0.1 at points 9, 12, 17, 30, 33, 34, disregarding points with zero Th content. Most of these points intercept the dark CL zones or zones showing changes in the crystal evolution. Especially decrease at the outer zones at which Th/U ratio drops off to 0.025 is noteworthy.

The zircon crystal [Z9(11)] is characterized by median values of 65.52% (±0.35) ZrO_2, 32.33% (±0.12) SiO_2 and 1.51% (±0.26) HfO_2 (Table 6.2). Th/U ratio ranges from 0 to 0.62, while Th varies between 0-1986 ppm, and U varies between 899-6958 ppm.

Chondrite-normalized spider-diagram of the zircon crystal [Z9(11)] is given in the Figure 6.28. The crystal has similar abundances with [Z9(1)], considering depletion in Y, Fe and Ti, enrichment in Ta compared with averaged granitic zircons (Belousova et al., 2002).

Profiles of elemental abundances in ppm of [Z9(11)] are presented in the Figure 6.29. Light luminescent area of the core reflects high Zr-supersaturation that is consistent with the characteristics of initial skeletal growth as discussed in Chapter 5. At the dark part of the core point 7 lies with pronounced decrease in Si, and increase in U, Hf, Th and REE+Y. In addition drop in the CL-intensity is accompanied by increase in U and Y at this point. Moreover at points 14 and 18 that are on the corrosion zone, U, Th, Sc and REE+Y increase (Figure 6.29), against low abundances of Zr and Si. Next to point 18, at point 19 Th/U ratio drops off to 0.081. Slight elemental variations from core to rim continue to point B, where Zr, Si and Hf decrease, while U, Th and REE+Y increase.

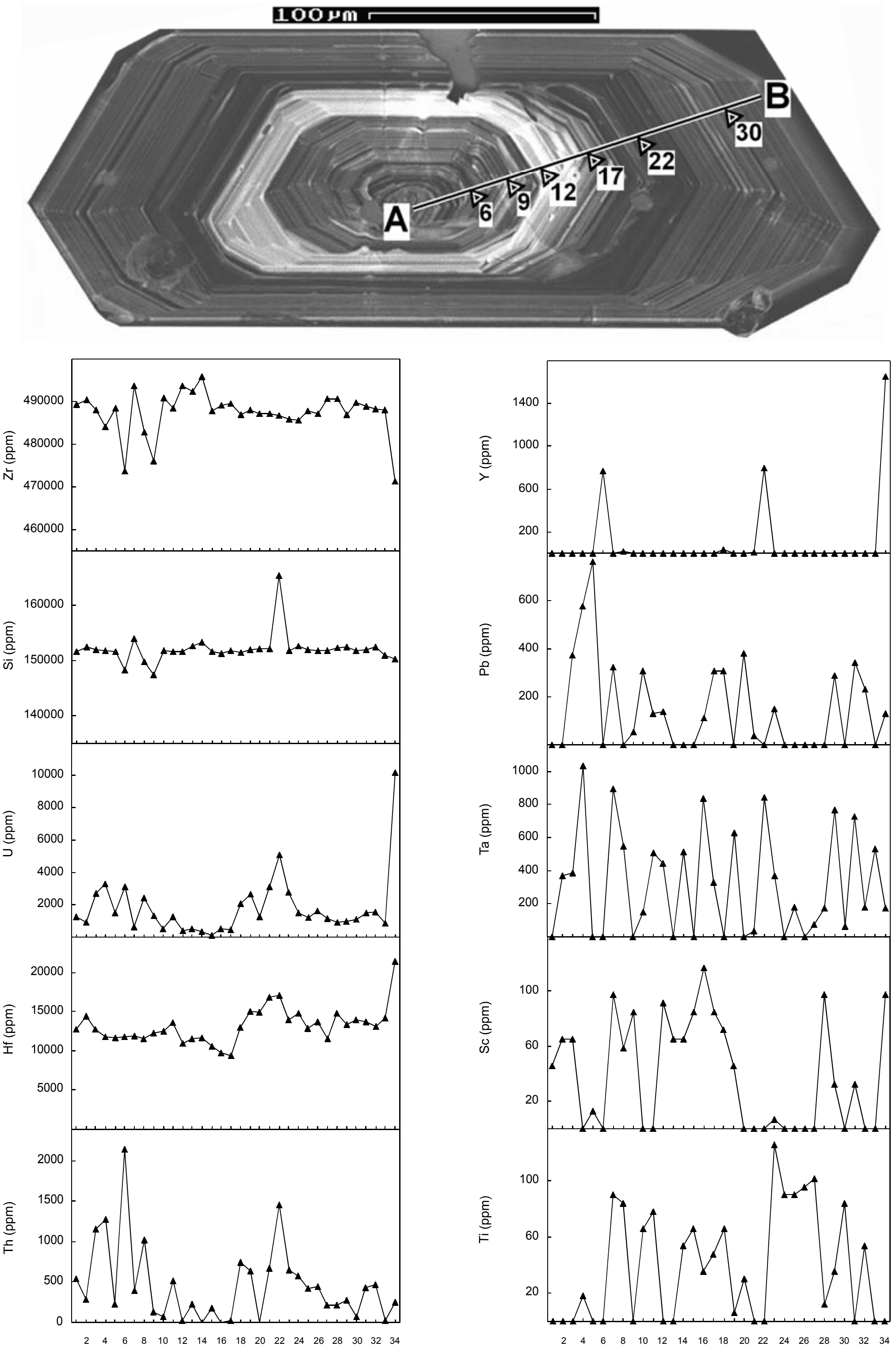

Figure 6.27. Chemical variations within the zircon crystal [Z9(1)] from the Yenişabanlı granitoid (sample SK-9): Numbers on the x-axis of the diagrams denote analyzed points along the line from A to B (in the photograph) with an equal distance.

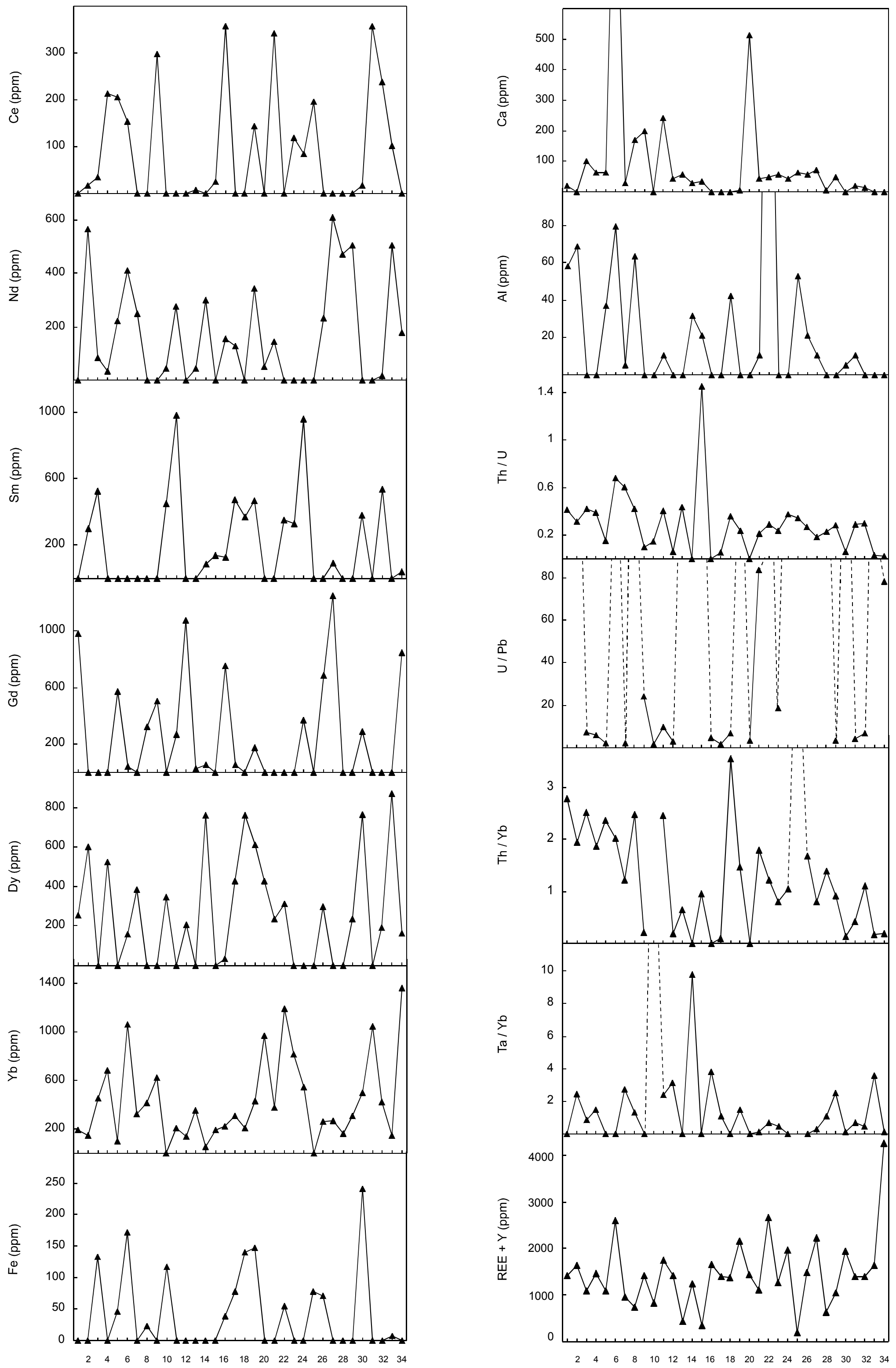

Figure 6.27 (cont'd).

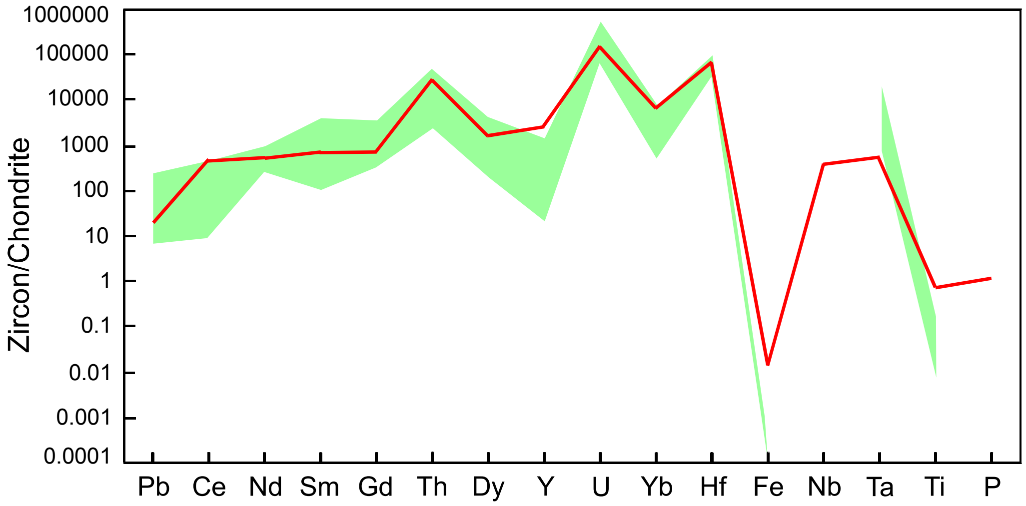

Figure 6.28. Chondrite-normalized trace element abundances of the zircon crystal [Z9(11)] from the Yenişabanlı granitoid (sample SK-9) (shaded area) and the averaged values of zircons from granitoids (solid line) (average of 154 samples; data from Belousova et al., 2002). Chondrite values are from Taylor and McLennan (1985). Zero values are not plotted.

6.3.2.3. Çimkalesi Monzogranite

The chemical characteristics of the zircons from the Çimkalesi monzogranite can be summed up in the following manner:

The zircon crystal [Z12(21)] is marked by median values of 65.64% (±8.18) ZrO_2, 32.81% (±5.37) SiO_2 and 1.45% (±0.23) HfO_2 (Table 6.2). Within the crystal Th/U is 0.04-0.89, Th is 88-4262 ppm, and U is 454-5968 ppm.

Chondrite-normalized trace element abundances of the zircon crystal [Z12(21)] exhibit depletion in Y, Yb, Fe and Ti, and enrichment Ta with respect to abundances in averaged granitic zircons (Belousova et al., 2002) (Figure 6.30).

The elemental profiles drawn for the crystal [Z12(21)] are presented in the Figure 6.31. Point 2 falls onto the titanite inclusion visible on the CL-image. This occasion is also evident from sudden decrease in Zr, beside remarkable increases in Ca, Ti and Si. The core is overgrown by a dark zone of corrosion where Zr and Si decrease, U, Th, Pb and REE+Y increase.

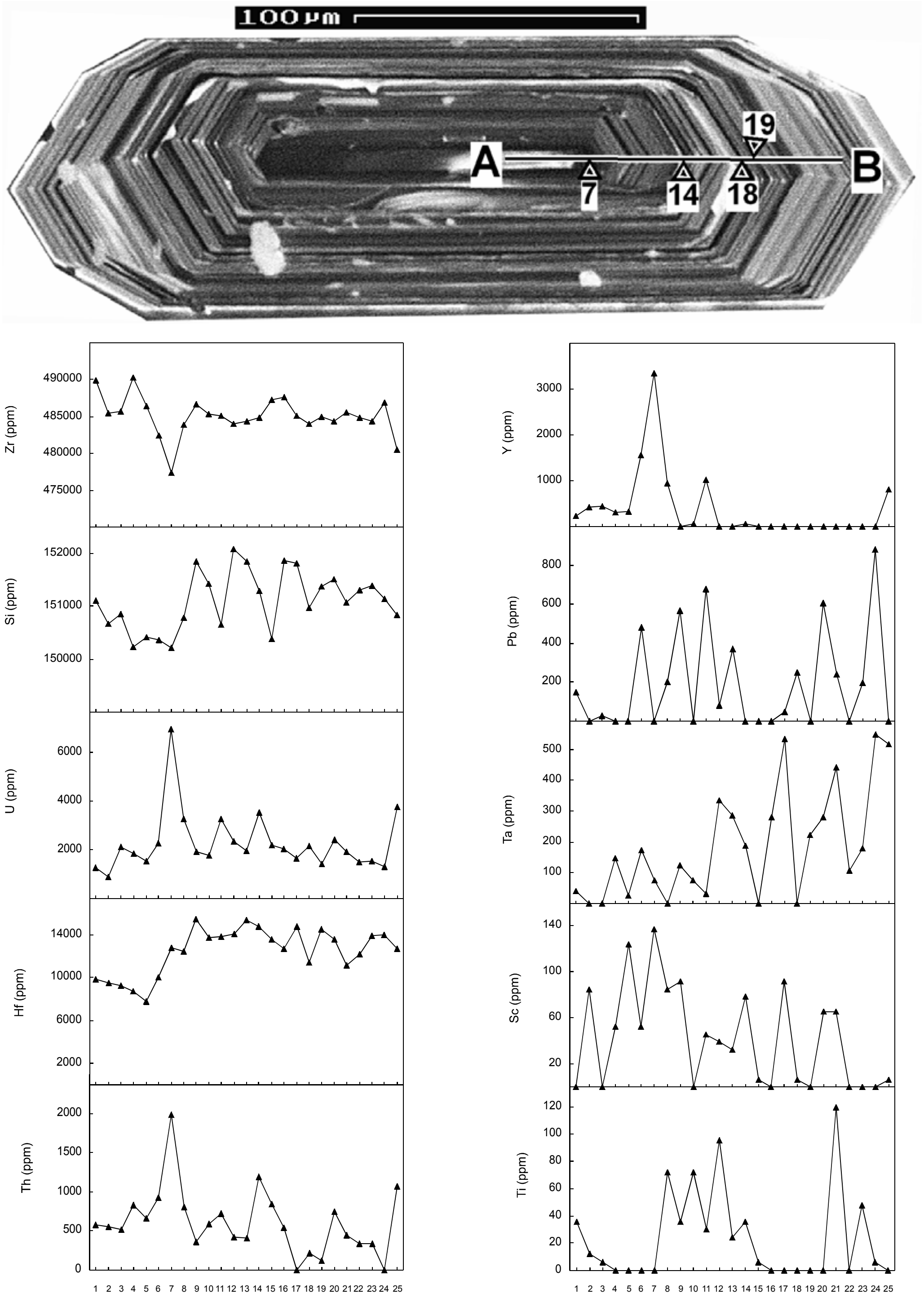

Figure 6.29. Chemical variations within the zircon crystal [Z9(11)] from the Yenişabanlı granitoid (sample SK-9): Numbers on the x-axis of the diagrams denote analyzed points along the line from A to B (in the photograph) with an equal distance.

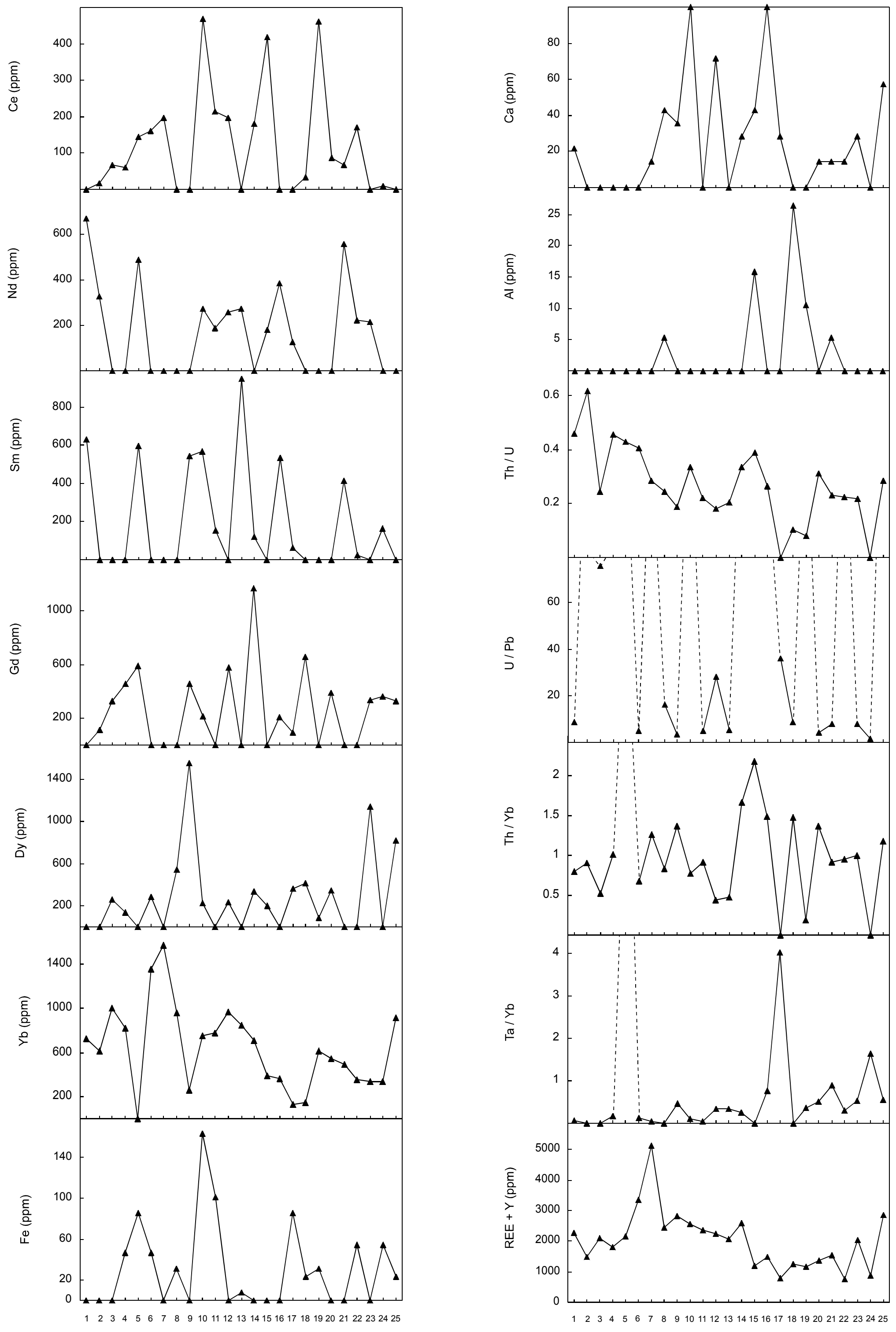

Figure 6.29 (cont'd).

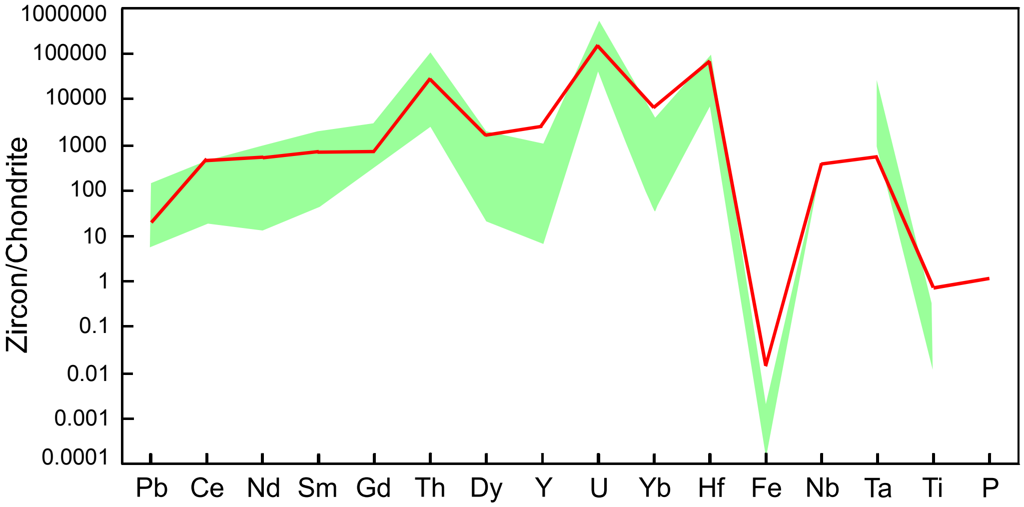

Figure 6.30. Chondrite-normalized trace element abundances of the zircon crystal [Z12(21)] from the Çimkalesi monzogranite (sample SK-12) (shaded area) and the averaged values of zircons from granitoids (solid line) (average of 154 samples; data from Belousova et al., 2002). Chondrite values are from Taylor and McLennan (1985). Zero values are not plotted.

At point 5 (Figure 6.31), Th/U ratio drops off to 0.079. Moreover point 7 is prominent with its low Zr, besides high U, Th, Pb, Sc and REE+Y contents. This point marks the corrosion stage overgrowing the core with low-CL intensity. From C to D (Figure 6.32) oscillation in the elements is observable in the chemical profiles. Point 14, reflecting significant drops in Zr, with increase in U, Th and REE+Y is at one of the thin corrosion zones along the line C-D. Point 22 is on the recrystallized patch within the crystal. Loss of Pb is accompanied by drop in Si, Zr and REE+Y abundances. Additionally at point D near to rim Zr, Si, Th and Th/U decrease, whilst Ca and REE+Y increase.

The zircon crystal [Z12(22)] is represented by median values of 65.70% (±0.27) ZrO_2, 32.26% (±0.23) SiO_2 and 1.41% (±0.12) HfO_2 (Table 6.2). Additionally, [Z12(22)] is characterized by Th/U ratio from 0 to 1.21, and Th abundance of 0-2188 ppm and U abundance of 0-3225 ppm.

Chondrite-normalized trace element patterns of the zircon crystal [Z12(22)] are very similar to those of the other crystal from the Çimkalesi granitoid, i.e. [Z12(21)] (Figure 6.33). Depletion in Y, Yb, Fe and Ti are notable in this crystal, compared with averaged values of Belousova et al. (2002).

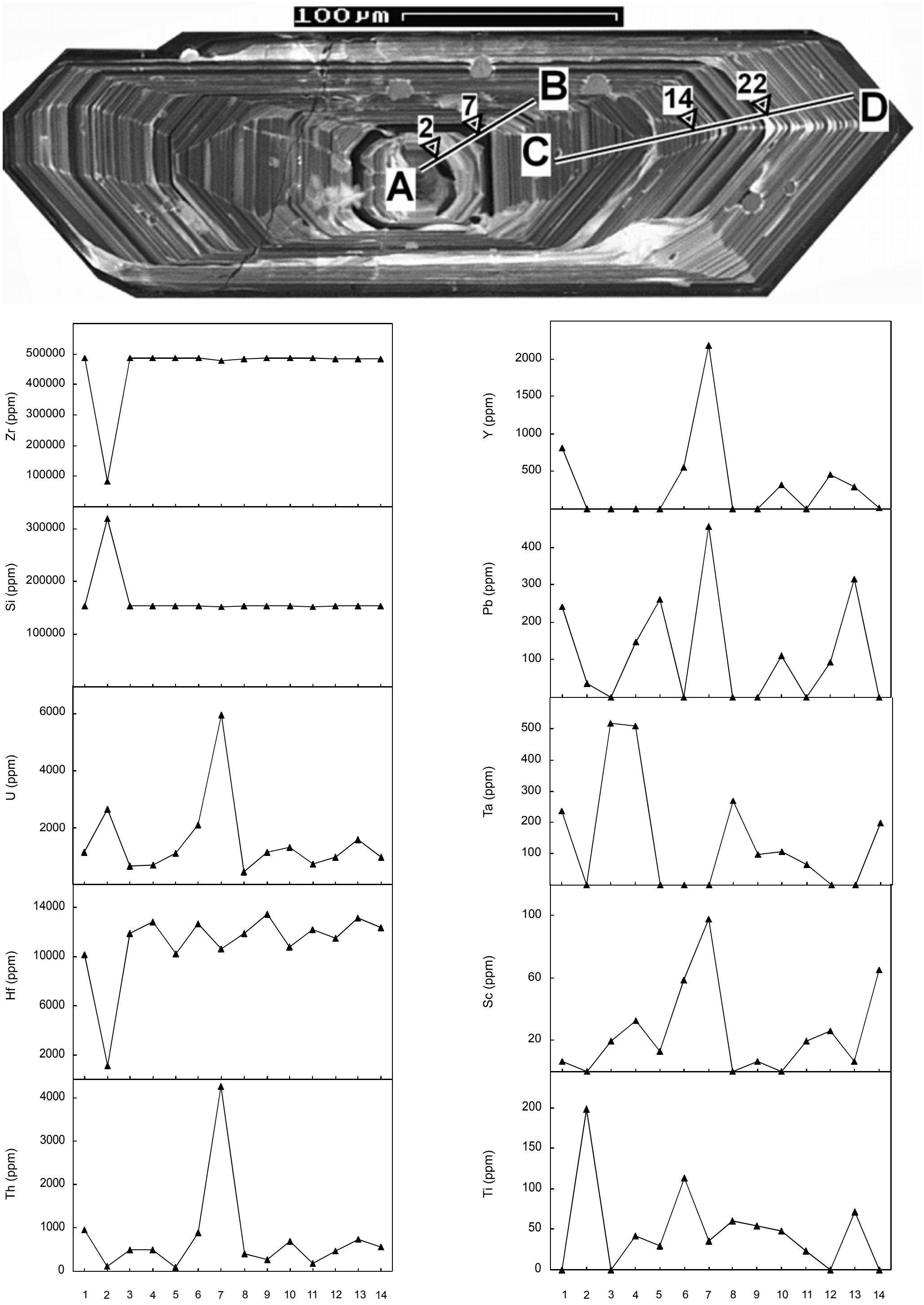

Figure 6.31. Chemical variations within the zircon crystal [Z12(21)] from the Çimkalesi monzogranite (sample SK-12): Numbers on the x-axis of the diagrams denote analyzed points along the line from A to B (in the photograph) with an equal distance.

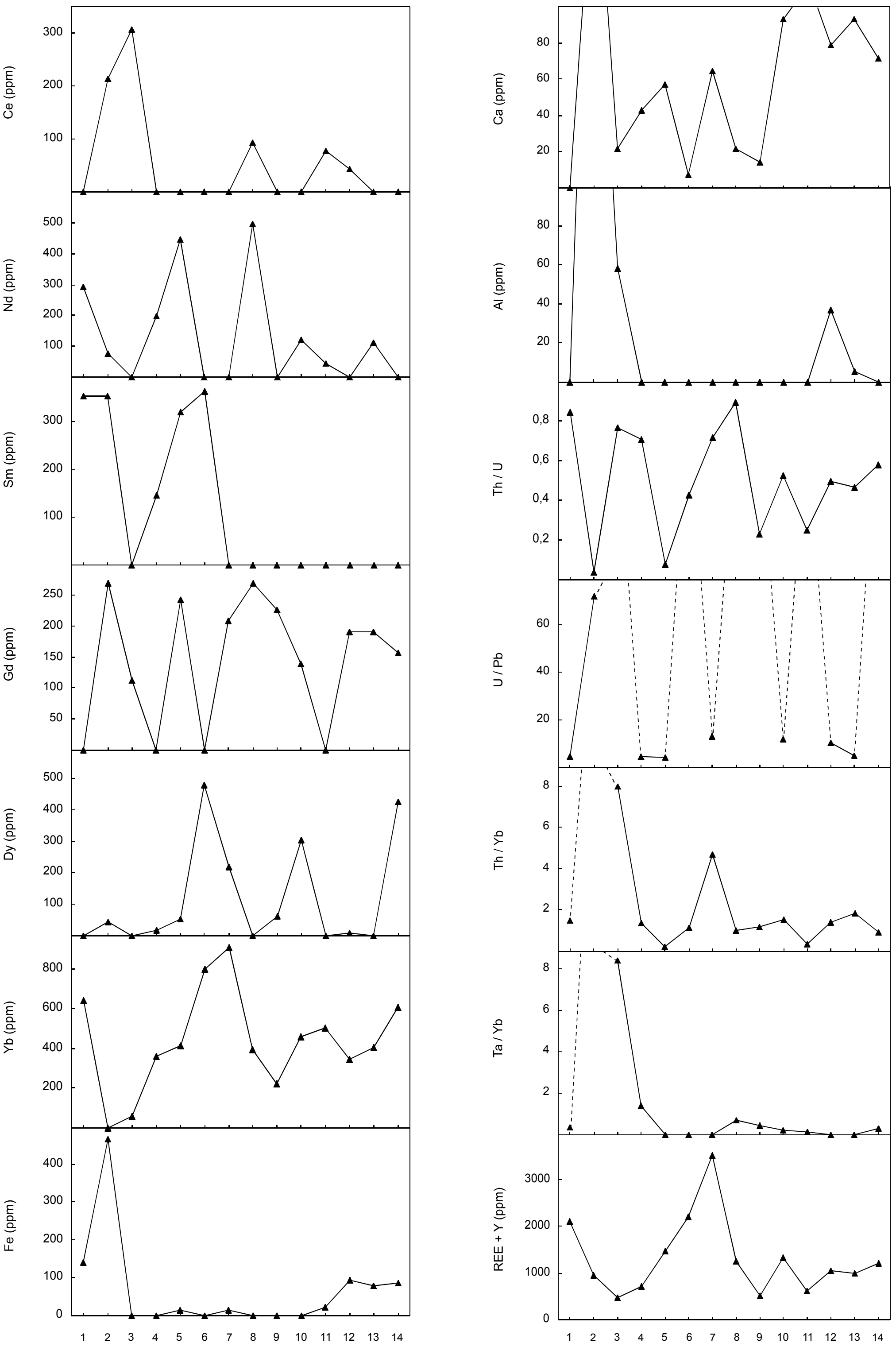

Figure 6.31 (cont'd).

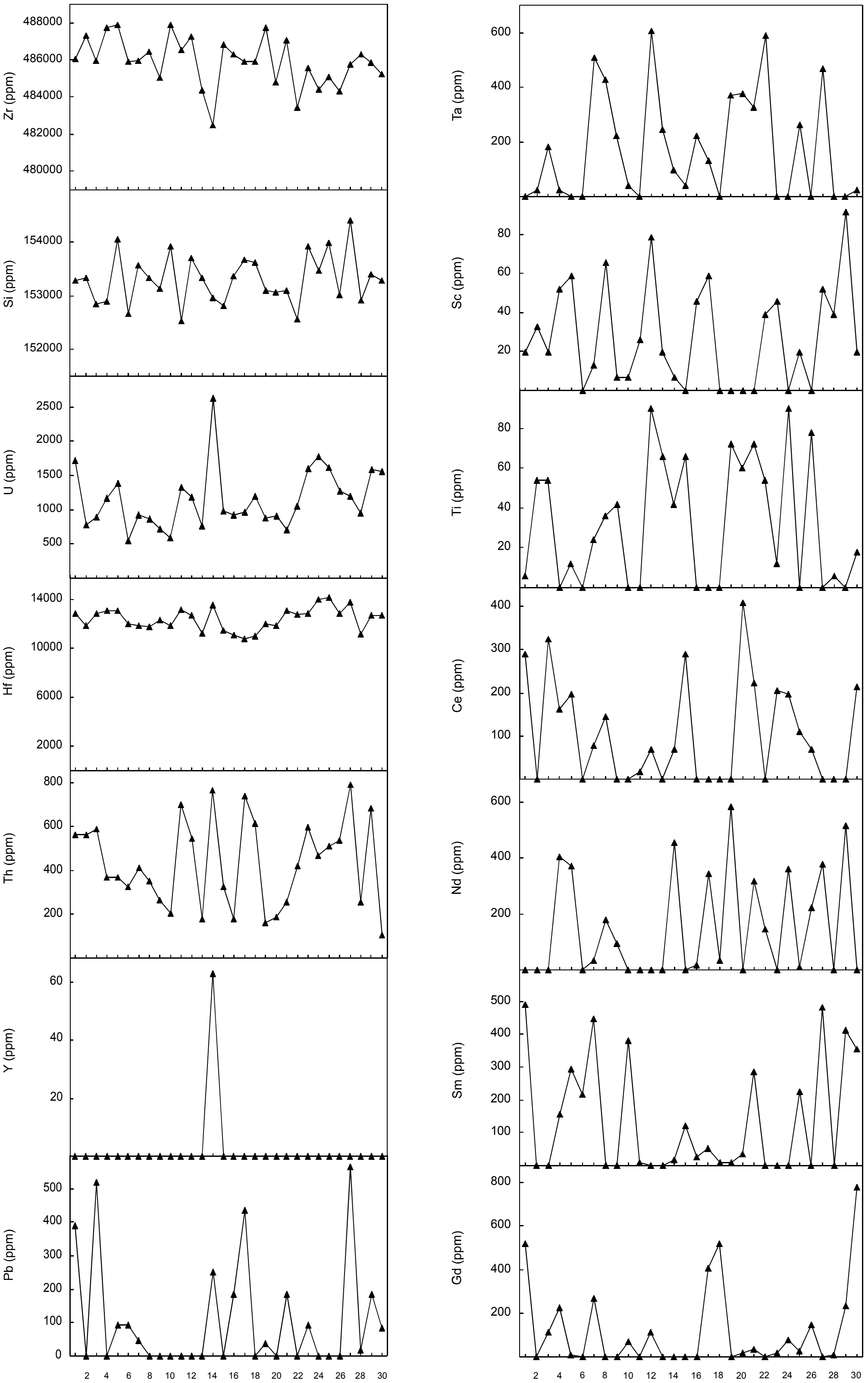

Figure 6.32. Chemical variations within the zircon crystal [Z12(21)] along the line from C to D (see CL-photograph in the Figure 6.31).

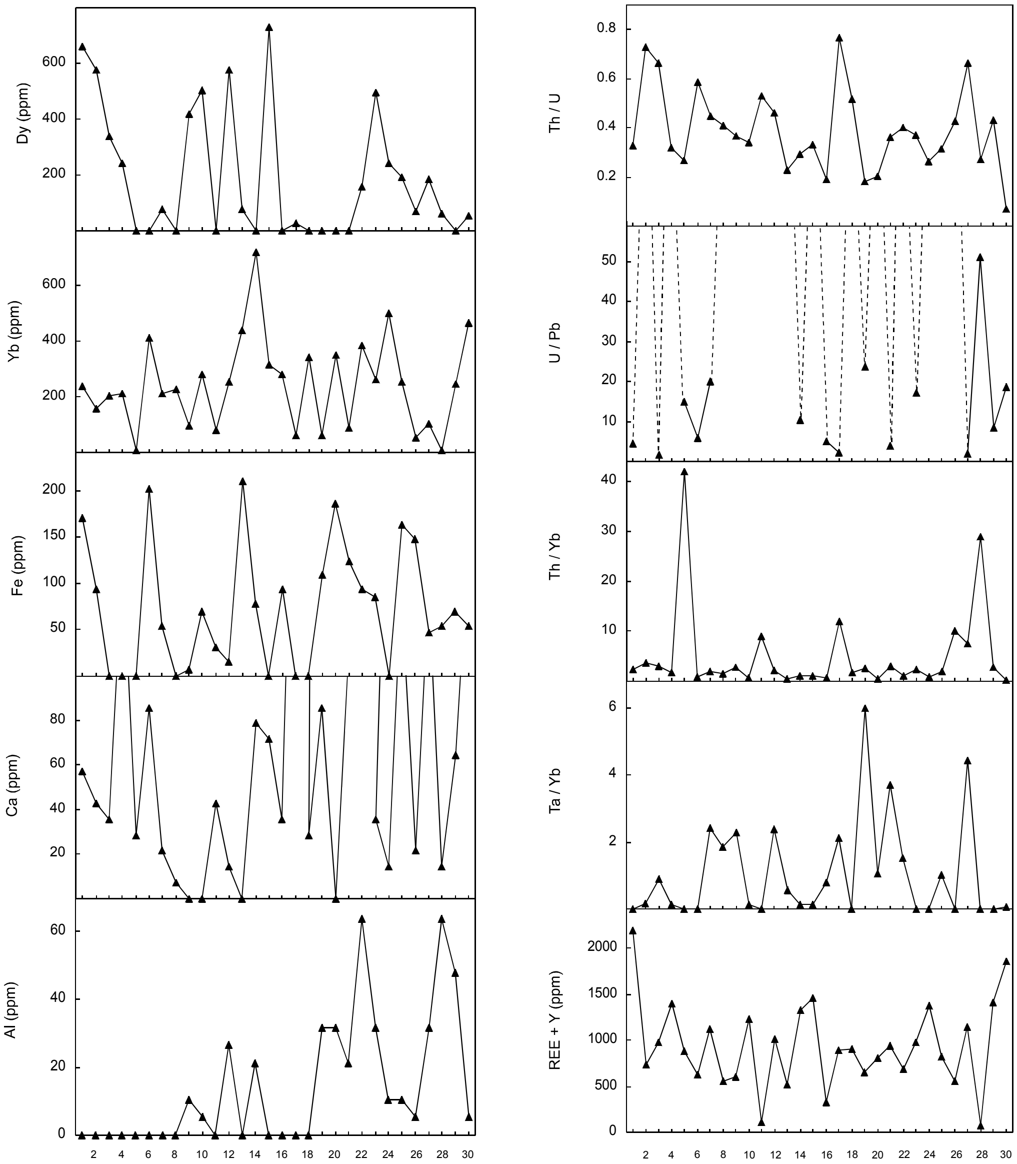

Figure 6.32 (cont’d).

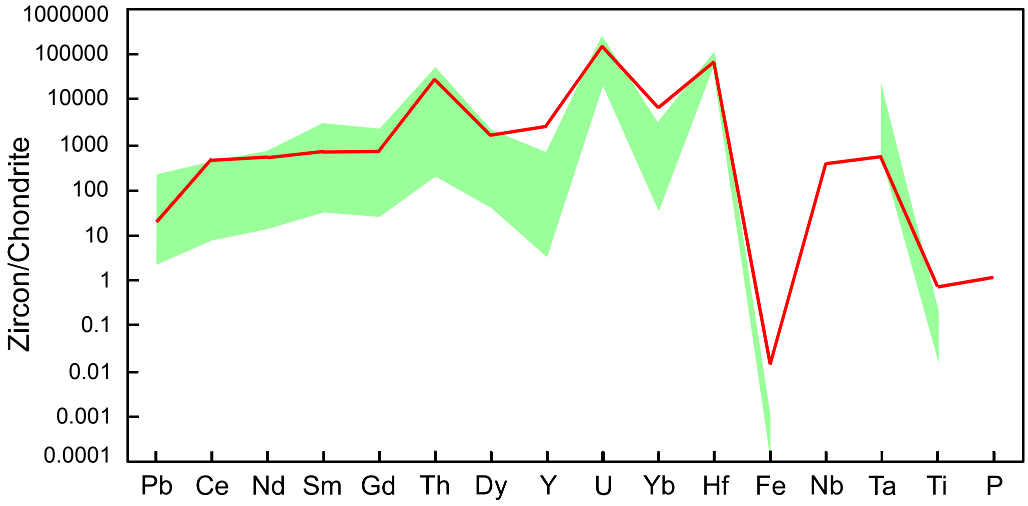

Figure 6.33. Chondrite-normalized trace element abundances of the zircon crystal [Z12(22)] from the Çimkalesi monzogranite (sample SK-12) (shaded area) and the averaged values of zircons from granitoids (solid line) (average of 154 samples; data from Belousova et al., 2002). Chondrite values are from Taylor and McLennan (1985). Zero values are not plotted.

Chemical variation within the zircon crystal [Z12(22)] are given in the Figures 6.34 and 6.35. Point 18 (on the A-B line) is at the rounded interface between the recrystallized and composite core and the overgrowing zones (Figure 6.34). Analysis of this point 18 outcomes sharp decrease in Zr is accompanied by abrupt increase in U, Th and REE+Y. Furthermore, point 20, which is at the corrosion surface, also shows decrease in Zr, besides increase in U and REE+Y. Moreover, point 32 also falls onto the corrosion zone and is marked by drop in Zr, combined with increase in U and Th. At points 12, 17 and 31, which are located on the dark CL zones Th/U ratio is less than 0.1. Through the outer zones decline in Zr and Si abundance is visible, although other elements show no systematic variations disregarding oscillations.

The line C-D passes through the zones of which are also cut by the line A-B (Figures 6.35). For instance, on the line C-D, point 8 falling onto the same zone with point 18 of line A-B, shows decrease in Zr, increase in U, Hf, Th, Sc, Ti and REE+Y. Moreover, Point D, located near to rim, reflects low Zr and Si abundances with high Ca and Al contents.

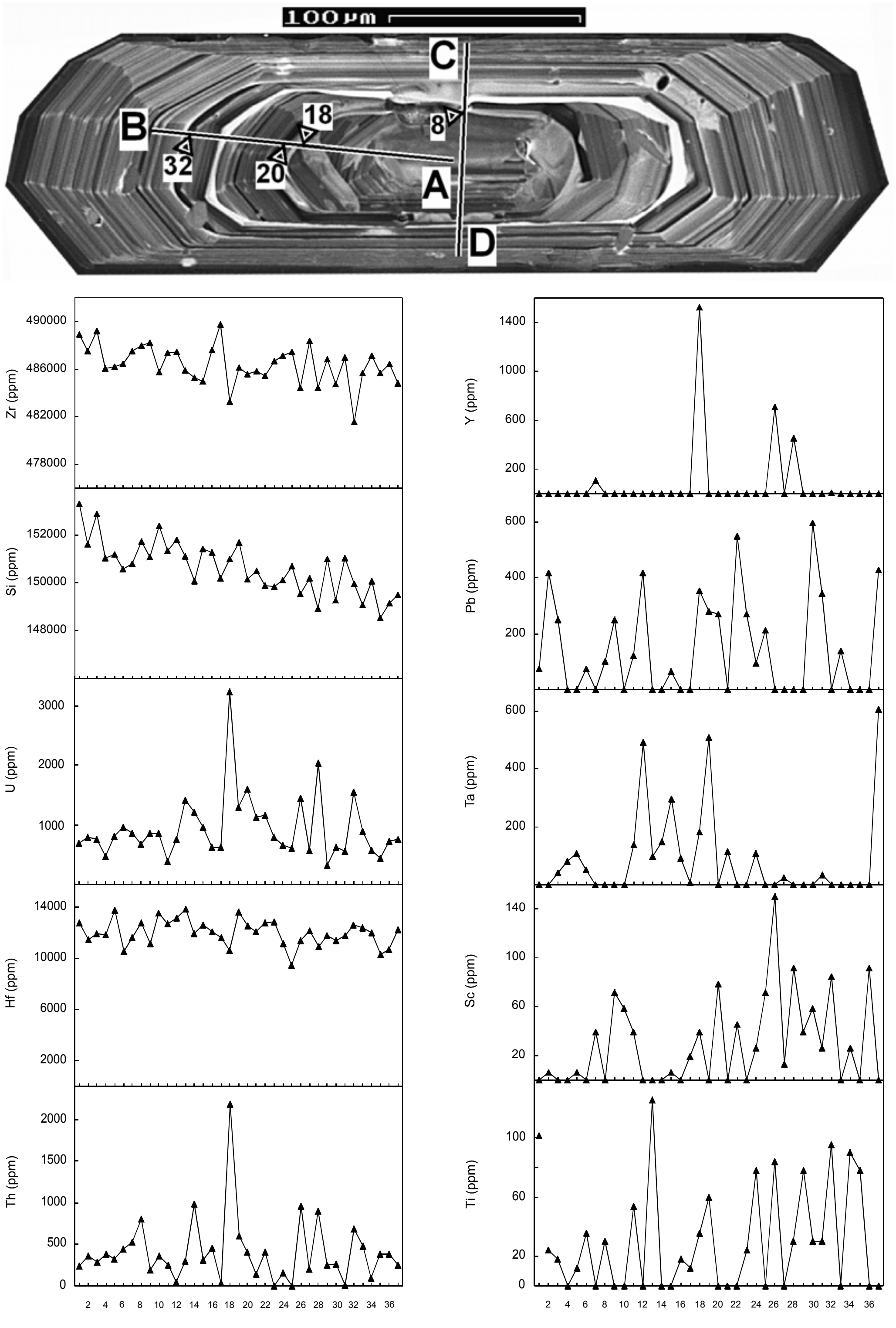

Figure 6.34. Chemical variations within the zircon crystal [Z12(22)] from the Çimkalesi monzogranite (sample SK-12): Numbers on the x-axis of the diagrams denote analyzed points along the line from A to B (in the photograph) with an equal distance.

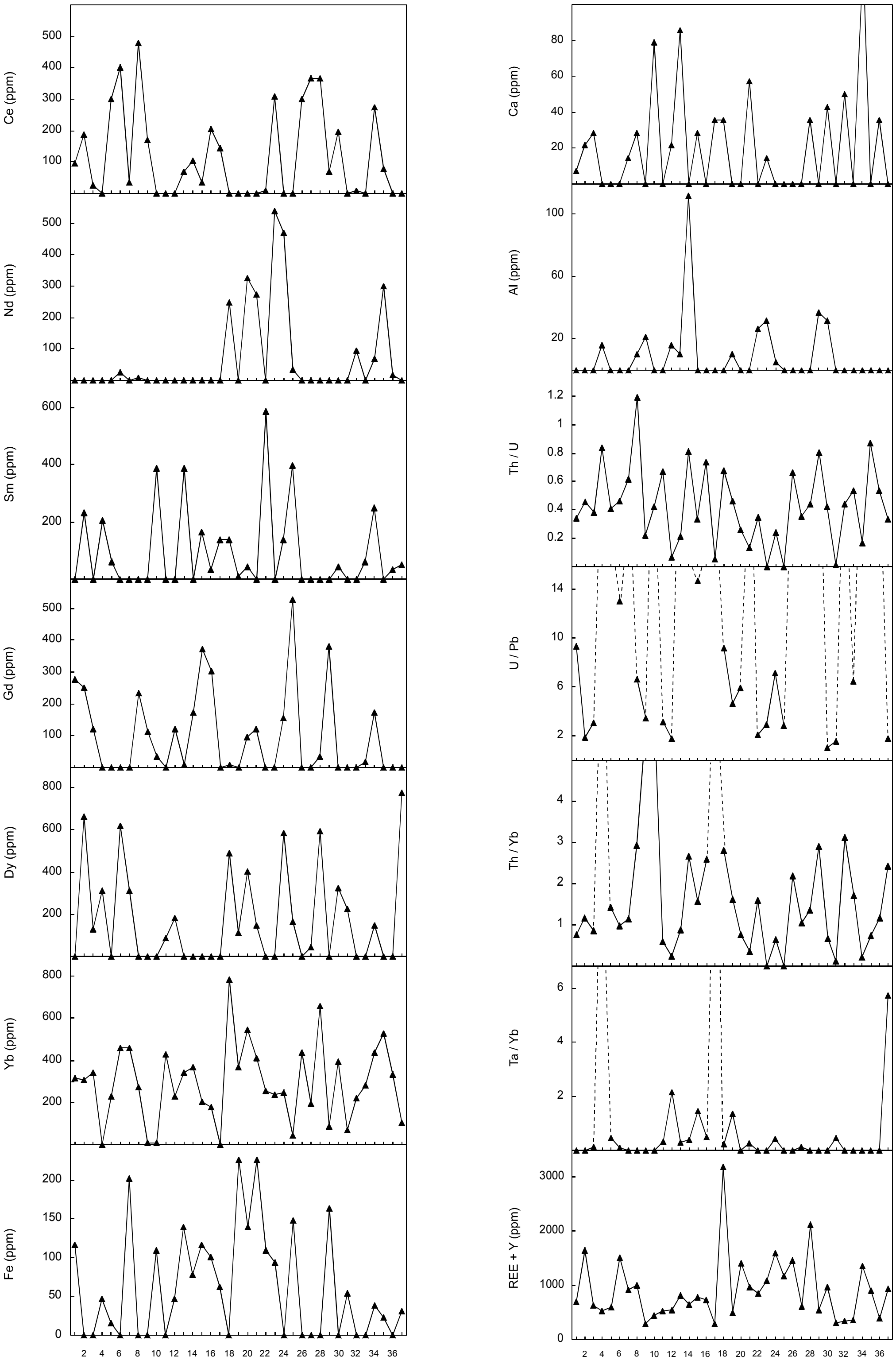

Figure 6.34 (cont'd).

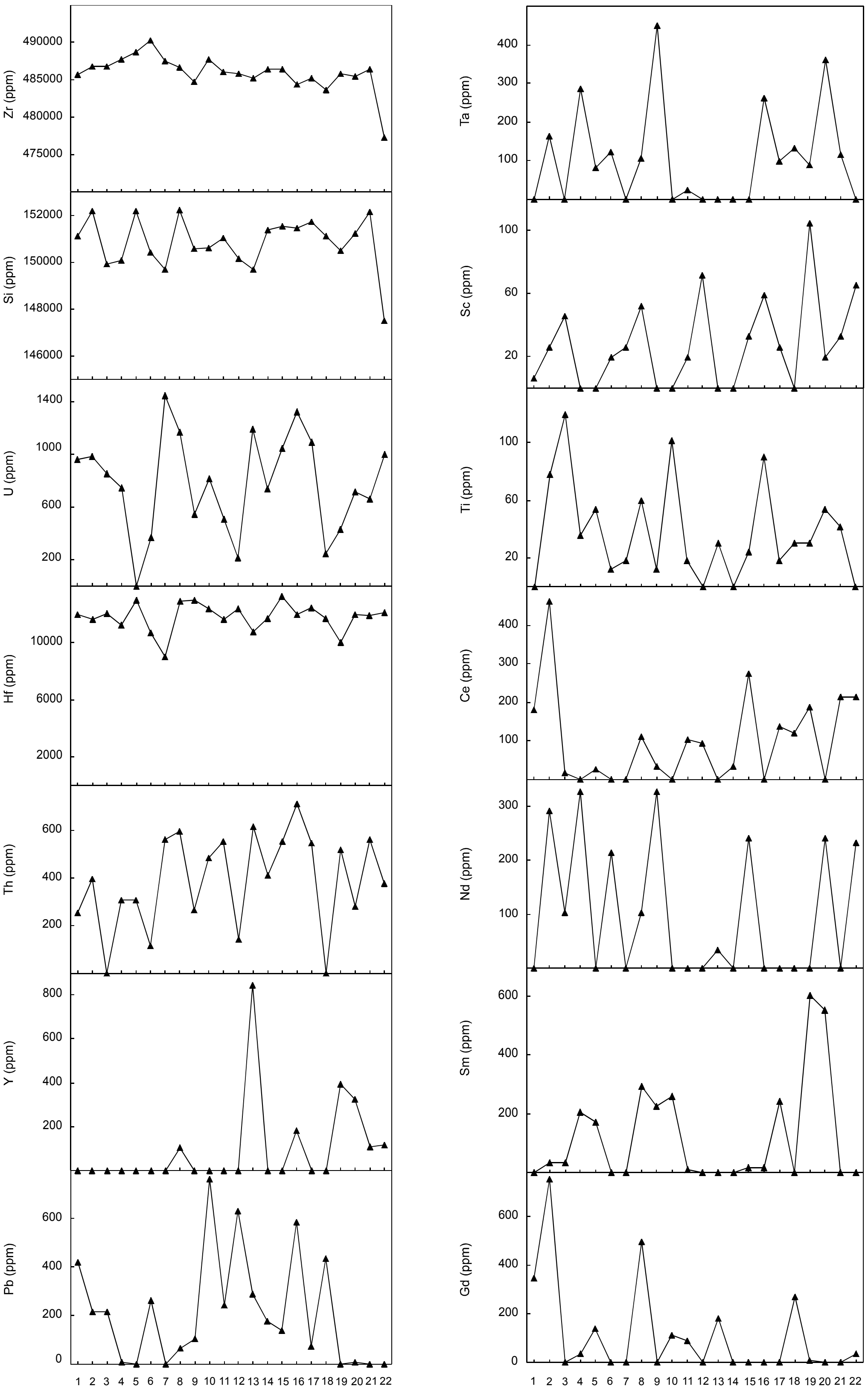

Figure 6.35. Chemical variations within the zircon crystal [Z12(22)] along the line from C to D (see CL-photograph in the Figure 6.34).

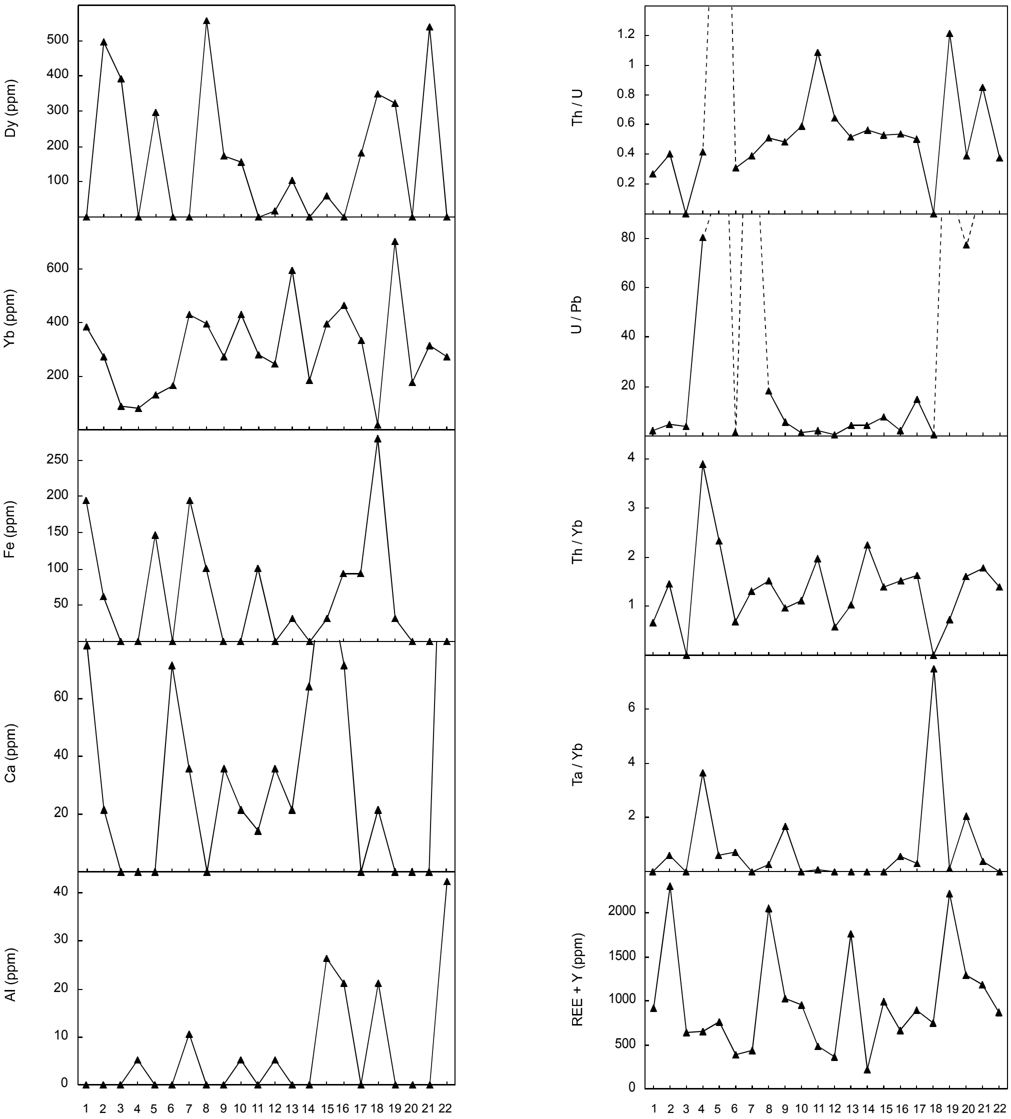

Figure 6.35 (cont'd).

Consequently, chemical data confirm the inferences from the CL images, and provide further evidence that most of the zircons in the scope of this study had a complex history of growth and resorption. Moreover, chemical data combined with the CL images indicate elemental concentrations range widely within zircon crystals.

Evaluated with the CL images, chemical data also show that the high contents of U and Y (also Th and REE in some extent) suppress the CL-intensity, whereas Zr and Si abundances decrease in the dark-CL zones.

CHAPTER 7

DISCUSSION

Zircon growth encompasses a range of processes and characteristics reflecting physical and chemical states of evolving magma. For that reason zircon is a critical mineral in (petrological) studies, particularly of granitoids.

Zircon typology method (cf. Pupin, 1980), based on morphological study regarding prismal and pyramidal proportions of zircon crystals, is a spectacular approach to the zircon growth and its link with the granitoid petrology. This method was applied on a variety of granitoids from distinct tectonic settings and supplied information consistent with the geological and geochemical data (e.g. Pupin, 1980). The present research, in this manner, aimed to investigate zircon crystals from granitoids by the typology method expressed by Pupin (1980).

In the previous studies, the CAG were described in various aspects including field, petrographical, isotopic and whole-rock geochemical characteristics. Apart from these studies mineralogical studies on the granitoids from the CACC are very limited. Zircon, in spite of being a key mineral for granitoid petrology, has not been a subject of the studies on the CAG. This phenomenon was the triggering point for selecting the CACC granitoids as a case study in the present research.

In the scope of this research, zircons, enriched and purified from the granitoids within the CACC, were studied. The granitoid samples were selected from the Ekecikdağ, Ağaçören and Terlemez plutons within the western part of the CACC, because they were well-studied by various authors (e.g. Türeli, 1991; Göncüoğlu and Türeli, 1993, 1994; Kadıoğlu, 1996; Güleç, 1994; Güleç and Kadıoğlu, 1998; Kadıoğlu et al., 2003; Yalınız, 1996, Yalınız et al., 1999) and their field, petrographical, isotopic and whole-rock geochemical characteristics were presented in detail. In this manner, it was possible to discuss the data obtained from zircon crystals in comparison with the existing knowledge.

Zircon crystals were examined under binocular microscope and SEM, and their morphological characteristics are presented in Chapter 4. On the "Typology Diagram" of Pupin (1980), distribution of the zircon types and typological evolutionary trends are determined. The results of the typology study are discussed below, but essential information obtained from this study was that the zircon investigation solely depending on the morphology of the crystals would not be adequate for evaluation of the petrology of granitoids and not capable of providing data about the evolving magma.

As a consequence, zircon intracrystalline features are examined by CL-imaging to reveal the growth histories of the studied zircons (Chapter 5). CL-imaging provided significant information on the internal features (e.g. zoning, inherent cores, overgrowths, resorption surfaces) and their relation with morphological features of zircons. Delineation of the development of crystal faces and internal structures gives data not only about the evolution of zircon crystals but also of host granitoids.

Zircon typology and CL studies supplied valuable information on the zircon crystals. However, to better constrain the growth mechanisms and evolutionary histories of zircons and thus granitoids, supplementary chemical data were crucially necessary. Hence, EMP analyses were performed along traverses through selected zircon crystals and chemical characteristics of zircons were presented in Chapter 6. In this way, chemical characteristics of the zircon crystals and their variation throughout the growth history could be evaluated. Naturally, chemical data obtained from zircon crystals are reflection of the chemical state of granitoids in different episodes and therefore provide basis for petrological interpretation of the CAG concerned.

Moreover, field, petrographic and whole-rock geochemical properties of the granitoids concerned are studied (Chapter 3) to combine the results with the information obtained from the zircon studies.

Consequently, the present research intended to characterize zircons considering their morphologies, internal structures and chemical features, and to provide new insights into the petrology of the granitoids from the CACC.

7.1. Petrography and Whole-Rock Geochemistry

In the present research, field and petrographical indications and whole-rock geochemical studies combined with evidences of previous work suggest that the Kalebalta and Hisarkaya granitoids are of S-type granitoids, whereas others (Borucu, Sinandı, Namlıkışla, Yenişabanlı, Sipahiler, Torunobası, Camili, Çimkalesi and Terlemez) can be defined as H-type granitoids.

H-type granitoids commonly found as intruding to both metamorphic rocks and gabbros from the ophiolitic rocks that were overthrusted the metamorphic rocks (e.g. Türeli, 1991), however occurrence of gabbroic rocks cutting granitoids is also suggested by some authors (e.g. Kadıoğlu et al, 1998, 2003). Furthermore, H- and S-type granitoids do not show clear-cut relationships in between within the studied areas.

Petrographically, H- and S-type granitoids are composed mainly of quartz, orthoclase, plagioclase, biotite (+muscovite in S-type granitoids) ± hornblende ± microcline, besides accessory phases of opaques, zircon ± titanite ± allanite ± apatite (Figures 3.1 and 3.3). Zircon is commonly found as associated with biotite (Figure 3.5), however contemporaneous growth of zircon and allanite (Figure 3.4b), and inclusions of zircon in quartz, orthoclase and plagioclase are also observed.

H-type granitoids concerned consist abundant mafic microgranular enclaves that are elliptical to spherical with sharp contact to their host and finer grained than their host rock (Figure 3.2). Besides mafic microgranular enclaves, K-feldspar megacrysts and abundance of mafic minerals (with hornblende>biotite) are common features in the H-type CAG. These characteristics represent that magma mingling/ mixing processes were evident in the evolution of these granitoids (Didier and Barbarin, 1991). Moreover, the relative proportion of mantle and crustal components, as constrained from the Sr-isotope data, exceeds the limits for complete hybridization, but infers incomplete mixing (commingling) of mafic and felsic magmas (Güleç and Kadıoğlu, 1998).

H-type granitoids have calc-alkaline metaluminous to peraluminous characters, whereas, S-type granitoids exhibit calc-alkaline peraluminous features (Table 7.1 and Figure 3.7). H- and S-type granitoids exhibit geochemical trends discrete from each other on the Harker diagrams (Figure 3.8). Chondrite-normalized REE patterns of the H- and S-type have granitoids steep LREE-enriched and almost flat HREE patterns, where H-type granitoids show LREE enrichment and HREE depletion with respect to S-type ones (Figure 3.11).

In brief, H- and S-type granitoids from the Ekecikdağ, Ağaçören and Terlemez areas geochemically differ in: (1) the S-type granitoids are more depleted in Sr, Ba, Zr, Ti, LREE, and more enriched in Rb, Nb, HREE (Figures 3.9 and 3.11), (2) the S-type granitoids have variable and larger negative Eu anomalies than the H-type granitoids (Figure 3.11 and Table 7.1), (3) the S-type granitoids have lower LREE/HREE ratios (e.g. Rb/Nb). Distinct geochemical trends observed between H- and S-type granitoids in Harker plots, also recognizable in the normalized multi-element and REE patterns, and element/element ratio plots (e.g. Figure 3.13).

Depending on these features, it is reasonable to assume that the H- and S-type CAG formed from different magma sources, i.e. they were not produced by fractional crystallization from a single magma source, or formed in different tectonic environments that affect their source characteristics. S-type granitoids of the CACC represent the collision stage, whereas H-type granitoids having enriched and hybridized mantle sources modified by subduction-related component characterize the post-collision period (Table 7.1).

Table 7.1. Summary of the geochemical characteristics of the H- and S-type granitoids from the Ekecikdağ, Ağaçören and Terlemez plutons.

GRANITOID	**General Character**	**Relative Enrichment**	**Eu-anomaly**	**Tectonic Setting**
H-TYPE (Borucu, Sinandı, Namlıkışla, Yenişabanlı, Sipahiler, Torunobası, Camili, Çimkalesi and Terlemez granitoids)	Calc-alkaline, metalumious to peraluminous	LILE, LREE	0.39-0.69	Post-collision
S-TYPE (Kalebalta and Hisarkaya granitoids)	Calc-alkaline, peraluminous	HFSE	0.12-0.52	Syn-collision

7.2. Studies on Zircons

Zircon is an early crystallizing mineral in magma, hence it reflects the properties of the magma in formation and crystallization stages, and prevents these characteristics superior than the other minerals. For that reason the origin and petrogenesis of the CAG were intended to explain by investigation of zircon, besides petrography and whole-rock geochemistry.

In the scope of this research, totally 3001 zircon crystals were examined under microscope, 295 of them were imaged by SEM and 138 of them were imaged by CL. EMP analysis were conducted on 14 zircon crystals at ca. 400 points.

7.2.1. Zircon Typology: Pupin's Method

Studies on crystal habits of zircon provide an approach to detailed petrogenetic investigation of the granitic rocks. Pupin (1980)'s zircon typology in this respect is an important method for identifying zircon populations and their growth histories. Examination of main zircon types of P, S and G, besides some minor types, e.g. J, L, K, gives way to enlighten the petrogenesis of granitoids. Zircon typology method (Pupin, 1980) based on the morphological research of zircon crystals was applied to the CAG (Chapter 4 and Table 7.2).

Zircon crystals of the Kalebalta and Hisarkaya granitoids (within Ekecikdağ pluton) show overgrowths and epitaxial growths (e.g. Figures 4.19, 4.20, 4.21) implying their autochthonous (Group 1 of Pupin, 1980) nature, although they resemble hybrid type in terms of crystal habits and typologic evolution trends (Group 4 or 5 of Pupin, 1980). Therefore, these granitoids are described as autochthonous granitoids, even though the zircon types do not fit with the Pupin (1980)'s classification. Additionally, the Kalebalta and Hisarkaya granitoids show similarities in mineral content and petrographical textures to the well-defined examples of Group 1 granitoids (e.g. Echassiéres, Villeret from the French Central Massif, Pupin, 1980), which are hyperaluminous granitoids commonly called as intrusive aluminous leucogranites. Autochthonous nature of the Kalebalta and Hisarkaya granitoids is also consistent with S-type description based on petrography and geochemistry discussed in Chapter 3.

Borucu and Sinandı granitoids from Ekecikdağ pluton and other granitoids from the Ağaçören (excluding Namlıkışla granitoid) and Terlemez suites are differentiated into the Group 4 of Pupin (1980), i.e. hybrid granitoids, considering their zircon morphologies and typologic evolution trends (e.g. Figure 4.4 to 4.11, and Figures 4.50 to 4.81). This interpretation coincides with the field, petrographical and whole-rock geochemical indications revealing hybridization processes within the evolution of these granitoids.

Most of the Group 4 granitoids belong to 4b stock of Pupin (1980)'s classification (i.e. Borucu, Sinandı, Sipahiler, Torunobası, Camili and Terlemez granitoids), except for Yenişabanlı and Çimkalesi, which are of stock 4c type. Group 4 granitoids are expressed as calc-alkaline series granites (within the chief group of "granites of crustal+mantle origin-hybrid granites") by Pupin (1980). The H-type CAG are comparable to other hybrid granitoids from the world (e.g. Monte Capanne monzogranite in Elba and Pont-de-Montvert monzogranite from the French Central Massif, Pupin, 1980), not only in terms of zircon typology but also petrographical and geochemical characteristics (mineral content, presence of mafic enclaves, calc-alkaline nature etc.).

Namlıkışla granitoid on the other hand is of Group 3 type (cf. Pupin, 1980) representing intrusive aluminous monzogranites and granodiorites (Figures 4.42 to 4.49). Namlıkışla granitoid have petrographical and geochemical features similar to those of well-described Group 3 granitoids (e.g. La Souterraine, Margeride, Tournon from the French Central Massif; Pupin, 1980). Namlıkışla granitoid includes basic microgranular xenoliths, although in lesser amounts than the Group 4 granitoids (i.e. Borucu, Terlemez, etc.), contrary to the Group 1 granitoids (i.e. Kalebalta and Hisarkaya). Having restricted amount of basic microgranular xenoliths is a characteristic feature of Group 3 granitoids (e.g. Pupin, 1980).

Table 7.2. Summary of the zircon typology (cf. Pupin, 1980) study of the Ekecikdağ, Ağaçören and Terlemez plutons.

GRANITOID	**n***	**Zircon types**	**Typological classification**
H-TYPE			
Borucu (SK-1)	584	$S_{18-19-23-24-12-13-5-10}$ P_{1-2-3} G_{1}	Hybrid Group 4(b)
Sinandı (SK-6)	57	$S_{7-12-13-18}$ $S_{2-9-10-17-19-23-24}$	Hybrid Group 4(b)
Namlıkışla (SK-8)	312	$S_{1-2-3-4-5-6-7-8-11-12-13-16}$ $L_{1-2-3-4-5}$	Autochthonous-Hybrid Group 3
Yenişabanlı (SK-9)	214	$S_{9-10-13-14-15-18-19-20}$ P_{2-3-4}	Hybrid Group 4(c)
Sipahiler (SK-10)	212	G_{1} P_{1-2-3} $S_{5-8-9-10-13-14}$	Hybrid Group 4(b)
Torunobası (SK-11a)	104	$S_{4-5-7-8-9-10-12-13-14-15-17-18-19-23-24}$ G_{1}	Hybrid Group 4(b)
Camili (SK-11b)	103	$S_{12-13-17-18-19-22-23-24}$ J_{3-4}	Hybrid Group 4(b)
Çimkalesi (SK-12)	352	$S_{13-17-18-19-20-22-23-24-25}$ J_{3-4-5}	Hybrid Group 4(c)
Terlemez (SK-7)	223	$S_{13-18-19-20-23-24-25}$	Hybrid Group 4(b)
S-TYPE			
Kalebalta (SK-3)	230	G_{1-3} $P_{1-2-3-4}$ $S_{5-10-13-14-15-20}$	Autochthonous Group 1
Hisarkaya (SK-4, 5)	610	$P_{1-2-3-4}$ G_{1-2-3} $S_{4-5-7-9-10-11-12-13-14-15-19-20}$	Autochthonous Group 1

* number of crystals examined

Although they are not observed in this study, zircons from the A-type CAG illustrating the morphological characteristics of alkaline zircons (Group 6 of Pupin, 1980) were also reported (e.g. Köksal et al., 2004b).

7.2.2. Cathodoluminescence Studies

Present research confirmed the validity of Pupin's method to the CAG, except for S-type granitoids (i.e. Kalebalta and Hisarkaya). Alternatively, autochthonous nature of S-type granitoids verified from the additional structures as epitaxial growths. On the other hand, hybridic origin, revealed by geologic and geochemical aspects, of the studied H-type CAG is supported by this method.

However, ongoing discussion infers that the crystallographic features of zircon crystals only reflect the latest stages of granitoid evolution. According to Vavra (1990), Pupin (1980)'s model, assuming that prismal and pyramidal proportions are controlled independently from each other by external conditions, is in contradiction to a kinematic consideration of crystal growth. Additionally, Vavra (1990) stated that the growth-rate of a single prism form ({110} or {100}) should have effects on the proportions of pyramidal forms besides proportions of prism forms so that it was not possible to discuss the evolution of prisms and pyramids independently. Kinetic factors known to control the growth rates of individual crystal faces are supersaturation, diffusion rates, and adsorption of foreign particles (e.g. Vavra, 1993). Vavra (1993) further indicated that the growth rates are immediately controlled by the environmental conditions at any instant, whereas crystal morphology is only the final result from the integration of variable growth rates during previous growth, which may have proceeded in a changing crystallization environment.

Taking into account of this interpretation, the present study is directed to search the internal structures of zircons and to acquire detailed data and combine with the typological results. CL imaging in this manner provides in-depth investigation of the zircon crystals.

CL studies on the granitoids of the CACC disclose that morphology may not be permanent throughout the crystal growth history. It may change from one typological type to another, e.g. from P to S. Likewise a crystal face that is typical for one type may disappear via center to rim, or vice versa. For instance in the crystals [Z4(6)] (Figure 5.13) and [Z10(2)] (Figure 5.33) {121}-pyramid is prominent in the inner parts, however, it disappears in the final shape. Furthermore, two crystals [Z4(1)] (Figure 5.12) and [Z4(10)] (Figure 5.16), very distinct concerning their internal structures, are very similar in their outer morphologies. On the other hand, in some CL-images, it is determined that a crystal was broken and new growth proceeded on the broken crystal (e.g. [Z7(8)] in Figure 5.51). Therefore it is not relevant to define a given zircon crystal by only considering its outer morphology.

Investigation of internal structures of the CACC granitoid zircons showed that they generally include euhedral to subhedral cores exhibiting zoning, although sometimes faint, but inherent and embayed cores also exist (Table 7.3). Studied zircons reveal either (1) large scale, first order, and/or small-scale second order oscillatory zoning parallel the major prism faces ({100}, {110}) and pyramidal faces ({101}, {211}) representing magmatic growth zonations, which should incorporate changing relative proportions of minor and trace elements (i.e. Hf, U, Th, Y, REE, Pb, P) in the crystal lattice (e.g. Vavra, 1990, 1993; Benisek and Finger, 1993) or (2) small-scale oscillatory zoning, which can be explained by self-organizational crystallization (e.g. Mattinson et al., 1996).

Revealed from CL-imaging, zircons from the CAG were subjected to intense corrosion, which is distinguishable by remarkable dissolution surfaces around small cores or cores with instantaneously surrounding zones (e.g. Çimkalesi granitoid in Figure 5.40). These resorption surfaces combined with sharp transition in zoning probably characterize an abrupt change in the growth history. Generally zoning develops from these resorption surfaces up to another pronounced corrosion event. Afterwards, crystals show new cycle of zoning/oscillatory zoning with minor interspersed corrosion events up to rims.

Incorporation of cations such as Na, K and Al, and impurity elements like U, Th, Y, P and REE leads to the differential growth rates of the crystal faces (e.g. Vavra, 1994). Zircon rims in the studied samples generally showing low-CL are characterized by reduced growth rate of {010} prism and growth inhibition of {110} prism, which may indicate low Zr-supersaturation and enrichment of H_2O in the growth medium at the latest stages of evolution (e.g.

Vavra, 1994). Additionally, increased concentration of impurity elements like U, Th, Y, P and REEs results in the drop in CL intensity and growth units dramatically change the morphological evolution of the studied crystals (e.g. Vavra, 1994).

Besides evaluation of development of crystal faces and zoning, more detailed information can be obtained from the CL-imaging. For instance, individual crystals may have unique properties distinguishable only in the CL-images, such as inherited cores (e.g. [Z3(18)] in Figure 5.9; [Z4(6)] in Figure 5.13), multiple cores (e.g. igneous clustering: [Z3(16)] in Figures 5.8 and 7.1a), metamictization (e.g. [Z8(20)] in Figure 5.25; [Z11a(10)] in Figure 5.37), inclusions (e.g. [Z12(21)] in Figures 5.44 and 7.1b), etc.

Moreover, formation of a distinct sector zoning is observed in some of the crystals (e.g. [Z3(4)] in Figure 5.5; [Z12(18)] in Figure 5.43). Furthermore, patchy zircon domains and flow structures, usually interpreted as signifying partial recrystallization and/or redistribution of elements, most probably during metamorphic overprinting at moderate to high temperatures (e.g. Vavra, 1990, 1993; Pidgeon, 1992; Benisek and Finger, 1993) are the case for some crystals (e.g. [Z12(26)] in Figure 5.46; [Z8(18)] in Figure 5.24). Additionally, some of the studied crystals exhibit metamictized cores surrounded by growth zoning, owing to interpretation that these crystals undergone metamictization before they were enclosed by the host magma (e.g. [Z8(20)] in Figure 5.25).

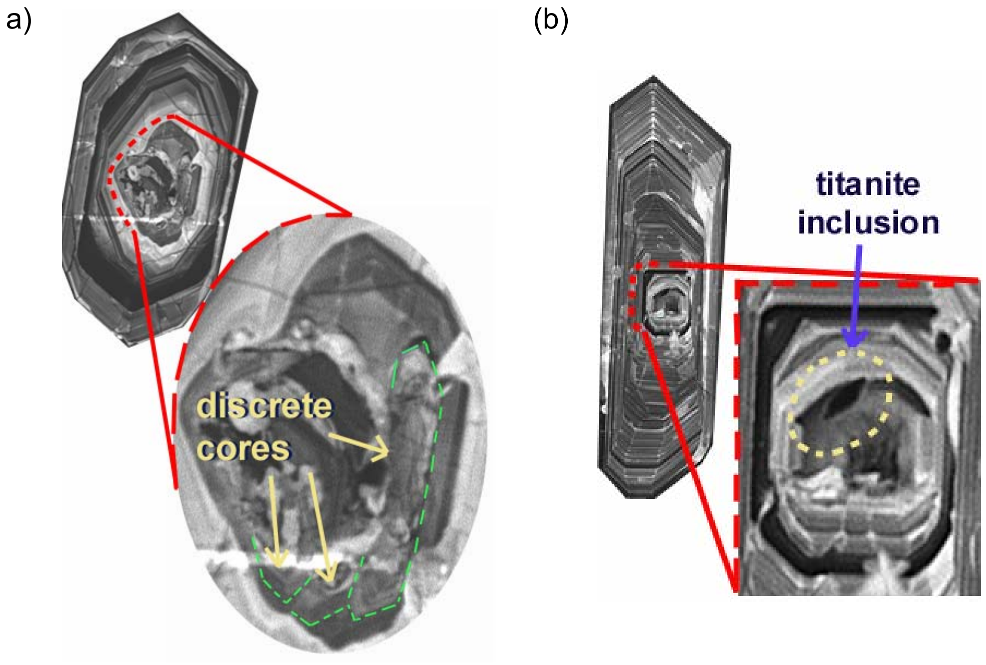

Figure 7.1. (a) Igneous clustering within the core of the zircon crystal [Z3(16)] from the Kalebalta leucogranite (sample SK-3); (b) Titanite inclusion on the zircon crystal [Z12(21)] from the Çimkalesi monzogranite (sample SK-12).

Furthermore, CL-study reveals that S-type granitoids (e.g. Kalebalta and Hisarkaya) exhibit changing of crystal habits at the latest stages of crystallization (e.g. [Z3(13)] in Figure 5.7; [Z3(16)] in Figure 5.8; [Z4(6)] in Figure 5.13; [Z5(11)] in Figure 5.19). In these figures, it is obvious that in the initial stages of growth, zircon crystals exhibit {121}-prism dominated forms, which are characteristic for crustal granitoids (i.e. autochthonous and intrusive aluminous leucogranites, Group 1 of Pupin, 1980), whereas outer morphologies are similar to those of hybrid granitoids (i.e. Group 4 of Pupin, 1980). This abrupt change in crystal forms may be related with the temperature and chemistry of the medium in the late stages of zircon crystallization (e.g. Benisek and Finger, 1993). This situation may explain the cause deflection of TETs (i.e. Figures 4.18, 4.34, 4.35) of these granitoids. Hence, it is evident that the results of the typology method should be evaluated along with the CL-imaging.

Even supposing the quality of CL data is substantial; it is not always possible to correlate growth stages of zircon crystals based on CL images even in a single pluton. In nature, zircon crystals even from a small intrusion can demonstrate slightly different growth histories. Some crystals show longer growth histories, while others may reflect shorter and interrupted ones. As indicated by Pidgeon and Compston (1992), magma may be inhomogeneous over an unspecified scale, and zircons experienced different crystallization histories in different parts of the magma before being finally brought together in the volume of granitoid represented by the present samples. In spite of these factors, zircon crystals from different granitoid bodies are tried to correlate based on CL-images.

In the scope of this study, zircons from two different exposures from the same granitoid (i.e. SK-4 and SK-5 from Hisarkaya granitoid), show similar structures, but with slight differences (Chapters 4 and 5). In such a manner, it is possible to correlate different outcrops belong to same granitoid sample based on the external and internal features of zircons.

Alternatively, combination of SEM and CL makes possible to compare different granitoid exposures. Accordingly, two separate granitoids (i.e. SK-7-Terlemez granitoid and SK-12-Çimkalesi granitoid), which are far from each other, display similar zircon external and internal structures. Both granitoids show zircon populations dominated by S_{24}-type, and long zircon growth histories demonstrating oscillatory zoning interrupted by multiple resorption faces (Table 7.3). Therefore, it is plausible to assume that zircons from both granitoids were subjected to similar conditions in their magma chambers. This interpretation provides comparison of different evolutionary conditions in regional concept.

7.2.3. Zircon Chemistry

In addition to zircon typology and CL studies, chemical properties of zircons from the CAG are investigated by using EMP. In this way it is possible to correlate the typological and intracrystalline features of crystals with their chemical characteristics.

Table 7.3. Some internal structures revealed by the CL-imaging of the Ekecikdağ, Ağaçören and Terlemez plutons.

GRANITOID	Inherited core	Overgrowth /epitaxial overgrowth	Resorption /corrosion surface	Metamictized domain	Recrystallized /flow domain	Sector zoning
H-TYPE						
Borucu (SK-1)			+		+	
Sinandı (SK-6)			+		+	+
Namlıkışla (SK-8)	+		+	+	+	
Yenişabanlı (SK-9)	+		+		+	
Sipahiler (SK-10)	+		+	+	+	
Torunobası (SK-11a)	+		+	+	+	
Camili (SK-11b)	+		+		+	
Çimkalesi (SK-12)	+		+		+	+
Terlemez (SK-7)	+		+		+	+
S-TYPE						
Kalebalta (SK-3)	+	+	+	+	+	+
Hisarkaya (SK-4, 5)	+	+	+	+	+	+

Variability in the intracrystalline structures within zircon crystals is also reflected in their chemistry, in terms of changing elemental concentrations. Cherniak et al. (1997) indicated that the very slow diffusion rates measured for the REEs suggest that they are essentially immobile under most geologic conditions, therefore permitting the preservation of fine-scale chemical zoning. Furthermore, Lee et al. (1997) indicated that radiation damage, fracturing due to differential expansion and pressure release, recrystallization, self-annealing, chemical reaction and leaching or alteration by fluids are possible processes that may modify the zircon crystal lattice. Otherwise, especially U and Th are exceedingly sluggish, even at high magmatic temperatures (Cherniak et al., 1997; Lee et al., 1997; Miller and Wooden, 2004). Therefore, it is plausible to expect pronounced U, Th and REE (+Y) growth zoning in response to enrichment or depletion of these elements at the crystal-melt interface during zircon growth.

Numerous factors such as magma composition, degree of melt polymerization, temperature, and pressure may together play an important role in determining indigenous trace element abundances in zircon (Heaman et al., 1990). Möller et al. (2001) indicated that geochemical characterization of zircon based on trace elements could be indicative for the determination of the growth environment of zircon when the mechanisms controlling trace element behavior are strictly evaluated.

Considering the whole EMP data set in this study, ZrO_2 content is around 65%, SiO_2 is 32%, and HfO_2 is 1.5% (Table 6.2) for the granitoids from the CACC. Th abundances change generally between 1000-2000 ppm within crystals. Zircons from the Kalebalta granitoid, on the other hand, have higher Th concentrations even more than 9000 ppm, whereas those from Namlıkışla have less than 500 ppm Th content (Table 6.2). U shows wide range from 0-10200 ppm within the granitoids in concern. The abundances of U and Th of zircons from the CACC are similar to those typically observed in granitic zircon, but in some zones the contents approach to other rock types (e.g. basalt, dolerite or syenite). Ratio of Th/U, then again, is commonly above 0.1, i.e. likewise other igneous zircons (e.g. Zeck and Williams, 2002; Belousova et al., 2002). However, it decreases to less than 0.1 at some inner and outer zones, and enormous values up to 15.96 (Figure 6.22, Appendix B [Table B.1] and Table 6.2) are also revealed. Changes in abundances of U, Th, and ratio of Th/U are probably due to variation in magma compositions and/or open-system behavior of the crystals. Y abundances, on the other hand, are commonly very low, whereas at maximum U and Th values, Y concentrations considerably increase.

Moreover, chondrite-normalized trace element patterns provide basis for comparison with other granitoids. Chondrite-normalized spider-diagrams suggests that zircons from the CAG broadly show depletion in Y, Yb, Fe and Ti, and enrichment in Ta with respect to that of average granitic zircons reported by Belousova et al. (2002) (e.g. Figures 6.1).

Furthermore, chemical profiles supply powerful data not only about the general characteristics, but also on the internal variations within the zircon crystals. The rims of zoned zircon crystals can be enriched in certain trace elements by as much as ten times the level found in the core (e.g. Exley, 1980), possibly as a consequence of the elevated trace element concentrations in the magma during the final stages of zircon crystallization (Heaman et al., 1990). Most of the zircons from the CAG show this behavior, owing to presence of enriched levels of U, Th, Y and REE at rims in almost all crystals, which is also definite by the {110} prism dominated morphologies (e.g. Benisek and Finger, 1993) (e.g. Figures 6.4 and 6.16).

In view of elemental profiles, alternating trace element enriched and depleted growth bands characterize the geochemical zoning in zircons from the CACC granitoids. Disregarding oscillations, abrupt changes in resorbed surfaces and elevated trace element concentrations at rims, chemical data for zircon crystals from the CAG do not reveal systematic compositional variation, i.e. there is no important increase or decrease in certain elements, from central part to the rim.

Slight decrease in Zr and Si, and insignificant increase in U, Th, REE+Y, Ca and Al are rarely observed from center to rim in zircon crystals, naturally as a cooling granite would become enriched in U, Th, Y and REE by fractional crystallization (e.g. Benisek and Finger, 1993). Nevertheless, it is hard to use this occasion for identifying the magma source characteristics of all granitoids concerned. Because such differences in initial and final chemistry are not valid for all studied zircon crystals. Instead the elemental variation due to oscillation portrays the patterns of profiles in most cases.

However, points intercepting the zones of corrosion, which were defined by the CL study, present outstanding chemical discrepancies. It is noteworthy that Zr and Si abundances decrease at the zones of corrosion in almost all analyzed crystals whereas U, Th, Sc and REE+Y contents increase (Chapter 6). Beside these elements, at these zones, rise in the contents of Hf, Ta, Ti, and Fe is infrequently observed, and particularly, Ca and Al reach anomalous levels at these zones or at the rims of the crystals (e.g. Figure 6.8).

These elemental changes are likely to be related with the progressive zircon crystallization in an evolving and/or cyclically rejuvenated magma (Vavra, 1990; Pidgeon, 1992; Hanchar and Miller, 1993; Hanchar and Rudnick, 1995; Connelly, 2000). Chemistry of the melt and elemental exchange between the crystal and the adjacent melt play an important role in this respect. In most of the crystals, sharp changes in elemental abundances are observable more than one time through the profile, suggesting that the new influx of magma during distinct episodes results in such structural and chemical changes within the crystal.

Zircon crystals from the granitoids defined as S-type (i.e. Kalebalta leucogranite and Hisarkaya porphyritic granite) depending on the aforementioned studies show unique chemical properties. Cores of zircons from S-type granitoids have exceptionally high (even thousands of ppm) Al contents (e.g. Figure 6.6) suggesting a crustal origin.

7.2.4. Understanding of Zircon Systematics

In the granitic zircons from the CACC, inherent, embayed or zoned euhedral cores are overgrown by zoning/oscillatory zoning. One of the most remarkable characteristics of the studied zircon crystals is the interruption of growth zoning by intermittent multi-resorption/corrosion stages. Multi-corrosion stages, determined by CL and chemistry studies, possibly formed by a thermal input as a result of renewed influx of fresh and hot magma, infer hybridization processes in the magma chamber (e.g. Vavra, 1990, 1994).

This is in accordance with the geological, geochemical and zircon typological interpretations suggesting a hybrid source, i.e. evidences of mixing/mingling processes, for granitoids concerned. Naturally it is not unexpected to observe the evidences of magma mixing/mingling processes within the zircon characteristics.

The interpretation of corrosion by hybridization processes can elucidate resorption/dissolution surfaces observed within zircons, though it still needs to be explained in terms of mechanism responsible for these multi-processes. Basically such a mechanism should involve (1) zircon growth, (2) heating zircon resulting in resorption, (3) zircon growth in a hybridization period revealing low Zr and Si, and high U, Th and REE+Y composition, (4) cooling and crystallization of zircon with chemical zoning/oscillatory zoning, (5) repetition of these processes more than one time, and (5) followed by zircon growth in a continuous manner up to a solidification of the host magma.

Dissolution and re-growth can be caused by transient heating of the resident felsic magma by mafic melt contribution, which is an effective way of raising the temperature in felsic magma for short periods of time, even for a modest amount of basalt input (e.g. Sparks and Marshall, 1986; Miller and Wooden, 2004). In the CL-images cores (or cores with surrounding zones) of zircons prior to corrosion are fairly large (usually >50 μm) (Chapter 5). This deduces relatively short duration of remelting or thermal events (e.g. Watson, 1996) so that zircons could survive and were not completely dissolved. One exclusive character is the resorbed and eroded/smoothed surfaces of these corrosion zones reflecting high heat input and disequilibrium conditions hindering euhedral crystal face development. Resorbed zircons would lose their euhedral morphologies and yield rounded forms in the CL-images (e.g. Figures 5.49 and 5.50). Transient heating by mafic melt impulse may result in dissolution of outer crystal surface or heat can be induced through interior zones.

The quenched mafic inclusions present in the H-type CAG provide apparent evidence of mafic magma input into the felsic magma chamber that fed the plutons in the Ağaçören, Ekecikdağ and Terlemez suites (Figure 3.2). After dissolving of zircons by mafic magma involvement, new zircon would grow once the magma cooled back to temperature below that of zircon crystallization. Decreased Zr and Si abundances, besides increased U, Th, Sc and REE+Y contents within the corrosion zones of studied zircons, give clues about the nature of the hybridization processes. These periods are usually characterized by low Zr-supersaturation and sometimes abrupt changes in the crystal form. Moreover, high abundances of U, Th, Sc and REE+Y at the zones of corrosion show that at the time of mixing/mingling, magma in which zircons grow reflects a mafic character (e.g. Heaman et al., 1990; Hoskin et al., 2000). In a hotter mafic melt the fast diffusion rates of trace elements (e.g. U, Th, Sc and REE+Y) prevents strong enrichment and depletion at the crystal-melt interface so that the chemical zoning of the growing crystal is weaker, broader and sometimes gradual (Rubatto and Gebauer, 2000). Therefore it is reasonable to conclude that the mafic melts not only generated heat to dissolve zircons but also affect to their compositions. Mafic magma pulses resulted in temperature increase owing to resorption of zircon crystals, and then resorbed zircon crystals re-grow in a more mafic magma chamber.

Zircon growth during this period would involve several factors such as

-contemporaneous crystallization of zircon and other minerals (Th and/or U-rich minerals monazite, thorite, etc.) leading to local geochemical disequilibrium,

-different diffusion rates of elements in melt and crystal,

-changes in the associated K-values depending on degree of supersaturation,

-crystallization kinetics controlled by melt volume and solid-solid vs. melt-solid reactions,

-the growth blocking effect of elements on certain crystallographic faces, and other crystallographic and crystallochemical features (Vavra, 1990; Benisek and Finger, 1993; Mattinson et al., 1996; Klötzli, 1999).

All these parameters may interplay a role in the degree of effectiveness of mafic melt injection to the crystal and growth characteristics of zircon in this period. Therefore, zircon crystals concerned would show diverse intracrystalline features within the CL-images.

A further theme to be discussed is the existence of repeated resorption surfaces in the growth history of a single crystal. These resorption surfaces may be related to (1) a single hybridization event or (2) multi-episodes of hybridization.

If the item (1) is the case, those crystals displaying several corrosion zones might have been resorbed and transported during a single hybridization period, and subjected to corrosion by penetrating hot magma in different parts of the magma chamber. Zircon crystals can be transported in a magma chamber by the forced convection by mafic melt injection (e.g. Snyder and Tait, 1996; Couch et al., 2001; Miller and Wooden, 2004). However, this explanation needs more supplementary data not only about the behavior of zircon crystals but also on time-scale relations and geometry of the invasion of magma.

If item (2) is relevant, multiple processes might have been realized in distinct periods of hybridization. Although no age data are available, CL imaging suggests relatively discrete periods of zircon growth between periods of no growth or limited growth, i.e. variability in zircon supersaturation. These discrete periods may possibly represent either long or short periods of time. Long time interval theory is likely to cover millions of years and several magma sources, with diverse mafic melt contribution. On the other hand, an underplated mafic magma can be a source region for episodic mafic melt injections into the felsic magma chamber, in relatively short periods.

Certainly, exact explanation related to these scenarios can only be achieved by accurate dating of distinct episodes of hybridization in a single crystal. However favored explanation would be that the evolution histories of the H-type CAG concerned include cyclic hybridization processes by episodic mafic melt injections.

Prominent similarities within zircon crystals suggest that the H-type granitoids, in the Ağaçören, Ekecikdağ and Terlemez suites, might have been generated from a common magma source. However, some slight intrinsic disparities in chondrite-normalized element patterns and element profiles imply that they are products of discrete magma pulses although they are fed by the same magma source. Additionally, circumstances come across throughout the evolution of granitoids, such as fractional crystallization and crustal contamination, may cause chemical variations within zircons. A model of multiple batches of felsic magma that solidify partially and re-melt by transient heating of mafic melts may explain the textural evidence for pronounced resorption and distinctive chemical characteristics of zircons (e.g. Miller and Wooden, 2004).

Moreover, zircon crystals from S-type granitoids, also point up resorption surfaces, revealed by CL-imaging, similar to those in the H-type granitoids. This is also the case for the Namlıkışla biotite-granite, which is defined to be an intrusive aluminous granitoid based on Pupin (1980)'s classification. These resorption surfaces commonly exhibit high abundances of U, Th and REE+Y akin to those in the H-type granitoids. On the other hand, zircon typology studies reveal that their morphologies fit with those of the hybrid granitoids.

Nevertheless, there are no whole-rock geochemical, macroscopic and microscopic evidences available about the mafic melt contribution within the evolution histories of the S-type CAG. They do not include mafic microgranular enclaves, and they present different whole-rock geochemical features than the H-type granitoids.

Zircon structures and chemical variations in S-type granitoids may be related with the physical and chemical processes encountered within the magma chamber, but not with the mafic melt contribution. At some stage in generation of these S-type granitoids, resorption surfaces of zircons likely to be formed by crystal interaction with the adjacent hot melt. For instance, settling of zircons of the S-type CACC granitoids from the upper part of the chamber through the interior into hotter and deeper layers would cause them to be resorbed, and they would also settle into a different chemical environment (e.g. Miller and Wooden, 2004). Moreover, detachment of mushy zircon-bearing rinds from the walls within a zoned magma body might provide a way for the zircons to be carried in crystal-laden plumes into deeper and hotter parts of the chamber (Miller and Wooden, 2004). These two processes should include the transportation of resorbed zircons to the cooler edges or walls of the magma body by lateral convection, where they would begin to grow again to avoid complete dissolution (Miller and Wooden, 2004). These processes, may be encountered within evolution of zircons from S-type granitoids, might also take place within the growth histories of zircons from H-type granitoids. These processes can imply multi-resorption surfaces but do not bring adequate explanation for distinct chemical characteristics.

Alternatively, intrusions of hybrid granitoids into the previously formed S-type ones may result in heat generation and lead to resorption and regrowth of zircons within S-type granitoids. However, intrusion of H-type granitoid into S-type granitoid likely to have limited effect, owing to formation of relatively thin hybrid zones (e.g. Altherr et al., 1999).

One plausible explanation will be the formation of S-type CACC granitoids by gaining significant thermal energy from mantle-derived magma without direct contribution (e.g. Düzgören-Aydın et al., 2001). Accordingly, transient heating of mantle melt injections probably caused melting of crustal rocks, which may exhibit heterogeneous nature comprising mafic constituents. Transient heating even causes resorption of previously formed zircons, showing either inherent or clustered cores and subsequent zonation. Higher diffusion rates of trace elements (e.g. U, Th, REE+Y) in a hotter melt resulted in broad low-CL zones around resorbed zircons (e.g. Rubatto and Gebauer, 2000). New zircon growths likely occur during subsequent cooling and crystallization, in equilibrium with partial melt have compositions relatively rich in U, Th, Y and HREE.

Mentioned explanations about the genesis of S- and H-type granitoids yet again need to be confirmed by accurate dating and comparison of resorption zones within S- and H-type granitoids, respectively.

7.3. Implications for Geochronological Studies

Investigation of zircon crystals from the granitoids of the CACC reveals complex growth histories comprising distinct phases of evolution. It is important to note that evaluation of exact growth history of a given crystal needs complementary dating studies. The present study, therefore, should be harmonized by age data to best describe the evolution of zircons and to extent information to magmatic system.

One of the aims of the present research is to compose a guideline for further geochronological studies on zircons of the CAG, apart from petrological indications. In this manner, investigation of zircons of 12 granitoids from three plutons within the western part of the CACC in this research showed that the dating of these minerals might yield discordant data in Thermal Ionization Mass Spectrometry (TIMS) applications. Because many (though certainly not all) crystals have inherent cores and/or cores likely to belong distinct age and petrogenetic environment (Table 7.3). In addition, there are secondary structures such as inclusions of other minerals, like apatite and titanite, and metamictized and recrystallized domains within these zircons (Chapter 4 and 5). Moreover, there are zones of corrosion interrupting the evolution histories of zircons. Preferably, zircon crystals with continuous igneous zoning determined by CL-studies will be most appropriate for dating. Furthermore typology study revealed that within a single granitoid body more than one zircon type, which may represent different generations, are present.

Single zircon Pb-evaporation technique can be useful for identifying distinct populations, but during application of this method Pb-loss due to recrystallized domains within crystals may affect the results. It is also important to note that zircons of the studied granitoids contain a large number of inclusions, which result in complex mixing of Pb from zircon and inclusions during evaporation (e.g. Klötzli, 1999).

Alternatively, in-situ and microsampling techniques, like Secondary Ion Mass Spectrometry (SIMS), Laser Ablation ICPMS (LA-ICP-MS), Laser Ablation Multi-Collector ICPMS (LA-MC-ICP-MS), Nuclear Microprobe (PIXE) and Sensitive High Mass-Resolution Ion Microprobe (SHRIMP) can acquire prevailing data on the zircon geochronology, besides chemistry of the granitoids of the CACC. These data would be used for interpreting protolith age and time-scale interpretations of processes in the magma chamber. In this manner, timing of magma mixing/mingling or hybridization events and distinct episodes of evolution would be possible. However, these studies should be accompanied by careful examination of CL-images of zircon crystals.

7.4. Petrological Constraints on the CACC Granitoids Based on Zircon Data

Existing controversy on the petrology of the CAG is mentioned in detail in Chapter 2. In spite of existing detailed petrological data, comprising isotopic, whole-rock and limited mineral chemistry, ongoing discussion implies that it is essential to conduct specific studies on individual minerals. Accordingly, in the present research, the study of granitic zircons revealing complex external and internal (involving chemical) characteristics give ideas about the processes encountered in an evolving magma.

Zircon crystals from the Kalebalta and Hisarkaya granitoids (from Ekecikdağ pluton) were experienced severe alteration during their growth. Typological characteristics and intracrystalline features of zircon crystals indicate that the host granitoids have crustal origin and fit to the S-type granitoid classification. S-type granitoids, being the earlier granitoid phase in the CACC, might have been emplaced into the lower crust following lithospheric delamination by melting of crustal rocks (e.g. Aydın et al., 1998; Boztuğ, 1998, 2000; Düzgören-Aydın et al., 2001). On the other hand, episodes of corrosion subsequent to development of cores and surrounding zones not only changed the habits of zircon crystals, but also affected their chemical features, especially at the late stages of growth. These corrosion stages should be accommodated by transient heating from melt injections but without direct contribution from mantle-derived magma as deduced from nonexistence of mafic microgranular enclaves. Another explanation for these resorption surfaces may be the physical and chemical factors due to the intrusion of H-type granitoids into the S-type granitoids.

Moreover, evidences of mingling/mixing processes within the studied H-type CACC granitoids (from the Ağaçören, Ekecikdağ and Terlemez plutons) are well defined by the CL imaging, chemical and typological studies on zircon crystals. Periodic freezing and thawing of crustal-derived felsic magma bodies by mafic melt injections from mantle and periodic remobilization of near-solidus crystal mush (e.g. Mahood, 1990; Miller and Wooden, 2004) may provide a model to explain the polycyclic nature of the zircons from the CAG. Magma mingling/mixing processes between co-existing mantle-derived mafic and crustal–derived felsic magmas probably gave rise to H-type granitoids in the CACC in a continuous or episodic extensional regime (e.g. Aydın et al., 1998; Boztuğ, 1998, 2000; Düzgören-Aydın et al., 2001), and resulted in the multi-corrosion stages within zircon crystals.

Despite of having relevant age data, investigations of zircon crystals from the CAG in terms of typological/intracrystalline structural and chemical evidences with supplementary field, petrography and whole-rock geochemistry data show that magmatism in central Anatolia ranges from peraluminous to metaluminous (and possibly to alkaline considering other parts of the CACC) nature and fingerprints of mafic melt contributions are definitely reflected in zircon zones of episodic hybridization.

In the scope of this study, external and internal features of the zircon crystals from granitoids in the western part of the CACC were investigated. Extension of this study to the other parts of the CACC would supply comprehensive data on granitoids of whole central Anatolia.

CHAPTER 8

CONCLUSIONS

Typological and chemical studies focused on zircons of the granitoids from central Anatolia revealed the following conclusions:

1. Plutonic rocks cropping out in the Ekecikdağ, Ağaçören and Terlemez regions within the western part of the CACC, are differentiated into S- and H-type granitoids on the basis of petrographical and whole-rock geochemical features.
2. H-type granitoids from the Ekecikdağ, Ağaçören and Terlemez regions are composed mainly of quartz, orthoclase, plagioclase, biotite ± hornblende ± microcline, besides accessory phases of opaques, zircon ± titanite ± allanite ± apatite. The H-type CAG concerned comprise abundant mafic microgranular enclaves suggesting mixing/mingling processes.
3. S-type granitoids from the Ekecikdağ region are generally composed of quartz, orthoclase, plagioclase and biotite as major phases, whereas muscovite (coexists with biotite), titanite, apatite, allanite, zircon, and opaque minerals are also accessorily present in these rocks. They do not include mafic enclaves contrary to H-type granitoids.
4. H-type CAG show calc-alkaline metaluminous to peraluminous nature, whereas, S-type granitoids demonstrate calc-alkaline peraluminous characteristic.
5. S-type CAG are more depleted in Sr, Ba, Zr, Ti, LREE, and more enriched in Rb, Nb, HREE, and have variable and larger negative Eu anomalies than the H-type granitoids.
6. Zircon exists associated with biotite, allanite and plagioclase. Inclusions of other minerals, such as apatite and titanite are present on zircons.

7. Zircon crystals are commonly white, yellow, limpid, transparent, pale yellow or brownish yellow with some brown to dark brown varieties. Most of the crystals are euhedral with well-defined crystal outlines but corroded and metamictized grains are also present.

8. P- and S-type zircon crystals mainly define the zircon populations of the granitoids concerned, whereas G, L and J-types also exist.

9. Zircon typology method (Pupin, 1980) combined with CL imaging revealed that, the Borucu, Sinandı granitoids from the Ekecikdağ pluton, Yenişabanlı, Sipahiler, Camili, Torunobası and Çimkalesi granitoids from the Ağaçören Pluton and the Terlemez granitoid belong to Group 4 (of Pupin's classification), which characterizes H-type granitoids. On the other hand, the Kalebalta and Hisarkaya granitoids from the Ekecikdağ region are described as Group 1 (of Pupin's classification) characterizing intrusive aluminous autochthonous leucogranites, whereas the Namlıkışla granitoid is defined as Group 3 (Intrusive aluminous monzogranites and granodiorites of Pupin's classification) with little mantle contribution. These interpretations are consistent with the whole-rock geochemical characteristics of the studied granitoids.

10. Internal structures of the CACC granitoid zircons, revealed from CL-imaging showed that they generally include euhedral to subhedral cores exhibiting zoning, although sometimes faint, but inherent and embayed cores also exist. Large scale, first order, and/or small-scale second order oscillatory zoning are observed within zircon crystals.

11. Chondrite-normalized spider-diagrams infer that zircons from granitoids concerned show depletion in Y, Yb, Fe and Ti, and enrichment in Ta with respect to that of averaged granitic zircons (reported by Belousova et al., 2002). Element patterns do not show systematic variation throughout growth histories of zircons, i.e. from cores to rims.

12. Zircons from both H- and S-type CAG were subjected to intense corrosion, which is distinguishable by remarkable dissolution surfaces around small cores or cores with instantaneously surrounding zones. The zones of corrosion in studied zircons reflect decreased Zr and Si abundances and increased U, Th, Sc and REE+Y contents. Beside these elements, at these zones, increase in Hf, Ta, Ti, Ca, Al and Fe are also observed.

13. Corrosion zones within zircons of the H-type CAG are interpreted to be formed by transient heating of the resident felsic magma due to mafic melt contribution, at the time of mixing/mingling of these granitoids, and then zircons re-grow in magma source reflecting a mafic character.

14. S-type CAG, on the other hand, do not reflect direct contribution from mantle-derived magma; although, especially in late stages of crystallization corrosion surfaces are found. Mantle-derived magma might likely to produce heat for resorption of zircons of the S-type CAG without direct contribution.

15. In further studies, analyses of representative zircon crystals by in-situ techniques (e.g. LA-ICP-MS, SHRIMP, PIXE) will provide more accurate chemical data, especially on REEs. In this manner, it will be possible to correlate REE patterns of zircons from different plutons. Moreover, characterizations of melt inclusions within zircon crystals, reflecting the composition of magma at the time of hybridization, will be a critical theme.

16. Dating of cores, corrosion zones and rims of the zircon crystals by U-Pb SHRIMP method will provide powerful data for timing of mixing/mingling processes within magma chamber, besides earliest and latest stages of magma evolution.

REFERENCES

Ajaji, T., Weis, D., Giret, A., and Bouabdellah, M., 1998. Coeval potassic and sodic calc-alkaline series in the post-collisional Hercynian Tanncherfi intrusive complex, northeastern Morocco: geochemical, isotopic and geochronological evidence. Lithos, v: 45, p. 371-393.

Akıman, O., Erler, A., Göncüoğlu, M.C., Güleç, N., Geven, A., Türeli, K., and Kadıoğlu, Y.K., 1993. Geochemical characteristics of granitoids along the western margin of the Central Anatolian Crystalline Complex and their tectonic implications. Geol J, v: 28, p. 371-382.

Alpaslan, M., Frei, R., Boztuğ, D., Kurt, M.A., and Temel, A., 2004. Geochemical and Pb-Sr-Nd isotopic constraints indicating an enriched-mantle source for Late Cretaceous to Early Tertiary volcanism, central Anatolia, Turkey. Int Geol Rev, v: 46, p. 1022-1041.

Altherr, R., Henjes-Kunst, F., Langer, C., and Otto, J., 1999. Interaction between crustal-derived felsic and mantle-derived mafic magmas in the Oberkirch pluton (European Variscides, Schwarzwald, Germany). Contrib Mineral Petrol, v: 137, p. 304-322.

Ataman, G., 1972. The preliminary study on the radiometric age of Cefalık Dağı that is one of the granitic-granidioiritic bodies in the SW of Ankara. Journal of Hacettepe Fen ve Mühendislik Bilimleri, v: 2, p. 44-49 (in Turkish).

Ayan, M., 1963. Contribution a l’ etude petrographique et geologique de la region situee au Nord - Est de Kaman. Bull Mineral Res Explor Inst Turkey, v: 115, 332 p.

Aydın, N.S., Göncüoğlu, M.C., and Erler, A., 1998. Latest Cretaceous magmatism in the Central Anatolian Crystalline Complex: review of field, petrographic and geochemical features. Turk J Earth Sci, v: 7, p. 259-268.

Aydın, N.S., and Önen P, 1999. Field, petrographic and geochemical features of the Baranadag quartz monzonite of the central Anatolian granitoids, Turkey. Turk J Earth Sci, v: 8, p. 113-123.

Barbarin, B., 1990. Granitoids: mineral petrogenetic classifications in relation to origin and tectonic setting. Geol J, v: 25, p. 227-238.

Barbey, P., Allé, P, Brouand, M., and Albarède, F., 1995. Rare-earth patterns in zircons from the Manaslu granite and Tibetian Slab migmatites (Himalaya): insights in the origin and evolution of a crustally-derived granite magma. Chem Geol, v: 125, p. 1-17.

Belousova, E.A., Griffin, W.L, O'Reilly, S.Y., and Fisher, N.I., 2002. Igneous zircon: trace element composition as an indicator of source rock type. Contrib Mineral Petrol, v: 143, p. 602-622.

Benisek, A., and Finger, F., 1993. Factors controlling the development of prism faces in granite zircons: a microprobe study. Contrib Mineral Petrol, v: 114, p. 441-445.

Black, L.P., Williams, I.S., and Compston, W., 1984. Four zircon ages from one rocks: the history of a 3,930 Ma-old granulite from Mount Somes, Enderby Land, Antarctica. Contrib Mineral Petrol, v: 94, p. 427-447.

Bonin, B., Azzouni-Sekkal, A., Bussy, F., and Ferrag, S., 1998. Alkali-calcic and alkaline post-orogenic (PO) granite magmatism: petrological constraints and geodynamic settings. Lithos, v: 45, p. 45-70.

Boztuğ, D., 1998. Post-collisional central Anatolian alkaline plutonism, Turkey. Turk J Earth Sci, v: 7, p. 145-165.

Boztuğ, D., 2000. S-I-A-type intrusive associations: geodynamic of significance of synchronism between metamorphism and magmatism in Central Anatolia, Turkey. In: Bozkurt, E., Winchester, J.A., and Piper, J.D.A. (eds), Tectonics and Magmatism in Turkey and the Surrounding Area, Geological Society, London, Special Publications, v: 173, p. 441-458.

Broska, I., and Uher. P., 1991. Regional typology of zircon and its relationship to allanite/monazite antagonism. Geol Carpathica, v: 42, p. 265-269.

Cesbron, F., Blanc, P., Ohnenstetter, D., and Rémond, G., 1995. Cathodoluminescence of rare earth doped zircons I. Their possible use as reference materials: Scanning Microscopy, Supplements, v: 9, p. 35-56.

Chappell, B.W., and White, A.J.R., 1992. I- and S-type granites in the Lachlan fold belt. Trans. R. Soc. Edinburgh Earth Sci, v: 83, p. 1-26.

Cherniak, D.J., Hanchar, J.M., and Watson, E.B., 1997. Rare-earth diffusion in zircon. Chem Geol, v: 134, p. 289-301.

Collins, W.J., Beams, S.D., White, A.J.R., and Chappell, B.W., 1982. Nature and origin of A-type granites with particular reference to south-eastern Australia. Contrib Mineral Petrol, v: 80, p. 189-200.

Connelly, J.N., 2000. Degree of preservation of igneous zonation in zircon as a signpost for concordancy in U/Pb geochronology. Chem Geol, v: 172, p. 25-39.

Couch, S., Sparks, R.S.J., and Carroll, M.R., 2001. Mineral disequilibrium in lavas explained by convective self-mixing in open magma chambers. Nature, v: 411, p. 1037-1039.

Çevikbaş, A., and Öztunalı, Ö., 1992. Geology of the Ulukışla-Çamardı (Niğde) Basin. Bull Mineral Res Explor Inst Turkey, v: 114, p. 155-172.

Didier, J., and Barbarin, B., 1991. Enclaves and granite petrology. Elsevier, Amsterdam, 625 p.

Dirik, K., Göncüoğlu, M.C., and Kozlu, H., 1999. Stratigraphy and pre-Miocene tectonic evolution of the southwestern part of the Sivas Basin, central Anatolia, Turkey. Geol J, v: 34, p: 303-319.

Donaldson, C.H., 1985. A comment on crystal shapes resulting from dissolution in magmas. Mineral Mag, v: 49, p. 129-132.

Düzgören-Aydın, N.S., Malpas, J., Göncüoğlu, and M.C., Erler, A., 2001. A review of the nature of magmatism in central Anatolia during the Mesozoic post-collisional period. Int Geol Rev, v: 43, p. 695-710.

Ekici, T., and Boztuğ, D., 1997. Anatolid-Pontid çarpışma sisteminin pasif kenarında yeralan Yozgat batolitinde syn-COLG ve post-COLG granitoyid birlikteliği. Geosound, v: 30, p. 519-538 (in Turkish).

Erkan, Y., and Ataman, G., 1981. An investigation on metamorphism age of Central Anatolian Massif by K - Ar method. Journal of Hacettepe Univ. Yerbilimleri, v: 8, p. 27-31 (in Turkish).

Erler, A., and Bayhan, H., 1995. General evaluation and problems of Cental Anatolian Granitoids. Journal of Hacettepe Univ. Yerbilimleri, v: 17, p. 49-67 (in Turkish).

Erler, A., and Göncüoğlu, M.C., 1996. Geologic and tectonic setting of the Yozgat batholith, northern Central Anatolian Crystalline Complex, Turkey. Int Geol Rev, v: 38, p. 714-726.

Erler, A., Akıman, O., Unan, C., Dalkılıç, F., Dalkılıç, B., Geven, A., and Önen, P., 1991. Petrology and geochemistry of the magmatic rocks of Kırşehir Massif in Kaman (Kırşehir) ve Yozgat regions. Turk J Earth Sci, v: 15, p. 76-100 (in Turkish).

Exley, R.A., 1980. Microprobe studies of REE-rich accessory minerals: implications for Skye granite petrogenesis and REE mobility in hydrothermal systems. Earth Planet Sci Lett, v: 48, p. 97-110.

Fayon, A.K., Whitney, D.L., Teyssier, C., Garver, J.I., and Dilek, Y., 2001. Effects of plate convergence obliquity on timing and mechanisms of exhumation of a mid-crustal terrain, the Central Anatolian Crystalline Complex. Earth Planet Sci Lett, v: 192, p. 191-205.

Fekkak, A., Boualoul, M., Badra, L., Amenzou, M., Saquaque, A., and El-Amrani, I. E., 2000. Origin and geotectonic setting of lower NeoproterozoicKelaat Mgouna detrital material (eastern Anti-Atlas, Morocco). J African Earth Sci, v: 30, no: 2, p. 295-311.

Floyd, P.A., Göncüoğlu, M.C., Winchester, J.A., and Yalınız, M.K., 2000. Geochemical character and tectonic environment of Neotethyan ophiolitic fragments and metabasites in the Central Anatolian Crystalline Complex, Turkey. In: Bozkurt, E., Winchester, J.A., and Piper, J.D.A. (eds.), Tectonics and Magmatism in Turkey and the Surrounding Area. Geological Society of London, Special Publication, v: 173, p. 183-202.

Fourcade, S., and Allegre, C.J., 1981. Trace element behavior in granite genesis: a case study the calc-alkaline plutonic association from the Quérigut Complex (Pyrénées, France). Contrib Mineral Petrol, v: 76, p. 177-195.

Förster, H.J., Tischendorf, G., and Trumbull, R.B., 1997. An evaluation of the Rb vs. (Y+Nb) discrimination diagram to infer tectonic setting of silicic igneous rocks. Lithos, v: 40, p. 261-293.

Fowler, A., Prokoph, A., Stern, R., and Dupuis, C., 2002. Organization of oscillatory zoning in zircon: analysis, scaling, geochemistry, and model of a zircon from Kipawa, Quebec, Canada. Geochim Cosmochim Acta, v: 66, no: 2, p. 311-328.

Gautier, P., Bozkurt, E., Hallot, E., and Dirik, K., 2001. Pre-Eocene Exhumation of the Nigde Metamorphic Dome, Central Anatolia, Turkey. 11th EUG Meeting, Strasbourg, J Conf Abstr, v: 6, p. 316.

Geven, A., 1992. Mineralogy, petrography and geochemistry of the Cefalikdag plutonic rocks (Kaman region, central Anatolia). M.E.T.U., Unpubl PhD. Thesis, Ankara, 165 p.

Gill, J.B., 1981. Orogenic andesites and plate tectonics. Springer, New York, 385 p.

Gökten, E., and Floyd, P.A., 1987. Geochemistry and tectonic environment of the Sarkisla area volcanic rocks in central Anatolia, Turkey. Mineral Mag, v: 51, p. 533-559.

Göncüoğlu, M.C., 1986. Geochronological data from the southern part (Niğde Area) of the Central Anatolian Massif. Bull Mineral Res Explor Inst Turkey, v: 105/106, p. 83-96.

Göncüoğlu, M.C., Erler, A., Toprak, V., Olgun, E., Yalınız, K., Kuşçu, I., Köksal, S., and Dirik, K., 1993, Geology of the central part of the Central Anatolian Massif: part III geological evolution of the Tertiary Basin of the Central Kizilirmak: Unpubl. Report No: 3313, Turkish Petroleum Company (in Turkish).

Göncüoğlu, M.C., Erler, A., Toprak, V., Yalınız, K., Olgun, E., and Rojay, B., 1992, Geology of the western part of the Central Anatolian Massif: part II central part: Unpubl. Report No: 3155, Turkish Petroleum Company (in Turkish).

Göncüoğlu, M.C., Toprak, G.M.V., Kuşçu, İ., Erler, A., and Olgun, E., 1991, Geology of the western part of the Central Anatolian Massif: part I southern part: Unpubl. Report No: 2909, Turkish Petroleum Company (in Turkish).

Göncüoğlu, M.C., and Türeli, T.K., 1993. Petrology and geodynamic interpretation of plagiogranites from Central Anatolian ophiolites (Aksaray, Turkey): Ofioliti, v: 18, no: 2, p. 187.

Göncüoğlu, M.C., and Türeli, T.K., 1994. Alpine collision-type granitoids in the western central Anatolian Crystalline Complex, Journal of Kocaeli Univ., v: 1, p. 39-46.

Göncüoğlu, M.C., Köksal, S., and Floyd, P.A., 1997. Post-collisional A-Type magmatism in the Central Anatolian Crystalline Complex: petrology of the İdiş Dağı intrusives (Avanos, Turkey). Turk J Earth Sci, v: 6, no: 2, p. 65-76.

Görür, N., Oktay, F.Y., Seymen, İ., and Şengör, A.M.C., 1984. Paleotectonic evolution of Tuzgölü basin complex, central Turkey: In: Dixon, J.E., Robertson, A.H.F. (eds), The geological evolution of the Eastern Mediterranean. Geol Soc London Spec Publ, London, v: 17, p. 81-96.

Görür, N., Tüysüz, O., and Şengör, A.M.C., 1998. Tectonic evolution of the central Anatolian basins. Int Geol Rev, v: 40, p. 831- 850.

Gucsik, A., Koeberl, C., Brandstätter, F., Reimold, W.U., and Libowitzky, E., 2002. Cathodoluminescence, electron microscopy, and Raman spectroscopy of experimentally shock-metamorphosed zircon. Earth Planet Sci Lett, v: 202, p. 495-509.

Güleç N., and Kadıoğlu, Y.K., 1998. Relative involvement of mantle and crustal components in the Agaçören Granitoid (central Anatolia-Turkey): estimates from trace element and Sr-isotope data. Chem Erde, v: 58, p. 23-37.

Güleç, N., 1994. Rb-Sr Isotope data from the Ağaçören granitoid (East of Tuz Gölü): geochronological and genetical implications. Turk J Earth Sci, v: 3, p. 39-43.

Gündoğdu, N.N., Bros, R., Kuruç, A., and Bayhan, H., 1988. Rb-Sr whole-rock systematic of the Bayındır Feldspathoidal Syenites (Kaman-Kırşehir). Proc 20th Ann of Earth Sci at Hacettepe Univ Symp, Ankara, Abstr, p. 55.

Hanchar, J.M., and Miller, C.F., 1993. Zircon zonation patterns as revealed by cathodoluminescence and back-scattered electron images: Implications for interpretation of complex crustal histories. Chem Geol, v: 110, p. 1-13.

Hanchar, J.M., and Rudnick, R.L., 1995. Revealing hidden structures: the application of cathodoluminescence and back-scattered electron imaging to dating zircons from lower crustal xenoliths. Lithos, v: 6, p. 289-303.

Harris, N.B.W., Pearce, J.A., and Tindle, A.G., 1986. Geochemical characteristics of collision-zone magmatism: In: Coward, M.P., Ries, A.C. (eds), Collision Tectonics. Geol Soc Spec Publ, London, v: 19, p. 67-81.

Hartman, P., 1973. Structure and morphology. In: Hartman, P. (ed), Crystal Growth: An Introduction, North-Holland Publ. Co., Amsterdam-London, American Elsevier Publ. Co., New York, p. 358-402.

Hawkesworth, C., Turner, S., Gallagher, K., Hunter, A., Bradshaw, T., and Rogers, N., 1995. Calc-alkaline magmatism, lithospheric thinning and extension in the Basin and Range. J Geophys Res, v: 100, p. 10271-10286.

Heaman, L.M., Bowins, R., and Crocket, J., 1990. The chemical composition of igneous zircon suites: implications for geochemical tracer studies. Geochim Cosmochim Acta, v: 54, p. 1597-1607.

Hinton, R.W., and Upton, B.G.J., 1991. The chemistry of zircon: variations within and between large crystals from syenite and alkali basalt xenoliths. Geochim Cosmochim Acta, v: 55, p. 3287-3302.

Hoskin, P.W.O., 2000. Patterns of chaos: fractal statistics and the oscillatory chemistry of zircon. Geochim Cosmochim Acta, v: 64, no: 11, p. 1905-1923.

Hoskin, P.W.O., Kinny, P.D., Wyborn, D., and Chappell, B.W., 2000. Identifying accessory mineral saturation during differentiation in granitoid magmas: an integrated approach. J Petrol, v: 41, p. 1365-1396.

İlbeyli, N., and Pearce, J.A., 1997. Petrogenesis of the collision-related central Anatolian granitoids, Turkey. 9th EUG Meeting, Strasbourg, J Conf Abstr, p. 502.

İlbeyli, N., Pearce, J.A., Thirlwall, M.F., and Mitchell, J.G., 2004. Petrogenesis of collision-related plutonics in central Anatolia, Turkey. Lithos, v: 72, p. 163-182.

Irvine, T.N., and Baragar, W.R.A., 1971. A guide to the geochemical classification of the common volcanic rocks. Canadian J Earth Sci, v: 8, p. 523-548.

Kadıoğlu, Y.K., 1996. Geology, petrography and geochemistry of Ağaçören (Aksaray) magmatic rocks. M.E.T.U., Unpubl Ph.D. Thesis, 242 p.

Kadıoğlu, Y.K., and Güleç N., 1999. Types and genesis of the enclaves in central Anatolian granitoids. Geol J, v: 34, p. 243-256.

Kadıoğlu, Y.K., Ateş, A., and Güleç, N., 1998. Structural interpretation of gabbroic rocks in Ağaçören Granitoid, central Turkey: field observations and aeromagnetic data. Geol Mag, v: 135, no: 2, p. 245-254.

Kadıoğlu, Y.K., Dilek, Y., Güleç, N., and Foland, K.A., 2003. Tectonomagmatic evolution of bimodal plutons in the Central Anatolian Crystalline Complex, Turkey. Geol J, v: 111, p. 671-690.

Klötzli, U.S., 1999. Th/U zonation in zircon derived from evaporation analysis: a model and its implications. Chem Geol, v: 158, p. 325-333.

Klötzli, U.S., Koller, F., Scharbert, S., and Höck, V., 2001. Cadomian lower-crustal contributions to Variscan granite petrogenesis (South Bohemian Pluton, Austria): constraints from zircon typology and geochronology, whole-rock and feldspar Pb-Sr isotope systematics, J Petrol, v: 42, no: 9, p. 1621-1642.

Köksal, S., 1996. The geological and petrological characteristics of the İdiş Dağı-Avanos Area (Nevşehir-central Anatolia). M.E.T.U., Unpubl M. Sc. Thesis, Ankara, 141 p.

Köksal, S., Romer, R.L., Göncüoğlu, M.C., and Toksoy-Köksal, F., 2004a. Timing of post-collisional H-type to A-type granitic magmatism: U-Pb titanite ages from Alpine central Anatolian Granitoids (Turkey). Int J Earth Sci, v: 93, p. 974-989.

Köksal, S., Toksoy-Köksal, F., and Göncüoğlu, M.C., 2004b. H-tipi ve A-tipi granitoyidlerin birlikteliğine bir örnek: Baranadağ ve Çamsarı granitoyidleri (Kaman, Kırşehir)'nin zirkon tipolojisi metodu ve jeokimyasal çalışmalarla karşılaştırılması. I. Ulusal Jeokimya Sempozyumu, Bursa, Abstr, p. 40 (in Turkish).

Köksal, S., Göncüoğlu, M.C., and Floyd, P.A., 2001. Extrusive members of postcollisional A-Type magmatism in central Anatolia: Karahidir volcanics, Idisdagi-Avanos area, Turkey. Int Geol Rev, v: 43, p. 683-694.

Koschek, G., 1993. Origin and significance of the SEM cathodoluminescence from zircon: J Microscopy, v: 171, p. 223-232.

Kostov, I., and Kostov, R.I., 1999. Crystal Habits of Minerals. Bulgarian Academic Monographs (1). Prof. M. Drinov Academic Publishing House and Pensoft Publishers, Sofia, 415 p.

Kuruç, A., 1990. Rb/Sr geochemistry of syenitoids from Kaman-Kırşehir region. Hacettepe University, Unpubl M Sc Thesis, Ankara, 97 p.

Kuşcu, İ., Gençalioğlu, Kuşcu, G., Meinert, L.D., and Floyd, P.A., 2002. Tectonic setting and petrogenesis of the Çelebi granitoid, (Kirikkale-Turkey) and comparison with world skarn granitoids. J Geochem Expl, v: 76, p. 175-194.

Lee, J.K.W., Williams, I.S., and Ellis, D.J., 1997. Pb, U and Th diffusion in natural zircon. Nature, v: 390, p. 159-162.

Liégeois, J.P., and Black, R., 1987. Alkaline magmatism subsequent to collision in the Pan-African belt of the Adrar des Iforas. In: Fitton, J.G., Upton, B.G.J. (eds), Alkaline igneous rocks. Geol Soc Spec Publ, v: 30, p. 381-401.

Mahood, G., 1990. Second reply to comment of R.S.J. Sparks, H.E. Huppert and C.J.N. Wilson on evidence for long residence times of rhyolitic magma in the Long Valley magmatic system: the isotopic record in the precaldera lavas of Glass Mountain. Earth Planet Sci Lett, v: 99, p. 395-399.

Maniar P.D., and Piccoli, P.M., 1989. Tectonic discrimination of granitoids. Geol Soc Am Bull, v: 101, p. 635-643.

Marshall, D.J., 1988. Cathodoluminescence of Geological Materials: Boston, Unwin Hyman, 146 p.

Mattinson, J.M., Graubard, C.M., Parkinson, D.L., and McClelland, W.C., 1996. U-Pb reverse discordance in zircons: the role of fine scale oscillatory zoning and sub-micron transport of Pb. In: Basu, A., Hart, S. (eds.), Earth Processes, Reading The Isotopic Code. Geophysical Monograph 95. American Geophysical Union, p. 355-370.

Miller, C.F., Hanchar, J.M., Wooden, J.L., Bennett, V.C., Harrison, T.M., Wark, D.A., and Foster, D. A., 1992. Source region of a granite batholith: evidence from lower crustal xenoliths and inherited accessory minerals. Trans. R. Soc. Edinburgh Earth Sci., v: 83, p. 49-62.

Miller, J.S., and Wooden, J.L., 2004. Residence, resorption and recycling of zircons in Devils Kitchen Rhyolite, Coso volcanic field, California. J Petrol, v: 45, no: 11, p. 2155-2170.

Möller, A., Poller, U., Kennedy, A., and Kröner, A., 2001. Trace and rare earth element geochemistry of magmatic and metamorphic zircon: caveats for geochronological interpretation based on Th/U and morphology only. 11th EUG Meeting, Strasbourg, J Conf Abstr, p. 599-600.

Moser D.E., and Heaman, L.M., 1997. Proterozoic zircon growth in Archean lower crustal xenoliths, southern Superior craton - a consequence of Matachewan ocean opening. Contrib Mineral Petrol, v: 128, p. 164-175.

Murakami, T., Chakoumakos, B.C., Ewing, R.C., Lumpkin, G.R., and Weber, W.J., 1991. Alpha-decay event damage in zircon: Am Mineral, v: 76, p. 1510-1532.

Murali, A.V., Parthasarayth, R., Mahadevan, T.M., and Sankar Das, M., 1983. Trace element characteristics, REE patterns and partition coefficients of zircons from different geological environments-a case study on Indian zircons. Geochim Cosmochim Acta, v: 47, p. 2047-2052.

Nasdala, L, Beran, A., Libowitzky, E., and Wolf, D., 2001. The incorporation of hydroxyl groups and molecular water in natural zircon ($ZrSiO_4$). Am J Sci, v: 301, p. 831-857.

Nasdala, L., Pidgeon, R.T., Wolf, D., and Irmer, G., 1998, Metamictization and U-Pb isotopic discordance in single zircons: a combined Raman microprobe and SHRIMP ion probe study: Mineral Petrol, v: 62, p. 1-27.

Otlu, N., and Boztuğ, D., 1998. The coexistence of the silica oversaturated (ALKOS) and undersaturated (ALKUS) rocks in the Kortundag and Baranadag plutons from the central Anatolian alkaline plutonism, E Kaman/NW Kirsehir, Turkey. Turk J Earth Sci, v: 7, p. 241-257.

Paterson, B. A., Stephens, W. E., Rogers, G., Williams, I. S., Hinton, R. W., and Herd, D. A., 1992. The nature of zircon inheritance in two granite plutons. Trans. R. Soc. Edinburgh Earth Sci, v: 83, p. 459-471.

Pearce, J.A., 1996. Sources and settings of granitic rocks, Episodes, v: 19, no: 4, p. 120-125.

Pearce, J.A, Harris N.B.W., and Tindle, A.G.W., 1984. Trace element discrimination diagrams for the tectonic interpretation of granitic rocks. J Petrol, v: 25, p. 956-983.

Pidgeon, R.T., and Compston, W., 1992. Zircon Th-U-Pb systems as indicators of source rocks and magmatic processes: a SHRIMP study of four granites from the Scottish Highlands. Trans. R. Soc. Edinburgh Earth Sci, v: 83, p. 473-483.

Pidgeon, R.T., 1992. Recrystallization of oscillatory zoned zircon: some geochronological and petrological implications. Contrib Mineral Petrol, v: 110, p. 463-472.

Pidgeon, R.T., Nemchin, A. A., and Hitchen, G.J., 1998. Internal structures of zircons from Archean granites from the Darling Range batholith: implications for zircon stability and the interpretation of zircon U-Pb ages. Contrib Mineral Petrol, v: 132, p. 288-299.

Poldervaart, A., 1956. Zircon in rocks 2. Igneous rocks. Am. J. Sci., v: 254, p. 521-554.

Poller, U., Huth, J., Hoppe, P., and Williams, I.S., 2001. REE, U, Th, and Hf distribution in zircon from western Carpathian Variscan granitoids: a combined cathodoluminescence and ion microprobe study. Am J Sci, v: 301, p. 358-376.

Potts, P.J., 1987. Handbook of Silicate Rock Analysis. Blackie, 602 p.

Pupin, J.P., and Turco, G., 1972. Une typologie originale du zircon accessoire. Bull Soc Fr Mineral Cristallogr, v: 95, p. 348-359.

Pupin, J.P., and Persoz, F., 1999. Magma mixing revealed by zircon study of ferro-K subalkaline granite series. C. R. Acad. Sci. Paris, Sciences de la terre et des planètes, v: 328, p. 9-16.

Pupin, J.P., 1980. Zircon and granite petrology. Contrib Mineral Petrol, v: 73, p. 207-220.

Rémond, G., Blanc, P., Cesbron, F., Ohnenstetter, D., and Rouer, O., 1995, Cathodoluminescence of rare earth doped zircons II. The distribution of the doping elements and the contrasts of images. Scanning Microscopy Supplement, v: 9, p. 57-76.

Roberts, M.P., Pin, C., Clemens, J.D., and Paquette, J.L., 2000. Petrogenesis mafic to felsic plutonic rock association: the calc-alkaline Quérigut complex, French Pyrenees. J Petrol, v. 41, no: 6, p. 809-844.

Rollinson, H., 1993. Using Geochemical Data: Evaluation, Presentation, Interpretation. Longman, 352 p.

Romer, R.L., 2003. Alpha-recoil in U-Pb geochronology : effective sample size matters. Contrib Mineral Petrol, v: 145, p. 481-491.

Romer, R.L., Förster H.J., and Breitkreuz, C., 2001. Intracontinental extensional magmatism with a subduction fingerprint: the late Carboniferous Halle volcanic complex (Germany). Contrib Mineral Petrol, v: 141, p. 201-221.

Rubatto, D., and Gebauer, D., 2000. Use of cathodoluminescence for U-Pb zircon dating by ion microprobe : some examples from the western Alps. In: Pagel, M., Barbin, V., Blanc, P., and Ohnenstetter (eds), Cathodoluminescence in Geosciences, Springer-Verlag, Berlin, Heidelberg, Abstr, p. 373-400.

Rubatto, D., 2002. Zircon trace element geochemistry: partitioning with garnet and the link between and metamorphism. Chem Geol, v: 184, p. 123-138.

Schaltegger, U., Fanning, C.M., Gunther, D., Maurin, J.C., Schulman, K., and Gebauer, D., 1999. Growth, annealing and recrystallization of zircon and preservation of monazite in high-grade metamorphism: conventional and in-situ U-Pb isotope, cathodoluminescence and microchemical evidence. Contrib Mineral Petrol, v: 134, p.186-201.

Schersten, A., Årebäck, H., Cornell, D., Hoskin, P., Åberg, A., and Armstrong, R., 2000. Dating mafic-ultramafic intrusions by ion-microprobing contact-melt zircon : examples from SW Sweden. Contrib Mineral Petrol, v: 139, p. 115-125.

Scheepers, R., Cousin, L.E., Przbylowicz, W.J., and Prozesky, V.M., 1999. Nuclear microprobe (PIXE) analyses of zircons as indicators of granite type. Nuclear Instruments and Methods in Physics Research B, v: 158, p. 599-605.

Snyder, D., and Tait, S., 1996. Magma mixing by convective entrainment. Nature, v: 379, p. 529-531.

Sommerauer, J., 1974. Trace element distribution patterns and the mineralogical stability of zircon. An application for combined electron microprobe techniques. Proc. Electron. Microsc. Soc. S.A., v: 4, p. 71-72.

Sparks, R.S.J., and Marshall, L.A., 1986. Thermal and mechanical constraints on mixing between mafic and silicic magmas. J Volcan Geothermal Research, v: 29, p. 99-129.

Speer, J.A., 1982. Zircon. In: P. H. Ribbe (ed.), Orthosilicates, 2nd edition, Reviews in Mineralogy, Min Soc Am, v: 5, p. 67-112.

Steiger, R.H., and Jäger E., 1977. Subcommission on geochronology: convention on the use of decay constants in geo- and cosmochronology. Earth Planet Sci Lett, v: 36, p. 359-362.

Sun, S.S., and McDonough, W.F., 1989. Chemical and isotopic systematics of ocean basalts: implication for mantle composition and processes. In: Saunders, A.D., Norry, M.J. (eds.), Magmatism in Ocean Basins, Geological Society of London, Special Publication, v: 42, p. 313-345.

Şengör, A.M.C., and Yılmaz, Y., 1981. Tethyan evolution of Turkey: a plate tectonic approach. Tectonophysics, v: 75, p. 181-241.

Tatar, S., Boztuğ, D., Harlavan, Y., and Arehart, G.B., 2003. The composite Behrekdag batholith: an igneous record for the collision between Anatolides and Pontides along İzmir-Ankara-Erzincan Zone around Kırıkkale region, central Anatolia, Turkey. 56th Geological Congress of Turkey, Ankara, Abstr, p. 28-31.

Taylor, S.R., and McLennan, S.M., 1985. The Continental Crust: its Composition and Evolution, Blackwell Scientific, Oxford, 312 p.

Tikhomirova, M., 2002. Zircon inheritance in diatexite granodiorites and its consequence on geochronology-a case study in Lusatia and Erzebirge (Saxo-Thuringia, eastern Germany), Chem Geol, v: 191, p. 209-224.

Toksoy-Köksal F., Göncüoğlu, M.C., and Yalınız, M.K., 2001. Petrology of the Kurancali phlogopite metagabbro: an island arc-type ophiolitic sliver in the Central Anatolian Crystalline Complex. Int Geol Rev, v: 43, p. 624-639.

Trocellier, P., and Delmas, R., 2001. Chemical durability of zircon. Nuclear Instruments and Methods in Physics Research B, v: 181, p. 408-412.

Türeli, T.K., 1991. Geology, petrography and geochemistry of Ekecikdağ (Aksaray) Plutonic Rocks: M.E.T.U., Unpubl PhD. Thesis, Ankara, 194 p.

Türeli, T.K., Göncüoğlu, M.C., and Akıman, O., 1993. Ekecikdağ granitoyidinin petrolojisi ve kökeni (Orta Anadolu Kristalen Kütlesi batısı). Bull Mineral Res Explor Inst Turkey, v: 115, p. 15-28.

Vavra, G., 1990. On the kinematics of zircon growth and its petrogenetic significance: a cathodoluminescence study. Contrib Mineral Petrol, v: 106, p. 90-99.

Vavra, G., 1993. A guide to quantitative morphology of accessory zircon. Chem Geol, v: 110, p. 15-28.

Vavra, G., 1994. Systematics of internal zircon morphology in major Variscan granitoid types. Contrib Mineral Petrol, v: 117, p. 331-344.

Vavra, G., Gebauer, D., Schmid, R., and Compston, W., 1996. Multiple zircon growth and recrystallization during polyphase Late Carboniferous to Triassic metamorphism in granulites of the Ivrea Zone (Southern Alps): an ion microprobe (SHRIMP) study. Contrib Mineral Petrol, v: 122, p. 337-358.

Vavra, G., Schmid, R., and Gebauer, D., 1999. Internal morphology, habit and U-Th-Pb microanalysis of amphibole-to-granulite facies zircons:

geochronology of the Ivrea Zone (Southern Alps). Contrib Mineral Petrol, v: 134, p. 380-404.

Wark, D.A., and Miller, C.F., 1993. Accessory mineral behavior during differentiation of a granite suite: monazite, xenotime and zircon in Sweetwater Wash pluton, southeastern California, U.S.A. Chem Geol, v: 110, p. 49-67.

Watson, E.B., 1979. Zircon saturation in felsic liquids: experimental results and applications to trace element geochemistry. Contrib Mineral Petrol, v: 70, p. 407-419.

Watson, E.B., 1996. Dissolution, growth and survival of zircons during crustal fusion: kinetic principles, geological models and implications of isotopic inheritance. Trans. R. Soc. Edinburgh Earth Sci, v: 87, p. 43-56.

Wenzel, T., Mertz, D.F., Oberhaensli, R., Becker, T., and Renne, P.R., 1997. Age, geodynamic setting, and mantle enrichment processes of a K-rich intrusion from the Meissen massif (northern Bohemian massif) and implications for related occurrences from the mid-European Hercynian. Geol Rundsch, v: 86, p. 556-570.

Whalen, J.B., Currie, K.L., and Chappell, W., 1987. A-type granites: geochemical characteristics, discrimination and petrogenesis. Contrib Mineral Petrol, v: 95, p. 407-419.

Whalen, J.B., Jenner, G.A., Longstaffe, F.J., Robert, F., and Gariéty, C., 1996. Geochemical and isotopic (O, Nd, Pb and Sr) constraints on A-type granite petrogenesis based on the Topsails igneous suite, Newfoundland Appalachians. J Petrol, v: 37, p. 1463-1489.

Whitehouse, M.J., and Kamber, B.S., 2002. On the overabundance of light rare earth elements in terrestrial zircons and its implications for Earth's earliest magmatic differentiation. Earth Planet Sci Lett, v: 204, p. 333-346.

Whitehouse, M.J., and Kamber, B.S., 2003. A rare earth element study of complex zircons from early Archean Amîsoq gneisses, Godthåbsfjord, south-west Greenland. Precamb Res, v: 126, p. 363-377.

Whitney, D.L, Teyssier, C., Fayon, A.K., Hamilton, M.A., and Heizler M., 2003. Tectonic controls on metamorphism, partial melting, and intrusion:

timing and duration of regional metamorphism and magmatism in the Nigde Massif, Turkey. Tectonophysics, v: 376, no: 1-2, p. 37-60.

Whitney, D.L., and Dilek, Y., 1997. Core complex development in central Anatolia. Geology, v: 25, p. 1023-1026.

Williams, I.S., 1992. Some observations on the use of zircon U-Pb geochemistry in the study of granitic rocks, Trans. R. Soc. Edinburgh Earth Sci, v: 83, p. 447-458.

Williams, I.S., Shah, J.S., and Stowe, S., 1996. Elemental and isotopic microanalysis of zircons and backscattered electron contrast: Proceedings of the 6th European Conference on Applications of Surface and Interface Analysis, p. 1007-1010.

Willner, A.P., Sindern, S., Metzger, R., Ermolaeva, T., Kramm, U., Puchkov, V., and Kronz, A., 2003. Typology and single grain U/Pb ages of detrital zircons from Proterozoic sandstones in the SW Urals (Russia): early time marks at the eastern margin of Baltica. Precamb Res, v: 124, p. 1-20.

Yalınız, M.K., Parlak, O., Özkan-Altıner, S., and Göncüoğlu M.C., 1997. Formation and emplacement ages of supra-subduction-type ophiolites in central Anatolia: Sarikaraman ophiolites, central Turkey. 20th Anniversary of Geol Education, Çukurova Univ, Adana, Abstr, p. 61-62.

Yalınız, M.K., 1996, Petrogenesis of Sarıkaraman Ophiolites (Ortaköy, Central Anatolia) M.E.T.U., Unpubl PhD. Thesis, Ankara, 270 p.

Yalınız, M.K., Aydın, N.S., Göncüoğlu, M.C., and Parlak, O., 1999. Terlemez quartz monzonite of Central Anatolia (Aksaray-Sarıkaraman): age, petrogenesis and geotectonic implications for ophiolite emplacement. Geol J, v: 34, p. 233-242.

Yılmaz, S., and Boztuğ, D., 1998. Petrogenesis of the Çiçekdag Igneous Complex, N of Kırşehir, central Anatolia, Turkey. Turk J Earth Sci, v: 7, p. 185-199.

Zeck, H.P., and Williams, I.S., 2002. Inherited and magmatic zircon from Neogene Hoyazo cordierite dacite, SE Spain-anatectic source rock provenance and magmatic evolution. J Petrol, v: 43, no: 6, p. 1089-1104.

Zheng, J., Griffin, W.L., O'Reilly, S.Y., Lu, F., Yu, C., Zhang, M., and Li, H., 2004. U-Pb and Hf-isotope analysis of zircons in mafic xenoliths from Fuxian kimberlites: evolution of the lower crust beneath the North China craton. Contrib Mineral Petrol, v: 148, p. 79-103.

APPENDIX A.

Geochemical Data Source for Central Anatolian Granitoids and Typical Granitoid Types:

Typical S-type granite: av. of 704 samples (Chappell and White, 1992).

Typical post-collision granite: Quérigut (central biotite granite) (av. of 46 samples, Fourcade and Allegre, 1981), Nb and Zr from Roberts et al. (2000).

Typical A-type granite: av. of 148 samples (Whalen et al., 1987), REE from Collins et al. (1982).

Central Anatolian S-type granitoid area: compiled from Üçkapılı (av. of 4 samples, Göncüoğlu, 1986), Kalebalta (av. of 7 samples, Türeli et al., 1993; Göncüoğlu and Türeli, 1994); Sarıhacılı (av. of 3 samples, Boztuğ, 2000); REE from Yozgat (sample Yz76-Düzgören-Aydın et al., 2001).

Central Anatolian H-type granitoid area: compiled from Ağaçören (av. of 35 samples, Kadıoğlu, 1996), Baranadağ (Otlu and Boztuğ, 1998; Boztuğ, 1998, 2000; Aydın and Önen, 1999); Çamsarı (Otlu and Boztuğ, 1998; Boztuğ, 1998, 2000); Ekecikdağ (Borucu granitoid) (av. of 19 samples, Türeli, 1991), Terlemez (av. of 15 samples, Yalınız et al., 1999), Yozgat (av. of 9 samples, Düzgören-Aydın et al., 2001), Cefalıkdağ (av. of 11 samples, Geven, 1992) and Çelebi granitoids (av. of 7 leucocratic and 7 mesocratic granitoids, Kuşcu et al., 2002);

Central Anatolian A-type granitoid area: compiled from Bayındır (av. of 10 samples, Otlu and Boztuğ, 1998), Hamit (av. of 15 samples, Otlu and Boztuğ, 1998), İdişdağ (sample SK-6, Köksal, 1996; Göncüoğlu et al., 1997) and Eğrialan syenitoids (av. of 13 samples, Yılmaz and Boztuğ, 1998).

APPENDIX B.

Table B.1. Electron microprobe analyses of zircon crystals from the granitoids

Sample no	SK-1														
Crystal no	[Z1(19)]														
Cross section	A-B	A-B	A-B	A-B	A-B	A-B	A-B	A-B	A-B	A-B	A-B	A-B	A-B	A-B	A-B
Analyses no	1	2	3	4	5	6	7	8	9	10	11	12	13	14	15
ZrO_2 %	64.116	64.631	64.613	64.052	63.580	64.183	63.796	64.565	64.759	64.422	64.876	64.695	64.792	64.966	38.787
SiO_2 %	32.218	32.296	32.009	32.489	32.005	32.319	32.237	32.224	32.121	32.245	32.383	32.292	32.285	32.531	20.439
CaO %			0.010		0.006	0.003	0.010		0.003	0.005	0.003	0.008	0.004	0.013	18.901
Al_2O_3 %				0.012	0.011		0.009			0.002			0.005	0.010	
Zr (ppm)	474657	478469	478336	474183	470689	475153	472288	477981	479417	476922	480283	478943	479661	480949	287144
Si (ppm)	150598	150963	149621	151865	149603	151070	150687	150626	150145	150724	151369	150944	150911	152061	95539
Ca (ppm)			71		43	21	71		21	36	21	57	29	93	135086
Al (ppm)				64	58		48			11			26	53	
Pb (ppm)	84		724	232		28	102		149	316		325			520
Ce (ppm)	43	359		145	145				68	145	265	137			598
Nd (ppm)			249	197	94			34		17		694		180	480
Sm (ppm)		190	371				1009			267		630		155	241
Gd (ppm)		104	130	17	243	95				208	182		503		850
Th (ppm)	70	88	255		334	290	237	378	272	149	9	308	158	70	9
Dy (ppm)		209			70		35	340	1019						
Y (ppm)		79													
U (ppm)	164	363	518	500	1372	1126	1962	91	681	981	554	699	745	372	600
Yb (ppm)		26	474			316	255	228	316	132	114	553	272	360	
Hf (ppm)	11134	12168	11202	12262	14255	17172	14297	12779	11855	13016	14424	11897	10701	12898	7929
Fe (ppm)	70							109	47						47
Nb (ppm)															
Ta (ppm)	450		385				377	336	74			221	287		
Ti (ppm)	12	36	6	12	90						18	24	54		36
P (ppm)															59480
Sc (ppm)		91	33	20	235	65	26	20		26	26	78		59	
RATIOS															
Th/U	0.430	0.242	0.492		0.244	0.258	0.121	4.160	0.400	0.152	0.016	0.440	0.212	0.189	0.015
Th/Yb		3.336	0.537			0.917	0.932	1.655	0.862	1.134	0.077	0.556	0.581	0.195	
Ta/Yb			0.812				1.479	1.471	0.233			0.400	1.053		
U/Pb	1.957		0.715	2.153		40.447	19.215		4.587	3.108		2.153			1.153
REE+Y (ppm)	43	967	1224	360	552	412	1298	602	1404	770	561	2014	775	695	2169

(Values below detection limit or zero values are not shown)

(REE = Ce+Nd+Sm+Gd+Dy+Yb)

Table B.1. (cont'd)

Sample no	SK-1					SK-1										
Crystal no	[Z1(19)]					[Z1(23)]										
Cross section	A-B	A-B	A-B	A-B	A-B	A-B	A-B	A-B	A-B	A-B	A-B	A-B	A-B	A-B	A-B	A-B
Analyses no	16	17	18	19	20	1	2	3	4	5	6	7	8	9	10	11
ZrO_2 %	65.046	65.420	65.039	65.822	0.976	64.938	64.893	65.459	65.473	65.337	65.483	65.066	65.004	65.533	65.232	65.351
SiO_2 %	32.414	32.420	32.544	32.923	1.452	32.594	32.391	32.630	32.512	32.603	32.655	32.542	32.603	32.608	32.584	32.393
CaO %		0.003			0.008	0.005	0.014						0.010	0.008		
Al_2O_3 %			0.002		0.017		0.004	0.013					0.058	0.045		
Zr (ppm)	481541	484310	481490	487286	7225											
Si (ppm)	151514	151542	152122	153894	6787	480742	480409	484599	484703	483696	484777	481690	481231	485147	482918	483799
Ca (ppm)		21			57	152356	151407	152524	151972	152398	152641	152113	152398	152421	152309	151416
Al (ppm)			11		90	36	100						71	57		
Pb (ppm)			399	186	149											
Ce (ppm)	120					362	130		232	260	288				46	56
Nd (ppm)					206		17					51	34	213	17	102
Sm (ppm)				198		171	446						137			369
Gd (ppm)	165		243	607	147	130	243	286	599	113	113	182	165			
Th (ppm)		246	606	132	79	202	246	378	185	316	114	360	475	395	589	466
Dy (ppm)	96				35	610						235			383	200
Y (ppm)			102								94	94	118		55	
U (ppm)	554	1117	2980	2689		1190	1072	1335	999	1145	1408	1862	1762	1335	1490	1008
Yb (ppm)	299	624	861	869	26	632	211	501	457	132	580	808	536	413	386	149
Hf (ppm)	13390	13144	12609	12397	17	13678	12779	14000	12542	14653	14797	13466	13678	13440	13805	10930
Fe (ppm)					342		117	163	109	39		101	295		47	47
Nb (ppm)					24											
Ta (ppm)			131	238		98	106	532	393	467	41		491	884	57	41
Ti (ppm)	78		12	78	18			30					48		48	96
P (ppm)					31											
Sc (ppm)	78				7		13			20	52	52	26	52		13
RATIOS																
Th/U		0.220	0.204	0.049		0.170	0.230	0.283	0.185	0.276	0.081	0.194	0.269	0.296	0.395	0.462
Th/Yb		0.395	0.705	0.152	3.002	0.320	1.168	0.755	0.404	2.402	0.197	0.446	0.886	0.958	1.524	3.120
Ta/Yb			0.152	0.273		0.155	0.505	1.064	0.861	3.544	0.071		0.917	2.143	0.148	0.274
U/Pb			7.464	14.483		3.287	8.248		4.306	4.404	4.893				32.097	18.103
REE+Y (ppm)	679	624	1206	1675	414	1544	917	787	1055	245	787	1371	990	626	842	821

Table B.1. (cont'd)

Sample no	SK-1															SK-3		
Crystal no	[Z1(23)]															[Z3(18)]		
Cross section	A-B	A-B	A-B	A-B	A-B	A-B	A-B	A-B	A-B	A-B	A-B	A-B	A-B	A-B	A-B	A-B	A-B	A-B
Analyses no	12	13	14	15	16	17	18	19	20	21	22	23	24	25	26	1	2	3
ZrO_2 %	65.427	65.429	65.556	65.207	64.035	64.460	65.340	65.856	64.012	64.646	65.220	67.203	65.503	64.580	64.509	64.896	65.288	64.317
SiO_2 %	32.519	32.632	32.386	32.299	31.713	32.360	32.420	32.618	31.508	32.072	32.298	33.748	32.488	32.553	32.579	32.185	32.467	32.193
CaO %	0.018	0.008	0.001	0.012	0.006	0.040	0.007		0.010	0.006	0.016	0.010	0.002	0.003	0.005		0.007	
Al_2O_3 %				0.001			0.001	0.002							0.005		0.007	
Zr (ppm)																480431	483333	476145
Si (ppm)	484362	484377	477914	482733	474057	477203	483718	487538	473887	478580	482830	497510	484925	478092	477566	150444	151762	150481
Ca (ppm)	152005	152533	151383	150977	148238	151262	151542	152468	147279	149916	150972	157750	151860	152164	152286		50	
Al (ppm)	129	57	7	86	43	286	50		71	43	114	71	14	21	36		37	
Pb (ppm)																	241	
Ce (ppm)	455		241		223	19	427	214	121	408	186				390	34		495
Nd (ppm)	231	213				213		282		85		51	154	239		369	600	51
Sm (ppm)	180	446	377	935		574	360			34		163		746			250	
Gd (ppm)		442	468	165	95	512	260	364	434		26				17	87	130	217
Th (ppm)	817	826	1301	580	422	1450	237	70	334	193	255	896	809	2197	1389	2962	1582	6345
Dy (ppm)	488		218			932				558	105	592		366	52		462	322
Y (ppm)			1567			1126							244	638	677	4158	2221	3756
U (ppm)	2289	2380	5723	1590	1762	4587	1889	1681	1808	1199	1154	3198	4360	8257	8703	3479	2071	5896
Yb (ppm)	281		1133	246	483	1019	448	571	281	624	255	711	711	755	790	1475	553	1352
Hf (ppm)	14602	13992	13152	12075	13457	13551	13491	13602	12983	13067	12440	15535	14059	15510	17943	11516	11431	11202
Fe (ppm)	23	132		225	264	86			350	54	171		117					23
Nb (ppm)																		
Ta (ppm)	377	557			385	25		123			614	565	794	238		98		188
Ti (ppm)		66	96	18	78	12		60	48	66		42	84	6		66	48	
P (ppm)																		
Sc (ppm)		20	176	52	26	78	98	26	26			13	72	85	39	241	156	235
RATIOS																		
Th/U	0.357	0.347	0.227	0.365	0.239	0.316	0.126	0.042	0.185	0.161	0.221	0.280	0.185	0.266	0.160	0.851	0.764	1.076
Th/Yb	2.908		1.148	2.359	0.874	1.423	0.530	0.123	1.188	0.310	1.000	1.260	1.137	2.909	1.575	2.007	2.859	4.692
Ta/Yb	1.341				0.797	0.024		0.215			2.412	0.794	1.117	0.315		0.067		0.139
U/Pb	5.033		23.711		7.910	247.065	4.425	7.871	14.979	2.936	6.214				22.320		8.581	
REE+Y (ppm)	1180	1102	3763	1345	578	4377	1068	1217	715	1301	385	1518	1109	2744	1537	6123	4216	6194

Table B.1. (cont'd)

Sample no	SK-3																		
Crystal no	[Z3(18)]																		
Cross section	A-B	A-B	A-B	A-B	A-B	A-B	A-B	A-B	A-B	A-B	A-B	A-B	A-B	A-B	A-B	A-B	A-B	A-B	A-B
Analyses no	4	5	6	7	8	9	10	11	12	13	14	15	16	17	18	19	20	21	22
ZrO_2 %	63.860	66.154	66.453	66.165	66.320	62.547	65.988	65.997	66.248	65.977	64.081	66.466	65.694	65.849	66.150	63.710	65.674	66.249	64.469
SiO_2 %	32.098	32.598	32.653	32.632	32.773	31.704	32.627	32.687	32.527	32.493	31.573	32.771	32.548	32.522	32.422	31.639	32.383	32.528	32.222
CaO %		0.003	0.011			0.056				0.013	0.018	0.009		0.001	0.004	0.024			
Al_2O_3 %			0.008			0.041	0.006		0.005						0.004	0.009		0.001	
Zr (ppm)	472761	489744	491958	489826	490973	463041	488515	488582	490440	488434	474397	492054	486339	487486	489714	471651	486191	490447	477270
Si (ppm)	150037	152374	152632	152533	153192	148196	152510	152790	152043	151884	147583	153183	152141	152019	151552	147892	151369	152047	150617
Ca (ppm)		21	79			400				93	129	64		7	29	172			
Al (ppm)			42			217	32		26						21	48		5	
Pb (ppm)	9	139	492	297		316	288	214			19	325			316	576	46	882	93
Ce (ppm)	43	34	384	572	26		410	137			666	128	128	282	256		60		
Nd (ppm)					146			463				17	360			326			94
Sm (ppm)	190	233	52		561						724	845	586			474	95		
Gd (ppm)	87	382		633		434	295	191	321	208	156	547	477		182	468	174	165	147
Th (ppm)	9298	1019	334	598	536	6187	483		44	580	993	308	1406	1345	158	6196	2645	422	475
Dy (ppm)	157	1028	383		349	1333	35	349			44	1063	340		174	366		261	410
Y (ppm)	3457	63				6764							1701	386		2480	236		2315
U (ppm)	7867	1063	191	282	808	9665	1635	400	781	1417	836	1072	2162	2089	1154	5441	2725	1136	4887
Yb (ppm)	1598	659	422	650	527	3847	553	588	457	386	676	667	1616	711	474	1449	457	430	1475
Hf (ppm)	9430	11176	8658	9709	11533	14102	11083	11329	10625	10634	11092	10871	9803	12694	11600	7852	11142	11558	16934
Fe (ppm)	93		39	31	62	326		124	187		132	78	155	109		117	218	70	23
Nb (ppm)						620													
Ta (ppm)		238		483		647		295	82			131		311		409	205	1155	221
Ti (ppm)	48	12	126	48		150		108			138	12	36			6		60	12
P (ppm)																			
Sc (ppm)	170	98	33	7	72	163	39	72	72	65		39	189	104	39	104	46		104
RATIOS																			
Th/U	1.182	0.959	1.751	2.122	0.663	0.640	0.296		0.056	0.409	1.188	0.287	0.650	0.644	0.137	1.139	0.971	0.372	0.097
Th/Yb	5.817	1.548	0.793	0.920	1.017	1.608	0.874		0.096	1.501	1.469	0.461	0.870	1.890	0.334	4.276	5.793	0.980	0.322
Ta/Yb		0.361		0.744		0.168		0.501	0.179			0.196		0.438		0.283	0.448	2.684	0.150
U/Pb	847.429	7.633	0.388	0.948		30.623	5.682	1.872			45.014	3.299			3.655	9.454	58.713	1.288	52.646
REE+Y (ppm)	5531	2399	1241	1855	1607	12378	1293	1727	778	595	2266	3267	5208	1379	1087	5564	1021	857	4442

Table B.1. (cont'd)

Sample no	SK-3												SK-3					
Crystal no	[Z3(16)]												[Z3(16)]					
Cross section	A-B	A-B	A-B	A-B	A-B	A-B	A-B	A-B	A-B	A-B	A-B		B-C	B-C	B-C	B-C	B-C	B-C
Analyses no	1	2	3	4	5	6	7	8	9	10	11		1	2	3	4	5	6
ZrO_2 %	65.482	50.130	31.193	51.932	65.938	65.821	66.077	65.866	63.846	56.898	66.343		66.205	66.065	50.679	66.286	66.272	66.092
SiO_2 %	32.778	36.655	43.039	39.816	32.637	32.398	32.414	32.371	32.596	33.504	32.516		32.461	32.985	34.297	32.563	32.547	32.392
CaO %	0.002	2.227	0.908	0.918	0.014	0.018	0.005	0.011	0.063	0.207	0.006		0.004	0.020	0.194			
Al_2O_3 %	0.045	2.558	10.383	2.288	0.055	0.046	0.009	0.002	0.136	1.037				0.044	1.139		0.002	
Zr (ppm)	484769	371117	230925	384457	488145	487279	489174	487612	472658	421221	491143		490122	489085	375181	490721	490618	489285
Si (ppm)	153216	171338	201179	186114	152557	151440	151514	151313	152365	156609	151991		151734	154183	160316	152211	152136	151412
Ca (ppm)	14	15916	6489	6561	100	129	36	79	450	1479	43		29	143	1387			
Al (ppm)	238	13538	54952	12109	291	243	48	11	720	5488				233	6028		11	
Pb (ppm)	223	158	19	241			74	334	334		687				195	28		
Ce (ppm)			213	68	94	171	43	188			34		77	162	418	265	94	85
Nd (ppm)	146				77			214		26			111					
Sm (ppm)		198	26		241			43	190	405	26				121	224	190	371
Gd (ppm)	694			243	1050			9	156	312	373		278		651	460	451	95
Th (ppm)	448	3911	2601	2970	650	255		378	3753	5449	97		97	1933	4921			220
Dy (ppm)			52		166	70	967			880	662		70		244	305	279	444
Y (ppm)	24	465	173					126	331						71			
U (ppm)	1535	1054	845	372	690	1090	273	1027	917		118		227	345	427			754
Yb (ppm)	457	1019	220	53	676	422	738	413	369	518	281		167	465	457	88	272	465
Hf (ppm)	15594	10473	7810	11405	14933	14382	13610	13678	14161	10956	13712		13992	10651	10210	12372	12881	11032
Fe (ppm)	62	27338	26654	14512	101		272	303	5791	27517	233		101	1049	45644	396	109	16
Nb (ppm)															72			
Ta (ppm)	41	164		41			131	82	532	205	450		729	8	434		262	
Ti (ppm)	6		174	6		18			12	54	36		96	126		12	36	
P (ppm)		1091																
Sc (ppm)	248		20	52	176	202	163	202		20	124		85	111	72	39		72
RATIOS																		
Th/U	0.292	3.711	3.079	7.976	0.942	0.234		0.368	4.090		0.819		0.426	5.601	11.527			0.291
Th/Yb	0.981	3.839	11.848	56.372	0.962	0.605		0.916	10.174	10.516	0.344		0.579	4.154	10.777			0.472
Ta/Yb	0.090	0.161		0.777			0.178	0.198	1.443	0.395	1.603		4.368	0.018	0.951		0.963	
U/Pb	6.890	6.677	45.503	1.543			3.670	3.072	2.745		0.172				2.190			
REE+Y (ppm)	1320	1682	684	364	2304	662	1748	993	1045	2142	1376		702	628	1961	1341	1286	1461

Table B.1. (cont'd)

Sample no	SK-3											SK-4						
Crystal no	[Z3(16)]											[Z4(7)]						
Cross section	B-C	B-C	B-C	B-C	B-C	B-C	B-C	B-C	B-C	B-C	B-C	A-B	A-B	A-B	A-B	A-B	A-B	A-B
Analyses no	7	8	9	10	11	12	13	14	15	16	17	1	2	3	4	5	6	7
ZrO_2 %	66.422	65.674	66.067	66.132	47.676	63.900	66.529	66.302	64.562	64.299	64.304	63.965	61.333	64.788	63.763	40.018	62.818	65.448
SiO_2 %	32.398	32.398	32.507	32.507	32.103	33.563	32.564	32.384	32.923	32.073	31.901	31.949	31.063	31.963	31.799	34.858	31.308	32.007
CaO %		0.006			0.553	0.099	0.002	0.010	0.007		0.086	0.041	0.206	0.080	0.066	0.585	0.035	0.011
Al_2O_3 %					1.307	0.262					0.002	0.114	0.208	0.062	0.093	5.723	0.024	
Zr (ppm)	491728	486191	489100	489581	352950	473058	492520	490840	477958	476011	476048	473539	454054	479631	472043	296257	465047	484518
Si (ppm)	151440	151440	151949	151949	150061	156885	152216	150907	149219	149920	149116	149341	145199	149406	148640	162938	146345	149612
Ca (ppm)		43			3952	708	14	71	50		615	293	1472	572	472	4181	250	79
Al (ppm)					6917	1387					11	603	1101	328	492	30289	127	
Pb (ppm)	585		260			278	74		418	473		9	111	427		251		418
Ce (ppm)			26	188	171	256		145	452		657		239	222	60		888	
Nd (ppm)				257		352	214		403					86	111		566	412
Sm (ppm)	655		276		216	181	379		155		699							595
Gd (ppm)	121		920	980	772			78	668	946	373		1111		677	703	390	555
Th (ppm)	413	1670	272	334	6512	2109		123	1643	1274	1318	615	1362	352	352	141	879	466
Dy (ppm)	183	17		723	192	645	253			697	645		9	1263	279	235	61	
Y (ppm)		1213			1110				3662	4197	3882	2378	9654	528	1126	1425	6087	2441
U (ppm)	500	2553	1653	1117	3679	409	690	391	6822	7758	7077	5450	7140	518	4742	1899	10065	3606
Yb (ppm)	378	852	334	79	738	342	334	720	1572	1273	1914	984	2731	527	1449	1256	2599	1484
Hf (ppm)	11982	13949	14212	14467	10125	11142	11651	9964	14814	16544	15917	19673	16332	17307	19063	14153	19775	14102
Fe (ppm)	16			163	52764	8698	16	194			179	591	1376	404	272	32997	241	47
Nb (ppm)																		
Ta (ppm)	229		491	205	238	303	753		360		663	74	811	221	573			
Ti (ppm)		36			114		30		102	36		66	30	12	48	312	12	72
P (ppm)																		
Sc (ppm)	7	156	46		39			189	176	91	124	78	143	20	91	163	313	150
RATIOS																		
Th/U	0.827	0.654	0.165	0.299	1.770	5.160		0.315	0.241	0.164	0.186	0.113	0.191	0,679	0.074	0.074	0.087	0.129
Th/Yb	1.094	1.960	0.816	4.225	8.828	6.158		0.171	1.045	1.000	0.689	0.625	0.499	0,667	0.243	0.112	0.338	0.314
Ta/Yb	0.607		1.472	2.590	0.322	0.885	2.258		0.229		0.347	0.075	0.297	0,420	0.396			
U/Pb	0.854		6.361			1.468	9.296		16.331	16.386		587.133	64.095	1.213		7.575		8.633
REE+Y (ppm)	1337	2082	1555	2228	3198	1776	1180	943	6912	7113	8170	3362	13744	2626	3702	3619	10592	5487

Table B.1. (cont'd)

Sample no	SK-4														SK-4			
Crystal no	[Z4(7)]														[Z4(1)]			
Cross section	A-B	A-B	A-B	A-B	A-B	A-B	A-B	A-B	A-B	A-B	A-B	A-B	A-B		A-B	A-B	A-B	A-B
Analyses no	8	9	10	11	12	13	14	15	16	17	18	19	20		1	2	3	4
ZrO_2 %	66.203	66.31	65.982	66.119	66.271	66.085	66.902	66.223	66.08	66.208	65.302	66.3	65.923		66.258	66.206	64.837	64.775
SiO_2 %	32.293	32.417	32.394	32.383	32.335	32.353	32.546	32.27	32.334	32.079	32.251	32.534	32.364		32.076	32.189	31.689	31.764
CaO %	0.011	0.006	0.002	0.010	0.020	0.007	0.017	0.032	0.945	0.785	0.009	0.010	0.001		0.002	0.010	0.024	
Al_2O_3 %			0.004		0.010	0.005	0.004	0.009	0.005						0.001	0.002	0.019	0.003
Zr (ppm)	490107	490899	488471	489485	490610	489233	495282	490255	489196	490144	483437	490825	488034		490514	490129	479994	479535
Si (ppm)	150949	151528	151421	151369	151145	151229	152131	150841	151140	149948	150752	152075	151281		149934	150463	148125	148476
Ca (ppm)	79	43	14	71	143	50	121	229	6754	5610	64	71	7		14	71	172	
Al (ppm)			21		53	26	21	48	26						5	11	101	16
Pb (ppm)			297	418	19	678	511	353			9	65	863			223	297	343
Ce (ppm)		17	43				333	444	333	205	111						120	
Nd (ppm)	249	394	857		69		43	557				300					317	206
Sm (ppm)	276	586		492				86				397	17				69	224
Gd (ppm)	399		668		234	763	434		52	191	607		330		434		668	
Th (ppm)	193	105	167	237	316	677	211	905	79	360	1397	255	606		518		756	905
Dy (ppm)		322	784		732		209					331	183			70		87
Y (ppm)											1953		55				2221	2291
U (ppm)	808	699	881	1172	1335	563	590	727	927	1045	4070	1281	2171		55	91	2525	4270
Yb (ppm)	44	299		439	404	439		465	430	114	1071	571	448			439	1001	826
Hf (ppm)	12152	12347	9548	11821	12788	13551	11643	10566	11524	11778	12677	14619	15069		9404	12270	14238	14823
Fe (ppm)	86				70		62	8					155		132		839	233
Nb (ppm)																		
Ta (ppm)	74	180			82	180	8		622		377	729	139			369	336	
Ti (ppm)			30		12	78			66	162			66		96	96	162	66
P (ppm)									2239									
Sc (ppm)		52	13	33	13	78		52	72	20	7	52	72		13	33	176	248
RATIOS																		
Th/U	0.239	0.151	0.190	0.203	0.237	1.202	0.357	1.246	0.085	0.345	0.343	0.199	0.279		9.513		0.299	0.212
Th/Yb	4.403	0.353		0.540	0.783	1.541		1.945	0.184	3.156	1.304	0.447	1.354				0.755	1.096
Ta/Yb	1.679	0.603			0.203	0.410			1.446		0.352	1.277	0.311			0.839	0.335	
U/Pb			2.966	2.805	71.924	0.831	1.157	2.060			438.393	19.711	2.515			0.408	8.501	12.430
REE+Y (ppm)	968	1619	2352	931	1439	1203	1019	1553	815	510	3743	1599	1033		434	509	4.396	3.634

Table B.1. (cont'd)

Sample no	SK-4									SK-4						
Crystal no	[Z4(1)]									[Z4(1)]						
Cross section	A-B	A-B	A-B	A-B	A-B	A-B	A-B	A-B	A-B	C-D	C-D	C-D	C-D	C-D	C-D	C-D
Analyses no	5	6	7	8	9	10	11	12	13	1	2	3	4	5	6	7
ZrO_2 %	65.865	66.193	66.392	66.136	66.391	66.427	65.846	66.100	66.034	66.244	65.962	65.489	65.417	64.977	65.115	65.936
SiO_2 %	31.891	32.170	32.185	32.224	32.185	31.995	32.064	32.033	32.075	32.008	31.767	31.924	31.795	31.488	31.686	31.877
CaO %	0.004	0.004	0.010	0.002	0.009	0.002	0.008	0.010	0.007		0.016	0.003	0.002	0.016	0.001	
Al_2O_3 %	0.004	0.034			0.005					0.003	0.006	0.001	0.004			0.001
Zr (ppm)	487.605	490.033	491.506	489.611	491.499	491.765	487.464	489.344	488.856	490.410	488.323	484.821	484.288	481.031	482.052	488.130
Si (ppm)	149.070	150.374	150.444	150.626	150.444	149.556	149.878	149.733	149.930	149.617	148.490	149.224	148.621	147.186	148.111	149.004
Ca (ppm)	29	29	71	14	64	14	57	71	50		114	21	14	114	7	
Al (ppm)	21	180			26					16	32	5	21			5
Pb (ppm)				269		446	111		46		46	473		111	473	
Ce (ppm)				102	222		120	563	324		290		213	572	273	393
Nd (ppm)		77	51			249	574	429	1.115		180	986				
Sm (ppm)		250	155		34		724			733	216	621	535			388
Gd (ppm)			78	529		599			121		555		295			
Th (ppm)	545	105	237	167	308	510			598	264	466	431	2.250	1.134	958	457
Dy (ppm)		497					35		253	436	418				357	
Y (ppm)									197				827	1.465	402	
U (ppm)	827	799	354		200	164	336	36	1.045	472	154	1.008	2.198	4.587	2.534	1.499
Yb (ppm)	746		369		202	167	61	422	316	228		325	413	1.642	861	571
Hf (ppm)	10.235	11.431	11.524	10.439	11.405	10.388	13.432	12.652	11.176	11.490	9.022	12.525	10.523	13.932	11.660	11.872
Fe (ppm)	70	8	47	225			86	210	39	39		54	117			16
Nb (ppm)																
Ta (ppm)	794	524		270	688			639	197		467	295	409	803		
Ti (ppm)	24		36				6		36	60			12	48		
P (ppm)																
Sc (ppm)	52	13		33		7		91	150		13	33	20	98	98	20
RATIOS																
Th/U	0.659	0.132	0.670		1.539	3.117			0.572	0.558	3.016	0.427	1.023	0.247	0.378	0.305
Th/Yb	0.730		0.643		1.523	3.055			1.890	1.155		1.325	5.451	0.690	1.113	0.800
Ta/Yb	1.064				3.406			1.515	0.622			0.907	0.992	0.489		
U/Pb						0.367	3.017		22.507		3.327	2.130		41.181	5.353	
REE+Y (ppm)	746	824	654	632	458	1.014	1.515	1.414	2.326	1.397	1.659	1.932	2.283	3.679	1.893	1.352

Table B.1. (cont'd)

Sample no	**SK-4**							**SK-6**									**SK-6**				
Crystal no	**[Z4(1)]**							**[Z6(19)]**									**[Z6(19)]**				
Cross section	**C-D**	**C-D**	**C-D**	**C-D**	**C-D**	**C-D**		**A-B**	**A-B**	**A-B**	**A-B**	**A-B**	**A-B**	**A-B**	**A-B**		**C-D**	**C-D**	**C-D**	**C-D**	**C-D**
Analyses no	**8**	**9**	**10**	**11**	**12**	**13**		**1**	**2**	**3**	**4**	**5**	**6**	**7**	**8**		**9**	**10**	**11**	**12**	**13**
ZrO_2 %	63.736	63.551	65.319	65.052	65.064	62.443		64.924	65.398	65.172	64.692	64.410	65.109	65.728	65.570		**65.326**	**65.511**	**63.731**	**65.213**	**65.207**
SiO_2 %	31.276	31.243	31.608	31.568	31.576	28.861		31.94	31.523	31.623	31.515	31.670	31.517	31.582	31.699		31.686	31.402	31.063	31.537	31.537
CaO %	0.006	0.001				0.023		0.015	0.002	0.006		0.008	0.004		0.008						
Al_2O_3 %			0.006		0.005	0.017		0.106		0.003	0.006	0.013	0.008				0.003	0.007			0.007
Zr (ppm)	471.843	470.474	483.563	481.586	481.675	462.271		480.638	484.147	482.474	478.921	476.833	482.008	486.590	485.421		483.614	484.984	471.806	482.778	482.733
Si (ppm)	146.195	146.041	147.747	147.560	147.597	134.906		149.299	147.350	147.817	147.312	148.037	147.321	147.625	148.172		148.111	146.784	145.199	147.415	147.415
Ca (ppm)	43	7				164		107	14	43		57	29		57						
Al (ppm)			32		26	90		561		16	32	69	42				16	37			37
Pb (ppm)	631		687		46			455	56	102		186			74		325	149		176	158
Ce (ppm)		179		77	137	623			34			521			9		34	290	111		290
Nd (ppm)	334	240	634	214	283	960		609		94		583	463		472		386	197	412	129	
Sm (ppm)		448	69		147	52				233		285	164	164			492		888		
Gd (ppm)		269	156	139	737	69		503	139	390	946	1.006		295			512				35
Th (ppm)	1.555	1.459	606	360	554	1.380		1.037	35	185	26	483	228	35	193			369	404	932	483
Dy (ppm)	148	261			322	514			357	1.011	836			270	619		688		9	505	
Y (ppm)	3.000	3.449		165		1.386		992			472	1.756	118						2.575		
U (ppm)	6.395	7.858	1.399	1.690	1.853	3.316		1.517	263	400	391	1.653	1.908	590	1.117			82	1.980	2.925	1.662
Yb (ppm)	1.598	1.888	430	255	571	1.063		1.036	202	325	790	1.001	711	334	360		404	562	1.633	667	
Hf (ppm)	13.517	15.348	12.652	12.771	13.695	12.559		13.712	13.059	14.305	14.348	15.713	13.152	11.948	12.508		16.247	13.576	16.146	14.043	13.407
Fe (ppm)		210	86	23		179		93									31			62	
Nb (ppm)																					
Ta (ppm)		188			328			516				925			115			672	459		
Ti (ppm)			90		6			60		30				12					120	108	
P (ppm)																					
Sc (ppm)	170	143	78	39	33	72		137	346	326	372	163	124		20		254	528	313		13
RATIOS																					
Th/U	0.243	0.186	0.434	0.213	0.299	0.416		1	0	0	0	0	0	0	0			4.515	0.204	0.319	0.291
Th/Yb	0.973	0.773	1.409	1.415	0.970	1.298		1	0	1	0	0	0	0	1			0.657	0.248	1.400	
Ta/Yb		0.100			0.574			0				1			0			1.195	0.281		
U/Pb	10.131		2.036		39.925			3	5	4		9			15			0.550		16.584	10.534
REE+Y (ppm)	5.081	6.735	1.290	850	2.197	4.667		3.140	732	2.053	3.045	5.152	1.456	1.063	1.459		2.516	1.050	5.628	1.301	325

Table B.1. (cont'd)

Sample no	SK-6											SK-6						
Crystal no	[Z6(19)]											[Z6(17)]						
Cross section	C-D	C-D	C-D	C-D	C-D	C-D	C-D	C-D	C-D	C-D	C-D	A-B	A-B	A-B	A-B	A-B	A-B	A-B
Analyses no	14	15	16	17	18	19	20	21	22	23	24	1	2	3	4	5	6	7
ZrO_2 %	**64.546**	**64.834**	**65.209**	**64.761**	**64.954**	**64.661**	**65.040**	**65.051**	**64.768**	**66.162**	**65.575**	**63693**	**63764**	**64200**	**63933**	**64106**	**63675**	**64539**
SiO_2 %	31.435	31.398	31.537	31.330	31.402	31.456	31.469	31.656	31.409	31.612	31.315	30859	30864	30670	30237	30521	30.67	30601
CaO %	0.005		0.002		0.006	0.002					0.007	0.007	0.018	0.008	0.007	0.002	0.010	
Al_2O_3 %		0.007		0.004	0.002	0.004		0.008	0.008		0.012	0.002	0.053	0.012		0.008		
Zr (ppm)	477.840	479.972	482.748	479.432	480.860	478.691	481.497	481.578	479.483	489.803	485.458	471525	472051	475278	473302	474583	471392	477788
Si (ppm)	146.938	146.765	147.415	146.447	146.784	147.036	147.097	147.971	146.817	147.766	146.377	144246	144269	143362	141338	142666	143362	143040
Ca (ppm)	36		14		43	14					50	50	129	57	50	14	71	
Al (ppm)		37		21	11	21		42	42		64	11	281	64		42		
Pb (ppm)	56	668			130	603	306		37	158	334	195				278	139	548
Ce (ppm)			145	102	581	34		17	487	359	282	85						256
Nd (ppm)	472	429						977	592	283	240	214		69		300		
Sm (ppm)	121	43	86			112		293		207		397						17
Gd (ppm)	69		599		43				200			52		408		972	416	
Th (ppm)	299	492	360	562	193	237	255	422	123	281	571				53		334	1063
Dy (ppm)		192					636	941	584			889		958	871		497	35
Y (ppm)														63		8		
U (ppm)	1.090	1.154	1.045	899	300	745	999	1.290	999	754	1.490		245	3470	463	645	908	1117
Yb (ppm)		685	325	61		35		123	79	193		527	255	1572	782	905	360	
Hf (ppm)	11.499	13.695	13.127	11.643	12.940	13.814	13.364	13.551	12.966	14.407	12.185	12771	15272	16510	12542	12177	11956	11397
Fe (ppm)	86				140	23		109							23		8	124
Nb (ppm)																		
Ta (ppm)				369	16	745			131	287	385	139	672	1204	270			901
Ti (ppm)					60				12		30					6		
P (ppm)																		
Sc (ppm)	150		26	26	91					59		176		437	267	254		91
RATIOS																		
Th/U	0.274	0.427	0.345	0.625	0.645	0.319	0.255	0.327	0.123	0.373	0.383				0.114		0.368	0.952
Th/Yb		0.719	1.109	9.149		6.755		3.431	1.557	1.456					0.067		0.928	
Ta/Yb				5.995		21.216			1.658	1.484		0.264	2637	0.766	0.346			
U/Pb	19.571	1.726			2.307	1.235	3.262		26.910	4.778	4.458					2316	6524	2040
REE+Y (ppm)	662	1.348	1.155	164	624	181	636	2.352	1.941	1.042	522	2164	255	3070	1653	2184	1273	308

Table B.1. (cont'd)

Sample no	SK-6						SK-6										SK-8		
Crystal no	[Z6(17)]						[Z6(17)]										[Z8(21)]		
Cross section	A-B	A-B	A-B	A-B	A-B	A-B	C-D	C-D	C-D	C-D	C-D	C-D	C-D	C-D	C-D	C-D	A-B	A-B	A-B
Analyses no	8	9	10	11	12	13	1	2	3	4	5	6	7	8	9	10	1	2	3
ZrO_2 %	**64352**	**63831**	**64660**	**64546**	**63496**	**64725**	**63880**	**63296**	**63872**	**63205**	**63603**	**64365**	**63588**	**63297**	**54344**	**31461**	**65.699**	**65.756**	**64.812**
SiO_2 %	30553	30335	30670	30658	30565	30825	30874	30524	30895	30761	30750	31024	30649	30590	26361	20374	31.966	31.887	31.962
CaO %	0.006		0.016	0.004	0.001		0.007	0.007	0.006	0.014	0.016	0.031	0.045	0.123	35643	20790	0.024		0.018
Al_2O_3 %		0.005	0.002					0.004		0.005	0.001	0.002	0.001	0.002	0.008	0.879		0.001	0.020
Zr (ppm)	476404	472547	478684	477840	470067	479165	472909	468586	472850	467912	470859	476500	470748	468593	402314	232909	486376	486798	479809
Si (ppm)	142815	141796	143362	143306	142871	144087	144316	142680	144414	143788	143736	145017	143264	142988	123221	95235	149420	149051	149402
Ca (ppm)	43		114	29	7		50	50	43	100	114	222	322	879	64109	148586	172		129
Al (ppm)		26	11					21		26	5	11	5	11	42	4652		5	106
Pb (ppm)	260	399	9		306	214		789	149		678			464	214	594	576	436	9
Ce (ppm)	248		350		299	60	77	751			256	128	299	290	777	282	359	188	51
Nd (ppm)		86	472		60				300			283	369			189			317
Sm (ppm)	17		103	742	181	241	207			103				517		733		431	181
Gd (ppm)		495			373				87	720	26						347		234
Th (ppm)	316	1099	35	905	220	712	642	1520	466	879	79	466	404	677	615	141		290	457
Dy (ppm)	288		78		357	9	410	401	218	183		479		767	122	105		680	1133
Y (ppm)								976		181						1039		874	1913
U (ppm)	1417	2098	1290	1608	945	1481	1417	3988	1199	3107	1499	1726	1499	1626	654	600	118	18	
Yb (ppm)	97	913	237	536		465	114	1238	571	1238		641	342	738	711	571		931	861
Hf (ppm)	12847	10515	12720	13474	13313	14093	11600	13593	13067	11346	14628	13534	13966	11549	9268	9811	8599	9243	10634
Fe (ppm)		171	78						124		389				140			233	
Nb (ppm)																			
Ta (ppm)	385	860			1065	581		74	221	57				74	680	1114			
Ti (ppm)	30	102	42	108	30		72		36			30	6			54	96	66	42
P (ppm)															24588	44083			
Sc (ppm)	59	65			91	33	170			72			72	20			346	254	404
RATIOS																			
Th/U	0.223	0.523	0.027	0.563	0.233	0.481	0.453	0.381	0.388	0.283	0.053	0.270	0.270	0.416	0.941	0.235		15.962	
Th/Yb	3275	1203	0.148	1690		1529	5619	1228	0.816	0.710		0.727	1180	0.917	0.865	0.246		0.312	0.531
Ta/Yb	3985	0.942				1249		0.060	0.387	0.046				0.100	0.956	1951			
U/Pb	5452	5257	139955		3084	6935		5054	8073		2212			3503	3063	1010	0.205	0.042	
REE+Y (ppm)	649	1494	1241	1277	1270	775	807	3367	1175	2426	282	1531	1010	2312	1610	2918	706	3104	4691

Table B.1. (cont'd)

Sample no	SK-8											SK-8							
Crystal no	[Z8(21)]											[Z8(21)]							
Cross section	**A-B**	**A-B**	**A-B**	**A-B**	**A-B**	**A-B**	**A-B**	**A-B**	**A-B**	**A-B**		**C-D**	**C-D**	**C-D**	**C-D**	**C-D**	**C-D**	**C-D**	**C-D**
Analyses no	**4**	**5**	**6**	**7**	**8**	**9**	**10**	**11**	**12**	**13**		**1**	**2**	**3**	**4**	**5**	**6**	**7**	**8**
ZrO_2 %	65.983	65.224	65.870	64.936	65.566	66.145	65.749	66.079	65.674	65.661		65.872	65.488	65.242	65.608	64.947	65.585	65.326	65.080
SiO_2 %	31.997	32.04	32.231	32.015	31.959	32.193	31.946	32.115	32.051	32.300		32.054	32.222	32.117	31.969	32.152	31.994	31.940	32.004
CaO %	0	0	0	0	0	0.004	0	0.003	0	0.005		0	0.011	0.002	0.002	0.012	0.007	0.003	0
Al_2O_3 %	0	0.006	0	0.006	0	0.004	0.005	0.008	0.003	0		0.006	0.007	0	0	0	0	0.002	0.004
Zr (ppm)	488478	482859	487642	480727	485391	489677	486746	489189	486191	486094		487656	484814	482992	485702	480809	485532	483614	481793
Si (ppm)	149565	149766	150659	149649	149388	150481	149327	150117	149818	150981		149832	150617	150126	149434	150290	149551	149299	149598
Ca (ppm)	0	0	0	0	0	29	0	21	0	36		0	79	14	14	86	50	21	0
Al (ppm)	0	32	0	32	0	21	26	42	16	0		32	37	0	0	0	0	11	21
Pb (ppm)	130	334	0	0	0	9	0	316	0	149		520	0	0	9	0	121	0	204
Ce (ppm)	0	461	0	0	120	94	111	94	0	0		0	0	17	0	0	0	34	0
Nd (ppm)	0	0	0	0	394	514	51	0	0	0		0	386	0	609	463	0	412	0
Sm (ppm)	86	60	0	0	0	0	0	440	0	0		0	0	43	0	0	0	362	379
Gd (ppm)	512	0	0	0	442	0	0	460	0	1006		434	0	139	0	87	0	0	0
Th (ppm)	483	0	387	360	237	53	0	167	0	35		176	167	202	378	53	0	0	149
Dy (ppm)	566	87	0	627	0	157	218	122	0	0		131	0	0	296	0	218	0	0
Y (ppm)	409	0	0	0	0	0	0	0	0	0		0	0	0	0	0	0	0	0
U (ppm)	436	227	182	154	391	363	209	127	127	0		118	254	291	609	1081	609	382	1790
Yb (ppm)	606	562	263	0	527	18	35	176	18	746		0	0	360	474	422	88	667	184
Hf (ppm)	8802	9820	11380	10973	13407	11575	10685	10523	10362	12262		11270	12219	11651	13652	14967	12669	12177	12957
Fe (ppm)	0	39	0	70	163	0	233	0	280	194		0	47	0	132	0	0	31	0
Nb (ppm)	0	0	0	0	0	0	0	0	0	0		0	0	0	0	0	0	0	0
Ta (ppm)	958	106	0	0	713	598	0	0	0	0		483	0	156	0	0	0	82	0
Ti (ppm)	12	0	72	78	0	0	102	0	102	72		54	150	84	90	18	0	0	6
P (ppm)	0	0	0	0	0	0	0	0	0	0		0	0	0	0	0	0	0	0
Sc (ppm)	215	163	189	202	150	176	196	52	130	59		85	78	72	176	65	13	91	0
RATIOS																			
Th/U	1.109	0	2.128	2.333	0.607	0.145	0	1.313	0			1.488	0.657	0.695	0.621	0.049	0	0	0.084
Th/Yb	0.798	0	1.468		0.450	3.002	0	0.951	0	0.047				0.561	0.797	0.125	0	0	0.810
Ta/Yb	1.581	0.189	0		1.352	34.038	0	0	0	0				0.432	0	0	0	0.123	0
U/Pb	3.355	0.680				39.142		0.403		0		0.227			65.563		5.043		8.762
REE+Y (ppm)	2180	1171	263	627	1483	783	415	1291	18	1753		564	386	559	1379	971	306	1475	564

Table B.1. (cont'd)

Sample no	SK-8				SK-8								SK-8									
Crystal no	[Z8(21)]				[Z8(20)]								[Z8(20)]									
Cross section	C-D	C-D	C-D		A-B	A-B	A-B	A-B	A-B	A-B	A-B		C-D	C-D	C-D	C-D	C-D	C-D	C-D	C-D	C-D	C-D
Analyses no	9	10	11		1	2	3	4	5	6	7		1	2	3	4	5	6	7	8	9	10
ZrO_2 %	65.120	64.978	64.912		65.128	65.590	65.844	65.230	64.775	65.085	65.651		65.237	65.186	64.731	64.760	64.370	65.020	64.454	65.251	65.035	64.970
SiO_2 %	32.074	31.908	31.989		31.906	32.065	32.092	32.171	32.249	32.292	32.367		32.085	32.146	31.753	31.830	31.909	31.918	31.780	31.879	31.908	31.965
CaO %	0	0	0		0.003	0	0.002	0.006	0	0.004	0		0	0.004	0	0	0	0.003	0	0.007	0.019	0.002
Al_2O_3 %	0	0	0.003		0	0.009	0.001	0.008	0.006	0	0.002		0.011	0.010	0	0.003	0	0.001	0.004	0	0	0.003
Zr (ppm)	482089	481038	480549		482149	485569	487449	482904	479535	481830	486020		482955	482578	479209	479424	476537	481349	477159	483059	481460	480979
Si (ppm)	149925	149149	149528		149140	149883	150009	150378	150743	150944	151295		149976	150262	148425	148785	149154	149196	148551	149014	149149	149416
Ca (ppm)	0	0	0		21	0	14	43	0	29	0		0	29	0	0	0	21	0	50	136	14
Al (ppm)	0	0	16		0	48	5	42	32	0	11		58	53	0	16	0	5	21	0	0	16
Pb (ppm)	0	260	0		0	176	0	0	0	0	0		0	0	251	0	0	0	0	0	0	0
Ce (ppm)	0	0	94		0	0	0	0	68	68	9		0	231	0	0	0	196	256	222	0	0
Nd (ppm)	0	0	0		0	257	0	523	69	163	26		291	506	0	0	0	171	0	0	0	274
Sm (ppm)	285	0	0		112	319	0	0	0	181	302		129	147	0	0	457	0	69	526	0	52
Gd (ppm)	304	95	798		0	0	69	0	0	217	191		226	0	460	147	0	0	1111	980	373	0
Th (ppm)	0	0	26		0	149	0	0	0	35	290		0	88	0	325	228	0	0	62	325	18
Dy (ppm)	0	0	0		0	314	157	0	0	0	549		0	0	941	401	131	732	0	61	653	662
Y (ppm)	0	276	543		0	0	0	0	0	0	0		0	0	362	543	669	173	0	8	394	402
U (ppm)	663	945	382		91	45	236	863	2262	363	945		527	0	799	291	400	536	363	191	300	1553
Yb (ppm)	176	448	562		0	184	0	395	0	35	378		0	0	246	984	992	597	263	878	1142	1001
Hf (ppm)	12576	13254	16247		11838	12135	13669	13627	14229	16103	15993		13101	14093	12754	13966	14568	13050	14187	13347	14695	16553
Fe (ppm)	179	23	148		117	350	0	0	62	0	0		70	0	0	0	62	124	171	0	8	0
Nb (ppm)	0	0	0		0	0	0	0	0	0	0		0	0	0	0	0	0	0	0	0	0
Ta (ppm)	188	123	328		123	0	0	516	82	0	0		0	0	1024	0	0	49	483	713	0	0
Ti (ppm)	30	144	6		60	24	0	42	0	78	0		84	0	0	42	138	0	12	150	78	0
P (ppm)	0	0	0		0	0	0	0	0	0	0		0	0	0	0	0	0	0	0	0	0
Sc (ppm)	98	248	300		98	52	26	150	7	0	0		111	137	261	319	241	170	215	117	300	52
RATIOS																						
Th/U	0	0	0.069		0	3.289	0	0	0	0.097	0.307		0		0	1.118	0.572	0	0	0.322	1.085	0.011
Th/Yb	0	0	0.047			0.810		0		1.000	0.768				0	0.331	0.230	0	0	0.070	0.285	0.018
Ta/Yb	1.072	0.274	0.583			0		1.306		0	0				4.163	0	0	0.082	1.834	0.811	0	0
U/Pb		3.635				0.258									3.189							
REE+Y (ppm)	764	819	1997		112	1074	226	918	137	664	1454		646	883	2009	2075	2249	1870	1699	2675	2562	2391

Table B.1. (cont'd)

Sample no	SK-9																
Crystal no	[Z9(1)]																
Cross section	A-B	A-B	A-B	A-B	A-B	A-B	A-B	A-B	A-B	A-B	A-B	A-B	A-B	A-B	A-B	A-B	A-B
Analyses no	1	2	3	4	5	6	7	8	9	10	11	12	13	14	15	16	17
ZrO_2 %	66.092	66.238	65.910	65.394	65.976	63.993	66.679	65.221	64.323	66.299	65.976	66.676	66.525	66.99	65.907	66.083	66.138
SiO_2 %	32.442	32.638	32.533	32.484	32.437	31.723	32.960	32.033	31.530	32.472	32.438	32.460	32.662	32.809	32.456	32.386	32.497
CaO %	0.003		0.014	0.009	0.009	1.409	0.004	0.024	0.028		0.034	0.006	0.008	0.004	0.005		
Al_2O_3 %	0.011	0.013			0.007	0.015	0.001	0.012			0.002			0.006	0.004		
Zr (ppm)	489285	490366	487938	484118	488426	473746	493631	482837	476189	490818	488426	493609	492491	495933	487916	489218	489626
Si (ppm)	151645	152561	152071	151842	151622	148284	154067	149733	147382	151785	151627	151729	152674	153361	151711	151383	151902
Ca (ppm)	21		100	64	64	10070	29	172	200		243	43	57	29	36		
Al (ppm)	58	69			37	79	5	64			11			32	21		
Pb (ppm)			371	576	761		325		56	306	130	139				111	306
Ce (ppm)		17	34	213	205	154			299				9		26	359	
Nd (ppm)		566	86	34	223	412	249			43	274		43	300		154	129
Sm (ppm)		302	526							448	983			86	138	129	474
Gd (ppm)	980				573	43		321	503		269	1076	26	52		755	52
Th (ppm)	536	290	1151	1274	228	2136	395	1019	132	70	518	26	228		185		26
Dy (ppm)	253	601		523		157	383			349		209		758		35	427
Y (ppm)						772		16									
U (ppm)	1290	917	2734	3288	1472	3134	654	2435	1335	491	1281	418	527	363	127	509	481
Yb (ppm)	193	149	457	685	97	1063	325	413	624		211	141	351	53	193	220	307
Hf (ppm)	12762	14475	12796	11812	11711	11795	11889	11549	12304	12533	13534	10922	11566	11651	10549	9769	9353
Fe (ppm)			132		47	171		23		117						39	78
Nb (ppm)																	
Ta (ppm)		369	385	1032			893	549		147	508	442		516		835	328
Ti (ppm)				18			90	84		66	78			54	66	36	48
P (ppm)						1205											
Sc (ppm)	46	65	65		13		98	59	85			91	65	65	85	117	85
RATIOS																	
Th/U	0.416	0.316	0.421	0.388	0.155	0.681	0.605	0.419	0.099	0.143	0.405	0.063	0.434		1.451		0.055
Th/Yb	2.775	1.943	2.521	1.860	2.365	2.010	1.217	2.470	0.211		2.460	0.188	0.650		0.955		0.086
Ta/Yb		2.469	0.843	1.506			2.747	1.329			2.409	3.147		9.792		3.805	1.066
U/Pb			7.364	5.713	1.933		2.013		23.975	1.601	9.855	3.001				4.567	1.572
REE+Y (ppm)	1426	1635	1103	1456	1097	2600	957	750	1426	840	1737	1425	429	1249	357	1651	1389

Table B.1. (cont'd)

Sample no	SK-9																
Crystal no	[Z9(1)]																
Cross section	**A-B**	**A-B**	**A-B**	**A-B**	**A-B**	**A-B**	**A-B**	**A-B**	**A-B**	**A-B**	**A-B**	**A-B**	**A-B**	**A-B**	**A-B**	**A-B**	**A-B**
Analyses no	**18**	**19**	**20**	**21**	**22**	**23**	**24**	**25**	**26**	**27**	**28**	**29**	**30**	**31**	**32**	**33**	**34**
ZrO_2 %	65.778	65.920	65.807	65.801	65.743	65.627	65.593	65.894	65.805	66.281	66.270	65.777	66.164	66.056	65.950	65.919	63.662
SiO_2 %	32.419	32.509	32.535	32.547	35.395	32.496	32.654	32.500	32.464	32.494	32.605	32.632	32.493	32.515	32.630	32.286	32.160
CaO %		0.001	0.072	0.006	0.007	0.008	0.006	0.009	0.008	0.010	0.001	0.007		0.003	0.002		
Al_2O_3 %	0.008			0.002	18.577			0.010	0.004	0.002			0.001	0.002			
Zr (ppm)	486961	488012	487175	487131	486701	485843	485591	487819	487160	490684	490603	486953	489818	489019	488234	488004	471296
Si (ppm)	151538	151958	152080	152136	165449	151898	152636	151916	151748	151888	152407	152533	151884	151986	152524	150916	150327
Ca (ppm)		7	515	43	50	57	43	64	57	71	7	50		21	14		
Al (ppm)	42			11	98319			53	21	11			5	11			
Pb (ppm)	306		381	37		149						288		343	232		130
Ce (ppm)		145		342		120	85	196					17	359	239	102	
Nd (ppm)		343	51	146					231	609	472	506			17	506	180
Sm (ppm)	371	466			354	328	957			95			379		535		43
Gd (ppm)		174					373		685	1249			286				850
Th (ppm)	747	633		677	1459	650	571	422	439	220	220	281	70	431	466	26	255
Dy (ppm)	758	610	427	235	314				296			235	767		192	871	166
Y (ppm)	31			8	795												1654
U (ppm)	2062	2680	1245	3107	5078	2762	1526	1235	1617	1181	945	981	1081	1472	1562	890	10174
Yb (ppm)	211	430	966	378	1194	817	544		263	272	158	307	501	1045	422	149	1361
Hf (ppm)	13016	15043	14882	16832	17027	13924	14831	12881	13720	11566	14738	13296	13992	13712	13161	14204	21420
Fe (ppm)	140	148			54			78	70				241			8	
Nb (ppm)																	
Ta (ppm)		631		33	844	369		180		74	172	770	66	729	180	532	172
Ti (ppm)	66	6	30			126	90	90	96	102	12	36	84		54		
P (ppm)																	
Sc (ppm)	72	46				7					98	33		33			98
RATIOS																	
Th/U	0.362	0.236		0.218	0.287	0.236	0.374	0.341	0.272	0.186	0.233	0.287	0.065	0.293	0.298	0.030	0.025
Th/Yb	3.544	1.470		1.792	1.221	0.796	1.049		1.668	0.807	1.390	0.915	0.141	0.412	1.105	0.177	0.187
Ta/Yb		1.465		0.087	0.706	0.451				0.271	1.088	2.505	0.131	0.698	0.427	3.566	0.126
U/Pb	6.731		3.270	83.667		18.593						3.409		4.285	6.733		78.285
REE+Y (ppm)	1371	2168	1444	1108	2657	1264	1960	196	1477	2225	630	1048	1950	1404	1404	1629	4254

Table B.1. (cont'd)

Sample no	SK-9																			
Crystal no	**[Z9(11)]**																			
Cross section	**A-B**	**A-B**	**A-B**	**A-B**	**A-B**	**A-B**	**A-B**	**A-B**	**A-B**	**A-B**	**A-B**	**A-B**	**A-B**	**A-B**	**A-B**	**A-B**	**A-B**	**A-B**	**A-B**	**A-B**
Analyses no	**1**	**2**	**3**	**4**	**5**	**6**	**7**	**8**	**9**	**10**	**11**	**12**	**13**	**14**	**15**	**16**	**17**	**18**	**19**	**20**
ZrO_2 %	66.186	65.568	65.614	66.222	65.700	65.173	64.474	65.357	65.737	65.567	65.523	65.377	65.424	65.494	65.814	65.862	65.528	65.383	65.513	65.435
SiO_2 %	32.327	32.232	32.271	32.138	32.177	32.169	32.137	32.257	32.483	32.395	32.229	32.536	32.484	32.366	32.173	32.488	32.478	32.299	32.382	32.412
CaO %	0.003						0.002	0.006	0.005	0.014		0.010		0.004	0.006	0.014	0.004			0.002
Al_2O_3 %								0.001							0.003			0.005	0.002	
Zr (ppm)	489981	485406	485746	490247	486383	482482	477307	483844	486657	485398	485073	483992	484340	484858	487227	487582	485110	484036	484999	484421
Si (ppm)	151108	150664	150846	150224	150407	150369	150220	150780	151837	151426	150650	152085	151842	151290	150388	151860	151814	150977	151365	151505
Ca (ppm)	21						14	43	36	100		71		29	43	100	29			14
Al (ppm)								5							16			26	11	
Pb (ppm)	149		28			483		204	566		678	84	371				46	251		603
Ce (ppm)		17	68	60	145	162	196			470	213	196		179	418			34	461	85
Nd (ppm)	669	326			489					274	189	257	274		180	386	129			
Sm (ppm)	630				595				543	569	155		949	121		535	60			
Gd (ppm)		113	330	460	590				460	217		581		1171		208	95	659		390
Th (ppm)	580	554	518	835	659	923	1986	800	360	589	721	422	404	1186	844	536		220	114	747
Dy (ppm)			261	139		288		549	1560	227		235		340	200		366	418	87	349
Y (ppm)	236	425	441	307	331	1551	3347	937		55	1016			63						
U (ppm)	1263	899	2117	1835	1535	2280	6958	3270	1917	1762	3252	2353	1980	3543	2180	2035	1671	2144	1408	2407
Yb (ppm)	729	615	1001	826		1361	1572	957	263	755	782	966	852	711	386	360	132	149	615	544
Hf (ppm)	9854	9497	9294	8768	7784	10015	12804	12440	15459	13797	13814	14085	15442	14772	13627	12737	14823	11414	14534	13627
Fe (ppm)				47	86	47		31		163	101		8				86	23	31	
Nb (ppm)																				
Ta (ppm)	41			147	25	172	74		123	74	33	336	287	188		278	532		221	278
Ti (ppm)	36	12	6					72	36	72	30	96	24	36	6					
P (ppm)																				
Sc (ppm)		85		52	124	52	137	85	91		46	39	33	78	7		91	7		65
RATIOS																				
Th/U	0.459	0.616	0.245	0.455	0.429	0.405	0.285	0.245	0.188	0.334	0.222	0.179	0.204	0.335	0.387	0.264		0.103	0.081	0.310
Th/Yb	0.796	0.901	0.518	1.011		0.678	1.263	0.835	1.368	0.780	0.922	0.437	0.475	1.668	2.183	1.489		1.472	0.186	0.372
Ta/Yb	0.056			0.179		0.126	0.047		0.466	0.098	0.042	0.348	0.337	0.265		0.773	4.041		0.360	0.511
U/Pb	8.501		76.001			4.723		16.013	3.385		4.799	28.161	5.333				36.011	8.553		3.990
REE+Y (ppm)	2263	1496	2101	1792	2150	3362	5115	2443	2826	2567	2355	2236	2075	2585	1185	1489	782	1261	1163	1369

Table B.1. (cont'd)

Sample no	SK-9					SK-12													
Crystal no	[Z9(11)]					[Z12(21)]													
Cross section	A-B	A-B	A-B	A-B	A-B	A-B	A-B	A-B	A-B	A-B	A-B	A-B	A-B	A-B	A-B	A-B	A-B	A-B	A-B
Analyses no	21	22	23	24	25	1	2	3	4	5	6	7	8	9	10	11	12	13	14
ZrO_2 %	65.597	65.486	65.424	65.772	64.910	65.641	11.356	65.875	65.881	65.728	65.688	64.620	65.573	65.705	65.657	65.740	65.489	65.426	65.351
SiO_2 %	32.319	32.369	32.387	32.334	32.269	32.868	68.395	32.93	32.947	32.802	32.839	32.500	32.882	32.868	32.679	32.634	32.911	32.831	32.872
CaO %	0.002	0.002	0.004		0.008		0.933	0.003	0.006	0.008	0.001	0.009	0.003	0.002	0.013	0.016	0.011	0.013	0.010
Al_2O_3 %	0.001						11.465	0.011									0.007	0.001	
Zr (ppm)	485621	484799	484340	486916	480535	485946	84070	487679	487723	486590	486294	478388	485443	486420	486065	486679	484821	484355	483799
Si (ppm)	151070	151304	151388	151140	150837	153637	319702	153926	154006	153328	153501	151916	153702	153637	152753	152543	153838	153464	153655
Ca (ppm)	14	14	29		57		6668	21	43	57	7	64	21	14	93	114	79	93	71
Al (ppm)	5						60679	58									37	5	
Pb (ppm)	241		195	882		241	37		149	260		455			111		93	316	
Ce (ppm)	68	171		9			213	307					94			77	43		
Nd (ppm)	557	223	214			291	77		197	446			497		120	43		111	
Sm (ppm)	414	26		164		354	354		147	319	362								
Gd (ppm)			338	364	330		269	113		243		208	269	226	139		191	191	156
Th (ppm)	448	334	334		1072	949	105	492	492	88	896	4262	404	264	694	176	475	738	554
Dy (ppm)			1141		819		44		17	52	479	218		61	305		9		427
Y (ppm)					803	819					551	2181			315		457	291	16
U (ppm)	1926	1499	1526	1317	3788	1126	2671	645	699	1108	2098	5968	454	1154	1326	709	954	1590	954
Yb (ppm)	492	351	334	334	913	641		61	360	413	799	905	395	220	457	501	342	404	606
Hf (ppm)	11142	12194	13966	13992	12703	10193	1136	11897	12864	10278	12720	10617	11906	13517	10820	12228	11533	13127	12389
Fe (ppm)		54		54	23	140	466			16		16				23	93	78	86
Nb (ppm)							151												
Ta (ppm)	442	106	180	549	516	238		516	508				270	98	106	66			197
Ti (ppm)	120		48	6			198		42	30	114	36	60	54	48	24		72	
P (ppm)																			
Sc (ppm)	65				7	7		20	33	13	59	98		7		20	26	7	65
RATIOS																			
Th/U	0.233	0.223	0.219		0.283	0.843	0.040	0.763	0.704	0.079	0.427	0.714	0.890	0.228	0.524	0.248	0.4998	0.464	0.581
Th/Yb	0.911	0.951	1.001		1.173	1.481		8.006	1.367	0.213	1.122	4.712	1.023	1.201	1.520	0.351	1.386	1.827	0.914
Ta/Yb	0.899	0.303	0.540	1.644	0.565	0.371		8.393	1.410				0.684	0.448	0.233	0.131			0.324
U/Pb	7.979		7.828	1.494		4.667	71.924		4.709	4.264		13.121			11.906		10.275	5.037	
REE+Y (ppm)	1531	771	2028	870	2865	2105	957	482	721	1473	2192	3512	1255	506	1335	620	1041	998	1205

Table B.1. (cont'd)

Sample no	SK-12																		
Crystal no	[Z12(21)]																		
Cross section	**C-D**	**C-D**	**C-D**	**C-D**	**C-D**	**C-D**	**C-D**	**C-D**	**C-D**	**C-D**	**C-D**	**C-D**	**C-D**	**C-D**	**C-D**	**C-D**	**C-D**	**C-D**	**C-D**
Analyses no	**1**	**2**	**3**	**4**	**5**	**6**	**7**	**8**	**9**	**10**	**11**	**12**	**13**	**14**	**15**	**16**	**17**	**18**	**19**
ZrO_2 %	65.654	65.826	65.642	65.887	65.902	65.635	65.644	65.707	65.516	65.905	65.719	65.819	65.424	65.17	65.762	65.691	65.633	65.638	65.883
SiO_2 %	32.794	32.802	32.699	32.710	32.957	32.661	32.854	32.803	32.761	32.928	32.631	32.881	32.805	32.724	32.691	32.809	32.875	32.863	32.754
CaO %	0.008	0.006	0.005	0.016	0.004	0.012	0.003	0.001			0.006	0.002		0.011	0.010	0.005	0.035	0.004	0.012
Al_2O_3 %									0.002	0.001		0.005		0.004					0.006
Zr (ppm)	486043	487316	485954	487767	487879	485902	485969	486435	485021	487901	486524	487264	484340	482459	486842	486316	485887	485924	487738
Si (ppm)	153291	153328	152847	152898	154053	152669	153571	153333	153136	153917	152529	153697	153342	152963	152809	153361	153669	153613	153104
Ca (ppm)	57	43	36	114	29	86	21	7			43	14		79	71	36	250	29	86
Al (ppm)									11	5		26		21					32
Pb (ppm)	390		520		93	93	46							251		186	436		37
Ce (ppm)	290		324	162	196		77	145			17	68		68	290				
Nd (ppm)				403	369		34	180	94					454		17	343	34	583
Sm (ppm)	492			155	293	216	448			379	9			17	121	26	52	9	9
Gd (ppm)	521		113	226	9		269			69		113					408	521	
Th (ppm)	562	562	589	369	369	325	413	352	264	202	703	545	176	765	325	176	738	615	158
Dy (ppm)	662	575	340	244			78		418	505		575	78		732		26		
Y (ppm)														63					
U (ppm)	1717	772	890	1163	1381	554	927	863	718	590	1326	1181	763	2625	981	917	963	1190	881
Yb (ppm)	237	158	202	211	9	413	211	228	97	281	79	255	439	720	316	281	61	342	61
Hf (ppm)	12847	11838	12872	13042	13084	12024	11838	11761	12304	11829	13152	12694	11227	13576	11499	11066	10803	10964	12024
Fe (ppm)	171	93				202	54		8	70	31	16	210	78		93			109
Nb (ppm)																			
Ta (ppm)		25	180	25			508	426	221	41		606	246	98	41	221	131		369
Ti (ppm)	6	54	54		12		24	36	42			90	66	42	66				72
P (ppm)																			
Sc (ppm)	20	33	20	52	59		13	65	7	7	26	78	20	7		46	59		
RATIOS																			
Th/U	0.328	0.728	0.661	0.317	0.267	0.587	0.446	0.407	0.367	0.342	0.530	0.461	0.230	0.291	0.331	0.192	0.767	0.517	0.180
Th/Yb	2.372	3.558	2.915	1.751	42.029	0.788	1.960	1.540	2.729	0.719	8.895	2.139	0.400	1.062	1.028	0.625	12.008	1.796	2.573
Ta/Yb		0.155	0.892	0.117			2.409	1.865	2.289	0.146		2.380	0.560	0.137	0.130	0.787	2.132		5.995
U/Pb	4.404		1.712		14.874	5.969	19.963							10.474		4.942	2.207		23.730
REE+Y (ppm)	2202	733	979	1401	876	628	1118	554	609	1235	105	1011	518	1323	1459	324	890	906	653

Table B.1. (cont'd)

Sample no	SK-12												SK-12					
Crystal no	[Z12(21)]												[Z12(22)]					
Cross section	C-D	C-D	C-D	C-D	C-D	C-D	C-D	C-D	C-D	C-D	C-D		A-B	A-B	A-B	A-B	A-B	A-B
Analyses no	20	21	22	23	24	25	26	27	28	29	30		1	2	3	4	5	6
ZrO_2 %	65.485	65.791	65.304	65.591	65.432	65.528	65.423	65.619	65.689	65.628	65.547		66.042	65.858	66.079	65.651	65.678	65.704
SiO_2 %	32.745	32.752	32.638	32.928	32.831	32.944	32.735	33.032	32.713	32.818	32.794		32.796	32.437	32.707	32.309	32.349	32.213
CaO %		0.016	0.081	0.005	0.002	0.019	0.003	0.019	0.002	0.009	0.022		0.001	0.003	0.004			
Al_2O_3 %	0.006	0.004	0.012	0.006	0.002	0.002	0.001	0.006	0.012	0.009	0.001					0.003		
Zr (ppm)	484791	487057	483451	485576	484399	485110	484332	485783	486302	485850	485250		488915	487553	489189	486020	486220	486413
Si (ppm)	153062	153094	152561	153917	153464	153992	153015	154403	152912	153403	153291		153300	151622	152884	151024	151211	150575
Ca (ppm)		114	579	36	14	136	21	136	14	64	157		7	21	29			
Al (ppm)	32	21	64	32	11	11	5	32	64	48	5					16		
Pb (ppm)		186		93				566	19	186	84		74	418	251			74
Ce (ppm)	410	222		205	196	111	68				213		94	188	26		299	401
Nd (ppm)		317	146		360	9	223	377		514								26
Sm (ppm)	34	285				224		483		414	354			233		207	60	
Gd (ppm)	17	35		17	78	26	147		9	234	781		278	252	121			
Th (ppm)	185	255	422	598	466	510	536	791	255	685	105		237	360	290	387	325	448
Dy (ppm)			157	497	244	192	70	183	61		52			662	131	314		619
Y (ppm)																		
U (ppm)	908	709	1054	1608	1771	1617	1263	1190	945	1590	1553		690	790	763	463	799	963
Yb (ppm)	351	88	386	263	501	255	53	105	9	246	465		316	307	342		228	457
Hf (ppm)	11855	13076	12762	12864	14009	14119	12821	13788	11134	12703	12694		12754	11439	11940	11838	13746	10532
Fe (ppm)	187	124	93	86		163	148	47	54	70	54		117			47	16	
Nb (ppm)																		
Ta (ppm)	377	328	590			262		467			25				41	82	106	49
Ti (ppm)	60	72	54	12	90		78		6		18		102	24	18		12	36
P (ppm)																		
Sc (ppm)			39	46		20		52	39	91	20			7			7	
RATIOS																		
Th/U	0.203	0.360	0.400	0.372	0.263	0.315	0.425	0.665	0.270	0.431	0.068		0.344	0.456	0.380	0.835	0.407	0.466
Th/Yb	0.525	2.902	1.092	2.268	0.931	2.001	10.174	7.505	29.020	2.788	0.227		0.751	1.172	0.847		1.424	0.981
Ta/Yb	1.072	3.730	1.526			1.029		4.430			0.053				0.120		0.466	0.108
U/Pb		3.816		17.320				2.102	50.885	8.562	18.593		9.296	1.892	3.044			12.966
REE+Y (ppm)	813	946	689	982	1379	816	561	1149	78	1408	1866		688	1642	620	521	588	1502

Table B.1. (cont'd)

Sample no	SK-12																			
Crystal no	[Z12(22)]																			
Cross section	A-B	A-B	A-B	A-B	A-B	A-B	A-B	A-B	A-B	A-B	A-B	A-B	A-B	A-B	A-B	A-B	A-B	A-B	A-B	A-B
Analyses no	7	8	9	10	11	12	13	14	15	16	17	18	19	20	21	22	23	24	25	26
ZrO_2 %	65.849	65.920	65.952	65.616	65.828	65.845	65.632	65.547	65.508	65.866	66.152	65.276	65.670	65.587	65.628	65.575	65.740	65.798	65.842	65.439
SiO_2 %	32.263	32.457	32.324	32.599	32.378	32.477	32.332	32.104	32.393	32.363	32.131	32.308	32.454	32.124	32.198	32.066	32.054	32.111	32.238	31.993
CaO %	0.002	0.004		0.011		0.003	0.012		0.004		0.005	0.005			0.008		0.002			
Al_2O_3 %		0.002	0.004			0.003	0.002	0.021					0.002			0.005	0.006	0.001		
Zr (ppm)	487486	488012	488249	485761	487331	487457	485880	485250	484962	487612	489729	483244	486161	485547	485850	485458	486679	487109	487434	484451
Si (ppm)	150809	151715	151094	152379	151346	151809	151131	150065	151416	151276	150192	151019	151701	150159	150505	149888	149832	150098	150692	149546
Ca (ppm)	14	29		79		21	86		29		36	36			57		14			
Al (ppm)		11	21			16	11	111					11			26	32	5		
Pb (ppm)		102	251		121	418			65			353	278	269		548	269	93	214	
Ce (ppm)	34	478	171				68	102	34	205	145					9	307			299
Nd (ppm)		9										249		326	274		540	472	34	
Sm (ppm)				388			388		164	34	138	138	9	43		586		138	397	
Gd (ppm)		234	113	35		121	9	174	373	304		9		95	121			156	529	
Th (ppm)	527	800	193	360	255	53	299	984	316	457	35	2188	598	413	149	404		158		958
Dy (ppm)	314				87	183						488	113	401	148			584	166	
Y (ppm)	110											1520								709
U (ppm)	854	672	863	854	382	763	1408	1217	954	618	627	3225	1290	1599	1136	1163	790	663	609	1444
Yb (ppm)	457	272	9	9	430	228	342	369	202	176		782	369	544	413	255	237	246	44	439
Hf (ppm)	11643	12762	11185	13534	12686	13144	13864	11931	12592	12041	11643	10617	13585	12525	12075	12779	12813	11168	9480	11414
Fe (ppm)	202			109		47	140	78	117	101	62		225	140	225	109	93		148	
Nb (ppm)																				
Ta (ppm)					139	491	98	147	295	90	8	180	508		115			106		
Ti (ppm)		30			54		126			18	12	36	60				24	78		84
P (ppm)																				
Sc (ppm)	39		72	59	39				7		20	39		78		46		26	72	150
RATIOS																				
Th/U	0.618	1.190	0.224	0.422	0.668	0.069	0.212	0.809	0.332	0.740	0.056	0.679	0.463	0.258	0.132	0.348		0.239		0.663
Th/Yb	1.155	2.938	22.015	41.028	0.592	0.231	0.872	2.669	1.566	2.602		2.800	1.620	0.759	0.362	1.587		0.643		2.182
Ta/Yb					0.324	2.152	0.287	0.400	1.460	0.513		0.231	1.376		0.278			0.433		
U/Pb		6.583	3.443		3.161	1.827			14.678			9.142	4.632	5.939		2.123	2.936	7.144	2.851	
REE+Y (ppm)	915	993	292	432	517	533	808	645	773	719	283	3185	491	1410	957	850	1085	1595	1170	1447

Table B.1. (cont'd)

Sample no	SK-12												SK-12							
Crystal no	[Z12(22)]												[Z12(22)]							
Cross section	A-B	A-B	A-B	A-B	A-B	A-B	A-B	A-B	A-B	A-B	A-B		C-D	C-D	C-D	C-D	C-D	C-D	C-D	C-D
Analyses no	27	28	29	30	31	32	33	34	35	36	37		1	2	3	4	5	6	7	8
ZrO_2 %	65.968	65.435	65.763	65.482	65.785	65.054	65.604	65.806	65.599	65.708	65.486		65.605	65.747	65.754	65.879	66.019	66.231	65.845	65.741
SiO_2 %	32.130	31.856	32.305	31.934	32.311	32.080	31.889	32.104	31.781	31.909	31.984		32.326	32.558	32.071	32.106	32.559	32.178	32.027	32.567
CaO %		0.005		0.006		0.007		0.015		0.005			0.011	0.003				0.010	0.005	
Al_2O_3 %			0.007	0.006												0.001			0.002	
Zr (ppm)	488367	484421	486849	484769	487012	481601	485672	487168	485635	486442	484799		485680	486731	486783	487708	488745	490314	487457	486687
Si (ppm)	150187	148906	151005	149271	151033	149953	149060	150065	148555	149154	149504		151103	152187	149911	150075	152192	150411	149705	152230
Ca (ppm)		36		43		50		107		36			79	21				71	36	
Al (ppm)			37	32												5			11	
Pb (ppm)				594	343		139				427		418	214	214	9		260		65
Ce (ppm)	367	367	68	196		9		273	77				179	461	17		26			111
Nd (ppm)						94		69	300	17				291	103	326		214		103
Sm (ppm)				43			60	250		34	52			34	34	207	172			293
Gd (ppm)		35	382				17	174					347	755		35	139			495
Th (ppm)	202	896	255	264	9	685	483	97	387	387	255		255	395		308	308	114	562	598
Dy (ppm)	44	592		322	227			148			775			497	392		296			558
Y (ppm)		457				8														102
U (ppm)	572	2035	318	627	554	1553	899	572	445	718	763		963	981	854	745		372	1444	1172
Yb (ppm)	193	659	88	395	70	220	281	439	527	334	105		386	272	88	79	132	167	430	395
Hf (ppm)	12177	10913	11753	11422	11770	12584	12423	11965	10278	10668	12253		11999	11651	12016	11244	12966	10693	9031	12949
Fe (ppm)			163		54			39	23		31		194	62			148		194	101
Nb (ppm)																				
Ta (ppm)	25				33						606			164		287	82	123		106
Ti (ppm)		30	78	30	30	96		90	78					78	120	36	54	12	18	60
P (ppm)																				
Sc (ppm)	13	91	39	59	26	85		26		91			7	26	46			20	26	52
RATIOS																				
Th/U	0.353	0.441	0.802	0.421	0.016	0.441	0.538	0.169	0.869	0.539	0.334		0.265	0.403		0.413		0.307	0.389	0.510
Th/Yb	1.046	1.361	2.902	0.667	0.125	3.122	1.720	0.220	0.734	1.159	2.418		0.660	1.453		3.892	2.335	0.685	1.307	1.512
Ta/Yb	0.127				0.466						5.751			0.602		3.627	0.622	0.736		0.269
U/Pb				1.055	1.613		6.459				1.787		2.305	4.595	3.999	80.242		1.433		18.033
REE+Y (ppm)	604	2110	538	957	297	330	359	1353	904	385	933		913	2311	634	647	765	381	430	2057

Table B.1. (cont'd)

Sample no	SK-12													
Crystal no	[Z12(22)]													
Cross section	C-D	C-D	C-D	C-D	C-D	C-D	C-D	C-D	C-D	C-D	C-D	C-D	C-D	C-D
Analyses no	9	10	11	12	13	14	15	16	17	18	19	20	21	22
ZrO_2 %	65.475	65.877	65.657	65.618	65.544	65.698	65.702	65.427	65.548	65.330	65.620	65.583	65.713	64.464
SiO_2 %	32.211	32.225	32.312	32.12	32.022	32.385	32.416	32.399	32.464	32.326	32.195	32.357	32.549	31.554
CaO %	0.005	0.003	0.002	0.005	0.003	0.009	0.071	0.010		0.003				0.025
Al_2O_3 %		0.001		0.001			0.005	0.004		0.004				0.008
Zr (ppm)	484717	487693	486065	485776	485228	486368	486398	484362	485258	483644	485791	485517	486479	477233
Si (ppm)	150565	150631	151038	150140	149682	151379	151524	151444	151748	151103	150491	151248	152145	147494
Ca (ppm)	36	21	14	36	21	64	507	71		21				179
Al (ppm)		5		5			26	21		21				42
Pb (ppm)	102	761	241	631	288	176	139	585	74	436		9		
Ce (ppm)	34		102	94		34	273		137	120	188		213	213
Nd (ppm)	326				34		240					240		231
Sm (ppm)	224	259	9				17	17	241		604	552		
Gd (ppm)		113	87		182					269	9			35
Th (ppm)	264	483	554	141	615	413	554	712	545		518	281	562	378
Dy (ppm)	174	157		17	105		61		183	349	322		540	
Y (ppm)					843			181			394	323	110	118
U (ppm)	545	818	509	218	1190	736	1045	1326	1090	245	427	718	663	999
Yb (ppm)	272	430	281	246	597	184	395	465	334	18	703	176	316	272
Hf (ppm)	12966	12406	11668	12380	10786	11745	13262	11982	12431	11711	10023	11973	11906	12109
Fe (ppm)			101		31		31	93	93	280	31			
Nb (ppm)														
Ta (ppm)	450		25					262	98	131	90	360	115	
Ti (ppm)	12	102	18		30		24	90	18	30	30	54	42	
P (ppm)														
Sc (ppm)			20	72			33	59	26		104	20	33	65
RATIOS														
Th/U	0.484	0.591	1.088	0.645	0.517	0.561	0.530	0.537	0.500		1.214	0.392	0.848	0.378
Th/Yb	0.968	1.123	1.970	0.572	1.030	2.240	1.401	1.529	1.633		0.738	1.601	1.779	1.388
Ta/Yb	1.655		0.087					0.563	0.295	7.460	0.128	2.052	0.363	
U/Pb	5.338	1.074	2.108	0.345	4.135	4.172	7.502	2.268	14.678	0.562		77.306		
REE+Y (ppm)	1031	959	479	357	1761	219	987	664	895	755	2219	1290	1180	870

VITA

Serhat Köksal was born in Ankara, on October 30, 1970. He was graduated from High School of Bahçelievler Deneme Lisesi. He received his B.S. degree in Faculty of Engineering, Department of Geological Engineering from the Middle East Technical University in June 1992. He received his M.S. degree in Graduate School of Natural and Applied Sciences, Department of Geological Engineering from the Middle East Technical University in January 1996. He worked in Ministry of Energy and Natural Resources from 1993 to 1995, in General Directorate of Bank of Provinces from 1995 to 1997, and in Ministry of Energy and Natural Resources from 1997 to 2004. Since 2004 he has been working in the Thermal Ionization Mass Spectrometry Laboratory of the Research and Development Education and Measurement Center of Central Laboratory, Middle East Technical University. His main areas of interest are geochronology, isotope geochemistry, zircon typology and chemistry. He has two papers published in international journals, one is in International Journal of Earth Sciences, and the other is in International Geology Review. Additionally he has two more papers in national journals and four presentations in national and international congresses.